from experiments at equivalent motored conditions.[35] The turbulence quantity obtained during motoring experiments was the ensemble-averaged root mean square velocity fluctuation defined by Eq. (8.18). Values of S_b/S_L and u'_F/S_L were determined at two points in the combustion process: at a flame radius of 30 mm (the end of the flame development process) and at mass fraction burned equal to 0.5 (halfway through the rapid burning phase). To correct the motored turbulence data for the higher pressure levels corresponding to engine firing conditions, a simple rapid distortion model (see Sec. 14.4.2) based on conservation of angular momentum in turbulent eddies was used. A linear correlation between S_b and u'_F results, as shown in Fig. 9-30, for the rapid burning combustion phase. Note that as u'_F/S_L goes to zero, S_b/S_L approaches a value close to unity.

Once the flame front reaches the far cylinder wall (see Fig. 9-27) the front can no longer propagate: however, combustion continues behind the front until all the unburned mixture entrained into the enflamed region is consumed. This final burning or termination phase of the combustion process can be approximated by an exponential decay in the mass burning rate with a characteristic time constant τ_b of order 1 ms. Since these "islands" or "pockets" of unburned mixture behind the leading edge of the flame have a characteristic scale l_T based on the laminar flame area [Eqs. (9.41) and (9.48)], it follows that

$$l_T = \tau_b S_L \tag{9.49}$$

In summary, the above flame data analysis procedures show that the relationships between r_f and r_b, V_f and V_b, A_f and A_L, u_f, S_b and S_L are distinctly different in the three phases of combustion: (1) the development phase, where a highly wrinkled reaction-sheet "thick"-overall turbulent flame evolves from the essentially spherical flame kernal established by the spark discharge; (2) the rapid-burning phase, where this thick "developed" turbulent flame propagates across the combustion chamber to the far wall, during which most of the mass is burned; and (3) the termination phase after the flame front has reached the far wall and propagation of the front is no longer possible, when the remaining unburned mixture within the flame burns up. The burning velocity, in the rapid-burning phase of the combustion process, scales with turbulence intensity, which in turn scales with engine speed.

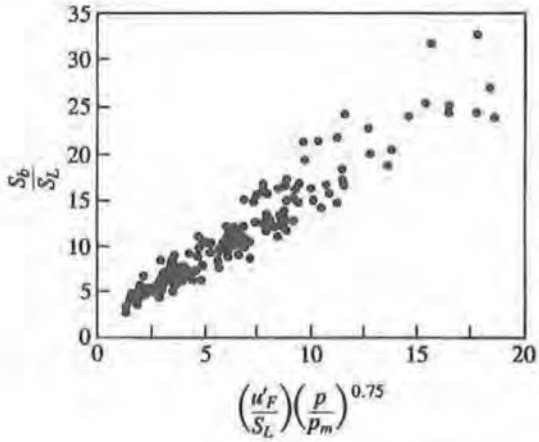


FIGURE 9-30
Variation of burning speed with turbulence intensity. The ensemble-averaged rms velocity fluctuation was measured during motoring engine operation. The ratio p/p_m (firing pressure/motoring pressure) corrects for the effect of additional compression on the turbulence intensity. Range of engine speeds and spark timings.[35]

9.4 CYCLIC VARIATIONS IN COMBUSTION, PARTIAL BURNING, AND MISFIRE

9.4.1 Observations and Definitions

Observation of cylinder pressure versus time measurements from a spark-ignition engine, for successive operating cycles, shows that substantial variations on a cycle-by-cycle basis exist. Since the pressure development is uniquely related to the combustion process, substantial variations in the combustion process on a cycle-by-cycle basis are occurring. In addition to these variations in each individual cylinder, there can be significant differences in the combustion process and pressure development between the cylinders in a multicylinder engine. Cyclic variations in the combustion process are caused by variations in mixture motion within the cylinder at the time of spark cycle-by-cycle, variations in the amounts of air and fuel fed to the cylinder each cycle, and variations in the mixing of fresh mixture and residual gases within the cylinder each cycle, especially in the vicinity of the spark plug. Variations between cylinders are caused by differences in these same phenomena, cylinder-to-cylinder.

Cycle-by-cycle variations in the combustion process are important for two reasons. First, since the optimum spark timing is set for the "average" cycle, faster-than-average cycles have effectively overadvanced spark-timing and slower-than-average cycles have retarded timing, so losses in power and efficiency result. Second, it is the extremes of the cyclic variations that limit engine operation. The fastest burning cycles with their overadvanced spark timing are most likely to knock. Thus, the fastest burning cycles determine the engine's fuel octane requirement and limit its compression ratio (see Sec. 9.6.3). The slowest burning cycles, which are retarded relative to optimum timing, are most likely to burn incompletely. Thus these cycles set the practical lean operating limit of the engine or limit the amount of exhaust gas recycle (used for NO emissions control) which the engine will tolerate. Due to cycle-by-cycle variations, the spark timing and average air/fuel ratio must always be compromises, which are not necessarily the optimum for the average cylinder combustion process. Variations in cylinder pressure have been shown to correlate with variations in brake torque which directly relate to vehicle driveability.

An example of the cycle-by-cycle variations in cylinder pressure and the variations in mixture burning rate that cause them are shown in Fig. 9-31. Pressure and gross heat-release rate [calculated from the cylinder pressure using Eq. (9.27)] for several successive cycles at a mid-load, mid-speed point are shown as a function of crank angle. The maximum heat-release rate and the duration of the heat release or burning process vary by a factor of two from the slowest to the fastest burning cycle shown. The peak cylinder pressure varies accordingly. The faster burning cycles have substantially higher values of maximum pressure than do the slower burning cycles; with the faster burning cycles peak pressure occurs closer to TC.

The heat-release rate data in Fig. 9-31 show that there are cycle-by-cycle variations in the early stages of flame development (from zero to a few percent of

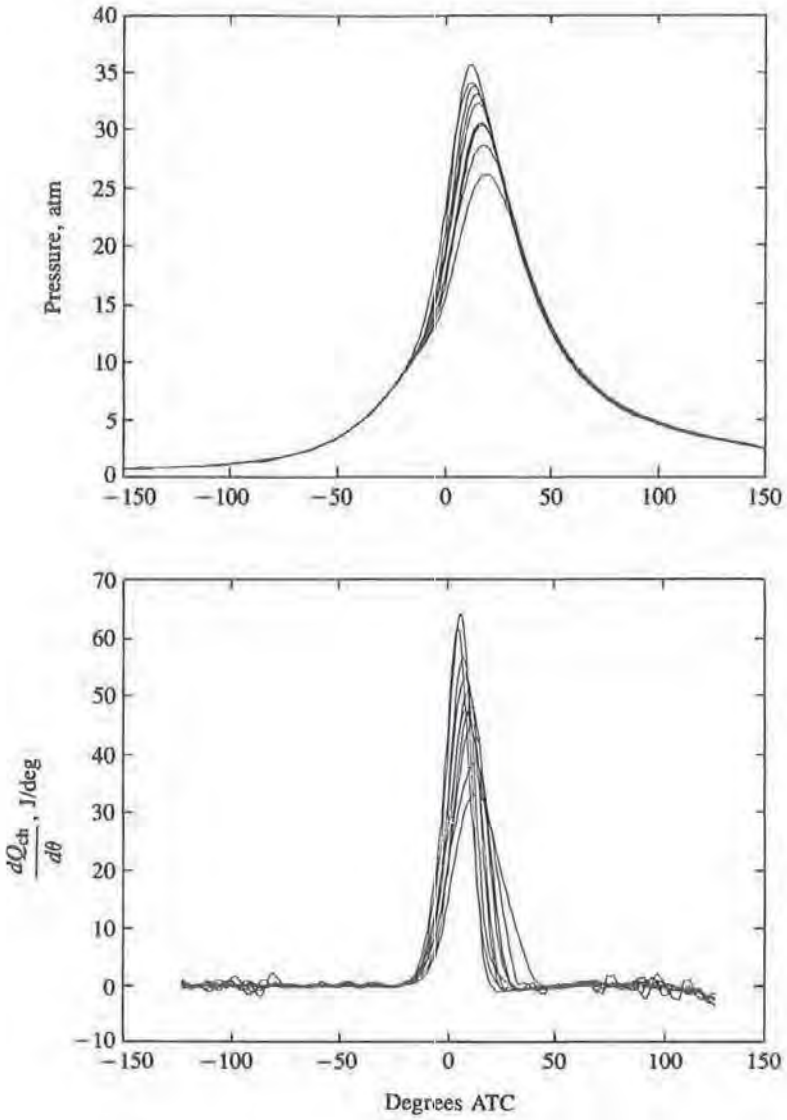


FIGURE 9-31
Measured cylinder pressure and calculated gross heat-release rate for ten cycles in single-cylinder spark-ignition engine operating at 1500 rev/min, $\phi = 1.0$, $p_{inlet} = 0.7$ atm, MBT timing 25° BTC.[14]

the total heat release) and in the major portion of the combustion process—the rapid-burning phase—indicated by the variations in the maximum burning rate.

As the mixture becomes leaner with excess air or more dilute with a higher burned gas fraction from residual gases or exhaust gas recycle, the magnitude of cycle-by-cycle combustion variations increases. Eventually, some cycles become sufficiently slow burning that combustion is not completed by the time the exhaust opens: a regime where *partial burning* occurs in a fraction of the cycles is encountered. For even leaner or more dilute mixtures, the *misfire* limit is reached. At this point, the mixture in a fraction of the cycles fails to ignite. While spark-ignition engines will continue to operate with a small percentage of the cycles in the partial-burn or misfire regimes, such operation is obviously undesirable from

the point of efficiency, hydrocarbon emissions, torque variations, and roughness. The partial-burn and misfire regimes are discussed in Sec. 9.4.3.

Various measures of cycle-by-cycle combustion variability are used. It can be defined in terms of variations in the cylinder pressure between different cycles, or in terms of variations in the details of the burning process which cause the differences in pressure. The following quantities have been used:

1. *Pressure-related parameters.* The maximum cylinder pressure p_{max}; the crank angle at which this maximum pressure occurs θ_{pmax}; the maximum rate of pressure rise $(dp/d\theta)_{max}$; the crank angle at which $(dp/d\theta)_{max}$ occurs; the indicated mean effective pressure [which equals $\int p\, dV/V_d$, see Eqs. (2.14), (2.15), and (2.19)].
2. *Burn-rate-related parameters.* The maximum heat-release rate (net or gross, see Sec. 9.2.2); the maximum mass burning rate; the flame development angle $\Delta\theta_d$ and the rapid burning angle, $\Delta\theta_b$ (see Sec. 9.2.3).
3. *Flame front position parameters.* Flame radius, flame front area, enflamed or burned volume, all at given times; flame arrival time at given locations.

Pressure-related quantities are easiest to determine; however, the relation between variations in combustion rate and variations in cylinder pressure is complex.[38] Equation (9.26) defines the factors that govern this relationship. Because the rate of change of pressure is substantially affected by the rate of change of cylinder volume as well as rate of burning, changes in the phasing of the combustion process relative to TC (e.g., which result from changes in flame development angle) as well as changes in the shape and magnitude of the heat-release rate profile affect the pressure. Figure 9-32 illustrates how the magnitude of the maximum cylinder pressure p_{max} and the crank angle at which it occurs θ_{pmax} vary as the crank angle at which combustion effectively starts (e.g., θ at which 1 percent of the cylinder mass has burned) and the burning rate are varied. Curve $CABE$ shows how p_{max} and θ_{pmax} vary for a fixed fast-burning heat-release profile (the duration of the heat-release process and its maximum value are held

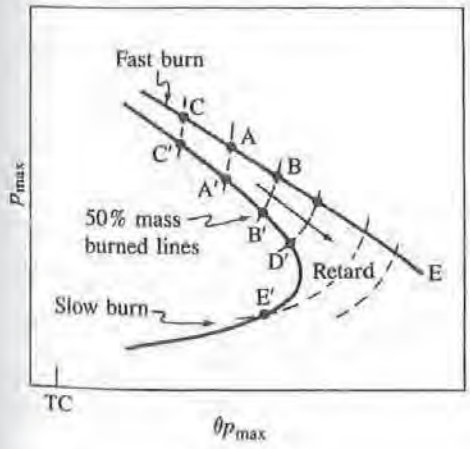


FIGURE 9-32
Schematic of variation in maximum cylinder pressure and crank angle at which it occurs, in individual cycles. $CABE$ typical of fast heat-release process; $C'A'B'D'E'$ typical of slow heat-release process. (*From Marekunas.*[38])

constant), as the phasing of this combustion process relative to TC is varied. A corresponds to MBT timing where the start of combustion is phased to give maximum brake torque, B corresponds to retarded timing, and C to over-advanced timing. $C'A'B'D'E'$ is a similar curve for a slow-burning heat-release profile. A' corresponds to MBT timing, and B' and D' to increasingly retarded timing. Note that with a sufficiently slow-burning heat-release profile, beyond D', $\theta_{p\max}$ decreases as the burn process is increasingly retarded. This occurs when the rate of increase of pressure due to combustion becomes so low that it is more than offset by the pressure decrease due to volume increase: eventually for extremely slow and late burning, the maximum pressure approaches the motored pressure at TC. The dashed lines show the constant start-of-combustion timing *relative* to MBT for each burn rate curve. Note that $\theta_{p\max}$ for constant relative timing varies little as the heat-release profile or burn rate varies.[38]

We can now explain the effects of variations in the heat-release profile (both in the development stage of the burning process, which effectively changes the location of the start of combustion, and in the rate of burning throughout the process) on $p_{\max}$ and $\theta_{p\max}$, when the spark timing occurs at a fixed crank angle. For a fixed burning rate profile (duration of burn and maximum burning rate) as the start of combustion is delayed to be closer to TC, $p_{\max}$ decreases and $\theta_{p\max}$ initially increases (A to B or A' to B'). This is the effect of a change in relative timing or phase of the burning process due to a slower initial rate of flame development with fixed spark timing. If, in addition to the flame development being slower, the heat-release rate throughout the burning process is lower, then that combustion process is even more retarded from the optimum and $p_{\max}$ decreases and $\theta_{p\max}$ increases further, to their values at D'. The effect of a faster initial flame development and faster burning rate, with fixed spark time, is the opposite. The magnitudes of the changes in $p_{\max}$ and $\theta_{p\max}$ depend, obviously, on the extent of the cyclic variations; they also depend on whether the average burn process is fast or slow. For fast-burning engines, a larger fraction of the heat release occurs near TC when the chamber volume is changing relatively slowly. Thus pressure variations are mainly due to combustion variations. With slow-burning engines, where a significant fraction of the energy release occurs well after TC, the effect of volume change also becomes significant and augments the effect of combustion variations. For large variations and a slow average burning process, $p_{\max}$ can fall below E', and $\theta_{p\max}$ then decreases. A fast-burning combustion process significantly reduces the impact of cyclic combustion variations on engine performance.[39]

We can now evaluate the various measures of combustion variability. The maximum pressure variation has been shown to depend on both changes in phasing and burning rate. The magnitude of this variation depends on whether the combustion chamber is faster or slower burning, on average. It also depends on whether the burning process is substantially retarded relative to MBT. It depends, too, on cyclic cylinder fuel and air charging variations. Thus the interpretation of variations in $p_{\max}$ [or in the maximum rate of pressure rise $(dp/d\theta)_{\max}$] in terms of variations in the rate and phasing of the burning process

must be done with care. The location of maximum pressure θ_{pmax} also depends on relative phasing of combustion and on the burn rate profile. In addition, for slow-burning chambers and retarded timing (around E') variations produce little change in θ_{pmax}. However, for fast-burning chambers, with MBT or only slightly retarded timing, the location of peak pressure depends essentially on the phasing of each combustion process relative to its MBT phasing, and is independent of charging variations. For these reasons, θ_{pmax} is a useful measure of variability in combustion event phasing.[38]

One important measure of cyclic variability, derived from pressure data, is the *coefficient of variation* in *indicated mean effective pressure*. It is the standard deviation in imep divided by the mean imep, and is usually expressed in percent:

$$\text{COV}_{\text{imep}} = \frac{\sigma_{\text{imep}}}{\text{imep}} \times 100 \tag{9.50}$$

It defines the cyclic variability in indicated work per cycle, and it has been found that vehicle driveability problems usually result when COV_{imep} exceeds about 10 percent.

Figure 9-33 illustrates the relationships between p_{max}, θ_{pmax}, and imep for 120 cycles of an engine cylinder at fixed operating conditions and three different spark timings.[38] The MBT timing data show a spread in imep at a fixed value of θ_{pmax}. This imep data band is relatively flat and is centered around $\theta_{pmax} \approx 16°$; only at later values of θ_{pmax} does imep fall off significantly. The vertical spread in imep around $\theta_{pmax} = 16°$ is due to variations in the amount of fuel entering the cylinder each cycle; normal variations in the burn profile under these conditions, which effectively change the phasing of the combustion process, produce only modest reductions in imep. For early θ_{pmax} (the extreme upper left of Fig. 9-33*a*), the variations in p_{max} are also due mainly to these fuel-charging variations, cycle-by-cycle; these are the fastest burning cycles with the most advanced phasing. As

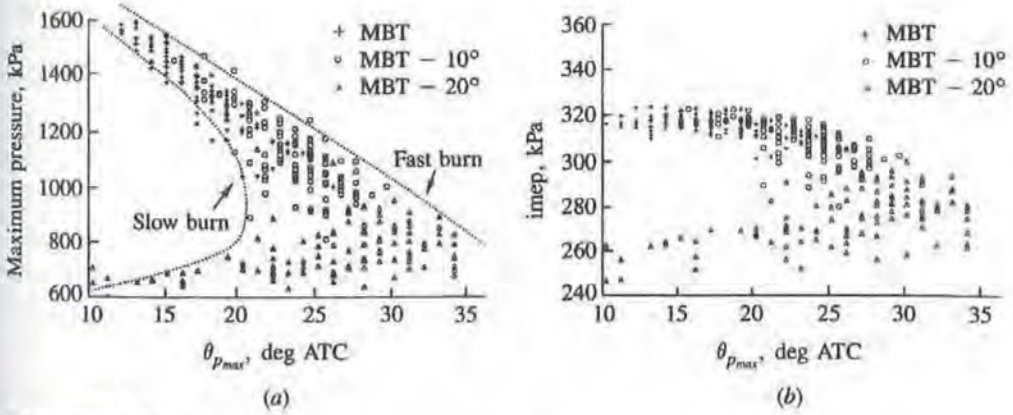


FIGURE 9-33
(*a*) Individual-cycle maximum pressure versus crank angle at which p_{max} occurs. (*b*) Individual-cycle indicated mean effective pressure versus θ_{pmax}.[38]

$\theta_{p\max}$ increases, the dispersion increases as cyclic variations in phasing and burning rate have increasing impact.

An important issue is whether variations in the early stages of flame development and variations in subsequent portions of the burning process are independent of each other or are correlated. Plots of early flame development angle (spark to 1 percent mass burned) against the burning angle (1 to 90 percent burned) from individual cycles for several different combustion chambers indicate the following. There is a trend with increasing flame development angle for the burning angle to increase (or the burning rate to decrease); however, there is much scatter about this trend (for a given value of flame development angle different cycles show a substantial range in burning angle), and the quantitative aspects of the trend depend on operating conditions and on combustion chamber design. In addition, as the mean rapid burning angle increases (due to changing operating conditions or a slower-burning chamber design) the mean flame development angle, the cyclic variation in the flame development angle, and the cyclic variation in the rapid burning angle all increase.[40] This topic is discussed more fully in the following section.

The shapes of the frequency distributions in individual-cycle pressure data (e.g., in $p_{\max}$, $(dp/d\theta)_{\max}$, $\theta_{p\max}$) and in burn rate data such as $\Delta\theta_d$, $\Delta\theta_b$, $(dQ/d\theta)_{\max}$ depend on whether the combustion process is fast and "robust" (e.g., with close-to-stoichiometric mixtures at higher loads at optimum timing—well away from the lean operating limit of the engine) or slower and less repeatable, closer to the lean or dilute-mixture operating limit. Under robust combustion conditions these distributions are close to normal distributions.[41–43] When the combustion process is much slower, the cyclic variability becomes large and the distribution becomes skewed toward the slower burning cycles which have low imep (due to the substantial retard of these slower cycles). When partial burning and then misfire occur, the low-pressure tail of the distribution approaches the motored pressure value at TC.[44] Examples of the frequency distributions of imep in these two combustion variability regimes are shown later in Fig. 9-36.

Cylinder pressure data are often averaged over many cycles to obtain the mean cylinder pressure at each crank angle. The primary use of this average pressure versus crank angle data is in calculating the average indicated mean effective pressure (which is a linear function of p). Since combustion parameters are not linearly related to the cylinder pressure [see Eq. (9-27)], analysis of the *average* pressure data will not necessarily yield accurate values of average combustion parameters. The error will be most significant when the combustion variability is largest. It is best to determine mean combustion parameters by averaging their values obtained from a substantial number of individual cycle analysis results. The number of cycles which must be averaged to obtain the desired accuracy depends on the extent of the combustion variability. For example, while 40 to 100 cycles may define imep to within a few percent when combustion is highly repeatable, several hundred cycles of data may be required when cyclic combustion variations are large.[12]

9.4.2 Causes of Cycle-by-Cycle and Cylinder-to-Cylinder Variations

Cycle-by-cycle combustion variations are evident from the beginning of the combustion process. Analysis of flame photographs from many engine cycles taken in special research engines with windows in the combustion chamber has shown that dispersion in the fraction of the combustion chamber volume inflamed is present from the start of combustion (e.g., see Refs. 3 and 23). Dispersion in burning rate is also evident throughout the combustion process (see Figs. 9-2 and 9-31). Three factors have been found to influence this dispersion:[45]

1. The variation in gas motion in the cylinder during combustion, cycle-by-cycle
2. The variation in the amounts of fuel, air, and recycled exhaust gas supplied to a given cylinder each cycle
3. Variations in mixture composition within the cylinder each cycle—especially near the spark plug—due to variations in mixing between air, fuel, recycled exhaust gas, and residual gas

The relative importance of these factors is not yet fully defined, and depends on engine design and operating variables. The variation in the velocity field within the engine cylinder throughout the cycle, and from one cycle to the next, has been reviewed in Sec. 8.2.2. Toward the end of the compression stroke, the ensemble-averaged rms velocity fluctuation is of comparable magnitude to the mean piston speed, and may be larger than the mean flow velocity if there is no strongly directed local mean flow pattern (see Figs. 8-8 and 8-9). This ensemble-averaged velocity fluctuation combines both cycle-by-cycle variation in the mean flow and the turbulent velocity fluctuations. During compression, these two components are of comparable magnitude (see Figs. 8-9 and 9-29). While this data base is limited, it indicates that substantial variations in the mean flow exist, cycle-by-cycle, both in the vicinity of the spark plug *and* throughout the combustion chamber. Velocity variations contribute in a major way to variations in the initial motion of the flame center as it grows from the kernel established by the spark, and in the initial rate of growth of the flame; they can also affect the burning rate once the flame has developed to fill a substantial fraction of the combustion chamber. Variations in gas motion near the spark plug convect the flame in its early stages in different directions and at different velocities, cycle-by-cycle. This affects the flame's interaction with the cylinder walls, changing the flame area development with time. Variations in the turbulent velocity fluctuations near the spark plug will result in variations in the rate at which the small initially laminarlike flame kernel develops into a turbulent flame. Variations in the mean flow throughout the chamber will produce differences in flame front shape; also, they may produce differences in turbulence which affect the propagation velocity of the front (see Fig. 9-30 for the relation between mean burning speed and turbulence intensity).

It is well known that, on a time-averaged basis, the fuel, air, and recycled exhaust gas flows into each cylinder of a multicylinder engine are not identical. These flow rate differences are typically a few percent (see Secs. 7.6.2 and 7.6.3). It is also known that the flow patterns within the different cylinders are not necessarily identical due to differences between the individual intake manifold runner and port geometries in many production engines. All these factors contribute to cylinder-to-cylinder variations in the combustion process: there can be significant differences in the mean burn rate parameters as well as in the cyclic variations in these parameters.[41] Also, the limited data available on the variation in mixture composition within each cylinder for each cycle indicates that cyclic charging variations in individual cylinders are comparable in magnitude to cylinder-to-cylinder differences (i.e., of order ± 5 percent[46]). Whether the amount of residual gas left in the cylinder varies significantly, cycle-by-cycle, is not known. At higher loads, where the combustion process is more repeatable (and always completed relatively early in the expansion stroke) and the residual gas fraction smaller (see Sec. 6.4), variations in the total amount of residual are not expected to be significant. At light loads (particularly at idle), where combustion variability is much higher and partial-burning cycles may occur, and especially with high valve overlap engine designs, variations in the residual gas mass and its composition may become important.

In addition, mixing of fuel, air, recycled exhaust, and residual is not complete: nonuniformities in composition exist within the cylinder at the start of combustion. Composition variations, cycle-by-cycle, in the vicinity of the spark plug electrode gap will affect the early stages of flame development, especially as the flame grows through the laminarlike burning phase following the creation of a small flame kernel by the spark discharge (see Sec. 9.5.1). Figure 9-34 indicates the extent of these composition nonuniformities. The available data comes from experiments where a small rapid-acting sampling valve located in the spark plug center electrode was used to extract gas from the vicinity of the electrode gap, close to the start of combustion, for individual cycle composition analysis. Figure 9-34*a* shows the cycle-by-cycle air/fuel ratio fluctuations in the burned gases sampled from one cylinder of a four-cylinder gasoline-fueled carbureted engine just after combustion has started. The standard deviation was typically 2 to 6 percent of the mean (A/F).[46–48] Figure 9-34*b* shows the relationship between total hydrocarbon and CO_2 concentrations in unburned mixture, sampled just before spark discharge. The CO_2 concentration is a measure of the burned gas fraction in the sampled unburned mixture; hence on average it correlates inversely with the total hydrocarbon concentration. However, there is substantial fluctuation in CO_2 concentration about the mean value, at a given fuel fraction, indicating significant fluctuations, cycle-by-cycle, in the mixing of fresh mixture with residual gas. Nonuniformities in EGR distribution between cylinders and EGR mixing within the cylinder would also increase the variations in burned gas fraction locally at the spark gap, cycle-by-cycle.[48]

Experiments in a multicylinder production SI engine, where the fuel/air ratio nonuniformities and the nonuniform mixing of fresh mixture with residual

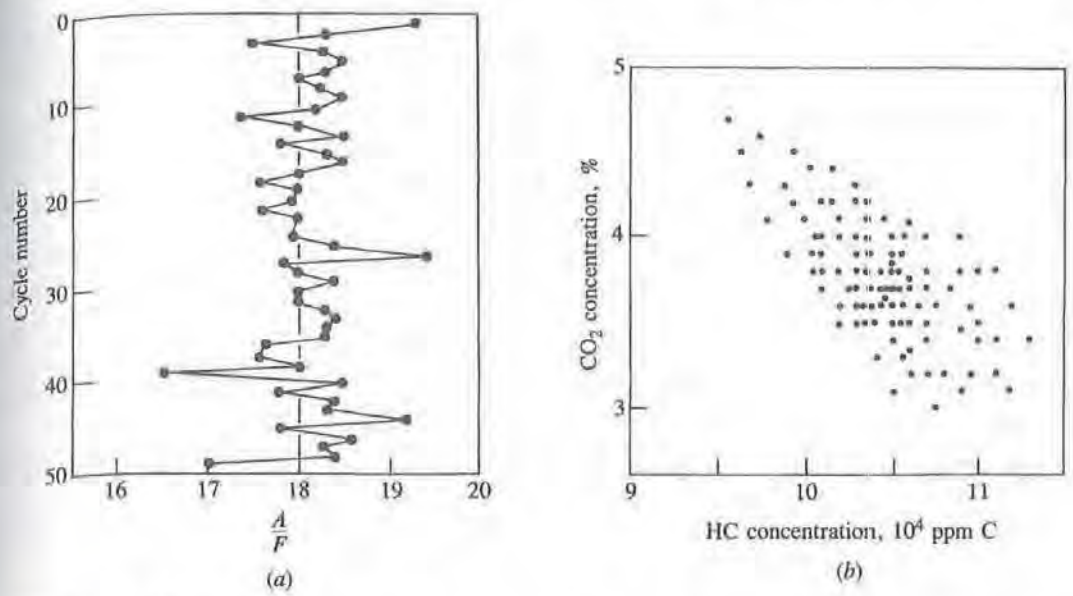


FIGURE 9-34
(*a*) Air/fuel ratio in 50 consecutive cycles, in vicinity of spark plug, measured just after ignition with a rapid-acting sampling valve located in the plug center electrode. Engine operated at 1400 rev/min, MBT timing, imep = 314 kPa.[47] (*b*) CO_2 and unburned HC concentrations in gas sampled in individual cycles from the vicinity of the spark plug just prior to ignition. Engine operated at 1200 rev/min, $\phi = 0.98$, $p_{\text{inlet}} = 0.5$ atm, gasoline fuel.[48]

gas were removed in turn as contributors to cycle-by-cycle variations (by comparing premixed propane operation with conventional carbureted operation with gasoline, and by removing residual gas by purging with nonfiring cycles), showed that the three contributing factors to cyclic combustion variations—velocity variations, fuel/air ratio variations, and residual gas mixing variations—are of comparable importance at road-load conditions.[45]

An explanation for cycle-by-cycle variations can be developed from the description of the turbulent flame propagation process in Sec. 9.3. Conditions in the *vicinity* of the spark plug will influence the initial stages of the flame propagation process—establishing a stable kernel and its development into a turbulent flame. During the developed flame propagation phase, the *average* conditions in the bulk gas within the combustion chamber will be the determining factors since the flame front spans the chamber, effectively averaging out local nonuniformities. By conditions are meant the turbulent velocity fluctuations and length scales in the flow, proportions of fuel, air, and burned gas in the mixture, and the mixture state.

Using the turbulent combustion model described in Sec. 14.4.2 (which is based on the description of the flame development and propagation process in Sec. 9.3), the flame development angle $\Delta\theta_d$ (the time to burn a few large eddies and establish a developed turbulent flame) can be expressed as[20]

$$\Delta\theta_d = C\left(\frac{l_I}{u'}\right)^{1/3}\left(\frac{l_M}{S_L}\right)^{2/3} \tag{9.51}$$

The turbulent flow field influences $\Delta\theta_d$ through l_I, u', and l_M, the integral scale, the turbulence intensity, and the microscale, respectively. The mixture composition influences $\Delta\theta_d$ through the laminar flame speed S_L. There is therefore a variability in the flame development period, since all of these quantities can vary in the vicinity of the spark plug on a cycle-by-cycle basis.

The pressure development during the rapid-burning developed turbulent flame propagation phase, when the flame spans the combustion chamber, depends on the average rate of burning in the flame. Thus, variations in the turbulent flow field and mixture composition across the gas entering the flame front are averaged out and are not important. However, variation in chamber-average quantities are significant. The combustion model in Sec. 14.4.2 leads to the following expression for the maximum burning rate:

$$\left(\frac{dm_b}{dt}\right)_{\max} = \frac{Cm_f(h^*/B)(\rho_u^*/\rho_i)^{10/9}[(\bar{u}'^* S_L^*)/h_i]^{2/3}}{\nu^{*1/3}} \tag{9.52}$$

Here, m_f is the mass of fuel in the chamber, h is the instantaneous (mean) clearance height, B is the bore, ρ the density, $\bar{u}'$ the average turbulence intensity across the flame front, and ν the kinematic viscosity; the * denotes the value at the time of the maximum burning rate and the subscript i the value at spark; C is a constant depending on engine design. It can be seen from Eq. (9.52) that cycle-by-cycle variations in the maximum burning rate can result from variations in the overall flow pattern within the combustion chamber (which vary $\bar{u}'^*$) and from variations in the amount of fuel (m_f) that enters the cylinder each cycle.† Also, it can be seen that variations in the flame development process will result in variations in the maximum burning rate because the crank angle at which the maximum burning rate occurs is shifted, and all the starred parameters in Eq. (9.52) will have different values.

From the discussion of flame development and structure in Sec. 9.3, and Eqs. (9.51) and (9.52) above, we would expect that mixture conditions and motion leading to slower flame development rates (longer flame development angles, $\Delta\theta_d$)—lower turbulence intensities and more dilute mixtures—would also give lower burning rates (longer rapid burning angles, $\Delta\theta_b$). Data from many different engines and a wide range of operating cases show that this is the case, on average, though there is substantial variation about the mean trend. Figure 9-35 shows these trends; it also shows that the standard deviation of $\Delta\theta_d$ and the standard deviation of $\Delta\theta_b$ for a given chamber and operating condition generally increase as the average burning process becomes slower.[40]

One final factor of importance is how variations in flame development and burning rate affect engine torque. With fixed spark timing, such variations in the combustion process cycle-by-cycle result in slower developing and/or burning

† Variations in the total amount of air, recycled exhaust gas, and residual in the chamber could also, for some operating regimes, be significant.

cycles being retarded and faster developing and/or burning cycles being overadvanced. The curve of torque versus combustion timing (relative to optimum timing), Fig. 9-3*b*, is almost independent of the burning rate; i.e., a given magnitude retard (of say 10°) relative to optimum timing gives almost the same reduction in torque for a very fast burn as it does for a very slow burn. This is because the burning process, for optimum timing, is centered at about 10° ATC independent of the burn rate, and retard or advance shifts this "center" by equal amounts for all burn rates.[16] One of the major advantages of fast-burn engines is now apparent. The magnitude of the variations in the flame development process and subsequent flame propagation rate are decreased as the burning rate is increased (see Fig. 9-35): the ratio of standard deviation in $\Delta\theta_d$ and $\Delta\theta_b$ to the mean values remains approximately constant. Thus, these smaller combustion variations in fast-burn engines, which correspond to modest retard and overadvance in nonaverage burn rate cycles, have little effect on torque. In contrast, the larger combustion variations of slow-burning engines result in significant cyclic torque variations.

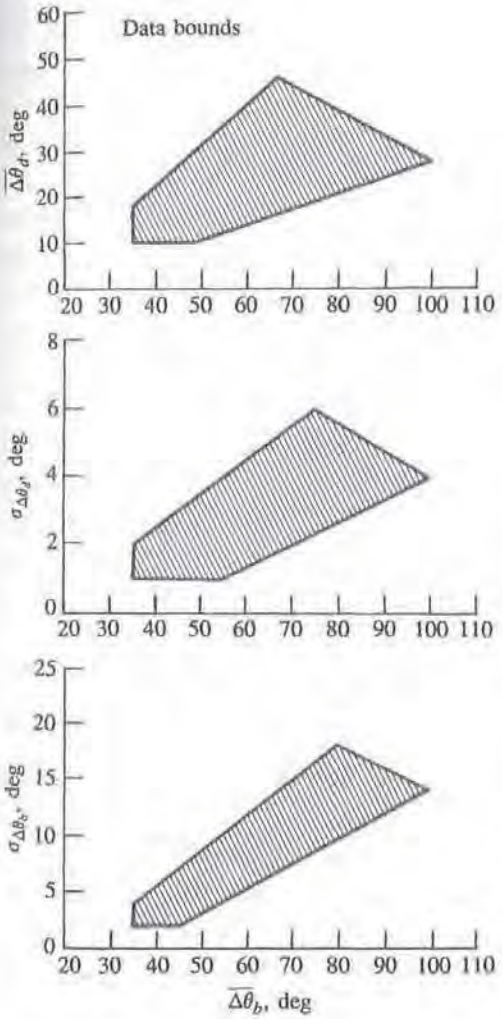


FIGURE 9-35
Variation in mean value of flame development angle $\overline{\Delta\theta_d}$ (spark to 1 percent mass burned) and standard deviations of flame development angle and rapid burning angle $\Delta\theta_b$ (1 to 90 percent mass burned) with mean rapid burning angle $\overline{\Delta\theta_b}$. Range of combustion chamber geometries and engine operating conditions.[40]

9.4.3 Partial Burning, Misfire, and Engine Stability

As the unburned mixture in a spark-ignition engine is leaned out with excess air or is diluted with increasing amounts of burned residual gas and exhaust gas recycle, the flame development period, the duration of the rapid burning phase, and the cycle-by-cycle fluctuations in the combustion process all increase. Eventually a point is reached where engine operation becomes rough and unstable, and hydrocarbon emissions increase rapidly. The point at which these phenomena occur effectively defines the engine's *stable operating limit.*† These phenomena result from the lengthening of all stages of the combustion process as the unburned mixture is diluted. With increasing dilution, first a fraction of the cycles burns so slowly that combustion is only just completed prior to exhaust valve opening. Then as burning lengthens further, in some cycles there is insufficient time to complete combustion within the cylinder; also, flame extinguishment before the exhaust valve opens and before the flame has propagated across the chamber may start to occur in some cycles. Finally, misfiring cycles where the mixture never ignites may start to occur. The proportion of partial burning or nonburning cycles increases rapidly if the mixture is made even more lean or dilute, and the point is soon reached where the engine will not run at all.

The impact on engine stability of increasing combustion variability, due to increased exhaust gas recycle at part-load, is shown in Fig. 9-36. Figure 9-36*a* shows the distributions of individual-cycle indicated mean effective pressure values for 0, 20, and 28 percent EGR. Without EGR at these conditions, the spread in imep is narrow. Increasing EGR widens the distribution significantly and cycles with low imep, and eventually zero imep, occur. Figure 9-36*b* shows how the coefficient of variation of imep and hydrocarbon emissions increase as EGR is increased. Slow burn, then partial burn, and then misfire cycles occur with increasing frequency. In the slow-burn cycles, combustion is complete but ends after 80° ATC and the indicated mean effective pressure is low (between 85 and 46 percent of the mean value). Imep in partial-burn cycles was less than 46 percent of the mean. In misfiring cycles, imep < 0. Empirically, it has been found that COV_{imep} [see Eq. (9.50)] is about 10 percent at the engine's stable operating limit, which here occurs just before the onset of partial-burning cycles[49].

An explanation of combustion phenomenon at the engine stable operating limit has been developed by Quader.[50] It involves the following terms:

> **Ignition-limited spark timing** or the **ignition limit.** The spark timing [advanced from maximum brake torque (MBT) timing] at which *misfire* (i.e., failure of flame initiation) first occurs at a given mixture composition, in a given small but arbitrary fraction of cycles (e.g., 0.5 to 1 percent).

† This limit has often been called the *lean operating limit.* Since what limits engine operation in practice is excessive torque fluctuations, cycle-by-cycle, and high hydrocarbon emissions, resulting from the use of mixtures made overly dilute with either air or burned gases (or with both), *stable operating limit* is a more appropriate term.

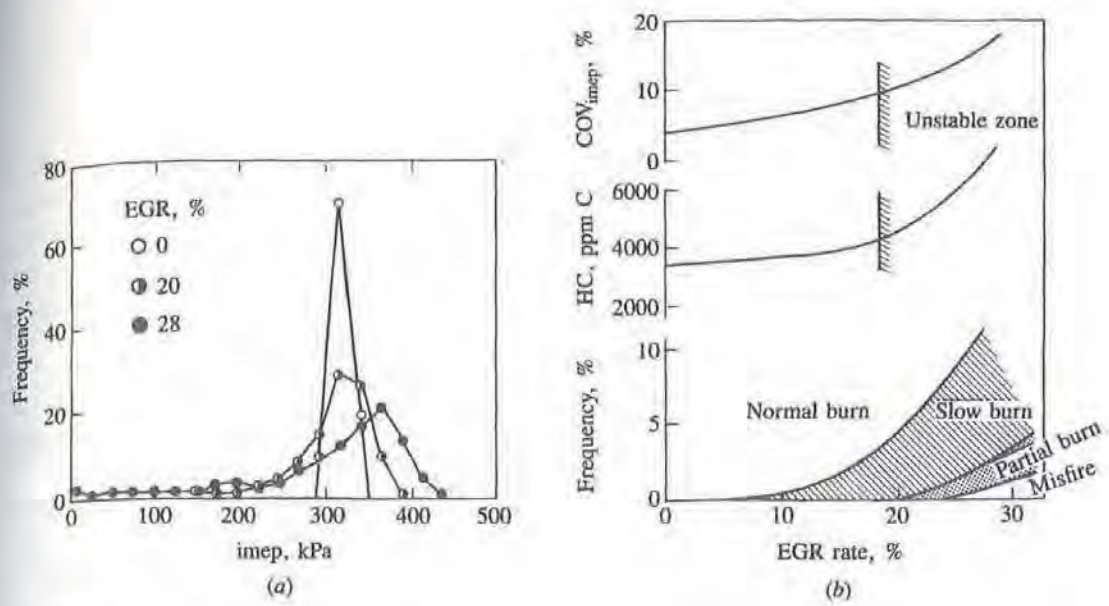


FIGURE 9-36
(*a*) Frequency distributions in indicated mean effective pressure at different EGR rates; 0 percent gave excellent engine stability, 20 percent acceptable stability, and 28 percent poor stability. (*b*) Coefficient of variation in imep, HC emissions, and percentage of normal, slow, partial-burn, and misfire cycles. Engine conditions: 1400 rev/min, $\phi = 1.0$, MBT timing, imep = 324 kPa.[49]

Partial-burn-limited spark timing or the **partial-burn limit.** The spark timing (retarded from MBT) at which incomplete flame propagation occurs at a given mixture composition in a given small percent of the cycles (again, this frequency is selected arbitrarily for experimental convenience).

Lean misfire limit at MBT spark. The leanest mixture stoichiometry at which the engine could be stabilized to operate at MBT spark timing with a misfire frequency below a specified value (again, this frequency, usually a percent or less of the cycles, is selected arbitrarily for convenience). A *dilute misfire limit*, the maximum amount of exhaust gas recycle that can be absorbed at a given stoichiometry for stable engine operation, can be similarly defined.

Engine experiments have defined the locations of the ignition limit line and the partial-burn limit line; they are shown qualitatively in Fig. 9-37. At a given spark timing, on this spark timing versus equivalence ratio plot, progressive leaning of the mixture fed to the engine will lead to the onset of misfire or to the onset of partial burning, depending on the location of the lines and the spark timing selected. The individual figures show the possible interactions of the maximum brake torque (MBT) timing line—leaner mixtures require greater advance—with the ignition limit and partial-burn limit lines. At MBT timing, the partial-burn limit may or may not be reached prior to misfire or the ignition limit. It will depend on the engine and ignition system design and operating conditions. For spark timings retarded relative to MBT, partial burning and not failure of flame initiation is the primary cause of unstable engine operation.

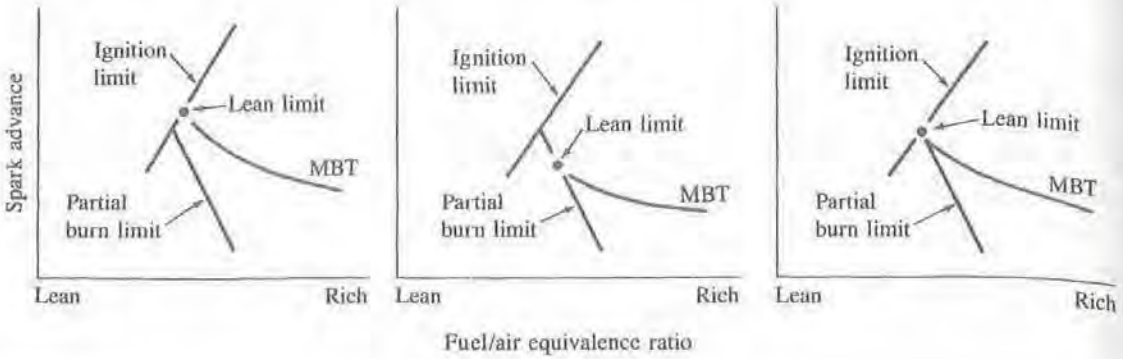


FIGURE 9-37
Schematics of three possible combinations of ignition limit, partial-burn limit, and MBT timing curves as function of fuel/air equivalence ratio. (*From Quader.*[50])

An example of these limiting combustion regimes for lean engine operation is shown in Fig. 9-38. With MBT timing, as the mixture is leaned out (at constant air flow rate), complete combustion in all cycles changes to partial burning in some cycles which changes to no ignition in some cycles at the ignition limit. In the partial-burning regime, the most common type of incomplete-combustion cycle was a slow-burning cycle which required more time to complete burning than was available: flame extinguishment during expansion was much less common. Engine performance measurements showed that the engine stability limit—evidenced by minimum fuel consumption and onset of rapid increase in HC emissions—occurred at $\phi = 0.65$, just before the partial-burn limit line where some slow-burning cycles occur but combustion is still complete in all cycles.[44]

From the above it is clear that flame initiation is a necessary but not sufficient condition for complete combustion. Too-slow flame development and prop-

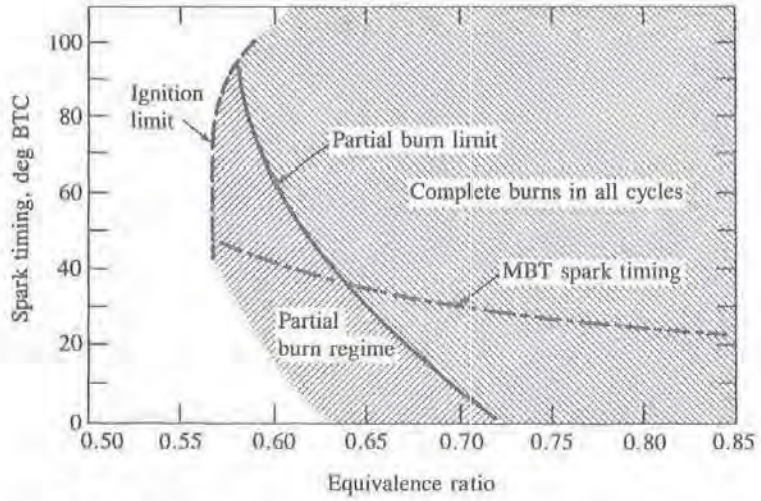


FIGURE 9-38
Actual limiting combustion regimes for lean-operating engine. 1200 rev/min, volumetric efficiency ≈ 60 percent, methane fuel, 40 mJ spark energy, 2.5 ms spark duration.[44]

agation following successful ignition is usually the factor which limits engine operation with dilute mixtures. Experiments have shown that a limited interval, of order 80 crank angle degrees (depending on engine geometry and spark plug location), is available during the engine cycle when conditions are favorable for complete flame propagation.[49, 51] Outside of this interval, the mixture pressure and temperature are too low, and the turbulence intensity is too low to sustain a sufficiently rapid rate of combustion. Thus, it is factors which increase the flame development and propagation rates which primarily extend the partial-burn limit.

9.5 SPARK IGNITION

In spark-ignition engines, the electrical discharge produced between the spark plug electrodes by the ignition system starts the combustion process close to the end of the compression stroke. The high-temperature plasma kernel created by the spark develops into a self-sustaining and propagating flame front—a thin reaction sheet where the exothermic combustion chemical reactions occur. The function of the ignition system is to initiate this flame propagation process, in a repeatable manner cycle-by-cycle, over the full load and speed range of the engine at the appropriate point in the engine cycle. Shadowgraph and schlieren photographs of the kernel created by the discharge between the plug electrodes, the growth of that kernal, and its transition to a propagating flame have already been presented in Figs. 9-19 and 9-20, and described in the accompanying text. A spark can arc from one electrode to another when a sufficiently high voltage is applied. Ignition systems commonly used to provide this spark are: battery ignition systems where the high voltage is obtained with an ignition coil (coil ignition systems); battery systems where the spark energy is stored in a capacitor and transferred as a high-voltage pulse to the spark plug by means of a special transformer (capacitive-discharge ignition systems); and magneto ignition systems where the magneto—a rotating magnet or armature—generates the current used to produce a high-voltage pulse.

This section reviews our basic understanding of electrical discharges in inflammable gas mixtures relevant to engine ignition (Sec. 9.5.1), the major design and operating characteristics of conventional engine ignition systems (Sec. 9.5.2), and, briefly, some alternative approaches to generating a propagating flame (Sec. 9.5.3).

9.5.1 Ignition Fundamentals

A spark can arc from one plug electrode to the other only if a sufficiently high voltage is applied. In a typical spark discharge, the electrical potential across the electrode gap is increased until breakdown of the intervening mixture occurs. Ionizing streamers then propagate from one electrode to the other. The impedance of the gap decreases drastically when a streamer reaches the opposite electrode, and the current through the gap increases rapidly. This stage of the

discharge is called the *breakdown phase*. It is followed by the *arc phase*, where the thin cylindrical plasma expands largely due to heat conduction and diffusion and, with inflammable mixtures, the exothermic reactions which lead to a propagating flame develop. This may be followed by a *glow discharge phase* where, depending on the details of the ignition system, the energy storage device (e.g., the ignition coil) will dump its energy into the discharge circuit.[52, 53]

Figure 9-39 shows the behavior of the discharge voltage and current as a function of time for a conventional coil ignition system. Typical values are shown; actual values depend on the details of the electrical components. The breakdown phase is characterized by a high-voltage (~10 kV), high-peak current (~200 A), and an extremely short duration (~10 ns). A narrow (~40 μm diameter) cylindrical ionized gas channel is established very early. The energy supplied is transferred almost without loss to this plasma column. The temperature and pressure in the column rise very rapidly to values up to about 60,000 K and a few hundred atmospheres, respectively. A strong shock or blast wave propagates outward, the channel expands, and, as a result, the plasma temperature and pressure fall. Some 30 percent of the plasma energy is carried away by the shock wave; however, most of this is regained since spherical blast waves transfer most of their energy to the gas within a small (~2 mm diameter) sphere into which the breakdown plasma soon expands.[52, 53]

A breakdown phase always precedes arc and glow discharges: it creates the electrically conductive path between the electrodes. The arc phase voltage is low

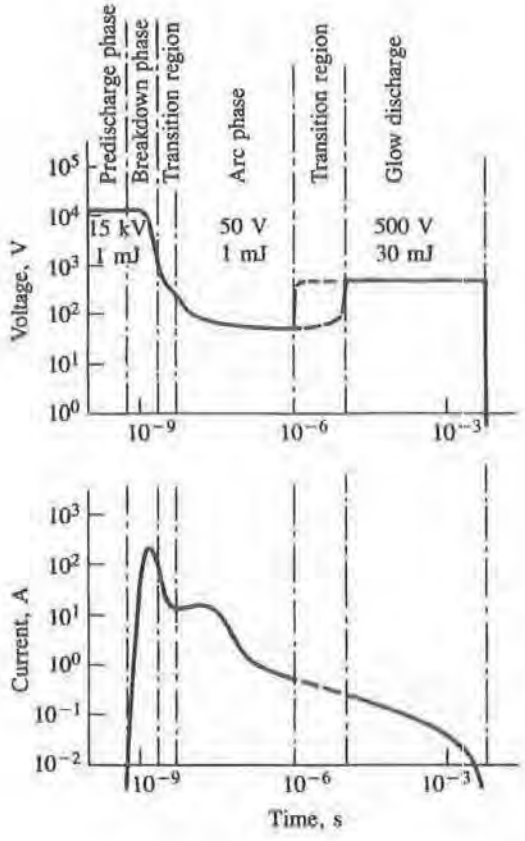


FIGURE 9-39
Schematic of voltage and current variation with time for conventional coil spark-ignition system. Typical values for energy and voltage in the three phases—breakdown, arc, and glow discharge—are given.[52]

(<100 V), though the current can be as high as the external circuit permits. In contrast to the breakdown phase where the gas in the channel is fully dissociated and ionized, in the arc phase the degree of dissociation may still be high at the center of the discharge, but the degree of ionization is much lower (about 1 percent). Voltage drops at the cathode and anode electrodes are a significant fraction of the arc voltage, and the energy deposited in these electrode sheath regions, which is conducted away by the metal electrodes, is a substantial fraction of the total arc energy (see Table 9.4 below). The arc requires a hot cathode spot, so evaporation of the cathode material occurs. The arc increases in size due primarily to heat conduction and mass diffusion. Due to these energy transfers the gas temperature in the arc is limited to about 6000 K: the temperature and degree of dissociation decrease rapidly with increasing distance from the arc axis. Currents less than 200 mA, a large electrode voltage drop at the cathode (300 to 500 V), a cold cathode, and less than 0.01 percent ionization are typical for the glow discharge. Energy losses are higher than in the arc phase, and peak equilibrium gas temperatures are about 3000 K.[52]

About 0.2 mJ of energy is required to ignite a quiescent stoichiometric fuel-air mixture at normal engine conditions by means of a spark. For substantially leaner and richer mixtures, and where the mixture flows past the electrodes, an order of magnitude greater energy (~3 mJ) may be required.[54] Conventional ignition systems deliver 30 to 50 mJ of electrical energy to the spark. Due to the physical characteristics of the discharge modes discussed above, only a fraction of the energy supplied to the spark gap is transmitted to the gas mixture. The energy balance for the breakdown, arc, and glow phases of the discharge is given in Table 9.4. Radiation losses are small throughout. The end of the breakdown phase occurs when a hot cathode spot develops, turning the discharge into an arc; heat losses to the electrodes then become substantial. The breakdown phase reaches the highest power level (~1 MW), but the energy supplied is small (0.3 to 1 mJ). The glow discharge has the lowest power level (~10 W) but the highest energy (30 to 100 mJ), due to its long discharge time. The arc phase lies between.

The proportions of the electrical energy supplied, which can be transferred to the plasma in these three phases of the discharge, are shown in Fig. 9-40.[53, 55] The different transfer capabilities for breakdown arc and glow discharges arise

TABLE 9.4
Energy distribution for breakdown, arc, and glow discharges†

	Breakdown, %	Arc, %	Glow, %
Radiation loss	<1	5	<1
Heat loss to electrodes	5	45	70
Total losses	6	50	70
Plasma energy	94	50	30

† Typical values, under idealized conditions with small electrodes.
Source: Maly and Vogel.[52]

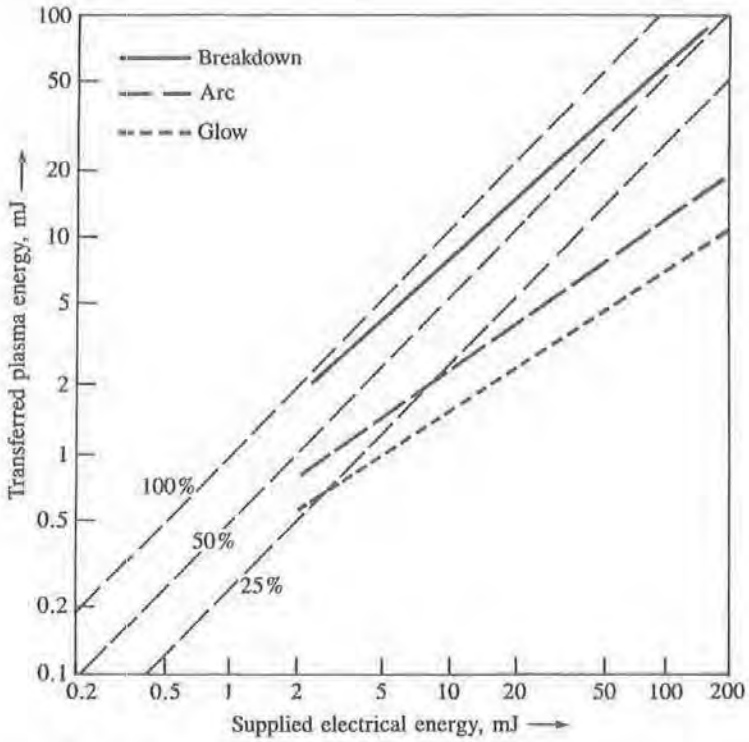


FIGURE 9-40
Energy transferred to the spark kernal as a function of supplied electrical energy for breakdown, arc, and glow discharges.[55]

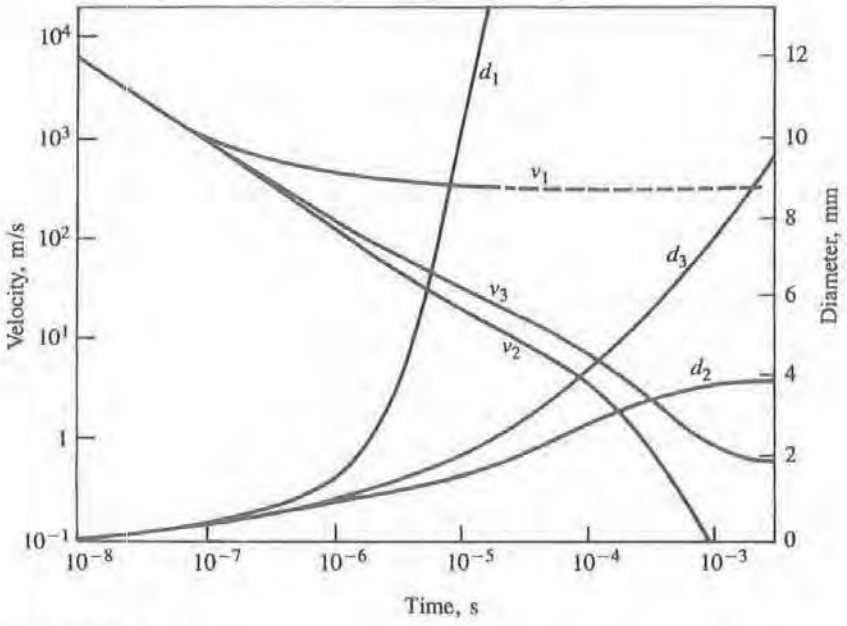


FIGURE 9-41
Diameters (d) and expansion velocities (v) of volumes activated by a capacitive-discharge ignition system: 3 mJ electrical energy, 100 μs duration. Subscripts denote: 1, shock in air at 1 atm; 2, plasma in air at 1 atm; 3, electrical and chemical plasma in stoichiometric methane-air mixture at 1 atm.[52]

primarily from the differences in heat losses to the electrodes, as explained above. These losses increase with increasing supplied energy. In arc and glow discharges, increases in either discharge time or discharge current (or in both) always lead to substantial decreases in energy-transfer efficiency. If the glow discharge current is increased above about 100 mA, the discharge changes to the arc mode and heavy electrode erosion will result. Thus there are practical limits to the arc and glow discharge currents; also, the time available for ignition in the engine limits increases in discharge time.

The initial expansion velocities in the discharge are much higher than those in self-propagating flames. Figure 9-41 shows the expansion velocities and diameters of the volumes activated by a 3-mJ, 100-μs discharge from a capacitor-discharge ignition system as a function of time after spark onset.[52] The curves shown are (1) for the shock wave following a discharge in air at 1 atm; (2) the plasma in air at 1 atm; (3) the electrical and chemical plasma following a discharge in a stoichiometric methane-air mixture at 1 atm. The initially strong shock wave attenuates rapidly to the local sound speed. Up to times of order microseconds, the effects of fuel combustion chemistry are small. The change in slope of the velocity curves for the plasmas at about 100 μs indicates the transition from an expansion caused by the initial high pressure in the breakdown discharge to expansion resulting from heat conduction and diffusion.

The temperature distributions within the three different types of discharge provide additional insight. During the breakdown discharge, on a time scale of nanoseconds, the temperature rises to 60,000 K. Increasing the breakdown energy does not produce *higher* kernel temperatures; instead the channel diameter increases, producing a larger plasma volume. The kernel temperatures then decrease to the order of 10,000 K on a microsecond time scale as the plasma expands behind the shock wave. Arc and glow discharges, because their power inputs are much lower, do not increase the kernel temperatures; rather, they extend the cooling period on a microsecond and millisecond time scale, respectively.[52]

The characters of the temperature profiles that each of these three types of discharge create in air, with essentially the same total electrical energy input (30 to 33 mJ), are indicated in Fig. 9-42. The radial profiles in the undisturbed midplane of the arc are shown. The expansion-wave-induced expansion of the plasma behind the shock with the breakdown discharge produces a larger plasma, earlier, with a steep temperature front. Thus it creates favorable conditions for transferring heat and radicals to the surrounding unburned mixture. In addition cold gas flows into the central region of the plasma, due to the boundary layers which the rapidly expanding flow sets up on the electrodes, effectively insulating the hottest plasma region from the cold electrode surfaces.[53] The arc and glow discharges, each preceded by a much lower energy initial breakdown process, show a much slower expansion rate and the more gradual temperature profile produced by heat conduction and diffusion.

Chemical reactions can be observed spectroscopically a few nanoseconds after spark onset. They are initiated by the very high radical density in the break-

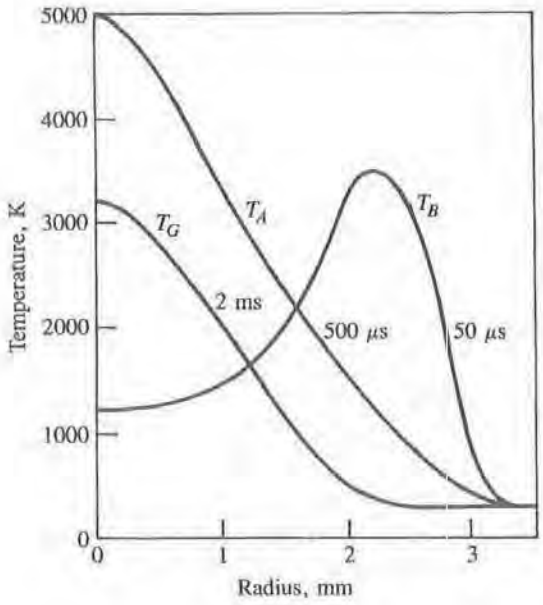


FIGURE 9-42
Radial temperature profiles at selected times after spark onset for ignition systems with different electrical energies and discharge times in air at 1 atm. T_B, breakdown discharge, 30 mJ energy, 60 ns duration; T_A, capacitive discharge, 3 mJ energy, 100 μs duration with superimposed current arc of 2 A, 30 mJ energy, for 230 μs; T_G, capacitive-discharge system, 3 mJ energy, 100 μs duration with superimposed constant-current glow discharge of 60 mA, 30 mJ energy, 770 μs duration.[52]

down plasma where all the heavy particles are present as highly excited atoms and ions. Since the kernel temperatures are much too high to allow the species present in normal combustion products to exist, combustion reactions take place at the outer plasma surface where the conditions are ideal for rapid chemical activity (temperatures of one thousand to a few thousand kelvins). The chemical energy released is added to the plasma energy and becomes evident when the plasma velocity falls below about 100 m/s (see Fig. 9-41). At this point, the inte-

TABLE 9.5
Equilibrium composition of stoichiometric isooctane-air combustion products

	Temperature, K†			
Species	**2000**	**3000**	**4000**	**5000**
CO	2.4(−3)	6.1(−2)	9.4(−2)	9.0(−2)
CO_2	1.2(−1)	5.7(−2)	5.0(−3)	3.5(−4)
H	2(−5)	9.7(−3)	1.2(−1)	1.9(−1)
H_2	6.1(−4)	1.5(−2)	2.4(−2)	3.5(−3)
H_2O	1.4(−1)	1.0(−1)	1.1(−2)	1.2(−4)
N	*n*	1(−5)	6.6(−4)	1.2(−2)
NH	*n*	*n*	2(−5)	6(−5)
NO	5.7(−4)	1.5(−2)	2.9(−2)	1.7(−2)
N_2	7.3(−1)	6.9(−1)	5.7(−1)	5.1(−1)
O	1(−5)	8.6(−3)	9.8(−2)	1.6(−1)
OH	4.5(−4)	2.2(−2)	3.3(−2)	5.6(−3)
O_2	1.1(−3)	2.3(−2)	1.7(−2)	2.2(−3)

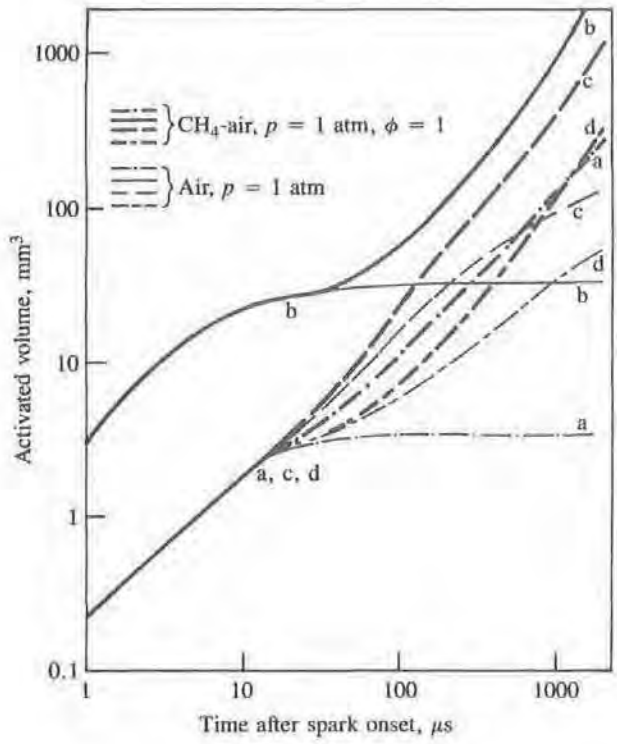
† At 4 atm pressure: mole fractions, $9.0(-2) = 9.0 \times 10^{-2}$. $n = < 5 \times 10^{-6}$

rior of the plasma still consists of a fully dissociated reacted gas mixture with most of its energy stored in radicals. An indication of the gas composition across the steep temperature profile at the plasma interface can be obtained from Table 9.5, which shows the equilibrium composition of C_8H_{18}-air combustion products over the relevant temperature range. Note, however, that the gas will not be in equilibrium. The different radicals have different diffusivities, with the hydrogen atom some five times that of other species. Thus the H radical will diffuse furthest into the as-yet unreacted mixture. On the high-temperature side of the inflammation zone, the large number of radical particles transfer their energy to the mixture molecules within a few collisions. On the low-temperature side of the zone, above-equilibrium concentrations of combustion-initiating radicals (O and H) build up. In addition, a high heat flux into the region occurs, from the plasma core, by conduction down the steep temperature gradient. As a consequence of these conditions, reactions will occur and energy will be released more rapidly than in a normal flame.[53]

Figure 9-43*a* shows the size of the activated volume as a function of time for several types of discharge, both in a stoichiometric mixture and in air. It can be seen from the air curves for the capacitive discharge (CDI) and breakdown discharge that, after about 10 μs, the plasma ceases to be the energy source for continued growth of the activated volume. At this time, the plasma temperature at the interface has fallen to a value comparable to flame temperatures. With combustible mixtures, molecules such as OH, CH, C_2, CO, etc., appear, indicating that combustion reactions are now occurring. Figure 9-43*a* shows that for $t \geq 20$ μs, the volume activated by the discharge with the combustible mixture grows much faster than the volume activated in air. Continuing the supply of electrical energy in the arc and glow discharge does produce a higher expansion rate in both the combustible mixture and in air, due to additional heat conduction and diffusion to the interface, but the onset of inflammation is not significantly affected. The radial temperature profiles across the discharge at selected times, shown in Fig. 9-43*b*, illustrate these points. This, therefore, is the critical point in the inflammation process: at some 20 μs after onset of the discharge the flame reactions must be proceeding sufficiently rapidly to be self-sustaining; i.e., chemical energy release must more than offset heat losses across the front to the surrounding unburned mixture via diffusion and conduction.[53]

Thus the characteristics of the breakdown phase of the discharge have the greatest impact on inflammation. The size of the activated volume a given time interval after spark initiation, the temperature difference across the kernel interface, and the velocity of the interface are all substantially increased by increasing the breakdown phase energy (see Fig. 9-43). Additional energy input during the arc and glow discharge phases has a more modest effect on these critical kernel properties. This is graphically illustrated by Fig. 9-44 where the same energy input into breakdown, arc, and glow discharge modes produces substantially different ignition limits.

Several models of the plasma–unburned mixture interface have been developed in attempts to quantify the complex phenomena described above (e.g., Refs.



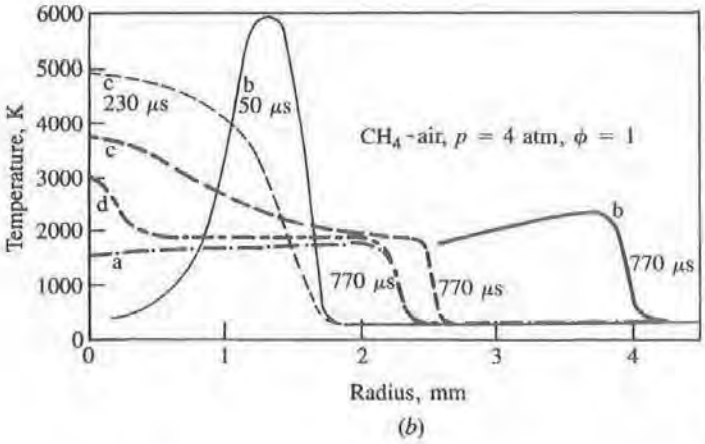


FIGURE 9-43
(*a*) Size of discharge-activated volume as function of time for several types of discharge in air and in stoichiometric methane-air mixture at 1 atm. a: CDI, 3 mJ energy, 100 μs duration; b: breakdown discharge, 30 mJ energy, 20 ns duration; c: CDI plus arc discharge, 1.5 A, 40 V, 500 μs duration; d: CDI + glow discharge, 30 mA, 500 V, 2 ms duration. (*b*) Temperature profiles for different discharge modes at different times in stoichiometric methane-air mixture at 300 K, 4 atm. a: CDI, 3 mJ energy, 100 μs duration; b: breakdown discharge, 20 mJ energy, 80 ns duration; c: CDI, 3 mJ energy, 100 μs duration, plus 2 A, 30 mJ energy, 230 μs duration arc; d: CDI, 3 mJ energy, 100 μs duration, plus 60 mA, 30 mJ energy, 770 μs duration glow discharge.[53]

56 and 57). They are based on the requirement that the energy release due to chemical reaction in the plasma front (and production of radical species) exceed the losses due to conduction and diffusion to the unburned gas ahead of the front. While these models are incomplete, they do provide a theoretical basis for the well-known fact that the minimum energy required to ignite a premixed fuel-air mixture depends strongly on mixture composition. Figure 9-45 shows a typical set of results on the minimum ignition energy as a function of the equivalence ratio under quiescent conditions.[58] The curve shows a minimum for slightly rich-of-stoichiometric mixtures; the minimum energy required for successful ignition increases rapidly as the mixture is leaned out. While the initial plasma kernel

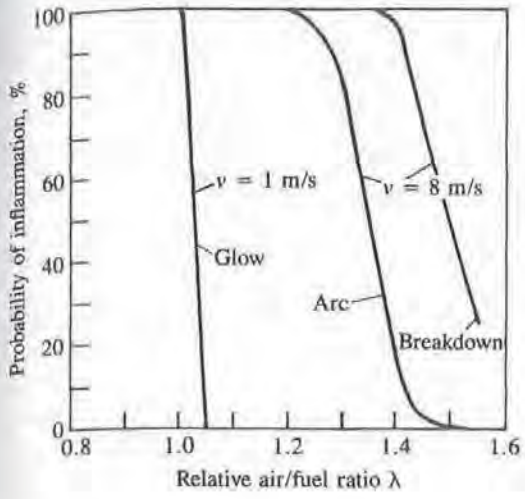


FIGURE 9-44
Probability of inflammation of stoichiometric methane-air mixture, at 300 K, 4 atm, as function of relative air/fuel ratio λ ($= 1/\phi$) for different ignition discharges with equal total electrical energy (30–33 mJ). Breakdown: 30 mJ, 60 ns duration. Arc: CDI, 3 mJ, 100 μs duration; plus 2 A, 30 mJ, 230 μs duration arc. Glow: CDI, 3 mJ, 100 μs duration; plus 60 mA, 30 mJ, 770 μs duration glow discharge. v = mixture velocity.[52]

growth (up to 10 to 100 μs) is not greatly affected by the mixture equivalence ratio, the inflammation process and the thickness and rate of propagation of the resulting flame are strongly affected. The lean side of the minimum is of more practical interest than the rich side. Because the chemical energy density of the mixture and flame temperature decrease as the mixture is leaned out, the flame speed decreases and the flame becomes thicker. Thus more time is available for heat losses from the inflammation zone, less energy is available to offset these losses, and the rate of energy transfer into the zone decreases. The consequence is that, as the mixture is leaned out, the approximately spherical discharge-created plasma must grow to a larger size before inflammation will occur. Substantially, more energy must therefore be supplied to the discharge.[53]

In engines, the mixture is not quiescent: mean and fluctuating velocities in the range 1 to 10 m/s exist in the clearance volume at TC (see Sec. 8.2.2). On the time scale of the breakdown discharge phase (10 ns), this fluid motion is not important. In the arc and glow discharge phases, however, the arc is convected

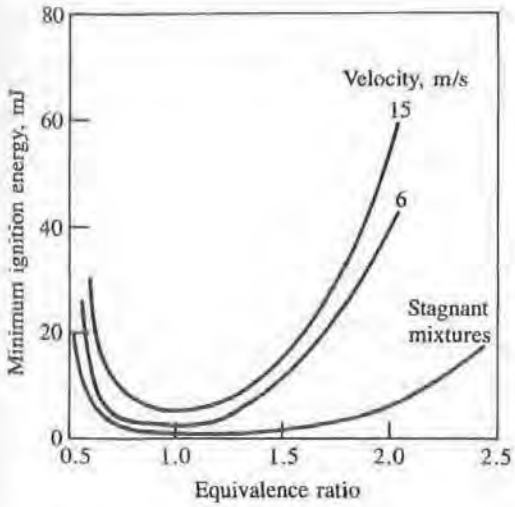


FIGURE 9-45
Effect of mixture equivalence ratio and flow velocity on minimum ignition energy for propane-air mixtures at 0.17 atm.[58]



FIGURE 9-46
Photographs of single glow discharge (30 mJ, 0.77–1.5 ms) in air at 2 atm flowing perpendicular to axis of electrodes. Below 25 m/s almost no multiple discharges; above 25 m/s only multiple discharges. 1.2 mm electrode gap.[56]

by the flow and lengthened accordingly, as illustrated in Fig. 9-46. For velocities below 15 m/s a steady increase in discharge channel length occurs. For higher velocities, an increasing number of reignitions occur, so the discharge energy is distributed into many separate channels. As the channel lengthens, the ratio of total discharge voltage to anode plus cathode voltage drop increases substantially, and the relative importance of heat losses to the electrodes decreases. Thus more energy is transferred to the gas—the energy-transfer efficiency increases. However, as the channel is lengthened, the energy transferred is spread over a larger volume. Depending on flow velocity, and mixture and discharge conditions, increasing velocity may increase or decrease the minimum ignition energy or the lean ignition limit for a specific ignition system. Both the mean flow velocity and turbulence levels are important.[53–58] With a conventional coil ignition system, increasing mean flow velocity up to the point where reignitions start to occur extends the lean limit. With breakdown discharge systems, the lean ignition limit decreases as flow velocity increases.[53] With capacitive-discharge systems at low flow velocities, the flow has little impact: at high flow velocities the minimum ignition energy increases.[59]

Maly[53] has summarized these fundamental aspects of spark-discharge ignited flames as follows:

1. Of the total electrical energy supplied to the spark, only that fraction contained within the outer surface layer of the plasma (of thickness of the order of the inflammation zone) is available for initiating the flame propagation process. The energy density and the temperature gradient in this layer depend on the discharge mode. Highest energy densities and temperature gradients are achieved if the ignition energy is supplied in the shortest time interval.
2. A minimum radius of the spark plasma is required for inflammation of the fuel-air mixture to occur. This radius increases rapidly as the mixture is leaned out (or diluted); it decreases with increasing pressure and increasing plasma expansion velocity.
3. After inflammation, burning rates are proportional to flame surface area. Thus discharges and plasma geometries that produce the largest inflammation zone surface area, most rapidly, are advantageous.

4. The time over which the ignition energy can be used effectively for inflammation decreases as the initial flame velocity increases. Ignition energy supplied after inflammation has occurred will have only a modest impact on flame propagation.

9.5.2 Conventional Ignition Systems

The ignition system must provide sufficient voltage across the spark plug electrodes to set up the discharge and supply sufficient energy to the discharge to ignite the combustible mixture adjacent to the plug electrodes under all operating conditions. It must create this spark at the appropriate time during the compression stroke. Usually spark timing is set to give maximum brake torque for the specific operating condition, though this maximum torque may be constrained by emission control or knock control requirements. For a given engine design, this optimum spark timing varies as engine speed, inlet manifold pressure, and mixture composition vary. Thus, in most applications, and especially the automotive applications, the system must have means for automatically changing the spark timing as engine speed and load vary.

With an equivalence ratio best suited for ignition and with homogeneous mixture distribution, spark energies of order 1 mJ and durations of a few microseconds would suffice to initiate the combustion process. In practice, circumstances are less ideal. The air, fuel, and recycled exhaust are not uniformly distributed between cylinders; the mixture of air, fuel, recycled exhaust gas, and residual gas within each cylinder is not homogeneous. Also, the pressure, temperature, and density of the mixture between the spark plug electrodes at the time the spark is needed affect the voltage required to produce a spark. These vary significantly over the load and speed range of an engine. The spark energy and duration, therefore, has to be sufficient to initiate combustion under the most unfavorable conditions expected in the vicinity of the spark plug over the complete engine operating range. Usually if the spark energy exceeds 50 mJ and the duration is longer than 0.5 ms reliable ignition is obtained.

In addition to the spark requirements determined by mixture quality, pressure, temperature, and density, there are others determined by the state of the plugs. The erosion of the plug electrodes over extended mileage increases the gap width and requires a higher breakdown voltage. Also, spark plug fouling due to deposit buildup on the spark plug insulator can result in side-tracking of the spark. When compounds formed by the burning of fuel, lubricating oil, and their additives are deposited on the spark plug insulator, these deposits provide an alternative path for the spark current. If the resistance of the spark plug deposits is sufficiently low, the loss of electrical energy through the deposits may prevent the voltage from rising to that required to break down the gas. The influence of side-tracking on spark generation decreases with lower source impedance of the high-voltage supply, and therefore with a higher available energy.

The fundamental requirements of the high-voltage ignition source can be summarized as: (1) a high ignition voltage to break down the gap between the

plug electrodes; (2) a low source impedance or steep voltage rise; (3) a high energy storage capacity to create a spark kernel of sufficient size; (4) sufficient duration of the voltage pulse to ensure ignition. There are several commonly used concepts that partly or fully satisfy these requirements.[54, 60]

COIL IGNITION SYSTEMS. Breaker-operated inductive ignition systems have been used in automotive engines for many years. While they are being replaced with more sophisticated systems (such as transistorized coil ignition systems), they provide a useful introduction to ignition system design and operation. Figure 9-47 shows the circuit of a typical breaker ignition system. The system includes a battery, switch, resistor, coil, distributor, spark plugs, and the necessary wiring. The circuit functions as follows. If the breaker point is closed when the ignition is switched on, current flows from the battery, through the resistor, primary winding of the ignition coil, contacts, and back to the battery through ground. This current sets up a magnetic field within the iron core of the coil. When ignition is required, the breaker points are opened by the action of the distributor cam, interrupting the primary current flow. The resulting decay of magnetic flux in the coil induces a voltage in both the primary and secondary windings. The voltage induced in the secondary winding is routed by the distributor to the correct spark plug to produce the ignition spark.

The current and voltage waveforms are shown in Fig. 9-48. The primary current for any given time of contact closure t is given by

$$I_p = \frac{V_0}{R}(1 - e^{-Rt/L_p}) \tag{9.53}$$

where I_p is the primary current, V_0 is the supply voltage, R is the total primary circuit resistance, and L_p is the primary circuit inductance. The primary current requires time to build up. At low speeds the time of contact closure is sufficient for the primary current to reach the maximum permitted by the circuit resistance; at high speeds the primary current may not reach its maximum. Thus, only at higher engine speeds does the term e^{-Rt/L_p} become significant. When the points open the primary current falls to zero and a voltage of order 15 kV is induced in the secondary winding. If the coil is not connected to a spark plug,

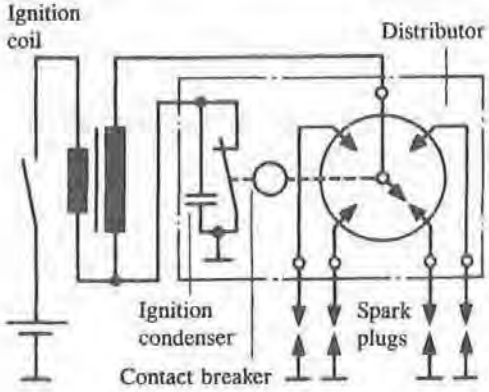


FIGURE 9-47
Schematic of conventional coil ignition system. (*Courtesy Robert Bosch GmbH and SAE.*[54])

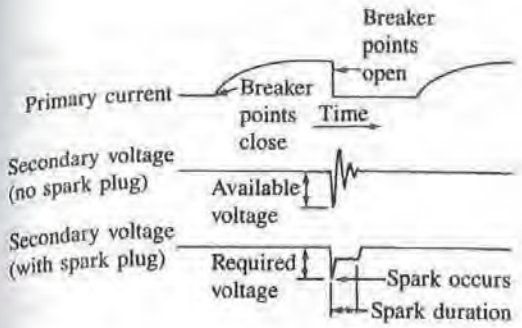


FIGURE 9-48
Current and voltage waveforms for breaker ignition system.[61]

this induced voltage will have a damped sinusoidal waveform, as shown in the center trace. The peak value of this voltage is the maximum voltage that can be produced by the system and is called the *available voltage* V_a of the system. The maximum energy transferred to the secondary system is given by

$$E_{s,\,\max} = \frac{1}{2} C_s V_a^2$$

where C_s is the total capacitance of the secondary circuit. Hence, the available voltage of the system is given by

$$V_a = \left(\frac{2E_{s,\,\max}}{C_s}\right)^{1/2} \tag{9.54}$$

If all the energy stored in the primary circuit of the coil, $\frac{1}{2}L_p I_p^2$, is transferred to the secondary,

$$V_a = I_p\left(\frac{L_p}{C_s}\right)^{1/2} \tag{9.55}$$

When the coil is connected to a spark plug, the secondary voltage will rise to the breakdown potential of the spark plug, and a discharge between the plug electrodes will occur. This alters the waveform as shown in the bottom trace of Fig. 9-48. After the spark occurs, the voltage is reduced to a lower value until all the energy is dissipated and the arc goes out. The value of this voltage which caused breakdown to occur is called the *required voltage* of the spark plug. The interval during which the spark occurs is called the *spark duration*. The available voltage of the ignition system must always exceed the required voltage of the spark plug to ensure breakdown. The spark must then possess sufficient energy and duration to initiate combustion under all conditions of operation.

The major limitations of the breaker-operated induction-coil system are the decrease in available voltage as engine speed increases due to limitations in the current switching capability of the breaker system, and the decreasing time available to build up the primary coil stored energy. Also, because of the high source impedance (about 500 kΩ) the system is sensitive to side-tracking across the spark plug insulator. A further disadvantage is that due to their high current

load, the breaker points are subject to electrical wear in addition to mechanical wear, which results in short maintenance intervals. The life of the breaker points is dependent on the current they are required to switch. Acceptable life is obtained with $I_p \approx 4$ A; increased currents cause a rapid reduction in breaker point life and system reliability.

TRANSISTORIZED COIL IGNITION (TCI) SYSTEMS. In automotive applications, the need for much reduced ignition system maintenance, extended spark plug life, improved ignition of lean and dilute mixtures, and increased reliability and life has led to the use of coil ignition systems which provide a higher output voltage and which use electronic triggering to maintain the required timing without wear or adjustment (see Refs. 54 and 61). These are called transistorized coil ignition (TCI) or high-energy electronic-ignition systems. The higher output voltage is required because spark plugs are now set to wider gaps (e.g., about 1 mm) to extend the ability to ignite the fuel mixture over a wider range of engine operation, and because during the extended mileage between spark plug replacement electrode erosion further increases the gap. In automotive applications an available ignition voltage of 35 kV is now usually provided. In addition to higher voltage, longer spark duration (about 2 ms) has been found to extend the engine operating conditions over which satisfactory ignition is achieved.

Most of the solid-state ignition systems now in use operate on the same basic principle. Figure 9-49 shows the block circuit diagram of a transistorized coil ignition system. The distributor points and cam assembly of the conventional ignition system are replaced by a magnetic pulse generating system which detects the distributor shaft position and sends electrical pulses to an electronic control module. The module switches off the flow of current to the coil primary windings, inducing the high voltage in the secondary windings which is distributed to the

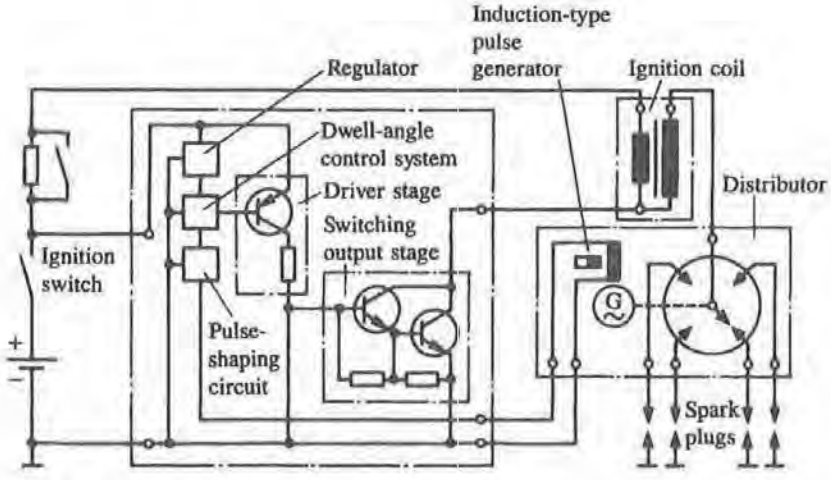


FIGURE 9-49
Schematic of transistorized coil ignition system with induction pulse generator. (*Courtesy Robert Bosch GmbH and SAE.*[54])

spark plugs as in the conventional breaker system. The control module contains timing circuits which then close the primary circuit so that buildup of primary circuit current can occur. There are many types of pulse generators that could trigger the electronic circuit of the ignition system.[60] A magnetic pulse generator, where a gear-shaped iron rotor driven by the distributor shaft rotates past the stationary pole piece of the pickup, is usually used. The number of teeth on the rotor is the same as the number of cylinders. A magnetic field is provided by a permanent magnet. As each rotor tooth passes the pole piece it first increases and then decreases the magnetic field strength ψ linked with the pickup coil, producing a voltage signal proportional to $d\psi/dt$. The electronic module switches off the coil current to produce the spark as the rotor tooth passes through alignment and the pickup coil voltage abruptly reverses and passes through zero. The increasing portion of the voltage waveform, after this voltage reversal, is used by the electronic module to establish the point at which the primary coil current is switched on for the next ignition pulse.

CAPACITIVE-DISCHARGE IGNITION (CDI) SYSTEMS. With this type of system (shown schematically in Fig. 9-50) a capacitor, rather than an induction coil, is used to store the ignition energy. The capacitance and charging voltage of the capacitor determine the amount of stored energy. The ignition transformer steps up the primary voltage, generated at the time of spark by the discharge of the capacitor through the thyristor, to the high voltage required at the spark plug. The CDI trigger box contains the capacitor, thyristor power switch, charging device (to convert battery voltage to the charging voltage of 300 to 500 V by means of pulses via a voltage transformer), pulse shaping unit, and control unit.

The principal advantage of CDI is its insensitivity to electrical shunts in the high-voltage ignition circuit that result from spark plug fouling. Because of the fast capacitive discharge, the spark is strong but short (0.1 to 0.3 ms). This can lead to ignition failure at operating conditions where the mixture is very lean or dilute.[54]

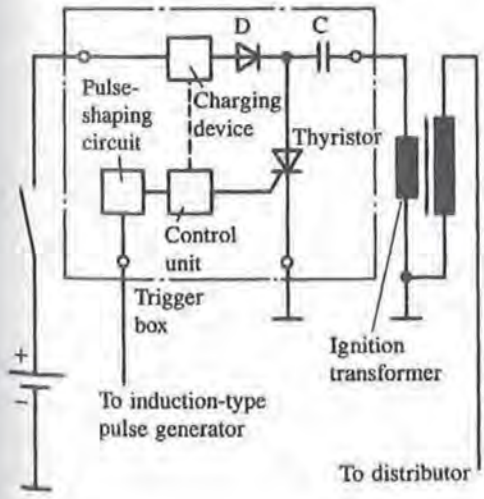


FIGURE 9-50
Schematic of capacitive-discharge system. (*Courtesy Robert Bosch GmbH and SAE.*[54])

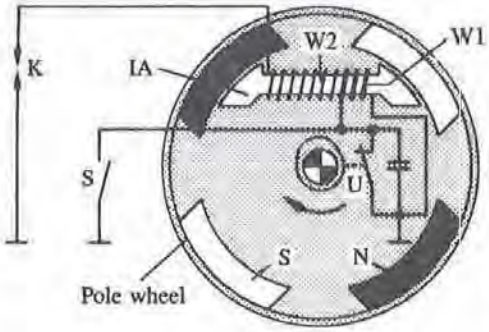


FIGURE 9-51
Schematic of breaker-triggered magneto system with ignition armature. (*Courtesy Robert Bosch GmbH and SAE.*[54])

MAGNETO IGNITION. With this type of ignition system, a magneto supplies the ignition voltage for the spark discharge independent of a battery or generator. Magneto ignition is commonly used in small four-stroke and two-stroke engines. Figure 9-51 illustrates the system and its operation. A time-varying magnetic flux Φ_0 is set up in the ignition armature (IA) as the rotating permanent magnets on the pole wheel generate a current in the closed primary winding W1. This primary current generates an additional flux Φ_I, giving a resultant flux $\Phi_R = \Phi_0 + \Phi_I$. To generate the ignition voltage, the primary current flow is interrupted and the flux collapses rapidly from Φ_R to Φ_0, producing a high-voltage pulse in the winding which is connected to the spark plug electrode. The current can be interrupted with contact breakers (breaker-triggered magneto) or with a transistor (semiconductor magneto). Since the flux generated by the rotating pole wheel depends on engine speed, the magnitude of the ignition voltage varies with speed.[54]

SPARK PLUG DESIGN. The function of the spark plug is to provide an electrode gap across which the high-voltage discharge occurs which ignites the compressed mixture of fuel vapor and air in the combustion chamber. In addition, it must provide a gas-tight conducting path from the high-voltage wire to the electrode gap. Figure 9-52 shows a typical spark plug design. There are three principal

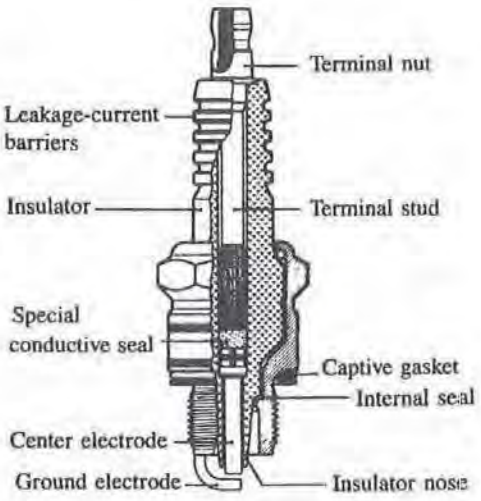


FIGURE 9-52
Cutaway drawing of conventional spark plug. (*Courtesy Robert Bosch GmbH and SAE.*[54])

components: an insulator, electrodes, and a shell. The insulated material must have adequate thermal shock resistance, tensile and compressive strength, and impact strength. It must also have low porosity to limit absorption of combustion gases and high resistivity to prevent leakage of high-voltage charge at both ambient temperatures and normal operating temperatures. Alumina is usually used as the insulator material.

The electrodes are normally made of high-nickel alloys to withstand the high ignition voltage, high temperatures, and corrosive gases with minimum erosion. The center-electrode surface temperatures can average 650–700°C under normal operating conditions. A wide range of electrode geometries are available.

The location of the special conductive seal within the shell affects the *heat rating* of the spark plug. For a "hot" plug, an insulator with a long conical nose is used; for a "cold" plug a short-nosed insulator is used. The length of the heat conduction path from the insulator nose to the shell is changed in this way to vary and control the temperature of the exposed part of the insulator. The spark plug insulator tip temperature increases with increasing speed. It is desirable to have the tip hotter than about 350°C to prevent fouling at low speed. High-speed high-load tip temperatures must be kept below about 950°C to prevent preignition. Normally, the gap between the center and ground electrodes is 0.7 to 0.9 mm. For extremely dilute mixtures this is usually increased to 1.2 mm. Magneto ignition systems use smaller gaps (~0.5 mm). High-compression-ratio racing engines use smaller gaps (0.3 to 0.4 mm).[54]

9.5.3 Alternative Ignition Approaches

A large number of methods for initiating combustion in spark-ignition engines with electrical discharges, in addition to those described in the previous section, have been proposed and examined. These include different designs of spark plug, use of more than one plug, use of higher power, higher energy, or longer-duration discharges, and ignition systems that initiate the main combustion process with a high-temperature reacting jet—plasma-jet and flame-jet ignition systems.[62] Conventional ignition systems normally ignite the unburned fuel, air, burned gas mixture within the cylinder and perform satisfactorily under conditions away from the lean or dilute engine stable operating limit. Thus, these alternative ignition approaches have the goal of extending the engine stability limit (and/or of reducing the cyclic combustion variability near the stability limit), usually by achieving a faster initial burning rate than can be obtained with conventional systems. This section describes the more interesting of these alternative ignition approaches.

ALTERNATIVE SPARK-DISCHARGE APPROACHES. There are many different designs of spark plugs. These use different geometry electrodes, gap widths, and gap arrangements. The effects of the major plug electrode design features on the engine's stable lean operating limit are illustrated in Fig. 9-53.[63] Ignition system effects are important when misfire due to the quenching effect of the spark plug

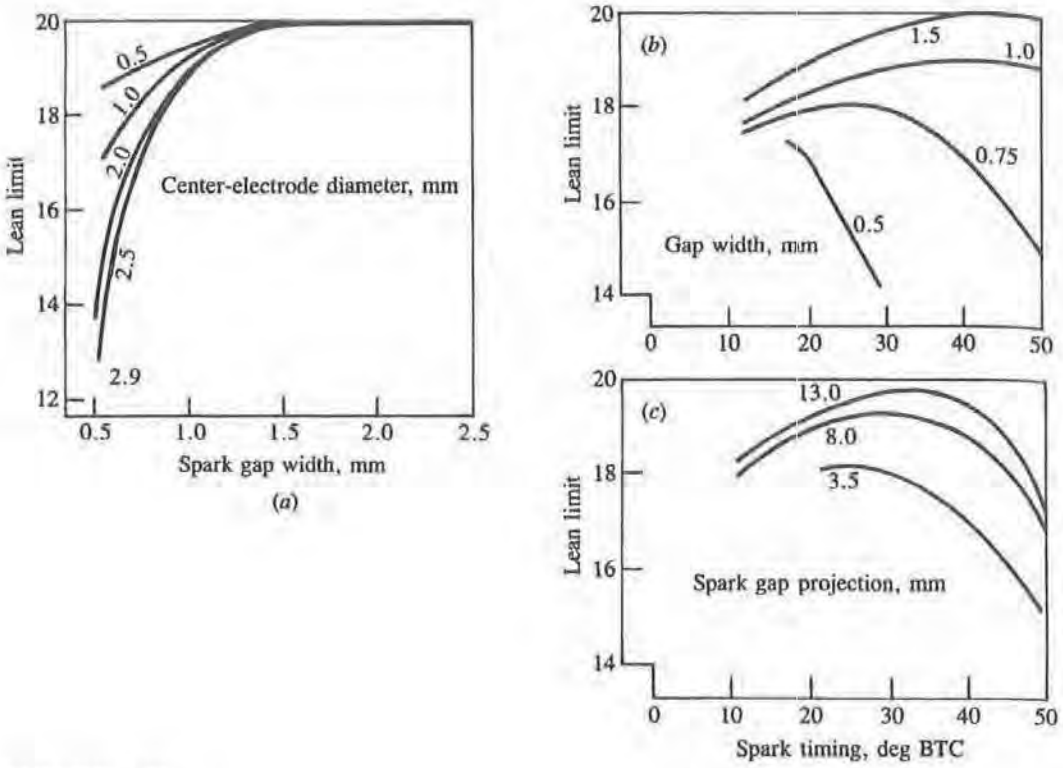


FIGURE 9-53
Effect of spark plug electrode diameter, plug gap width, and projection of gap into chamber on air/fuel ratio at engine's lean stable operating limit. Baseline conditions: 30 mJ spark energy, 3.5 mm projection, center electrode diameter 2.5 mm, gap width 0.75 mm, 40° BTC spark timing. 1600 rev/min, intake pressure 300 mmHg.[63]

electrodes determines the stable operating limit.† Thus, smaller spark plug center-electrode diameters (Fig. 9-53*a*), larger electrode gap widths (Fig. 9-53*b*), and higher electrode temperatures (obtained by projecting the gap further into the combustion chamber; Fig. 9-53*c*), all extend the lean stability limit to leaner (or more dilute) mixtures for the more advanced spark timings and smaller gap widths. For spark timing closer to TC and for larger gap widths, these data show the lean stability limit to be much less sensitive (or not sensitive at all) to plug geometry or spark energy. Multigap plugs, designed to produce a series of discharges which together form a long arc, have also been used to generate a larger initial flame kernel and thereby extend the lean limit.

Use of more than one plug, at separate locations in the combustion chamber and fired simultaneously, is also common.[49] The advantages are twofold. First, the effective flame area in the early stages of flame development is increased substantially (e.g., by almost a factor of two for two widely spaced plugs). Second, the variations in flow velocity and mixture composition in the vicinity of the (multiple) plugs produce less variability in the initial mixture burning rate than occurs with a single plug. Studies of heat-release rates, flame

† See Sec. 9.4.3 for a detailed discussion of the stable operating limit.

development angle, and rapid-burning angle, and imep and torque fluctuations have defined the effects of both increasing the number of ignition sites from 1 to 12 and of changing their geometric location.[64] These results confirm that increasing the number of simultaneously developing flame kernels increases the initial mixture burning rate, as anticipated. It also extends the lean stable operating limit and reduces cyclic combustion variability under conditions where slow and occasional partial-burning cycles would occur with fewer spark plug gaps.

Many studies have examined the effects of higher-energy discharges on engine operation near the lean operating limit. It is useful to differentiate between higher current discharges and longer duration discharges: most high-energy (conventional-type) ignition systems have both these features. The results of these studies show that away from the lean or dilute stable operating limit, increasing the discharge current or duration has no significant effect on engine operating characteristics. The higher current does, as would be expected, result in a larger flame kernel during the inflammation process and thereby modestly reduces the spark advance required for maximum brake torque with a given combustion chamber and set of operating conditions. Figure 9-54 shows these trends for rich, stoichiometric, and slightly lean mixtures. The figure also shows that both higher

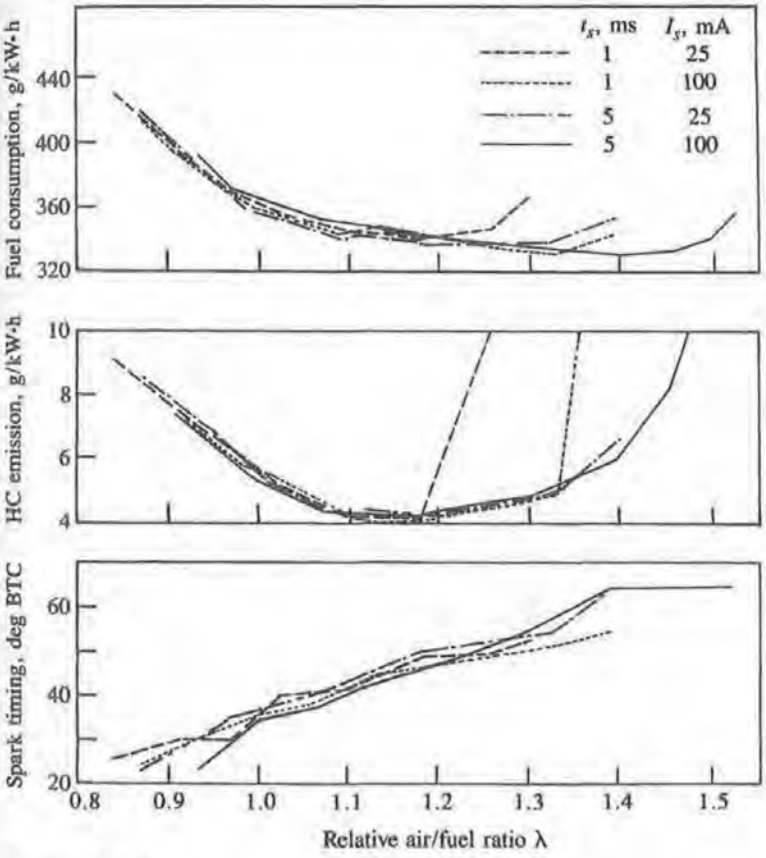


FIGURE 9-54
Effect of higher spark currents I_s and longer spark durations t_s on fuel consumption, HC emissions, and MBT spark timing, as a function of relative air/fuel ratio λ ($=1/\phi$). 2000 rev/min, bmep = 3 atm, 2.8-dm^3 six-cylinder engine.[65]

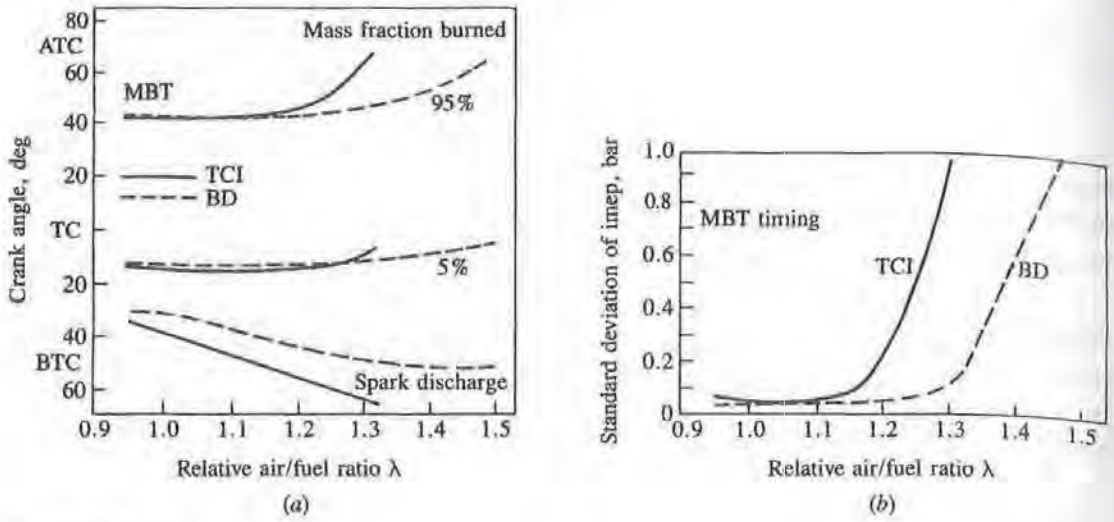


FIGURE 9-55
(*a*) MBT spark timing and location of 5 and 95 percent mass fraction burned points for conventional transistorized coil ignition (TCI) system (43 mJ energy, 2 ms duration) and breakdown system (BD) (43 mJ energy, ~10 ns duration) as function of relative air/fuel ratio λ ($=1/\phi$). (*b*) Standard deviation in indicated mean effective pressure as a function of relative air/fuel ratio λ for TCI and BD systems.[66]

currents and longer duration discharges do extend the lean engine stability limit [and also the dilute (with EGR) stability limit]. Note the HC emissions data, which indicate that longer discharges have a greater impact than higher currents on extending the *misfire* limit. The increase in fuel consumption as the lean operating limit is approached is due to the rapidly increasing cycle-by-cycle combustion variability.

The discussion of discharge fundamentals in Sec. 9.5.1 showed that depositing energy into the discharge during the initial short breakdown phase resulted in faster flame kernel growth than did depositing the same energy at slower rates. Ignition systems of this type have been used. In such systems, a capacitor is connected in parallel with the spark plug electrodes, and a low-impedance discharge path allows the energy stored in the capacitor to be discharged into the gap very rapidly. The anticipated effects on the engine's combustion process are observed. Away from the lean engine stability limit, the primary impact is a reduction in the flame development period due to the more rapid initial flame kernel growth. Thus MBT timing is less advanced with these breakdown systems than with conventional systems (see Fig. 9-55*a*). The lean limit can also be extended, and acceptable engine stability obtained (i.e., tolerable cycle-by-cycle combustion variations) for leaner or more dilute engine operation, as shown in Fig. 9-55*b*.[66, 67]

PLASMA-JET IGNITION. In a plasma-jet ignitor, the spark discharge is confined within a cavity that surrounds the plug electrodes, which connects with the combustion chamber via an orifice. The electrical energy supplied to the plug elec-

trodes is substantially increased above values used in normal ignition systems by allowing a capacitor to discharge at a relatively low voltage and high current through the spark generated in a conventional manner with a high-voltage low-current ignition system. Stored energies of about 1 J are typically used, and this energy is discharged in some 20 μs. This high-power discharge creates a high-temperature plasma so rapidly that the pressure in the cavity increases substantially, causing a supersonic jet of plasma to flow from the cavity into the main combustion chamber. The plasma enters the combustion chamber as a turbulent jet, preceded by a hemispherical blast wave. The gas dynamic effects of the blast wave are dissipated by the time combustion starts, which is typically of order 1 ms after the discharge commences. Ignition in the main combustion chamber takes place in the turbulent jet; the flame starts out as a turbulent flame in contrast to the flame with conventional ignition systems, which is initially laminarlike. The penetration of the jet depends on its initial momentum; it thus depends on the amount of energy deposited, cavity size, and orifice area. If the cavity is filled prior to ignition with a hydrocarbon (or a mixture of hydrocarbons) the ignition capabilities are enhanced due to the large increase in hydrogen atoms created in the plasma.[62]

The effects of plasma-jet ignitors on engine combustion are similar to those of breakdown ignition systems: the flame development period is significantly shortened, and the engine's lean stable operating limit is extended. In addition, the phenomenon of misfire, which is the failure to initiate combustion in a fraction of the engine's operating cycles, no longer occurs.[68] The lean operating limit of the engine is, however, normally controlled by flame extinguishment.

FLAME-JET IGNITION. With this type of system, ignition occurs in a prechamber cavity which is physically separated from the main chamber above the piston and is connected to it via one or more orifices or nozzles. As the flame develops in this cavity the pressure of the gases in the prechamber rises, forcing gas out into the main chamber through the orifice (or orifices) as one or more turbulent burning jets. The jet or jets penetrate into the main chamber, igniting the unburned mixture in the main chamber, thereby initiating the primary combustion process. Ignition within the cavity is usually achieved with a conventional spark discharge. The function of the prechamber or cavity is to transform the initial flame around the spark plug electrodes into one or more flame jets in the main chamber, which have a substantial surface area that can ignite extremely lean or dilute mixtures in a repeatable manner. Many different systems for achieving this goal have been developed; some of these have been used in production spark-ignition engines. Examples of the three major types of flame-jet ignition systems are shown in Fig. 9-56.

Figure 9-56*a* shows an example of the simplest type of flame-jet ignition concept (often called a *torch cell*). The cavity has no separate valve so is unscavenged; nor is there any prechamber fuel metering system. The function of the prechamber cavity is to increase the initial growth rate of the flame immediately following spark discharge by having this flame growth take place in a

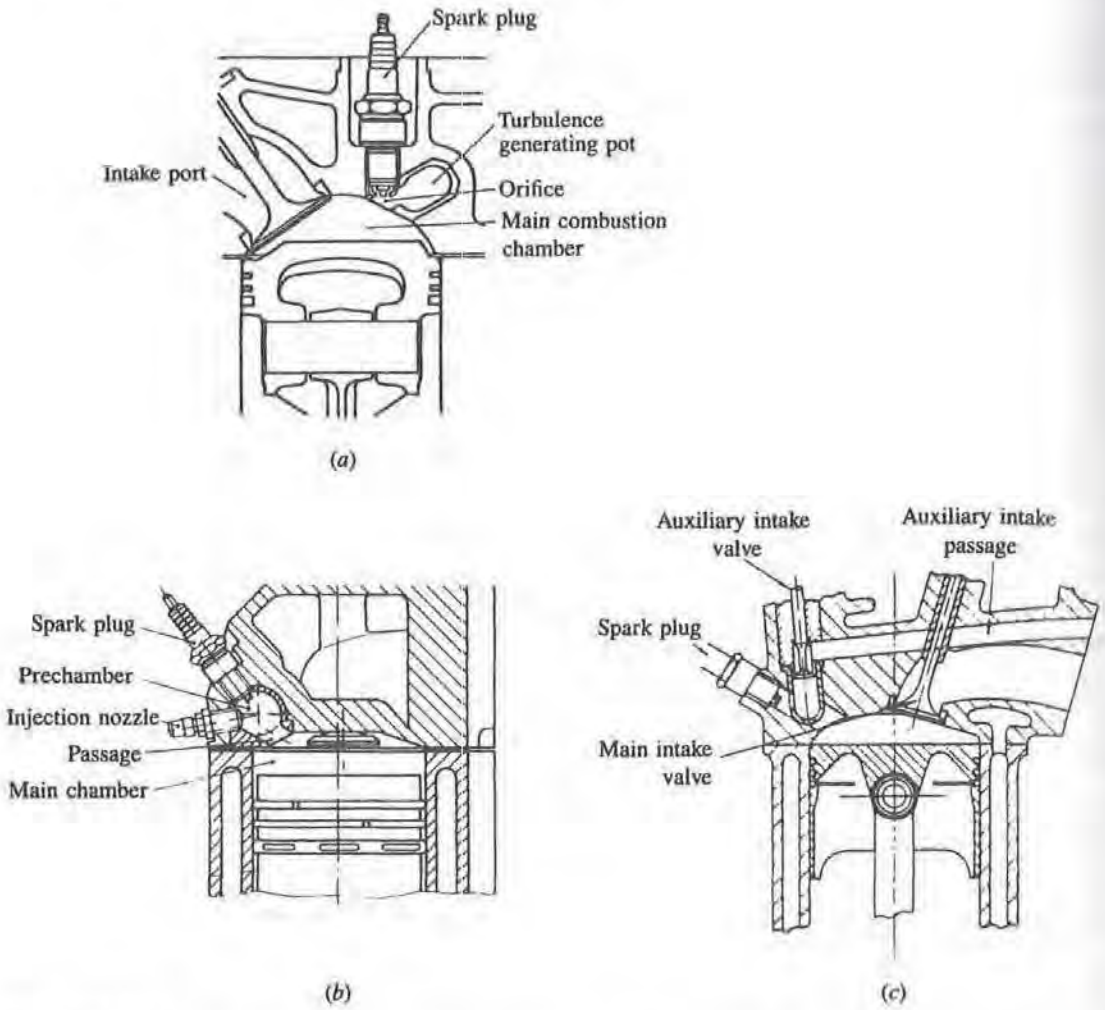


FIGURE 9-56
Flame-jet ignition concepts: (*a*) turbulence-generating torch cell;[69] (*b*) prechamber stratified-charge engine with auxiliary fuel injector with no prechamber scavenging;[70] (*c*) prechamber stratified-charge engine with prechamber inlet valve and auxiliary carburetor.[71]

more turbulent region than the main combustion chamber: the flame jet or jets which then emerge from the cavity produce a large initial flame surface area in the main chamber to start the bulk charge combustion process. The prechamber system shown was called a turbulent generating pot.[69] Another approach is to incorporate the cavity into the spark plug. Systems with prechamber volumes varying from 20 percent of the clearance volume to less than 1 percent have been developed. The flow pattern produced within the prechamber by the flow into the cavity during compression and the location of the spark plug electrodes within the cavity and of the nozzle or orifice are critical design issues. A major problem with these systems is that the prechamber is never completely scavenged by fresh mixture between cycles, so the burned gas fraction in the unburned mixture within the prechamber is always substantially higher than the burned gas fraction in the unburned main chamber mixture.[72]

Figure 9-56*b* and *c* shows two *prechamber stratified-charge* engine flame-jet ignition concepts. Here the mixture in the prechamber cavity is enriched by addition of fuel so that it ends up being slightly rich-of-stoichiometric at the time of spark discharge. The initial inflammation process in the cavity then occurs more rapidly and more repeatably. The operating principle of these stratified-charge systems is described briefly in Sec. 1.9. Figure 9-56*b* shows a system where the prechamber is unscavenged and fuel is injected directly into the prechamber cavity (in addition to the main fuel-injection process which occurs into the fresh charge in the intake system) to richen the mixture (which is lean overall) at the time of spark to an easily ignitable rich-of-stoichiometric composition. With this approach, the prechamber volume is usually 20 to 25 percent of the clearance volume. Figure 9-56*c* shows a prechamber stratified-charge flame-jet ignition system where the prechamber is scavenged between each combustion event. With this approach, a separate small intake valve feeds very rich mixture into the prechamber during the intake process, while the main fuel metering system feeds lean mixture to the main intake valve. During intake the prechamber is completely scavenged by the rich intake stream. During compression the lean mixture flowing from the main chamber to the prechamber brings the prechamber mixture equivalence ratio to slightly rich-of-stoichiometric at the time of spark discharge.[71]

The number and size of the orifices connecting the prechamber and the main chamber have a significant effect on the development of the main chamber burning process. Two different approaches are shown in the flame development stage in Fig. 9-57. Figure 9-57*a* shows the jets produced when the prechamber has more than one small nozzle which direct the burning prechamber mixture deep into the main chamber charge. A fast burning of the lean main-chamber charge results. With this approach, prechamber volumes of 2 to 3 percent of the clearance volume and nozzle area/prechamber volume ratios of 0.03 to 0.04 cm^{-1} are used. Figure 9-57*b* shows the approach used by Honda in their CVCC engine.

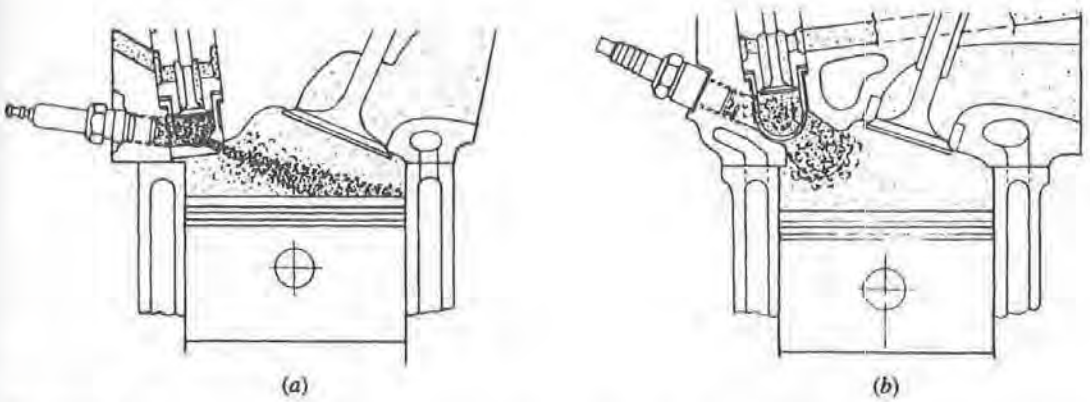


FIGURE 9-57
Two different approaches to prechamber orifice design with the prechamber stratified-charge carbureted and scavenged engine: (*a*) one or more small orifice(s) for deep jet penetration and faster burning process; (*b*) large orifice for lower-velocity jet and slower burn.[73]

A larger prechamber (5 to 12 percent) and larger orifice (orifice area/prechamber volume ratio of 0.04 to 0.2 cm^{-1}) gives a lower velocity jet which penetrates the main chamber charge more slowly, resulting in a slower burn.

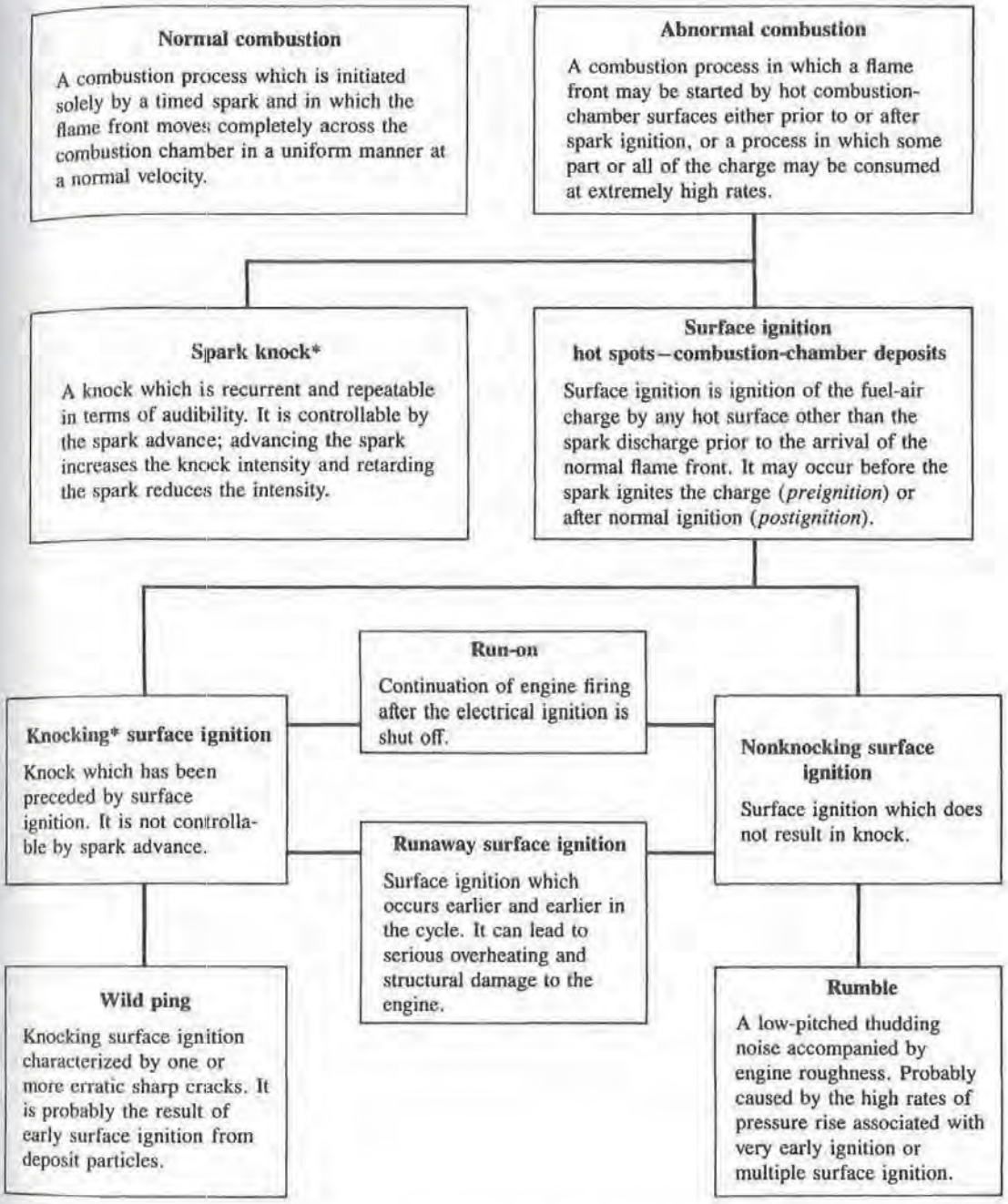
All these concepts extend the engine's lean stable operating limit, relative to equivalent conventional engines, by several air/fuel ratios. For example, the unscavenged cavity without auxiliary fueling can operate satisfactorily at part-load with air/fuel ratios of 18 (equivalence ratio $\phi \approx 0.8$, relative air/fuel ratio $\lambda \approx 1.25$). The prechamber stratified-charge flame-jet ignition concepts can operate much leaner than this; however, the best combination of fuel consumption and emissions characteristics is obtained with $\phi \approx 0.9 - 0.75$, $\lambda \approx 1.1 - 1.3$.[70, 71] One performance penalty associated with all these flame-jet ignition concepts is the additional heat losses to the prechamber walls due to increased surface area and flow velocities. The stratified-charge prechamber concepts also suffer an efficiency penalty, relative to equivalent operation with uniform air/fuel ratios, due to the presence of fuel-rich regions during the combustion process.

9.6 ABNORMAL COMBUSTION: KNOCK AND SURFACE IGNITION

9.6.1 Description of Phenomena

Abnormal combustion reveals itself it many ways. Of the various abnormal combustion processes which are important in practice, the two major phenomena are knock and surface ignition. These abnormal combustion phenomena are of concern because: (1) when severe, they can cause major engine damage; and (2) even if not severe, they are regarded as an objectionable source of noise by the engine or vehicle operator. *Knock* is the name given to the noise which is transmitted through the engine structure when essentially spontaneous ignition of a portion of the end-gas—the fuel, air, residual gas, mixture ahead of the propagating flame—occurs. When this abnormal combustion process takes place, there is an extremely rapid release of much of the chemical energy in the end-gas, causing very high local pressures and the propagation of pressure waves of substantial amplitude across the combustion chamber. *Surface ignition* is ignition of the fuel-air mixture by a hot spot on the combustion chamber walls such as an overheated valve or spark plug, or glowing combustion chamber deposit: i.e., by any means other than the normal spark discharge. It can occur before the occurrence of the spark (*preignition*) or after (*postignition*). Following surface ignition, a turbulent flame develops at each surface-ignition location and starts to propagate across the chamber in an analogous manner to what occurs with normal spark ignition.

Because the spontaneous ignition phenomenon that causes knock is governed by the temperature and pressure history of the end gas, and therefore by the phasing and rate of development of the flame, various combinations of these two phenomena—surface ignition and knock—can occur. These have been categorized as indicated in Fig. 9-58. When autoignition occurs repeatedly, during



*Knock: The noise associated with autoignition of a portion of the fuel-air mixture ahead of the advancing flame front. Autoignition is the spontaneous ignition and the resulting very rapid reaction of a portion or all of the fuel-air mixture.

FIGURE 9-58
Definition of combustion phenomena—normal and abnormal (knock and surface ignition)—in a spark-ignition engine. (*Courtesy Coordinating Research Council.*)

otherwise normal combustion events, the phenomena is called *spark-knock*. Repeatedly here means occurring more than occasionally: the knock phenomenon varies substantially cycle-by-cycle, and between the cylinders of a multicylinder engine, and does not necessarily occur every cycle (see below). Spark-knock is controllable by the spark advance: advancing the spark increases the knock severity or intensity and retarding the spark decreases the knock. Since surface ignition usually causes a more rapid rise in end-gas pressure and temperature than occurs with normal spark ignition (because the flame either starts propagating sooner, or propagates from more than one source), knock is a likely outcome following the occurrence of surface ignition. To identify whether or not surface ignition causes knock, the terms knocking surface ignition and nonknocking surface ignition are used. Knocking surface ignition usually originates from preignition caused by glowing combustion chamber deposits: the severity of knock generally increases the earlier that preignition occurs. Knocking surface ignition cannot normally be controlled by retarding the spark timing, since the spark-ignited flame is not the cause of knock. Nonknocking surface ignition is usually associated with surface ignition that occurs late in the operating cycle.

The other abnormal combustion phenomena in Fig. 9-58, while less common, have the following identifying names. Wild ping is a variation of knocking surface ignition which produces sharp cracking sounds in bursts. It is thought to result from early ignition of the fuel-air mixture in the combustion chamber by glowing loose deposit particles. It disappears when the particles are exhausted and reappears when fresh particles break loose from the chamber surfaces. Rumble is a relatively stable low-frequency noise (600 to 1200 Hz) phenomenon associated with deposit-caused surface ignition in high-compression-ratio engines. This type of surface ignition produces very high rates of pressure rise following ignition. Rumble and knock can occur together. Run-on occurs when the fuel-air mixture within the cylinder continues to ignite after the ignition system has been switched off. During run-on, the engine usually emits knocklike noises. Run-on is probably caused by compression ignition of the fuel-air mixture, rather than surface ignition. Runaway surface ignition is surface ignition that occurs earlier and earlier in the cycle. It is usually caused by overheated spark plugs or valves or other combustion chamber surfaces. It is the most destructive type of surface ignition and can lead to serious overheating and structural damage to the engine.[74]

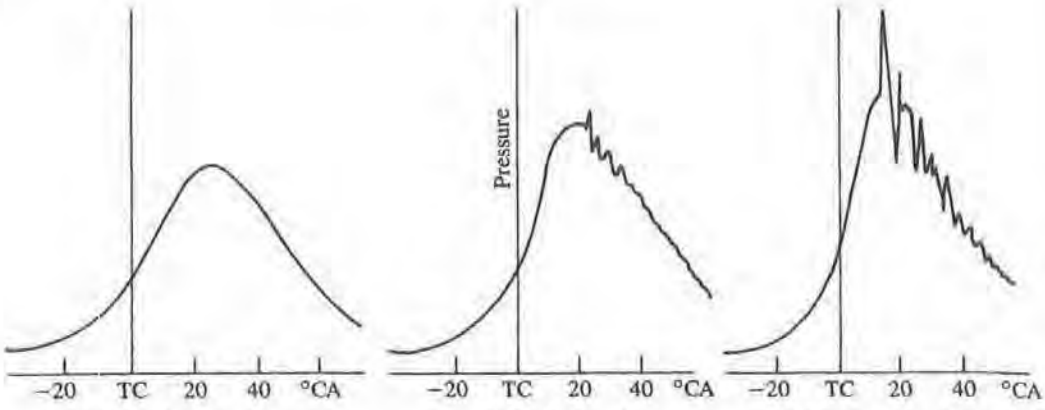
After some additional description of surface-ignition phenomena, the remainder of Sec. 9.6 will focus on knock. This is because surface ignition is a problem that can be solved by appropriate attention to engine design, and fuel and lubricant quality. In contrast, knock is an inherent constraint on engine performance and efficiency since it limits the maximum compression ratio that can be used with any given fuel.

Of all the engine surface-ignition phenomena in Fig. 9-58, preignition is potentially the most damaging. Any process that advances the start of combustion from the timing that gives maximum torque will cause higher heat rejection because of the increasing burned gas pressures and temperatures that result.

Higher heat rejection causes higher temperature components which, in turn, can advance the preignition point even further until critical components can fail. The parts which can cause preignition are those least well cooled and where deposits build up and provide additional thermal insulation: primary examples are spark plugs, exhaust valves, metal asperities such as edges of head cavities or piston bowls. Under normal conditions, using suitable heat-range spark plugs, preignition is usually initiated by an exhaust valve covered with deposits coming from the fuel and from the lubricant which penetrates into the combustion chamber. Colder running exhaust valves and reduced oil consumption usually alleviate this problem: locating the exhaust valve between the spark plug and the end-gas region avoids contact with both the hottest burned gas near the spark plug and the end-gas. Engine design features that minimize the likelihood of preignition are: appropriate heat-range spark plug, removal of asperities, radiused metal edges, well-cooled exhaust valves with sodium-cooled valves as an extreme option.[75, 76]

Knock primarily occurs under wide-open-throttle operating conditions. It is thus a direct constraint on engine performance. It also constrains engine efficiency, since by effectively limiting the temperature and pressure of the end-gas, it limits the engine compression ratio. The occurrence and severity of knock depend on the knock resistance of the fuel and on the antiknock characteristics of the engine. The ability of a fuel to resist knock is measured by its octane number: higher octane numbers indicate greater resistance to knock (see Sec. 9.6.3). Gasoline octane ratings can be improved by refining processes, such as catalytic cracking and reforming, which convert low-octane hydrocarbons to high-octane hydrocarbons. Also, antiknock additives such as alcohols, lead alkyls, or an organomanganese compound can be used. The octane-number requirement of an engine depends on how its design and the conditions under which it is operated affect the temperature and pressure of the end-gas ahead of the flame and the time required to burn the cylinder charge. An engine's tendency to knock, as defined by its *octane requirement*—the octane rating of the fuel required to avoid knock—is increased by factors that produce higher temperatures and pressures or lengthen the burning time. Thus knock is a constraint that depends on both the quality of available fuels and on the ability of the engine designer to achieve the desired normal combustion behavior while holding the engine's propensity to knock at a minimum.[74]

The pressure variation in the cylinder during knocking combustion indicates in more detail what actually occurs. Figure 9-59 shows the cylinder pressure variation in three individual engine cycles, for normal combustion, light knock, and heavy knock, respectively.[77] When knock occurs, high-frequency pressure fluctuations are observed whose amplitude decays with time. Figures 9-59*a* and *b* have the same operating conditions and spark advance. About one-third of the cycles in this engine at these conditions had no trace of knock and had normal, smoothly varying, cylinder pressure records as in Fig. 9-59*a*. Knock of varying severity occurred in the remaining cycles. With light or trace knock, knock occurs late in the burning process and the amplitude of the pressure fluctuations



(*a*) Normal combustion, spark 28°BTC

(*b*) Slight knock, spark 28°BTC

(*c*) Intense knock, spark 32°BTC

FIGURE 9-59
Cylinder pressure versus crank angle traces of cycles with (*a*) normal combustion, (*b*) light knock, and (*c*) heavy knock. 4000 rev/min, wide-open throttle, 381-cm^3 displacement single-cylinder engine.[77]

is small (Fig. 9-59*b*). With heavy knock, illustrated here with more advanced spark timing and by selecting an especially high intensity knocking cycle, knock occurs closer to top-center earlier in the combustion process and the initial amplitude of the pressure fluctuation is much larger. These pressure fluctuations produce the sharp metallic noise called "knock." They are the result of the essentially spontaneous release of much of the end-gas fuel's chemical energy. This produces a substantial *local* increase in gas pressure and temperature, thereby causing a shock wave to propagate away from the end-gas region across the combustion chamber. This shock wave, the expansion wave that accompanies it, and the reflection of these waves by the chamber walls create the oscillatory pressure versus time records shown in Fig. 9-59*b* and *c*. Note that once knock occurs, the pressure distribution across the combustion chamber is no longer uniform: transducers located at different points in the chamber will record different pressure levels at a given time until the wave propagation phenomena described above have been damped out.[78]

Many methods of knock detection and characterization have been used. The human ear is a surprisingly sensitive knock detector and is routinely used in determining the octane requirement of an engine—the required fuel quality the engine must have to avoid knock. Knock detectors used for knock control systems normally respond to the vibration-driven acceleration of parts of the engine block caused by knocking combustion pressure waves. A high-intensity flash is observed when knock occurs; this is accompanied by a sharp increase in ionization. Optical probes and ionization detectors have therefore been used. The spark plug can serve as an ionization detector. For more detailed studies of knock in engines, the piezoelectric pressure transducer is the most useful monitoring device. Often the transducer signal is filtered so that the pressure fluctuations caused by knock are isolated.[75]

The amplitude of the pressure fluctuation is a useful measure of the inten-

sity of knock because it depends on the amount of end-gas which ignites spontaneously and rapidly, and because engine damage due to knock results from the high gas pressures (and temperatures) in the end-gas region. Use of this measure of knock severity or intensity shows there is substantial variation in the extent of knock, cycle-by-cycle. Figure 9-60 shows the knock intensity in one hundred consecutive cycles in a given cylinder of a multicylinder engine operating at fixed conditions for knocking operation. The intensity varies randomly from essentially no knock to heavy knock.[79] Cylinder-to-cylinder variations are also substantial due to variations in compression ratio, mixture composition and conditions, burn rate, and combustion chamber cooling. One or more cylinders may not knock at all while others may be knocking heavily.[80]

Since the knock phenomenon produces a nonuniform state in the cylinder, and since the details of the knock process in each cycle and in each cylinder are different, a fundamental definition of knock intensity or severity is extremely difficult. The ASTM-CFR method for rating fuel octane quality (see Sec. 9.6.3) by the severity of knocking combustion uses the time derivative of pressure during the cycle. Cylinder pressure is determined with a pressure transducer. The low-frequency component of pressure change due to normal combustion is filtered out and the rate of pressure rise is averaged over many cycles during the pressure fluctuations following knock. This approach obviously provides only an average relative measure of knock intensity. The maximum rate of pressure rise has been used to quantify knock severity. An accelerometer mounted on the engine can give indications of relative knock severity provided that it is mounted in the same location for all tests. The most precise measure of knock severity is the maximum amplitude of the pressure oscillations that occur with knocking combustion. The cylinder pressure signal (from a high-frequency response pressure transducer) is filtered with a band-pass filter so that only the component of the pressure signal that corresponds to the fluctuations occurring after knock remains. The filter is set for the first transverse mode of gas vibration in the cylinder (in the 3 to 10 kHz range, depending on bore and chamber geometry). The maximum amplitude of pressure oscillation gives a good indication of the severity of knock.[81] The knock intensities in individual cycles shown in Fig. 9-60 were determined in

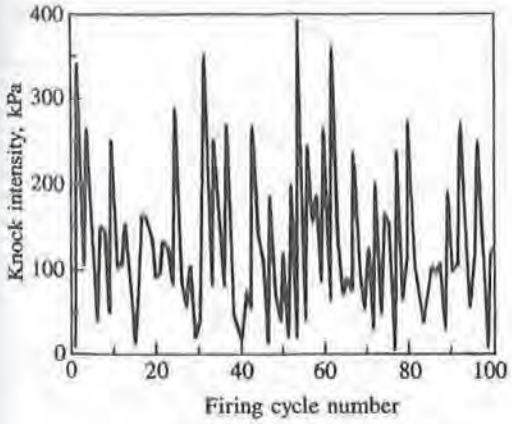


FIGURE 9-60
Knock intensity (maximum amplitude of band-pass-filtered pressure signal) in one hundred individual consecutive cycles. One cylinder of V-8 engine, 2400 rev/min, wide-open throttle.[79]

this manner.[79] Note that because the pressure fluctuations are the consequence of a wave propagation phenomenon, the location of the pressure transducer in relation to the location of the knocking end-gas and the shape of the combustion chamber will affect the magnitude of the maximum recorded pressure-fluctuation amplitude.

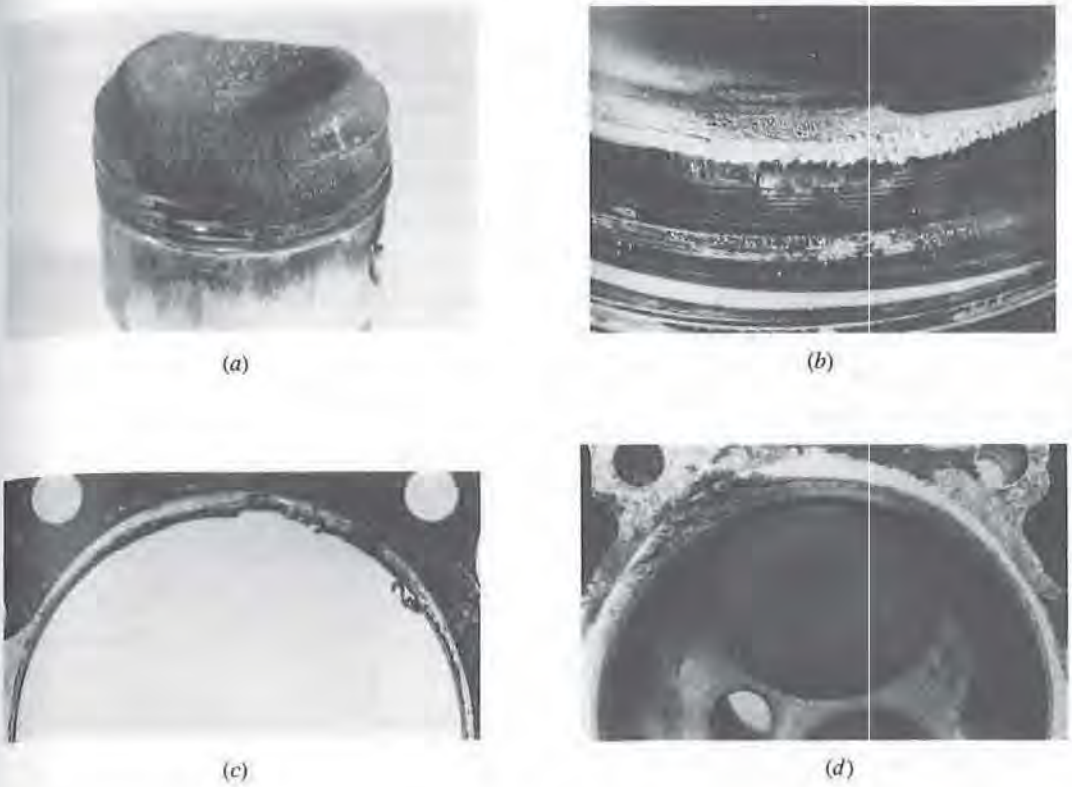
The impact of knock depends on its intensity and duration. Trace knock has no significant effect on engine performance or durability. Heavy knock can lead to extensive engine damage. In automobile applications, a distinction is usually made between "acceleration knock" and "constant-speed knock." Acceleration knock is primarily an annoyance, and due to its short duration is unlikely to cause damage. Constant-speed knock, however, can lead to two types of engine damage. It is especially a problem at high engine speeds where it is masked by other engine noises and is not easily detected. Heavy knock at constant speed can easily lead to:

1. Preignition, if significant deposits are present on critical combustion chamber components. This could lead to runaway preignition.†
2. Runaway knock—spark-knock occurring earlier and earlier, and therefore more and more intensely. This soon leads to severe engine damage.
3. Gradual erosion of regions of the combustion chamber, even if runaway knock does not occur.

The engine can be damaged by knock in different ways: piston ring sticking; breakage of the piston rings and lands; failure of the cylinder head gasket; cylinder head erosion; piston crown and top land erosion; piston melting and holing. Examples of component damage due to preignition and knock are shown in Fig. 9-61.[82–84]

The mechanisms that cause this damage are thought to be the following. Preignition damage is largely thermal as evidenced by fusion of spark plugs or pistons. When knock is very heavy, substantial additional heat is transferred to the combustion chamber walls and rapid overheating of the cylinder head and piston results. Under these conditions, knock is not stable: the overheating increases the engine's octane requirement which in turn increases the intensity of knock. It becomes heavier and heavier, and the uncontrolled running away of this phenomena can lead to engine failure in minutes. This damage is due to overheating of the engine: the piston and rings seize in the bore. The damage due to heavy knock over extended periods—erosion of piston crowns and (aluminum) cylinder heads in the end-gas region—is due primarily to the high gas pressures in this region. Extremely high pressure pulses of up to 180 atm due to heavy knock can occur locally in the end-gas region, in the 5 to 10 kHz frequency

† Note that heavy knock can also remove deposits from the combustion chamber walls, thereby decreasing the octane requirement of the engine.



(*a*) (*b*) (*c*) (*d*)

FIGURE 9-61
Examples of component damage from abnormal engine combustion. (*a*) Piston holing by preignition;[83] (*b*) piston crown erosion after 10 hours of high-speed knocking;[82] (*c*) cylinder head gasket splitting failure due to heavy knock;[83] (*d*) erosion of aluminum cylinder head along the top of the cylinder liner due to heavy knock.[83]

range. These high local pressures are combined with the higher-than-normal local surface temperatures which occur with the higher knocking heat fluxes and weaken the material. Pitting and erosion due to fatigue with these excessive mechanical stresses, and breakage of rings and lands, can then occur.[78, 82–84]

9.6.2 Knock Fundamentals

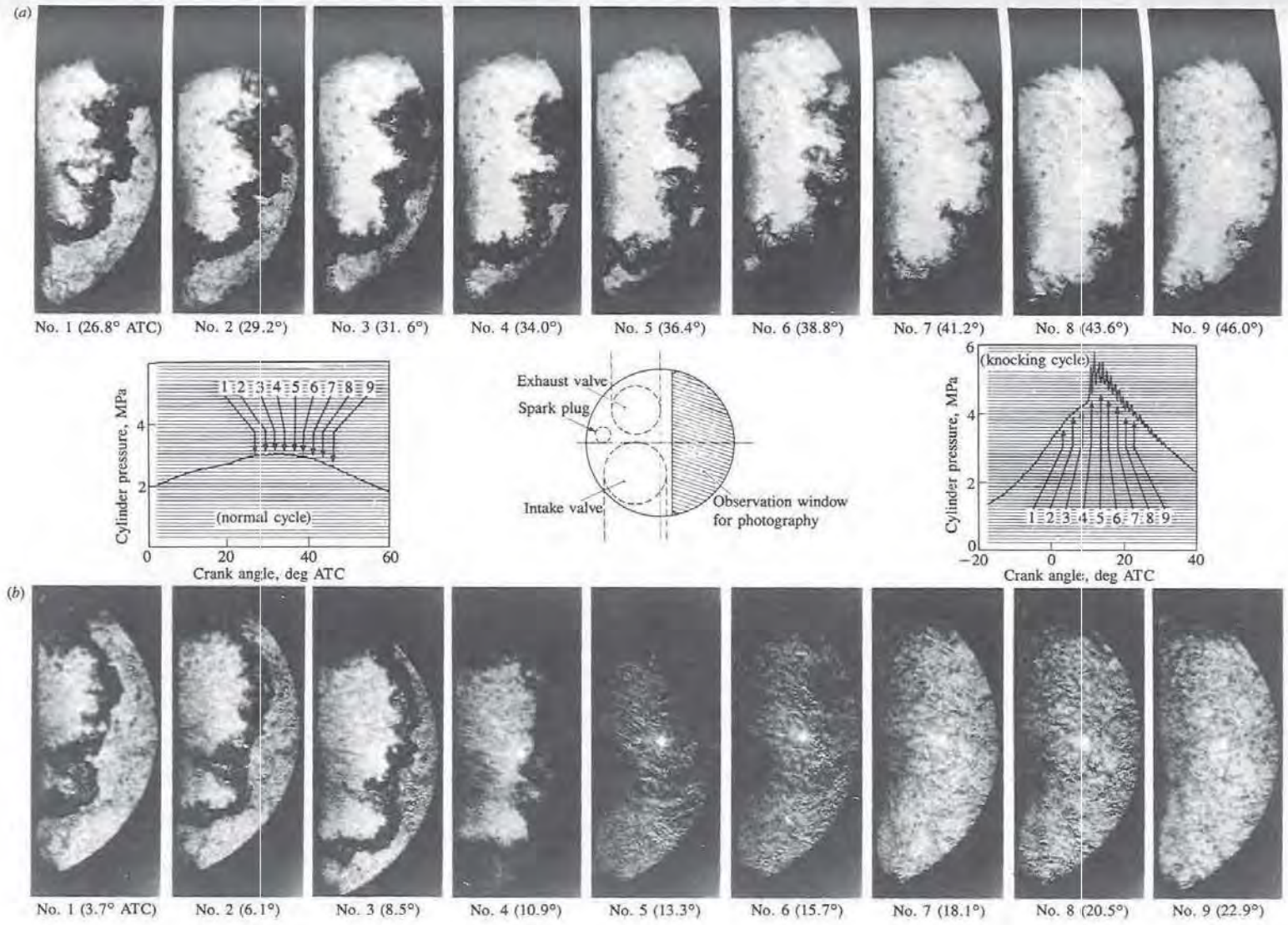
As yet, there is no complete fundamental explanation of the knock phenomenon over the full range of engine conditions at which it occurs. It is generally agreed that knock originates in the extremely rapid release of much of the energy contained in the end-gas ahead of the propagating turbulent flame, resulting in high local pressures. The nonuniform nature of this pressure distribution causes pressure waves or shock waves to propagate across the chamber, which may cause the chamber to resonate at its natural frequency. Two theories have been advanced to explain the origin of knock: the autoignition theory and the detonation theory. The former holds that when the fuel-air mixture in the end-gas region is compressed to sufficiently high pressures and temperatures, the fuel oxidation process—starting with the preflame chemistry and ending with rapid

energy release—can occur spontaneously in parts or all of the end-gas region. The latter theory postulates that, under knocking conditions, the advancing flame front accelerates to sonic velocity and consumes the end-gas at a rate much faster than would occur with normal flame speeds.[75] These theories attempt to describe what causes the rapid release of chemical energy in the end-gas which creates very high pressures, locally, in the end-gas region. The engine phenomenon "knock" includes also the propagation of strong pressure waves across the chamber, chamber resonance, and transmission of sound through the engine structure. The detonation theory has led many to call knock "detonation." However, the more general term "knock" is preferred, since this engine phenomenon includes more than the end-gas energy release, and there is much less evidence to support the detonation theory than the autoignition theory as the initiating process. Most recent evidence indicates that knock originates with the spontaneous or autoignition of one or more local regions within the end-gas. Additional regions (some adjacent to already ignited regions and some separated from these regions) then ignite until the end-gas is essentially fully reacted. This sequence of processes can occur extremely rapidly. Thus, the autoignition theory is most widely accepted.

Photographic studies of knocking combustion have been an important source of insight into the fundamentals of the phenomenon over the past fifty years.† Figure 9-62 shows two sets of schlieren photographs, one from a cycle with normal combustion and the other from a cycle with knock.[88] These photographs were taken in an overhead valve engine with a disc-shaped combustion chamber, with a window which permits observation of the chamber opposite to the spark plug. A reflecting mirror on the piston crown permits use of the schlieren technique which identifies regions where changes in gas density exist. Operating conditions, except for spark advance, were the same for both cycles. In the normal combustion sequence, the turbulent flame front moves steadily through the end-gas as combustion goes to completion. The cylinder pressure varies smoothly throughout this process. When the spark is advanced by 15°, the end-gas temperature and pressure are increased significantly and knock occurs. In this sequence of photographs (*b*), the initial flame propagation process (photographs 1 to 3) is like that of the normal combustion sequence: then almost

† See Refs. 85 to 87 for early high-speed photographic studies. See Refs. 88 to 91 for some recent studies.

FIGURE 9-62
Schlieren photographs from high-speed movies of (*a*) normal flame propagation through the end gas and (*b*) knocking combustion (autoignition occurs in photograph 4), with corresponding cylinder pressure versus crank angle traces. Disc-shaped combustion chamber with details of window shown in insert. 1200 rev/min, 80 percent volumetric efficiency, $(A/F) = 12.5$; spark timing: (*a*) 10° BTC, (*b*) 25° BTC.[88]


(a)
No. 1 (26.8° ATC)
No. 2 (29.2°)
No. 3 (31. 6°)
No. 4 (34.0°)
No. 5 (36.4°)
No. 6 (38.8°)
No. 7 (41.2°)
No. 8 (43.6°)
No. 9 (46.0°)
Cylinder pressure, MPa
1 2 3 4 5 6 7 8 9
(normal cycle)
Crank angle, deg ATC
Exhaust valve
Spark plug
Intake valve
Observation window for photography
(knocking cycle)
(b)
No. 1 (3.7° ATC)
No. 2 (6.1°)
No. 3 (8.5°)
No. 4 (10.9°)
No. 5 (13.3°)
No. 6 (15.7°)
No. 7 (18.1°)
No. 8 (20.5°)
No. 9 (22.9°)

the entire region ahead of the flame appears dark (photograph 4). Between photographs 3 and 4 substantial changes in the density and temperature throughout most of the end-gas region have occurred. Examination of the cylinder pressure trace shows that this corresponds closely to the time when the pressure recorded by the pressure transducer rises rapidly. Immediately after this, pressure oscillations (at 6 to 8 kHz) are detected. In photograph 5 the flame is no longer visible: the end-gas expansion has pushed the flame back out of the field of view. Subsequent photographs are alternatively lighter and darker, indicative of changing local density fields as pressure waves propagate back and forth across the chamber.

More extensive studies of this type, which relate photographs from high-speed movies of the combustion process to the cylinder pressure development, indicate that the location or locations where ignition of one or more portions of the end-gas first occur and the subsequent rate with which the ignition process develops throughout the rest of the end-gas vary substantially cycle-by-cycle and with the intensity of the knocking process. Figure 9-63 shows five shadowgraph photographs from a knocking engine cycle in a research engine similar to that shown in Fig. 9-62.[89] The photographs are 33 μs apart; the total sequence shown lasts 1°. The first photograph shows the flame front prior to onset of knock. The second photograph shows the onset of autoignition with the appearance of dark regions near the wall (two identified by arrows) where substantial density gradients resulting from local energy release exist. The third, fourth, and fifth photographs show the spread of these ignited regions with time through the remaining end-gas. The exact location where autoignition occurred was identified with a photodigitizing system which ranked regions of the photograph by their brightness or darkness. The digitized version of the second photograph is also shown in Fig. 9-63. Additional smaller regions of autoignition are evident adjacent to the wall and in the vicinity of the flame front. While the location of autoig-

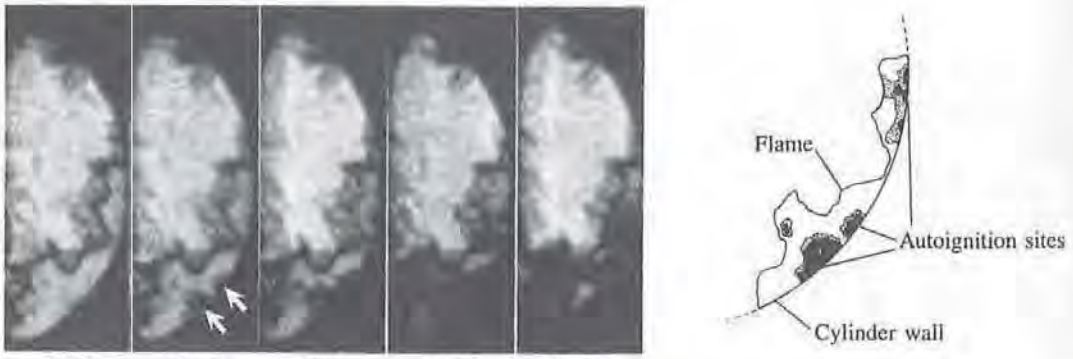


FIGURE 9-63
Five shadowgraph photographs of knocking combustion cycle identifying location of autoignition sites (arrows). Crank angle of each photo indicated: 33 μs between frames. Operating conditions and engine details as in Fig. 9-62. Photodigitized picture of second photograph showing additional details of the autoignition sites in the end-gas region on right.[89]

nition sites varied with engine operating conditions, the majority of occurrences in this study were in the vicinity of the cylinder wall. The rate of spread of the autoignited end-gas region also varied significantly. Under heavy knocking conditions the entire end-gas region became ignited very rapidly and high-amplitude pressure oscillations occurred. Under trace knock conditions, autoignition could occur; yet the spread of the autoignited region could be sufficiently slow for no pressure oscillations to be detected.

When the above-described end-gas ignition process occurs rapidly, the gas pressure in the end-gas region rises substantially due to the rapid release of the end-gas fuel's chemical energy. The erosion damage that knock can produce, due to stress-induced material fatigue as described in the previous section, indicates the location of this high-pressure region. With the chamber geometry typical of most engines where the flame propagates toward the cylinder wall, the damage is confined to the thin crescent-shaped region on the opposite side of the chamber to the spark plug, where one expects the end-gas to be located. A shock wave propagates from the outer edge of this high-pressure end-gas region across the chamber at supersonic velocity, and an expansion wave propagates into the high-pressure region toward the near wall. The presence of such a shock wave has been observed photographically.[90] The shock wave and expansion wave reflect off the walls of the chamber, eventually producing standing waves. Usually these standing waves are due to transverse gas vibration and are of substantial amplitude. The amplitude of the pressure oscillations builds up as the standing waves are established, and then decays as the gas motion is damped out. The frequency of the pressure oscillations (normally in the 5 to 10 kHz range) decreases with time as the initially finite-amplitude supersonic pressure waves decay to small-amplitude sound waves.[80] Thus the pressure signal detected with a transducer during a knocking combustion cycle will depend on the details of the end-gas ignition process, the combustion chamber geometry, and the location of the transducer in relation to the end-gas region.

The pressure variation across the cylinder bore, due to knock, can be illustrated by the following example. Consider the disc-shaped combustion chamber with the spark plug located in the cylinder wall shown in Fig. 9-64*a*. Figure 9-64*b* shows the pressure and temperature distribution across the combustion chamber due to the normal flame propagation process, at the time rapid ignition of the end-gas occurs. If the end-gas ignites completely and instantaneously, its pressure and temperature will suddenly rise, as shown. A shock wave will now propagate to the right and an expansion wave to the left, as shown in the distance-time diagram in Fig. 9-64*c*. These waves reflect off the walls and interact. The pressures at the cylinder wall, in the end-gas region and on the opposite side of the chamber at the spark plug, develop as shown in Fig. 9-64*d*. Figure 9-65 shows two simultaneously recorded pressure traces with heavy knock from two transducers at the top of the cylinder liner, one located near the spark plug and one in the end-gas region. In the end-gas region the pressure rises extremely rapidly when knock occurs, to a value considerably higher than that recorded on the opposite side of the chamber where the pressure rises more gradually. Standing

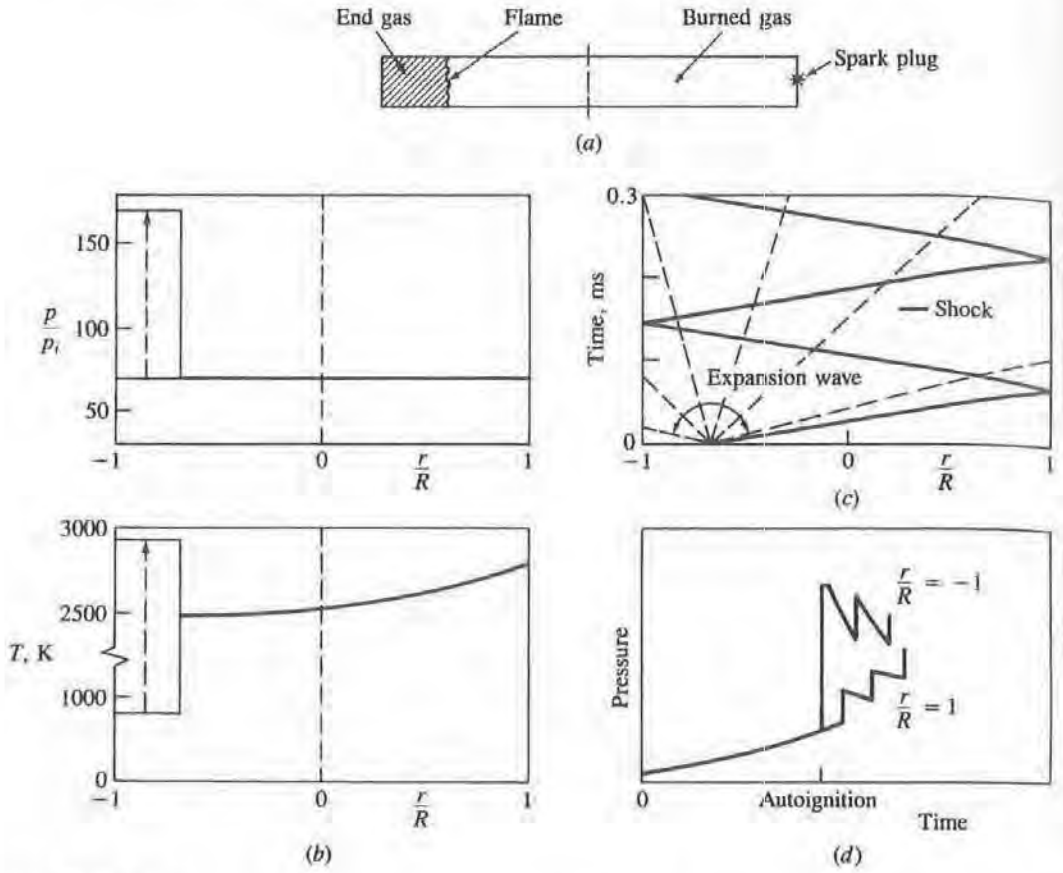


FIGURE 9-64
Illustration of how cylinder pressure distribution develops following knock. (*a*) Schematic of disc-shaped combustion chamber at time of knock. (*b*) Pressure and temperature across the diameter of a disc-shaped engine combustion chamber, before and after end-gas autoignition (assumed to occur very rapidly, at constant end-gas density). (*c*) Schematic of shock and expansion wave pattern following end-gas autoignition on distance-time plot. (*d*) Pressure variation with time at cylinder wall in the end-gas region, and at the opposite side of the cylinder.

waves are then set up and the amplitudes of the oscillations decay as the waves are damped out.[78]

The fundamental theories of knock are based on models for the autoignition of the fuel-air mixture in the end-gas. *Autoignition* is the term used for a rapid combustion reaction which is not initiated by any external ignition source. Often in the basic combustion literature this phenomenon is called an explosion. Before discussing the relevant theories of hydrocarbon oxidation, the necessary terminology will be defined and illustrated with the autoignition behavior of the much simpler hydrogen-oxygen system. For the hydrocarbons commonly found in practical fuels, the chemical reaction schemes by which the fuel molecules are broken down and react to form products are extremely complicated, and are as yet imperfectly understood.

The autoignition of a gaseous fuel-air mixture occurs when the energy re-

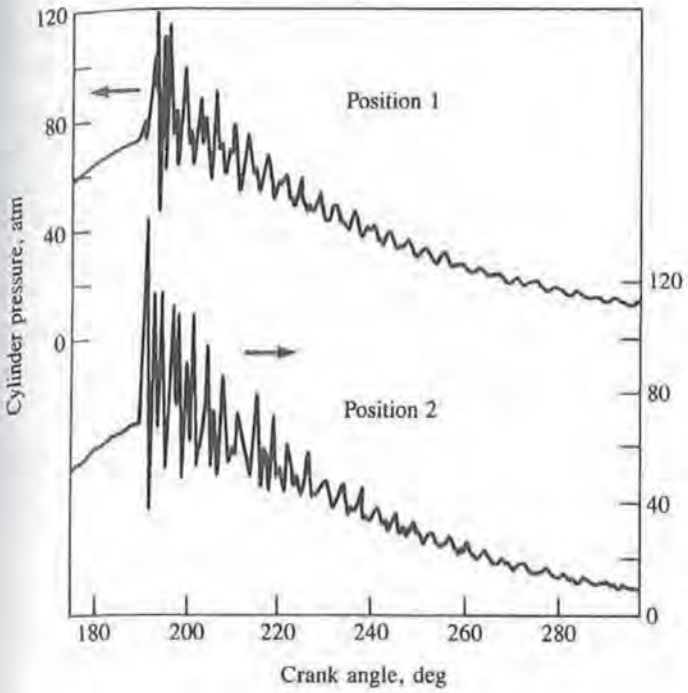


FIGURE 9-65
Simultaneously recorded pressure traces on opposite sides of spark-ignition engine combustion chamber in heavily knocking cycle. Position 1: at top of cylinder liner closest to spark plug. Position 2: at top of cylinder liner farthest from spark plug. 2000 rev/min, wide-open throttle, $(A/F) = 12.3$, spark advance 20° BTC.[78]

leased by the reaction as heat is larger than the heat lost to the surroundings; as a result the temperature of the mixture increases, thereby rapidly accelerating, due to their exponential temperature dependence, the rates of the reactions involved. The state at which such spontaneous ignition occurs is called the *self-ignition temperature* and the resulting self-accelerating event where the pressure and temperature increases rapidly is termed a *thermal explosion.*

In complex reacting systems such as exist in combustion, the "reaction" is not a single- or even a few-step process; the actual chemical mechanism consists of a large number of simultaneous, interdependent reactions or *chain reactions.* In such chains there is an *initiating* reaction where highly reactive intermediate species or *radicals* are produced from stable molecules (fuel and oxygen). This step is followed by *propagation* reactions where radicals react with the reactant molecules to form products and other radicals to continue the chain. The process ends with *termination* reactions where the chain propagating radicals are removed. Some propagating reactions produce two reactive radical molecules for each radical consumed. These are called *chain-branching* reactions. When, due to chain-branching, the number of radicals increases sufficiently rapidly, the reaction rate becomes extremely fast and a *chain-branching explosion* occurs. While the terms thermal and chain-branching explosions have been introduced separately, in many situations the self-accelerations in temperature and radicals occur simultaneously and the two phenomena must be combined.[92, 93]

The oxidation of hydrogen at high pressures and temperatures provides a good illustration of these phenomena. For stoichiometric hydrogen-oxygen mixtures, no reaction occurs below 400°C unless the mixture is ignited by an external

source such as a spark; above 600°C explosion occurs spontaneously at all pressures.†

The initiating steps proceed primarily through hydrogen peroxide (H_2O_2) to form the hydroxyl radical (OH) at lower temperatures, or through dissociation of H_2 at higher temperatures to form the hydrogen atom radical H. The basic radical-producing chain sequence is composed of three reactions:

$$\begin{aligned} &\text{(R1)} \quad H + O_2 = O + OH \\ &\text{(R2)} \quad O + H_2 = H + OH \\ &\text{(R3)} \quad H_2 + OH = H_2O + H \end{aligned} \tag{9.56}$$

The first two reactions are chain-branching; two radicals are produced for each one consumed. The third reaction is necessary to complete the chain sequence: starting with one hydrogen atom, the sequence R1 then R2 and R3 produces two H; starting with OH, the sequence R3, then R1, then R2 produces two OH. Since all three reactions are required, the multiplication factor is less than 2 but greater than 1. Repeating this sequence over and over again rapidly builds up high concentrations of radicals from low initial levels.

However, these three reactions do not correspond to the overall stoichiometry

$$H_2 + \tfrac{1}{2}O_2 = H_2O$$

and other reactions must become important. In flames, the chain-branching process ceases when the reverse of reactions R1–R3 become significant. A quasi equilibrium is established; while the overall process has proceeded a considerable way toward completion, a substantial amount of the available energy is still contained in the high radical concentrations. Over a longer time scale, this energy is released through three-body recombination reactions (the principal chain terminating reactions):

$$\begin{aligned} &\text{(R4)} \quad H + H + M = H_2 + M \\ &\text{(R5)} \quad O + O + M = O_2 + M \\ &\text{(R6)} \quad H + OH + M = H_2O + M \end{aligned} \tag{9.57}$$

M refers to any available third-body species, required in these recombination reactions to remove the excess energy.[92]

With this introductory background let us now turn to the autoignition of hydrocarbon-air mixtures. The process by which a hydrocarbon is oxidized can exhibit four different types of behavior, or a sequential combination of them, depending on the pressure and temperature of the mixture: slow reactions; single

† In between, three separate explosion limits—pressure-temperature boundaries for specific mixture ratios of fuel and oxidizer that separate regions of slow and fast reaction—exist; these are not, however, of interest to us here.

or multiple cool flames (slightly exothermic reactions); two-stage ignition (cool flame followed by a hot flame); single-stage ignition (hot flame). Slow reactions are a low-pressure, low-temperature (<200°C) phenomenon not normally occurring in engines. At 300 to 400°C one or more combustion waves often appear, accompanied by faint blue light emission; the reaction is quenched, however, when only a small fraction of the reactants have reacted and the temperature rise is only tens of degrees. These are called *cool flames.* Depending on conditions and the fuel, a cool flame may be followed by a "hot flame" or high-temperature explosion where the reaction accelerates rapidly after ignition. This is termed *two-stage ignition.* As the temperature of the mixture increases, a transition from two-stage to single-stage ignition occurs. While all hydrocarbons exhibit induction intervals which are followed by a very rapid reaction rate, some hydrocarbon compounds do not exhibit the cool flame or two-stage ignition behavior.

Figure 9-66 shows these ignition limits for isooctane, methane, and benzene. For isooctane, ignition in the low-temperature regions is by a two-stage process: there is a first time interval before the cool flame appears and then a second time interval from the appearance of the cool flame to the hot flame combustion process. Ignition in the high-temperature region is by a continuous one-stage process. The cool flame phenomena vary enormously with hydrocarbon structure. Normal paraffins give strong cool flames, branched-chain paraffins are more resistant. Olefins give even lower luminosity cool flames with longer induction periods. Methane shows only the high-temperature ignition limit, as indicated in Fig. 9-66. Benzene, also, does not exhibit the cool flame phenomenon and other aromatics give hardly detectable luminosity.[75] It is thought that some com-

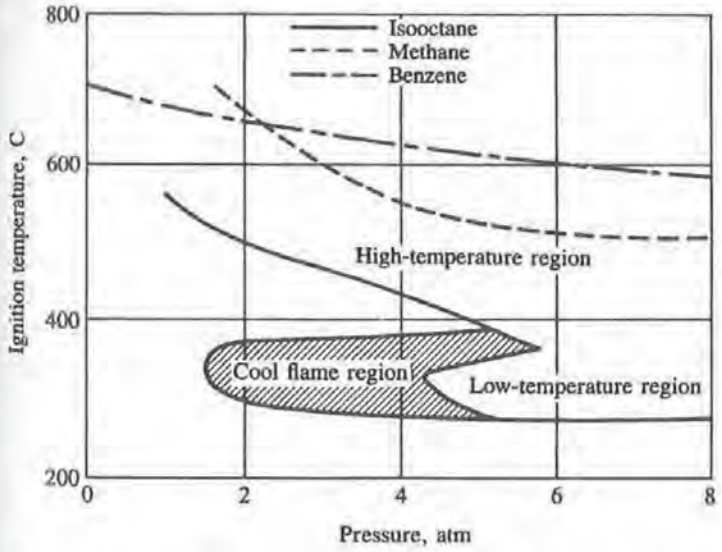


FIGURE 9-66
Ignition diagrams for isooctane, methane, and benzene. Two-stage ignition occurs in the low-temperature region; the first stage may be a cool flame. Single-stage ignition occurs in the high-temperature region.[94]

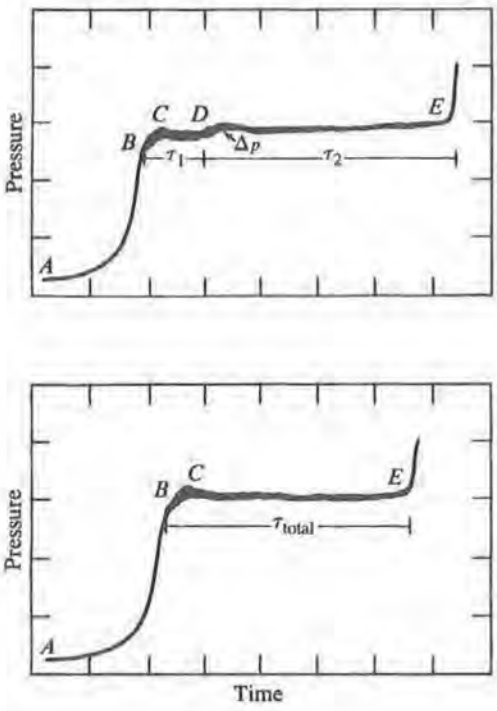


FIGURE 9-67
Pressure records of the autoignition of isooctane-air mixture ($\phi = 0.9$) in a rapid compression machine. $A \rightarrow B \rightarrow C$ is the compression process. Top: two-stage ignition (at D, then at E) at postcompression pressure of 1.86 MPa and temperature of 686 K. Bottom: single-stage ignition at E at post-compression conditions of 2.12 MPa and 787 K. Vertical scale: 690 kPa/division. Horizontal scale: 1 ms/division.[95]

pounds knock by a low-temperature two-stage ignition mechanism, some via a high-temperature single-stage ignition mechanism, and for some fuels both mechanisms may play a role.

Examples of these two mechanisms in rapid-compression machine experiments, where a homogeneous isooctane-air mixture was compressed to different final conditions in a piston-cylinder apparatus and allowed to autoignite, are shown in Fig. 9-67. $A \rightarrow B \rightarrow C$ is the piston-motion-produced compression. The top trace shows a well-defined cool flame at D, preceding hot ignition at E. The lower trace, at a higher temperature, shows a single-stage ignition process.[95]

Many of the above phenomena—long induction periods, initial slow increase in reaction rate, two-stage ignition process—cannot be explained with simple mechanisms like the hydrogen oxidation process reviewed above. Although chain-branching reactions are taking place, the radical generation process must be more complex. Explanations of the long induction periods are based on the formation of unstable but long-lived intermediates. These intermediates can then either react to form stable molecules or to form active radicals, the dominance and rate of either of these paths depending on the temperature: i.e.,[93]

$$\mathrm{A} \rightarrow \mathrm{M}^* \begin{cases} \text{I} & \text{Stable molecules} \\ \text{II} & \text{Radicals} \end{cases} \tag{9.58}$$

This is called a *degenerate-branching* mechanism. Hydroperoxides are an important metastable intermediate produced in the chain propagation process in the low-temperature ignition process. They have the form ROOH, where R is an

organic radical (formed by abstracting a hydrogen atom from a fuel hydrocarbon molecule). However, at higher temperatures, ROOH is no longer the major product of the chain propagation process: instead, it is hydrogen peroxide, H_2O_2. While H_2O_2 is relatively stable at lower temperatures, above 500°C it decomposes into two OH radicals.

An outline of the basic hydrocarbon (RH) oxidation process due to Semenov is as follows:[93]

(R1)	$RH + O_2 \dashrightarrow \dot{R} + H\dot{O}_2$	}	Chain initiation
(R2)	$\dot{R} + O_2 \dashrightarrow R\dot{O}_2$	⎫	
(R3)	$\dot{R} + O_2 \dashrightarrow$ olefin $+ H\dot{O}_2$	⎪	
(R4)	$R\dot{O}_2 + RH \dashrightarrow ROOH + \dot{R}$	⎬	Chain propagation
(R5)	$R\dot{O}_2 \dashrightarrow R'CHO + R''O$	⎪	(9.59)
(R6)	$H\dot{O}_2 + RH \dashrightarrow H_2O_2 + \dot{R}$	⎭	
(R7)	$ROOH \dashrightarrow R\dot{O} + \dot{O}H$	⎫	Degenerate branching
(R8)	$R'CHO + O_2 \dashrightarrow R'\dot{C}O + H\dot{O}_2$	⎭	
(R9)	$R\dot{O}_2 \dashrightarrow$ destruction	}	Chain termination

The dot denotes an active radical; each dash denotes the number of free bonds on the organic radical R.

Reaction R1 is slow and explains the induction period in hydrocarbon combustion. R2 is fast and of near-zero activation energy. R3 leads to olefins known to occur in the oxidation of saturated hydrocarbons. R4 and R5 yield the main intermediates. The degenerate branching comes about from the delay in decomposition of the reactive species in R7 and R8. As one radical is used up to form the reactants in R7 and R8, the multiple radicals do not appear until these reactants decompose.[93] A more extensive discussion of hydrocarbon oxidation mechanisms can be found in Benson.[96]

The following evidence indicates the relevance of the above mechanism to knock in engines. End-gas sampling studies have identified products of slow combustion reactions of isooctane; these principally include olefins, cyclic ethers, aldehydes (R'CHO), and ketones (R''CO).[97] Such studies have shown increasing concentrations of peroxides (predominantly H_2O_2 with traces of organic peroxides) with isoparaffinic fuels which show two-stage ignition behavior. Higher temperature, single-stage ignition fuels such as benzene and toluene gave no detectable peroxide. Aldehydes and ketones have been measured in significant and increasing concentrations in motored engines where the peak cycle temperature was steadily increased. In motored engines, the occurrence of cool flames, the two-stage nature of the autoignition ignition process at intermediate compression temperatures, and the transition to a single-stage ignition process at very high compression ratios (i.e., motored-engine gas temperatures with a peak much higher than normal to simulate end-gas conditions in a firing engine) have also been demonstrated.[75, 94]

Two types of models of this autoignition process have been developed and used: (1) empirical induction-time correlations; (2) chemical mechanisms which embody many or all of the features of the "full" hydrocarbon oxidation process given in Eq. (9.59).

Induction-time correlations are derived by matching an Arrhenius function to measured data on induction or autoignition times, for given fuel-air mixtures, over the relevant mixture pressure and temperature ranges. It is then assumed that autoignition occurs when

$$\int_{t=0}^{t_i} \frac{dt}{\tau} = 1 \tag{9.60}$$

where τ is the induction time at the instantaneous temperature and pressure for the mixture, t is the elapsed time from the start of the end-gas compression process ($t = 0$), and t_i is the time of autoignition. This equation can be derived by assuming that the overall rate of production of the critical species in the induction period chemistry, for a given mixture, depends only on the gas state and that the concentration of the critical species required to initiate autoignition is fixed (i.e., independent of the gas state).[98]

A number of empirical relations for induction time for individual hydrocarbons and blended fuels have been developed from fundamental or engine studies of autoignition (see Ref. 99). These relations have the form

$$\tau = Ap^{-n} \exp\left(\frac{B}{T}\right) \tag{9.61}$$

where A, n, and B are fitted parameters that depend on the fuel. The ability of these types of equations to predict the onset of knock with sufficient accuracy is unclear. The most extensively tested correlation is that proposed by Douaud and Eyzat:[100]

$$\tau = 17.68\left(\frac{\text{ON}}{100}\right)^{3.402} p^{-1.7} \exp\left(\frac{3800}{T}\right) \tag{9.62}$$

where τ is in milliseconds, p is absolute pressure in atmospheres, and T is in kelvin. ON is the appropriate octane number of the fuel (see Sec. 9.6.3). If the temperature and pressure time history of the end-gas during an individual cycle are known, Eqs. (9.60) and (9.62) together can be used to determine whether autoignition occurs before the normally propagating flame consumes the end-gas.

An important question with any model of the end-gas autoignition process is characterizing the end-gas temperature. During intake, the combustion chamber walls are hotter than the entering gases: thus, heat is transferred from the walls to the fresh mixture. During compression, the mixture temperature rises to levels substantially above the wall temperature. A thermal boundary layer will build up adjacent to the wall, as heat is now transferred to the wall. Unburned mixture away from the wall will be compressed essentially adiabatically (see Sec. 12.6.5). In addition, any unburned mixture which for some portion of time during intake and compression has been in close proximity to the exhaust valve and

piston (which run at higher temperatures than the water-cooled wall regions) could be at higher temperatures than adiabatically compressed mixture, due to substantial heat transfer to the unburned mixture. Thus, the end-gas temperature is not uniform and the distribution of temperature is extremely complex. Often, the *mean* unburned mixture temperature is used to characterize its state. Alternatively, the *core* temperature corresponding to adiabatic compression of mixture from conditions at the start of compression is used. In the absence of substantial heating by the exhaust valve and piston, the core temperature is a better representation of the maximum unburned mixture at any point in the cycle.

While more complex and complete chemical models of the autoignition process are being developed for simple paraffinic hydrocarbon fuel compounds (e.g., Refs. 91 and 101), no detailed models are yet available for use with real blended fuels in engines. However, a generalized kinetic model for hydrocarbon oxidation based on a degenerate branched-chain mechanism, known as the Shell model, has been developed and tested with some success. The model uses generic chemical entities representative of a variety of individual species which undergo a set of generalized reactions. This is justified by the broadly similar (though complex) ignition behavior of a variety of different fuel molecules and the similar kinetics exhibited by the organic radicals of the same type in the hydrocarbon oxidation process [Eq. (9.59)].[95, 102]

The Shell model is based on a generic eight-step degenerate chain-branching reaction scheme. The scheme involves the fuel (RH), oxygen, radicals formed from the fuel (R), products (P), intermediate product (Q), and degenerate-branching agent (B). The rate constants are either fixed at values consistent with the literature or fitted so that measured induction times (such as those illustrated in Fig. 9-67) are adequately predicted.[102] An example of results obtained with this scheme is shown in Fig. 9-68. It shows the calculated pressure, temperature, and species concentrations in the end-gas region of an operating spark-ignition

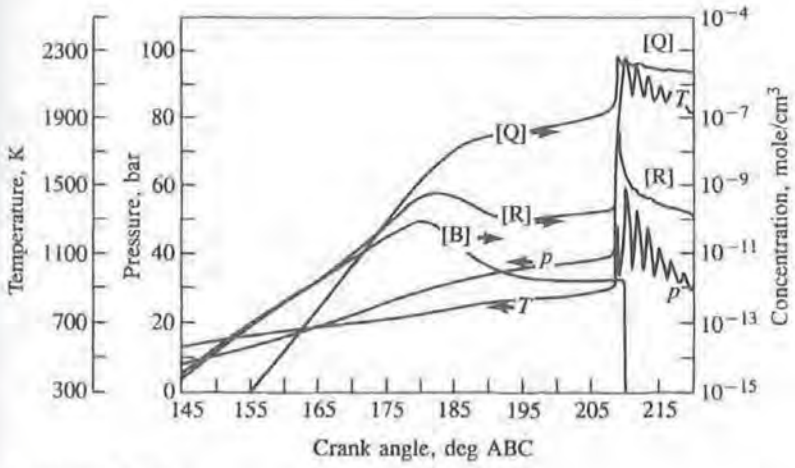


FIGURE 9-68
Pressure, temperature, and composition in the end-gas, before, during, and after autoignition, predicted by the Shell model in spark-ignition engine combustion process. B, Q, R defined in text.[103]

engine, leading up to knock at 209° ABC. In this example, the autoignition model has been incorporated in a multidimensional model of the flow and flame propagation processes within the combustion chamber (see Sec. 14.5).[103]

9.6.3 Fuel Factors

The tendency to knock depends on engine design and operating variables which influence end-gas temperature, pressure, and the time spent at high values of these two properties before flame arrival. Thus, for example, the tendency to knock is decreased through reductions in the end-gas temperature that follow from decreasing the inlet air temperature and retarding the spark from MBT timing. However, knock is a phenomenon that is governed by both engine and fuel factors; its presence or absence in an engine depends primarily on the antiknock quality of the fuel.

Individual hydrocarbon compounds vary enormously in their ability to resist knock, depending on their molecular size and structure. Their tendency to knock has been measured by the *critical compression ratio* of an engine: i.e., the compression ratio at which, under specified operating conditions, the specific fuel compound will exhibit incipient knock. Knocking tendency is related to molecular structure† as follows:[105, 106]

Paraffins

1. Increasing the length of the carbon chain increases the knocking tendency.
2. Compacting the carbon atoms by incorporating side chains (thereby shortening the length of the basic chain) decreases the tendency to knock.
3. Adding methyl groups (CH_3) to the side of the basic carbon chain, in the second from the end or center position, decreases the knocking tendency.

Olefins

4. The introduction of one double bond has little antiknock effect; two or three double bonds generally result in appreciably less knocking tendency.
5. Exceptions to this rule are acetylene (C_2H_2), ethylene (C_2H_4), and propylene (C_3H_6), which knock much more readily than the corresponding saturated hydrocarbons.

Napthenes and aromatics

6. Napthenes have significantly greater knocking tendency than have the corresponding size aromatics.
7. Introducing one double bond has little antiknock effect; two and three double bonds generally reduce knocking tendency appreciably.

† See Sec. 3.3 for a review of hydrocarbon structure and its nomenclature. A more extensive discussion is given by Goodger.[104]

8. Lengthening the side chain attached to the basic ring structure increases the knocking tendency in both groups of fuels, whereas branching of the side chain decreases the knocking tendency.

Figure 9-69 identifies the magnitude of these trends on a plot of the critical compression ratio against the number of carbon atoms in the molecule. The strong dependence of knocking tendency on fuel molecular size and structure is apparent.

Practical fuels are blends of a large number of individual hydrocarbon compounds from all the hydrocarbon series of classes: alkanes (paraffins), cyclanes (napthenes), alkenes (olefins), and aromatics (see Sec. 3.3). A practical measure of a fuel's resistance to knock is obviously required.[107, 108] This property is defined by the fuel's *octane number*. It determines whether or not a fuel will knock in a given engine under given operating conditions: the higher the octane number, the higher the resistance to knock. Octane number is not a single-valued quantity, and may vary considerably depending on engine design, operating conditions during test, ambient weather conditions during test, mechanical condition of engine, and type of oil and fuel used in past operation. The octane number (ON) scale is based on two hydrocarbons which define the ends of the scale. By definition, normal heptane (n-C_7H_{16}) has a value of zero and isooctane (C_8H_{18}: 2,2,4-trimethylpentane) has an octane number of 100. These hydrocarbons were chosen because of the great difference in their ability to resist knock and the fact that isooctane had a higher resistance to knock than any of the gasolines available at the time the scale was established. Blends of these two hydrocarbons define the knock resistance of intermediate octane numbers: e.g., a blend of 10 percent n-heptane and 90 percent isooctane has an octane number of 90. A fuel's octane number is determined by measuring what blend of these two hydrocarbons matches the fuel's knock resistance.

Several octane rating methods for fuels have been developed. Two of these—the research method (ASTM D-2699)† and the motor method (ASTM D-2700)—are carried out in a standardized single-cylinder engine. In the motor method, the engine operating conditions are more severe; i.e., the conditions are more likely to produce knock. In addition, road octane rating methods have been developed to define the antiknock quality of fuels in cars operated on the road or on chassis dynamometers. The engine used in the ASTM research and motor methods is the single-cylinder engine developed under the auspices of the Cooperative Fuel Research Committee in 1931—the CFR engine.‡ This test engine is a robust four-stroke overhead-valve engine with an 82.6-mm (3.25-in) bore and 114.3-mm (4.5-in) stroke. The compression ratio can be varied from 3 to 30 while

† ASTM denotes American Society for Testing and Materials; the letter and number defines the specific testing code.

‡ The Cooperative Fuel Research Committee is now the Coordinating Research Council, Inc.

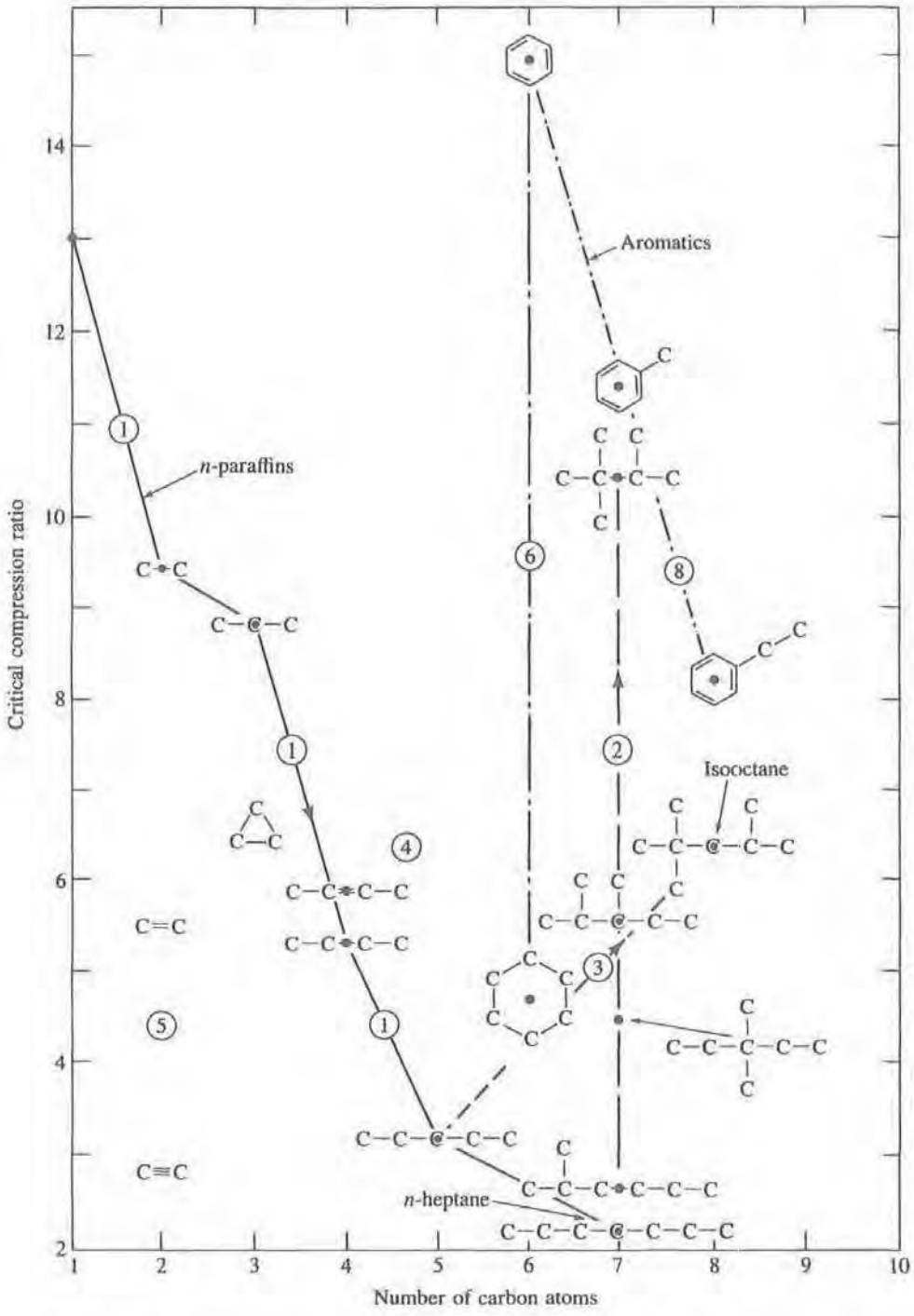


FIGURE 9-69
Critical compression ratio (for incipient knock at 600 rev/min and 450 K coolant temperature) as a function of number of carbon atoms in hydrocarbon molecule, illustrating the effects of changes in molecular structure. (*Developed from Lovell.*[105])

TABLE 9.6
Operating conditions for research and motor methods

	Research method	Motor method
Inlet temperature	52°C (125°F)	149°C (300°F)
Inlet pressure	Atmospheric	
Humidity	0.0036–0.0072 kg/kg dry air	
Coolant temperature	100°C (212°F)	
Engine speed	600 rev/min	900 rev/min
Spark advance	13° BTC (constant)	19–26° BTC (varies with compression ratio)
Air/fuel ratio	Adjusted for maximum knock	

the engine is operating, with a mechanism which raises or lowers the cylinder and cylinder head assembly relative to the crankcase. A special valve mechanism maintains a constant tappet clearance with vertical adjustment of the head. The engine is equipped with multiple-bowl carburetors so two reference fuels (usually blends of *n*-heptane and isooctane) and the fuel being rated can be placed in separate bowls. By means of a selector valve, the engine can be operated on any of the three fuels. The engine operating conditions of the research and motor methods are summarized in Table 9.6. The test conditions are chosen to represent the engine operating range where knock is most severe. With the fuel under test, the fuel/air ratio is adjusted for maximum knock. The compression ratio is then adjusted to produce knock of a standardized intensity, as measured with a magnetostriction knock detector. The level of knock obtained with the test fuel is bracketed by two blends of the reference fuels not more than two octane numbers apart (with one knocking more and one less than the test fuel). The octane number of the gasoline is then obtained by interpolation between the knockmeter scale readings for the two reference fuels and their octane numbers. For fuels below 100 ON, the *primary reference fuels* are blends of isooctane and *n*-heptane; the percent by volume of isooctane in the blend is the octane number. For fuels above 100 ON, the antiknock quality of the fuel is determined in terms of isooctane plus milliliters of the antiknock additive, tetraethyl lead, per U.S. gallon.†

The octane ratings of several individual hydrocarbon compounds and common blended fuels are summarized in App. D, Table D.4. Practically all fuels exhibit a difference between their research and motor octane numbers. The motor method of determining ON uses more severe operating conditions than the

† The octane number of the fuel is calculated from $ON = 100 + 28.28T/[1.0 + 0.736T + (1.0 + 1.472T - 0.035216T^2)^{1/2}]$, where T is milliliters of tetraethyl lead per U.S. gallon. Tetraethyl lead, $(C_2H_5)_4Pb$, contains 64.06 weight percent lead; 1 ml of TEL contains 1.06 grams of lead.

research method (higher inlet mixture temperature, more advanced timing). Thus, the motor octane number (MON) is usually lower than the research octane number (RON). The numerical difference between these octane numbers is called the *fuel sensitivity*:

$$\text{Fuel sensitivity} = \text{RON} - \text{MON} \tag{9.63}$$

Fuel sensitivity varies with the source of crude petroleum and refining processes used. The primary reference fuels themselves (mixtures of isooctane and *n*-heptane), by definition, have the same octane numbers by both the research and motor methods. Since the primary reference fuels are paraffins, we would expect other paraffins to have little or no sensitivity. In contrast, olefins and aromatics have high sensitivity. In general, therefore, straight-run gasolines containing high percentages of saturated hydrocarbons have low sensitivity, while cracked or reformed gasolines containing large percentages of unsaturated hydrocarbons have high sensitivity. Fuels having high sensitivity generally, but not always, have lower road octane ratings (i.e., octane ratings determined in cars in on-the-road use) than do low-sensitivity fuels of the same research octane number. Regular grade unleaded gasoline typically has a RON of at least 91 and a MON of about 83, giving a sensitivity of 8.

Research and motor octane number fuel ratings are made in a single-cylinder engine run at constant speed, wide-open throttle and fixed spark timing. These methods do not always predict how a fuel will behave in an automobile engine operated under a variety of speed, load, and weather conditions. Several methods of rating a gasoline in actual vehicles, either on the road or on chassis dynamometers which duplicate outdoor road conditions, have, therefore, been developed. These methods determine the fuel's *road octane number*.[107] The road ratings of current fuels usually lie between the motor and research ratings. Road octane number can be related to motor and research ratings with equations of the form

$$\text{Road ON} = a\,(\text{RON}) + b\,(\text{MON}) + c$$

where a, b, and c are experimentally derived constants. Recent studies show $a \approx b \approx 0.5$ gives good agreement. An *antiknock index* which is the mean of the research and motor octane numbers is now used in the United States to characterize antiknock quality:

$$\text{Antiknock index} = \frac{\text{RON} + \text{MON}}{2} \tag{9.64}$$

Refiners and automobile manufacturers are interested in the octane number requirement of engines or vehicles on the road. The *octane number requirement* (usually abbreviated to OR) of an engine or vehicle-engine combination is defined as the minimum fuel octane number that will resist knock throughout the engine's operating speed and load range. The octane number requirement of a single engine or vehicle does not usually provide adequate information for that particular model; every model has a range of requirements due to production tolerances and variations in engine and vehicle condition.

Modern gasolines contain a number of chemical additives designed to improve fuel quality. These additives are used to raise the octane number of the fuel, control surface ignition, reduce spark plug fouling, resist gum formation, prevent rust, reduce carburetor icing, remove carburetor or injector deposits, minimize deposits in the intake system, and prevent valve sticking. The octane number of hydrocarbon fuels can be increased by antiknock agents. Their use generally allows an increase in antiknock quality to be achieved at less expense than modifying the fuel's hydrocarbon composition by refinery processing. The most effective antiknock agents are lead alkyls. Tetraethyl lead (TEL), $(C_2H_5)_4Pb$, was first introduced in 1923. Tetramethyl lead (TML), $(CH_3)_4Pb$, was introduced in 1960. Since TML boils in the mid-range of a gasoline (110°C), whereas TEL boils at the high end (200°C), the introduction of TML permitted better distribution of octane amongst the cylinders of an engine. In 1959 a manganese antiknock compound (methylcyclopentadienyl manganese tricarbonyl), now known as MMT, was introduced as a supplementary antiknock agent for TEL. It is also an antiknock agent in its own right.

About 1970, in the United States, low-lead and unleaded gasolines were introduced. Two factors influenced the reduction in the use of lead alkyls: concern about the toxicological aspects of lead in the urban environment and the use of catalytic devices for emission control that are poisoned by lead. Unleaded and reduced-lead-content gasolines are now required in the United States. Japan has almost completely converted to unleaded fuel. In Europe, requirements which reduce the lead content of gasolines and introduce unleaded fuel were implemented in the late 1980s. MMT is sometimes used as an antiknock additive in unleaded gasoline. However, its role as a deposit in plugging exhaust catalytic converters limits its use to low concentrations. The expanding use of unleaded fuels has increased interest in other methods of boosting the octane rating of gasolines. The use of oxygenates—alcohols and ethers—as gasoline extenders, which due to their excellent antiknock quality increase the fuel's octane rating, is becoming more common. A brief review of the mechanism by which these additives and compounds improve the knock resistance of gasolines follows.

Lead is the most effective antiknock element known. In the form of lead alkyls, it is stable and fuel-soluble. The precise mechanism by which lead alkyls control knock is not fully known. It is generally agreed that the alkyls decompose before they exert their antiknock action. The decomposed material—lead oxide, PbO—either as a vapor or as a fog (a dispersion of fine particles), inhibits the preflame chain-branching reaction which leads to autoignition of the fuel-air charge, thus slowing the reaction rate. However, lead has little effect on two-stage ignition until after the cool flame.[109] Commercially available tetraalkyl lead antiknock fluids are based on TEL, TML, physical mixtures of TEL and TML, and mixed ethyl-methyl compounds produced by reacting TML and TEL. This range of compounds offers volatilities between the extremes of TEL and TML. The individual alkyls vary in antiknock behavior as a function of fuel composition and combustion conditions. The average effect of various amounts of TEL in a large number of regular gasolines is summarized in Fig. 9-70: the effectiveness of

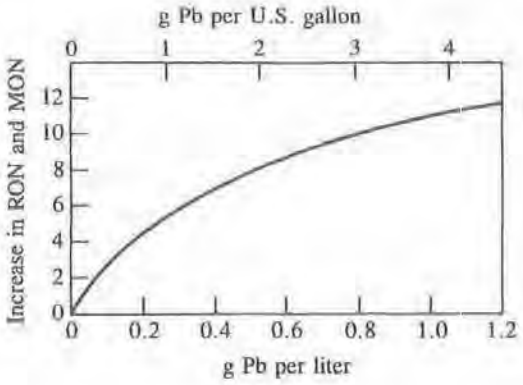


FIGURE 9-70
Gasoline octane number increase resulting from use of antiknock additive tetraethyl lead. Varies with fuel composition: average values shown.

each successive increment added steadily decreases. The addition of about 0.8 g lead per liter (3 g Pb per U.S. gallon, the maximum economic limit to lead concentration) provides an average gain of about 10 octane numbers in modern gasolines, though effectiveness varies with chemical composition of the fuel. TML offers a greater octane number gain than TEL in many gasolines, particularly in highly aromatic fuels with a low sulfur content. One of its major values, however, is in overcoming engine knock that results from fuel component segregation in the intake manifold; gasoline fractions of different volatility separate in the intake manifold of a multicylinder engine and the heavier fractions lag behind (see Sec. 7.6.3). When a gasoline containing a lead alkyl is burned in a spark-ignition engine, it produces nonvolatile combustion products. These deposit on the walls of the combustion chamber and on the spark plug, causing lead-fouling of the spark plug electrodes and tracking across the plug insulator, and hot corrosion of the exhaust valve. Commercial antiknock fluids, therefore, contain scavenging agents—combinations of ethylene dibromide and ethylene dichloride—which transfer the lead oxides which would otherwise deposit into volatile lead-bromine compounds which are largely exhausted with the combustion gases.

Low concentrations of methylcyclopentadienyl manganese tricarbonyl (MMT) act as an octane promoter; it is most effective in highly paraffinic gasolines. It is sometimes used as a supplement to TEL. MMT-TEL antiknock fluids are tailored to optimize octane cost effectiveness and the average fluid contains about 0.03 g Mn/g Pb. The octane gains vary significantly with fuel composition. In unleaded fuels MMT is sometimes used in low concentrations to provide from 0.5 to 1 octane number gain. On a weight of metal basis, MMT is about twice as effective as TEL in terms of research octane number gain and about equally effective in terms of motor octane number gain.[109]

The use of oxygenates (oxygen containing organic compounds) as extenders or substitutes for gasoline is increasing.[110] In some cases, this is because the oxygenate can be produced from nonpetroleum sources (e.g., biomass, coal) and thus may offer strategic or economic benefits. In other cases, the good antiknock blending characteristics of oxygenates can aid in meeting octane quality demands where increasingly stringent regulations limit lead alkyl use. Several oxygenates have been used as automotive fuels; those of major interest are methanol

(CH_3OH), ethanol (C_2H_5OH), tertiary butyl alcohol (TBA) (C_4H_9OH), and methyl tertiary butyl ether (MTBE).

Table 9.7 lists the antiknock characteristics of these compounds and their physical and chemical characteristics relative to gasoline. The blending value of antiknock index [Eq. (9.64)] given in the table is not necessarily the same as the compound's antiknock index [$(R + M)/2$ from App. D, Table D.4] when used alone as a fuel, and depends on the gasoline composition with which the compound is blended. MTBE-gasoline blends have good water stability, and MTBE has little effect on vapor pressure and material compatibility. TBA is moderately susceptible to water extraction and loss. Ethanol is technically feasible as a high octane supplement or substitute for gasoline; economically it is less attractive than methanol.

Methanol, because it can be made from natural gas, coal, or cellulose materials, has near- and long-term potential. Its high octane quality (130 RON, 95 MON), when used in low-concentration ($\sim$5 percent) methanol-cosolvent-gasoline blends, can help offset the octane loss from lead alkyl phase-out. Problems with these blends include poor solubility in gasoline in the presence of water; toxicity; an energy content about half that of gasoline; high latent heat of vaporization and oxygen content which contribute to poor driveability; incompatibility with many commonly used metals and elastomers; blending effects on gasoline volatility which may force the displacement of large volumes of butane. Some of these problems can be partially reduced by using cosolvents such as TBA or isobutanol. Use of methanol as a neat fuel in specially designed engines permits advantage to be taken of its high octane rating via high compression ratios. Problems include its energy content of one-half that of gasoline; engine starting problems which require starting aids such as 5 to 10 percent isopentane at temperatures below 10°C or intake system heaters; toxicity; extensive engine modifications.[110]

The octane requirement of an engine-vehicle combination usually increases during use, primarily due to the buildup of combustion chamber deposits within the engine cylinder. While these deposits increase the engine's compression ratio modestly, their largest effect is to increase the temperature of the outer surface of

TABLE 9.7
Oxygenate properties[110]

	Methanol	Ethanol	TBA	MTBE	Gasoline
Typical $(R + M)/2$ blending value	112	110	98	105	87–93
Weight percent oxygen	50	35	22	18	0
Stoichiometric (A/F)	6.5	9.0	11.2	11.7	14.5
Specific gravity	0.796	0.794	0.791	0.746	0.74
Lower heating value, MJ/kg	20.0	26.8	32.5	35.2	44.0
Latent heat of vaporization, MJ/kg	1.16	0.84	0.57	0.34	0.35
Boiling temperature, °C	65	78	83	55	27–227

TBA, tertiary butyl alcohol; MTBE, methyl teriary butyl ether.

the combustion chamber. This *increases* heat transfer *to* the fresh mixture during induction and *decreases* heat transfer from the unburned charge during compression. End-gas temperatures are therefore higher, thus increasing the likelihood of knock. As the combustion chamber deposits stabilize (over 15,000 to 25,000 km of driving), the engine's octane requirement typically increases by about 5 octane numbers; the increase can vary from between 1 to over 13 octane numbers.

Essentially all of the octane requirement increase results from the buildup of deposits on the combustion chamber walls: when the deposits are completely removed from the engine the octane requirement returns to close to its original value. The volume of deposits for leaded and unleaded fuels which build up inside the engine cylinder are similar in magnitude, and are in the range 0.3 to 1 cm^3 per cylinder. The compression ratio increase associated with this volume of deposits is small (0.1 compression ratio) and contributes therefore on the order of 10 percent of the octane requirement increase. The primary effect of the deposits is thought to be changes in heat transfer between the end-gas and the combustion chamber walls, as explained above. In an experiment where the deposits were removed from various regions of the combustion chamber in sequence and the octane requirement after each removal was determined, it was found that the deposits on the cylinder head around the end-gas region were the cause of about two-thirds of the total ORI observed. Though the volume of the deposits for leaded and unleaded fuels are comparable, the composition and density are substantially different. For unleaded fuels the major element is carbon (one-third to one-half by mass). The deposit density with leaded fuels is 2 to 5 g/cm^3; with unleaded fuels it is a factor of 5 lower.[111]

PROBLEMS

9.1. The table gives relevant properties of three different spark-ignition engine fuels. The design and operating parameters of a four-cylinder 1.6-liter displaced volume engine are to be optimized for each fuel over the engine's operating load and speed range. You may assume that for each engine-fuel combination, the gross indicated fuel conversion efficiency and imep at any operating condition are given by 0.8 times the fuel-air cycle efficiency at those conditions. Also, assume that for every five research octane number increase above 95 (the gasoline value) in fuel antiknock rating, the compression ratio can be increased by one unit. For gasoline, the engine compression ratio is 9, so if the octane number of the fuel is 100, a compression ratio of 10 can be used.

(*a*) At part-throttle operation—at an intake pressure of 0.5 atm and a speed of 2500 rev/min—estimate the gross indicated fuel conversion efficiency and specific fuel consumption for each engine-fuel combination. Each engine-fuel combination operates at the lean limit given.

(*b*) At the appropriate equivalence ratio for maximum power, with 1 atm inlet pressure at the same speed (2500 rev/min), the volumetric efficiencies are as shown. Explain these volumetric efficiency values. Each fuel is fully vaporized in the inlet manifold and the inlet mixture temperature is held constant for all fuels. Manifold and valve design remains the same.

(*c*) Estimate the ratios of the maximum indicated mean effective pressure, at the same conditions as in (*b*), of the natural gas and methanol fueled engines to the maximum imep of the gasoline engine.

(*d*) If the methane engine burns 33 percent faster than the gasoline engine (i.e., its combustion event takes three-quarters of the time), sketch a *carefully drawn qualitative* cylinder pressure versus crank angle curve for the two engines, from halfway through the compression stroke to halfway through the expansion stroke. Put both curves on the same graph. Conditions are as in (*b*). Show the motored *and* firing pressure curves for each engine. The spark timing should be set for maximum brake torque for each engine. Show the location of spark timing, the location of maximum cylinder pressure, and the approximate location of the end of combustion.

Fuel properties

Fuel	Formula	Research octane number	ϕ at lean operating limit	Stoichiometric air/fuel ratio	Heating value, MJ/kg	η_u
Natural gas	CH_4	120	0.7	17.2	50	0.78
Methanol	CH_3OH	105	0.8	6.4	20	0.75
Gasoline	$(CH_2)_n$	95	0.9	14.9	44	0.85

ϕ = fuel/air equivalence ratio.

9.2. The figure shows the flame propagating radially outward from the center of a disc-shaped combustion chamber. Combustion in such a device has many features in common with spark-ignition engine combustion. The chamber diameter is 10 cm and the height is 1.5 cm. For this problem, the flame can be thought of as a thin cylindrical sheet. Its radius increases approximately linearly with time. The volume of the chamber is constant. The fuel is a typical hydrocarbon fuel; the mixture is stoichiometric; the initial temperature is room temperature.

(*a*) Sketch qualitative but *carefully proportioned* graphs of the following quantities versus time from the start of combustion to the end of combustion:
  (1) The ratio of actual pressure in the chamber to the initial pressure
  (2) The ratio of average density of the gas *ahead* of the flame to the initial density
  (3) The ratio of the average density of the gas *behind* the flame to the initial density

(*b*) On a qualitative but *carefully proportioned* graph of r/R_0 versus time show how the radial positions of gas elements, initially at $r/R_0 = 0$, 0.5, and 1.0 before combustion, change during the combustion process as the flame propagates radially outward from the center ($r = 0$) to the outer wall ($r = R_0$).

Note: Accurate numerical calculations are not required to answer this question. You will be graded on the amount of physical insight your diagrams and the supporting brief explanations of your logic communicate. You should write down any equations or approximate numerical values for relevant quantities that help explain your reasoning.

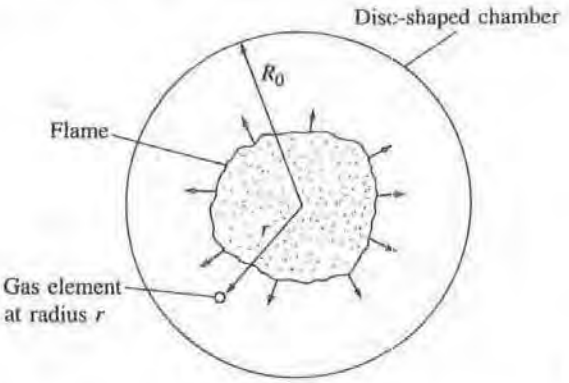


FIGURE P9-2

9.3. Highly compact bowl-in-piston or bowl-in-head combustion chambers permit SI engine operation at higher-than-normal compression ratios and with leaner mixtures. A vigorous swirling flow in the combustion chamber just prior to combustion is achieved by these chamber designs. The table compares the characteristics of a compact-chamber spark-ignition engine (Fig. P9-3) with a more conventional spark-ignition engine which has an open chamber (see Fig. 9-4).

	Compact chamber 1.5 liter	**Conventional 1.5 liter**
Compression ratio	14 : 1	9 : 1
Fuel octane requirement	97 RON	97 RON
Maximum bmep	980 kPa	965 kPa
Air/fuel ratio at WOT	17 : 1	13 : 1
MBT timing at 2000 rev/min and WOT	5° BTC	25° BTC
Air/fuel ratio at cruise conditions	22 : 1	16 : 1

For gasoline, the stoichiometric air/fuel ratio is 14.6. RON = research octane number, WOT = wide-open throttle, MBT = maximum brake torque.

Use the data provided, and any additional quantitative information you have or can generate easily, to answer the following questions:

(*a*) Explain whether the combustion process rate in the compact-chamber engine will be faster, slower, or about the same rate as the conventional engine combustion process.

(*b*) The compact-chamber engine has a higher compression ratio than the conventional engine, yet it has about the same maximum bmep at WOT in the mid-speed range. Explain quantitatively how the differences in compression ratio, air/fuel ratio, and MBT spark timing at WOT between the two engines influence maximum bmep and result in negligible total change.

(*c*) Both engines have been designed to have the same fuel octane requirement, yet the compact-chamber engine has a much higher compression ratio. Explain which features of the engine allow it to operate without knock at a 14 : 1 compression ratio while the conventional engine can only operate without knock at 9 : 1.

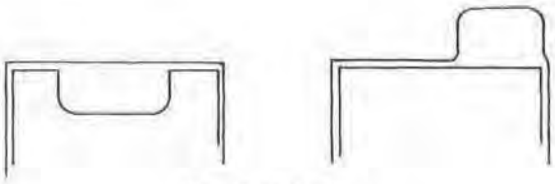


FIGURE P9-3

(*d*) The efficiency of the compact-chamber engine at part-throttle conditions is higher than that of the conventional engine. Briefly explain why this is the case and estimate approximately the ratio of the two engine efficiencies.

9.4. In a spark-ignition engine, a turbulent flame propagates through the uniform premixed fuel-air mixture within the cylinder and extinguishes at the combustion chamber walls.

(*a*) Draw a carefully proportioned qualitative graph of cylinder pressure p and mass fraction burned x_b as a function of crank angle θ for $-90° < \theta < 90°$ for a typical SI engine at wide-open throttle with the spark timing adjusted for maximum brake torque. Mark in the crank angles of spark discharge, and of the flame development period (0 to 10 percent burned) and end of combustion, on both p and x_b versus θ curves relative to the top-center crank position.

(*b*) Estimate approximately the fraction of the cylinder volume occupied by burned gases when the mass fraction burned is 0.5 (i.e., halfway through the burning process).

(*c*) A simple model for this turbulent flame is shown on the left in Fig. P9-4. The rate of burning of the charge dm_b/dt is given by

$$\frac{dm_b}{dt} = A_f \rho_u S_T$$

where A_f is the area of the flame front (which can be approximated by a portion of a cylinder whose axis is at the spark plug position), ρ_u is the unburned mixture

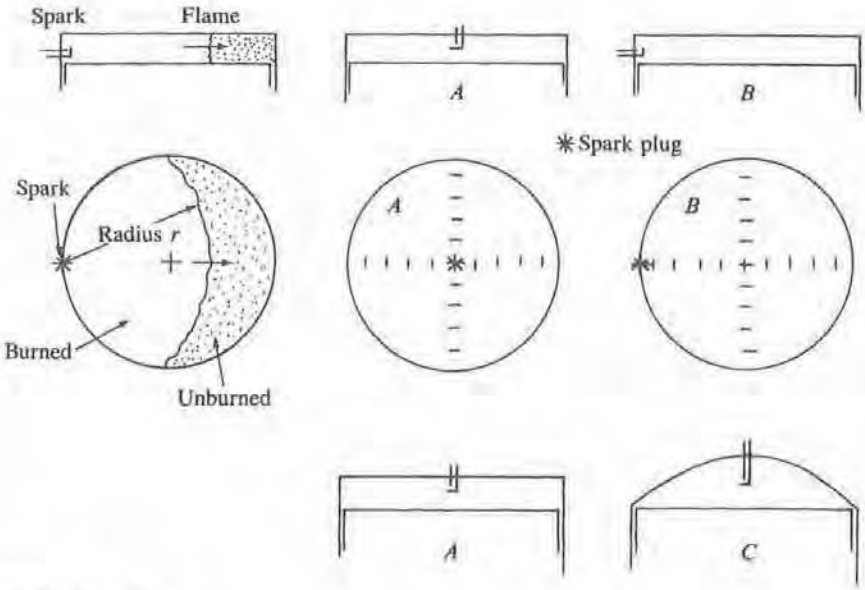


FIGURE P9-4

density, and S_T is the turbulent flame speed (the speed at which the front moves relative to the unburned mixture ahead of it). The rate of mass burning is influenced therefore by combustion chamber geometry (through A_f) as well as those factors that influence S_T (turbulent intensity, fuel/air ratio, residual gas fraction, and EGR). Compare combustion chambers *A* and *B* shown in Fig. P9-4. Sketch the *approximate* location of the flame front when 50 percent of the mass has been burned. (A careful qualitative sketch is sufficient; however, provide a quantitative justification for your sketch.) Sketch the mass fraction burned versus crank angle curves for these two combustion chambers on the same graph, each with its spark timing set for maximum brake torque. You may assume the value of S_T is the same for *A* and *B*.

(*d*) Compare combustion chambers *A* and *C* in Fig. P9-4 which have the same flame travel distance but have different chamber shapes. Which chamber has
(1) the faster rate of mass burning during the first half of the combustion process;
(2) the faster rate of mass burning during the second half of the combustion process;
(3) the more advanced timing for maximum brake torque?
Explain your answers.

9.5. A new synthetic fuel with chemical formula $(CH_2O)_n$ is being developed from coal for automotive use. You are making an evaluation of what changes in the spark-ignition engines you produce might be required if gasoline is replaced by this fuel "X." First make the following calculations:

(*a*) What is the stoichiometric air/fuel ratio for "X"? How does this compare with the stoichiometric air/fuel ratio for gasoline?

(*b*) Given that in a constant-volume calorimeter experiment to determine the heating value of "X" the combustion of 50 g of fuel with excess air at standard conditions resulted in a temperature rise of 1.25°C of the water and calorimeter (of combined heat capacity 650 kJ/K), what is the heating value of a stoichiometric mixture of "X" and air, *per kilogram of mixture*? How does this value compare with a stoichiometric gasoline-air mixture?

Then,

(*c*) Compare *approximately* the specific fuel consumption of a spark-ignition engine operated on stoichiometric gasoline and "X" mixtures. What do you conclude about the relative size of the fuel systems required to provide equal power?

(*d*) "X"-air mixtures take twice as long to burn as gasoline-air mixtures (the crank angle between the spark and end of combustion is twice as large). Sketch carefully drawn pressure-time curves over the entire engine four-stroke cycle for the two mixtures, for the same displacement and compression ratio engines, for the same *imep* (for throttled engine operation) for stoichiometric mixtures, with optimum spark timing, indicating the relative crank angle location of spark, peak cylinder pressure, and end of combustion, and the relative values of intake pressure, peak cylinder pressure, and pressure at the exhaust valve opening, for the two mixtures at the same equivalence ratio. (You do not need to make calculations to sketch these graphs.)

(*e*) Though "X"-air mixtures are slower burning than gasoline-air mixtures, the engine compression ratio can be increased to 14 : 1 from the 8 : 1 values typical for gasoline. Using typical fuel-air cycle efficiencies and the relation between the fuel-air cycle and real cycle efficiency, determine whether the slower-burning

higher-compression-ratio engine using "X" will be more efficient, have about the same efficiency, or be less efficient than the faster-burning lower-compression-ratio gasoline engine.

9.6. Knock in spark-ignition engines is an abnormal combustion condition. Almost everyone who rides a motorcycle or drives a car experiences this phenomenon at some time and usually changing into a lower gear will take the engine away from this condition. Use your experience of what changes in other variables do, and consult this and other textbooks to complete a table with the dependent variables shown at the top of the columns.

The independent variables are: speed, compression ratio, chamber surface/volume ratio, spark plug distance from cylinder axis, percent EGR, inlet mixture temperature, inlet mixture pressure, (F/A), wall temperature, air swirl, squish motion, fuel octane number. In these columns show the corresponding influence on the dependent variables by a "+" for an increase and a "−" for a decrease. Show the effect of increase in engine system independent variables on: cylinder pressure and temperature, flame speed, total burn time, autoignition induction period, tendency to knock. Provide in the extreme right-hand column brief comments to explain your answers.

Effect of increase in engine independent variable	Dependent variables						
	Cylinder		Flame speed	Total burn time	Induction period	Tendency to knock	Explanation
	Pressure	Temperature					
Speed, rev/min							
Etc.							

9.7. The attached graph gives the pressure–crank angle curve for a spark-ignition engine running at $\phi = 1.0$. The mass fraction burned x_b is also shown. Estimate the tem-

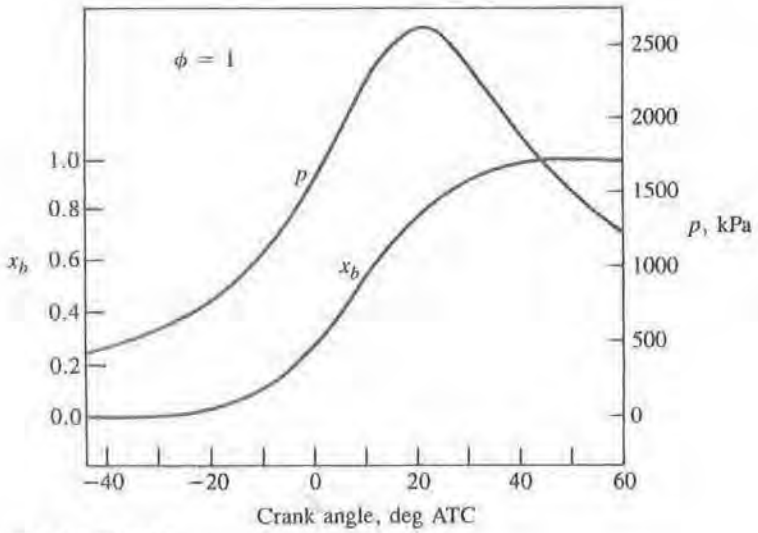


FIGURE P9-7

perature of the reactants at a number of crank angles and plot a graph of T_u versus θ. Assume the reactants in the cylinder are at 333 K and 1 atm pressure at the start of compression. It is necessary to make simplifications in order to do this and you should explain clearly what other assumptions you make; they should be compatible with Prob. 9.8 below.

9.8. If the combustion takes place progressively through a large number of very small zones of gas and there is no mixing between the zones, determine:

(*a*) the temperature at $-30°$, just after combustion, of the zone which burns at $-30°$;

(*b*) the temperature at $0°$, just after combustion, of the zone which burns at $0°$;

(*c*) the temperature at $+30°$, just after combustion of the zone which burns at $+30°$;

(*d*) the temperature of the products in these three zones at $+30°$.

Plot your results versus crank angle to show whether there is a spatial distribution of temperature in the cylinder after combustion.

Note: Each small unburned gas element burns at essentially constant pressure and is subsequently compressed and/or expanded. Use charts (Chap. 4) or an equilibrium computer code. The unburned gas state is given by Prob. 9.7.

9.9. An approximate way to calculate the pressure in the end-gas just after knock occurs is to assume that all the end-gas (the unburned gas ahead of the flame) burns instantaneously at constant volume. We assume that the inertia of the burned gases prevents significant gas motion while the end-gas autoignites.

For the pressure data in Fig. P9-7, assume autoignition occurs at 10 crank angle degrees after the top-center position. Determine the maximum pressure reached in the end-gas after knock occurs. From the mass fraction burned and approximate average burned gas conditions at this time, estimate the volume occupied by the end-gas as a fraction of the cylinder volume just before autoignition occurs. Use the charts (Chap. 4) or an equilibrium computer code.

9.10. At spark timing (30° BTC) in an automobile spark-ignition engine (with bore = stroke = 85 mm and $r_c = 9$) at 2000 rev/min, operating on gasoline, the cylinder pressure is 7.5 atm and the mixture temperature is 650 K. The fuel-air mixture is stoichiometric with a residual gas fraction of 8 percent. The rapid burning angle $\Delta\theta_b$ (10 to 90 percent mass burned) is 35°. Estimate (*a*) the mean piston speed; (*b*) the average flame travel speed based on $\Delta\theta_b$ (the spark plug is located 15 mm from the cylinder axis); (*c*) the turbulence intensity at TC [see Eq. (8.23)]; (*d*) the laminar flame speed at spark; (*e*) the turbulent burning speed S_b at TC using Fig. 9-30 (appropriate firing and motored pressures are given in Fig. 9-2*a*); (*f*) the mean expansion speed of the burned gases u_b at TC. Discuss briefly the relative magnitudes of these velocities.

9.11. The following combustion chamber design changes increase the mass burning rate in a spark-ignition engine at fixed compression ratio, bore, speed, and inlet mixture conditions. Explain how each change affects the burning rate.

(*a*) Reducing the amount of EGR.

(*b*) Using two spark plugs per cylinder instead of one.

(*c*) Generating swirl within the cylinder using a mask on the cylinder head (see Fig. 8-14).

(*d*) Using a combustion chamber with higher clearance height near the spark plug and a more central plug location.

9.12. Explain why SI engine torque varies, at fixed speed and inlet mixture conditions, as

the spark timing is varied from very advanced (e.g., 60° before TC) to close to TC. What is the "best" spark timing? Explain how it varies with engine speed and load.

9.13. (*a*) Explain the causes of the observed variation in cylinder pressure versus crank angle and imep in spark-ignition engines, cycle-by-cycle.

(*b*) What impacts do these cylinder pressure variations have on engine operation?

9.14. (*a*) Describe briefly what occurs when a spark-ignition engine "knocks."

(*b*) SI engine knock is primarily a problem at wide-open throttle and lower engine speeds. Explain why this is the case.

(*c*) With a knock sensor, the normal knock control strategy is to retard the spark timing when knock is detected, until knock no longer occurs. Explain why this strategy is effective and is preferred over other possible approaches (e.g., throttling the inlet, adding EGR).

(*d*) In a knocking engine, the crank angle at which autoignition occurs and the magnitude of the pressure oscillations which result vary substantially, cycle-by-cycle. Suggest reasons why this happens.

9.15. (*a*) The electrical energy stored in a typical ignition system coil is 50 mJ. Almost all this energy is transferred from the coil during the glow discharge phase. If the glow discharge lasts for 2 ms, use the data in Fig. 9-39 to estimate the glow discharge voltage and current.

(*b*) Only a fraction of this energy is transferred to the fuel-air mixture between the spark plug electrodes. Estimate the energy transferred during the breakdown and glow phases of the discharge, using the data in Fig. 9-40.

(*c*) Overall about one-tenth of the coil energy is transferred to the fuel-air mixture. What fraction of the cylinder contents' chemical energy ($m_f Q_{LHV}$) does this correspond to at a typical part-load condition ($p_i = 0.5$ atm, $\phi = 1.0$)? Assume 500 cm^3 per cylinder displaced volume. If the average burned gas temperature within the flame kernal just after spark is 3500 K and the cylinder pressure is 6 atm, what radius of kernal has fuel chemical energy equal to the electrical energy transferred to the kernal?

REFERENCES

1. Nakamura, H., Ohinouye, T., Hori, K. Kiyota, Y., Nakagami, T., Akishino, K., and Tsukamoto, Y.: "Development of a New Combustion System (MCA-JET) in Gasoline Engine," SAE paper 780007, *SAE Trans.*, vol. 87, 1978.
2. Rassweiler, G. M., and Withrow, L.: "Motion Pictures of Engine Flames Correlated with Pressure Cards," *SAE Trans.*, vol. 83, pp. 185–204, 1938. Reissued as SAE paper 800131, 1980.
3. Nakanishi, K., Hirano, T., Inoue, T., and Ohigashi, S.: "The Effects of Charge Dilution on Combustion and Its Improvement—Flame Photograph Study," SAE paper 750054, *SAE Trans.*, vol. 84, 1975.
4. Beretta, G. P., Rashidi, M., and Keck, J. C.: "Turbulent Flame Propagation and Combustion in Spark Ignition Engines," *Combust. Flame*, vol. 52, pp. 217–245, 1983.
5. Amann, C. A.: "Cylinder-Pressure Measurement and Its Use in Engine Research," SAE paper 852067, 1985.
6. Lavoie, G. A., Heywood, J. B., and Keck, J. C.: "Experimental and Theoretical Investigation of Nitric Oxide Formation in Internal Combustion Engines," *Combust. Sci. Technol.*, vol. 1, pp. 313–326, 1970.
7. Rassweiler, G. M., and Withrow, L.: "Flame Temperatures Vary with Knock and Combustion-Chamber Position," *SAE Trans.*, vol. 36, pp. 125–133, 1935.

8. Lavoie, G. A.: "Spectroscopic Measurement of Nitric Oxide in Spark-Ignition Engines," *Combust. Flame*, vol. 15, pp. 97–108, 1970.
9. Heywood, J. B., and Keck, J. C.: "Formation of Hydrocarbons and Oxides of Nitrogen in Automobile Engines," *Env. Sci. Technol.*, vol. 7, pp. 216–223, 1973.
10. Kreiger, R. B., and Borman, G. L.: "The Computation of Apparent Heat Release for Internal Combustion Engines," ASME paper 66-WA/DGP-4, 1966.
11. LoRusso, J. A., and Tabaczynski, R. J.: "Combustion and Emissions Characteristics of Methanol, Methanol-Water, and Gasoline-Methanol Blends in a Spark-Ignition Engine," SAE paper 769019, *Proceedings of Eleventh Intersociety Energy Conversion Engineering Conference*, Lake Tahoe, Nev., pp. 122–132, Sept. 12–17, 1976.
12. Lancaster, D. R., Kreiger, R. B., and Lienesch, J. H.: "Measurement and Analysis of Engine Pressure Data," SAE paper 750026, *SAE Trans.*, vol. 84, 1975.
13. Caris, D. F., and Nelson, E. E.: "A New Look at High Compression Engines," *SAE Trans.*, vol. 67, pp. 112–124, 1959.
14. Gatowski, J. A., Balles, E. N., Chun, K. M., Nelson, F. E., Ekchian, J. A., and Heywood, J. B.: "Heat Release Analysis of Engine Pressure Data," SAE paper 841359, *SAE Trans.*, vol. 93, 1984.
15. Chun, K. M., and Heywood, J. B.: "Estimating Heat-Release and Mass-of-Mixture Burned from Spark-Ignition Engine Pressure Data," *Combust. Sci. Technol.*, vol. 54, pp. 133–144, 1987.
16. Heywood, J. B., Higgins, J. M., Watts, P. A., and Tabaczynski, R. J.: "Development and Use of a Cycle Simulation to Predict SI Engine Efficiency and NO_x Emissions," SAE paper 790291, 1979.
17. Gatowski, J. A., Heywood, J. B., and Deleplace, C.: "Flame Photographs in a Spark-Ignition Engine," *Combust. Flame*, vol. 56, pp. 71–81, 1984.
18. Witze, P. O.: "The Effect of Spark Location on Combustion in a Variable-Swirl Engine," SAE paper 820044, *SAE Trans.*, vol. 91, 1982.
19. Taylor, C. F.: *The Internal Combustion Engine in Theory and Practice*, vol. II, *Combustion, Fuels, Materials, Design*, MIT Press, 1968.
20. Hires, S. D., Tabaczynski, R. J., and Novak, J. M.: "The Prediction of Ignition Delay and Combustion Intervals for a Homogeneous Charge, Spark Ignition Engine," SAE paper 780232, *SAE Trans.*, vol. 87, 1978.
21. Heywood, J. B.: "Combustion Chamber Design for Optimum Spark-Ignition Engine Performance," *Int. J. Vehicle Design*, vol. 5, no. 3, pp. 336–357, 1984.
22. Abraham, J., Williams, F. A., and Bracco, F. V.: "A Discussion of Turbulent Flame Structure in Premixed Charges," SAE paper 850345, in *Engine Combustion Analysis: New Approaches*, P-156, 1985.
23. Namazian, M., Hansen, S. P., Lyford-Pike, E. J., Sanchez-Barsse, J., Heywood, J. B., and Rife, J.: "Schlieren Visualization of the Flow and Density Fields in the Cylinder of a Spark-Ignition Engine," SAE paper 800044, *SAE Trans.*, vol. 89, 1980.
24. Keck, J. C.: "Turbulent Flame Structure and Speed in Spark-Ignition Engines," *Proceedings of the Nineteenth International Symposium on Combustion*, The Combustion Institute, pp. 1451–1466, 1982.
25. Heywood, J. B., and Vilchis, F. R.: "Comparison of Flame Development in a Spark-Ignition Engine Fueled with Propane and Hydrogen," *Combust. Sci. Technol.*, vol. 38, pp. 313–324, 1984.
26. Smith, J. R.: "Turbulent Flame Structure in a Homogeneous-Charge Engine," SAE paper 820043, *SAE Trans.*, vol. 91, 1982.
27. Smith, J. R.: "The Influence of Turbulence on Flame Structure in an Engine," in T. Uzkan (ed.), *Flows in Internal Combustion Engines*, pp. 67–72, ASME, New York, 1982.
28. Rallis, C. J., and Garforth, A. M.: "The Determination of Laminar Burning Velocity," *Prog. Energy Combust. Sci.*, vol. 6, pp. 303–330, 1980.
29. Metghalchi, M., and Keck, J. C.: "Laminar Burning Velocity of Propane-Air Mixtures at High Temperature and Pressure," *Combust. Flame*, vol. 38, pp. 143–154, 1980.
30. Metghalchi, M., and Keck, J. C.: "Burning Velocities of Mixtures of Air with Methanol, Isooctane, and Indolene at High Pressure and Temperature," *Combust. Flame*, vol. 48, pp. 191–210, 1982.
31. Milton, B. E., and Keck, J. C.: "Laminar Burning Velocities in Stoichiometric Hydrogen and

Hydrogen-Hydrocarbon Gas Mixtures," *Combust. Flame*, vol. 58, pp. 13–22, 1984.
32. Rhodes, D. B., and Keck, J. C.: "Laminar Burning Speed Measurements of Indolene-Air-Diluent Mixtures at High Pressures and Temperature," SAE paper 850047, 1985.
33. Metghalchi, M.: "Laminar Burning Velocity of Isooctane-Air, Methane-Air, and Methanol-Air Mixtures at High Temperature and Pressure," M.S. Thesis, Department of Mechanical Engineering, MIT, 1976.
34. Daneshyar, H., Mendes-Lopes, J. M. C., Ludford, G. S. S., and Tromans, P. S.: "The Influence of Straining on a Premixed Flame and Its Relevance to Combustion in SI Engines," paper C50/83, in *Combustion in Engineering*, vol. 1, pp. 191–199, Proceedings of an International Conference of the Institution of Mechanical Engineers, Mechanical Engineering Publications Ltd., London, 1983.
35. Groff, E. G., and Matekunas, F. A.: "The Nature of Turbulent Flame Propagation in a Homogeneous Spark-Ignited Engine," SAE paper 800133, *SAE Trans.*, vol. 89, 1980.
36. Witze, P. O., and Mendes-Lopes, J. M. C.: "Direct Measurement of the Turbulent Burning Velocity in a Homogeneous-Charge Engine," SAE paper 851531, 1986.
37. Hall, M. J., Bracco, F. V., and Santavicca, D. A.: "Cycle-Resolved Velocity and Turbulence Measurements in an IC Engine with Combustion," SAE paper 860320, 1986.
38. Matekunas, F. A.: "Modes and Measures of Cyclic Combustion Variability," SAE paper 830337, *SAE Trans.*, vol. 92, 1983.
39. Young, M. B.: "Cyclic Dispersion in the Homogeneous-Charge Spark-Ignition Engine—A Literature Survey," SAE paper 810020, *SAE Trans.*, vol. 90, 1981.
40. Young, M. B.: "Cyclic Dispersion—Some Quantitative Cause and Effect Relationships," SAE paper 800459, 1980.
41. Patterson, D. J.: "Cylinder Pressure Variations Present a Fundamental Combustion Problem," SAE paper 660129, *SAE Trans.*, vol. 75, 1966.
42. Fisher, R. V., and Macey, J. P.: "Digital Data Acquisition with Emphasis on Measuring Pressure Synchronously with Crank Angle," SAE paper 750028, 1975.
43. Douaud, A., and Eyzat, P.: "DIGITAP—An On-Line Acquisition and Processing System for Instantaneous Engine Data—Applications," SAE paper 770218, 1977.
44. Peters, B. D.: "Mass Burning Rates in a Spark Ignition Engine Operating in the Partial-Burn Regime," paper C92/79, Conference Proceedings on *Fuel Economy and Emissions of Lean Burn Engines*, Institution of Mechanical Engineers, London, June 12–14, 1979.
45. Hansel, J. G.: "Lean Automotive Engine Operation—Hydrocarbon Exhaust Emissions and Combustion Characteristics," SAE 710164, *SAE Trans.*, vol. 80, 1971.
46. Yu, H. T. C.: "Fuel Distribution Studies—A New Look at an Old Problem," *SAE Trans.*, vol. 71, pp. 596–613, 1963.
47. Nakagawa, Y., Nakai, M., and Hamai, K.: "A Study of the Relationship between Cycle-to-Cycle Variations of Combustion and Heat Release Delay in a Spark-Ignited Engine," *Bull. JSME*, vol. 25, no. 199, pp. 54–60, 1982.
48. Matsui, K., Tanaka, T., and Ohigashi, S.: "Measurement of Local Mixture Strength at Spark Gap of S.I. Engines," SAE paper 790483, *SAE Trans.*, vol. 88, 1979.
49. Kuroda, H., Nakajima, Y., Sugihara, K., Takagi, Y., and Muranaka, S.: "The Fast Burn with Heavy EGR, New Approach for Low NO_x and Improved Fuel Economy," SAE 780006, *SAE Trans.*, vol. 87, 1978.
50. Quader, A. A.: "What Limits Lean Operation in Spark Ignition Engines—Flame Initiation or Propagation?," SAE paper 760760, *SAE Trans.*, vol. 85, 1976.
51. Quader, A. A.: "Lean Combustion and the Misfire Limit in Spark Ignition Engines," SAE paper 741055, *SAE Trans.*, vol. 83, 1974.
52. Maly, R., and Vogel, M.: "Ignition and Propagation of Flame Fronts in Lean CH_4-Air Mixtures by the Three Modes of the Ignition Spark," *Proceedings of Seventeenth International Symposium on Combustion*, pp. 821–831, The Combustion Institute, 1976.
53. Maly, R.: "Spark Ignition: Its Physics and Effect on the Internal Combustion Process," in J. C. Hilliard and G. S. Springer (eds.), *Fuel Economy in Road Vehicles Powered by Spark Ignition Engines*, chap. 3, Plenum Press, New York, 1984.

54. Bosch: *Automotive Handbook*, Robert Bosch GmbH, Stuttgart, West Germany, 1976.
55. Maly, R., Saggau, B., Wagner, E., and Ziegler, G.: "Prospects of Ignition Enhancement," SAE paper 830478, *SAE Trans.*, vol. 92, 1983.
56. Maly, R.: "Ignition Model for Spark Discharges and the Early Phase of Flame Front Growth," *Proceedings of Eighteenth International Symposium on Combustion*, pp. 1747–1754, The Combustion Institute, 1981.
57. Refael, S., and Sher, E.: "A Theoretical Study of the Ignition of a Reactive Medium by Means of an Electrical Discharge," *Combust. Flame*, vol. 59, pp. 17–30, 1985.
58. Ballal, D. R., and Lefebvre, A. H.: "Influence of Flow Parameters on Minimum Ignition Energy and Quenching Distance," *Proceedings of Fifteenth International Symposium on Combustion*, pp. 1473–1481, The Combustion Institute, 1974.
59. Kono, M., Linuma, K., Kumagai, S., and Sakai, T.: "Spark Discharge Characteristics and Igniting Ability of Capacitor Discharge Ignition Systems," *Combust. Sci. Technol.*, vol. 19, pp. 13–18, 1978.
60. Rittmannsberger, N.: "Developments in High-Voltage Generation and Ignition Control," paper C106/72, in the Automobile Division Conference on *Automotive Electric Equipment*, Institution of Mechanical Engineers, London, 1972.
61. Huntzinger, G. O., and Rigsby, G. E.: "HEI—A New Ignition System Through New Technology," SAE paper 750346, *SAE Trans.*, vol. 84, 1975.
62. Dale, J. D., and Oppenheim, A. K.: "Enhanced Ignition for I.C. Engines with Premixed Gases," SAE paper 810146, *SAE Trans.*, vol. 90, 1981.
63. Tanuma, T., Sasaki, K., Kaneko, T., and Kawasaki, H.: "Ignition, Combustion, and Exhaust Emissions of Lean Mixtures in Automotive Spark Ignition Engines," SAE paper 710159, *SAE Trans.*, vol. 80, 1971.
64. Nakamura, N., Baika, T., and Shibata, Y.: "Multipoint Spark Ignition for Lean Combustion," SAE paper 852092, 1985.
65. Schwartz, H.: "Ignition Systems for Lean Burn Engines," paper C95/79, *Proceedings of Conference on Fuel Economy and Emissions of Lean Burn Engines*, pp. 87–96, Institution of Mechanical Engineers, London, June 1979.
66. Ziegler, G. F. W., Wagner, E. P., Saggau, B., and Maly, R. R.: "Influence of a Breakdown Ignition System on Performance and Emission Characteristics," SAE paper 840992, *SAE Trans.*, vol. 93, 1984.
67. Anderson, R. W., and Asik, J. R.: "Lean Air-Fuel Ignition System Comparison in a Fast-Burn Engine," SAE paper 850076, 1985.
68. Edwards, C. F., Oppenheim, A. K., and Dale, J. D.: "A Comparative Study of Plasma Ignition Systems," SAE paper 830479, 1983.
69. Noguchi, M., Sanda, S., and Nakamura, N.: "Development of Toyota Lean Burn Engine," SAE paper 760757, *SAE Trans.*, vol. 85, 1976.
70. Brandstetter, W. R., Decker, G., and Reichel, K.: "The Water-Cooled Volkswagen PCI-Stratified Charge Engine," SAE paper 750869, *SAE Trans.*, vol. 84, 1975.
71. Date, T., and Yagi, S.: "Research and Development of the Honda CVCC Engine," SAE paper 740605, 1974.
72. Konishi, M., Nakamura, N., Oono, E., Baika, T., and Sanda, S.: "Effects of a Prechamber on NO_x Formation Process in the SI Engine," SAE paper 790389, 1979.
73. Turkish, M. C.: "Prechamber and Valve Gear Design for 3-Valve Stratified Charge Engines," SAE paper 751004, *SAE Trans.*, vol. 84, 1975.
74. Ethyl Corporation: "Engine Combustion Noises," Ethyl technical note PCDTN-MS 117768 Rev. 774.
75. Wheeler, R. W.: "Abnormal Combustion Effects on Economy," in J. C. Hilliard and G. S. Springer (eds.), *Fuel Economy in Road Vehicles Powered by Spark-Ignition Engines*, chap. 6, pp. 225–276, Plenum Press, 1984.
76. Guibet, J. C., and Duval, A.: "New Aspects of Preignition in European Automotive Engines," SAE paper 720114, *SAE Trans.*, vol. 81, 1972.
77. Douaud, A., and Eyzat, P.: "DIGITAP—An On-Line Acquisition and Processing System for Instantaneous Engine Data—Applications," SAE paper 770218, 1977.

78. Lee, W., and Schaefer, H. J.: "Analysis of Local Pressures, Surface Temperatures and Engine Damages under Knock Conditions," SAE paper 830508, *SAE Trans.*, vol. 92, 1983.
79. Leppard, W. R.: "Individual-Cylinder Knock Occurrence and Intensity in Multicylinder Engines," SAE paper 820074, 1982.
80. Nakajima, Y., Onoda, M., Nagai, T., and Yoneda, K.: "Consideration for Evaluating Knock Intensity," *JSAE Rev.*, vol. 9, pp. 27–35, 1982.
81. Benson, G., Fletcher, E. A., Murphy, T. E., and Scherrer, H. C.: "Knock (Detonation) Control by Engine Combustion Chamber Shape," SAE paper 830509, 1983.
82. Cornetti, G. M., DeCristofaro, F., and Gozzelino, R.: "Engine Failure and High Speed Knock," SAE paper 770147.
83. Renault, F.: "A New Technique to Detect and Control Knock Damage," SAE paper 820073, 1982.
84. *The Relationship between Knock and Engine Damage*, Tentative Code of Practice, CEC Report M-07-T-83, Co-ordinating European Council (CEC), London, England, 1984.
85. Withrow, L., and Rassweiler, G. M.: "Slow-Motion Shows Knocking and Non-Knocking Explosions," *SAE J.*, vol. 39, no. 2, pp. 297–303, 312, 1936.
86. Miller, C. D., Olsen, H. L., Logan, W. O., and Osterstrom, G. E.: NACA report 857, 1946.
87. Male, T.: "Photography at 500,000 Frames per Second of Combustion and Detonation in a Reciprocating Engine," *Proceedings of Third Symposium on Combustion, Flame and Explosion Phenomena*, p. 721, Williams and Wilkins, Combustion Institute, Pittsburgh, 1949.
88. Nakajima, Y., Nagai, T., Iijima, T., Yokoyama, J., and Nakamura, K.: "Analysis of Combustion Patterns Effective in Improving Anti-Knock Performance of a Spark-Ignition Engine," *JSAE Rev.*, vol. 13, pp. 9–17, 1984.
89. Nakagawa, Y., Takagi, Y., Itoh, T., and Iijima, T.: "Laser Shadowgraphic Analysis of Knocking in S.I. Engine," SAE paper 845001; also in *XX FISITA Congress Proceedings*, vol. P-143, 1984.
90. Hayashi, T., Taki, M., Kojima, S., and Kondo, T.: "Photographic Observation of Knock with a Rapid Compression and Expansion Machine," SAE paper 841336, *SAE Trans.*, vol. 93, 1984.
91. Smith, J. R., Green, R. M., Westbrook, C. K., and Pitz, W. J.: "An Experimental and Modeling Study of Engine Knock," *Proceedings of Twentieth International Symposium on Combustion*, pp. 91–100, The Combustion Institute, 1984.
92. Barnard, J. A.: *Flame and Combustion*, 2d ed., Chapman and Hall, 1985.
93. Glassman, I.: *Combustion*, Academic Press, 1977.
94. Downes, D.: "Chemical and Physical Studies of Engine Knock," in *Six Lectures on the Basic Combustion Processes*, pp. 127–155, Ethyl Corporation, Detroit, Mich., 1954.
95. Halstead, M. P., Kirsch, L. J., Prothero, A., and Quinn, C. P.: "A Mathematical Model for Hydrocarbon Autoignition at High Pressures," *Proc. R. Soc.*, ser. A, vol. 346, pp. 515–538, 1975.
96. Benson, S. W.: "The Kinetics and Thermochemistry of Chemical Oxidation with Application to Combustion and Flames," *Prog. Energy Combust. Sci.*, vol. 7, pp. 125–134, 1981.
97. Alperstein, M., and Bradow, R. L.: "Investigations into the Composition of End Gases from Otto Cycle Engines," SAE paper 660410, *SAE Trans.*, vol. 75, 1966.
98. Livengood, J. C., and Wu, P. C.: "Correlation of Autoignition Phenomenon in Internal Combustion Engines and Rapid Compression Machines," *Proceedings of Fifth International Symposium on Combustion*, p. 347, Reinhold, 1955.
99. By, A., Kempinski, B., and Rife, J. M.: "Knock in Spark Ignition Engines," SAE paper 810147, 1981.
100. Douaud, A. M., and Eyzat, P.: "Four-Octane-Number Method for Predicting the Anti-Knock Behavior of Fuels and Engines," SAE paper 780080, *SAE Trans.*, vol. 87, 1978.
101. Cox, R. A., and Cole, J. A.: "Chemical Aspects of the Autoignition of Hydrocarbon-Air Mixtures," *Combust. Flame*, vol. 60, pp. 109–123, 1985.
102. Halstead, M. P., Kirsch, L. J., and Quinn, C. P.: "Autoignition of Hydrocarbon Fuels at High Temperatures and Pressures—Fitting of a Mathematical Model," *Combust. Flame*, vol. 30, pp. 45–60, 1977.
103. Schäpertöns, H., and Lee, W.: "Multidimensional Modelling of Knocking Combustion in SI Engines," SAE paper 850502, 1985.
104. Goodger, E. M.: *Hydrocarbon Fuels*, Macmillan, London, 1975.

105. Lovell, W. G.: "Knocking Characteristics of Hydrocarbons," *Ind. Engng. Chem.*, vol. 40, pp. 2388–2438, 1948.
106. Lichty, L. C.: *Combustion Engine Processes*, McGraw-Hill, 1967.
107. Ethyl Corporation: "Determining Road Octane Numbers," Ethyl technical note PCDTN SP-347 (113) Rev. 573.
108. Benson, J.: "What Good are Octanes," in *Chemtech*, pp. 16–22, American Chemical Society, January 1976.
109. Barusch, M. R., Macpherson, J. B., and Amberg, G. H.: "Additives, Engine Fuel," in J. J. McKetta and W. A. Cunningham (eds.), *Encyclopedia of Chemical Processing and Design*, vol. 2, pp. 1–77, Marcel Dekker, New York and Basel, 1977.
110. McCabe, L. J., Fitch, F. B., and Lowther, H. V.: "Future Trends in Automotive Fuels and Engine Oils," SAE paper 830935, in *Proceedings of Second International Pacific Conference on Automotive Engineering*, pp. 678–697, Tokyo, Japan, Nov. 7–10, 1983.
111. Benson, J. D.: "Some Factors Which Affect Octane Requirement Increase," SAE paper 750933, *SAE Trans.*, vol. 84, 1975.

CHAPTER 10

COMBUSTION IN COMPRESSION-IGNITION ENGINES

10.1 ESSENTIAL FEATURES OF PROCESS

The essential features of the compression-ignition or diesel engine combustion process can be summarized as follows. Fuel is injected by the fuel-injection system into the engine cylinder toward the end of the compression stroke, just before the desired start of combustion. Figures 1-17, 1-18, and 1-19 illustrate the major components of common diesel fuel-injection systems. The liquid fuel, usually injected at high velocity as one or more jets through small orifices or nozzles in the injector tip, atomizes into small drops and penetrates into the combustion chamber. The fuel vaporizes and mixes with the high-temperature high-pressure cylinder air. Since the air temperature and pressure are above the fuel's ignition point, spontaneous ignition of portions of the already-mixed fuel and air occurs after a delay period of a few crank angle degrees. The cylinder pressure increases as combustion of the fuel-air mixture occurs. The consequent compression of the unburned portion of the charge shortens the delay before ignition for the fuel and air which has mixed to within combustible limits, which then burns rapidly. It also reduces the evaporation time of the remaining liquid fuel. Injection continues until the desired amount of fuel has entered the cylinder. Atomization, vaporization, fuel-air mixing, and combustion continue until essentially all the fuel has passed through each process. In addition, mixing of the air remaining in the cylinder with burning and already burned gases continues throughout the combustion and expansion processes.

It will be clear from this summary that the compression-ignition combustion process is extremely complex. The details of the process depend on the characteristics of the fuel, on the design of the engine's combustion chamber and fuel-injection system, and on the engine's operating conditions. It is an unsteady, heterogeneous, three-dimensional combustion process. While an adequate conceptual understanding of diesel engine combustion has been developed, to date an ability to describe many of the critical individual processes in a quantitative manner is lacking.

Some important consequences of this combustion process on engine operation are the following:

1. Since injection commences just before combustion starts, there is no knock limit as in the spark-ignition engine resulting from spontaneous ignition of the premixed fuel and air in the end-gas. Hence a higher engine compression ratio can be used in the compression-ignition engine, improving its fuel conversion efficiency relative to the SI engine.
2. Since injection timing is used to control combustion timing, the delay period between the start of injection and start of combustion must be kept short (and reproducible). A short delay is also needed to hold the maximum cylinder gas pressure below the maximum the engine can tolerate. Thus, the spontaneous ignition characteristics of the fuel-air mixture must be held within a specified range. This is done by requiring that diesel fuel have a cetane number (a measure of the ease of ignition of that fuel in a typical diesel environment; see Sec. 10.6.2) above a certain value.
3. Since engine torque is varied by varying the amount of fuel injected per cycle with the engine air flow essentially unchanged, the engine can be operated unthrottled. Thus, pumping work requirements are low, improving part-load mechanical efficiency relative to the SI engine.
4. As the amount of fuel injected per cycle is increased, problems with air utilization during combustion lead to the formation of excessive amounts of soot which cannot be burned up prior to exhaust. This excessive soot or black smoke in the exhaust constrains the fuel/air ratio at maximum engine power to values 20 percent (or more) lean of stoichiometric. Hence, the maximum indicated mean effective pressure (in a naturally aspirated engine) is lower than values for an equivalent spark-ignition engine.
5. Because the diesel always operates with lean fuel/air ratios (and at part load with very lean fuel/air ratios), the effective value of γ ($=c_p/c_v$) over the expansion process is higher than in a spark-ignition engine. This gives a higher fuel conversion efficiency than the spark-ignition engine, for a given expansion ratio (see Sec. 5.5.3).

The major problem in diesel combustion chamber design is achieving sufficiently rapid mixing between the injected fuel and the air in the cylinder to complete combustion in the appropriate crank angle interval close to top-center. The

foregoing discussion indicates (and more detailed analysis will confirm) that mixing rates control the fuel burning rate. Commercial diesel engines are made with a very large range of cylinder sizes, with cylinder bores varying from about 70 to 900 mm. The mean piston speed at maximum rated power is approximately constant over this size range (see Sec. 2.2), so the maximum rated *engine* speed will be inversely proportional to the stroke [see Eq. (2.9)]. For a fixed crank angle interval for combustion (of order 40 to 50° to maintain high fuel conversion efficiency), the time available for combustion will, therefore, scale with the stroke. Thus, at the small end of the diesel engine size range, the mixing between the injected fuel and the air must take place on a time scale some 10 times shorter than in engines at the large end of this range. It would be expected, therefore, that the design of the engine combustion chamber (including the inlet port and valve) and the fuel-injection system would have to change substantially over this size range to provide the fuel and air motion inside the cylinder required to achieve the desired fuel-air mixing rate. As engine size decreases, more vigorous air motion is required while less fuel jet penetration is necessary. It is this logic, primarily, that leads to the different diesel combustion chamber designs and fuel injection systems found in practice over the large size range of commercial diesel engines.

10.2 TYPES OF DIESEL COMBUSTION SYSTEMS

Diesel engines are divided into two basic categories according to their combustion chamber design: (1) *direct-injection (DI) engines*, which have a single open combustion chamber into which fuel is injected directly; (2) *indirect-injection (IDI) engines*, where the chamber is divided into two regions and the fuel is injected into the "prechamber" which is connected to the main chamber (situated above the piston crown) via a nozzle, or one or more orifices. IDI engine designs are only used in the smallest engine sizes. Within each category there are several different chamber geometry, air-flow, and fuel-injection arrangements.

10.2.1 Direct-Injection Systems

In the largest-size engines, where mixing rate requirements are least stringent, quiescent direct-injection systems of the type shown in Fig. 10-1a are used. The momentum and energy of the injected fuel jets are sufficient to achieve adequate fuel distribution and rates of mixing with the air. Additional organized air motion is not required. The combustion chamber shape is usually a shallow bowl in the crown of the piston, and a central multihole injector is used.

As engine size decreases, increasing amounts of air swirl are used to achieve faster fuel-air mixing rates. Air swirl is generated by suitable design of the inlet port (see Sec. 8.3); the swirl rate can be increased as the piston approaches TC by forcing the air toward the cylinder axis, into a bowl-in-piston type of combustion

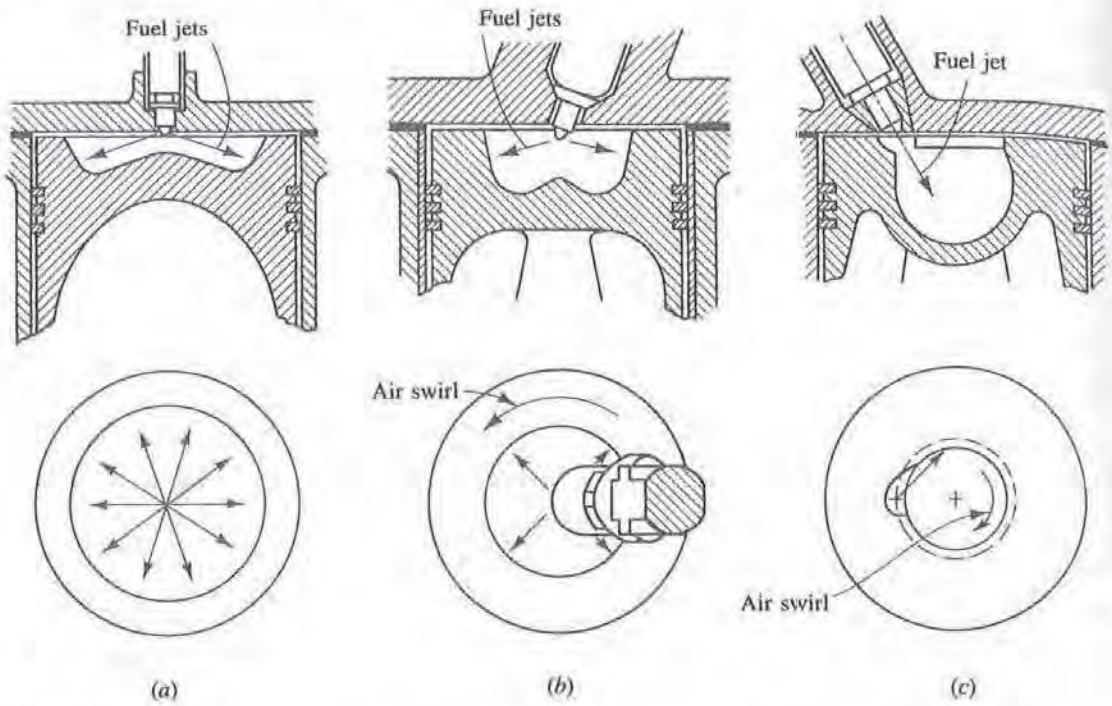


FIGURE 10-1
Common types of direct-injection compression-ignition or diesel engine combustion systems: (*a*) quiescent chamber with multihole nozzle typical of larger engines; (*b*) bowl-in-piston chamber with swirl and multihole nozzle; (*c*) bowl-in-piston chamber with swirl and single-hole nozzle. (*b*) and (*c*) used in medium to small DI engine size range.

chamber. Figure 10-1b and *c* shows the two types of DI engine with swirl in common use. Figure 10-1*b* shows a DI engine with swirl, with a centrally located multihole injector nozzle. Here the design goal is to hold the amount of liquid fuel which impinges on the piston cup walls to a minimum. Figure 10-1*c* shows the M.A.N. "M system" with its single-hole fuel-injection nozzle, oriented so that most of the fuel is deposited on the piston bowl walls. These two types of designs are used in medium-size (10- to 15-cm bore) diesels and, with increased swirl, in small-size (8- to 10-cm bore) diesels.

10.2.2 Indirect-Injection Systems

Inlet generated air swirl, despite amplification in the piston cup, has not provided sufficiently high fuel-air mixing rates for small high-speed diesels such as those used in automobiles. Indirect-injection or divided-chamber engine systems have been used instead, where the vigorous charge motion required during fuel injection is generated during the compression stroke. Two broad classes of IDI systems can be defined: (1) swirl chamber systems and (2) prechamber systems, as illustrated in Fig. 10-2*a* and *b*, respectively. During compression, air is forced from the main chamber above the piston into the auxiliary chamber, through the nozzle or orifice (or set of orifices). Thus, toward the end of compression, a vigorous flow in the auxiliary chamber is set up; in swirl chamber systems the connect-

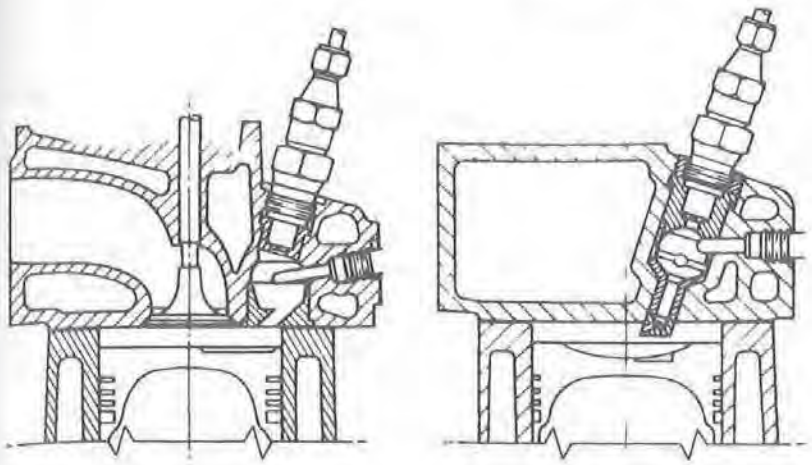


FIGURE 10-2
Two common types of small indirect-injection diesel engine combustion system: (*a*) swirl prechamber; (*b*) turbulent prechamber.

ing passage and chamber are shaped so that this flow within the auxiliary chamber rotates rapidly.

Fuel is usually injected into the auxiliary chamber at lower injection-system pressure than is typical of DI systems through a pintle nozzle as a single spray, as shown in Fig. 1-18. Combustion starts in the auxiliary chamber; the pressure rise associated with combustion forces fluid back into the main chamber where the jet issuing from the nozzle entrains and mixes with the main chamber air. The glow plug shown on the right of the prechamber in Fig. 10-2 is a cold-starting aid. The plug is heated prior to starting the engine to ensure ignition of fuel early in the engine cranking process.

10.2.3 Comparison of Different Combustion Systems

The number of different combustion chamber types proposed and tried since the beginnings of diesel engine development is substantial. Over the years, however, through the process of evolution and the increased understanding of the physical and chemical processes involved, only a few designs based on a sound principle have survived. The important characteristics of those chambers now most commonly used are summarized in Table 10.1. The numbers for dimensions and operating characteristics are typical ranges for each different type of diesel engine and combustion system.

The largest, slowest speed, engines for power generation or marine applications use open quiescent chambers which are essentially disc shaped; the motion of the fuel jets is responsible for distributing and mixing the fuel. These are usually two-stroke cycle engines. In the next size range, in large truck and locomotive engines, a quiescent chamber consisting of a shallow dish or bowl in the

TABLE 10.1
Characteristics of Common Diesel Combustion Systems

	Direct injection				Indirect injection	
System	Quiescent	Medium swirl	High swirl "M"	High swirl multispray	Swirl chamber	Pre-chamber
Size	Largest	Medium	Medium—smaller	Medium—small	Smallest	Smallest
Cycle	2-/4-stroke	4-stroke	4-stroke	4-stroke	4-stroke	4-stroke
Turbocharged/supercharged/naturally aspirated	TC/S	TC/NA	TC/NA	NA/TC	NA/TC	NA/TC
Maximum speed, rev/min	120–2100	1800–3500	2500–5000	3500–4300	3600–4800	4500
Bore, mm	900–150	150–100	130–80	100–80	95–70	95–70
Stroke/bore	3.5–1.2	1.3–1.0	1.2–0.9	1.1–0.9	1.1–0.9	1.1–0.9
Compression ratio	12–15	15–16	16–18	16–22	20–24	22–24
Chamber	Open or shallow dish	Bowl-in-piston	Deep bowl-in-piston	Deep bowl-in-piston	Swirl pre-chamber	Single/multi-orifice pre-chamber
Air-flow pattern	Quiescent	Medium swirl	High swirl	Highest swirl	Very high swirl in pre-chamber	Very turbulent in pre-chamber
Number of nozzle holes	Multi	Multi	Single	Multi	Single	Single
Injection pressure	Very high	High	Medium	High	Lowest	Lowest

piston crown is often used. The air utilization in these engines is low, but they are invariably supercharged or turbocharged to obtain high power density.

In the DI category, as engine size decreases and maximum speed rises, swirl is used increasingly to obtain high-enough fuel-air mixing rates. The swirl is generated by suitably shaped inlet ports, and is amplified during compression by forcing most of the air toward the cylinder axis into the deep bowl-in-piston combustion chamber. In about the same size range, an alternative system to the multihole nozzle swirl system is the M.A.N. "M" system (or wall-wetting system), where most of the fuel from the single-hole pintle nozzle is placed on the wall of the spherical bowl in the piston crown.

In the smallest engine sizes, the IDI engine has traditionally been used to obtain the vigorous air motion required for high fuel-air mixing rates. There are several different geometries in use. These either generate substantial swirl in the

auxiliary chamber during the latter part of the compression stroke, using a nozzle or connecting passage that enters the auxiliary chamber tangentially, or they generate intense turbulence in the prechamber through use of several small orifices and obstructions to the flow within the prechamber. The most common design of swirl chamber is the Ricardo Comet design shown in Fig. 10-2*a*. An alternative IDI engine to the two types listed in Table 10-1 is the air cell system. In that system the fuel is injected into the main chamber and not the auxiliary "air cell." The auxiliary chamber acts as a turbulence generator as gas flows into and out of the cell.

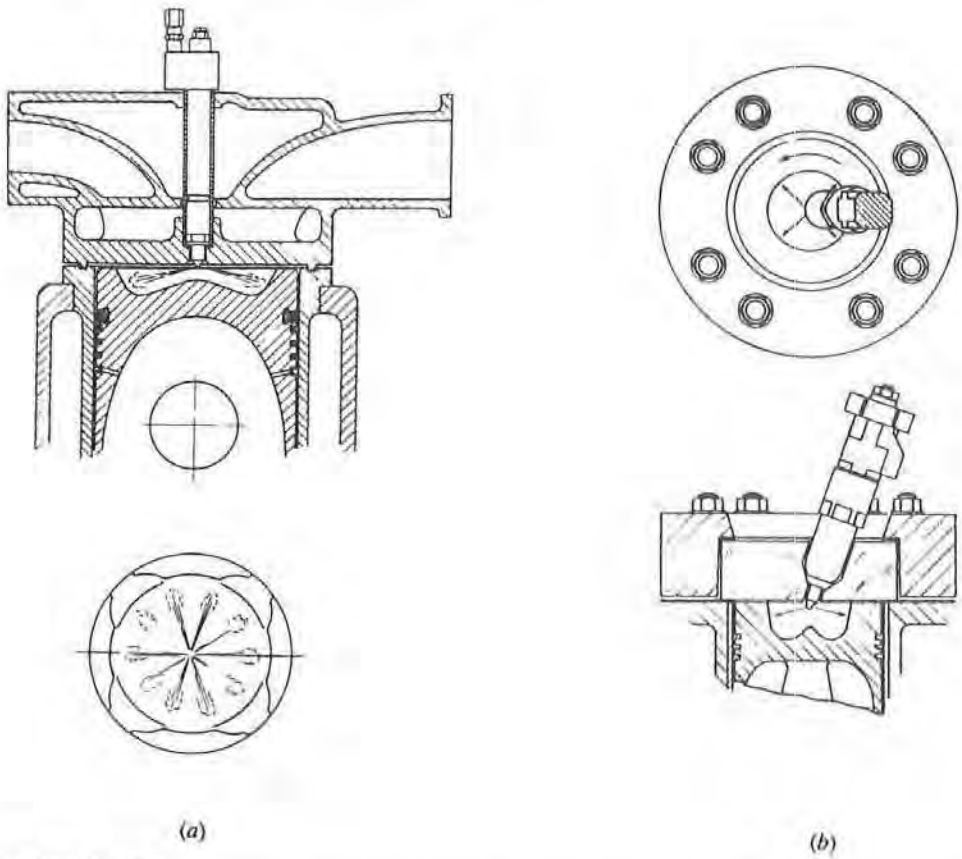
10.3 PHENOMENOLOGICAL MODEL OF COMPRESSION-IGNITION ENGINE COMBUSTION

Studies of photographs of diesel engine combustion, combined with analyses of engine cylinder pressure data, have led to a widely accepted descriptive model of the compression-ignition engine combustion process. The concept of *heat-release rate* is important to understanding this model. It is defined as the rate at which the chemical energy of the fuel is released by the combustion process. It can be calculated from cylinder pressure versus crank angle data, as the energy release required to create the measured pressure, using the techniques described in Sec. 10.4. The combustion model defines four separate phases of diesel combustion, each phase being controlled by different physical or chemical processes. Although the relative importance of each phase does depend on the combustion system used, and engine operating conditions, these four phases are common to all diesel engines.

10.3.1 Photographic Studies of Engine Combustion

High-speed photography at several thousand frames per second has been used extensively to study diesel engine combustion. Some of these studies have been carried out in combustion chambers very close to those used in practice, under normal engine operating conditions (e.g., Refs. 1 and 2). Sequences of individual frames from movies provide valuable information on the nature of the combustion process in the different types of diesel engines. Figure 10-3 shows four combustion chamber geometries that have been studied photographically. These are: (*a*) a quiescent chamber typical of diesel engines in the 3 to 20 dm^3/cylinder displacement used for industrial, marine, and rail traction applications (only the burning of a single fuel spray of the multispray combustion system could be studied[2]); (*b*) a smaller high-speed DI engine with swirl and four fuel jets centrally injected; (*c*) an M.A.N. "M" DI system; and (*d*) a Ricardo Comet V swirl chamber IDI system.[1]

The combustion sequences were recorded on color film and show the following features:



(*a*) (*b*)

FIGURE 10-3
Four diesel combustion chambers used to obtain photographs of the compression-ignition combustion process shown in Fig. 10-4 on color plate: (*a*) quiescent DI chamber; (*b*) multihole nozzle DI chamber with swirl: on p. 499; (*c*) M.A.N. "M" DI chamber; (*d*) Ricardo Comet IDI swirl chamber.[1,2]

Fuel spray(s). The fuel droplets reflect light from spot lamps and define the extent of the liquid fuel spray prior to complete vaporization.

Premixed flame. These regions are of too low a luminosity to be recorded with the exposure level used. The addition of a copper additive dope to the fuel gives these normally blue flames a green color bright enough to render them visible.

Diffusion flame. The burning high-temperature carbon particles in this flame provide more than adequate luminosity and appear as yellow-white. As the flame cools, the radiation from the particles changes color through orange to red.

Over-rich mixture. The appearance of a brown region, usually surrounded by a white diffusion flame, indicates an excessively rich mixture region where substantial soot particle production has occurred. Where this fuel-rich soot-laden cloud contacts unburned air there is a hot white diffusion flame.

Table 10.2 summarizes the characteristics of these different regions, discernable in the photographs shown in Fig. 10-4 on the color plate.

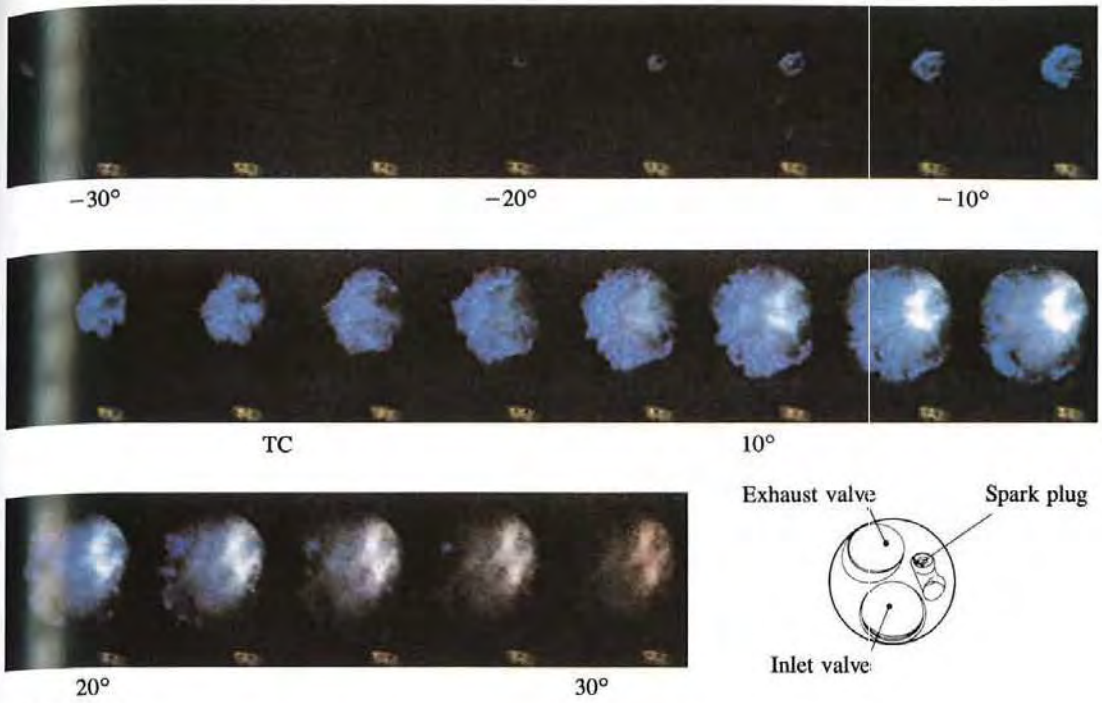


FIGURE 9-1

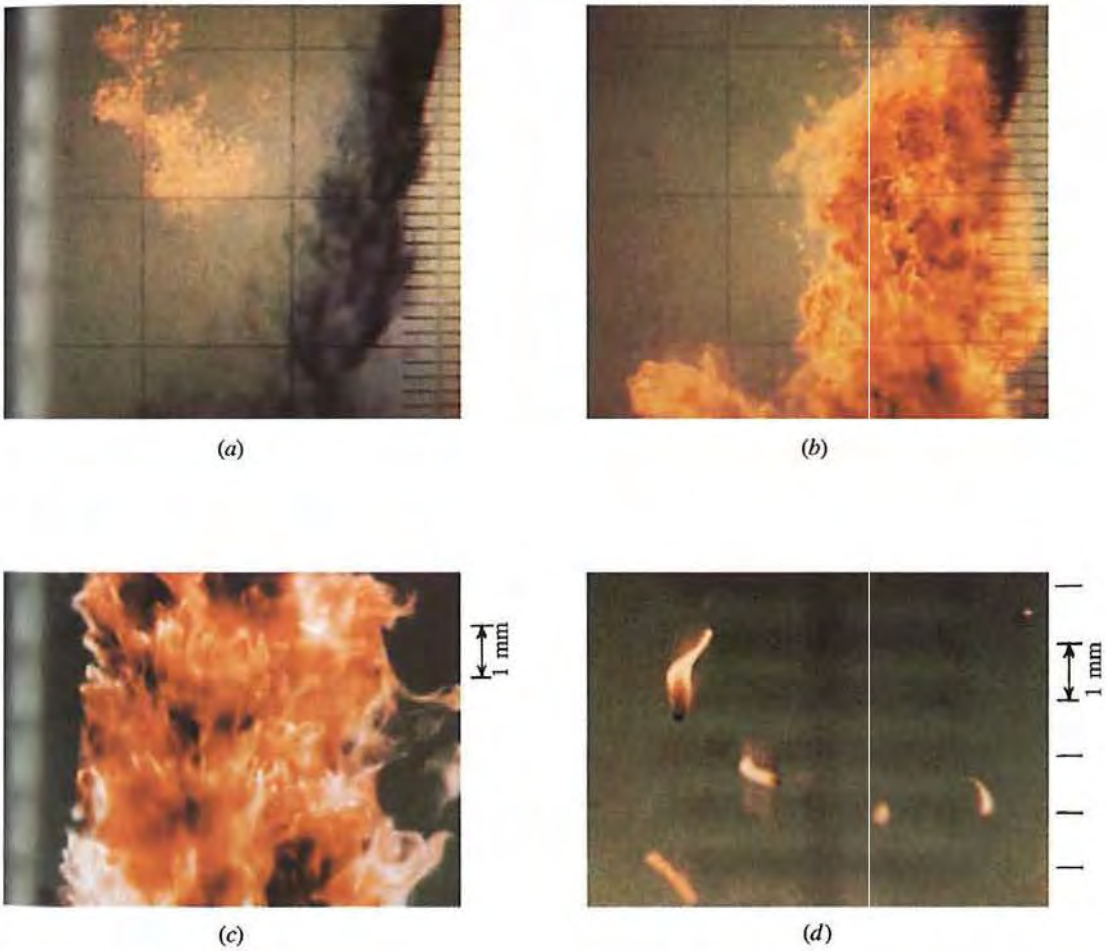


FIGURE 10-5

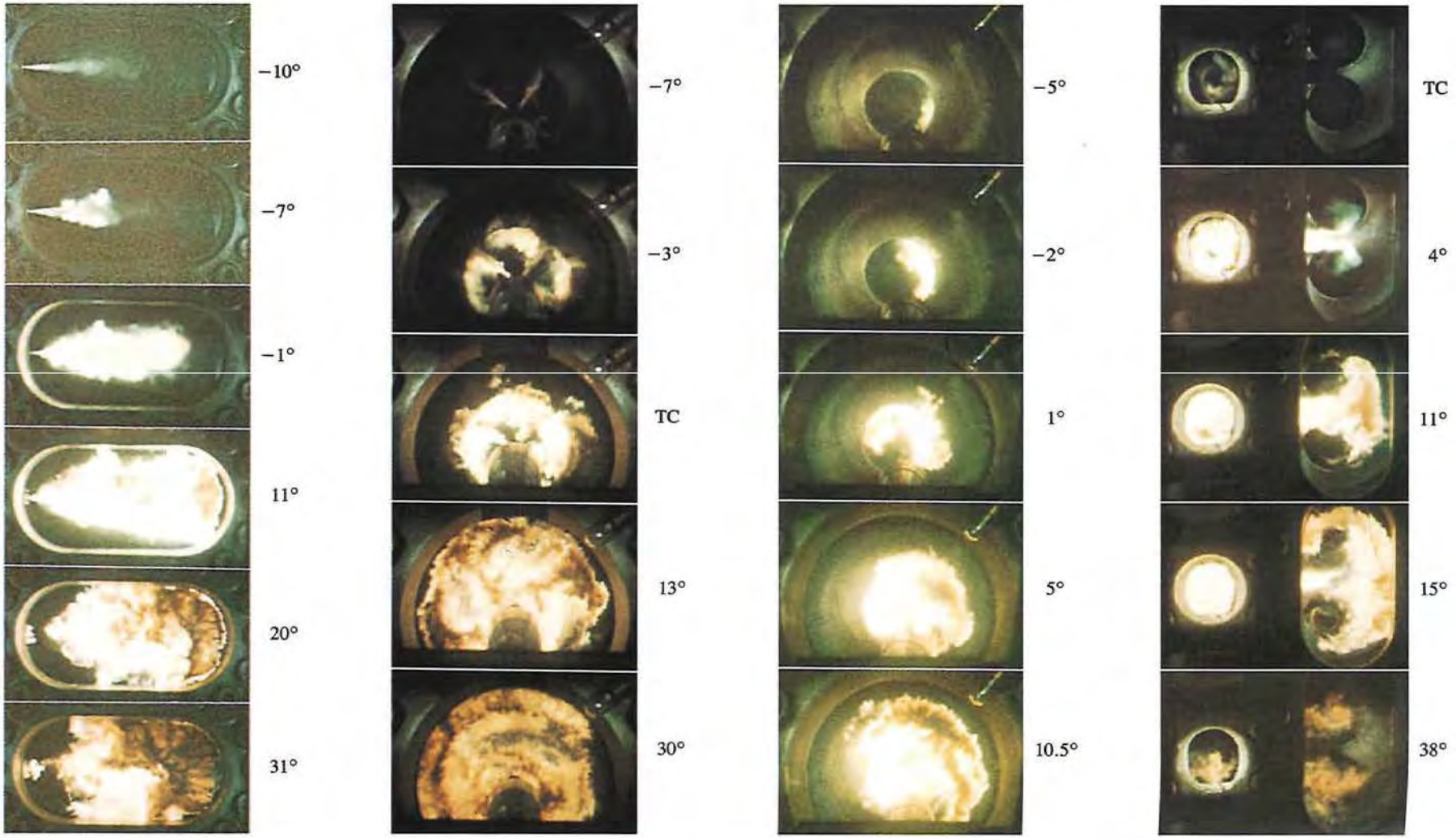
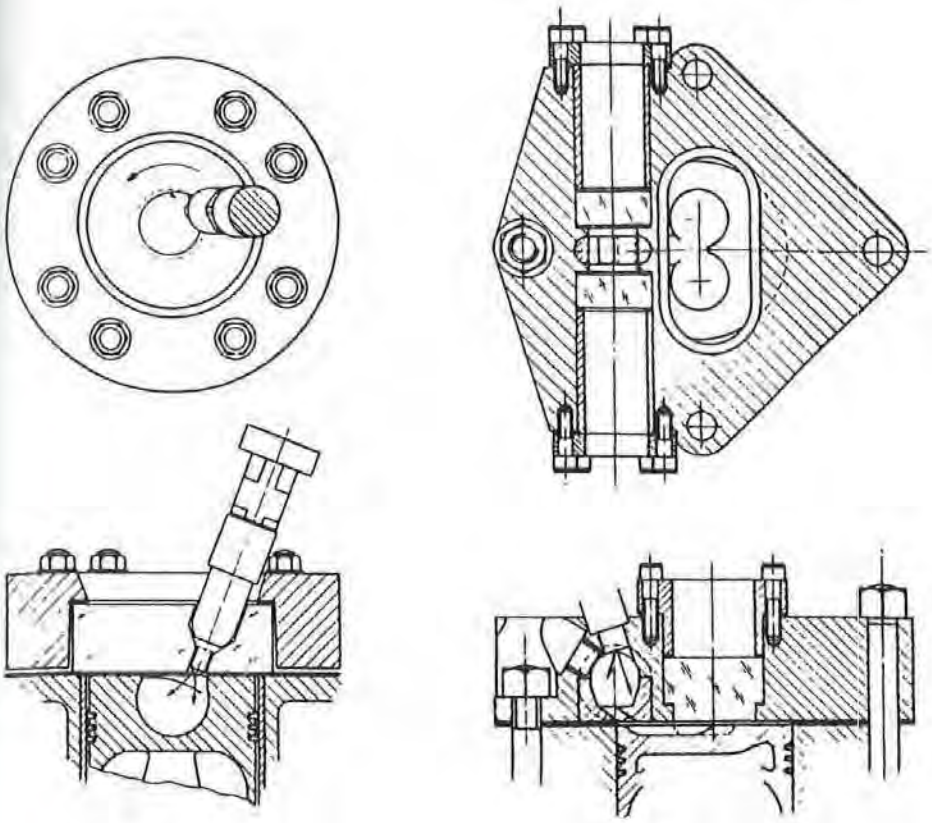


FIGURE 10-4



(*c*) (*d*)

Figure 10-4*a* shows a sequence of photographs from one combustion event of the single spray, burning under conditions typical of a large quiescent DI engine. The fuel spray is shown penetrating into the chamber. Ignition occurs at $-8°$ in the fuel-air mixture left behind on the edge of the spray not far from the injector. The flame then spreads rapidly ($-7°$) along the outside of the spray to the spray tip. Here some of the fuel, which has had a long residence time in the chamber, burns with a blue-green low-luminosity flame (colored green by the copper fuel additive). The flame engulfing the remainder of the spray is brilliant white-yellow from the burning of the soot particles which have been formed in

FIGURE 10-4 (On Color Plate, facing this page)
Sequence of photographs from high-speed movies taken in special visualization diesel engines shown in Fig. 10-3: (*a*) combustion of single spray burning under large DI engine conditions; (*b*) combustion of four sprays in DI engine with counterclockwise swirl; (*c*) combustion of single spray in M.A.N. "M" DI diesel; (*d*) combustion in prechamber (on left) and main chamber (on right) in Ricardo Comet IDI swirl chamber diesel. 1250 rev/min, imep = 827 kPa (120 lb/in^2)$^{1.2}$ (*Courtesy Ricardo Consulting Engineers.*)

TABLE 10.2
Interpretation of diesel engine combustion color photographs[1]

Color	Interpretation
Grey	Background; the gas (air in early stages, combustion products later) is transparent and not glowing
Green	Early in combustion process; low luminosity "premixed"-type flame, rendered visible by copper added to fuel. Later; burned gas above about 1800°C
White, and yellow-white	Carbon particle burnup in diffusion flame, 2000–2500°C
Yellow, orange-red	Carbon burnup in diffusion flame at lower temperatures; last visible in film at 1000°C
Brown	Soot clouds from very fuel-rich mixture regions. Where these meet air (grey) there is always a white fringe of hot flame

the fuel-rich spray core. At this stage (−1°), about 60 percent of the fuel has been injected. The remainder is injected into this enflamed region, producing a very fuel-rich zone apparent as the dark brown cloud (11°). This soot cloud moves to the outer region of the chamber (11° to 20°); white-yellow flame activity continues near the injector, probably due to combustion of ligaments of fuel which issued from the injector nozzle as the injector needle was seating. Combustion continues well into the expansion stroke (31°C).

This sequence shows that fuel distribution is always highly nonuniform during the combustion process in this type of DI engine. Also the air which is between the individual fuel sprays of the quiescent open-chamber diesel mixes with each burning spray relatively slowly, contributing to the poor air utilization with this type of combustion chamber.

Figure 10-4*b* shows a combustion sequence from the DI engine with swirl (the chamber shown in Fig. 10-3*b*). The inner circle corresponds to the deep bowl in the piston crown, the outer circle to the cylinder liner. The fuel sprays (of which two are visible without obstruction from the injector) first appear at −13°. At −7° they have reached the wall of the bowl; the tips of the sprays have been deflected slightly by the anticlockwise swirl. The frame at −3° shows the first ignition. Bright luminous flame zones are visible, one on each spray. Out by the bowl walls, where fuel vapor has been blown around by the swirl, larger greenish burning regions indicating the presence of premixed flame can be seen. The fuel downstream of each spray is next to ignite, burning yellow-white due to the soot

formed by the richer mixture. Flame propagation back to the injector follows extremely rapidly and at TC the bowl is filled with flame. At 5° ATC the flame spreads out over the piston crown toward the cylinder wall due to combustion-produced gas expansion and the reverse squish flow (see Sec. 8.4). The brown regions (13°) are soot-laden fuel-rich mixture originating from the fuel which impinges on the wall. The last frame (30° ATC) shows the gradual diminution of the soot-particle-laden regions as they mix with the excess air and burn up. The last dull-red flame visible on the film is at about 75° ATC, well into the expansion stroke.

Figure 10-4*c* shows the combustion sequence for the M.A.N. "M"-type DI engine. In the version of the system used for these experiments, the fuel was injected through a two-hole nozzle which produces a main jet directed tangentially onto the walls of the spherical cup in the piston crown, and an auxiliary spray which mixes a small fraction of the fuel directly with the swirling air flow. More recent "M" systems use a pintle nozzle with a single variable orifice.[3] At −5° the fuel spray is about halfway round the bowl. Ignition has just occurred of fuel adjacent to the wall which has mixed sufficiently with air to burn. The flame spreads rapidly (−2°, 1°) to envelop the fuel spray, and is convected round the cup by the high swirl air flow. By shortly after TC the flame has filled the bowl and is spreading out over the piston crown. A soot cloud is seen near the top right of the picture at 5° ATC which spreads out around the circumference of the enflamed region. There is always a rim of flame between the soot cloud and the cylinder liner as excess air is mixed into the flame zone (10.5°). The flame is of the carbon-burning type throughout; little premixed green flame is seen even at the beginning of the combustion process.

Figure 10-4*d* shows the combustion sequence in a swirl chamber IDI engine of the Ricardo Comet V design. The swirl chamber (on the left) is seen in the view of the lower drawing of Fig. 10-3*d* (with the connecting passageway entering the swirl chamber tangentially at the bottom left to produce clockwise swirl). The main chamber is seen in the plan view of the upper drawing of Fig. 10-3*d*. Two sprays emerge from the Pintaux nozzle after the start of injection at −11°. The smaller auxiliary spray which is radial is sharply deflected by the high swirl. Frame 1 shows how the main spray follows the contour of the chamber; the auxiliary spray has evaporated and can no longer be seen. The first flame occurs at −1° in the vaporized fuel from the auxiliary spray and is a green premixed flame. The flame then spreads to the main spray (TC), becoming a yellow-white carbon-particle-burning flame with a green fringe. At 4° ATC the swirl chamber appears full of carbon-burning flame, which is being blown down the throat and into the recesses in the piston crown by the combustion generated pressure rise in the prechamber. The flame jet impinges on the piston recesses entraining the air in the main chamber, leaving green patches where all carbon is burned out (4°, 11°, 15°). A brown soot cloud is emerging from the throat. By 15° ATC this soot cloud has spread around the cylinder, with a bright yellow-white flame at its periphery. This soot then finds excess air and burns up, while the yellow-white

flame becomes yellow and then orange-red as the gases cool on expansion. By 38° ATC most of the flame is burnt out.

Magnified color photographs of the flame around a single fuel spray under conditions typical of a direct-injection diesel engine, shown in Fig. 10-5 on the color plate, provide additional insight into the compression-ignition and flame-development processes.[4] These photographs were obtained in a rapid compression machine: this device is a cylinder-piston apparatus in which air is rapidly compressed by moving the piston to temperatures and pressures similar to those in the diesel engine combustion chamber at the time of injection. A single fuel spray was then injected into the disc-shaped combustion chamber. The air flow prior to compression was forced to swirl around the cylinder axis and much of that swirl remains after compression.

Figure 10-5*a* shows a portion of the liquid fuel spray (which appears black due to back lighting) and the rapidly developing flame 0.4 ms after ignition occurs. Ignition commences in the *fuel vapor*–air mixture region, set up by the jet motion and swirling air flow, away from the liquid core of the spray. In this region the smaller fuel droplets have evaporated in the hot air atmosphere that surrounds them and mixed with sufficient air for combustion to occur. Notice that the fuel vapor concentration must be nonuniform; combustion apparently occurs around small "lumps" of mixture of the appropriate composition and temperature. Figure 10-5*b* shows the same flame at a later time, 3.2 ms after ignition. The flame now surrounds most of the liquid spray core. Its irregular boundary reflects the turbulent character of the fuel spray and its color variation indicates that the temperature and composition in the flame region are not uniform.

Figure 10-5*c* shows a portion of this main flame region enlarged to show its internal structure. A highly convoluted flame region is evident, which has a similar appearance to a gaseous turbulent diffusion flame. The major portion of the diesel engine flame has this character, indicative of the burning of fuel vapor–air pockets or lumps or eddies of the appropriate composition. Only at the end of the combustion process is there visible evidence of individual fuel droplets burning with an envelope flame. Figure 10-5*d* shows the same region of the combustion chamber as Fig. 10-5*c*, but at the end of the burning process well after injection has been completed. A few large droplets are seen burning with individual droplet flames. It is presumed that such large drops were formed at the end of the injection process as the injector nozzle was closing.

FIGURE 10-5 (On Color Plate, facing page 498)
Photographs from high-speed movie of single fuel spray injected into a swirling air flow in a rapid-compression machine. (*a*) Spray and flame 0.4 ms after ignition; scale on right in millimeters. (*b*) Flame surrounding spray 3.2 ms after ignition. (*c*) Magnified photograph of main portion of flame. (*d*) Individual droplet burning late in combustion process after injection completed. Air temperature ~500°C. 50 mg fuel injected.[4] (*Courtesy Professor M. Ogasawara, Osaka University.*)

10.3.2 Combustion in Direct-Injection, Multispray Systems

Figure 10-6 shows typical data for cylinder pressure (p), fuel-injector needle-lift, and fuel pressure in the nozzle gallery through the compression and expansion strokes of a direct-injection diesel. The engine had central fuel injection through a four-hole nozzle into a disc-shaped bowl-in-piston combustion chamber. The rate of fuel injection can be obtained from the fuel-line pressure, cylinder pressure, nozzle geometry, and needle-lift profiles by considering the injector as one or more flow restrictions;[5] it is similar in phasing and comparable in shape to the needle-lift profile. There is a delay of 9° between the start of injection and start of combustion [identified by the change in slope of the $p(\theta)$ curve]. The pressure rises rapidly for a few crank angle degrees, then more slowly to a peak value about 5° after TC. Injection continues after the start of combustion. A rate-of-heat-release diagram† from the same study, corresponding to this rate of fuel injection and cylinder pressure data, is shown in Fig. 10-7. The general shape of the rate-of-heat-release curve is typical of this type of DI engine over its load and speed range. The heat-release-rate diagram shows negligible heat release until toward the end of compression when a slight loss of heat during the delay period (which is due to heat transfer to the walls and to fuel vaporization and heating) is

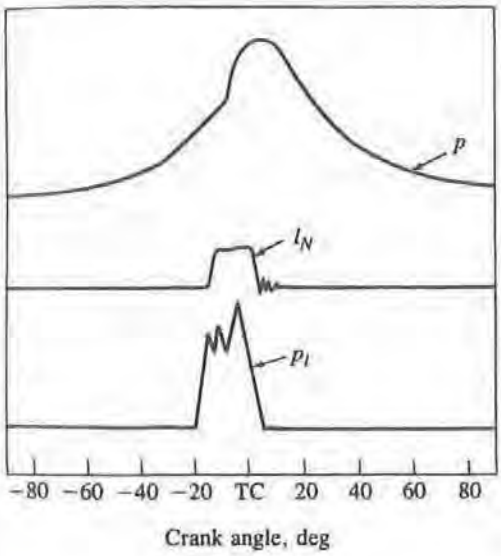


FIGURE 10-6
Cylinder pressure p, injector needle lift l_N, and injection-system fuel-line pressure p_l, as functions of crank angle for small DI diesel engine.[5]

† The heat-release rate plotted here is the net heat-release rate (see Sec. 10.4). It is the sum of the change of sensible internal energy of the cylinder gases and the work done on the piston. It differs from the rate of fuel energy released by combustion by the heat transferred to the combustion chamber walls. The heat loss to the walls is 10 to 25 percent of the fuel heating value in smaller engines; it is less in larger engine sizes. This net heat release can be used as an indicator of actual heat release when the heat loss is small.

evident. During the combustion process the burning proceeds in three distinguishable stages. In the first stage, the rate of burning is generally very high and lasts for only a few crank angle degrees. It corresponds to the period of rapid cylinder pressure rise. The second stage corresponds to a period of gradually decreasing heat-release rate (though it initially may rise to a second, lower, peak as in Fig. 10-7). This is the main heat-release period and lasts about 40°. Normally about 80 percent of the total fuel energy is released in the first two periods. The third stage corresponds to the "tail" of the heat-release diagram in which a small but distinguishable rate of heat release persists throughout much of the expansion stroke. The heat release during this period usually amounts to about 20 percent of the total fuel energy.

From studies of rate-of-injection and heat-release diagrams such as those in Fig. 10-7, over a range of engine loads, speeds, and injection timings, Lyn[6] developed the following summary observations. First, the total burning period is much longer than the injection period. Second, the absolute burning rate increases proportionally with increasing engine speed; thus on a crank angle basis, the burning interval remains essentially constant. Third, the magnitude of the initial peak of the burning-rate diagram depends on the ignition delay period, being higher for longer delays. These considerations, coupled with engine combustion photographic studies, lead to the following model for diesel combustion.

Figure 10-8 shows schematically the rate-of-injection and rate-of-burning diagrams, where the injected fuel as it enters the combustion chamber has been divided into a number of elements. The first element which enters mixes with air and becomes "ready for burning" (i.e., mixes to within combustible limits), as shown conceptually by the lowest triangle along the abscissa in the rate-of-burning figure. While some of this fuel mixes rapidly with air, part of it will mix much more slowly. The second and subsequent elements will mix with air in a similar manner, and the total "ready-for-burning" diagram, enclosed by the dashed line, is obtained. The total area of this diagram is equal to that of the rate-of-injection diagram. Ignition does not occur until after the delay period is over, however. At the ignition point, some of the fuel already injected has mixed with enough air to be within the combustible limits. That "premixed" fuel-air

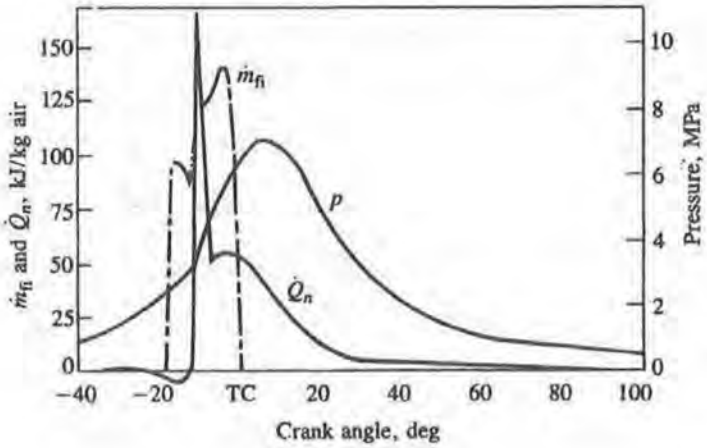


FIGURE 10-7
Cylinder pressure p, rate of fuel injection $\dot{m}_{fi}$, and net heat-release rate $\dot{Q}_n$ calculated from p for small DI diesel engine, 1000 rev/min, normal injection timing, bmep = 620 kPa.[5]

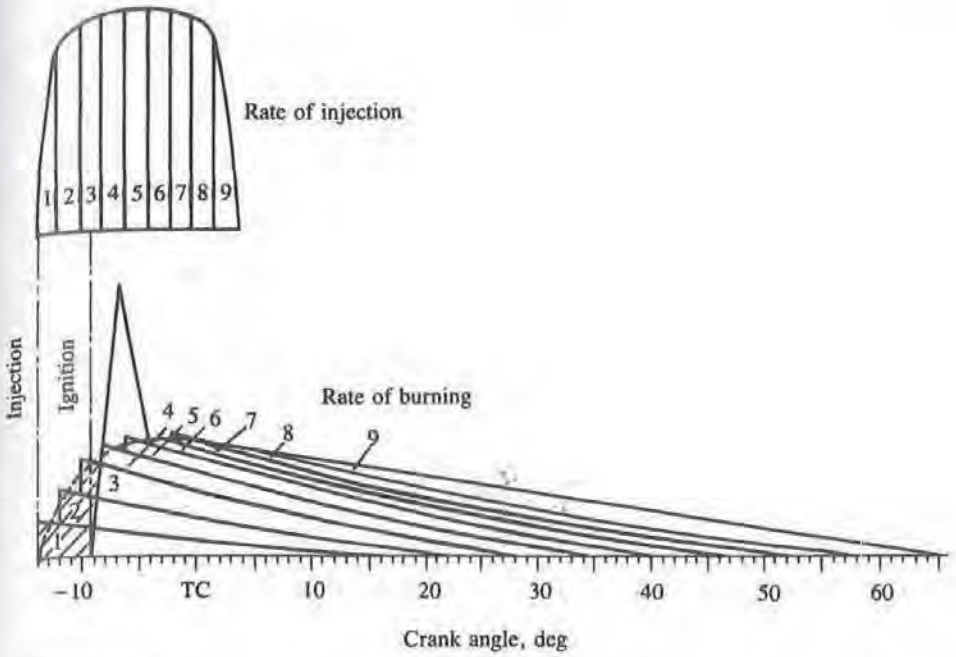


FIGURE 10-8
Schematic of relationship between rate of fuel injection and rate of fuel burning or energy release.[6]

mixture (the shaded region in Fig. 10-8) is then added to the mixture which becomes ready for burning after the end of the delay period, producing the high initial rate of burning as shown. Such a heat-release profile is generally observed with this type of naturally aspirated DI diesel engine. Photographs (such as those in Fig. 10-4*a* and *b*) show that up to the heat-release-rate peak, flame regions of low green luminosity are apparent because the burning is predominantly of the premixed part of the spray. After the peak, as the amount of premixed mixture available for burning decreases and the amount of fresh mixture mixed to be "ready for burning" increases, the spray burns essentially as a turbulent diffusion flame with high yellow-white or orange luminosity due to the presence of carbon particles.

To summarize, the following stages of the overall compression-ignition diesel combustion process can be defined. They are identified on the typical heat-release-rate diagram for a DI engine in Fig. 10-9.

Ignition delay (*ab*). The period between the start of fuel injection into the combustion chamber and the start of combustion [determined from the change in slope on the p-θ diagram, or from a heat-release analysis of the $p(\theta)$ data, or from a luminosity detector].

Premixed or rapid combustion phase (*bc*). In this phase, combustion of the fuel which has mixed with air to within the flammability limits during the ignition delay period occurs rapidly in a few crank angle degrees. When this burning mixture is added to the fuel which becomes ready for burning and burns during this phase, the high heat-release rates characteristic of this phase result.

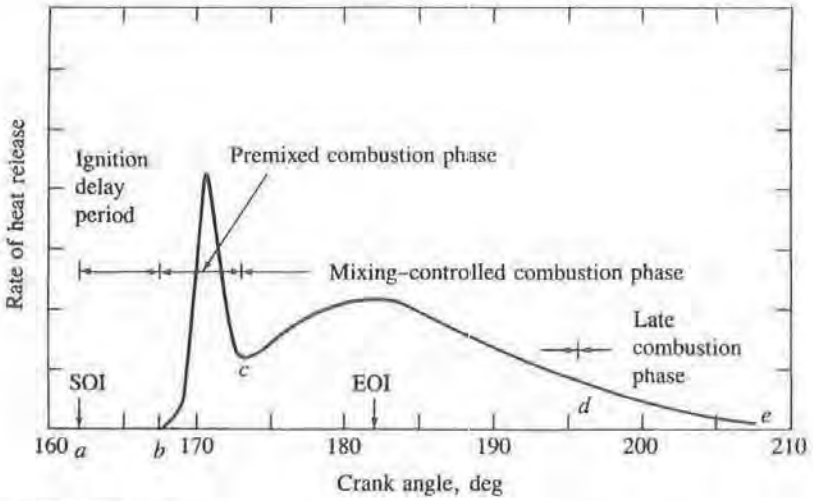


FIGURE 10-9
Typical DI engine heat-release-rate diagram identifying different diesel combustion phases.

Mixing-controlled combustion phase (*cd*). Once the fuel and air which premixed during the ignition delay have been consumed, the burning rate (or heat-release rate) is controlled by the rate at which mixture becomes available for burning. While several processes are involved—liquid fuel atomization, vaporization, mixing of fuel vapor with air, preflame chemical reactions—the rate of burning is controlled in this phase primarily by the fuel vapor–air mixing process. The heat-release rate may or may not reach a second (usually lower) peak in this phase; it decreases as this phase progresses.

Late combustion phase (*de*). Heat release continues at a lower rate well into the expansion stroke. There are several reasons for this. A small fraction of the fuel may not yet have burned. A fraction of the fuel energy is present in soot and fuel-rich combustion products and can still be released. The cylinder charge is nonuniform and mixing during this period promotes more complete combustion and less-dissociated product gases. The kinetics of the final burnout processes become slower as the temperature of the cylinder gases fall during expansion.

10.3.3 Application of Model to Other Combustion Systems

In the M.A.N. "M" DI engine system, and in IDI systems, the shapes of the heat-release-rate curve are different from those of the quiescent or moderate swirl DI shown in Figs. 10-7 and 10-9. With the "M" system, the initial heat-release "spike" is much less pronounced (in spite of the fact that a large fraction of the fuel is injected during the delay period) though the total burning period is about the same. Lyn[6] has suggested that the lower initial burning rate is due to the fact that the smaller number of nozzle holes (one or two instead of about four or more) and the directing of the main spray tangentially to the wall substantially reduce the free mixing surface area of the fuel jets. However, since the burning

rates after ignition are relatively high, mixing must speed up. This occurs due to the centrifugal forces set up in the swirling flow. Initially, the fuel is placed near the wall, and mixing is inhibited by the effect of the high centrifugal forces on the fuel vapor which is of higher density than the air and so tends to remain near the wall. Once ignition occurs, the hot burning mixture expands, decreases in density, and is then moved rapidly toward the center of the chamber. This strong radial mixing is the rate-determining process. An additional delaying mechanism exists if significant fuel is deposited on the wall. At compression air temperatures, the heat transferred to the fuel film on the wall from the gases in the cylinder is too small to account for the observed burning rates. Only after combustion starts will the gas temperature and heat-transfer rates be high enough to evaporate the fuel off the wall at an adequate rate.

In the swirl chamber IDI engine, where the air in the main chamber is not immediately available for mixing, again the rate-determining processes are different.[6] There is no initial spike on the rate-of-heat-release curve as was the case with DI engines. The small size of the chamber, together with the high swirl rate generated just before injection, results in considerable fuel impingement on the walls. This and the fact that the ignition delay is usually shorter with the IDI engine due to the higher compression ratio used account for the low initial burning rate.

Based on the above discussion Lyn[6] proposed three basic injection, mixing, and burning patterns important in diesel engines:

A. Fuel injection across the chamber with substantial momentum. Mixing proceeds immediately as fuel enters the chamber and is little affected by combustion.
B. Fuel deposition on the combustion chamber walls. Negligible mixing during the delay period due to limited evaporation. After ignition, evaporation becomes rapid and its rate is controlled by access of hot gases to the surface, radial mixing being induced by differential centrifugal forces. Burning is therefore delayed by the ignition lag.
C. Fuel distributed near the wall: mixing proceeds during the delay, but at a rate smaller than in mechanism A. After ignition, mixing is accelerated by the same mechanism as in mechanism B.

Figure 10-10 shows, schematically, the construction of the burning-rate or heat-release-rate diagrams (from the same injection-rate diagram) for the DI diesel combustion system with a central multihole nozzle, for the "M"-type DI diesel, and for the swirl chamber IDI. For the DI engine with multihole nozzle, mechanism A is predominant. For the DI engine with fuel sprayed tangentially to the wall, mechanisms B and C prevail; the delayed mixing prevents excessively high initial burning rates. For the IDI swirl chamber engine, the shorter ignition delay together with mixing process C during the delay period produces a gradual increase in burning rate, as shown in Fig. 10-10*c*.

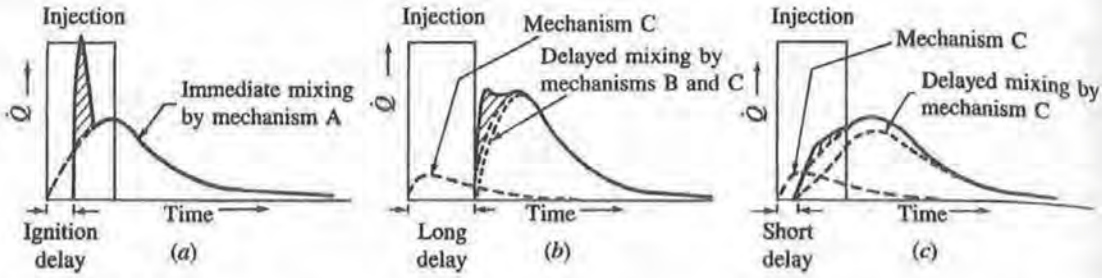


FIGURE 10-10
Schematic injection-rate and burning-rate diagrams in three different types of naturally aspirated diesel combustion system: (*a*) DI engine with central multihole nozzle; (*b*) DI "M"-type engine with fuel injected on wall; (*c*) IDI swirl chamber engine. Mechanisms A, B, and C defined in text.[6]

10.4 ANALYSIS OF CYLINDER PRESSURE DATA

Cylinder pressure versus crank angle data over the compression and expansion strokes of the engine operating cycle can be used to obtain quantitative information on the progress of combustion. Suitable methods of analysis which yield the rate of release of the fuel's chemical energy (often called heat release), or rate of fuel burning, through the diesel engine combustion process will now be described. The methods of analysis are similar to those described in Sec. 9.2.2 for spark-ignition engines and start with the first law of thermodynamics for an open system which is quasi static (i.e., uniform in pressure and temperature). The first law for such a system (see Fig. 9-11) is

$$\frac{dQ}{dt} - p\frac{dV}{dt} + \sum_i \dot{m}_i h_i = \frac{dU}{dt} \tag{10.1}$$

where dQ/dt is the heat-transfer rate across the system boundary into the system, $p(dV/dt)$ is the rate of work transfer done by the system due to system boundary displacement, $\dot{m}_i$ is the mass flow rate into the system across the system boundary at location i (flow out of the system would be negative), h_i is the enthalpy of flux i entering or leaving the system, and U is the energy of the material contained inside the system boundary.

The following problems make the application of this equation to diesel combustion difficult:

1. Fuel is injected into the cylinder. Liquid fuel is added to the cylinder which vaporizes and mixes with air to produce a fuel/air ratio distribution which is nonuniform and varies with time. The process is not quasi static.
2. The composition of the burned gases (also nonuniform) is not known.
3. The accuracy of available correlations for predicting heat transfer in diesel engines is not well defined (see Chap. 12).
4. Crevice regions (such as the volumes between the piston, rings, and cylinder wall) constitute a few percent of the clearance volume. The gas in these regions is cooled to close to the wall temperature, increasing its density and, therefore,

the relative importance of these crevices. Thus crevices increase heat transfer and contain a nonnegligible fraction of the cylinder charge at conditions that are different from the rest of the combustion chamber.

Due to difficulties in dealing with these problems, both sophisticated methods of analysis and more simple methods give only approximate answers.

10.4.1 Combustion Efficiency

In both heat-release and fuel mass burned estimations, an important factor is the completeness of combustion. Air utilization in diesels is limited by the onset of black smoke in the exhaust. The smoke is soot particles which are mainly carbon. While smoke and other incomplete combustion products such as unburned hydrocarbons and carbon monoxide represent a combustion inefficiency, the magnitude of that inefficiency is small. At full load conditions, if only 0.5 percent of the fuel supplied is present in the exhaust as black smoke, the result would be unacceptable. Hydrocarbon emissions are the order of or less than 1 percent of the fuel. The fuel energy corresponding to the exhausted carbon monoxide is about 0.5 percent. Thus, the combustion inefficiency [Eq. (4.69)] is usually less than 2 percent; the combustion efficiency is usually greater than about 98 percent (see Fig. 3-9). While these emissions are important in terms of their air-pollution impact (see Chap. 11), from the point of view of energy conversion it is a good approximation to regard combustion and heat release as essentially complete.

10.4.2 Direct-Injection Engines

For this type of engine, the cylinder contents are a single open system. The only mass flows across the system boundary (while the intake and exhaust valves are closed) are the fuel and the crevice flow. An approach which incorporates the crevice flow has been described in Sec. 9.2.2; crevice flow effects will be omitted here. Equation (10.1) therefore becomes

$$\frac{dQ}{dt} - p\frac{dV}{dt} + \dot{m}_f h_f = \frac{dU}{dt} \tag{10.2}$$

Two common methods are used to obtain combustion information from pressure data using Eq. (10.2). In both approaches, the cylinder contents are assumed to be at a uniform temperature at each instant in time during the combustion process. One method yields fuel energy- or heat-release rate; the other method yields a fuel mass burning rate. The term *apparent* is often used to describe these quantities since both are approximations to the real quantities which cannot be determined exactly.

HEAT-RELEASE ANALYSIS. If U and h_f in Eq. (10.2) are taken to be the sensible internal energy of the cylinder contents and the sensible enthalpy of the injected

fuel, respectively,† then dQ/dt becomes the difference between the chemical energy or heat released by combustion of the fuel (a positive quantity) and the heat transfer from the system (in engines, the heat transfer is from the system and by thermodynamic convention is a negative quantity). Since $h_{s,f} \approx 0$, Eq. (10.2) becomes

$$\frac{dQ_n}{dt} = \frac{dQ_{ch}}{dt} - \frac{dQ_{ht}}{dt} = p\frac{dV}{dt} + \frac{dU_s}{dt} \tag{10.3}$$

The apparent *net heat-release* rate, dQ_n/dt, which is the difference between the apparent *gross heat-release* rate dQ_{ch}/dt and the heat-transfer rate to the walls dQ_{ht}/dt, equals the rate at which work is done on the piston plus the rate of change of sensible internal energy of the cylinder contents.

If we further assume that the contents of the cylinder can be modeled as an ideal gas, then Eq. (10.3) becomes

$$\frac{dQ_n}{dt} = p\frac{dV}{dt} + mc_v\frac{dT}{dt} \tag{10.4}$$

From the ideal gas law, $pV = mRT$, with R assumed constant, it follows that

$$\frac{dp}{p} + \frac{dV}{V} = \frac{dT}{T} \tag{10.5}$$

Equation (10.5) can be used to eliminate T from Eq. (10.4) to give

$$\frac{dQ_n}{dt} = \left(1 + \frac{c_v}{R}\right)p\frac{dV}{dt} + \frac{c_v}{R}V\frac{dp}{dt}$$

or

$$\frac{dQ_n}{dt} = \frac{\gamma}{\gamma - 1}p\frac{dV}{dt} + \frac{1}{\gamma - 1}V\frac{dp}{dt} \tag{10.6}$$

Here γ is the ratio of specific heats, c_p/c_v. An appropriate range for γ for diesel heat-release analysis is 1.3 to 1.35; Eq. (10.6) is often used with a constant value of γ within this range. More specifically, we would expect γ for diesel engine heat-release analysis to have values appropriate to air at end-of-compression-stroke temperatures prior to combustion ($\approx$1.35) and to burned gases at the overall equivalence ratio following combustion ($\approx$1.26–1.3). The appropriate values for γ during combustion which will give most accurate heat-release information are not well defined.[7, 8]

More complete methods of heat-release analysis based on Eq. (10.2) have been proposed and used. These use more sophisticated models for the gas properties before, during, and after combustion, and for heat transfer and crevice effects.[8] However, it is also necessary to deal with the additional issues of: (1) mixture nonuniformity (fuel/air ratio nonuniformity *and* burned and unburned gas nonuniformities); (2) accuracy of any heat-transfer model used (see Chap. 12);

† That is, $U = U_s = U(T) - U(298\text{ K})$ and $h_f = h_{s,f} = h_f(T) - h_f(298\text{ K})$; see Sec. 5.5 for definition.

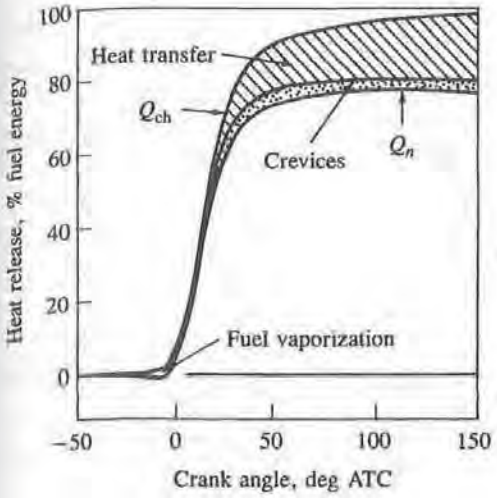


FIGURE 10-11
Gross and net heat-release profile during combustion, for a turbocharged DI diesel engine in mid-load, mid-speed range, showing relative magnitude of heat transfer, crevice, and fuel vaporization and heatup effects.

and (3) the effects of the crevice regions. These additional phenomena must be dealt with at an equivalent level of accuracy for more complex heat-release models to be worth while. For many engineering applications, Eq. (10.6) is adequate for diesel engine combustion analysis.

Additional insight can be obtained by incorporating a model for the largest of the effects omitted from Eq. (10.6), the heat transfer dQ_{ht}/dt (see Chap. 12); we thereby obtain a close approximation to the *gross* heat-release rate. The integral of the gross heat-release rate over the complete combustion process should then equal (to within a few percent only, since the analysis is not exact) the mass of fuel injected m_f times the fuel lower heating value Q_{LHV}: i.e.,

$$Q_{ch} = \int_{t_{start}}^{t_{end}} \frac{dQ_{ch}}{dt}\, dt = m_f Q_{LHV} \tag{10.7}$$

Of course, Eqs. (10.1) to (10.4), (10.6), and (10.7) also hold with crank angle θ as the independent variable instead of time t.

Figure 10-11 illustrates the relative magnitude of gross and net heat release, heat transfer, crevice effects, and heat of vaporization and heating up of the fuel for a turbocharged DI diesel engine operating in the mid-load, mid-speed range. The net heat release is the gross heat release due to combustion, less the heat transfer to the walls, crevice effects, and the effect of fuel vaporization and heatup (which was omitted above by neglecting the mass addition term in dU/dt). This last term is sufficiently small to be neglected. The enthalpy of vaporization of diesel fuel is less than 1 percent of its heating value; the energy change associated with heating up fuel vapor from injection temperature to typical compression air temperatures is about 3 percent of the fuel heating value. The heat transfer integrated over the duration of the combustion period is 10 to 25 percent of the total heat released.

FUEL MASS BURNING RATE ANALYSIS. If the internal energies of the fuel, air, and burned gases in Eq. (10.1) are evaluated relative to a consistent datum (such

as that described in Sec. 4.5.2), then this equation can be used to obtain an apparent *fuel mass burning rate* from cylinder pressure versus crank angle data. (With such a species energy datum the "heat release" is properly accounted for in the internal energy and enthalpy terms.) Following Krieger and Borman,[9] Eq. (10.2) can be written as

$$\frac{d}{dt}(mu) = -p\frac{dV}{dt} + \frac{dQ}{dt} + h_f\frac{dm}{dt} \tag{10.8}$$

Here Q is the heat transfer to the gas within the combustion chamber (that is, $Q = -Q_{ht}$), m is the mass within the combustion chamber, and dm/dt has been substituted for $\dot{m}_f$.

Since the properties of the gases in the cylinder during combustion (assumed to be uniform and in chemical equilibrium at the pressure p and average temperature T) are in general a function of p, T, and the equivalence ratio ϕ,

$$u = u(T, p, \phi) \qquad \text{and} \qquad R = R(T, p, \phi)$$

Therefore

$$\frac{du}{dt} = \frac{\partial u}{\partial T}\frac{dT}{dt} + \frac{\partial u}{\partial p}\frac{dp}{dt} + \frac{\partial u}{\partial \phi}\frac{d\phi}{dt} \tag{10.9a}$$

$$\frac{dR}{dt} = \frac{\partial R}{\partial T}\frac{dT}{dt} + \frac{\partial R}{\partial p}\frac{dp}{dt} + \frac{\partial R}{\partial \phi}\frac{d\phi}{dt} \tag{10.9b}$$

Also,

$$\phi = \phi_0 + \left(\frac{m}{m_0} - 1\right)\frac{1 + (F/A)_0}{(F/A)_s} \tag{10.10}$$

and

$$\frac{d\phi}{dt} = \frac{1 + (F/A)_0}{(F/A)_s m_0}\frac{dm}{dt} \tag{10.11}$$

(F/A) is the fuel/air ratio; the subscript 0 denotes the initial value prior to fuel injection and the subscript s denotes the stoichiometric value. It then follows that

$$\frac{1}{m}\frac{dm}{dt} = \frac{-(RT/V)(dV/dt) - (\partial u/\partial p)(dp/dt) + (1/m)(dQ/dt) - CB}{u - h_f + D(\partial u/\partial \phi) - C[1 + (D/R)(\partial R/\partial \phi)]} \tag{10.12}$$

where

$$B = \frac{1}{p}\frac{dp}{dt} - \frac{1}{R}\frac{\partial R}{\partial p}\frac{dp}{dt} + \frac{1}{V}\frac{dV}{dt}$$

$$C = \frac{T(\partial u/\partial T)}{1 + (T/R)(\partial R/\partial T)}$$

$$D = \frac{[1 + (F/A)_0]m}{(F/A)_s m_0}$$

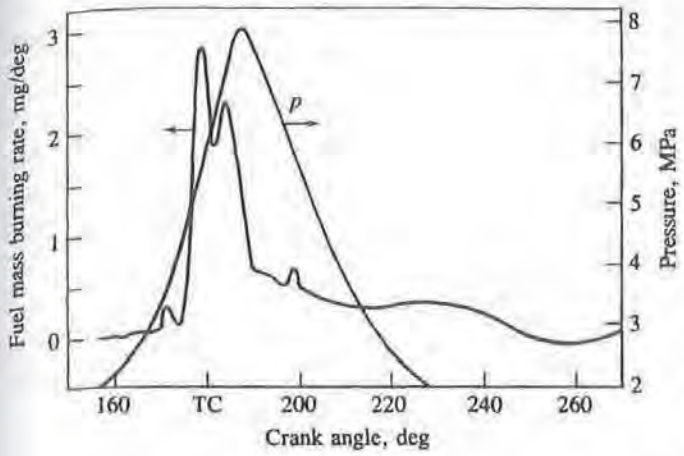


FIGURE 10-12
Cylinder pressure p and fuel mass burning rate calculated from p, as a function of crank angle, using the Krieger and Borman method[9] for DI diesel engine at 3200 rev/min and full load.

Equation (10.12) can be solved numerically for $m(t)$ given m_0, ϕ_0, $p(t)$, and appropriate models for the working fluid properties (see Sec. 4.7) and for the heat-transfer term dQ/dt (see Chap. 12).

Figure 10-12 shows cylinder pressure data for an open chamber DI diesel and fuel mass burning rate $dm/d\theta$ calculated from that data using the above method. The heat-transfer model of Annand was used (see Sec. 12.4.3). The result obtained is an *apparent* fuel mass burning rate. It is best interpreted, after multiplying by the heating value of the fuel, as the fuel chemical-energy or heat-release rate. The *actual* fuel burning rate is unknown because not all the fuel "burns" with sufficient air available locally to produce products of *complete* combustion. About 60 percent of the fuel has burned in the first one-third of the total combustion period. The integral of the fuel mass burning rate over the combustion process should equal the total fuel mass burned; in this case it is 3 percent less than the total fuel mass injected. Note that chemical energy continues to be released well into the expansion process. The accuracy of this type of calculation then decreases, however, since errors in estimating heat transfer significantly affect the apparent fuel burning rate.

Krieger and Borman also carried out sensitivity analyses for the critical assumptions and variables. They found that the effect of dissociation of the product gases was negligible. This permits a substantial simplification of Eq. (10.12). With no dissociation, $u = u(T, \phi)$, and $R = \tilde{R}/M$ can be taken as constant, since the molecular weight M changes little. Then

$$\frac{dm}{dt} = \frac{[1 + (c_v/R)]p(dV/dt) + (c_v/R)V(dp/dt) - (dQ/dt)}{h_f + (c_v/R)(pV/m) - u - D(\partial u/\partial \phi)} \tag{10.13}$$

where D, as before, is $[1 + (F/A)_0]m/[(F/A)_s m_0]$. Given the uncertainties inherent in the heat-transfer model and the neglect of nonuniformities and crevices, Eq. (10.13) represents an adequate level of sophistication.

The other sensitivity variations studied by Krieger and Borman were: shifting of the phasing of the pressure data 2° forward and 2° backward; translating the pressure data ± 34 kPa (5 lb/in^2); changing the heat transfer ± 50 percent;

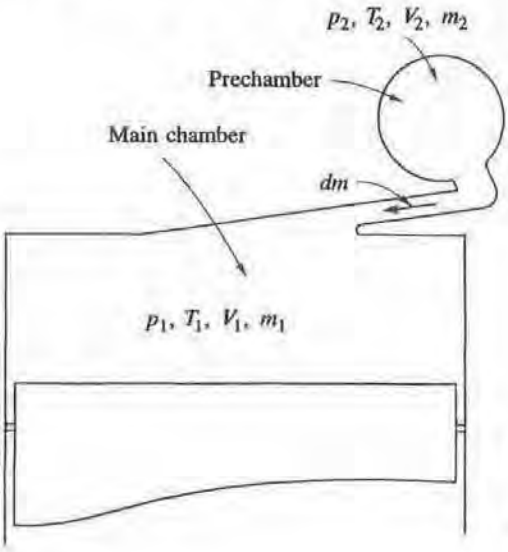


FIGURE 10-13
Schematic defining variables in main chamber (subscript 1) and prechamber (subscript 2) for IDI engine heat-release analysis.

increasing the initial mass 5 percent. The initial mass change had a negligible effect on the fuel burning rate calculations. The heat-transfer changes of ± 50 percent changed the mass of fuel burned by about ± 5 percent. The change in phasing of the pressure data was more significant. It needs to be stressed that *accurate* (in magnitude and phasing) pressure data are a most important requirement for useful heat-release or fuel mass burning rate analysis.

10.4.3 Indirect-Injection Engines

In IDI diesel engines, the pressures in each of the two chambers, main and auxiliary, are not the same during the combustion process. Since combustion starts in the auxiliary or prechamber, the fuel energy release in the prechamber causes the pressure there to rise above the main chamber pressure. Depending on combustion chamber design and operating conditions, the prechamber pressure rises to be 0.5 to 5 atm above that in the main chamber. This pressure difference causes a flow of fuel, air, and burning and burned gases into the main chamber, where additional energy release now occurs. The analysis of the DI diesel in the previous section was based on uniform pressure throughout the combustion chamber. For IDI engines the effect of the pressure difference between the chambers must usually be included.

Figure 10-13 shows an IDI combustion chamber divided at the nozzle into two open systems. Applying the first law [Eq. (10.1)] to the *main chamber* yields

$$\frac{dQ_1}{dt} - p_1 \frac{dV_1}{dt} + h_{2,1} \frac{dm}{dt} = \frac{dU_1}{dt} \tag{10.14}$$

and to the *auxiliary chamber* yields

$$\frac{dQ_2}{dt} - h_{2,1} \frac{dm}{dt} + h_f \frac{dm_f}{dt} = \frac{dU_2}{dt} \tag{10.15}$$

Here dm/dt is the mass flow rate between the chambers with positive flow from the prechamber to the main chamber. If $dm/dt > 0$, $h_{2,1} = h_2$; if $dm/dt < 0$, $h_{2,1} = h_1$. If we define U_1 and U_2 as sensible internal energies and h_f as the sensible enthalpy of the fuel, then dQ_1/dt and dQ_2/dt represent the net heat-release rates—the difference between the combustion energy-release rates and the rates of heat transfer to the walls.

If we use an ideal gas model for the working fluid in each chamber, with c_v, c_p, and M constant, the relation $p_1 V_1 = m_1 R T_1$ and $p_2 V_2 = m_2 R T_2$ can be used to eliminate m and T from the dU/dt terms and, with the fact that $h_{s,f} = 0$, can be used to write Eqs. (10.14) and (10.15) as

$$\frac{dQ_1}{dt} = \frac{\gamma}{\gamma - 1} p_1 \frac{dV_1}{dt} + \frac{1}{\gamma - 1} V_1 \frac{dp_1}{dt} - c_p T_{2,1} \frac{dm}{dt} \tag{10.16}$$

$$\frac{dQ_2}{dt} = \frac{1}{\gamma - 1} V_2 \frac{dp_2}{dt} + c_p T_{2,1} \frac{dm}{dt} \tag{10.17}$$

When Eqs. (10.16) and (10.17) are added together, the term representing the enthalpy flux between the two chambers cancels out, and the following equation for *total* net heat-release results:

$$\frac{dQ}{dt} = \frac{dQ_1}{dt} + \frac{dQ_2}{dt} = \frac{\gamma}{\gamma - 1} p_1 \frac{dV_1}{dt} + \frac{1}{\gamma - 1}\left(V_1 \frac{dp_1}{dt} + V_2 \frac{dp_2}{dt}\right) \tag{10.18}$$

The comments made in the previous section regarding the interpretation of the net heat release (it is the gross heat release due to combustion less the heat transfer to the walls, and other smaller energy transfers due to crevices, fuel vaporization, and heatup) also hold here.

In practice, Eq. (10.18) is difficult to use since it requires experimental data for both the main and auxiliary chamber pressures throughout the combustion process. Access for two pressure transducers through the cylinder head is not often available; even when access can be achieved, the task of obtaining pressure data from two different transducers under the demanding thermal loading conditions found in IDI diesels, of sufficient accuracy such that the difference between the pressures (of order 0.5 to 5 atm) at pressure levels of 60 to 80 atm can be interpreted, requires extreme diligence in technique.[10, 11] Figure 10-14*a* and *b* shows apparent net heat-release rate profiles for an IDI diesel obtained using Eq. (10.18) with $\gamma = 1.35$.[11] Curves of dQ/dt and $dQ/d\theta$ are shown at three different speeds and essentially constant fuel mass injected per cycle. While the absolute heat-release rates increase with increasing speed, the relative rates are essentially independent of speed, indicating that combustion rates, which depend on fuel-air mixing rates, scale approximately with engine speed.

Equation (10.18) (or its equivalent) has been used assuming $p_2 = p_1$ and using either main chamber or auxiliary chamber pressure data alone. The error associated with this approximation can be estimated as follows. If we write $p_2 =$

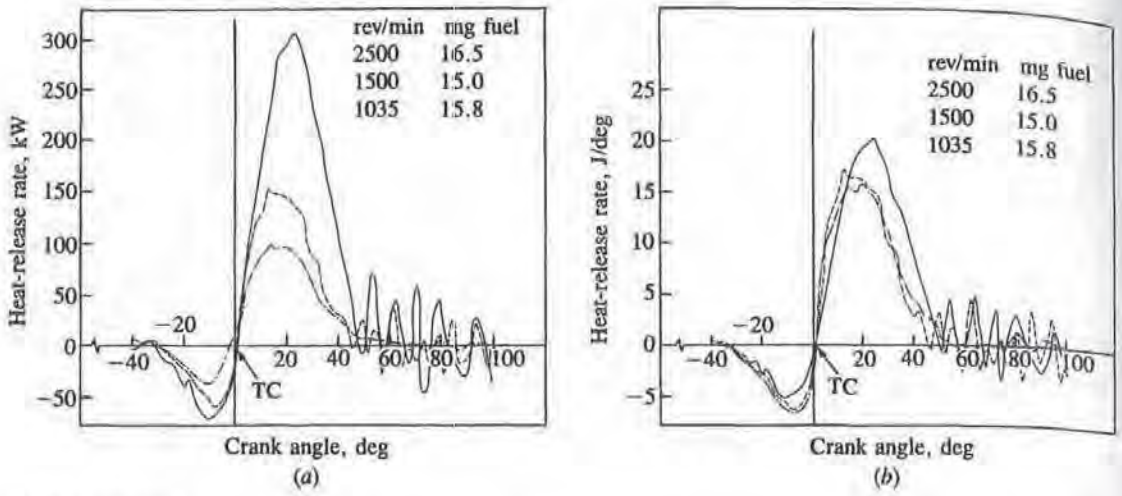


FIGURE 10-14
Calculated net heat-release-rate profiles for IDI diesel engine at constant load ($0.29 \leq \phi \leq 0.32$). (*a*) Heat-release rate in kilowatts. (*b*) Heat-release rate in joules per degree.[11]

$p_1 + \Delta p$ then Eq. (10.18) becomes

$$\frac{dQ}{dt} = \frac{\gamma}{\gamma - 1} p_1 \frac{dV_1}{dt} + \frac{V_1 + V_2}{\gamma - 1} \frac{dp_1}{dt} + \frac{V_2}{\gamma - 1} \frac{d(\Delta p)}{dt} \tag{10.19}$$

If the last term is omitted, Eq. (10.19) is identical to Eq. (10.6) derived for the DI diesel. Since the term $V(dp_1/dt)/(\gamma - 1)$ is much larger than the first term on the right-hand side of Eq. (10.19) during the early stages of the combustion process, the error involved in omitting the last term is given to a good approximation by $[V_2/(V_1 + V_2)]d(\Delta p)/dp_1$. In the initial stages of combustion this error can be quite large (of order 0.25 based on data in Ref. 10 close to TC). Later in the combustion process it becomes negligible (of order a few percent after 20° ATC).[10] Thus, neglecting Δp will lead to errors in predicting the initial heat-release *rate*. The magnitude of the error will depend on the design of the combustion chamber and on engine speed and load (with more restricted passageways, higher loads and speeds, giving higher values of Δp and, therefore, greater error). Later in the combustion process the error is much less, so *integrated* heat-release data derived ignoring Δp will show a smaller error.

A model analogous to the above, but using the approach of Krieger and Borman[9] (see Sec. 10.4.2), for the IDI diesel has been developed and used by Watson and Kamel.[10] The energy conservation equation for an *open* system developed in Sec. 14.2.2, with energy and enthalpy modeled using a consistent datum (see Sec. 4.5.2), with appropriate models for convective and radiation heat transfer and for gas properties, was applied to the main chamber and also to the prechamber. These equations were solved using accurately measured main chamber and prechamber pressure data to determine the apparent rate of heat release (here, the rate of fuel burning multiplied by the fuel heating value) in the main chamber and prechambers through the combustion process. The engine was a Ricardo Comet swirl chamber IDI design. Some results are shown in Fig.

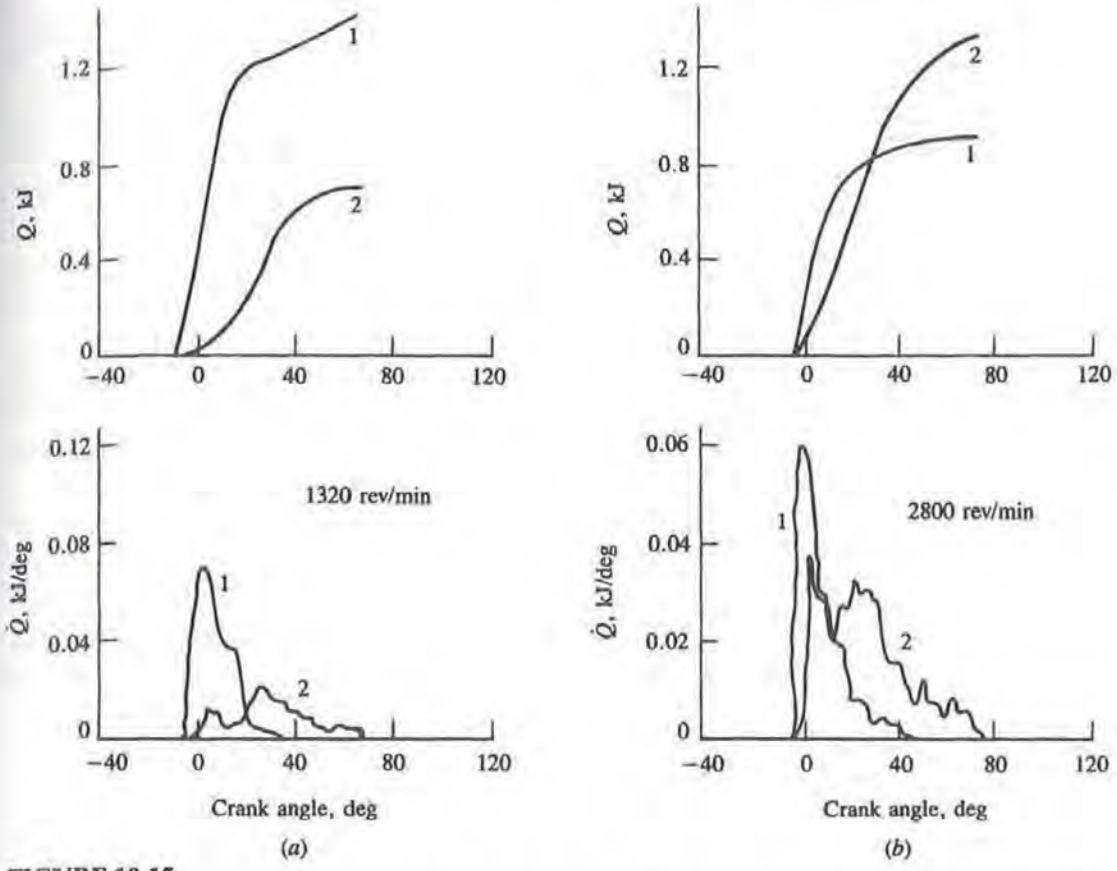


FIGURE 10-15
Calculated gross heat-release rates in IDI swirl-chamber diesel engine at full load. 1 Prechamber heat release. 2 Main chamber heat release. Top figures: integrated heat release. Bottom figures: heat-release rate. (*a*) 1320 rev/min; (*b*) 2800 rev/min.[10]

10-15. For this particular engine, at low engine speeds two-thirds of the heat release occurs in the prechamber; at higher engine speeds about two-thirds of the heat release occurs in the main chamber.

10.5 FUEL SPRAY BEHAVIOR

10.5.1 Fuel Injection

The fuel is introduced into the cylinder of a diesel engine through a nozzle with a large pressure differential across the nozzle orifice. The cylinder pressure at injection is typically in the range 50 to 100 atm. Fuel injection pressures in the range 200 to 1700 atm are used depending on the engine size and type of combustion system employed. These large pressure differences across the injector nozzle are required so that the injected liquid fuel jet will enter the chamber at sufficiently high velocity to (1) atomize into small-sized droplets to enable rapid evaporation and (2) traverse the combustion chamber in the time available and fully utilize the air charge.

Examples of common diesel fuel-injection systems were described briefly in Sec. 1.7 and illustrated in Figs. 1-17 to 1-19. (See also Refs. 12 and 13 for more

extensive descriptions of diesel fuel-injection systems.) The task of the fuel-injection system is to meter the appropriate quantity of fuel for the given engine speed and load to each cylinder, each cycle, and inject that fuel at the appropriate time in the cycle at the desired rate with the spray configuration required for the particular combustion chamber employed. It is important that injection begin and end cleanly, and avoid any secondary injections.

To accomplish this task, fuel is usually drawn from the fuel tank by a supply pump, and forced through a filter to the injection pump. The injection pump sends fuel under pressure to the nozzle pipes which carry fuel to the injector nozzles located in each cylinder head. Excess fuel goes back to the fuel tank. Figures 1-17 and 1-19 show two common versions of fuel systems used with multicylinder engines in the 20 to 100 kW per cylinder brake power range which operate with injection pressures between about 300 and 1200 atm.

In-line injection pumps (Fig. 1-17) are used in engines in the 40 to 100 kW per cylinder maximum power range. They contain a plunger and barrel assembly for each engine cylinder. Each plunger is raised by a cam on the pump camshaft and is forced back by the plunger return spring. The plunger stroke is fixed. The plunger fits sufficiently accurately within the barrel to seal without additional sealing elements, even at high pressures and low speeds. The amount of fuel delivered is altered by varying the *effective* plunger stroke. This is achieved by means of a control rod or rack, which moves in the pump housing and rotates the plunger via a ring gear or linkage lever on the control sleeve. The plunger chamber above the plunger is always connected with the chamber below the plunger helix by a vertical groove or bore in the plunger. Delivery ceases when the plunger helix exposes the intake port (port opening), thus connecting the plunger chamber with the suction gallery. When this takes place depends on the rotational position of the plunger. In the case of a lower helix, delivery always starts (port closing) at the same time, but ends sooner or later depending on the rotational position of the plunger. With a plunger with an upper helix, port closing (start of delivery) not port opening is controlled by the helix and is varied by rotating the plunger. Figure 1-18 illustrates how the plunger helix controls fuel delivery.[14]

Distributor-type fuel-injection pumps (such as that illustrated in Fig. 1-19) are normally used in multicylinder engines with less than 30 kW per cylinder maximum power with injection pressures up to 750 atm. These pumps have only one plunger and barrel. The pump plunger is made to describe a combined rotary and stroke movement by the rotating cam plate. The fuel is accurately metered to each injection nozzle in turn by this plunger which simultaneously acts as the distributor. Such units are more compact and cheaper than in-line pumps but cannot achieve such high injection pressures. The distributor-type fuel-injection pump is combined with the automatic timing device, governor, and supply pump to form a single unit.

Single-barrel injection pumps are used on small one- and two-cylinder diesel engines, as well as large engines with outputs of more than 100 kW per cylinder. Figure 10-16 shows the layout of the injection system and a section

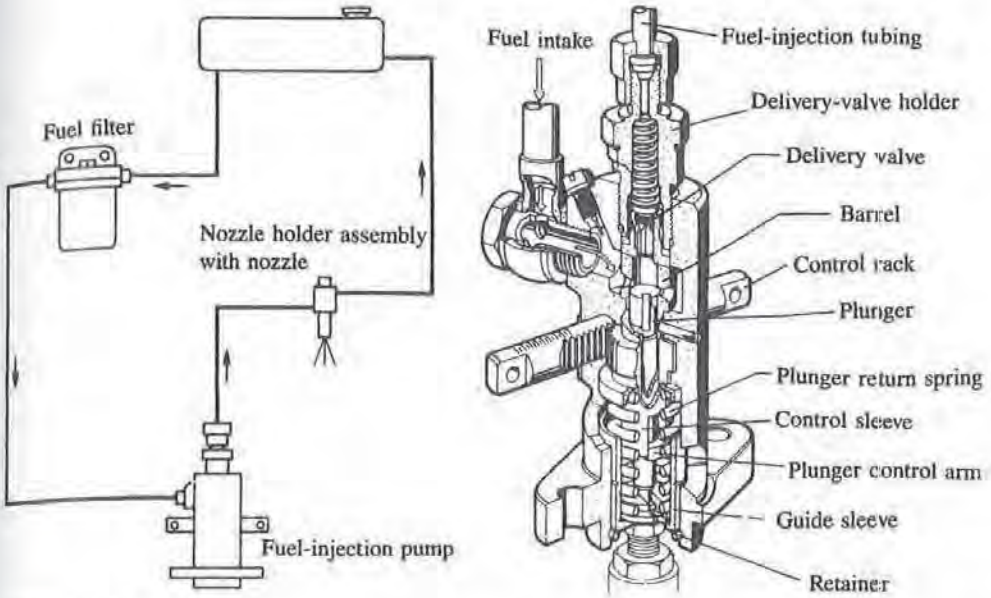


FIGURE 10-16
Fuel-injection system with single-barrel pump. Left: system layout. Right: section through fuel-injection pump. (*Courtesy Robert Bosch GmbH and SAE.*[14])

through the fuel-injection pump.[14] Such pumps are driven by an auxiliary cam on the engine camshaft. Also used extensively on larger engines are unit injectors where the pump and injector nozzle are combined into a single unit. An example of a unit injector and its driving mechanism used on a large two-stroke cycle diesel engine is shown in Fig. 10-17. Fuel, supplied to the injector through a fuel-distributing manifold, enters the cavity or plunger chamber ahead of the plunger through a metering orifice. When fuel is to be injected, the cam via the rocker arm pushes down the plunger, closing the metering orifice and compressing the fuel, causing it to flow through check valves and discharge into the cylinder through the injector nozzles or orifices. The amount of fuel injected is controlled by the rack, which controls the spill of fuel into the fuel drain manifold by rotating the plunger with its helical relief section via the gear.

The most important part of the injection system is the nozzle. Examples of different nozzle types and a nozzle holder assembly are shown in Fig. 1-18. The nozzles shown are fluid-controlled needle valves where the needle is forced against the valve seat by a spring. The pressure of the fuel in the pressure chamber above the nozzle aperture opens the nozzle by the axial force it exerts on the conical surface of the nozzle needle. Needle valves are used to prevent dribble from the nozzles when injection is not occurring. It is important to keep the volume of fuel left between the needle and nozzle orifices (the sac volume) as small as possible to prevent any fuel flowing into the cylinder after injection is over, to control hydrocarbon emissions (see Sec. 11.4.4). Multihole nozzles are used with most direct-injection systems; the M.A.N. "M" system uses a single-hole nozzle. Pintle nozzles, where the needle projects into and through the nozzle hole, are used in indirect-injection engine systems. The shape of the pin on the

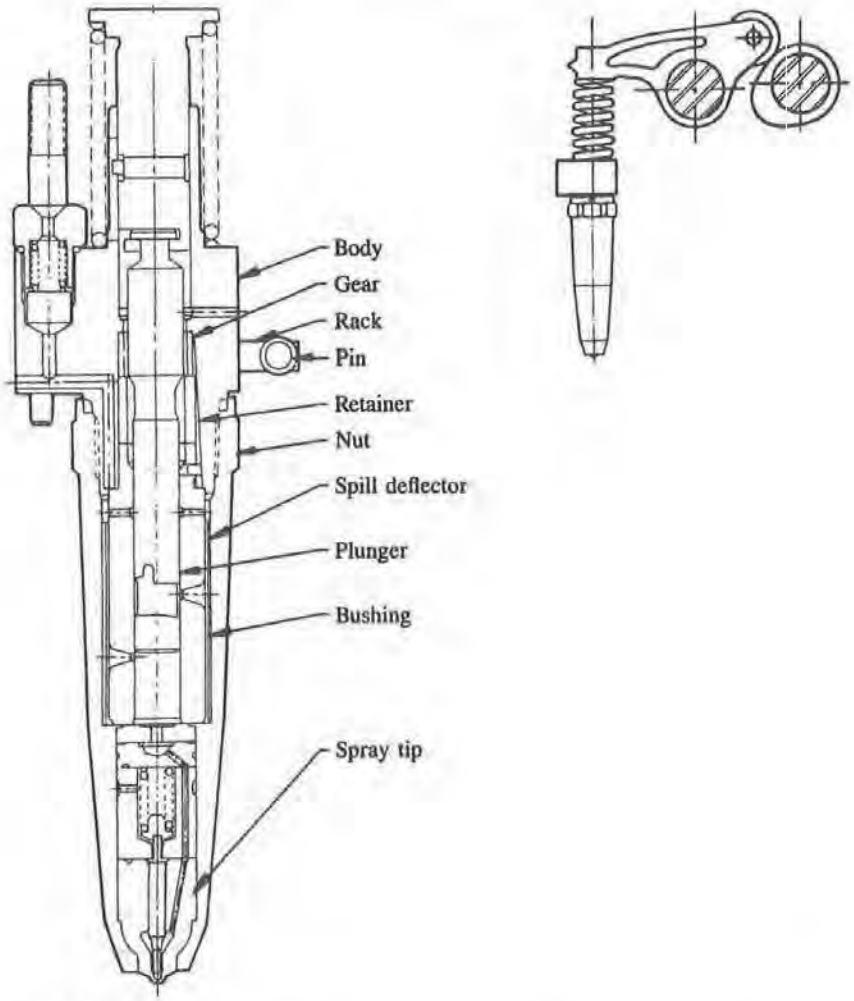


FIGURE 10-17
Unit fuel injector and its driving mechanism, typically used in large diesel engines.[15]

end of the nozzle needle controls the spray pattern and fuel-delivery characteristics. Auxiliary nozzle holes are sometimes used to produce an auxiliary smaller spray to aid ignition and starting. Open nozzle orifices, without a needle, are also used.

The technology for electronic control of injection is now available. In an electronic injector, such as that shown in Fig. 10-18, a solenoid operated control valve performs the injection timing and metering functions in a fashion analogous to the ports and helices of the mechanical injector. Solenoid valve closure initiates pressurization and injection, and opening causes injection pressure decay and end of injection. Duration of valve closure determines the quantity of fuel injected. The unit shown uses camshaft/rocker arm driven plungers to generate the injection pressure, and employs needle-valve nozzles of conventional design. Increased flexibility in fuel metering and timing and simpler injector mechanical design are important advantages.[16]

Accurate predictions of fuel behavior within the injection system require

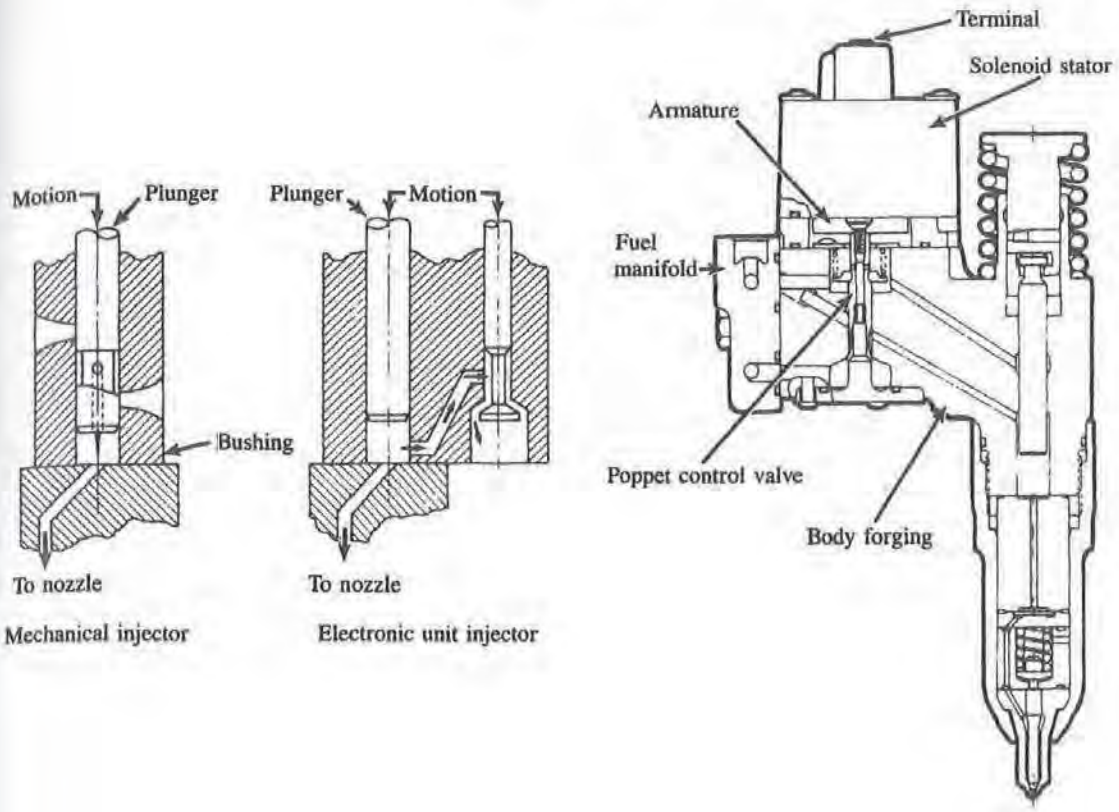


FIGURE 10-18
Electronically controlled unit fuel-injection system.[16]

sophisticated hydraulic models: Hiroyasu[17] provides an extensive reference list of such models. However, approximate estimates of the injection rate through the injector nozzles can be made as follows. If the pressure upstream of the injector nozzle(s) can be estimated or measured, and assuming the flow through each nozzle is quasi steady, incompressible, and one dimensional, the mass flow rate of fuel injected through the nozzle $\dot{m}_f$ is given by

$$\dot{m}_f = C_D A_n \sqrt{2\rho_f \Delta p} \tag{10.20}$$

where A_n is the nozzle minimum area, C_D the discharge coefficient, ρ_f the fuel density, and Δp the pressure drop across the nozzle. If the pressure drop across the nozzle and the nozzle open area are essentially constant during the injection period, the mass of fuel injected is then

$$m_f = C_D A_n \sqrt{2\rho_f \Delta p}\, \frac{\Delta\theta}{360N} \tag{10.21}$$

where $\Delta\theta$ is the nozzle open period in crank angle degrees and N is engine speed. Equations (10.20) and (10.21) illustrate the dependence of injected amounts of fuel on injection system and engine parameters.

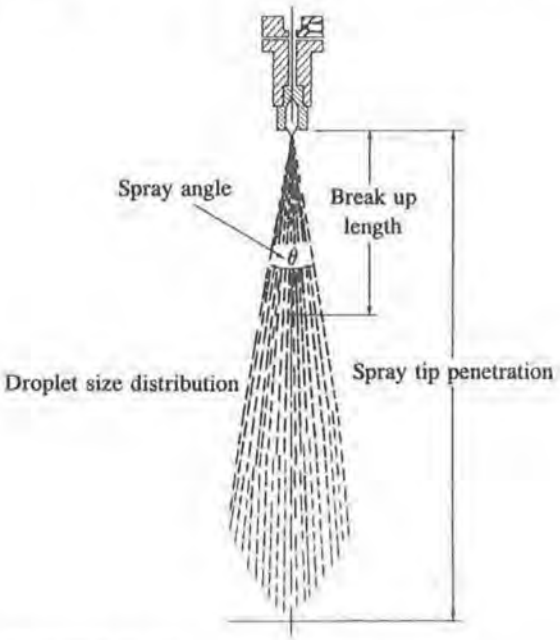


FIGURE 10-19
Schematic of diesel fuel spray defining its major parameters.[18]

10.5.2 Overall Spray Structure

The fuel is introduced into the combustion chamber of a diesel engine through one or more nozzles or orifices with a large pressure differential between the fuel supply line and the cylinder. Different designs of nozzle are used (e.g., single-orifice, multiorifice, throttle, or pintle; see Fig. 1-18), depending on the needs of the combustion system employed. Standard diesel injectors usually operate with fuel-injection pressures between 200 and 1700 atm. At time of injection, the air in the cylinder has a pressure of 50 to 100 atm, temperature about 1000 K, and density between 15 and 25 kg/m^3. Nozzle diameters cover the range 0.2 to 1 mm diameter, with length/diameter ratios from 2 to 8. Typical distillate diesel fuel properties are: relative specific gravity of 0.8, viscosity between 3 and 10 kg/m·s and surface tension about 3×10^{-2} N/m (at 300 K). Figure 10-19 illustrates the structure of a typical DI engine fuel spray. As the liquid jet leaves the nozzle it becomes turbulent and spreads out as it entrains and mixes with the surrounding air. The initial jet velocity is greater than 10^2 m/s. The outer surface of the jet breaks up into drops of order 10 μm diameter, close to the nozzle exit. The liquid column leaving the nozzle disintegrates within the cylinder over a finite length called the *breakup length* into drops of different sizes. As one moves away from the nozzle, the mass of air within the spray increases, the spray diverges, its width increases, and the velocity decreases. The fuel drops evaporate as this air-entrainment process proceeds. The tip of the spray penetrates further into the combustion chamber as injection proceeds, but at a decreasing rate. Figure 10-20 shows photographs of a diesel fuel spray injected into quiescent air in a rapid-compression machine which simulates diesel conditions.[19] Two different pho-

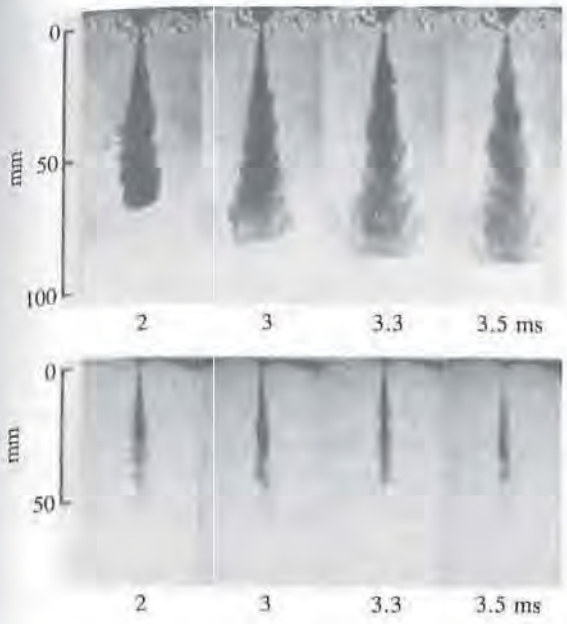


FIGURE 10-20
Shadowgraph and back-illuminated photographs of evaporating spray injected into nitrogen at 3.4 MPa and 670 K in rapid-compression machine. Times in milliseconds are after start of injection: injection duration 3.3 ms. Top (shadowgraph) photographs show full vapor and liquid region. Bottom (back-illuminated) photographs only show liquid-containing core.[19]

tographic techniques, back lighting and shadowgraph,† have been used to distinguish the liquid-containing core of the jet and the extent of the fuel vapor region of the spray which surrounds the liquid core. The region of the jet closest to the nozzle (until injection ceases at 3.3 ms) contains liquid drops and ligaments; the major region of the spray is a substantial vapor cloud around this narrow core which contains liquid fuel.

Different spray configurations are used in the different diesel combustion systems described earlier in this chapter. The simplest configuration involves multiple sprays injected into quiescent air in the largest-size diesels (Fig. 10-1*a*). Figures 10-19 and 10-20 illustrate the essential features of each spray under these circumstances until interactions with the wall occur. Each liquid fuel jet atomizes into drops and ligaments at the exit from the nozzle orifice (or shortly thereafter). The spray entrains air, spreads out, and slows down as the mass flow in the spray increases. The droplets on the outer edge of the spray evaporate first, creating a fuel vapor–air mixture sheath around the liquid-containing core. The highest velocities are on the jet axis. The equivalence ratio is highest on the centerline (and fuel-rich along most of the jet), decreasing to zero (unmixed air) at the spray boundary. Once the sprays have penetrated to the outer regions of the combustion chamber, they interact with the chamber walls. The spray is then forced to flow tangentially along the wall. Eventually the sprays from multihole nozzles

† The back lighting identifies regions where sufficient liquid fuel (as ligaments or drops) is present to attenuate the light. The shadowgraph technique responds to density gradients in the test section, so it identifies regions where fuel vapor exists.

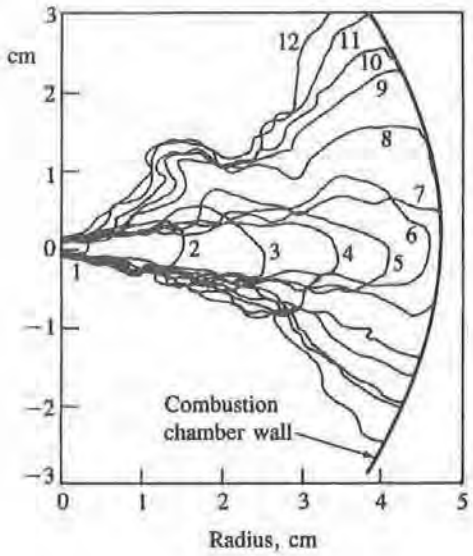


FIGURE 10-21
Sketches of outer vapor boundary of diesel fuel spray from 12 successive frames of rapid-compression-machine high-speed shadowgraph movie showing interaction of vaporizing spray with cylindrical wall of combustion chamber. Injection pressure 60 MPa. Time between frames 0.14 ms.[20]

interact with one another. Figure 10-21 shows diesel fuel sprays interacting with the cylindrical outer wall of a disc-shaped combustion chamber in a rapid-compression machine, under typical diesel-injection conditions. The cylinder wall causes the spray to split with about half flowing circumferentially in either direction. Adjacent sprays then interact forcing the flow radially inward toward the chamber axis.[20]

Most of the other combustion systems in Figs. 10-1 and 10-2 use air swirl to increase fuel-air mixing rates. A schematic of the spray pattern which results when a fuel jet is injected radially outward into a swirling flow is shown in Fig. 10-22. Because there is now relative motion in both radial and tangential directions between the initial jet and the air, the structure of the jet is more complex. As the spray entrains air and slows down it becomes increasingly bent toward the swirl direction; for the same injection conditions it will penetrate less with swirl than without swirl. An important feature of the spray is the large vapor-containing region downstream of the liquid-containing core. Figure 10-23 shows schlieren photographs of four fuel jets injected on the axis of an IDI diesel engine

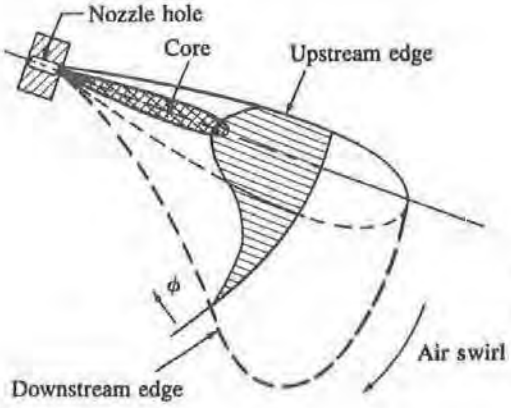


FIGURE 10-22
Schematic of fuel spray injected radially outward from the chamber axis into swirling air flow. Shape of equivalence ratio (ϕ) distribution within jet is indicated.



FIGURE 10-23
Schlieren photographs of vaporizing sprays injected into swirling air flow in transparent prechamber of special IDI diesel.[21] Left: high sensitivity, showing boundaries of the vapor regions of spray. Right: low sensitivity, showing liquid-containing core (dark) in relation to vapor regions (mottled).

prechamber with high clockwise swirl. The photograph on the left, with high sensitivity, shows the outer boundary of the fuel vapor region of the spray; the low-sensitivity photograph on the right locates the liquid phase regions of the spray.[21] The interaction between the swirl and both liquid and vapor spray regions is evident, as is the spray interaction with the chamber wall.

Other spray flow patterns are used. The spray may enter the swirling air flow tangentially as in the M.A.N. "M" system shown in Fig. 10-1*c*. The spray then interacts immediately with the combustion chamber walls.

To couple the spray-development process with the ignition phase of the combustion, it is important to know which regions of the spray contain the fuel injected at the beginning of the injection process. These regions of the sprays are likely to autoignite first. Each spray develops as follows. At the start of injection the liquid fuel enters the quiescent air charge, atomizes, moves outward from the nozzle, and slows down rapidly as air is entrained into the spray and accelerated. This start-up process forms a vortex or "puff" at the head of the spray. The injected fuel which follows encounters less resistance; thus drops from that fuel overtake the drops from first-injected fuel, forcing them outward toward the periphery of the spray. At the tip of the unsteady spray the drops meet the highest aerodynamic resistance and slow down, but the spray continues to penetrate the air charge because droplets retarded at the tip are continually replaced by new higher-momentum later-injected drops.[22] Accordingly, droplets in the periphery of the spray and behind the tip of the spray come from the earliest injected fuel.[23] As Figs. 10-20 and 10-23 indicate, these drops evaporate quickly.

10.5.3 Atomization

Under diesel engine injection conditions, the fuel jet usually forms a cone-shaped spray at the nozzle exit. This type of behavior is classified as the atomization breakup regime, and it produces droplets with sizes very much less than the nozzle exit diameter. This behavior is different from other modes of liquid jet

breakup. At low jet velocity, in the Rayleigh regime, breakup is due to the unstable growth of surface waves caused by surface tension and results in drops larger than the jet diameter. As jet velocity is increased, forces due to the relative motion of the jet and the surrounding air augment the surface tension force, and lead to drop sizes of the order of the jet diameter. This is called the first wind-induced breakup regime. A further increase in jet velocity results in breakup characterized by divergence of the jet spray after an intact or undisturbed length downstream of the nozzle. In this second wind-induced breakup regime, the unstable growth of short-wavelength waves induced by the relative motion between the liquid and surrounding air produces droplets whose average size is much less than the jet diameter. Further increases in jet velocity lead to breakup in the atomization regime, where the breakup of the outer surface of the jet occurs at, or before, the nozzle exit plane and results in droplets whose average diameter is much smaller than the nozzle diameter. Aerodynamic interactions at the liquid/gas interface appear to be one major component of the atomization mechanism in this regime.[22, 24]

A sequence of very short time exposure photographs of the emergence of a liquid jet from a nozzle of 0.34 mm diameter and $L_n/d_n = 4$ into high-pressure nitrogen at ambient temperature is shown in Fig. 10-24. The figure shows how the spray tip penetrates and the spray spreads during the early part of its travel.[25] Data such as these were used to examine the dependence of the spray development on gas and liquid density, liquid viscosity, and nozzle geometry.[24–26] The effects of the most significant variables, gas/liquid density ratio and nozzle geometry, on initial jet spreading angle are shown in Fig. 10-25. For a given geometry (cylindrical hole and length/diameter = 4), the initial jet spreading or spray angle increases with increasing gas/liquid density ratio as shown in Fig. 10-25*a*. Typical density ratios for diesel injection conditions are between 15×10^{-3} and 30×10^{-3}. Of several different nozzle geometry parameters examined, the length/diameter ratio proved to be the most significant (see Fig. 10-25*b*).

For jets in the atomization regime, the spray angle θ was found to follow the relationship

$$\tan \frac{\theta}{2} = \frac{1}{A} 4\pi \left(\frac{\rho_g}{\rho_l}\right)^{1/2} \frac{\sqrt{3}}{6} \tag{10.22}$$

where ρ_g and ρ_l are gas and liquid densities and A is a constant for a given nozzle geometry.† The data in Fig. 10-25*a* are fitted by $A = 4.9$. This behavior is in accord with the theory that aerodynamic interactions are largely responsible for jet breakup. Note that the data in Fig. 10-25*b* show a continuous trend as the jet breakup regime makes a transition from second wind-induced breakup (solid

† An empirical equation for A is $A = 3.0 + 0.28\,(L_n/d_n)$, where L_n/d_n is the length/diameter ratio of the nozzle.[25]

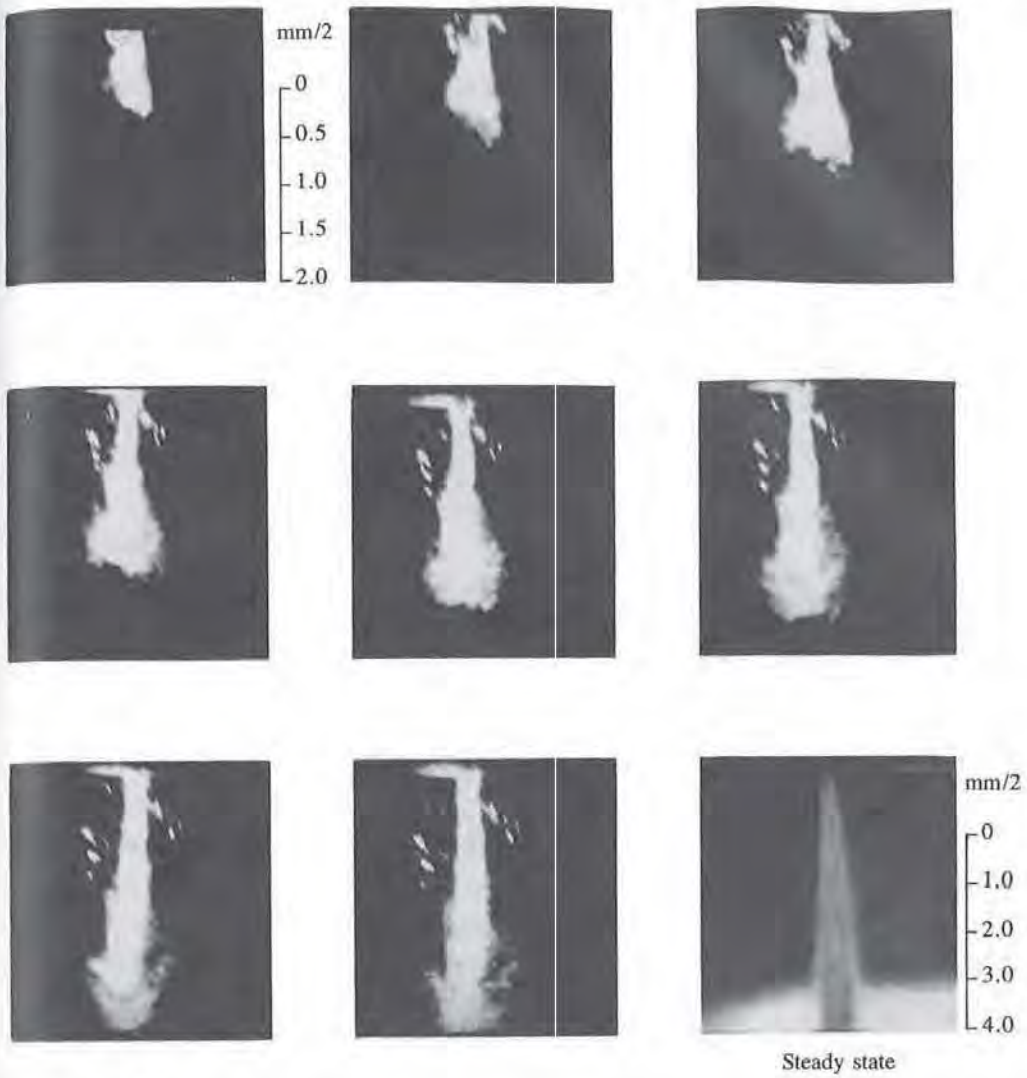
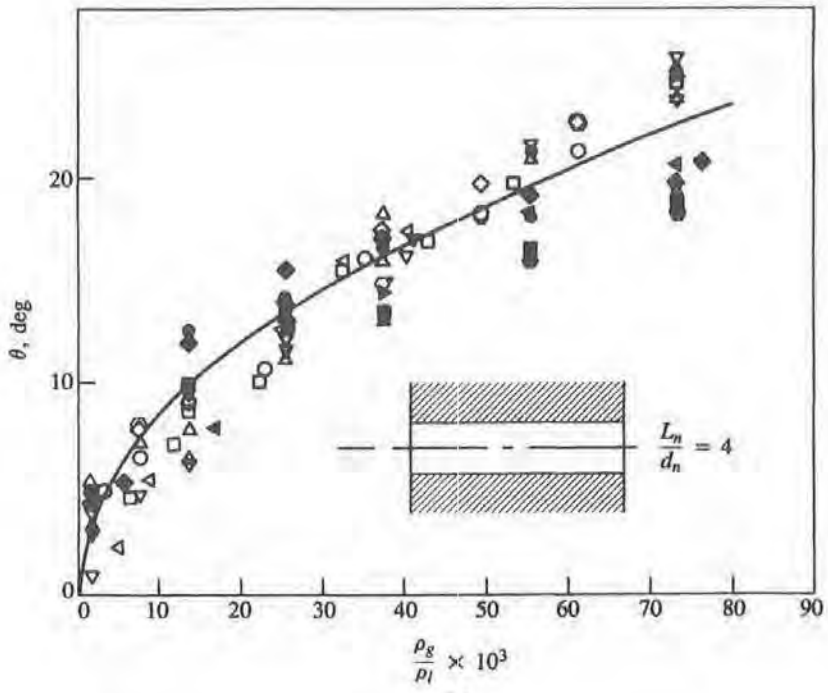


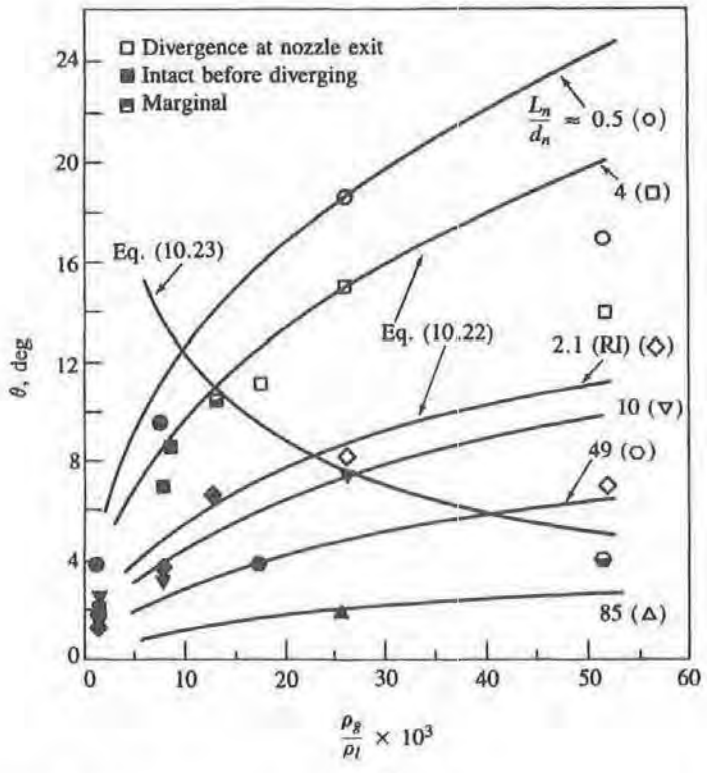
FIGURE 10-24
Photographs showing initial emergence and steady state (bottom right) of high-pressure liquid spray. Time between frames 2.1 μs. Liquid: water. Gas: nitrogen at 1380 kPa. Δp across nozzle 11 MPa. Nozzle diameter 0.34 mm.[25]

symbols) to atomization regime breakup (open symbols). The growth of aerodynamic surface waves is known to be responsible for jet breakup in the second wind-induced breakup regime. Such a mechanism can explain the observed data trends in the atomization regime, if an additional mechanism is invoked to explain nozzle geometry effects. One possible additional mechanism is liquid cavitation. A criterion for the onset of jet atomization at the nozzle exit plane was developed. For $(\rho_l/\rho_g)(\mathrm{Re}_l/\mathrm{We}_l)^2 > 1$ (which is true for distillate fuel injection applications) the design criterion is

$$\left(\frac{\rho_l}{\rho_g}\right)^{1/2} < k \tag{10.23}$$



(*a*)



(*b*)

FIGURE 10-25

(*a*) Initial spray angle of atomizing jets versus density ratio (ρ_g/ρ_l = gas density/liquid density) for fixed nozzle geometry shown. Various fluids and gases at liquid pressures of 3.4–92 MPa. Nozzle diameters $d_n = 0.254$, 0.343, and 0.61 mm.[22] (*b*) Initial spray angle versus density ratio for a wide range of nozzle geometries. L_n/d_n = nozzle length/diameter ratio (RI = rounded inlet geometry). Solid symbols indicate jets which break up and diverge downstream of nozzle exit. Open symbols indicate jet breakup at nozzle exit.[25]

where k is an empirical constant depending on nozzle geometry in the range 6 to 12 ($k = 18.3/\sqrt{A}$).

Jet breakup trends can be summarized as follows. The initial jet divergence angles increase with increasing gas density. Divergence begins progressively closer to the nozzle as gas density increases until it reaches the nozzle exit. Jet divergence angles increase with decreasing fuel viscosity; divergence begins at the nozzle exit once the liquid viscosity is below a certain level. Nozzle design affects the onset of the jet atomization regime. Jet divergence angles decrease with increasing nozzle length. For the same length, rounded inlet nozzles produce less divergent jets than sharp-edged inlet nozzles. The initial jet divergence angle and intact spray length are quasi steady with respect to changes in operating conditions which occur on time scales longer than about 20 μs.[25] Note that while all these results were obtained under conditions where evaporation was not occurring, the initial spray-development processes are not significantly affected by evaporation (see Sec. 10.5.6).

10.5.4 Spray Penetration

The speed and extent to which the fuel spray penetrates across the combustion chamber has an important influence on air utilization and fuel-air mixing rates. In some engine designs, where the walls are hot and high air swirl is present, fuel impingement on the walls is desired. However, in multispray DI diesel combustion systems, overpenetration gives impingement of liquid fuel on cool surfaces which, especially with little or no air swirl, lowers mixing rates and increases emissions of unburned and partially burned species. Yet underpenetration results in poor air utilization since the air on the periphery of the chamber does not then contact the fuel. Thus, the penetration of liquid fuel sprays under conditions typical of those found in diesel engines has been extensively studied.

Many correlations based on experimental data and turbulent gas jet theory have been proposed for fuel spray penetration.[17] These predict the penetration S of the fuel spray tip across the combustion chamber for injection into quiescent air, as occurs in larger DI engines, as a function of time. An evaluation of these correlations[27] indicated that the formula developed by Dent,[28] based on a gas jet mixing model for the spray, best predicts the data:†

$$S = 3.07\left(\frac{\Delta p}{\rho_g}\right)^{1/4}(td_n)^{1/2}\left(\frac{294}{T_g}\right)^{1/4} \tag{10.24}$$

where Δp is the pressure drop across the nozzle, t is time after the start of injection, and d_n is the nozzle diameter. All quantities are expressed in SI units: t in

† For nozzles where $2 \le L_n/d_n \le 4$, and for $t > 0.5$ ms. At exceptionally high chamber densities ($p > 100$ atm) Eq. (10.24) overpredicts penetration.

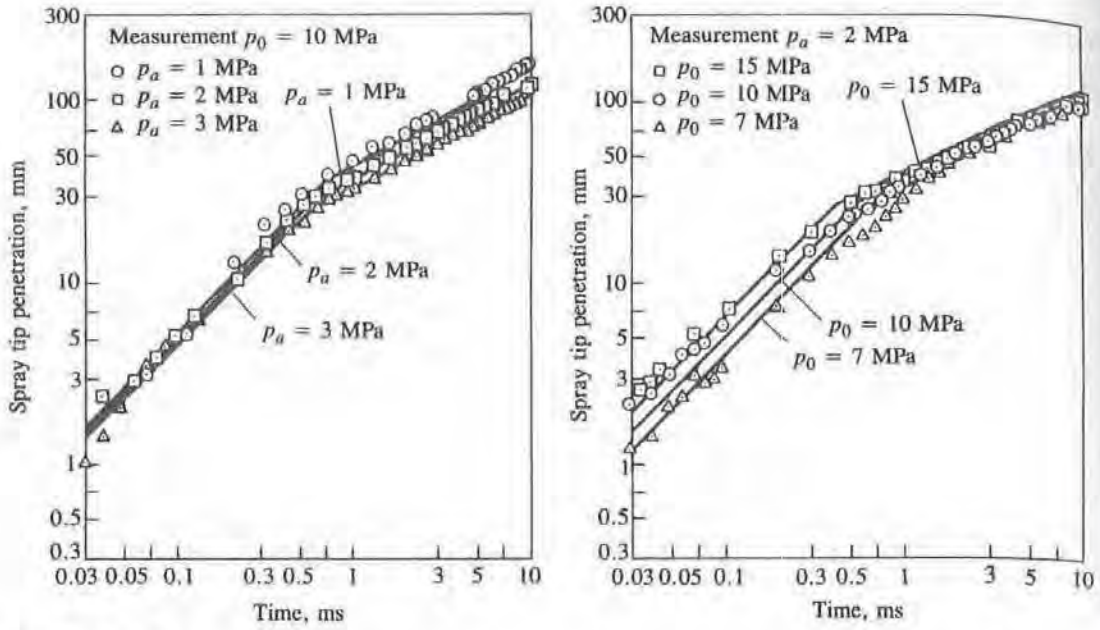


FIGURE 10-26
Spray tip penetration as function of time at various ambient pressures (p_a) and injection pressures (p_0). Fuel jets injected into quiescent air at room temperature.[29]

seconds, S and d_n in meters, Δp in pascals, ρ_g in kilograms per cubic meter, and T_g in kelvins.

More detailed studies have examined the spray tip location as a function of time, following start of a diesel injection process in high-pressure bombs. Data taken by Hiroyasu *et al.*,[29] shown in Fig. 10-26, illustrate the sensitivity of the spray tip position as a function of time to ambient gas state and injection pressure for fuel jets injected into quiescent air at room temperature. These data show that the initial spray tip penetration increases linearly with time t (i.e., the spray tip velocity is constant) and, following jet breakup, then increase as $\sqrt{t}$. Injection pressure has a more significant effect on the initial motion before breakup; ambient gas density has its major impact on the motion after breakup. Hiroyasu *et al.* correlated their data for spray tip penetration S(m) versus time as

$$\begin{aligned} t < t_{\text{break}}: \quad & S = 0.39\left(\frac{2\Delta p}{\rho_l}\right)^{1/2} t \\ t > t_{\text{break}}: \quad & S = 2.95\left(\frac{\Delta p}{\rho_g}\right)^{1/4} (d_n t)^{1/2} \end{aligned} \tag{10.25}$$

where

$$t_{\text{break}} = \frac{29\rho_l d_n}{(\rho_g \Delta p)^{1/2}} \tag{10.26}$$

and Δp is the pressure drop across the nozzle (pascals), ρ_l and ρ_g are the liquid and gas densities, respectively (in kilograms per cubic meter), d_n is the nozzle

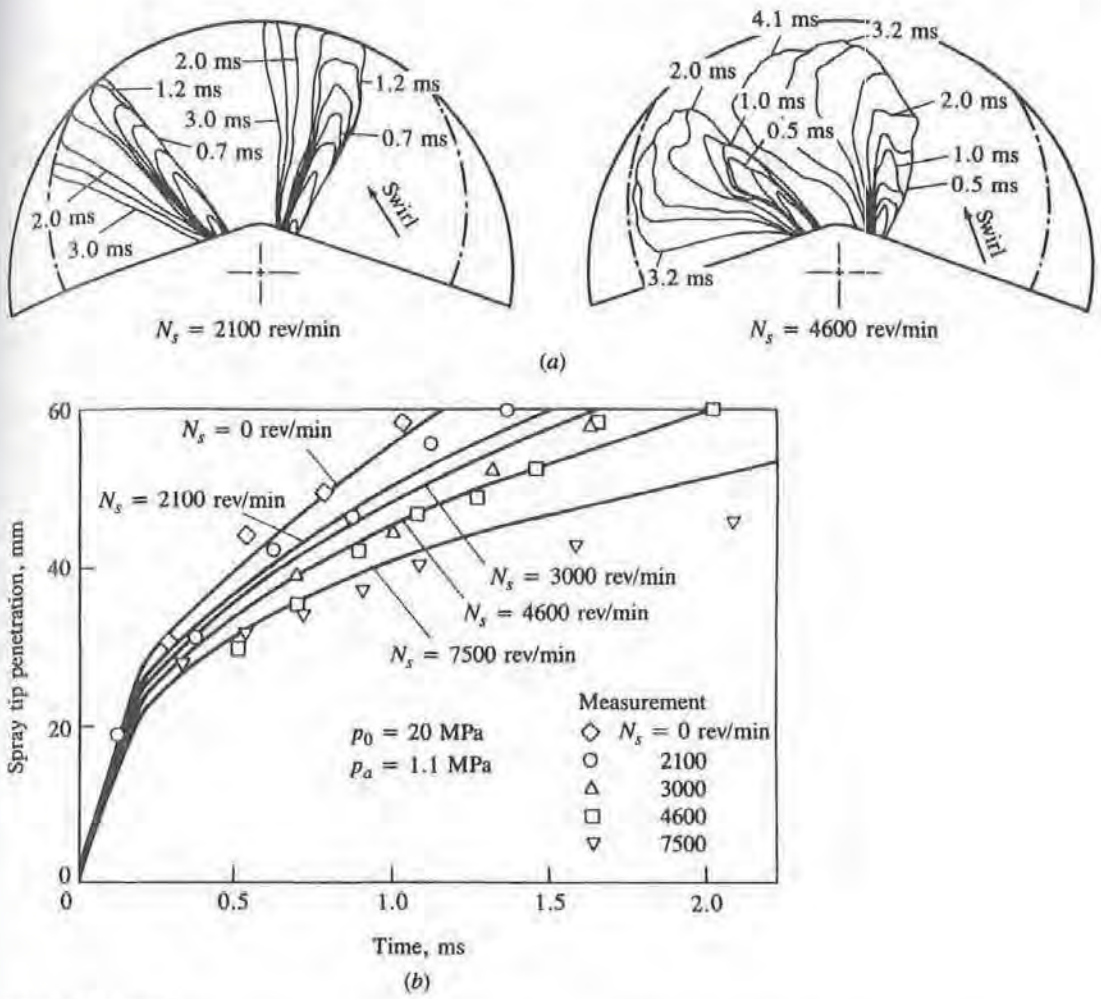


FIGURE 10-27
(*a*) Measured outer boundary of sprays injected into swirling air flow. (*b*) Spray tip penetration as a function of time for different swirl rates. Solid lines show Eq. (10.27).[29]

diameter (meters), and t is time (seconds). The results of Reitz and Bracco[25] indicate that the breakup or intact length depends on nozzle geometry details in addition to the diameter (see Fig. 10-25*b*). Note that under high injection pressures and nozzle geometries with short length/diameter ratios, the intact or breakup length becomes very short; breakup can occur at the nozzle exit plane.

The effect of combustion air swirl on spray penetration is shown in Fig. 10-27. Figure 10-27*a* shows how the spray shape and location changes as swirl is increased; Fig. 10-27*b* shows how spray tip penetration varies with time and swirl rate.[29] These authors related their data on spray tip penetration with swirl, S_s, through a correlation factor to the equivalent penetration, S, without swirl given by Eq. (10.25):

$$\frac{S_s}{S} = \left(1 + \frac{\pi R_s N S}{30 v_j}\right)^{-1} \tag{10.27}$$

where R_s is the swirl ratio which equals the swirl rate in revolutions per minute divided by the engine speed N (revolutions per minute), and v_j is the initial fuel jet velocity (meters per second). The curves in Fig. 10-27*b* correspond to Eq. (10.27). Swirl both reduces the penetration of the spray and spreads out the spray more rapidly.

10.5.5 Droplet Size Distribution

Previous sections in Sec. 10.5 have discussed the overall characteristics of the diesel engine fuel spray—its spreading rate and penetration into the combustion chamber. While the distribution of fuel via the spray trajectory throughout the combustion chamber is important, atomization of the liquid fuel into a large number of small drops is also necessary to create a large surface area across which liquid fuel can evaporate. Here we review how the drop size distribution in the fuel spray depends on injection parameters and the air and fuel properties. Since the measurement of droplet characteristics in an operating diesel engine is extremely difficult, most results have come from studies of fuel injection into constant-volume chambers filled with high-pressure quiescent air at room temperature.

During the injection period, the injection conditions such as injection pressure, nozzle orifice area, and injection rate may vary. Consequently, the droplet size distribution at a given location in the spray may also change with time during the injection period. In addition, since the details of the atomization process are different in the spray core and at the spray edge, and the trajectories of individual drops depend on their size, initial velocity, and location within the spray, the drop size distribution will vary with position within the spray.[29] None of these variations has yet been adequately quantified.

The aerodynamic theory of jet breakup in the atomization regime summarized in Sec. 10.5.3 (which is based on work by G. I. Taylor) leads to the prediction that the initial average drop diameter D_d is proportional to the length of the most unstable surface waves:[22]

$$\bar{D}_d = C \frac{2\pi\sigma}{\rho_g v_r^2} \lambda^* \tag{10.28}$$

where σ is the liquid-fuel surface tension, ρ_g is the gas density, v_r is the relative velocity between the liquid and gas (taken as the mean injection velocity v_j), C is a constant of order unity, and λ^* is the dimensionless wavelength of the fastest growing wave. λ^* is a function of the dimensionless number $(\rho_l/\rho_g)(\mathrm{Re}_j/\mathrm{We}_j)^2$, where the jet Reynolds and Weber numbers are given by $\mathrm{Re}_j = \rho_l v_j d_n/\mu_l$ and $\mathrm{We}_j = \rho_l v_j^2 d_n/\sigma$ and d_n is the nozzle orifice diameter. λ^* goes to 3/2 as this number increases above unity. Near the edge of the spray close to the nozzle, this equation predicts observed drop size trends with respect to injection velocity, fuel properties, nozzle L/d, and nozzle diameter, though measured mean drop sizes are larger by factors of 2 to 3.[30] However, within the dense early region of the spray, secondary atomization phenomena—coalescence and breakup—occur

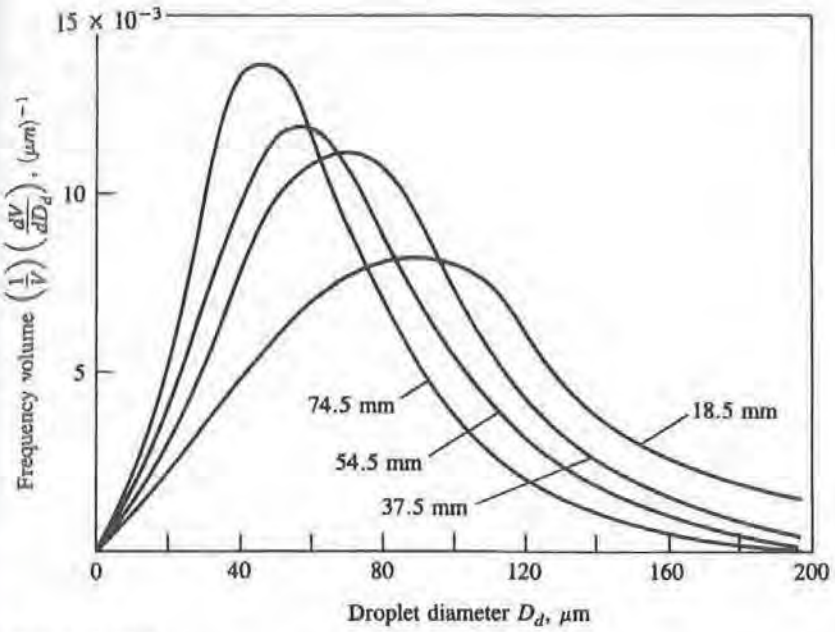


FIGURE 10-28
Droplet size distribution in diesel fuel spray injected through throttling pintle nozzle into quiescent room-temperature air at 11 atm. Nozzle opening pressure 9.9 MPa. Pump speed 500 rev/min. Droplets are sampled well downstream of injector at given radial distances from spray axis.[32]

which will change the droplet size distribution and mean diameter. The downstream drop size in the solid-cone sprays used in diesel-injection systems is markedly influenced by both drop coalescence and breakup. Eventually a balance is reached as coalescence decreases (due to the expansion of the spray) and breakup ceases (due to the reduced relative velocity between the drops and the entrained gas).[31]

Measurements of droplet size distributions within a simulated diesel spray indicate how size varies with location. Figure 10-28 shows the variation in drop size distribution with radial distance from the spray axis, at a fixed axial location. The drop sizes were measured with a liquid immersion technique where a sample of drops is collected in a small cell filled with an immiscible liquid. Size distributions can be expressed in terms of:

1. The incremental number of drops Δn within the size range $D_d - \Delta D_d/2 < D_d < D_d + \Delta D_d/2$
2. The incremental volume ΔV of drops in this size range
3. The cumulative number of drops n less than a given size D_d
4. The cumulative volume V of drops less than a given size D_d

Since the drops are spherical:

$$\frac{dn}{dD_d} = \frac{6}{\pi D_d^3}\frac{dV}{dD_d} \tag{10.29}$$

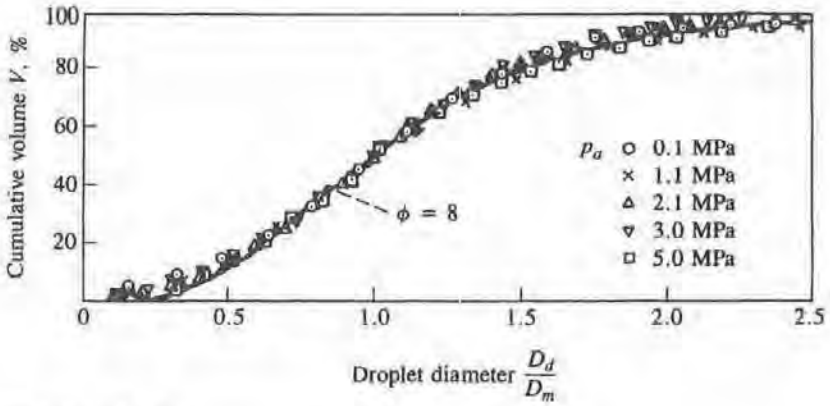


FIGURE 10-29
Normalized drop-size cumulative frequency distribution in spray injected into ambient-temperature air for air pressures from 0.1 to 5 MPa. Throttling pintle nozzle with nozzle opening pressure of 9.9 MPa. Median drop diameter $D_m = 1.224D_{SM}$.[32]

The distributions shown in the figure are frequency distributions of drop volume.[32] The peak in the distribution shifts to larger drop diameters as the radial position decreases: on average, the drops are smaller at the periphery of the spray.

To characterize the spray, expressions for drop size distribution and mean diameter are desirable. An appropriate and commonly used mean diameter is the *Sauter mean diameter*:

$$D_{SM} = \left(\int D_d^3 \, dn\right) \Big/ \left(\int D_d^2 \, dn\right) \tag{10.30}$$

where dn is the number of drops with diameter D_d in the range $D_d - dD_d/2 < D_d < D_d + dD_d/2$. The integration is usually carried out by summing over an appropriate number of drop size groups. The Sauter mean diameter is the diameter of the droplet that has the same surface/volume ratio as that of the total spray.

Various expressions for the distribution of drop sizes in liquid sprays have been proposed. One proposed by Hiroyasu and Kadota[32] based on the chi-square statistical distribution fits the available experimental data. Figure 10-29 shows how the chi-square distribution with a degree of freedom equal to 8 fits well to experimental measurements of the type shown in Fig. 10-28. Here D_m is the median drop diameter which for this chi-square curve is $1.224D_{SM}$. The nondimensional expression for drop size distribution in sprays injected through hole nozzles, pintle nozzles, and throttling pintle nozzles given by the chi-square distribution is

$$\frac{dV}{V} = 13.5\left(\frac{D_d}{D_{SM}}\right)^3 \exp\left[-3\left(\frac{D_d}{D_{SM}}\right)\right] d\left(\frac{D_d}{D_{SM}}\right) \tag{10.31}$$

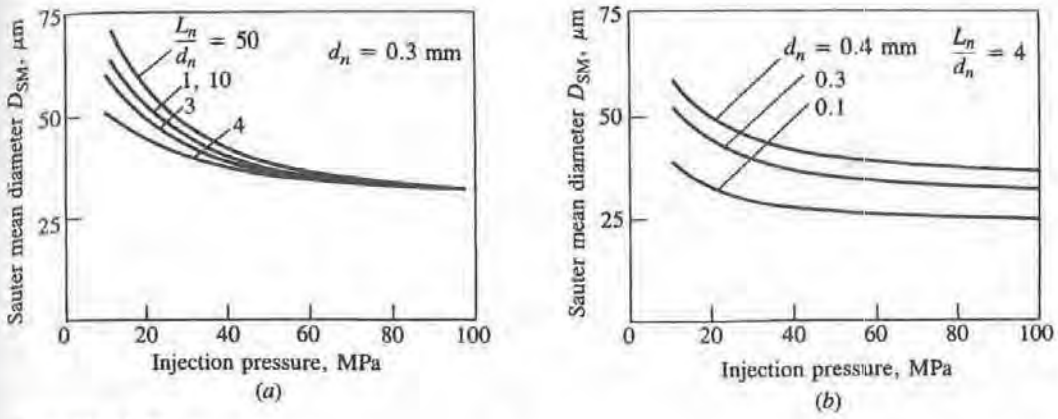


FIGURE 10-30
Effect of fuel-injection pressure and nozzle geometry and size on Sauter mean drop diameter. (*a*) Effect of nozzle length/diameter ratio L_n/d_n and injection pressure. (*b*) Effect of nozzle diameter d_n and injection pressure.[18]

An empirical expression for the Sauter mean diameter D_{SM} (in micrometers) for typical diesel fuel properties given by Hiroyasu and Kadota[32] is

$$D_{SM} = A(\Delta p)^{-0.135}\rho_a^{0.121}V_f^{0.131} \tag{10.32}$$

where Δp is the mean pressure drop across the nozzle in megapascals, ρ_a is the air density in kilograms per cubic meter, and V_f is the amount of fuel delivered per cycle per cylinder in cubic millimeters per stroke. A is a constant which equals 25.1 for pintle nozzles, 23.9 for hole nozzles, and 22.4 for throttling pintle nozzles. Other expressions for predicting D_{SM} can be found in Ref. 17.

The effects of injection pressure, nozzle geometry and size, air conditions, and fuel properties on Sauter mean diameter in sprays obtained with diesel fuel-injection nozzles have been extensively studied. Various immersion, photographic, and optical techniques for making such measurements have been used.[17] Some of the major effects are illustrated in Figs. 10-30 and 10-31 which show

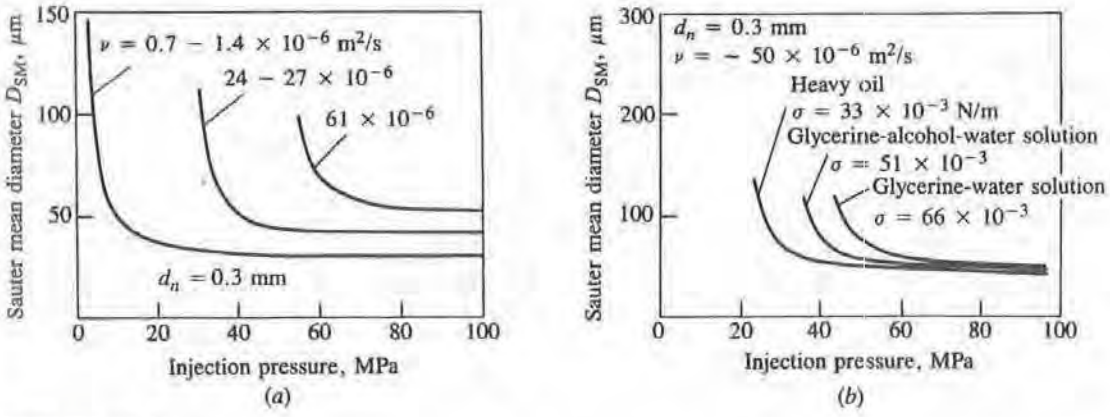


FIGURE 10-31
Effect of (*a*) liquid viscosity ν and (*b*) liquid surface tension σ on Sauter mean drop diameter as a function of injection pressure. Air conditions: 3 MPa and ambient temperature.[17]

average Sauter mean diameters determined optically from studies of steady diesel fuel sprays in a pressurized vessel. Figure 10-30 shows that nozzle size affects the mean drop size in the expected direction. Nozzle length/diameter ratio is also shown to be important: an $L_n/d_n = 4$ gives the minimum mean drop size at low and intermediate injection pressures. This L_n/d_n also corresponds to the minimum value of spray breakup length and to the maximum spray cone angle. Fuel viscosity and surface tension also affect mean drop size as shown in Fig. 10-31, with the effects being most significant at lower injection pressures.

10.5.6 Spray Evaporation

The injected liquid fuel, atomized into small drops near the nozzle exit to form a spray, must evaporate before it can mix with air and burn. Figure 10-20 showed the basic structure of an evaporating diesel spray under conditions typical of a large direct-injection engine. Back illumination showed that a core exists along the axis of the spray where the liquid fuel ligaments or drops are sufficiently dense to attenuate the light beam. Once the start-up phase of the injection process is over, the length of this core remains essentially constant until injection ends. This core is surrounded by a much larger vapor-containing spray region which continues to penetrate deeper into the combustion chamber: the core extends only partway to the spray tip. Additional insight into the physical structure of evaporating sprays can be obtained from the schlieren photographs taken just after the end of injection in a prechamber engine with air swirl, shown in Fig. 10-32. The lowest magnification picture (A) shows the overall structure of the spray. The only liquid-containing region evident is that part of the core nearest the nozzle which shows black on the left of the photograph. The spreading vapor region of the spray, carried around the chamber by the swirling air flow, appears mottled due to local turbulent vapor concentration and temperature fluctuations. The dark region within the spray vapor region is due to soot formed where the fuel vapor concentration is sufficiently high. It is probable that, after the breakup length, the dense black liquid core of the spray is composed of individual droplets but the concentration is so high along the optical path that the light beam is fully extinguished. However, the last part of the core close to the nozzle tip (B) disperses sufficiently for individual features to be resolved. The small black dots are liquid fuel drops in the size range 20 to 100 μm. Fuel drop vapor trails can be observed in the highest magnification photo (C) corresponding to various stages of evaporation. These range from drops showing little surrounding vapor to vapor trails with little liquid remaining at the head. The vapor trails show random orientations relative to the spray axis, presumably due to local air turbulence. The process of droplet evaporation under normal engine operating conditions appears to be rapid relative to the total combustion period.[21]

Let us examine the drop evaporation process in more detail. Consider a liquid drop at close to ambient temperature injected into air at typical end-of-compression engine conditions. Three phenomena will determine the history of the drop under these conditions:

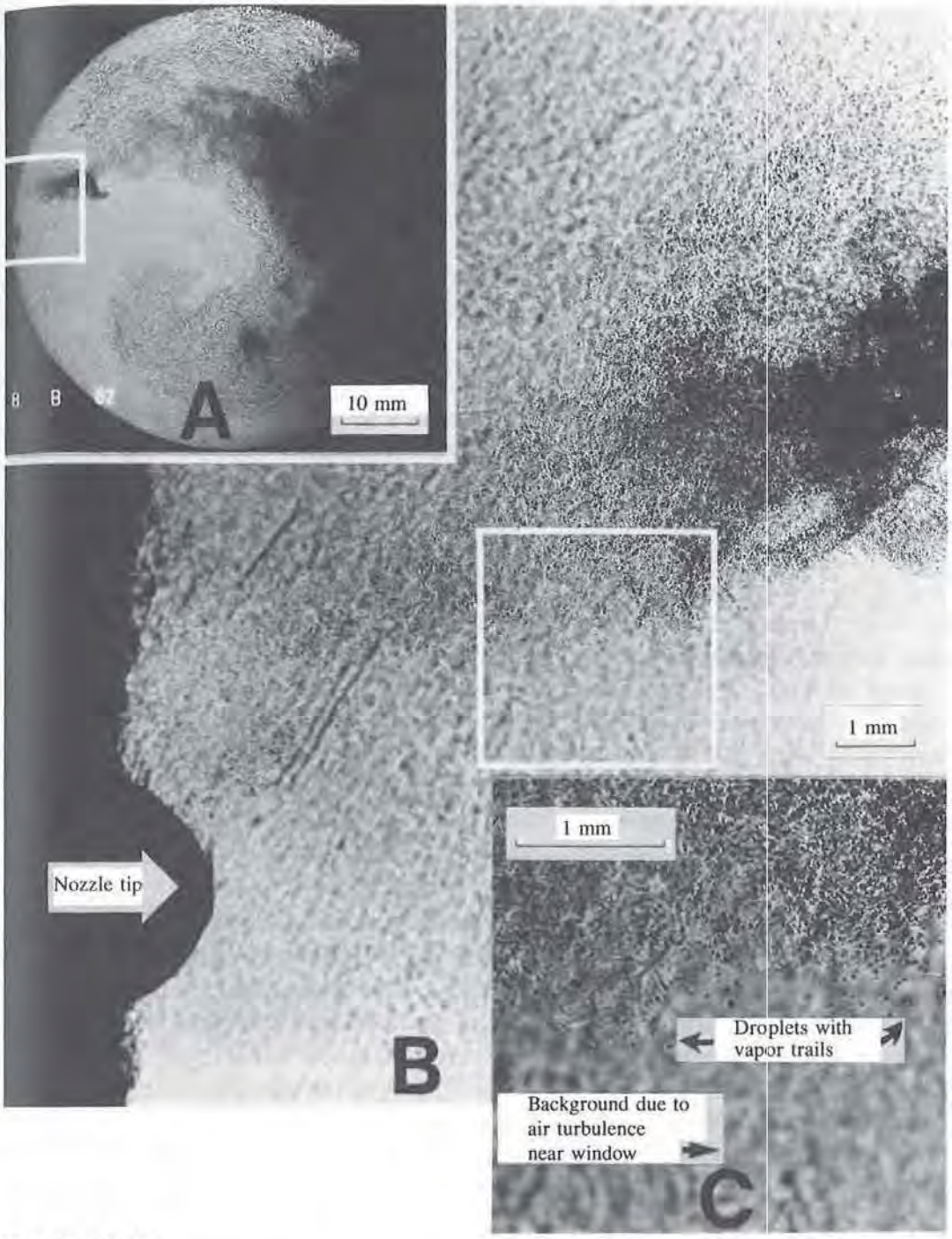


FIGURE 10-32
Shadowgraph photographs at three magnifications taken just after the end of injection of diesel-fuel spray into swirling air flow in prechamber of special diesel engine. Nozzle hole diameter = 0.25 mm.[21]

1. Deceleration of the drop due to aerodynamic drag
2. Heat transfer to the drop from the air
3. Mass transfer of vaporized fuel away from the drop

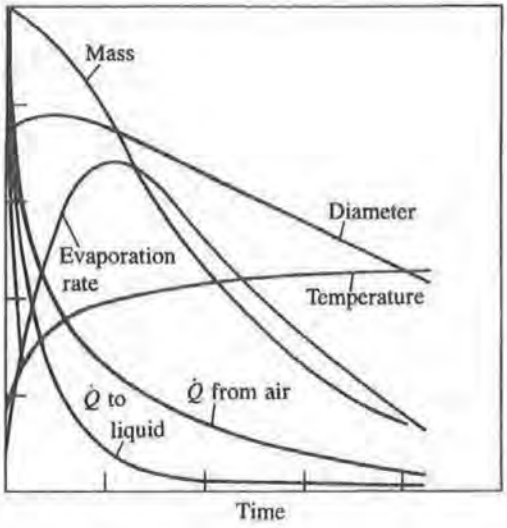


FIGURE 10-33
Schematic of variation of mass, diameter, temperature, evaporation rate, heat-transfer rate from air, and heat-transfer rate to liquid drop core as function of time during evaporation process of individual drop in diesel environment at the time of injection.

As the droplet temperature increases due to heat transfer, the fuel vapor pressure increases and the evaporation rate increases. As the mass transfer rate of vapor away from the drop increases, so the fraction of the heat transferred to the drop surface which is available to increase further the drop temperature decreases. As the drop velocity decreases, the convective heat-transfer coefficient between the air and the drop decreases. The combination of these factors gives the behavior shown in Fig. 10-33 where drop mass, temperature, velocity, vaporization rate, and heat-transfer rate from the air are shown schematically as a function of time following injection.[33] Analysis of individual fuel drops 25 μm in diameter, injected into air at typical diesel conditions, indicates that evaporation times are usually less than 1 ms.[34]

Such an analysis is relevant to drops that are widely separated (e.g., at the edge of the spray). In the spray core, where drop number densities are high, the evaporation process has a significant effect on the temperature and fuel-vapor concentration in the air within the spray. As fuel vaporizes, the local air temperature will decrease and the local fuel vapor pressure will increase. Eventually thermodynamic equilibrium would pertain: this is usually called adiabatic saturation.[33] Calculated thermodynamic equilibrium temperatures for diesel spray conditions are plotted in Fig. 10-34 as a function of the fuel/air mass ratio for *n*-dodecane and *n*-heptane. The initial liquid fuel temperature was 300 K. The ratio of fuel vapor to air mass at these equilibrium conditions is also shown. To the left of the peaks in the m_{fv}/m_a curves, only fuel vapor is present. To the right of these peaks, liquid fuel is also present because the vapor phase is saturated.[35] Liquid fuel vaporization causes substantial reductions in gas temperature. While this equilibrium situation may not be reached within the spray, these results are useful for understanding the temperature distribution within an evaporating spray.

To quantify accurately the fuel vaporization rate within a diesel fuel spray requires the solution of the coupled conservation equations for the liquid drop-

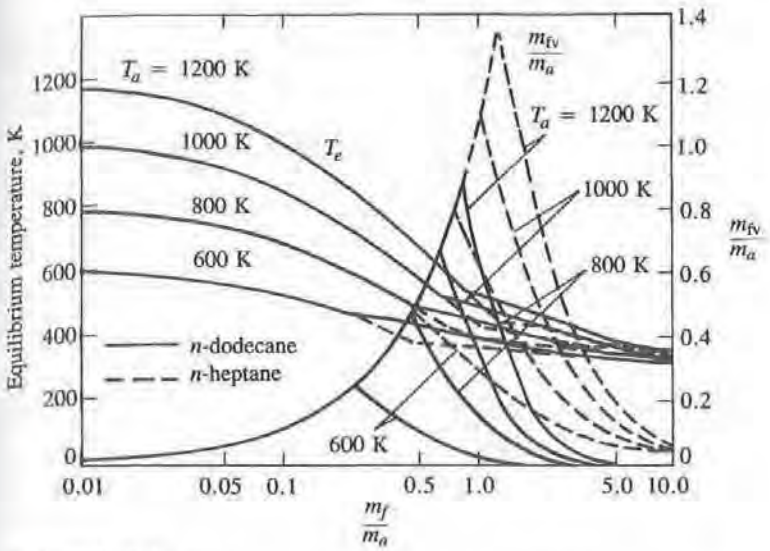


FIGURE 10-34
Adiabatic-saturation conditions for equilibrium mixtures formed by injecting *n*-dodecane and *n*-heptane, initially liquid at 300 K, into air at initial temperature T_a between 600 and 1200 K and initial density 6.5 kg/m^3. Equilibrium mixture temperature (T_e) and ratio of fuel vapor mass (m_{fv}) to air mass (m_a) shown as function of ratio of total fuel mass m_f to m_a. Fuel vapor only present to left of peaks in m_{fv}/m_a curves: liquid fuel also present to right of peaks.[35]

lets and the air within the combustion chamber. Various phenomenological models and computational fluid dynamic models have been developed for this purpose (see Secs. 14.4.3 and 14.5.5). In the most sophisticated of these, the spray is assumed to be composed of discrete computational particles each of which represents a group of droplets of similar size, temperature, etc. The distribution functions in droplet size, velocity, temperature, etc., produced by the fuel injector are statistically sampled and the resulting discrete particles are followed along lagrangian trajectories as they interact and exchange mass, momentum, and energy with the surrounding gas. Drops interact directly with each other via collisions and indirectly via evaporation by modifying the ambient vapor concentration and gas temperature. Studies with such models indicate that, under normal diesel engine conditions, 70 to 95 percent of the injected fuel is in the vapor phase at the start of combustion. Evaporation is more than 90 percent complete after 1 ms. However, only 10 to 35 percent of the vaporized fuel has mixed to within flammability limits in a typical medium-speed DI diesel engine. Thus combustion is largely mixing-limited, rather than evaporation-limited.[36] Of course, under cold-starting conditions, evaporation becomes a major constraint.

10.6 IGNITION DELAY

10.6.1 Definition and Discussion

The ignition delay in a diesel engine was defined as the time (or crank angle) interval between the start of injection and the start of combustion. The start of

injection is usually taken as the time when the injector needle lifts off its seat (determined by a needle-lift indicator). The start of combustion is more difficult to determine precisely. It is best identified from the change in slope of the heat-release rate, determined from cylinder pressure data using the techniques described in Sec. 10.4, which occurs at ignition. Depending on the character of the combustion process, the pressure data alone may indicate when pressure change due to combustion first occurs; in DI engines under normal conditions ignition is well defined, but in IDI engines the ignition point is harder to identify. Flame luminosity detectors are also used to determine the first appearance of the flame. Experience has shown that under normal conditions, the point of appearance of the flame is later than the point of pressure rise and results in greater uncertainty or error in determining the ignition point.

Both physical and chemical processes must take place before a significant fraction of the chemical energy of the injected liquid fuel is released. The physical processes are: the atomization of the liquid fuel jet; the vaporization of the fuel droplets; the mixing of fuel vapor with air. The chemical processes are the precombustion reactions of the fuel, air, residual gas mixture which lead to autoignition. These processes are affected by engine design and operating variables, and fuel characteristics, as follows.

Good atomization requires high fuel-injection pressure, small injector hole diameter, optimum fuel viscosity, and high cylinder air pressure at the time of injection (see Sec. 10.5.3). The rate of vaporization of the fuel droplets depends on the size of the droplets, their distribution, and their velocity, the pressure and temperature inside the chamber, and the volatility of the fuel. The rate of fuel-air mixing is controlled largely by injector and combustion chamber design. Some combustion chamber and piston head shapes are designed to amplify swirl and create turbulence in the air charge during compression. Some engine designs use a prechamber or swirl chamber to create the vigorous air motion necessary for rapid fuel-air mixing (see Sec. 10.2). Also, injector design features such as the number and spatial arrangement of the injector holes determine the fuel spray pattern. The details of each nozzle hole affect the spray cone angle. The penetration of the spray depends on the size of the fuel droplets, the injection pressure, the air density, and the air-flow characteristics. The arrangement of the sprays, the spray cone angle, the extent of spray penetration, and the air flow all affect the rate of air entrainment into the spray. These physical aspects of fuel-injection and fuel-spray behavior are reviewed in Sec. 10.5.

The chemical component of the ignition delay is controlled by the precombustion reactions of the fuel. A fundamental discussion of autoignition or spontaneous hydrocarbon oxidation in premixed fuel-air mixtures is given in Sec. 9.6.2. Since the diesel engine combustion process is heterogeneous, its spontaneous ignition process is even more complex. Though ignition occurs in vapor phase regions, oxidation reactions can proceed in the liquid phase as well between the fuel molecules and the oxygen dissolved in the fuel droplets. Also, cracking of large hydrocarbon molecules to smaller molecules is occurring. These chemical processes depend on the composition of the fuel and the cylinder charge tem-

perature and pressure, as well as the physical processes described above which govern the distribution of fuel throughout the air charge.

Since the ignition characteristics of the fuel affect the ignition delay, this property of a fuel is very important in determining diesel engine operating characteristics such as fuel conversion efficiency, smoothness of operation, misfire, smoke emissions, noise, and ease of starting. The ignition quality of a fuel is defined by its cetane number. Cetane number is determined by comparing the ignition delay of the fuel with that of primary reference fuel mixtures in a standardized engine test (see below). For low cetane fuels with too long an ignition delay, most of the fuel is injected before ignition occurs, which results in very rapid burning rates once combustion starts with high rates of pressure rise and high peak pressures. Under extreme conditions, when autoignition of most of the injected fuel occurs, this produces an audible knocking sound, often referred to as "diesel knock." For fuels with very low cetane numbers, with an exceptionally long delay, ignition may occur sufficiently late in the expansion process for the burning process to be quenched, resulting in incomplete combustion, reduced power output, and poor fuel conversion efficiency. For higher cetane number fuels, with shorter ignition delays, ignition occurs before most of the fuel is injected. The rates of heat release and pressure rise are then controlled primarily by the rate of injection and fuel-air mixing, and smoother engine operation results.

10.6.2 Fuel Ignition Quality

The ignition quality of a diesel fuel is defined by its *cetane number*. The method used to determine the ignition quality in terms of cetane number is analogous to that used for determining the antiknock quality of gasoline in terms of octane number. The cetane number scale is defined by blends of two pure hydrocarbon reference fuels. Cetane (*n*-hexadecane, $C_{16}H_{34}$), a hydrocarbon with high ignition quality, represents the top of the scale with a cetane number of 100. An isocetane, heptamethylnonane (HMN), which has a very low ignition quality, represents the bottom of the scale with a cetane number of 15.† Thus, cetane number (CN) is given by

$$\text{CN} = \text{percent } n\text{-cetane} + 0.15 \times \text{percent HMN} \tag{10.33}$$

The engine used in cetane number determination is a standardized single-cylinder, variable compression ratio engine with special loading and accessory equipment and instrumentation. The engine, the operating conditions, and the test procedure are specified by ASTM Method D613.[37] The operating requirements include: engine speed—900 rev/min; coolant temperature—100°C; intake air temperature—65.6°C (150°F); injection timing—13° BTC; injection

† In the original procedure α-methylnapthalene ($C_{11}H_{10}$) with a cetane number of zero represented the bottom of the scale. Heptamethylnonane, a more stable compound, has replaced it.

pressure—10.3 MPa (1500 lb/in^2). With the engine operating under these conditions, on the fuel whose cetane number is to be determined, the compression ratio is varied until combustion starts at TC: i.e., an ignition delay period of 13° (2.4 ms at 900 rev/min) is produced. The above procedure is then repeated using reference fuel blends. Each time a reference fuel is tried, the compression ratio is adjusted to give the same 13° ignition delay. When the compression ratio required by the actual fuel is bracketed by the values required by two reference blends differing by less than five cetane numbers, the cetane number of the fuel is determined by interpolation between the compression ratios required by the two reference blends.

Because of the expense of the cetane number test, many correlations which predict ignition quality based on the physical properties of diesel fuels have been developed.[38, 39] A calculated *cetane index* (CCI) is often used to estimate ignition quality of diesel fuels (ASTM D976[40]). It is based on API gravity and the mid-boiling point (temperature 50 percent evaporated). It is applicable to straight-run fuels, catalytically cracked stocks, and blends of the two. Its use is suitable for most diesel fuels and gives numbers that correspond quite closely to cetane number. A *diesel index* is also used. It is based on the fact that ignition quality is linked to hydrocarbon composition: *n*-paraffins have high ignition quality, and aromatic and napthenic compounds have low ignition quality. The aniline point (ASTM D611[41]—the lowest temperature at which equal volumes of the fuel and aniline become just miscible) is used, together with the API gravity, to give the diesel index:

$$\text{Diesel index} = \text{aniline point (°F)} \times \frac{\text{API gravity}\dagger}{100} \tag{10.34}$$

The diesel index depends on the fact that aromatic hydrocarbons mix completely with aniline at comparatively low temperatures, whereas paraffins require considerably higher temperatures before they are completely miscible. Similarly, a high API gravity denotes low specific gravity and high paraffinicity, and, again, good ignition quality. The diesel index usually gives values slightly above the cetane number. It provides a reasonable indication of ignition quality in many (but not all) cases.

10.6.3 Autoignition Fundamentals

Basic studies in constant-volume bombs, in steady-flow reactors, and in rapid-compression machines have been used to study the autoignition characteristics of fuel-air mixtures under controlled conditions. In some of these studies the fuel and air were premixed; in some, fuel injection was used. Studies with fuel injec-

† API gravity is based on specific gravity and is calculated from: API gravity, deg = (141.5/specific gravity at 60°F) − 131.5.

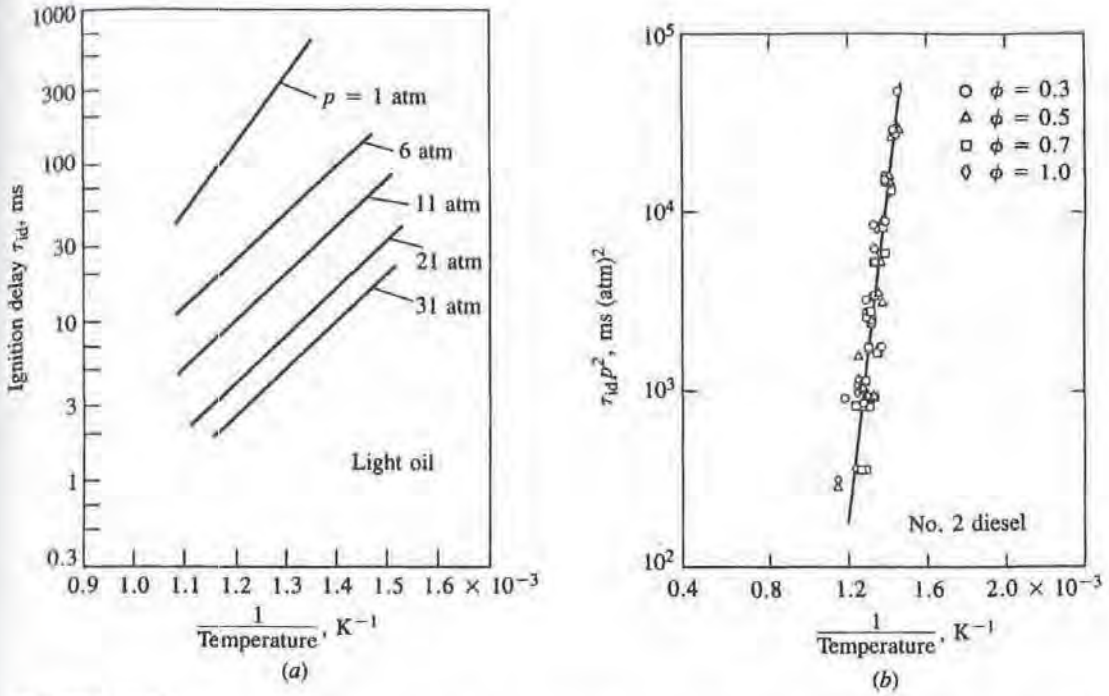


FIGURE 10-35
(*a*) Ignition delay as function of reciprocal air temperature for light oil spray injected into constant-volume combustion bomb. Injection pressure 9.8 MPa (100 atm). Air pressures indicated.[42] (*b*) Ignition delay × (pressure)^2 measured in steady-flow reactor for No. 2 diesel fuel as function of reciprocal temperature. Fuel/air equivalence ratio ϕ varied from 0.3 to 1.0.[43]

tion into constant-temperature and pressure environments have shown that the temperature and pressure of the air are the most important variables for a given fuel composition. Ignition delay data from these experiments have usually been correlated by equations of the form:

$$\tau_{id} = Ap^{-n} \exp\left(\frac{E_A}{\tilde{R}T}\right) \tag{10.35}$$

where τ_{id} is the ignition delay (the time between the start of injection and the start of detectable heat release), E_A is an apparent activation energy for the fuel autoignition process, $\tilde{R}$ is the universal gas constant, and A and n are constants dependent on the fuel (and, to some extent, the injection and air-flow characteristics).

Figure 10-35*a* shows ignition delay data obtained by injecting liquid fuel sprays into a high-pressure heated constant-volume bomb.[42] Figure 10-35*b* shows ignition delay data from a steady-flow high-pressure reactor where vaporized fuel was mixed rapidly with the heated air stream.[43] The match between the form of Eq. (10.35) and the data is clear. Figure 10-35*b* also shows an equivalence ratio dependence of the ignition delay. Representative values for A, n, and E_A for Eq. (10.35), taken from these and other studies, are given in Table 10.3. Ignition delay times calculated with these formulas for various diesel engines are given in

TABLE 10.3
Constants for Arrhenius equation for ignition delay:[44]

$$\tau_{id}(\text{ms}) = Ap^{-n} \exp\left[E_A/(\bar{R}T)\right]$$

	Conditions				Parameters		
Investigator	Apparatus	Fuel	p, atm	T, K	n	A	$E_A/\bar{R}$, K
Spadaccini and TeVelde[43] No. 1	Steady flow	No. 2 diesel	10–30	650–900	2	2.43×10^{-9}	20,926
Spadaccini and TeVelde[43] No. 2	Steady flow	No. 2 diesel	10–30	650–900	1	4.00×10^{-10}	20,080
Stringer *et al.*[45]	Steady flow	Diesel 45–50 cetane number	30–60	770–980	0.757	0.0405	5,473
Wolfer[46]	Constant-volume bomb	Fuel with cetane number >50	8–48	590–782	1.19	0.44	4,650
Hiroyasu *et al.*[29]	Constant-volume bomb	Kerosene	1–30	673–973	1.23	0.0276	7,280

Table 10.4. Air pressures and temperatures at TC piston position were estimated from measured cylinder pressure data. Measured ignition delay times in these types of engines are: 0.6 to 3 ms for low-compression-ratio DI diesel engines over a wide range of operating conditions; 0.4 to 1 ms for high-compression-ratio and turbocharged DI diesel engines; 0.6 to 1.5 ms for IDI diesel engines.[44]

The variation in the calculated delay times can be attributed to several factors:

1. In some cases the correlations are being extrapolated outside their original range of operating conditions.
2. The methods used to detect the start of combustion, and hence the duration of the delay, are not identical.
3. The experimental apparatus and the method of fuel-air mixture preparation are different.

The third factor is probably the most significant. As has been explained, the phenomenon of autoignition of a fuel spray consists of sequences of physical and chemical processes of substantial complexity. The relative importance of each process depends on the ambient conditions, on fuel properties, and on how the fuel-air mixture is prepared. For example, fuel evaporation times are significant in cold engines, but not under fully warmed-up conditions. Thus, an equation of the simple form of Eq. (10.35) can only fit the data over a limited range of conditions. The correlations of Spadaccini and TeVelde[43] have much higher activation energies. Normally, lower values of $E_A/\bar{R}$ imply that physical processes such as vaporization and mixing are important and relevant to chemical processes. Thus, fuel preparation, mixture inhomogeneity, heat loss, and nonuniform flow patterns

TABLE 10.4
Calculated ignition delay times[44]

Engine	Conditions			τ_{id}, ms				
				Spadaccini and TeVelde[43]				
	Speed, rev/min	p, atm	T, K	No. 1	No. 2	Stringer *et al.*[45]	Wolfer[46]	Hiroyasu *et al.*[39]
IDI Diesel								
1. Low swirl	600	45.6	690	17.3	38.2	6.26	3.94	9.60
	1200	49.3	747	1.47	3.83	3.22	2.15	3.90
	1800	52.5	758	0.86	2.44	2.76	1.82	3.13
2. High swirl	600	45.2	674	36.3	76.9	7.60	4.68	12.5
	1200	48.4	721	4.18	10.3	4.25	2.75	5.67
	1800	51.8	744	1.47	4.07	3.19	2.08	3.82
DI Diesel								
1. Low compression ratio		42.8	781	0.57	1.37	2.60	1.92	2.39
2. High compression ratio	1500	58.8	975	0.0015	0.0060	0.508	0.407	0.322

affect the ignition delay. While the work of Spadaccini and TeVelde probably describes the chemical ignition delay more accurately, since great care was taken to obtain a uniform mixture and flow, the experiments in constant-volume bombs with diesel-type fuel injectors are more relevant to the diesel engine compression-ignition combustion process because they include the appropriate physical and chemical processes. The available engine ignition delay data suggest that for delays less than about 1 ms, the rate of decrease in delay with increasing temperature becomes much less than that indicated by the data in Fig. 10-35. This is due to the increasing relative importance of physical processes relative to chemical processes during the delay period. Thus relations of the form of Eq. (10.35) should be used with caution.

In general, τ_{id} is a function of mixture temperature, pressure, equivalence ratio, and fuel properties (though no accepted form for the variation with equivalence ratio is yet established). In the above referenced studies, the fuel was injected into a uniform air environment where the pressure and temperature only changed due to the cooling effect of the fuel-vaporization and fuel-heating processes. In an engine, pressure and temperature change during the delay period due to the compression resulting from piston motion. To account for the effect of changing conditions on the delay the following empirical integral relation is usually used:

$$\int_{t_{si}}^{t_{si}+\tau_{id}} \left(\frac{1}{\tau}\right) dt = 1 \tag{10.36}$$

where t_{si} is the time of start of injection, τ_{id} is the ignition delay period, and τ is the ignition delay at the conditions pertaining at time t. Whether the variation in conditions is significant depends on the amount of injection advance before TC that is used and the length of the delay.

10.6.4 Physical Factors Affecting Delay

The physical factors that affect the development of the fuel spray and the air charge state (its pressure, temperature, and velocity) will influence the ignition delay. These quantities depend on the design of the fuel-injection system and combustion chamber, and the engine operating conditions. The injection system variables affecting the fuel-spray development are injection timing, quantity, velocity, rate, drop size, and spray form or type. The relevant charge conditions depend on the combustion system employed, the details of the combustion chamber design, inlet air pressure and temperature, compression ratio, injection timing, the residual gas conditions, coolant and oil temperature, and engine speed. Data on these interactions are available for different types of diesel engines. The trends observed with the different diesel combustion systems are generally similar, though some of the details are different. In this section the ignition delay trends during normal (fully warmed-up) engine operation are considered. The dependence of the ignition delay on engine design and operating variables during engine starting and warm-up is also very important, and may be different from fully warmed-up behavior due to lower air temperature and pressure.

INJECTION TIMING. At normal engine conditions (low to medium speed, fully warmed engine) the minimum delay occurs with the start of injection at about 10 to 15° BTC.[47] The increase in the delay with earlier or later injection timing occurs because the air temperature and pressure change significantly close to TC. If injection starts earlier, the initial air temperature and pressure are lower so the delay will increase. If injection starts later (closer to TC) the temperature and pressure are initially slightly higher but then decrease as the delay proceeds. The most favorable conditions for ignition lie in between.

INJECTION QUANTITY OR LOAD. Figure 10-36 shows the effect of increasing injection quantity or engine load on ignition delay. The delay decreases approximately linearly with increasing load for this DI engine. As load is increased, the residual gas temperature and the wall temperature increase. This results in higher charge temperature (and also, to a lesser extent, charge pressure) at injection, thus shortening the ignition delay. When adjustment is made for this increasing temperature, it is found that increasing the quantity of fuel injected has no significant effect on the delay period under normal operating conditions. Under engine starting conditions, however, the delay increases due to the larger drop in mixture temperature associated with evaporating and heating the increased amount of fuel.[47] This latter result should be expected since it is the first part of the injected fuel which ignites first; subsequent injected fuel (above the minimum required to maintain the fuel-air mixture within the flammability limits during the delay) does not influence the delay.

DROP SIZE, INJECTION VELOCITY, AND RATE. These quantities are determined by injection pressure, injector nozzle hole size, nozzle type, and geometry.

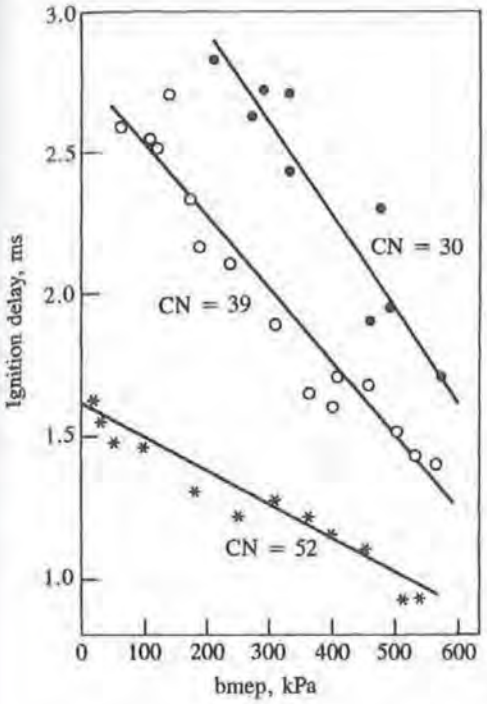


FIGURE 10-36
Ignition delays measured in a small four-stroke cycle DI diesel engine with $r_c = 16.5$ as a function of load at 1980 rev/min. Fuel cetane numbers 30, 39, and 52.[48]

Experiments by Lyn and Valdmanis[47] have shown that none of these factors has a significant effect on the delay. At normal operating conditions, increasing injection pressure produces only modest decreases in the delay. Doubling the nozzle hole diameter at constant injection pressure to increase the fuel flow rate (by a factor of about 4) and increase the drop size (by about 30 percent) had no significant effect on the delay. Studies of different nozzle hole geometries showed that the length/diameter ratio of the nozzle was not significant; nor did changes in nozzle type (multihole, pintle, pintaux) cause any substantial variation in delay at normal engine conditions.

INTAKE AIR TEMPERATURE AND PRESSURE. Figure 10-35 showed values of ignition delay for diesel fuels plotted against the reciprocal of charge temperature for several charge pressures at the time of injection. The intake air temperature and pressure will affect the delay via their effect on charge conditions during the delay period. Figure 10-37 shows the effects of inlet air pressure and temperature as a function of engine load. The fundamental ignition data available show a strong dependence of ignition delay on charge temperatures below about 1000 K at the time of injection. Above about 1000 K, the data suggest that the charge temperature is no longer so significant. Through this temperature range there is an effect of pressure at the time of injection on delay: the higher the pressure the shorter the delay, with the effect decreasing as charge temperatures increase and delay decreases. Since air temperature and pressure during the delay period are such important variables, other engine variables that affect the relation between the inlet air state and the charge state at the time of injection will influence the delay. Thus, an increase in the compression ratio will decrease the ignition delay,

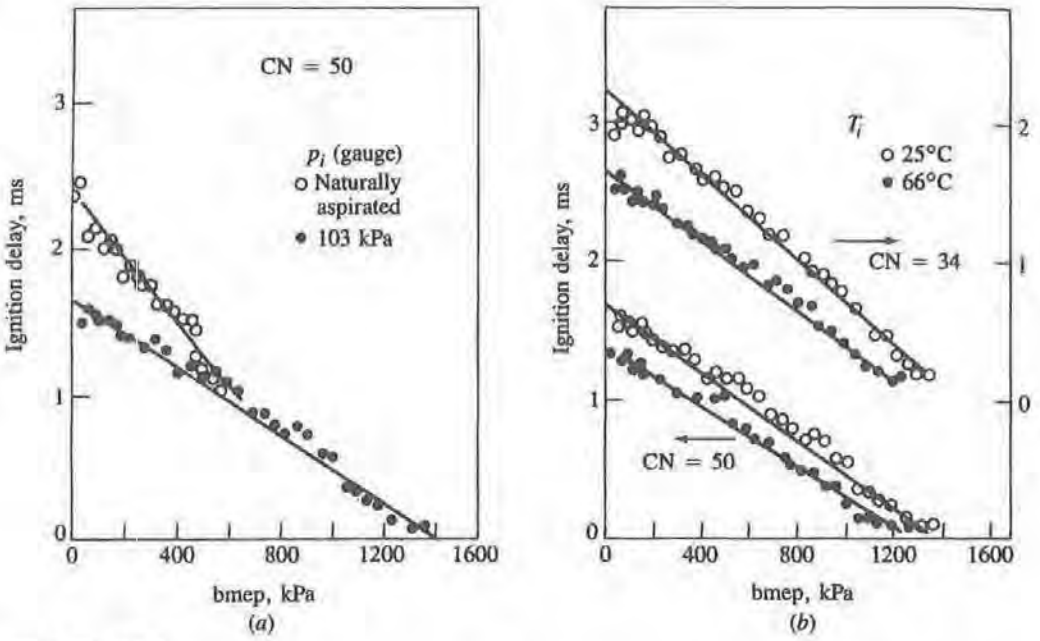


FIGURE 10-37
Effect of inlet air pressure and temperature on ignition delay over load range of small DI diesel at 1980 rev/min. (*a*) Engine naturally aspirated and with 1 atm boost; inlet air temperature $T_i = 25°C$; 50 cetane number fuel. (*b*) Engine naturally aspirated; $T_i = 25$ and 66°C; 34 and 50 cetane number fuel.[48]

and injection timing will affect the delay (as was discussed earlier), largely due to the changes in charge temperature and pressure at the time of injection.

ENGINE SPEED. Increases in engine speed at constant load result in a slight decrease in ignition delay when measured in milliseconds; in terms of crank angle degrees, the delay increases almost linearly.[48] A change in engine speed changes the temperature/time and pressure/time relationships. Also, as speed increases, injection pressure increases. The peak compression temperature increases with increasing speed due to smaller heat loss during the compression stroke.[47]

COMBUSTION CHAMBER WALL EFFECTS. The impingement of the spray on the combustion chamber wall obviously affects the fuel evaporation and mixing processes. Impingement of the fuel jet on the wall occurs, to some extent, in almost all of the smaller, higher speed engines. With the "M" system, this impingement is desired to obtain a smooth pressure rise. The ignition delay with the "M" system is longer than in conventional DI engine designs.[47] Engine and combustion bomb experiments have been carried out to examine the effect of wall impingement on the ignition delay. Figure 10-38 shows the effect of jet wall impingement on ignition delay measured in a constant-volume combustion bomb, for a range of air pressures and temperatures, and wall temperatures.[29] The wall was perpendicular to the spray and was placed 100 mm from the nozzle tip. The data shows that the presence of the wall reduces the delay at the lower

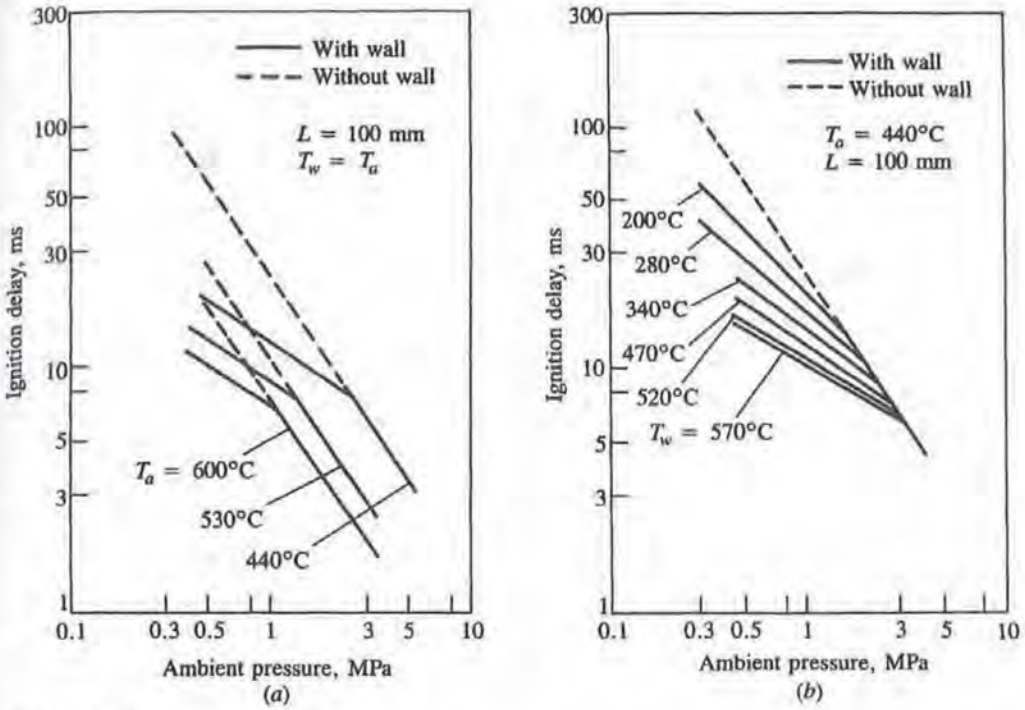


FIGURE 10-38
Effect of spray impingement on wall 100 mm from nozzle on ignition delay from combustion bomb studies. (*a*) Effect of air temperature as a function of air pressure; $T_w = T_{air}$. (*b*) Effect of wall temperature at 440°C air temperature.[29]

pressures and temperatures studied, but has no significant effect at the high pressures and temperatures more typical of normal diesel operation. Engine experiments where the delay was measured while the jet impingement process was varied showed analogous trends. The jet impingement angle (the angle between the fuel jet axis and the wall) was varied from almost zero (jet and wall close to parallel) to perpendicular. The delay showed a tendency to become longer as the impingement angle decreased. The most important result is not so much the modest change in delay but the difference in the initial rate of burning that results from the differences in fuel evaporation and fuel-air mixing rates.

SWIRL RATE. Changes in swirl rate change the fuel evaporation and fuel-air mixing processes. They also affect wall heat transfer during compression and, hence, the charge temperature at injection. Only limited engine studies of the effect of swirl rate variations on ignition delay have been made. At normal operating engine speeds, the effect of swirl rate changes on the delay are small. Under engine starting conditions (low engine speeds and compression temperatures) the effect is much more important,[47] due presumably to the higher rates of evaporation and mixing obtained with swirl.

OXYGEN CONCENTRATION. The oxygen concentration in the charge into which the fuel is injected would be expected to influence the delay. The oxygen concentration is changed, for example, when exhaust gas is recycled to the intake

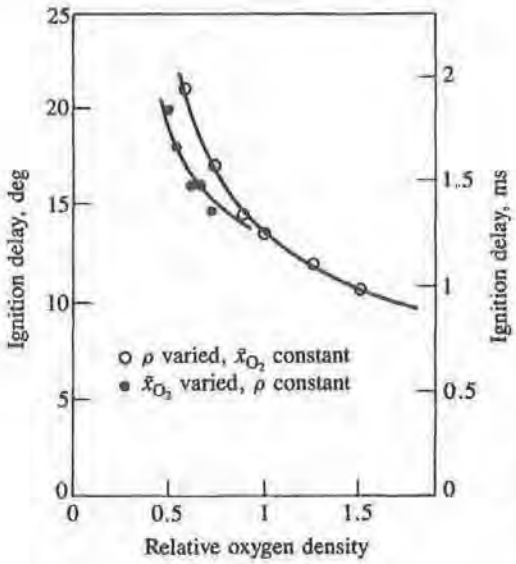


FIGURE 10-39
Effect of oxygen density in gas on ignition delay in single-cylinder DI engine of 1.3-dm^3 displacement with $r_c = 15$ at 1800 rev/min. Oxygen density changed by recycling exhaust gas at constant inlet density and by varying inlet pressure from 0.5 to 3 atm with air.[49]

for the control of oxides of nitrogen emissions (see Chap. 11). Results of a study carried out in a single-cylinder DI engine operated at a constant air/fuel ratio (30 : 1), manifold temperature, injection timing, and speed (1800 rev/min), where the oxygen concentration was varied by recirculating known amounts of cooled exhaust, are shown in Fig. 10-39.[49] Oxygen density is normalized by the naturally aspirated no-recirculation test value. As oxygen concentration is decreased, ignition delay increases.

10.6.5 Effect of Fuel Properties

Since both physical and chemical processes take place during the ignition delay, the effects of changes in the physical and chemical properties of fuels on the delay period have been studied. The chemical characteristics of the fuel are much the more important. The ignition quality of the fuel, defined by its cetane number, will obviously affect the delay. The dependence of cetane number on fuel molecular structure is as follows. Straight-chain paraffinic compounds (normal alkanes) have the highest ignition quality, which improves as the chain length increases. Aromatic compounds have poor ignition quality as do the alcohols (hence, the difficulties associated with using methanol and ethanol, possible alternative fuels, in compression-ignition engines). Figure 10-40 illustrates these effects. A base fuel was blended with pure paraffinic (normal, iso-, and cycloalkanes), aromatic, and olefinic hydrocarbons of various carbon numbers, by up to 20 percent by volume. The base fuel, a blend of 25 percent *n*-hexadecane and 75 percent isooctane, had a cetane number of 38.3. The figure shows that the resulting ignition delays correlate well as a function of cetane number at constant compression ratio and engine operating conditions. Addition of normal alkanes (excluding *n*-pentane and lower carbon number alkanes) improve the ignition quality. As the chain length of the added paraffin gets longer (higher carbon number) the cetane number improve-

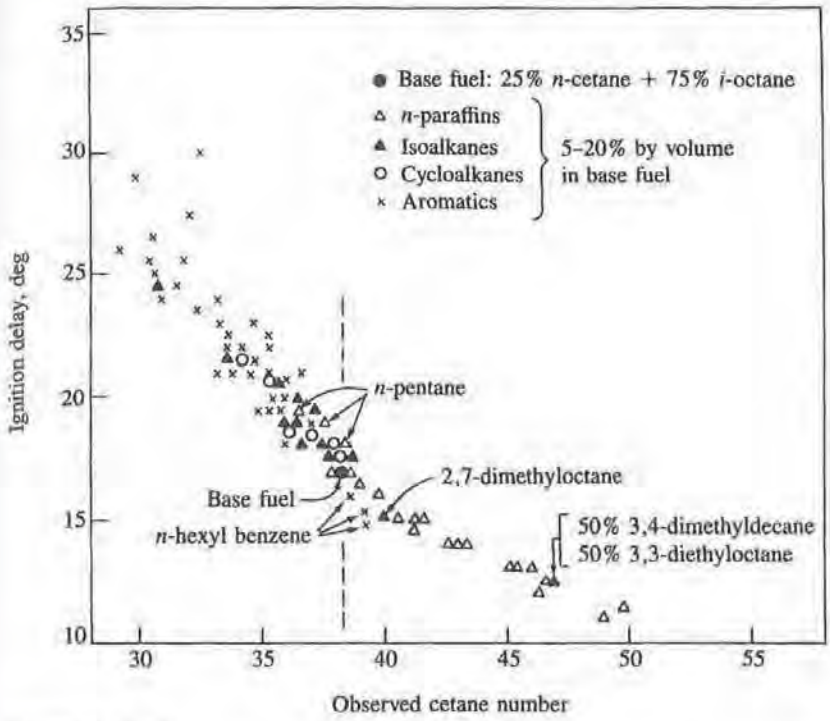


FIGURE 10-40
Effect of type of hydrocarbon structure on ignition quality of fuels in DI diesel combustion process at constant compression ratio and engine operating conditions.[50]

ment increases. Isoalkanes, depending on the degree of branching, degrade ignition quality (unless the branching is concentrated at one end of the molecule, when these types of isoalkanes improve ignition quality). Cycloalkanes and aromatics generally reduce the cetane number, unless they have a long *n*-alkane chain attached to the ring. The cetane number of a fuel (a measure of its ability to autoignite) generally varies inversely with its octane number (a measure of its ability to resist autoignition; see Fig. 9-69 for the effect of hydrocarbon structure on knock). The cetane number of commercial diesel fuel is normally in the range 40 to 55.

Engine ignition delay data with diesel fuels of different cetane number, at various constant loads and speeds, shown in Fig. 10-41, demonstrate similar trends. Within the normal diesel fuel cetane number range of 40 to 55, an approximately linear variation is evident. However, decreasing fuel cetane number below about 38 may result in a more rapid increase in ignition delay.

Cetane number is controlled by the source of crude oil, by the refining process, and by additives or ignition accelerators. Just as it is possible to reduce the tendency to knock or autoignite in spark-ignition engine fuels by adding antiknock agents, so there are additives that improve the ignition quality of compression-ignition engine fuels. Generally, substances that increase the tendency to knock enhance ignition, and vice versa. Ignition-accelerating additives include organic peroxides, nitrates, nitrites, and various sulfur compounds. The most important of these commercially are the alkyl nitrates (isopropyl nitrate,

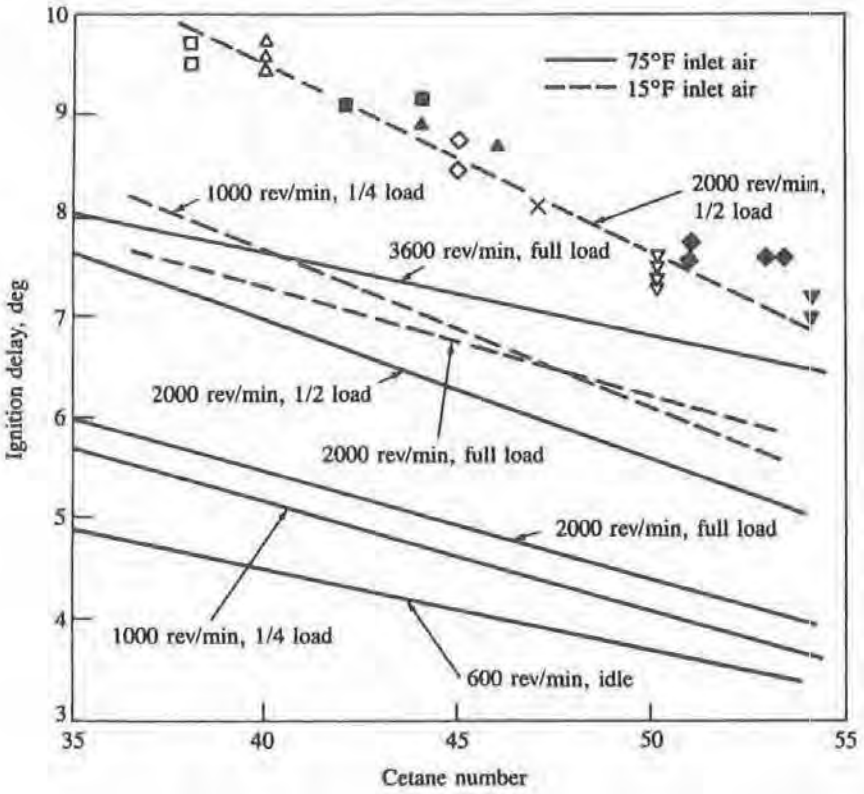


FIGURE 10-41
Effect of fuel cetane number on ignition delay over the load and speed range of 6.2-dm^3 eight-cylinder IDI swirl-chamber diesel engine. Top curve indicates typical fit between data and least-squares straight line over this cetane number range.[51]

primary amyl nitrates, primary hexyl nitrates, octyl nitrate).[52] Typically, about 0.5 percent of these additives by volume in a distillate fuel gives about a 10 cetane number increase in a fuel's ignition quality, though their effectiveness may depend on the composition of the base fuel. The incremental effect of increasing amounts of ignition-accelerating additives on cetane number decreases.[48] Usually, the ignition delay obtained with cetane improved blends are found to be equivalent to those obtained with natural diesel fuels of the same cetane number. Two potential practical uses for ignition accelerators are in upgrading the ignition characteristics of poorer quality diesel fuel and (in much larger amounts) making possible the use of alcohols in compression-ignition engines.

The physical characteristics of diesel fuel do not significantly affect the ignition delay in fully or partially warmed-up engines. Tests with fuels of different front-end volatility (over the cetane number range 38 to 53), and with substantially different front-end ignition quality for the same average cetane number, showed no discernible differences. Fuel viscosity variations over a factor of 2.5 were also tested and showed no significant effect.[48] Thus, in a warmed-up engine, variations in fuel atomization, spray penetration, and vaporization rate over reasonable ranges do not appear to influence the duration of the delay period significantly (see also Sec. 10.5.6 on fuel vaporization).

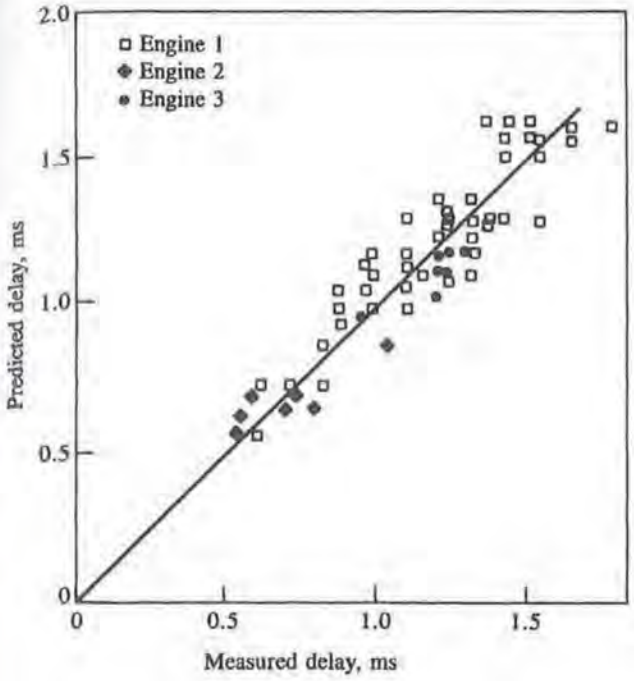


FIGURE 10-42
Comparison of engine ignition delays predicted with Eq. (10.37) with corresponding measured values.[54]

10.6.6 Correlations for Ignition Delay in Engines

Many correlations have been proposed for predicting ignition delay as a function of engine and air charge variables. These usually have the form of Eq. (10.35) and have been based on data from more fundamental experiments in combustion bombs and flow reactors. An important factor in assessing the appropriateness of any correlation is how it is to be used to predict the magnitude of the delay. If an equation for predicting the complete delay process (including all the physical and chemical processes from injection to combustion) is required, then the data show that such a simple form for the equation is unlikely to be adequate for the full range of engine conditions (see Table 10.4). However, if a model for the autoignition process of a premixed fuel-air mixture during the delay period is required, for use in conjunction with models for the physical processes of fuel evaporation and fuel-air mixing, then correlations such as those listed in Table 10.3 may be sufficiently accurate.

An empirical formula, developed by Hardenberg and Hase[53] for predicting the duration of the ignition delay period in DI engines, has been shown to give good agreement with experimental data over a wide range of engine conditions (see Fig. 10-42).[54] This formula gives the ignition delay (in crank angle degrees) in terms of charge temperature T (kelvins) and pressure p (bars) during the delay (taken as TC conditions) as

$$\tau_{id}(\text{CA}) = (0.36 + 0.22\bar{S}_p) \exp\left[E_A\left(\frac{1}{\bar{R}T} - \frac{1}{17{,}190}\right)\left(\frac{21.2}{p - 12.4}\right)^{0.63}\right] \quad (10.37)$$

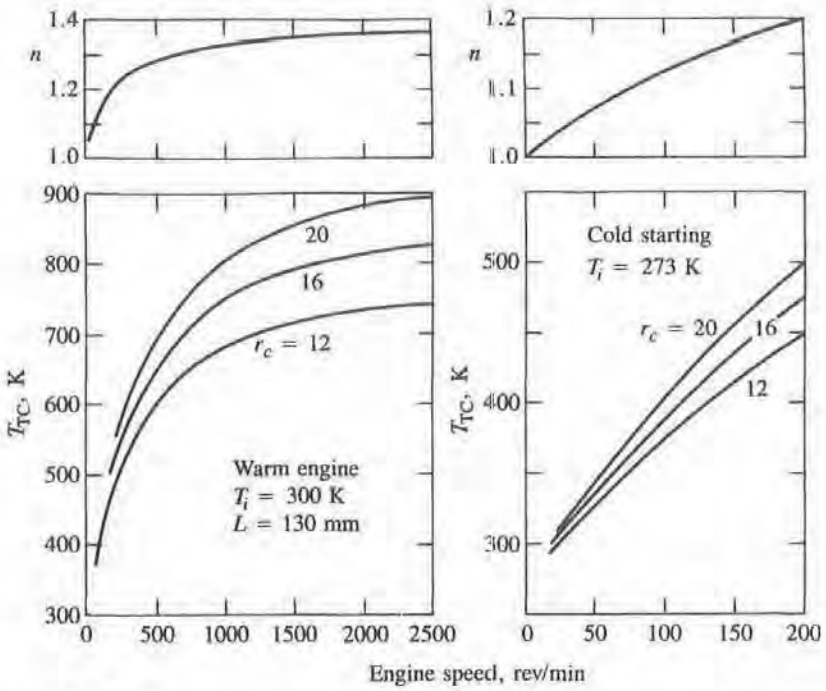


FIGURE 10-43
Exponent n for polytropic model of compression process in Eq. (10.39) and corresponding end-of-compression air temperature at TC. Warm and cold DI diesel engine with 130 mm stroke.[53]

where $\bar{S}_p$ is the mean piston speed (meters per second) and $\tilde{R}$ is the universal gas constant (8.3143 J/mol · K). E_A (joules per mole) is the apparent activation energy, and is given by

$$E_A = \frac{618{,}840}{\text{CN} + 25} \tag{10.38}$$

where CN is the fuel cetane number. The apparent activation energy decreases with increasing fuel cetane number. The delay in milliseconds is given by

$$\tau_{id}(\text{ms}) = \frac{\tau_{id}(\text{CA})}{0.006N}$$

where N, engine speed, is in revolutions per minute. Values for T and p can be estimated using a polytropic model for the compression process:

$$T_{TC} = T_i r_c^{n-1} \qquad p_{TC} = p_i r_c^n \tag{10.39a,b}$$

where n is the polytropic exponent (see Sec. 9.2.2), r_c is the compression ratio, and the subscript i denotes intake manifold conditions. Values of the polytropic exponent are given in Fig. 10-43 for a direct-injection diesel under warm and cold engine operating conditions.[49,53]

10.7 MIXING-CONTROLLED COMBUSTION

10.7.1 Background

Earlier sections of this chapter have developed our current understanding of the individual processes which together make up the total injection-mixing-burning sequence—atomization, vaporization, fuel spray development, air entrainment, ignition, and combustion. While the phenomenological model developed by Lyn[6] provides satisfactory logical links between these processes, quantitative links are still lacking. Especially difficult to quantify are the relations between fuel spray behavior, flame structure, and fuel burning rate—the area of focus of this section. The color photographs of the compression-ignition combustion process in different types of diesel engines in Figs. 10-4 and 10-5 (see color plate between 498 and 499) show how the flame immediately following ignition spreads rapidly and envelops the spray. Depending on the spray configuration, the visible flame may then fill almost the entire combustion chamber. The flame and spray geometries are closely related. Mixing processes are also critical during the ignition delay period: while the duration of the delay period is not influenced in a major way by the rates of spray processes which together control "mixing," the amount of fuel mixed with air to within combustible limits during the delay (which affects the rate of pressure rise once ignition has occurred) obviously is directly related to mixing rates. Thus substantial observational evidence supports the mixing-controlled character of diesel engine combustion.

However, while it is well accepted that diesel combustion is normally controlled by the fuel-air mixing rate, fundamentally based quantitatively accurate models for this coupled mixing and combustion process are not yet available. The difficulties are twofold. First, the spray geometry in real diesel combustion systems is extremely complex. Second, the phenomena which must be described (and especially the unsteady turbulent diffusion diesel engine flame) are inadequately understood. Current capabilities for modeling these phenomena are reviewed in Chap. 14. Thermodynamic-based models of the diesel combustion process with atomization, vaporization, and spray development described by empirical or turbulent-jet-based submodels have been developed and used to predict burning rates. These are described in Secs. 14.4.3 and 14.4.4, and show reasonable but not precise agreement with data. Fluid-mechanic-based models of air flow, fuel spray behavior, and combustion are under active development (see Sec. 14.5). While realistic air-flow predictions are now feasible, predictions of spray behavior are less well developed and combustion-rate predictions are still exploratory.

In the following sections, the evidence linking spray characteristics to flame structure and burning rates is summarized.

10.7.2 Spray and Flame Structure

The structure of each fuel spray is that of a narrow liquid-containing core (densely filled with drops of order 20 μm in diameter) surrounded by a much

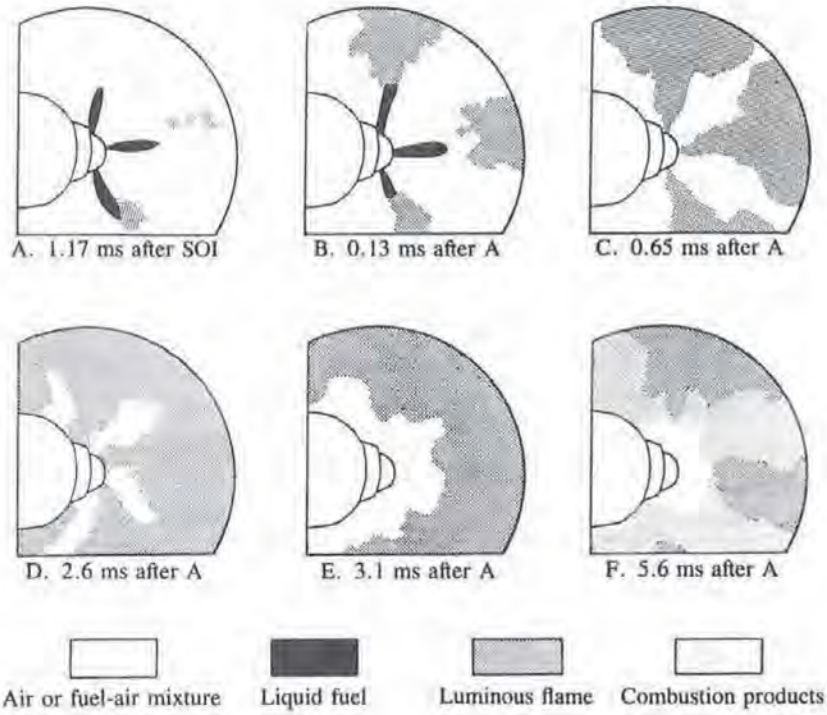
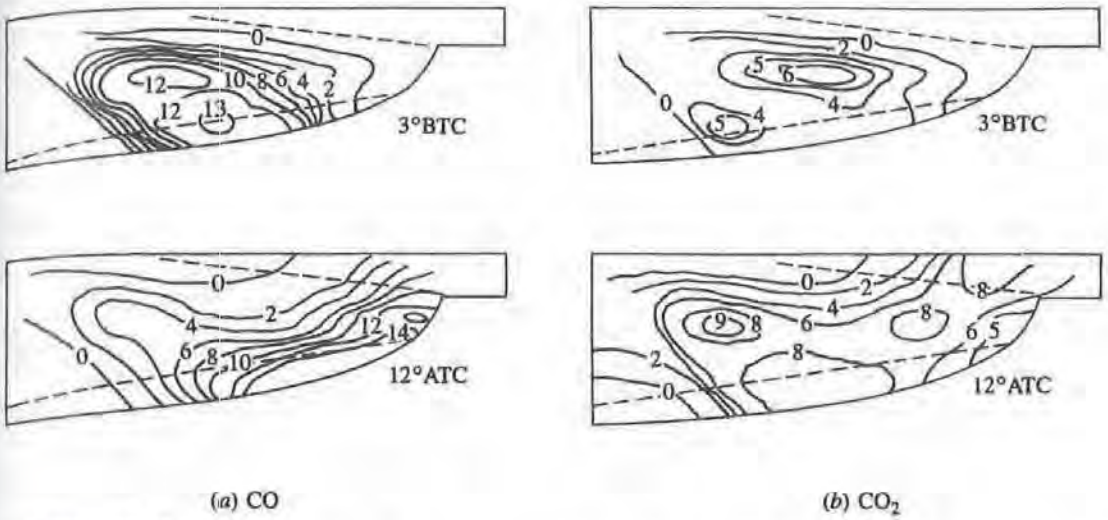


FIGURE 10-44
Tracings of outer boundary of liquid fuel spray and flame from high-speed movies of diesel combustion taken in a rapid-compression machine, looking down on piston through transparent head. First occurrence of luminous flame at A, 1.17 ms after start of injection. End of injection at D.[57]

larger gaseous-jet region containing fuel vapor (see Fig. 10-20). The fuel concentration in the core is extremely high: local fuel/air equivalence ratios near the nozzle of order 10 have been measured during the injection period. Fuel concentrations within the spray decrease with increasing radial and axial position at any given time, and with time at a fixed location once injection has ended.[55] The fuel distribution within the spray is controlled largely by turbulent-jet mixing processes. Fuel vapor concentration contours determined from interferometric studies of unsteady vaporizing diesel-like sprays, presented by Lakshminarayan and Dent,[56] confirm this gaseous turbulent-jet-like structure of the spray, with its central liquid-containing core which evaporates relatively quickly once fuel injection ends.

The location of the autoignition sites and subsequent spreading of the enflamed region in relation to the fuel distribution in the spray provides further evidence of the mixing-controlled character of combustion. Figure 10-44 shows how this process occurs under conditions typical of direct-injection quiescent-chamber diesel engines. It shows tracings of the liquid fuel spray and flame boundaries taken from high-speed movies of the injection and combustion processes with central injection of five fuel jets into a disc-shaped chamber in a rapid-compression machine.[57] These and other similar studies show that autoignition first occurs toward the edge of the spray, between the spray tip (which may by then have interacted with the combustion chamber walls, and which contains



(*a*) CO (*b*) CO_2

FIGURE 10-45
Contours of constant CO and CO_2 concentration in a plane along the spray axis calculated from gas composition data obtained with a rapid-acting sampling valve in a large 30.5-cm bore DI quiescent-chamber diesel engine with $r_c = 12.85$ operated at 500 rev/min. Injection starts 17° BTC, ignition occurs 8° BTC, injection ends 5° ATC.[60]

later-injected fuel as explained in Sec. 10.5.2) and the injector nozzle. Experiments where air/fuel ratio contours for a gaseous fuel jet injected into a swirling air flow in a rig simulated the fuel-air mixing process in open-chamber diesels,[58] under conditions chosen to match a set of diesel combustion rapid-compression-machine experiments where the autoignition sites and subsequent flame development were recorded on movies,[59] showed that autoignition occurred in a concentration band between the equivalence ratios of 1 and 1.5. Subsequent flame development, along mixture contours close to stoichiometric, occurs rapidly, as indicated in Fig. 10-44. Initially, this is thought to be due to spontaneous ignition of regions close to the first ignition site due to the temperature rise associated with the strong pressure wave which emanates from each ignition site due to local rapid chemical energy release. Also, spontaneous ignition at additional sites on the same spray, well separated from the original ignition location, can occur. Turbulent mixing provides another flame-spreading mechanism. From this point flame development is rapid, and the gas expansion which occurs on burning deforms the original spray form. These processes take place in each fuel spray in a closely comparable though not necessarily identical manner. Combustion movies such as those in Figs. 10-4 and 10-44 show that flame rapidly envelops each spray once spontaneous ignition occurs.

Gas-sampling data indicate that the burned gases within the flame-enveloped spray are only partially reacted and may be fuel-rich. Figure 10-45 shows CO and CO_2 concentration contours determined from rapid-acting sample valve measurements from the combustion chamber of a large quiescent-chamber two-stroke cycle diesel engine.[60] The contour maps shown correspond to the centerline of one of the five injected fuel sprays. Injection commenced at

17° BTC and ended about 5° ATC; ignition occurred at 8° BTC. The contours at 3° BTC show high CO concentrations in the burned gases which now occupy most of the spray region, indicating locally very fuel-rich conditions. Later, at 12° ATC, fuel injection has ceased, this rich core has moved outward to the piston-bowl wall, and combustion within the expanded spray region is much more complete. This oxidation of CO, as air is entrained into the spray region, mixes, and burns, releases substantial additional chemical energy.

The role of air swirl in promoting much more rapid fuel-air mixing in medium-size and smaller diesel engines is evident from similar gas-sampling studies in engines with these different combustion systems. The variation of gas species and unburned hydrocarbon concentrations within critical regions of the combustion chamber have been mapped out by a number of investigators.[61–63] These data show that during the early stages of injection and combustion, the boundaries of the individual sprays can be identified as they are convected around the combustion chamber bowl by the swirl. The fuel distribution within the combustion chamber is highly nonuniform. However, within each spray, sufficient air has mixed into the spray to bring the peak fuel/air equivalence ratios within the spray, in the outer regions of the chamber, to close to stoichiometric values.[63] This substantially different character of the spray with swirl is clear from the data in Fig. 10-46. Figure 10-46*a* shows equivalence ratio values determined from gas sampling, versus crank angle, from several studies with different designs of combustion chamber. While the local values obviously depend on the relation of the sample valve location to spray position at any given crank angle, the much lower values of equivalence ratio with swirl relative to quiescent chambers, during injection and the early stages of combustion, clearly indicate that swirl enhances mixing rates substantially. As combustion ends, these data indicate relatively uniform fuel distribution within the combustion chamber, at least on a gross geometric scale. However, early in the combustion process the high CO levels, found in all these combustion systems as shown in Fig. 10-46*b*, indicate that the burned gases are only partially reacted. With quiescent chambers this is largely due to lack of oxygen. With swirl, however, substantial oxygen is present. Whether the high CO with swirl is due to kinetic limitations or to smaller-scale mixture nonhomogeneities is unclear.

10.7.3 Fuel-Air Mixing and Burning Rates

The model of diesel combustion obtained from heat-release analyses of cylinder pressure data identifies two main stages of combustion (see Fig. 10-9). The first is the premixed-combustion phase, when the fuel which has mixed sufficiently with air to form an ignitable mixture during the delay period is consumed. The second is the mixing-controlled combustion phase, where rates of burning (at least in naturally aspirated engines) are lower. Experimental evidence from heat-release analysis indicates that the majority of the fuel (usually more than 75 percent) burns during the second mixing-controlled phase. Such evidence forms the basis for the heat-release models used in diesel engine cycle simulations. For example,

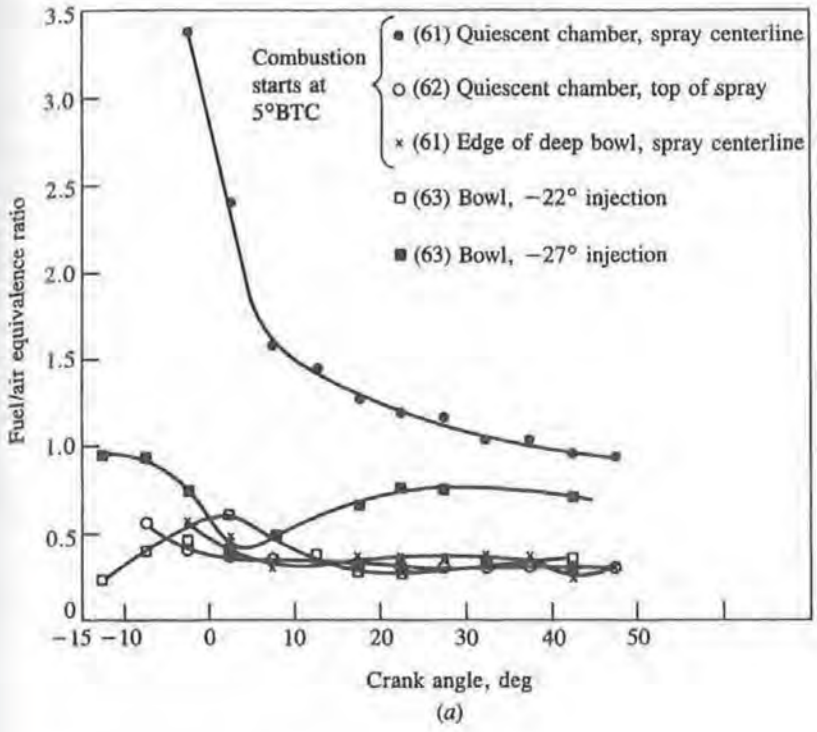


FIGURE 10-46
Time and space-resolved gas-composition data obtained from rapid-acting sampling valves from within the combustion chambers of quiescent and high-swirl bowl-in-piston DI diesel engines. (*a*) Local fuel/air equivalence ratios on spray centerline and periphery with quiescent chamber, edge of deep bowl with swirl, and within a shallow bowl with swirl, three-quarters of the way out to the bowl wall, for two injection timings (−22° and −27°). (*b*) CO concentration on spray centerline with quiescent chamber, edge of deep bowl, and within shallow bowl with swirl.[61–63]

the fraction of the fuel β which burns in the premixed phase has been correlated by Watson *et al.* (see Sec. 14.4.3) by the relation

$$\beta = 1 - \frac{a\phi^b}{\tau_{id}^c} \tag{10.40}$$

where ϕ is the fuel/air equivalence ratio, τ_{id} the ignition delay (in milliseconds), and $a \approx 0.9$, $b \approx 0.35$, and $c \approx 0.4$ are constants depending on engine design. Equation (10.40) shows the expected trends for the premixed fraction, with changes in the overall equivalence ratio ϕ (increasing injection duration as load is increased) and changes in the ignition delay.

That the fuel-burning or heat-release rate is predominantly mixing controlled is supported by the following types of evidence. Estimates of the rate at which fuel-air mixture with composition within the combustible limits is produced in diesel sprays under typical engine conditions, based on a variety of turbulent-jet models of the spray (e.g., see Refs. 29, 36, and 59 and also Sec. 14.4.3), show that mixing rates and burning rates are comparable in magnitude. Estimates of characteristic times for the turbulent-jet mixing processes in diesel combustion chambers show these to be comparable to the duration of the heat-release process, and much longer than characteristic times for evaporation and the combustion chemical kinetics.[36, 44]

Then, measured diesel-combustion heat-release profiles show trends with engine design and operating parameter changes that correspond to fuel-air mixing being the primary controlling factor. Examples of heat-release profiles measured in rapid-compression-machine studies of diesel combustion, shown in Fig. 10-47, illustrate this clearly. The rapid-compression machine had a disc-shaped chamber of 10 cm diameter with a 3.1 cm clearance height at the end of a compression process through a volume ratio of 15.4; a five-hole centrally located fuel-injector nozzle was used. Figure 10-47*a* shows the heat-release profiles for different initial air temperatures which produce different ignition delays. Longer delays allow more fuel to mix to within combustible limits during the delay, so the peak premixed heat-release rate increases. However, the mixing-controlled-phase heat-release-rate magnitudes are essentially the same because the spray-mixing processes are little affected by these changes in air temperature. Figure 10-47*b* and *c* shows that heat-release rates throughout the combustion process are increased by increased fuel-injection rate (achieved by increasing the fuel-injection pressure) and by swirl. Both these changes increase the fuel-air mixing rates within the fuel spray and therefore increase the heat-release rate during the mixing-controlled combustion phase.

Diesel engine heat-release rate trends, as design and operating variables are changed, can be related to mixing rates in analogous fashion. Table 10.5 summarizes the trends that have been investigated. The directional effects of changes in engine parameters on the ignition delay period and the fuel-air mixing rate are all consistent with the measured changes in premixed and mixing-controlled heat-release rates. The controlling role of fuel-air mixing in the diesel engine fuel spray on combustion is clear.

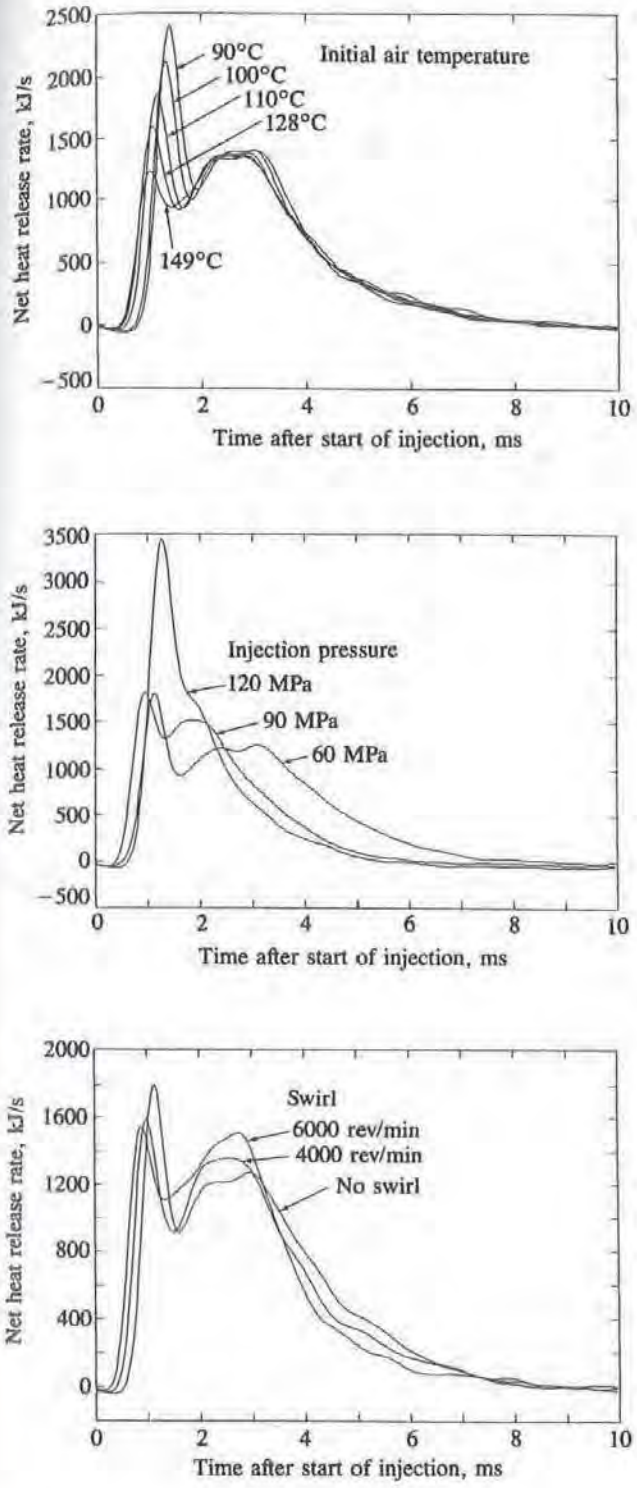


FIGURE 10-47
Net heat-release rates, as a function of time after start of injection, calculated from cylinder pressure data from rapid-compression-machine studies of DI diesel combustion. (*a*) Effect of varying initial air temperature: 4000 rev/min swirl, injection pressure 60 MPa. (*b*) Effect of varying injection pressure: no swirl. (*c*) Effect of varying swirl: injection pressure 60 MPa.[20]

TABLE 10.5
Effects of engine design and operating variables on heat-release rates

Reference	Parameter varied	Effect on τ_{id}	$\dot{m}_m$	$\dot{Q}_p$	$\dot{Q}_m$
5, 64	Injection rate ↑	*	↑	↑	↑
65	Turbocharger boost ↑	↓	*	↓	*
66	Compression ratio ↓	↑	*	↑	*
66	Number of injector holes ↑	*	↑	↑	↑
67, 68	Injection advance ↑	↑	*	↑	*
67, 68	Swirl ↑	*	↑	↑	↑
67	Intake-air temperature ↓	↑	*	↑	*
68, 69	Injection pressure ↑	*	↑	↑	↑
11, 69	Speed ↑	*	↑	↑	↑

τ_{id}, ignition delay; $\dot{m}_m = (dm/dt)_m$, fuel-air mixing rate; $\dot{Q}_p = (dQ/dt)_p$, heat-release rate during premixed-combustion phase; $\dot{Q}_m = (dQ/dt)_m$, heat-release rate during mixing-controlled-combustion phase. ↑ increase; ↓ decrease; * minor effect.
Source: From Plee and Ahmad.[44]

PROBLEMS

10.1. Describe the sequence of processes which must occur before the liquid fuel in the injection system in a direct-injection compression-ignition engine is fully burned.

10.2. Small high-swirl direct-injection CI engines have fuel conversion efficiencies which are about 10 percent higher than values typical of equivalent indirect-injection engines. (IDI engines are used because they achieve higher bmep.) What combustion-system-related differences contribute to this higher efficiency?

10.3. In a diesel engine, because the fuel distribution is nonuniform the burned gas temperature is nonuniform. Consider small fuel-air mixture elements initially at 1000 K and 6.5 MPa at top-center with a range of equivalence ratios. Each element burns at essentially constant pressure. Calculate (using the charts in Chap. 4, or an appropriate chemical equilibrium thermodynamic computer code) the burned gas temperature for mixture equivalence ratios of 0.4, 0.6, 0.8, 1.0, 1.2. Assume the fuel is isooctane.

10.4. The levels of combustible species in the exhaust of a direct-injection diesel engine are: HC, 0.8 g/kW · h; CO, 3 g/kW · h; particulates, 0.7 g/kW · h. If the specific fuel consumption is 210 g/kW · h calculate the combustion efficiency.

10.5. Consider the naturally aspirated direct-injection diesel engine in Fig. 1-23 operating at 2300 rev/min and an equivalence ratio of 0.7. Estimate the following:
(*a*) Mass of air in each cylinder per cycle, mass, and volume (as liquid) of diesel fuel injected per cylinder per cycle.
(*b*) Estimate the average drop size [e.g., use Eq. (10.32)]. The cylinder pressure at time of injection (close to TC) is 50 atm; the fuel injection pressure is 500 atm.
(*c*) Assuming all fuel droplets are the same size as the average drop, how many drops are produced per injection? If these drops are uniformly distributed throughout the air charge at TC, what is the approximate distance between drops? (Neither of these assumptions is correct; however, the calculations illustrate the difficulty of the fuel-air mixing process.)

10.6. Estimate the following quantities for a typical direct-injection diesel fuel spray. The injection pressure is 500 atm; the cylinder pressure during injection is 50 atm.
(*a*) Assuming that the flow through the nozzle orifice is incompressible and quasi steady, estimate the liquid fuel velocity at the orifice exit. At this velocity, how long would the fuel take to reach the cylinder wall? The bore is 125 mm.
(*b*) Each nozzle orifice diameter d_n is 0.34 mm and $L_n/d_n = 4$. Determine the spray angle and plot spray tip penetration versus time.
(*c*) Use Eq. (10.32) to estimate the initial average drop size assuming that the injection process in (*a*) above continues for 1 millisecond and the injector nozzle has four orifices.

10.7. Diesel fuel is injected as a liquid at room temperature into air at 50 atm and 800 K, close to TC at the end of compression. If the overall equivalence ratio is 0.7, estimate the reduction in average air temperature which would occur when the fuel is fully vaporized and uniformly mixed. Assume such mixing takes place at constant volume prior to any combustion.

10.8. Using Eq. (10.37) estimate the ignition delay in milliseconds and crank angle degrees for these operating conditions in Table 10.4: low swirl IDI diesel 600 and 1800 rev/min; high swirl IDI diesel 1800 rev/min; DI diesel low and high compression ratio. The fuel cetane number is 45; stroke = 0.1 m. Discuss whether the predicted trends with speed, swirl, and compression ratio are consistent with Sec. 10.6.4.

10.9. The compression ratio of truck diesel engines must be set at about 18 so that the engine will start when cold. Using Eqs. (10.37) to (10.39) develop a graph of τ_{id} (in degrees) as a function of compression ratio for $r_c = 12$ to 20. Assume $p_i = 1$ atm, $T_i = 255$ K, $n = 1.13$, speed = 100 rev/min, bore = stroke = 120 mm, fuel cetane number = 45. If the ignition delay must be less than 20° CA for satisfactory starting, what compression ratio is required?

10.10. Equation (10.40) predicts the fraction β of the fuel injected into a direct-injection diesel engine which burns in the premixed phase. Plot β as a function of τ_{id} for $\phi = 0.4$. Show that for turbocharged DI diesel engines where τ_{id} is 0.4 to 1 ms, the premixed combustion phase is much less important than it normally is for naturally aspirated engines where τ_{id} is between 0.7 and 3 ms.

REFERENCES

1. Alcock, J. F., and Scott, W. M.: "Some More Light on Diesel Combustion," *Proc. Auto. Div., Instn Mech. Engrs*, No. 5, pp. 179–191, 1962–1963.
2. Scott, W. M.: "Understanding Diesel Combustion through the Use of High Speed Moving Pictures in Color," SAE paper 690002, *SAE Trans.*, vol. 78, 1969.
3. Neitz, A., and D'Alfonso, N.: "The M.A.N. Combustion System with Controlled Direct Injection for Passenger Car Diesel Engines," SAE paper 810479, 1979.
4. Ogasawara, M., Tokunaga, Y., Horio, K., Uryu, M., and Hirofumi, N.: "Photographic Study on the Intermittent Spray Combustion by a Rapid Compression Machine" (in Japanese), *Internal Combustion Engine*, vol. 15, 1976.
5. Austen, A. E. W., and Lyn, W.-T.: "Relation between Fuel Injection and Heat Release in a Direct-Injection Engine and the Nature of the Combustion Processes," *Proc. Instn Mech. Engrs*, No. 1, pp. 47–62, 1960–1961.
6. Lyn, W.-T.: "Study of Burning Rate and Nature of Combustion in Diesel Engines," in *Proceedings of Ninth International Symposium on Combustion*, pp. 1069–1082, The Combustion Institute, 1962.
7. Cheng, W., and Gentry, R.: "Effects on Charge Non-Uniformity on Diesel Heat Release Analysis," SAE paper 861568, 1986.

8. Gatowski, J. A., Balles, E. N., Chun, K. M., Nelson, F. E., Ekchian, J. A., and Heywood, J. B.: "Heat Release Analysis of Engine Pressure Data," SAE paper 841359, *SAE Trans.*, vol. 93, 1984.
9. Krieger, R. B., and Borman, G. L.: "The Computation of Apparent Heat Release for Internal Combustion Engines," ASME paper 66-WA/DGP-4, in *Proc. Diesel Gas Power*, ASME, 1966.
10. Watson, N., and Kamel, M.: "Thermodynamic Efficiency Evaluation of an Indirect Injection Diesel Engine," SAE paper 790039, *SAE Trans.*, vol. 88, 1979.
11. Kort, R. T., Mansouri, S. H., Heywood, J. B., and Ekchian, J. A.: "Divided-Chamber Diesel Engine, Part II: Experimental Validation of a Predictive Cycle-Simulation and Heat Release Analysis," SAE paper 820274, *SAE Trans.*, vol. 91, 1982.
12. Obert, E. F.: *Internal Combustion Engines and Air Pollution*, Intext Educational Publishers, 1973 edition.
13. Weathers, Jr., T., and Hunter, C.: *Diesel Engines for Automobiles and Small Trucks*, Reston Publishing Company, a Prentice-Hall Company, Reston, Va. 1981.
14. Bosch: *Automotive Handbook*, 1st English ed., Robert Bosch GmbH, 1976.
15. Williams, Jr., H. A.: "The GM/EMD Model 710G Series Engine," in *Marine Engine Development*, SP-625, SAE, 1985. Also ASME paper 85-GGP-24, 1985.
16. Hames, R. J., Straub, R. D., and Amann, R. W.: "DDEC Detroit Diesel Electronic Control," SAE paper 850542, 1985.
17. Hiroyasu, H.: "Diesel Engine Combustion and Its Modeling," in *Diagnostics and Modeling of Combustion in Reciprocating Engines*, pp. 53–75, COMODIA 85, Proceedings of Symposium, Tokyo, Sept. 4–6, 1985.
18. Arai, M., Tabata, M., and Hiroyasu, H.: "Disintegrating Process and Spray Characterization of Fuel Jet Injected by a Diesel Nozzle," SAE paper 840275, *SAE Trans.*, vol. 93, 1984.
19. Kamimoto, T., Kobayashi, H., and Matsuoka, S.: "A Big Size Rapid Compression Machine for Fundamental Studies of Diesel Combustion," SAE paper 811004, *SAE Trans.*, vol. 90, 1981.
20. Balles, E.: "Fuel-Air Mixing and Diesel Combustion in a Rapid Compression Machine," Ph.D. Thesis, Department of Mechanical Engineering, MIT, June 1987.
21. Browne, K. R., Partridge, I. M., and Greeves, G.: "Fuel Property Effects on Fuel/Air Mixing in an Experimental Diesel Engine," SAE paper 860223, 1986.
22. Bracco, F. V.: "Modeling of Engine Sprays," SAE paper 850394, 1985.
23. Kuo, T., and Bracco, F. V.: "Computations of Drop Sizes in Pulsating Sprays and of Liquid-Core Length in Vaporizing Sprays," SAE paper 820133, *SAE Trans.*, vol. 91, 1982.
24. Reitz, R. D., and Bracco, F. V.: "Mechanism of Atomization of a Liquid Jet," *Phys. Fluid*, vol. 25, no. 10, pp. 1730–1742, 1982.
25. Reitz, R. D., and Bracco, F. V.: "On the Dependence of Spray Angle and Other Spray Parameters on Nozzle Design and Operating Conditions," SAE paper 790494, 1979.
26. Wu, K.-J., Su, C.-C., Steinberger, R. L., Santavicca, D. A., and Bracco, F. V.: "Measurements of the Spray Angle of Atomizing Jets," *J. Fluids Engng*, vol. 105, pp. 406–413, 1983.
27. Hay, N., and Jones, P. L.: "Comparison of the Various Correlations for Spray Penetration," SAE paper 720776, 1972.
28. Dent, J. C.: "Basis for the Comparison of Various Experimental Methods for Studying Spray Penetration," SAE paper 710571, *SAE Trans.*, vol. 80, 1971.
29. Hiroyasu, H., Kadota, T., and Arai, M.: "Supplementary Comments: Fuel Spray Characterization in Diesel Engines," in James N. Mattavi and Charles A. Amann (eds.), *Combustion Modeling in Reciprocating Engines*, pp. 369–408, Plenum Press, 1980.
30. Wu, K.-J., Reitz, R. D., and Bracco, F. V.: "Measurements of Drop Size at the Spray Edge near the Nozzle in Atomizing Liquid Jets," *Phys. Fluids*, vol. 29, no. 4, pp. 941–951, 1986.
31. Reitz, R. D., and Diwakar, R.: "Effect of Drop Breakup on Fuel Sprays," SAE paper 860469, 1986.
32. Hiroyasu, H., and Kadota, T.: "Fuel Droplet Size Distribution in Diesel Combustion Chamber," SAE paper 740715, *SAE Trans.*, vol. 83, 1974.
33. El Wakil, M. M., Myers, P. S., and Uyehara, O. A.: "Fuel Vaporization and Ignition Lag in Diesel Combustion," in *Burning a Wide Range of Fuels in Diesel Engines, SAE Progress in Technol.*, vol. 11, pp. 30–44, SAE, 1967.

34. Borman, G. L., and Johnson, J. H.: "Unsteady Vaporization Histories and Trajectories of Fuel Drops Injected into Swirling Air," in *Burning a Wide Range of Fuels in Diesel Engines, SAE Progress in Technology*, vol. 11, pp. 13–29, SAE, 1967; also SAE paper 598C, 1962.
35. Kamimoto, T., and Matsuoka, S.: "Prediction of Spray Evaporation in Reciprocating Engines," SAE paper 770413, *SAE Trans.*, vol. 86, 1977.
36. Kuo, T., Yu, R. C., and Shahed, S. M.: "A Numerical Study of the Transient Evaporating Spray Mixing Process in the Diesel Environment," SAE paper 831735, *SAE Trans.*, vol. 92, 1983.
37. ASTM Method D613, Cetane Test Procedure.
38. Henein, N. A., and Fragoulis, A. N.: "Correlation between Physical Properties and Autoignition Parameters of Alternate Fuels," SAE paper 850266, 1985.
39. Gulder, O. L., Glavincevski, B., and Burton, G. F.: "Ignition Quality Rating Methods for Diesel Fuels—A Critical Appraisal," SAE paper 852080, 1985.
40. ASTM D976, Calculated Cetane Index.
41. ASTM D611.
42. Igura, S., Kadota, T., and Hiroyasu, H.: "Spontaneous Ignition Delay of Fuel Sprays in High Pressure Gaseous Environments," *Trans. Japan Soc. Mech. Engrs*, vol. 41, no. 345, pp. 24–31, 1975.
43. Spadaccini, L. J., and TeVelde, J. A.: "Autoignition Characteristics of Aircraft-Type Fuels," *Combust. Flame*, vol. 46, pp. 283–300, 1982.
44. Plee, S. L., and Ahmad, T.: "Relative Roles of Premixed and Diffusion Burning in Diesel Combustion," SAE paper 831733, *SAE Trans.*, vol. 92, 1983.
45. Stringer, F. W., Clarke, A. E., and Clarke, J. S.: "The Spontaneous Ignition of Hydrocarbon Fuels in a Flowing System," *Proc. Instn Mech. Engrs*, vol. 184, pt. 3J, 1969–1970.
46. Wolfer, H. H.: "Ignition Lag in Diesel Engines," VDI-Forschungsheft 392, 1938; Translated by Royal Aircraft Establishment, Farnborough Library No. 358, UDC 621–436.047, August 1959.
47. Lyn, W.-T., and Valdmanis, E.: "Effects of Physical Factors on Ignition Delay," SAE paper 680102, 1968.
48. Wong, C. L., and Steere, D. E.: "The Effects of Diesel Fuel Properties and Engine Operating Conditions on Ignition Delay," SAE paper 821231, *SAE Trans.*, vol. 91, 1982.
49. Andree, A., and Pachernegg, S. J.: "Ignition Conditions in Diesel Engines," SAE paper 690253, *SAE Trans.*, vol. 78, 1969.
50. Glavincevski, B., Gülder, O. L., and Gardner, L.: "Cetane Number Estimation of Diesel Fuels from Carbon Type Structural Composition," SAE paper 841341, 1984.
51. Olree, R., and Lenane, D.: "Diesel Combustion Cetane Number Effects," SAE paper 840108, *SAE Trans.*, vol. 93, 1984.
52. Schaefer, A. J., and Hardenberg, H. O.: "Ignition Improvers for Ethanol Fuels," SAE paper 810249, *SAE Trans.*, vol. 90, 1981.
53. Hardenberg, H. O., and Hase, F. W.: "An Empirical Formula for Computing the Pressure Rise Delay of a Fuel from its Cetane Number and from the Relevant Parameters of Direct-Injection Diesel Engines," SAE paper 790493, *SAE Trans.*, vol. 88, 1979.
54. Dent, J. C., and Mehta, P. S.: "Phenomenological Combustion Model for a Quiescent Chamber Diesel Engine," SAE paper 811235, *SAE Trans.*, vol. 90, 1981.
55. Chang, Y. J., Kobayashi, H., Matsuzawa, K., and Kamimoto, T.: "A Photographic Study of Soot Formation and Combustion in a Diesel Flame with a Rapid Compression Machine," in *Diagnostics and Modeling of Combustion in Reciprocating Engines*, pp. 149–157, COMODIA 85, Proceedings of Symposium, Tokyo, Sept. 4–6, 1985.
56. Lakshminarayan, P. A., and Dent, J. C.: "Interferometric Studies of Vaporising and Combustion Sprays," SAE paper 830244, *SAE Trans.*, vol. 92, 1983.
57. Colella, K. J., Balles, E. N., Ekchian, J. A., Cheng, W. K., and Heywood, J. B.: "A Rapid Compression Machine Study of the Influence of Charge Temperature on Diesel Combustion," SAE paper 870587, 1987.
58. Morris, C. J., and Dent, J. C.: "The Simulation of Air Fuel Mixing in High Swirl Open Chamber Diesel Engines," *Proc. Instn Mech. Engrs*, vol. 190, no. 47/76, pp. 503–513, 1976.
59. Rife, J., and Heywood, J. B.: "Photographic and Performance Studies of Diesel Combustion with

a Rapid Compression Machine," SAE paper 740948, *SAE Trans.*, vol. 83, 1974.
60. Whitehouse, N. D., Cough, E., and Jeje, A. B.: "The Study of Combustion in a Quiescent Combustion Chamber Diesel Engine," ASME paper 82-HT-35, 1982.
61. Nightingale, D. R.: "A Fundamental Investigation into the Problem of NO Formation in Diesel Engines," SAE paper 750848, *SAE Trans.*, vol. 84, 1975.
62. Bennethum, J. E., Mattavi, J. N., and Toepel, R. R.: "Diesel Combustion Chamber Sampling-Hardware, Procedures, and Data Interpretation," SAE paper 750849, *SAE Trans.*, vol. 84, 1975.
63. Rhee, K. T., Myers, P. S., and Uyehara, O. A.: "Time- and Space-Resolved Species Determination in Diesel Combustion Using Continuous Flow Gas Sampling," SAE paper 780226, *SAE Trans.*, vol. 87, 1978.
64. Shipinsky, J., Uyehara, O. A., and Myers, P. S.: "Experimental Correlation between Rate-of-Injection and Rate-of-Heat-Release in a Diesel Engine," ASME paper 68–DGP-11, 1968.
65. Grigg, H. C., and Syed, M. H.: "The Problem of Predicting Rate of Heat Release in Diesel Engine," *Proc. Instn Mech. Engrs*, vol. 184, pt. 3J, 1969–1970.
66. Whitehouse, N. D., Clough, E., and Way, J. B.: "The Effect of Changes in Design and Operating Conditions on Heat Release in Direct-Injection Diesel Engines," SAE paper 740085, 1974.
67. Meguerdichian, M., and Watson, N.: "Prediction of Mixture Formation and Heat Release in Diesel Engines," SAE paper 780225, 1978.
68. Kamimoto, T., Aoyagi, Y., Matsui, Y., and Matsuoka, S.: "The Effects of Some Engine Variables on Measured Rates of Air Entrainment and Heat Release in a DI Diesel Engine," SAE paper 8000253, *SAE Trans.*, vol. 89, 1980.
69. Dent, J. C., Mehta, P. S., and Swan, J.: "A Predictive Model for Automotive DI Diesel Engine Performance and Smoke Emissions," paper C126/82, presented at the International Conference on *Diesel Engines for Passenger Cars and Light Duty Vehicles*, Institution of Mechanical Engineers, London, England, Oct. 5–7, 1982.

CHAPTER 11

POLLUTANT FORMATION AND CONTROL

11.1 NATURE AND EXTENT OF PROBLEM

Spark-ignition and diesel engines are a major source of urban air pollution. The spark-ignition engine exhaust gases contain oxides of nitrogen (nitric oxide, NO, and small amounts of nitrogen dioxide, NO_2—collectively known as NO_x), carbon monoxide (CO), and organic compounds which are unburned or partially burned hydrocarbons (HC). The relative amounts depend on engine design and operating conditions but are of order: NO_x, 500 to 1000 ppm or 20 g/kg fuel; CO, 1 to 2 percent or 200 g/kg fuel; and HC, 3000 ppm (as C_1) or 25 g/kg fuel. Piston blowby gases, and fuel evaporation and release to the atmosphere through vents in the fuel tank and carburetor after engine shut-down, are also sources of unburned hydrocarbons. However, in most modern engines these nonexhaust sources are effectively controlled by returning the blowby gases from the crankcase to the engine intake system and by venting the fuel tank and carburetor float bowl through a vapor-absorbing carbon cannister which is purged by some of the engine intake air during normal engine operation. In diesel engine exhaust, concentrations of NO_x are comparable to those from SI engines. Diesel hydrocarbon emissions are significant though exhaust concentrations are lower by about a factor of 5 than typical SI engine levels. The hydrocarbons in the exhaust may also condense to form white smoke during engine starting and warm-up.

Specific hydrocarbon compounds in the exhaust gases are the source of diesel odor. Diesel engines are an important source of particulate emissions; between about 0.2 and 0.5 percent of the fuel mass is emitted as small (~ 0.1 μm diameter) particles which consist primarily of soot with some additional absorbed hydrocarbon material. Diesel engines are not a significant source of carbon monoxide.

Use of alcohol fuels in either of these engines substantially increases aldehyde emissions. While these are not yet subject to regulation, aldehydes would be a significant pollutant if these fuels were to be used in quantities comparable to gasoline and diesel. Currently used fuels, gasoline and diesel, contain sulfur: gasoline in small amounts (≤ 600 ppm by weight S), diesel fuel in larger amounts (≤ 0.5 percent). The sulphur is oxidized (or burned) to produce sulfur dioxide, SO_2, of which a fraction can be oxidized to sulfur trioxide, SO_3, which combines with water to form a sulfuric acid aerosol.

In general, the concentrations of these pollutants in internal combustion engine exhaust differ from values calculated assuming chemical equilibrium. Thus the detailed chemical mechanisms by which these pollutants form and the kinetics of these processes are important in determining emission levels. For some pollutant species, e.g., carbon monoxide, organic compounds, and particulates, the formation and destruction reactions are intimately coupled with the primary fuel combustion process. Thus an understanding of the formation of these species requires knowledge of the combustion chemistry. For nitrogen oxides and sulfur oxides, the formation and destruction processes are not part of the fuel combustion process. However, the reactions which produce these species take place in an environment created by the combustion reactions, so the two processes are still intimately linked. A summary of the mechanisms by which these pollutants form in internal combustion engines provides an introduction to this chapter. In subsequent sections, the details of the basic formation mechanisms of each pollutant and the application of these mechanisms to the combustion process in both spark-ignition and compression-ignition engines will be developed.

The processes by which pollutants form within the cylinder of a conventional spark-ignition engine are illustrated qualitatively in Fig. 11-1. The schematic shows the combustion chamber during four different phases of the engine operating cycle: compression, combustion, expansion, and exhaust. Nitric oxide (NO) forms throughout the high-temperature burned gases behind the flame through chemical reactions involving nitrogen and oxygen atoms and molecules, which do not attain chemical equilibrium. The higher the burned gas temperature, the higher the rate of formation of NO. As the burned gases cool during the expansion stroke the reactions involving NO freeze, and leave NO concentrations far in excess of levels corresponding to equilibrium at exhaust conditions. Carbon monoxide also forms during the combustion process. With rich fuel-air mixtures, there is insufficient oxygen to burn fully all the carbon in the fuel to CO_2; also, in the high-temperature products, even with lean mixtures, dissociation ensures there are significant CO levels. Later, in the expansion stroke, the CO oxidation process also freezes as the burned gas temperature falls.

The unburned hydrocarbon emissions have several different sources.

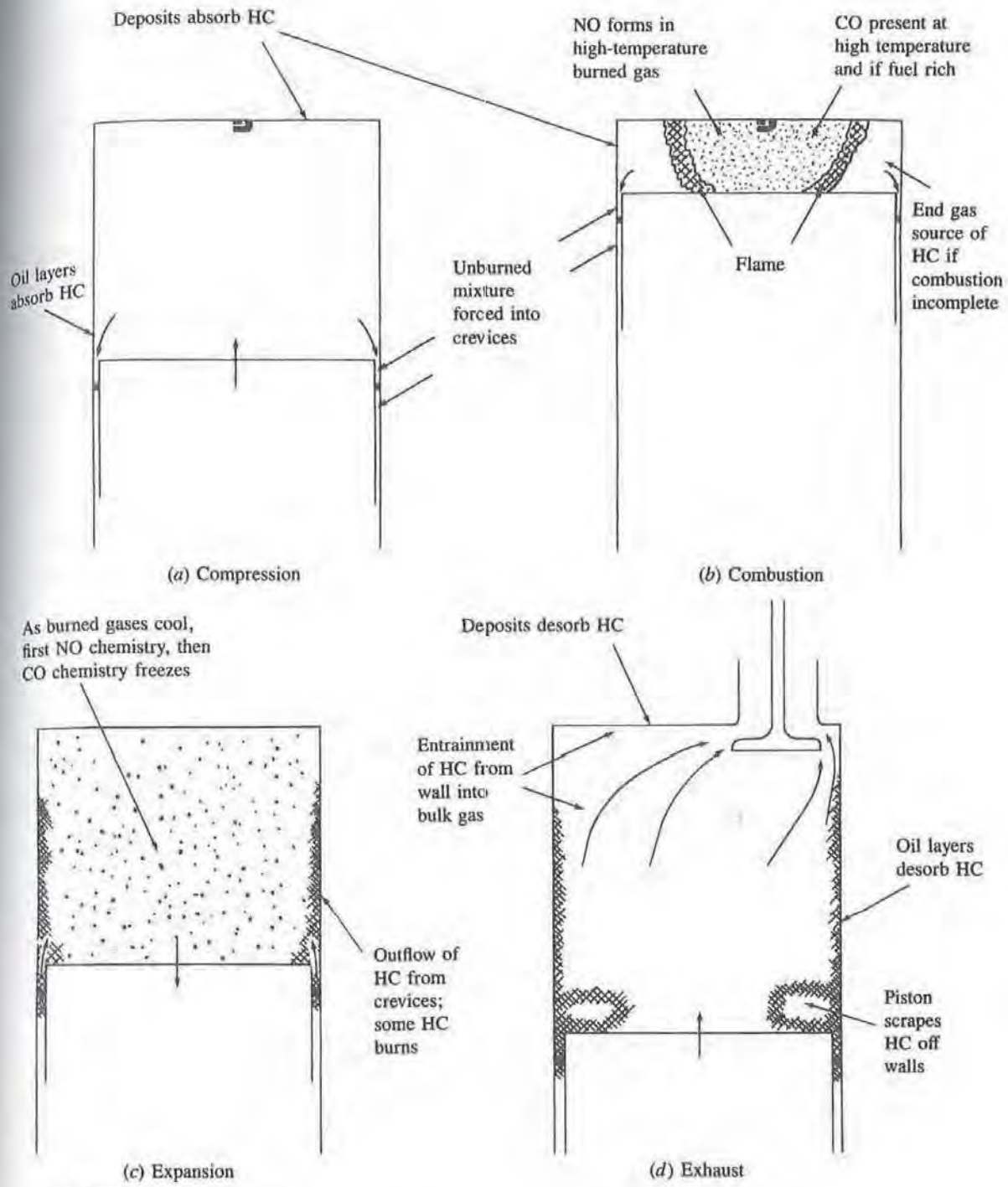


FIGURE 11-1
Summary of HC, CO, and NO pollutant formation mechanisms in a spark-ignition engine.

During compression and combustion, the increasing cylinder pressure forces some of the gas in the cylinder into crevices, or narrow volumes, connected to the combustion chamber: the volumes between the piston, rings, and cylinder wall are the largest of these. Most of this gas is unburned fuel-air mixture; much of it

escapes the primary combustion process because the entrance to these crevices is too narrow for the flame to enter. This gas, which leaves these crevices later in the expansion and exhaust processes, is one source of unburned hydrocarbon emissions. Another possible source is the combustion chamber walls. A quench layer containing unburned and partially burned fuel-air mixture is left at the wall when the flame is extinguished as it approaches the wall. While it has been shown that the unburned HC in these thin (≤ 0.1 mm) layers burn up rapidly when the combustion chamber walls are clean, it has also been shown that the porous deposits on the walls of engines in actual operation do increase engine HC emissions. A third source of unburned hydrocarbons is believed to be any engine oil left in a thin film on the cylinder wall, piston and perhaps on the cylinder head. These oil layers can absorb and desorb fuel hydrocarbon components, before and after combustion, respectively, thus permitting a fraction of the fuel to escape the primary combustion process unburned. A final source of HC in engines is incomplete combustion due to bulk quenching of the flame in that fraction of the engine cycles where combustion is especially slow (see Sec. 9.4.3). Such conditions are most likely to occur during transient engine operation when the air/fuel ratio, spark timing, and the fraction of the exhaust recycled for emission control may not be properly matched.

The unburned hydrocarbons exit the cylinder by being entrained in the bulk-gas flow during blowdown and at the end of the exhaust stroke as the piston pushes gas scraped off the wall out of the exhaust valve. Substantial oxidation of the hydrocarbons which escape the primary combustion process by any of the above processes can occur during expansion and exhaust. The amount of oxidation depends on the temperature and oxygen concentration time histories of these HC as they mix with the bulk gases.

One of the most important variables in determining spark-ignition engine emissions is the fuel/air equivalence ratio, ϕ. Figure 11-2 shows qualitatively how NO, CO, and HC exhaust emissions vary with this parameter. The spark-ignition engine has normally been operated close to stoichiometric, or slightly fuel-rich, to ensure smooth and reliable operation. Figure 11-2 shows that leaner mixtures give lower emissions until the combustion quality becomes poor (and eventually misfire occurs), when HC emissions rise sharply and engine operation becomes erratic. The shapes of these curves indicate the complexities of emission control. In a cold engine, when fuel vaporization is slow, the fuel flow is increased to provide an easily combustible fuel-rich mixture in the cylinder. Thus, until the engine warms up and this enrichment is removed, CO and HC emissions are high. At part-load conditions, lean mixtures could be used which would produce lower HC and CO emissions (at least until the combustion quality deteriorates) and moderate NO emissions. Use of recycled exhaust to dilute the engine intake mixture lowers the NO levels, but also deteriorates combustion quality. Exhaust gas recirculation (EGR) is used with stoichiometric mixtures in many engine control systems. Note that the highest power levels are obtained from the engine with slightly rich-of-stoichiometric mixtures and no recycled exhaust to dilute the incoming charge. As we will see, several emission control techniques are required

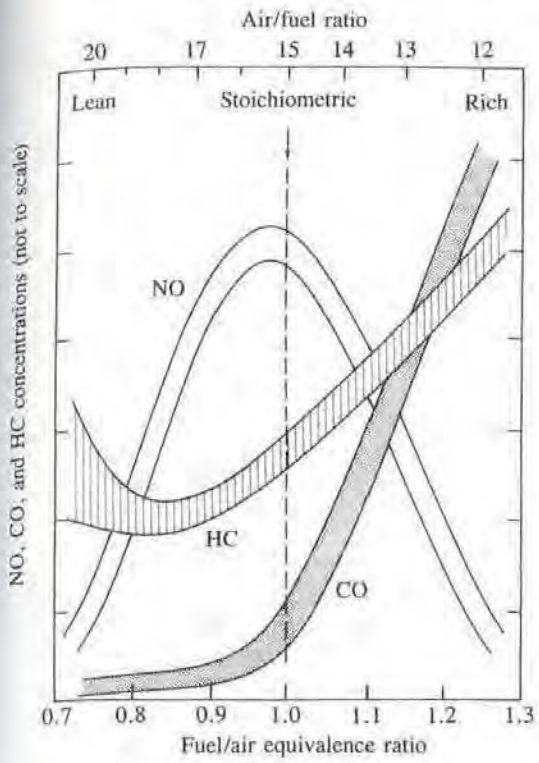


FIGURE 11-2
Variation of HC, CO, and NO concentration in the exhaust of a conventional spark-ignition engine with fuel/air equivalence ratio.

to reduce emissions of all three pollutants, over all engine operating modes, and achieve acceptable average levels.

In the diesel engine, the fuel is injected into the cylinder just before combustion starts, so throughout most of the critical parts of the cycle the fuel distribution is nonuniform. The pollutant formation processes are strongly dependent on the fuel distribution and how that distribution changes with time due to mixing. Figure 11-3 illustrates how various parts of the fuel jet and the flame affect the formation of NO, unburned HC, and soot (or particulates) during the "premixed" and "mixing-controlled" phases of diesel combustion in a direct-injection engine with swirl. Nitric oxide forms in the high-temperature burned gas regions as before, but temperature and fuel/air ratio distributions within the burned gases are now nonuniform and formation rates are highest in the close-to-stoichiometric regions. Soot forms in the rich unburned-fuel-containing core of the fuel sprays, within the flame region, where the fuel vapor is heated by mixing with hot burned gases. Soot then oxidizes in the flame zone when it contacts unburned oxygen, giving rise to the yellow luminous character of the flame. Hydrocarbons and aldehydes originate in regions where the flame quenches both on the walls and where excessive dilution with air prevents the combustion process from either starting or going to completion. Fuel that vaporizes from the nozzle sac volume during the later stages of combustion is also a source of HC. Combustion generated noise is controlled by the early part of the combustion process, the initial rapid heat release immediately following the ignition-delay period.

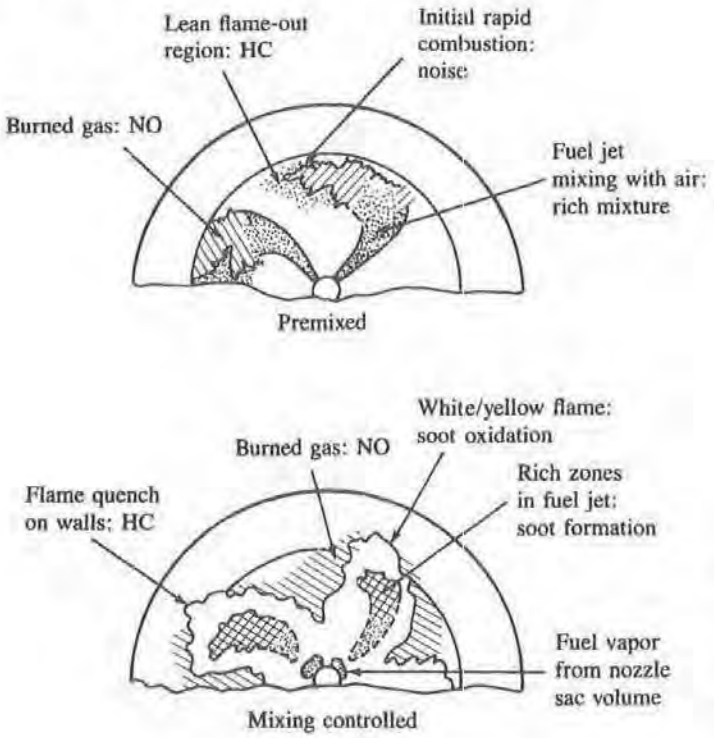


FIGURE 11-3
Summary of pollutant formation mechanisms in a direct-injection compression-ignition engine during "premixed" and "mixing-controlled" combustion phases.

11.2 NITROGEN OXIDES

11.2.1 Kinetics of NO Formation

While nitric oxide (NO) and nitrogen dioxide (NO_2) are usually grouped together as NO_x emissions, nitric oxide is the predominant oxide of nitrogen produced inside the engine cylinder. The principal source of NO is the oxidation of atmospheric (molecular) nitrogen. However, if the fuel contains significant nitrogen, the oxidation of the fuel nitrogen-containing compounds is an additional source of NO. Gasolines contain negligible amounts of nitrogen; although diesel fuels contain more nitrogen, current levels are not significant.

The mechanism of NO formation from atmospheric nitrogen has been studied extensively.[1] It is generally accepted that in combustion of near-stoichiometric fuel-air mixtures the principal reactions governing the formation of NO from molecular nitrogen (and its destruction) are†

$$O + N_2 = NO + N \tag{11.1}$$

$$N + O_2 = NO + O \tag{11.2}$$

$$N + OH = NO + H \tag{11.3}$$

† This is often called the extended Zeldovich mechanism. Zeldovich[1] was the first to suggest the importance of reactions (11.1) and (11.2). Lavoie *et al.*[2] added reaction (11.3) to the mechanism; it does contribute significantly.

TABLE 11.1
Rate constants for NO formation mechanism[1]

Reaction	Rate constant, $cm^3/mol \cdot s$	Temperature range, K	Uncertainty, factor of or %
(1) $O + N_2 \rightarrow NO + N$	$7.6 \times 10^{13} \exp[-38{,}000/T]$	2000–5000	2
(−1) $N + NO \rightarrow N_2 + O$	1.6×10^{13}	300–5000	±20% at 300 K 2 at 2000–5000 K
(2) $N + O_2 \rightarrow NO + O$	$6.4 \times 10^{9}\ T \exp[-3150/T]$	300–3000	±30% 300–1500 K 2 at 3000 K
(−2) $O + NO \rightarrow O_2 + N$	$1.5 \times 10^{9}\ T \exp[-19{,}500/T]$	1000–3000	±30% at 1000 K 2 at 3000 K
(3) $N + OH \rightarrow NO + H$	4.1×10^{13}	300–2500	±80%
(−3) $H + NO \rightarrow OH + N$	$2.0 \times 10^{14} \exp[-23{,}650/T]$	2200–4500	2

The forward and reverse rate constants (k_i^+ and k_i^-, respectively) for these reactions have been measured in numerous experimental studies. Recommended values for these rate constants taken from a critical review of this published data are given in Table 11.1. Note that the equilibrium constant for each reaction, $K_{c,i}$ (see Sec. 3.7.2), is related to the forward and reverse rate constants by $K_{c,i} = k_i^+/k_i^-$. The rate of formation of NO via reactions (11.1) to (11.3) is given by [see Eqs. (3.55) and (3.58)]

$$\frac{d[NO]}{dt} = k_1^+[O][N_2] + k_2^+[N][O_2] + k_3^+[N][OH] - k_1^-[NO][N] - k_2^-[NO][O] - k_3^-[NO][H] \quad (11.4)$$

where [ ] denote species concentrations in moles per cubic centimeter when k_i have the values given in Table 11.1. The forward rate constant for reaction (11.1) and the reverse rate constants for reactions (11.2) and (11.3) have large activation energies which results in a strong temperature dependence of NO formation rates.

A similiar relation to (11.4) can be written for $d[N]/dt$:

$$\frac{d[N]}{dt} = k_1^+[O][N_2] - k_2^+[N][O_2] - k_3^+[N][OH] - k_1^-[NO][N] + k_2^-[NO][O] + k_3^-[NO][H] \quad (11.5)$$

Since [N] is much less than the concentrations of other species of interest ($\sim 10^{-8}$ mole fraction), the steady-state approximation is appropriate: $d[N]/dt$ is set equal to zero and Eq. (11.5) used to eliminate [N]. The NO formation rate then becomes

$$\frac{d[NO]}{dt} = 2k_1^+[O][N_2] \frac{1 - [NO]^2/(K[O_2][N_2])}{1 + k_1^-[NO]/(k_2^+[O_2] + k_3^+[OH])} \quad (11.6)$$

where $K = (k_1^+/k_1^-)(k_2^+/k_2^-)$.

TABLE 11.2
Typical values of R_1, R_1/R_2, and $R_1/(R_2 + R_3)$†

Equivalence ratio	R_1‡	R_1/R_2	$R_1/(R_2 + R_3)$
0.8	5.8×10^{-5}	1.2	0.33
1.0	2.8×10^{-5}	2.5	0.26
1.2	7.6×10^{-6}	9.1	0.14

† At 10 atm pressure and 2600 K.
‡ Units gmol/cm^3 · s.

NO forms in both the flame front and the postflame gases. In engines, however, combustion occurs at high pressure so the flame reaction zone is extremely thin ($\sim$0.1 mm) and residence time within this zone is short. Also, the cylinder pressure rises during most of the combustion process, so burned gases produced early in the combustion process are compressed to a higher temperature than they reached immediately after combustion. Thus, NO formation in the postflame gases almost always dominates any flame-front–produced NO. It is, therefore, appropriate to assume that the combustion and NO formation processes are decoupled and to approximate the concentrations of O, O_2, OH, H, and N_2 by their equilibrium values at the local pressure and equilibrium temperature.

To introduce this equilibrium assumption it is convenient to use the notation $R_1 = k_1^+[O]_e[N_2]_e = k_1^-[NO]_e[N]_e$, where $[\ ]_e$ denotes equilibrium concentration, for the one-way equilibrium rate for reaction (11.1), with similiar definitions for $R_2 = k_2^+[N]_e[O_2]_e = k_2^-[NO]_e[O]_e$ and $R_3 = k_3^+[N]_e[OH]_e = k_3^-[NO]_e[H]_e$. Substituting $[O]_e$, $[O_2]_e$, $[OH]_e$, $[H]_e$, and $[N_2]_e$ for [O], $[O_2]$, [OH], [H], and $[N_2]$ in Eq. (11.6) yields

$$\frac{d[NO]}{dt} = \frac{2R_1\{1 - ([NO]/[NO]_e)^2\}}{1 + ([NO]/[NO]_e)R_1/(R_2 + R_3)} \tag{11.7}$$

Typical values of R_1, R_1/R_2 and $R_1/(R_2 + R_3)$ are given in Table 11.2. The difference between R_1/R_2 and $R_1/(R_2 + R_3)$ indicates the relative importance of adding reaction (11.3) to the mechanism.

The strong temperature dependence of the NO formation rate can be demonstrated by considering the initial value of $d[NO]/dt$ when $[NO]/[NO]_e \ll 1$. Then, from Eq. (11.7),

$$\frac{d[NO]}{dt} = 2R_1 = 2k_1^+[O]_e[N_2]_e \tag{11.8}$$

The equilibrium oxygen atom concentration is given by

$$[O]_e = \frac{K_{p(O)}[O_2]_e^{1/2}}{(\tilde{R}T)^{1/2}} \tag{11.9}$$

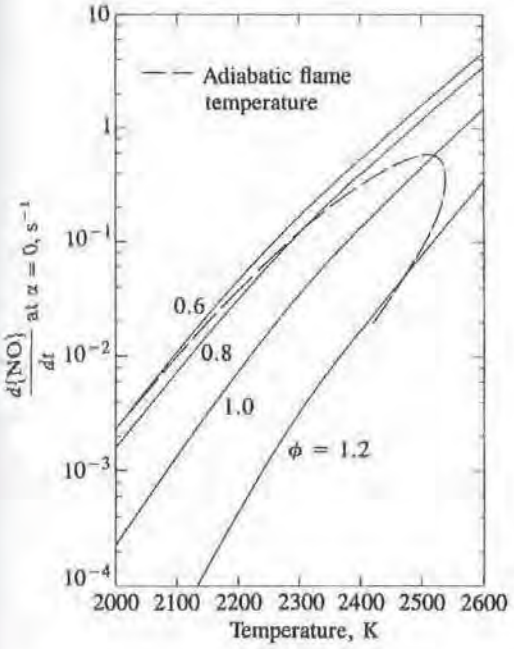


FIGURE 11-4
Initial NO formation rate, mass fraction per second (for $[NO]/[NO]_e \ll 1$), as a function of temperature for different equivalence ratios (ϕ) and 15 atm pressure. Dashed line shows adiabatic flame temperature for kerosene combustion with 700 K, 15 atm air.[3]

where $K_{p(O)}$ is the equilibrium constant for the reaction

$$\tfrac{1}{2}O_2 = O$$

and is given by

$$K_{p(O)} = 3.6 \times 10^3 \exp\left(\frac{-31{,}090}{T}\right) \quad \text{atm}^{1/2} \tag{11.10}$$

The initial NO formation rate may then be written [combining Eqs. (11.8), (11.9), and (11.10) with k_1^+ from Table 11.1] as

$$\frac{d[NO]}{dt} = \frac{6 \times 10^{16}}{T^{1/2}} \exp\left(\frac{-69{,}090}{T}\right)[O_2]_e^{1/2}[N_2]_e \quad \text{mol/cm}^3 \cdot \text{s} \tag{11.11}$$

The strong dependence of $d[NO]/dt$ on temperature in the exponential term is evident. High temperatures and high oxygen concentrations result in high NO formation rates. Figure 11-4 shows the NO formation rate as a function of gas temperature and fuel/air equivalence ratio in postflame gases. Also shown is the adiabatic flame temperature attained by a fuel-air mixture initially at 700 K at a constant pressure of 15 atm. For adiabatic constant-pressure combustion (an appropriate model for each element of fuel that burns in an engine), this initial NO formation rate peaks at the stoichiometric composition, and decreases rapidly as the mixture becomes leaner or richer.

A characteristic time for the NO formation process, τ_{NO}, can be defined by

$$\tau_{NO}^{-1} = \frac{1}{[NO]_e}\frac{d[NO]}{dt} \tag{11.12}$$

$[NO]_e$ can be obtained from the equilibrium constant

$$K_{NO} = 20.3 \times \exp(-21{,}650/T)$$

for the reaction

$$O_2 + N_2 = 2NO$$

as $[NO]_e = (K_{NO}[O_2]_e[N_2]_e)^{1/2}$. Equations (11.11) and (11.12) can be combined to give

$$\tau_{NO} = \frac{8 \times 10^{-16} T \exp(58{,}300/T)}{p^{1/2}} \tag{11.13}$$

where τ_{NO} is in seconds, T in kelvins, and p in atmospheres. Use has been made of the fact that $\tilde{x}_{N_2} \approx 0.71$. For engine combustion conditions, τ_{NO} is usually comparable to or longer than the times characteristic of changes in engine conditions so the formation process is kinetically controlled. However, for close-to-stoichiometric conditions at the maximum pressures and burned gas temperatures, τ_{NO} is of the same order as typical combustion times (1 ms) and equilibrium NO concentrations may be attained.

Evidence that this formation model is valid under conditions typical of those found in engines is provided by high-pressure combustion bomb studies. Newhall and Shahed[4] have measured the NO production, using the q-band absorption technique, behind hydrogen-air and propane-air planar flames propagating axially in a cylindrical bomb. Some results are compared with predictions made with this kinetic scheme (coupled with an "unmixed" combustion calculation to determine local pressure and temperature; see Sec. 9.2.1) in Fig. 11-5. The agreement is excellent. Note that the NO concentration rises smoothly from

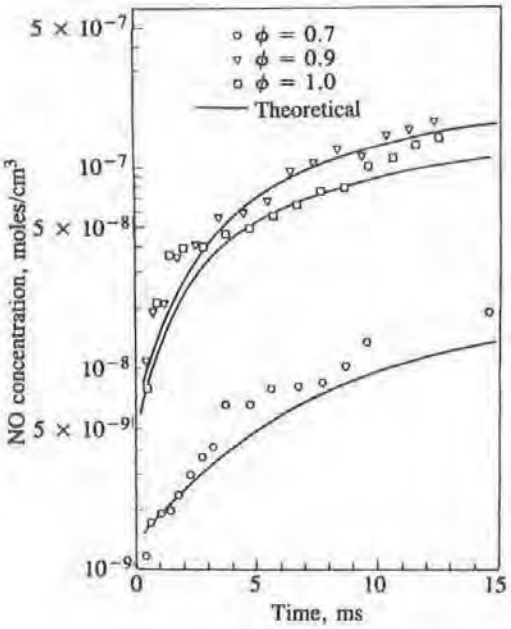


FIGURE 11-5
Measured and calculated rate-limited NO concentrations behind flame in high-pressure cylindrical bomb experiments with H_2-air mixture. ϕ = equivalence ratio.[4]

TABLE 11.3
Typical nitrogen content of distillate fuels[1]

Fraction	Average nitrogen, wt %	Range, wt %
Crude	0.65	—
Heavy distillates	1.40	0.60–2.15
Light distillates	0.07	0–0.60

close to zero, indicating that at these high pressures there is negligible NO production within the flame front itself.

Fuel nitrogen is also a source of NO via a different and yet to be fully explained mechanism. Table 11.3 shows the typical nitrogen content of petroleum-derived fuels. During distillation, the fuel nitrogen is concentrated in the higher boiling fractions. In distillate fuels, the nitrogen can exist as amines and ring compounds (e.g., pyridine, quinoline, and carbazoles). During combustion these compounds are likely to undergo some thermal decomposition prior to entering the combustion zone. The precursors to NO formation will therefore be low molecular weight nitrogen-containing compounds such as NH_3, HCN, and CN. The detailed information on the kinetics of NO formation from these compounds is limited. Oxidation to NO is usually rapid, occurring on a time scale comparable to that of the combustion reactions. The NO yield (amount of fuel nitrogen converted to NO) is sensitive to the fuel/air equivalence ratio. Relatively high NO yields (approaching 100 percent) are obtained for lean and stoichiometric mixtures; relatively low yields are found for rich mixtures. NO yields are only weakly dependent on temperature, in contrast to the strong temperature dependence of NO formed from atmospheric nitrogen.[1]

11.2.2 Formation of NO_2

Chemical equilibrium considerations indicate that for burned gases at typical flame temperatures, NO_2/NO ratios should be negligibly small. While experimental data show this is true for spark-ignition engines, in diesels NO_2 can be 10 to 30 percent of the total exhaust oxides of nitrogen emissions.[5] A plausible mechanism for the persistence of NO_2 is the following.[6] NO formed in the flame zone can be rapidly converted to NO_2 via reactions such as

$$NO + HO_2 \rightarrow NO_2 + OH \tag{11.14}$$

Subsequently, conversion of this NO_2 to NO occurs via

$$NO_2 + O \rightarrow NO + O_2 \tag{11.15}$$

unless the NO_2 formed in the flame is quenched by mixing with cooler fluid. This explanation is consistent with the highest NO_2/NO ratio occurring at light load in diesels, when cooler regions which could quench the conversion back to NO are widespread.[5]

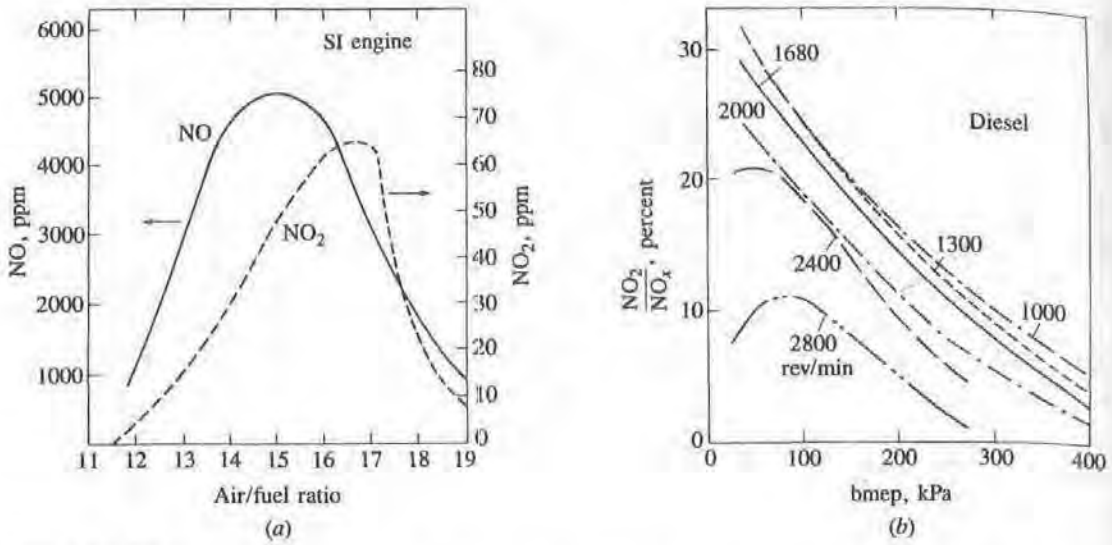


FIGURE 11-6
(*a*) NO and NO_2 concentrations in SI engine exhaust as function of air/fuel ratio, 1500 rev/min, wide-open throttle; (*b*) NO_2 as percent of total NO_x in diesel exhaust as function of load and speed.[5]

Figure 11-6 shows examples of NO and NO_2 emissions data from a spark-ignition and a diesel engine. The maximum value for the ratio (NO_2/NO) for the SI engine is 2 percent, at an equivalence ratio of about 0.85. For the diesel this ratio is higher, and is highest at light load and depends on engine speed.

It is customary to measure total oxides of nitrogen emissions, NO plus NO_2, with a chemiluminescence analyzer and call the combination NO_x. It is always important to check carefully whether specific emissions data for NO_x are given in terms of mass of NO or mass of NO_2, which have molecular weights of 30 and 46, respectively.

11.2.3 NO Formation in Spark-Ignition Engines

In conventional spark-ignition engines the fuel and air (and any recycled exhaust) are mixed together in the engine intake system, and vigorous mixing with the residual gas within the cylinder occurs during the intake process. Thus the fuel/air ratio and the amount of diluent (residual gas plus any recycled exhaust) is approximately uniform throughout the charge within the cylinder during combustion.† Since the composition is essentially uniform, the nature of the NO formation process within the cylinder can be understood by coupling the kinetic mechanism developed in Sec. 11.2.1 with the burned gas temperature distribution and pressure in the cylinder during the combustion and expansion processes. The

† It is well known that the mixture composition within the cylinder is not completely uniform and varies from one cycle to the next. Both these factors contribute to cycle-by-cycle combustion variations. For the present discussion, the assumption of mixture uniformity is adequate.

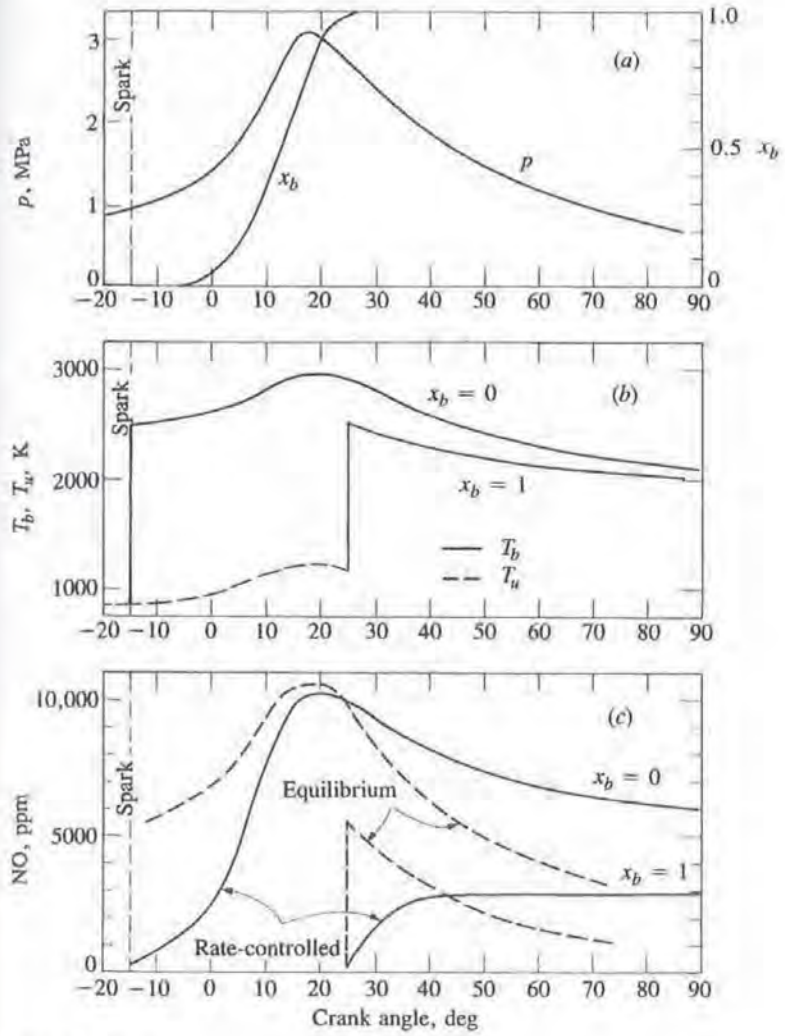


FIGURE 11-7
Illustration of SI engine NO formation model: (*a*) measured cylinder pressure p and calculated mass fraction burned x_b; (*b*) calculated temperature of unburned gas T_u and burned gas T_b in early- and late-burning elements; (*c*) calculated NO concentrations in early- and late-burning elements for rate-controlled model and at equilibrium.[7]

temperature distribution which develops in the burned gases due to the passage of the flame across the combustion chamber has been discussed in Sec. 9.2.1. Mixture which burns early is compressed to higher temperatures after combustion, as the cylinder pressure continues to rise; mixture which burns later is compressed primarily as unburned mixture and ends up after combustion at a lower burned gas temperature. Figure 11-7*a* and *b* shows measured cylinder pressure data from an operating engine, with estimates of the mass fraction burned (x_b) and the temperatures of a gas element which burned just after spark discharge and a gas element which burned at the end of the burning process. The model used to estimate these temperatures assumed no mixing between mixture elements which burn at different times. This assumption is more realistic than the

alternative idealization that the burned gases mix rapidly and are thus uniform (see Sec. 9.2.1). If the NO formation kinetic model [Eq. (11.7)] is used to calculate NO concentrations in these burned gas elements, using the equilibrium concentrations of the species O, O_2, N_2, OH, and H corresponding to the average fuel/air equivalence ratio and burned gas fraction of the mixture and these pressure and temperature profiles, the rate-limited concentration profiles in Fig. 11-7c are obtained. Also shown are the NO concentrations that would correspond to chemical equilibrium at these conditions. The rate-controlled concentrations rise from the residual gas NO concentration, lagging the equilibrium levels, then cross the equilibrium levels and "freeze" well above the equilibrium values corresponding to exhaust conditions. Depending on details of engine operating conditions, the rate-limited concentrations may or may not come close to equilibrium levels at peak cylinder pressure and gas temperature. Also, the amount of decomposition from peak NO levels which occurs during expansion depends on engine conditions as well as whether the mixture element burned early or late.[7]

Once the NO chemistry has frozen during the early part of the expansion stroke, integration over all elements will give the final average NO concentration in the cylinder which equals the exhaust concentration. Thus, if {NO} is the local mass fraction of NO, then the average exhaust NO mass fraction is given by

$$\{\overline{\mathrm{NO}}\} = \int_0^1 \{\mathrm{NO}\}_f \, dx_b \tag{11.16}$$

where $\{\mathrm{NO}\}_f$ is the final frozen NO mass fraction in the element of charge which burned when the mass fraction burned was x_b. Note that $\{\mathrm{NO}\} = [\mathrm{NO}]M_{\mathrm{NO}}/\rho$, where $M_{\mathrm{NO}} = 30$, the molecular weight of NO. The average exhaust concentration of NO as a mole fraction is given by

$$\tilde{x}_{\mathrm{NOav}} = \{\overline{\mathrm{NO}}\} \frac{M_{\mathrm{exh}}}{M_{\mathrm{NO}}} \tag{11.17}$$

and the exhaust concentration in ppm is $\tilde{x}_{\mathrm{NOav}} \times 10^6$. The earlier burning fractions of the charge contribute much more to the exhausted NO than do later burning fractions of the charge: frozen NO concentrations in these early-burning elements can be an order of magnitude higher than concentrations in late-burning elements. In the absence of vigorous bulk gas motion, the highest NO concentrations occur nearest the spark plug.

Substantial experimental evidence supports this description of NO formation in spark-ignition engines. The NO concentration gradient across the burned gas in the engine cylinder, due to the temperature gradient, has been demonstrated using gas sampling techniques[8,9] and using measurements of the chemiluminescent radiation from the reaction $\mathrm{NO} + \mathrm{O} \rightarrow \mathrm{NO}_2 + h\nu$ to determine the local NO concentration. Figure 11-8 shows NO concentration data as a function of crank angle, taken by Lavoie[10] through two different windows in the cylinder head of a specially constructed L-head engine where each window was a different distance from the spark plug. The stars indicate the estimated initial NO concentration that results from mixing of the residual gas with the fresh charge, at the

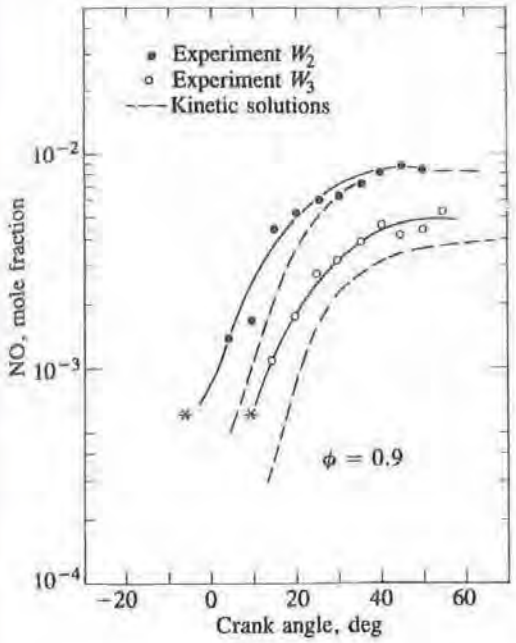


FIGURE 11-8
Spectroscopically measured NO concentrations through two windows W_3 and W_2 in special L-head SI engine (W_2 is closer to spark than W_3). The asterisks mark estimated initial conditions and flame arrival times. The dashed lines are calculated rate-limited concentrations for parts of charge burning at these flame arrival times with zero initial NO concentration.[10]

time of arrival of the flame at each window. The observed NO mole fractions rise smoothly from these initial values and then freeze about one-third of the way through the expansion process. NO levels observed at window W_2, closest to the spark plug, were substantially higher than those observed at window W_3. The dashed lines show calculated NO concentrations obtained using the NO formation kinetic model with an "unmixed" thermodynamic analysis for elements that burned at the time of flame arrival at each window. Since the calculated values started from zero NO concentration at the flame front (and not the diluted residual gas NO level indicated by the star), the calculations initially fall below the data. However, the difference between the two measurement locations and the frozen levels are predicted with reasonable accuracy. Thus, the rate-limited formation process, freezing of NO chemistry during expansion, and the existence of NO concentration gradients across the combustion chamber have all been observed.

The most important engine variables that affect NO emissions are the fuel/air equivalence ratio, the burned gas fraction of the *in-cylinder* unburned mixture, and spark timing. The burned gas fraction depends on the amount of diluent such as recycled exhaust gas (EGR) used for NO_x emissions control, as well as the residual gas fraction. Fuel properties will affect burned gas conditions; the effect of normal variations in gasoline properties is modest, however. The effect of variations in these parameters can be explained with the NO formation mechanism described above: changes in the time history of temperature and oxygen concentration in the burned gases during the combustion process and early part of the expansion stroke are the important factors.[11]

EQUIVALENCE RATIO. Figure 11-9 shows the effect of variations in the fuel/air equivalence ratio on NO emissions. Maximum burned gas temperatures occur at

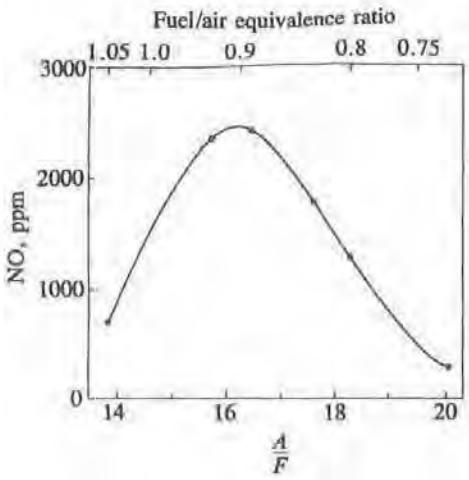


FIGURE 11-9
Variation of exhaust NO concentration with A/F and fuel/air equivalence ratio. Spark-ignition engine, 1600 rev/min, $\eta_v = 50$ percent, MBT timing.[12]

$\phi \approx 1.1$; however, at this equivalence ratio oxygen concentrations are low. As the mixture is enriched, burned gas temperatures fall. As the mixture is leaned out, increasing oxygen concentration initially offsets the falling gas temperatures and NO emissions peak at $\phi \approx 0.9$. Detailed predictions of NO concentrations in the burned gases suggest that the concentration versus time histories under fuel-lean conditions are different in character from those for fuel-rich conditions. In lean mixtures NO concentrations freeze early in the expansion process and little NO decomposition occurs. In rich mixtures, substantial NO decomposition occurs from the peak concentrations present when the cylinder pressure is a maximum. Thus in lean mixtures, gas conditions at the time of peak pressure are especially significant.[7]

BURNED GAS FRACTION. The unburned mixture in the cylinder contains fuel vapor, air, and burned gases. The burned gases are residual gas from the previous cycle and any exhaust gas recycled to the intake for NO_x emissions control. The residual gas fraction is influenced by load, valve timing (especially the extent of valve overlap), and, to a lesser degree, by speed, air/fuel ratio, and compression ratio as described in Sec. 6.4. The burned gases act as a diluent in the unburned mixture; the absolute temperature reached after combustion varies inversely with the burned gas mass fraction. Hence increasing the burned gas fraction reduces NO emissions levels. However, it also reduces the combustion rate and, therefore, makes stable combustion more difficult to achieve (see Secs. 9.3 and 9.4).

Figure 11-10 shows the effect of increasing the burned gas fraction by recycling exhaust gases to the intake system just below the throttle plate. Substantial reductions in NO concentrations are achieved with 15 to 25 percent EGR, which is about the maximum amount of EGR the engine will tolerate under normal part-throttle conditions. Of course, increasing the EGR at fixed engine load and speed increases the inlet manifold pressure, while fuel flow and air flow remain approximately constant.

The primary effect of the burned gas diluent in the unburned mixture on the NO formation process is that it reduces flame temperatures by increasing the

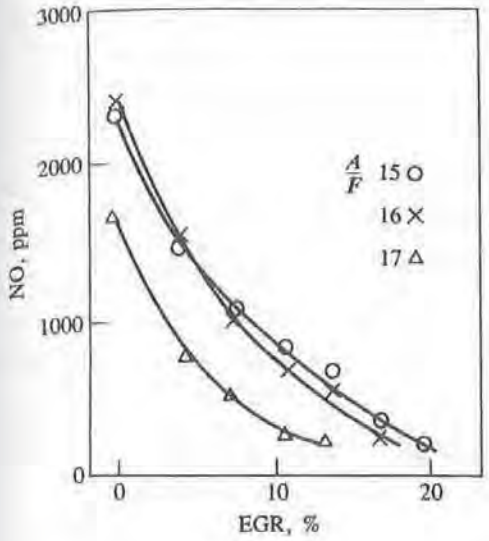


FIGURE 11-10
Variation of exhaust NO concentration with percent recycled exhaust gas (EGR). Spark-ignition engine, 1600 rev/min, $\eta_v = 50$ percent, MBT timing.[12]

heat capacity of the cylinder charge, per unit mass of fuel. Figure 11-11 shows the effect of different diluent gases added to the engine intake flow, in a single-cylinder engine operated at constant speed, fuel flow, and air flow.[13] The data in Fig. 11-11*a* show that equal volume percentages of the different diluents produce different reductions in NO emissions. The same data when plotted against diluent heat capacity (diluent mass flow rate × specific heat, c_p) collapse to a single

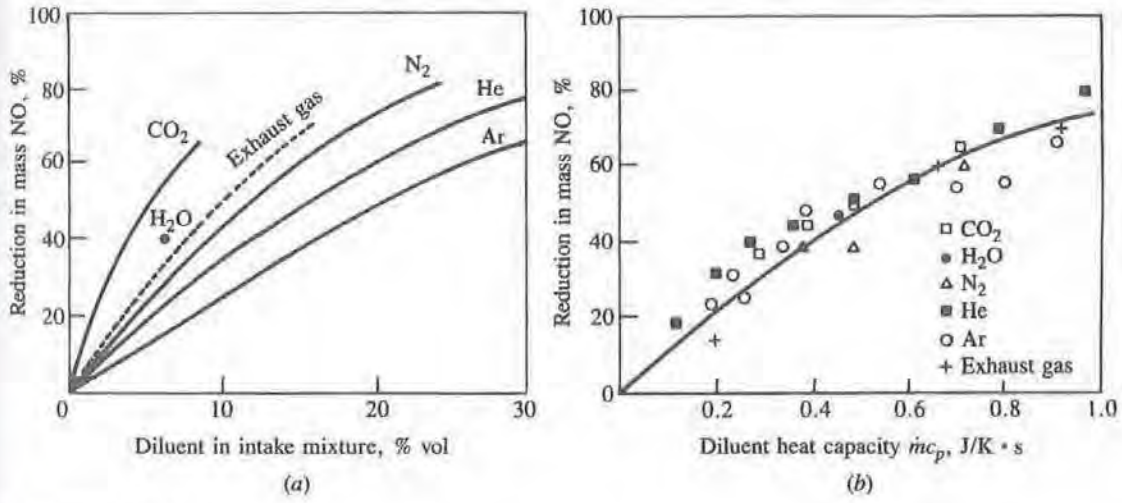


FIGURE 11-11
(*a*) Percentage reduction in mass NO emissions with various diluents. (*b*) Correlation of NO reduction with diluent heat capacity. Spark-ignition engine operated at 1600 rev/min, constant brake load (intake pressure ~0.5 atm), with MBT spark timing.[13]

curve.† A similiar study where the burned gas fraction in the unburned charge was varied by changing the valve overlap, compression ratio, and EGR, separately, showed that, under more realistic engine operating conditions, it is the heat capacity of the total diluent mass in the in-cylinder mixture that is important. Whether the diluent mass is changed by varying the valve overlap, EGR, or even the compression ratio is not important.[14]

EXCESS AIR AND EGR. Because of the above, it is possible to correlate the influence of engine operating variables (such as air/fuel ratio, engine speed, and load) and design variables (such as valve timing and compression ratio) on NO emissions with two parameters which define the in-cylinder mixture composition: the fuel/air equivalence ratio (often the air/fuel ratio is used instead) and the gas/fuel ratio. The gas/fuel ratio (G/F) is given by

$$\frac{G}{F} = \frac{\text{total mass in cylinder}}{\text{fuel mass in cylinder}} = \frac{A}{F}\left(1 + \frac{x_b}{1 - x_b}\right) \tag{11.18}$$

where x_b is the burned gas fraction [Eq. (4.3)]. These together define the relative proportions of fuel, air, and burned gases in the in-cylinder mixture, and hence

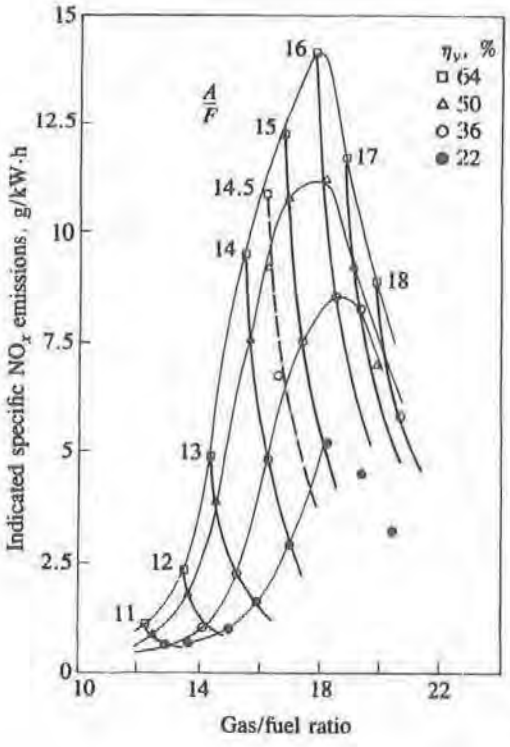


FIGURE 11-12
Correlation between gas/fuel ratio (G/F) and indicated specific NO_x emissions at various air/fuel ratios (A/F) and volumetric efficiencies (η_v). Spark-ignition engine operated at 1400 rev/min with spark timing retarded to give 0.95 of maximum brake torque.[15]

† Some of the scatter in Fig. 11-11 is due to the fact that the residual gas fraction is slightly different for each diluent.

will correlate NO emissions.† Figure 11-12 shows the correlation of specific NO emissions, from a four-cylinder engine, over a wide range of engine operating conditions with the air/fuel ratio and gas/fuel ratio. Lines of constant air/fuel ratio and volumetric efficiency are shown; the direction of increasing dilution with residual gas and EGR at constant air/fuel ratio is to the right. Excessive dilution results in poor combustion quality, partial burning, and, eventually, misfire (see Sec. 9.4.3). Lowest NO emissions consistent with good fuel consumption (avoiding the use of rich mixtures) are obtained with a stoichiometric mixture, with as much dilution as the engine will tolerate without excessive deterioration in combustion quality.[15]

Comparisons between predictions made with the NO formation model (described at the beginning of this section) and experimental data show good agreement with normal amounts of dilution.[16] With extreme dilution, at NO levels of about 100 ppm or less, the NO formed within the flame reaction zone cannot, apparently, be neglected. Within the flame, the concentrations of radicals such as O, OH, and H can be substantially in excess of equilibrium levels, resulting in much higher formation rates within the flame than in the postflame gases. It is believed that the mechanism [reactions (11.1) to (11.3)] and the formation rate equation (11.6) are valid. However, neglecting flame-front-formed NO is no longer an appropriate assumption.[17]

SPARK TIMING. Spark timing significantly affects NO emission levels. Advancing the timing so that combustion occurs earlier in the cycle increases the peak cylinder pressure (because more fuel is burned before TC and the peak pressure moves closer to TC where the cylinder volume is smaller); retarding the timing decreases the peak cylinder pressure (because more of the fuel burns after TC). Higher peak cylinder pressures result in higher peak burned gas temperatures, and hence higher NO formation rates. For lower peak cylinder pressures, lower NO formation rates result. Figure 11-13 shows typical NO emission data for a spark-ignition engine as a function of spark timing. NO emission levels steadily decrease as spark timing is retarded from MBT timing and moved closer to TC. Since exact determination of MBT timing is difficult (and not critical for fuel consumption and power where the variation with timing around MBT is modest), there is always considerable uncertainty in NO emissions at MBT timing. Often, therefore, an alternative reference timing is used, where spark is retarded from MBT timing to the point where torque is decreased by 1 or 2 percent from the maximum value. Great care with spark timing is necessary to obtain accurate NO emissions measurements under MBT-timing operating conditions.

† Spark timing also affects NO emissions, as discussed next. The above discussion relates to engines run with timing at MBT or with torque at a fixed percentage of (and close to) the maximum.

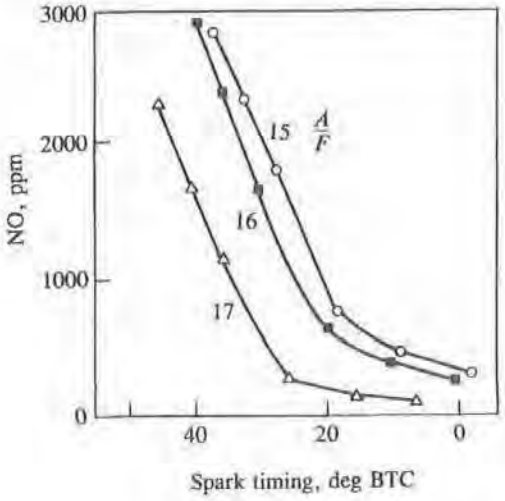


FIGURE 11-13
Variation of exhaust NO concentration with spark retard. 1600 rev/min, $\eta_v = 50$ percent; left-hand end of curve corresponds to MBT timing for each A/F.[13]

11.2.4 NO_x Formation in Compression-Ignition Engines

The kinetic mechanisms for NO and NO_2 formation described in Secs. 11.2.1 and 11.2.2 and the assumptions made regarding equilibration of species in the C—O—H system apply to diesels as well as to spark-ignition engines. The critical difference, of course, is that injection of fuel into the cylinder occurs just before combustion starts, and that nonuniform burned gas temperature and composition result from this nonuniform fuel distribution during combustion. The fuel-air mixing and combustion processes are extremely complex. During the "premixed" or uncontrolled diesel combustion phase immediately following the ignition delay, fuel-air mixture with a spread in composition about stoichiometric burns due to spontaneous ignition and flame propagation. During the mixing controlled combustion phase, the burning mixture is likely to be closer to stoichiometric (the flame structure is that of a turbulent, though unsteady, diffusion flame). However, throughout the combustion process mixing between already burned gases, air, and lean and rich unburned fuel vapor–air mixture occurs, changing the composition of any gas elements that burned at a particular equivalence ratio. In addition to these composition (and hence temperature) changes due to mixing, temperature changes due to compression and expansion occur as the cylinder pressure rises and falls.

The discussion in Sec. 11.2.1 showed that the critical equivalence ratio for NO formation in high-temperature high-pressure burned gases typical of engines is close to stoichiometric. Figure 11-4 is relevant here: it shows the initial NO formation rate in combustion products formed by burning a mixture of a typical hydrocarbon fuel with air (initially at 700 K, at a constant pressure of 15 atm). NO formation rates are within a factor of 2 of the maximum value for $0.85 \lesssim \phi \lesssim 1.1$.

The critical time period is when burned gas temperatures are at a maximum: i.e., between the start of combustion and shortly after the occurrence of peak cylinder pressure. Mixture which burns early in the combustion process

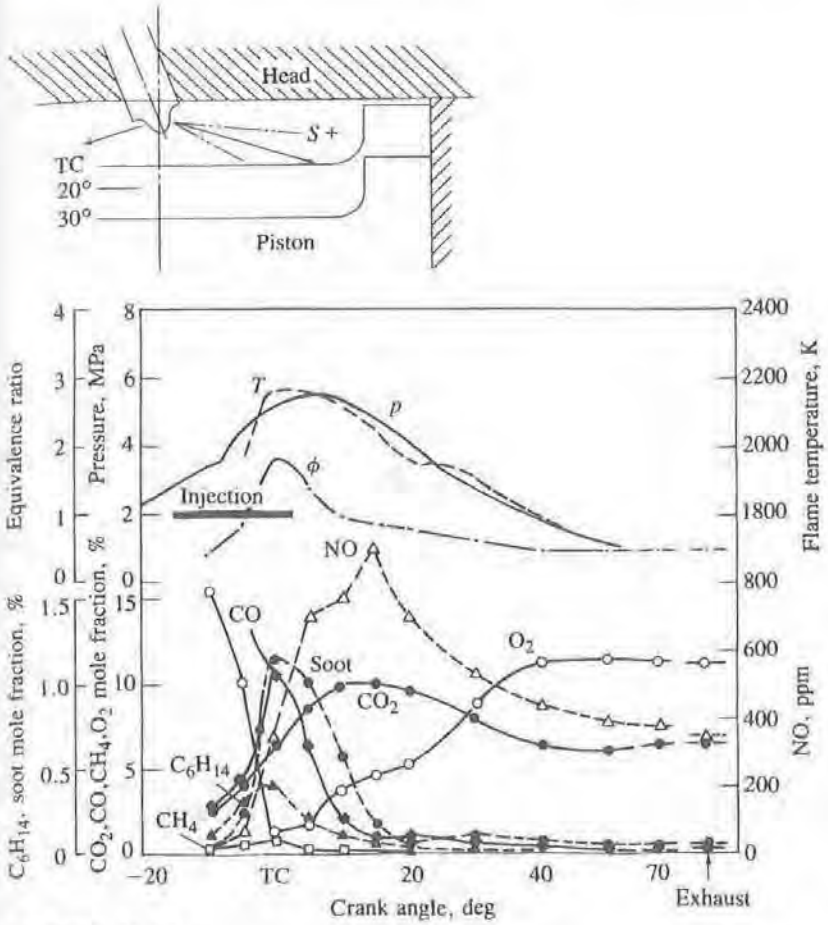


FIGURE 11-14
Concentrations of soot, NO, and other combustion product species measured at outer edge of bowl-in-piston combustion chamber (location *S*) of quiescent DI diesel with rapid sampling valve. Cylinder gas pressure p, mean temperature T, and local equivalence ratio ϕ shown. Bore = 95 mm, stroke = 110 mm, $r_c = 14.6$. Four-hole nozzle with hole diameter = 0.2 mm.[18]

is especially important since it is compressed to a higher temperature, increasing the NO formation rate, as combustion proceeds and cylinder pressure increases. After the time of peak pressure, burned gas temperatures decrease as the cylinder gases expand. The decreasing temperature due to expansion *and* due to mixing of high-temperature gas with air or cooler burned gas freezes the NO chemistry. This second effect (which occurs only in the diesel) means that freezing occurs more rapidly in the diesel than in the spark-ignition engine, and much less decomposition of the NO occurs.

The above description is supported by the NO concentration data obtained from experiments where gas was sampled from within the cylinder of normally operating diesel engines with special gas-sampling valves and analyzed. Figure 11-14 shows time histories of major species concentrations, through the combustion process, determined with a rapid-acting sampling valve (1 ms open time) in a quiescent *direct-injection diesel* engine. Concentrations at different positions in the combustion chamber were obtained; the sample valve location for the Fig.

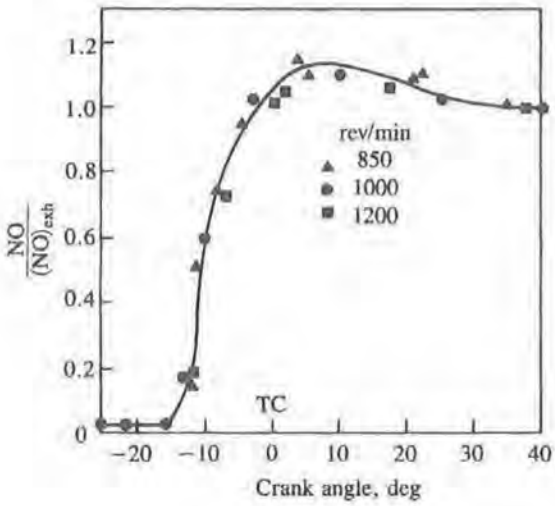


FIGURE 11-15
Ratio of cylinder-average NO concentration at given crank angle (determined from cylinder-dumping experiments) to exhaust NO concentration. DI diesel, equivalence ratio = 0.6, injection timing at 27° BTC.[19]

11-14 data is shown. Local NO concentrations rise from the residual gas value following the start of combustion, to a peak at the point where the local burned gas equivalence ratio changes from rich to lean (where the CO_2 concentration has its maximum value). As the local burned gas equivalence ratio becomes leaner due to mixing with excess air, NO concentrations decrease since formation becomes much slower as dilution occurs. At the time of peak NO concentrations within the bowl (15° ATC), most of the bowl region was filled with flame. The total amount of NO within the cylinder of this type of direct-injection diesel during the NO formation process has also been measured.[19] At a predetermined time in one cycle, once steady-state warmed-up engine operation had been achieved, the contents of the cylinder were dumped into an evacuated tank by rapidly cutting open a diaphragm which had previously sealed off the tank system. Figure 11-15 shows how the ratio of the average cylinder NO concentration divided by the exhaust concentration varies during the combustion process. NO concentrations reach a maximum shortly after the time of peak pressure. There is a modest amount of NO decomposition. Variations in engine speed have little effect on the shape of this curve. The 20 crank angle degrees after the start of combustion is the critical time period.

Results from similar cylinder-dumping experiments where injection timing and load (defined by the overall equivalence ratio) were varied also showed that almost all of the NO forms within the 20° following the start of combustion. As injection timing is retarded, so the combustion process is retarded; NO formation occurs later, and concentrations are lower since peak temperatures are lower. The effect of the overall equivalence ratio on NO_x concentrations is shown in Fig. 11-16. At high load, with higher peak pressures, and hence temperatures, and larger regions of close-to-stoichiometric burned gas, NO levels increase. Both NO and NO_x concentrations were measured; NO_2 is 10 to 20 percent of total NO_x. Though NO levels decrease with a decreasing overall equivalence ratio, they do so much less rapidly than do spark-ignition engine NO emissions (see Fig. 11-9) due to the nonuniform fuel distribution in the diesel. Though the

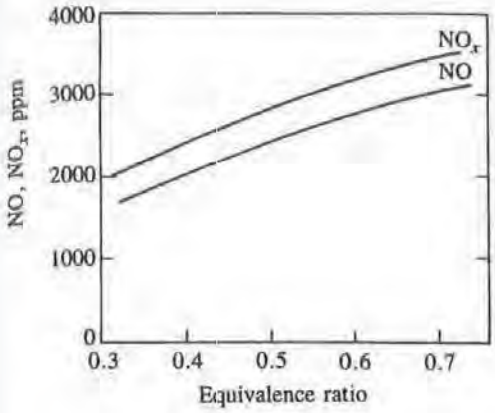


FIGURE 11-16
Exhaust NO_x and NO concentrations as a function of overall equivalence ratio or engine load. DI diesel, 1000 rev/min, injection timing at 27° BTC.[19]

amount of fuel injected decreases proportionally as the overall equivalence ratio is decreased, much of the fuel still burns close to stoichiometric. Thus NO emissions should be roughly proportional to the mass of fuel injected (provided burned gas pressures and temperatures do not change greatly).

Similar gas-sampling studies have been done with *indirect-injection* diesel engines. Modeling studies suggest that most of the NO forms within the prechamber and is then transported into the main chamber where the reactions freeze as rapid mixing with air occurs. However, the prechamber, except at light load, operates rich overall so some additional NO can form as the rich combustion products are diluted through the stoichiometric composition.[20] Figure 11-17 shows local NO concentrations and equivalence ratios as a function of crank angle determined with a rapid-acting sampling valve at different locations

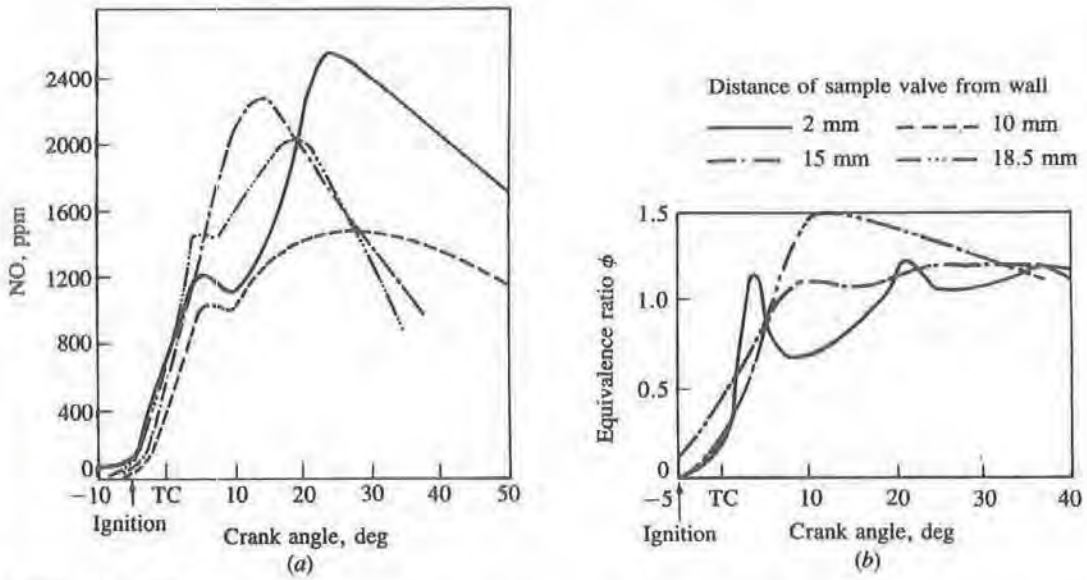


FIGURE 11-17
(*a*) NO concentrations measured with rapid sampling valve and (*b*) calculated equivalence ratios at different distances from the wall in swirl chamber of IDI diesel engine, as function of crank angle. Engine speed = 1000 rev/min, injection at 13° BTC, ignition at 5° BTC.[21]

within the prechamber of a Comet swirl chamber IDI engine.[21] The gas mixture rapidly becomes stoichiometric or fuel-rich. Composition nonuniformities across the prechamber are substantial. Peak NO concentrations, as expected, correspond approximately to locally stoichiometric regions. Because the mixture remains fuel-rich in the prechamber as the burned gases expand (after the time of peak pressure which occurs between 6 and 10° ATC), substantial NO decomposition within the prechamber can occur. However, by this time much of the gas (and NO) in the prechamber has been transferred to the main chamber where freezing of the NO chemistry will occur. Cylinder-gas dumping experiments, where both main chamber and prechamber gases were dumped and quenched, confirm this description. Cylinder average NO concentrations, determined by rapidly opening a diaphram which separated the engine cylinder from an evacuated tank at predetermined points in the cycle of an otherwise normally operated IDI engine, rise rapidly once combustion starts, until the NO chemistry is effectively frozen at about 15° ATC. Little net NO decomposition occurs.[22] Heat-release-rate diagrams obtained from pressure data analysis for the same IDI engine indicate that combustion is only about one-half complete at the time the NO formation process ceases.

Diluents added to the intake air (such as recycled exhaust) are effective at reducing the NO formation rate, and therefore NO_x exhaust emissions. As with spark-ignition engines, the effect is primarily one of reducing the burned gas temperature for a given mass of fuel and oxygen burned. Figure 11-18 shows the effect of dilution of the intake air with N_2, CO_2, and exhaust gas on NO_x exhaust levels.[23] The heat capacity of CO_2 (per mole) at the temperatures relevant to diesel combustion is about twice that of N_2. That of exhaust gas is slightly higher than that of N_2. Therefore these data show that the effect is primarily one of reduced burned gas temperatures. Note that the composition of the exhaust gas of a diesel varies with load. At idle, there is little CO_2 and H_2O, and the composition does not differ much from that of air. At high load the heat

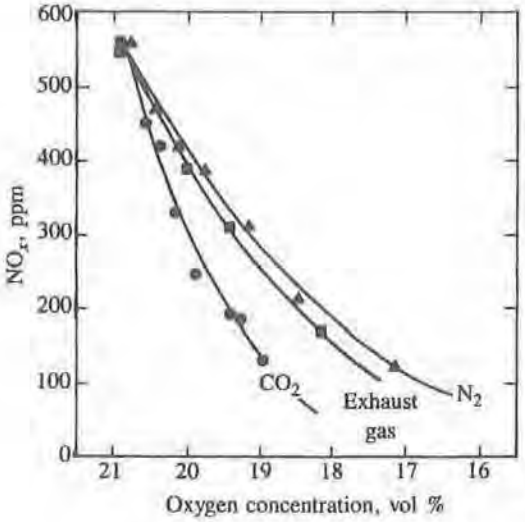


FIGURE 11-18
Effect of reduction in oxygen concentration by different diluents (exhaust gas, CO_2, N_2) on NO_x emissions in DI diesel. Bore = 140 mm, stroke = 152 mm, r_c = 14.3. Speed = 1300 rev/min, fuel rate = 142 mm^3/stroke, injection timing at 4° BTC.[23]

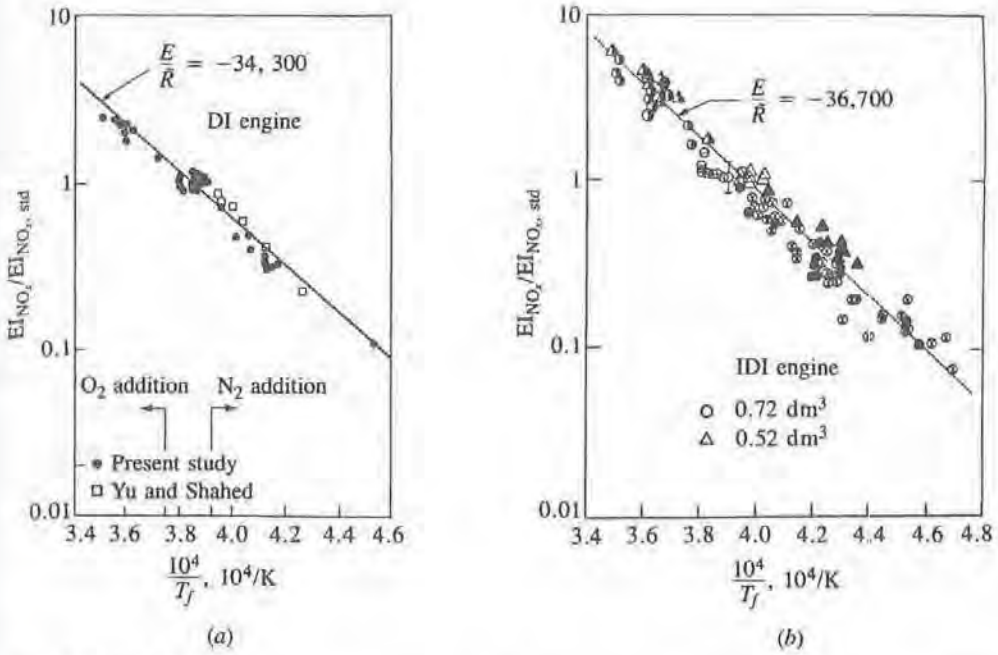


FIGURE 11-19
Correlation of NO_x emissions index EI_{NO_x} for a wide range of operating conditions with reciprocal of stoichiometric mixture flame temperature for: (*a*) DI engines; (*b*) IDI engines. Flame temperatures varied by addition of different diluents and oxygen.[25, 26] Values of EI_{NO_x} normalized with value at standard conditions.

capacity increases as the concentrations of CO_2 and H_2O are substantially higher. Similar studies in an *indirect-injection* engine show comparable trends. Addition of diluents [exhaust gas (EGR) and nitrogen] reduce peak flame temperatures and NO_x emissions; also, addition of oxygen (which corresponds to a *reduction* in diluent fraction) increases flame temperatures and therefore increases NO_x emissions.[24]

Confirmation that NO forms in the close-to-stoichiometric burned gas regions and the magnitude of the stoichiometric burned gas temperature controls NO_x emissions is given by the following. Plee *et al.*[25, 26] have shown that the effects of changes in intake gas composition (with EGR, nitrogen, argon, and oxygen addition) and temperature on NO_x emissions can be correlated by

$$EI_{NO_x} = \text{constant} \times \exp\left(\frac{E}{\tilde{R}T_f}\right) \tag{11.19}$$

T_f(kelvin) is the stoichiometric adiabatic flame temperature (evaluated at a suitable reference point: fuel-air mixture at top-center pressure and air temperature) and E is an overall activation energy. Figure 11-19 shows EI_{NO_x} for a range of intake air compositions and temperatures, and two DI and two IDI engines for several loads and speeds, normalized by the engine NO_x level obtained for standard air, plotted on a log scale against the reciprocal of the stoichiometric adiabatic flame at TC conditions. A single value of $E/\tilde{R}$ correlates the data over two

orders of magnitude. There is, of course, some scatter since the model used is overly simple, and load, speed, and other engine design and operating parameters affect the process. The overriding importance of the burned gas temperature of close-to-stoichiometric mixture is clear, however.

11.3 CARBON MONOXIDE

Carbon monoxide (CO) emissions from internal combustion engines are controlled primarily by the fuel/air equivalence ratio. Figure 11-20 shows CO levels in the exhaust of a conventional spark-ignition engine for several different fuel compositions.[27] When the data are plotted against the relative air/fuel ratio or the equivalence ratio, they are correlated by a single curve. For fuel-rich mixtures CO concentrations in the exhaust increase steadily with increasing equivalence ratio, as the amount of excess fuel increases. For fuel-lean mixtures, CO concentrations in the exhaust vary little with equivalence ratio and are of order 10^{-3} mole fraction.

Since spark-ignition engines often operate close to stoichiometric at part load and fuel rich at full load (see Sec. 7.1), CO emissions are significant and must be controlled. Diesels, however, always operate well on the lean side of stoichiometric; CO emissions from diesels are low enough to be unimportant, therefore, and will not be discussed further.

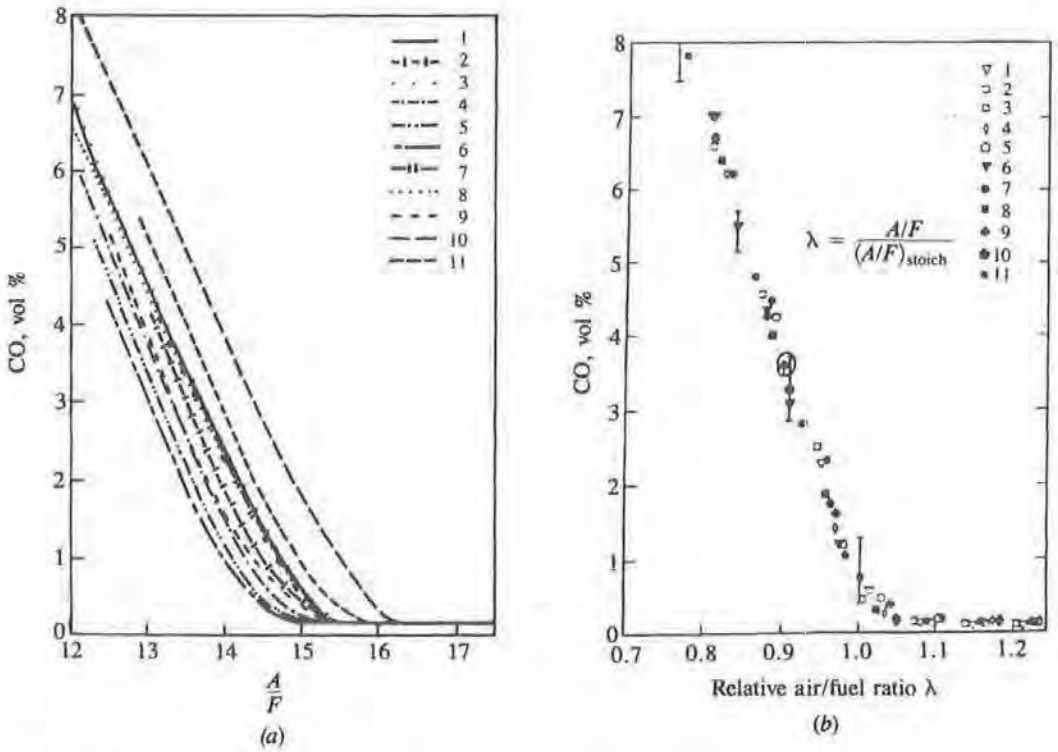


FIGURE 11-20
Variation of SI engine CO emissions with eleven fuels of different H/C ratio: (*a*) with air/fuel ratio; (*b*) with relative air/fuel ratio λ.[27]

The levels of CO observed in spark-ignition engine exhaust gases are lower than the maximum values measured within the combustion chamber, but are significantly higher than equilibrium values for the exhaust conditions. Thus the processes which govern CO exhaust levels are kinetically controlled. In premixed hydrocarbon-air flames, the CO concentration increases rapidly in the flame zone to a maximum value, which is larger than the equilibrium value for adiabatic combustion of the fuel-air mixture. CO formation is one of the principal reaction steps in the hydrocarbon combustion mechanism, which may be summarized by[1]

$$RH \rightarrow R \rightarrow RO_2 \rightarrow RCHO \rightarrow RCO \rightarrow CO \tag{11.20}$$

where R stands for the hydrocarbon radical. The CO formed in the combustion process via this path is then oxidized to CO_2 at a slower rate. The principal CO oxidation reaction in hydrocarbon-air flames is

$$CO + OH = CO_2 + H \tag{11.21}$$

The rate constant for this reaction is[1]

$$k_{CO}^{+} = 6.76 \times 10^{10} \exp\left(\frac{T}{1102}\right) \quad \text{cm}^3/\text{gmol} \tag{11.22}$$

It is generally assumed that in the postflame combustion products in a spark-ignition engine, at conditions close to peak cycle temperatures (2800 K) and pressures (15 to 40 atm), the carbon-oxygen-hydrogen system is equilibrated. Thus CO concentrations in the immediate postflame burned gases are close to equilibrium. However, as the burned gases cool during the expansion and exhaust strokes, depending on the temperature and cooling rate, the CO oxidation process [reaction (11.21)] may not remain locally equilibrated.

Newhall carried out a series of kinetic calculations for an engine expansion stroke assuming the burned gas at the time of peak cylinder pressure was uniform and in equilibrium.[28] Of the reactions important to CO chemistry, only three-body radical-recombination reactions such as

$$H + H + M = H_2 + M \tag{11.23}$$

$$H + OH + M = H_2O + M \tag{11.24}$$

$$H + O_2 + M = HO_2 + M \tag{11.25}$$

were found to be rate controlling. The bimolecular exchange reactions and the CO oxidation reaction (11.21) were sufficiently fast to be continuously equilibrated. Only during the later stages of the expansion stroke was the CO concentration predicted to depart from equilibrium, as shown in Fig. 11-21. Using this technique to predict average CO levels at the end of expansion over a range of equivalence ratios (rich to lean), Newhall obtained a good match to experimental data (see Fig. 11-22). The kinetically controlled aspects of the CO emissions mechanism have thus been confirmed.

These calculations showed that a partial equilibrium amongst the bimolecular exchange reactions occurred *a posteriori*. Analyses based explicitly on this partial equilibrium assumption (which are considerably simpler) have been

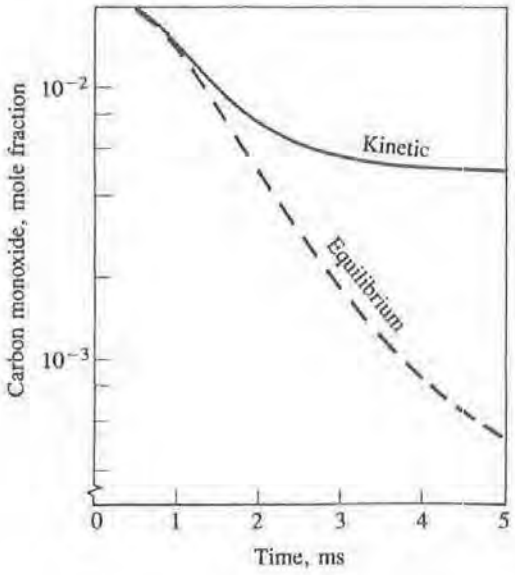


FIGURE 11-21
Results of kinetic calculations of CO concentrations during expansion stroke following TC combustion in SI engine; stoichiometric mixture.[28]

carried out.[29,30] The appropriate three-body atom and radical recombination reactions [e.g., (11.23) to (11.25)] were treated as the rate-limiting constraint on the total number of particles or moles per unit volume of burnt gases, i.e.,

$$\left(\frac{1}{V}\right)\frac{dn}{dt} = \sum_{i=1}^{k}(R_i^- - R_i^+) \tag{11.26}$$

V is the volume of the elemental system considered, n is the total number of moles, R_i^+ and R_i^- are the forward and backward rates for reaction i, and k represents the number of three-body recombination reactions included. All other

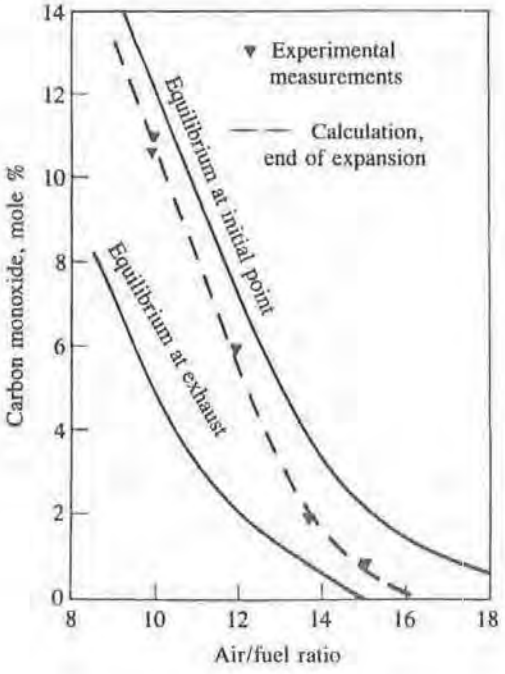


FIGURE 11-22
Predicted CO concentration at end of expansion stroke, compared with measured exhaust concentrations, as function of air/fuel ratio. Equilibrium levels at TC combustion and exhaust conditions also shown.[28]

reactions were assumed to be equilibrated. The studies using this simplified kinetic model have confirmed that at peak cylinder pressures and temperatures, equilibration times for CO are faster than times characteristic of changes in burnt gas conditions due to compression or expansion. Thus the CO concentration rapidly equilibrates in the burnt gases just downstream of the reaction zone following combustion of the hydrocarbon fuel. However, it has already been pointed out in Sec. 9.2.1 that the burnt gases are not uniform in temperature. Also, the blowdown of cylinder pressure to the exhaust manifold level during the exhaust process and the decrease in gas temperature that accompanies it occupies a substantial portion of the cycle—about 60 crank angle degrees. Thus, the temperature- and pressure-time profiles of parts of the charge at different locations throughout the cylinder differ, depending on when these parts of the charge burn and when they exit the cylinder through the exhaust valve and enter the exhaust manifold.

The results of an idealized calculation which illustrate these effects are shown in Fig. 11-23. The CO mole fractions in different elements or parts of the burnt gas mixture are plotted versus crank angle; x_b is the fraction of the total charge which had burned when each element shown burned; z is the mass fraction which had left the cylinder at the time each element left the cylinder. The partial equilibrium calculations show the burned gases are close to equilibrium until about 60 crank angle degrees after top-center. During the exhaust blowdown process after the exhaust valve opens, gas which leaves the cylinder early

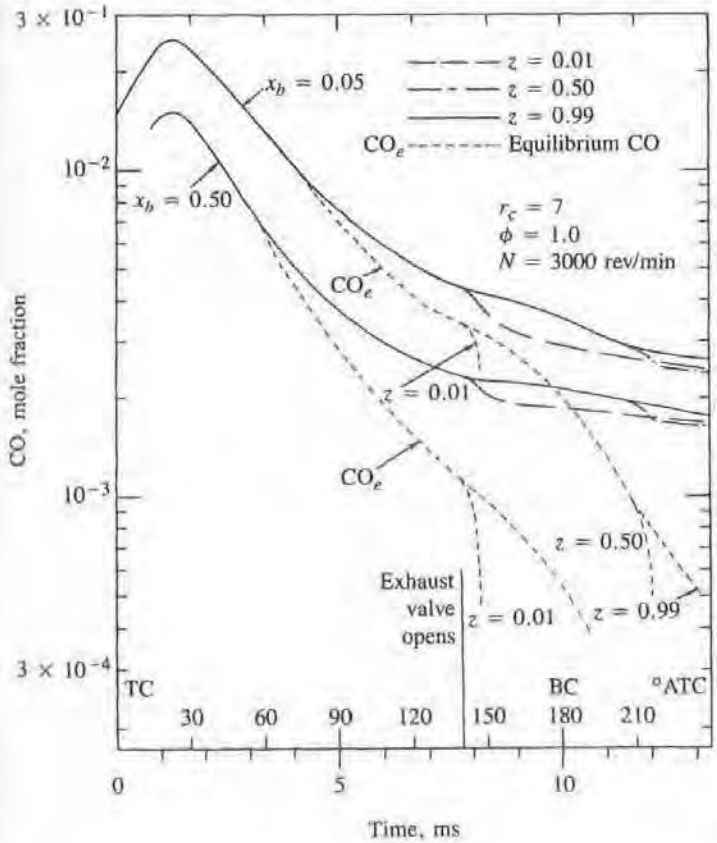


FIGURE 11-23
CO concentrations in selected elements of SI engine cylinder charge, which burn at different times and which exit the cylinder at different times. x_b is mass fraction burned when element burned. z is fraction of gas which has already left cylinder during exhaust process prior to element leaving cylinder. Speed = 3000 rev/min, $r_c = 7$, equivalence ratio = 1.0.[30]

($z \ll 1$) cools more rapidly than gas which leaves late ($z \approx 1$). In these calculations, mixing between gas elements which burn at different times was neglected. It can be seen that a CO gradient exists across the burned gases and that the CO concentration in the exhaust gases is unlikely to be uniform. Experiments with single-cylinder engines support these conclusions that CO is in equilibrium during the combustion process but deviates from equilibrium late in the expansion stroke (e.g., see Refs. 10 and 31).

Conclusions from these detailed studies are as follows. The measured average exhaust CO concentrations for fuel-rich mixtures are close to equilibrium concentrations in the burned gases during the expansion process. For close-to-stoichiometric mixtures, the partial equilibrium CO predictions are in agreement with measurements and are orders of magnitude above CO equilibrium concentrations corresponding to exhaust conditions. For fuel-lean mixtures, measured CO emissions are substantially higher than predictions from any of the models based on kinetically controlled bulk gas phenomena. One possible explanation of this lean-mixture discrepancy is that only partial oxidation to CO may occur of some of the unburned hydrocarbons emerging during expansion and exhaust from crevices in the combustion chamber and from any oil layers or deposits on the chamber walls.

While many questions about details of the CO oxidation mechanisms remain, as a practical matter exhaust emissions are determined by the fuel/air equivalence ratio. The degree of control achieved within the engine to date has come from improving mixture uniformity and leaning-out the intake mixture. In multicylinder engines, because CO increases rapidly as the inlet mixture becomes richer than stoichiometric, cylinder-to-cylinder variations in equivalence ratio about the mean value are important; nonuniform distribution can significantly increase average emissions. Thus improved cylinder-to-cylinder fuel/air ratio distribution has become essential. Also, because it is necessary to enrich the fuel-air mixture when the engine is cold, CO emissions during engine warm-up are much higher than emissions in the fully warmed-up state. Further, in transient engine operation during acceleration and deceleration, control of fuel metering has had to be improved. Additional reductions in CO beyond what can be achieved in the engine are possible with exhaust treatment devices, which are reviewed in Sec. 11.6. Oxidation of CO in the exhaust system without use of special exhaust treatment devices does not occur to any significant degree because the exhaust gas temperature is too low (Fig. 11-23 shows that the CO oxidation reactions effectively freeze as the gas passes through the exhaust valve).

11.4 UNBURNED HYDROCARBON EMISSIONS

11.4.1 Background

Hydrocarbons, or more appropriately organic emissions, are the consequence of incomplete combustion of the hydrocarbon fuel. The level of unburned hydrocarbons (HC) in the exhaust gases is generally specified in terms of the total hydro-

TABLE 11.4
Hydrocarbon composition of spark-ignition engine exhaust (by class)[33]

	Carbon, percent of total HC			
	Paraffins	Olefins	Acetylene	Aromatics
Without catalyst	33	27	8	32
With catalyst	57	15	2	26

carbon concentration expressed in parts per million carbon atoms (C_1).† While total hydrocarbon emission is a useful measure of combustion inefficiency, it is not necessarily a significant index of pollutant emissions. Engine exhaust gases contain a wide variety of hydrocarbon compounds. Table 11.4 shows the average breakdown by class of the hydrocarbons in spark-ignition engine exhaust gases, both with and without a catalytic converter, with gasoline fuel. Some of these hydrocarbons are nearly inert physiologically and are virtually unreactive from the standpoint of photochemical smog. Others are highly reactive in the smog-producing chemistry. (Some hydrocarbons are known carcinogens; see Sec. 11.5.2). Based on their potential for oxidant formation in the photochemical smog chemistry, hydrocarbon compounds are divided into nonreactive and reactive categories. Table 11.5 shows one reactivity scale which has been used to estimate the overall reactivity of exhaust gas hydrocarbon mixtures. Other scales are used for the same purpose.[34] Scales that assign high values for reactivity to the olefins (like Table 11.5), which react most rapidly in the photochemical smog reaction, probably best approximate smog-formation potential near the sources of hydrocarbon pollution. The simplest scale, which divides the HC into two classes—methane and nonmethane hydrocarbons—probably best approximates the end result for all HC emissions. All hydrocarbons except methane react, given enough time. More detailed breakdowns of the composition of spark-ignition and diesel engine exhaust HC are available in the literature.[33, 35]

Fuel composition can significantly influence the composition and magnitude of the organic emissions. Fuels containing high proportions of aromatics and olefins produce relatively higher concentrations of reactive hydrocarbons. However, many of the organic compounds found in the exhaust are not present

† This is because the standard detection instrument, a flame ionization detector (FID), is effectively a carbon atom counter: e.g., one propane molecule generates three times the response generated by one methane molecule. Some data in the literature are presented as ppm propane (C_3), or ppm hexane (C_6); to convert to ppm C_1 multiply by 3 or by 6, respectively. Older measurements of hydrocarbon emissions were made with nondispersive infrared (NDIR) detectors which had different sensitivities for the different hydrocarbon compounds. For gasoline-fueled engines, HC emissions determined by FID analyzers are about twice the levels determined by NDIR analyzers,[32] though this scaling is not exact.

TABLE 11.5
Reactivity of classes of hydrocarbons

Hydrocarbons	Relative reactivity†
C_1–C_4 paraffins Acetylene Benzene	0
C_4 and higher molecular weight paraffins Monoalkyl benzenes *Ortho-* and *para*-dialkyl benzenes Cyclic paraffins	2
Ethylene *Meta*-dialkyl benzenes Aldehydes	5
1-Olefins (except ethylene) Diolefins Tri- and tetraalkyl benzenes	10
Internally bonded olefins	30
Internally bonded olefins with substitution at the double bond Cycloolefins	100

† General Motors Reactivity Scale (0–100). Based on the NO_2 formation rate for the hydrocarbon relative to the NO_2 formation rate for 2,3-dimethyl-2-benzene.[34]

in the fuel, indicating that significant pyrolysis and synthesis occur during the combustion process.

Oxygenates are present in engine exhaust, and are known to participate in the formation of photochemical smog. Some oxygenates are also irritants and odorants. The oxygenates are generally categorized as carbonyls, phenols, and other noncarbonyls. The carbonyls of interest are low molecular weight aldehydes and aliphatic ketones. The volatile aldehydes are eye and respiratory tract irritants. Formaldehyde is a major component ($\lesssim$20 percent of total carbonyls). Carbonyls account for about 10 percent of the HC emissions from diesel passenger car engines, but only a few percent of spark-ignition engine HC emissions. Phenols are odorants and irritants: levels are much lower than aldehyde levels. Other noncarbonyls include methanol, ethanol, nitromethane, methyl formate. Whether these are significant with conventional hydrocarbon fuels is unclear.[35] Use of alcohol fuels increases oxygenate emissions. Both methanol and aldehyde emissions increase substantially above gasoline-fueled levels with methanol-fueled spark-ignition engines.

11.4.2 Flame Quenching and Oxidation Fundamentals

Flame quenching or extinction occurs at the walls of engine combustion chambers. The cool walls of the chamber act as a sink for heat and the active radical species generated within the flame. Quenching of the flame occurs under several different geometrical configurations: the flame may be propagating normal to, parallel to, or at an angle to the wall; the flame may quench at the entrance to a crevice—a thin volume with a narrow entrance to the combustion chamber such as the region between the piston crown and the cylinder wall. When the flame quenches, it leaves a layer or volume of unburned mixture ahead of the flame. (Whether this results in unburned hydrocarbon emissions depends on the extent to which these quench region hydrocarbons can subsequently be oxidized.)

Flame-quenching processes are analyzed by relating the heat release within the flame to the heat loss to the walls under conditions where quenching just occurs. This ratio, a Peclet number (Pe), is approximately constant for any given geometrical configuration. The simplest configuration for study is the two-plate quench process, where the minimum spacing between two parallel plates through which a flame will propagate is determined. The Peclet number for this two-plate configuration is given by:

$$\mathrm{Pe}_2 = \frac{\rho_u S_L c_{p,f}(T_f - T_u)}{k_f(T_f - T_u)/d_{q2}} = \frac{\rho_u S_L c_{p,f} d_{q2}}{k_f} \tag{11.27}$$

which is approximately constant over a wide range of conditions. ρ, S_L, c_p, T, and k are the density, laminar flame speed, specific heat at constant pressure, gas temperature, and thermal conductivity, respectively, with the subscripts u and f referring to unburned and flame conditions. d_{q2} is the two-plate quench distance. The wall temperature and unburned gas temperature are assumed to be equal; this assumption is also appropriate in the engine context since there is ample time during the compression stroke for a thermal boundary layer to build up to a thickness of at least the quench distance.

Lavoie[36] has developed empirical correlations for two-plate quench-distance data for propane-air mixtures: only limited data for liquid hydrocarbon fuels such as isooctane are available. The data in the pressure range 3 to 40 atm are well fitted by

$$\mathrm{Pe}_2 = \frac{9.5}{\phi}\left(\frac{p}{3}\right)^{0.26 \min(1,\, 1/\phi^2)} \tag{11.28}$$

where p is the pressure in atmospheres and ϕ is the fuel/air equivalence ratio. The two-plate quench distance d_{q2} is then obtained from Eq. (11.27) and Prandtl number and viscosity relations for the flame conditions (see Sec. 4.8 or Ref. 36). Thus the minimum size crevice region into which a flame will propagate can be determined.

For the process of a flame front quenching on a single wall, there are many possible geometries. The simplest is where the flame front is parallel to the wall

and approaches it head on. The one-wall quench distance d_{q1}, defined as the position of closest approach of the reaction zone to the wall, scales with flame properties in a similar way to the two-plate quench distance. Thus, a one-wall Peclet number relation can be formed:

$$\mathrm{Pe}_1 = \frac{\rho_u S_L c_{p,u} d_{q1}}{k_u} \approx 8 \tag{11.29}$$

where the subscript u denotes properties evaluated at unburned gas conditions.

Using the wall temperature as representative of the unburned gas temperature (because the thermal boundary-layer thickness is greater than typical quench distances), Lavoie showed that

$$\frac{d_{q1}}{d_{q2}} = \frac{\mathrm{Pe}_1}{\mathrm{Pe}_2} = 0.2 \tag{11.30}$$

is a reasonable fit to the single-wall quench data. Typical two-wall quench distances for spark-ignition engine conditions are 0.2 to 1 mm; these distances represent the minimum crevice size the flame will enter. Single-wall quench distances are, therefore, in the range 0.04 to 0.2 mm.

While a fraction of the fuel hydrocarbons can escape the primary combustion process unburned or only partially reacted, oxidation of some of these hydrocarbons can occur during the expansion and exhaust processes. Hydrocarbon oxidation rates have been determined in a number of different studies and several different empirical correlations of the data in the form of overall reaction rate equations have been proposed. A reasonable fit to the experimental data on unburned HC burnup is the rate expression:[36]

$$\frac{d[\mathrm{HC}]}{dt} = -6.7 \times 10^{15} \exp\left(\frac{-18{,}735}{T}\right) \tilde{x}_{\mathrm{HC}} \tilde{x}_{\mathrm{O_2}} \left(\frac{p}{RT}\right)^2 \tag{11.31}$$

where [ ] denotes concentration in moles per cubic centimeter, $\tilde{x}_{\mathrm{HC}}$ and $\tilde{x}_{\mathrm{O_2}}$ are the mole fractions of HC and $\mathrm{O_2}$, respectively, t is in seconds, T in kelvins, and the density term (p/RT) has units of moles per cubic centimeter. The spread in the data about this equation is substantial, however.

Studies of combustion of premixed fuel-air mixtures at high pressure in closed vessels or bombs have been useful in identifying the mechanisms by which hydrocarbons escape complete combustion. The residual unburned hydrocarbons left in the bomb following a combustion experiment have been shown to come primarily from crevices in the bomb walls. Unburned HC levels were proportional to total crevice volume, and decreased to very low values ($\sim$10 ppm C) as all the crevices were filled with solid material. Thus wall quench hydrocarbons apparently diffuse into the burned gases and oxidize following the quenching event.[37] Analytical studies of the flame quenching process, and postquench diffusion and oxidation with kinetic models of the hydrocarbon oxidation process, are in agreement with these bomb data.[38] Flame quenching can be thought of as a two-stage process. The first step is the extinction of the flame at a short distance from the cold wall, determined by a balance between thermal conduction of heat

from the hot reaction zone to the wall and heat released in the reaction zone by the flame reactions. The second step is the postquench diffusion and oxidation occurring on a time scale of one or a few milliseconds after quenching. The diffusion and oxidation process ultimately reduces the mass of wall quench hydrocarbons to several orders of magnitude below its value at the time of quenching.

Closed-vessel combustion experiments have also been used to show that oil layers on the walls of the bomb cause an increase in residual unburned HC levels after combustion is complete. The additional HC that result in experiments with oil films present are primarily (>95 percent) fuel molecules, and are directly proportional to the amount of oil placed on the walls of the reactor and the solubility of the specific fuel in the oil. These results show that absorption of fuel in the oil occurs prior to ignition. This dissolved fuel is then desorbed into the burned gases well after combustion is complete. Thus fuel absorption into and desorption from any oil layers is a potentially important engine HC mechanism.[39]

11.4.3 HC Emissions from Spark-Ignition Engines

Unburned hydrocarbon levels in the exhaust of a spark-ignition engine under normal operating conditions are typically in the range 1000 to 3000 ppm C_1. This corresponds to between about 1 and $2\frac{1}{2}$ percent of the fuel flow into the engine; the engine combustion efficiency is high. As indicated in Fig. 11-2, HC emissions rise rapidly as the mixture becomes substantially richer than stoichiometric. When combustion quality deteriorates, e.g., with very lean mixtures, HC emissions can rise rapidly due to incomplete combustion or misfire in a fraction of the engine's operating cycles. As outlined in Sec. 11.1, there are several mechanisms that contribute to total HC emissions. Also, any HC escaping the primary combustion process may oxidize in the expansion and exhaust processes. While a complete description of the HC emissions process cannot yet be given, there are sufficient fundamental data available to indicate which mechanisms are likely to be most important, and thus how major engine variables influence HC emission levels.

Four possible HC emissions formation mechanisms for spark-ignition engines (where the fuel-air mixture is essentially premixed) have been proposed: (1) flame quenching at the combustion chamber walls, leaving a layer of unburned fuel-air mixture adjacent to the wall; (2) the filling of crevice volumes with unburned mixture which, since the flame quenches at the crevice entrance, escapes the primary combustion process; (3) absorption of fuel vapor into oil layers on the cylinder wall during intake and compression, followed by desorption of fuel vapor into the cylinder during expansion and exhaust; (4) incomplete combustion in a fraction of the engine's operating cycles (either partial burning or complete misfire), occurring when combustion quality is poor (e.g., during engine transients when A/F, EGR, and spark timing may not be adequately controlled). In addition, as deposits build up on the combustion chamber walls,

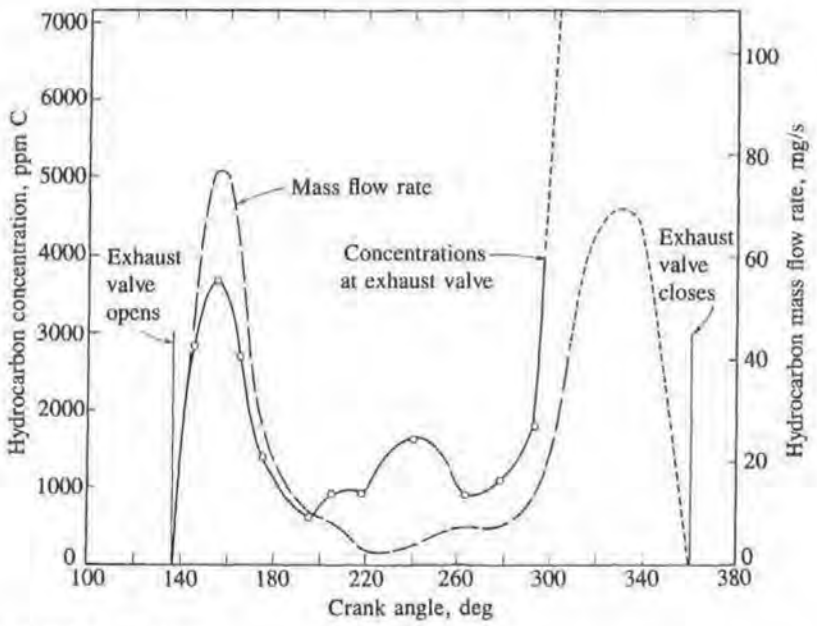


FIGURE 11-24
Variation in HC concentration and HC mass flow rate at the exhaust valve during the exhaust process. SI engine operating at 1200 rev/min and $\phi = 1.2$, unthrottled.[40]

HC emissions increase. Whether the deposits constitute an additional mechanism or merely modify one of the above mechanisms is unclear.

All these processes (except misfire) result in unburned hydrocarbons close to the combustion chamber walls, and not in the bulk of the cylinder gases. Thus, the distribution of HC in the exhaust gases would not be expected to be uniform. Experiments have been done to determine the unburned HC concentration distribution in the exhaust port during the exhaust process to provide insight into the details of the formation mechanisms. Gas concentrations were measured with a rapid-acting sampling valve placed at the exhaust port exit. Figure 11-24 shows results from these time-resolved HC concentration measurements. HC concentrations vary significantly during the exhaust process. Gas which remains in the exhaust port between exhaust pulses has a high HC concentration, so purging techniques where air or nitrogen was bled into the exhaust port were used to displace this high HC gas while the exhaust valve was closed. The high HC concentration in the blowdown exhaust gases is clearly discernible, as is the rapid rise in HC concentration toward the end of the exhaust stroke. The cylinder-exit HC concentrations were then multiplied by the instantaneous exhaust gas mass flow rate to obtain the instantaneous HC mass emission rate from the cylinder throughout the exhaust process, also shown in Fig. 11-24. The unburned HC are exhausted in two peaks of approximately equal mass: the first of these coincides with the exhaust blowdown mass flow pulse (which removes the majority of the *mass* from the cylinder); the second occurs toward the end of the exhaust stroke where HC concentrations are very high and the mass flow rate is relatively low.[40] Other experiments have confirmed these observations.[41] Clearly, mixing of

unburned HC with the bulk cylinder gases occurs during expansion and/or the exhaust blowdown process. Then, the final stages of piston motion during the exhaust stroke push most of the remaining fraction of the cylinder mass with its high HC concentration into the exhaust. This would be expected to leave a high concentration of HC in the residual gas in the cylinder. Experiments conducted in which the valve mechanism of a single-cylinder engine was arranged to disengage during operation and trap residual gases in the cylinder confirm this. For one set of typical engine operating conditions, approximately one-third of the hydrocarbons left unburned in an engine combustion event was retained in the cylinder and recycled.[42]

FLAME QUENCHING AT THE WALLS. The existence of quench layers on the cold combustion chamber walls of a spark-ignition engine was shown photographically by Daniel.[43] Photographs of the flame region immediately after flame arrival at the wall through a window in the cylinder head showed a thin nonradiating layer adjacent to the wall. The quench layer thicknesses measured were in the range 0.05 to 0.4 mm (thinnest at high load), in rough agreement with predictions based on experiments in combustion bombs. However, more recent work in bombs and engines indicates that diffusion of hydrocarbons from the quench layer into the burned gases and its subsequent oxidation occur on a time scale of a few milliseconds, at least with smooth clean combustion chamber walls. The constant-volume combustion bomb data which suggested this conclusion and the kinetic calculations which support this explanation of why quench layers are not significant with smooth clean walls have already been described in Sec. 11.4.2. The following evidence shows these conclusions are also valid in an engine.

A special rapid-acting poppet valve was used in a single-cylinder engine to sample the gases from a torus-shaped region, of height of order 0.25 mm and diameter about 6 mm, adjacent to the wall over a 1-ms period. Sampling was repeated every cycle to provide a steady stream of sampled gases for analysis. Figure 11-25 shows the variation in concentrations of HC species through the combustion, expansion, and exhaust processes. The fuel was propane (C_3H_8). The fuel concentration drops rapidly to a low value when the flame arrives at the valve; at the same time, intermediate hydrocarbon product concentrations rise and then fall sharply to values below 1 ppm. Beginning at 60° ATC, all HC concentrations rise and vary somewhat during the remainder of the cycle in a way that depends strongly on engine operating conditions. The observed rapid rise in partial oxidation products immediately after flame arrival is consistent with the flame quenching short of the wall. The presence of CH_2O and CH_3CHO in significant quantities indicates that low-temperature oxidation processes are occurring. However, since all HC product concentrations fall rapidly within 2 ms of flame arrival to very low values, the unburned HC in the quench layer diffuse into the bulk burned gases and oxidize. The increase in HC concentrations later in the cycle results from the sampling of hydrocarbons from sources other than quench layers.[44]

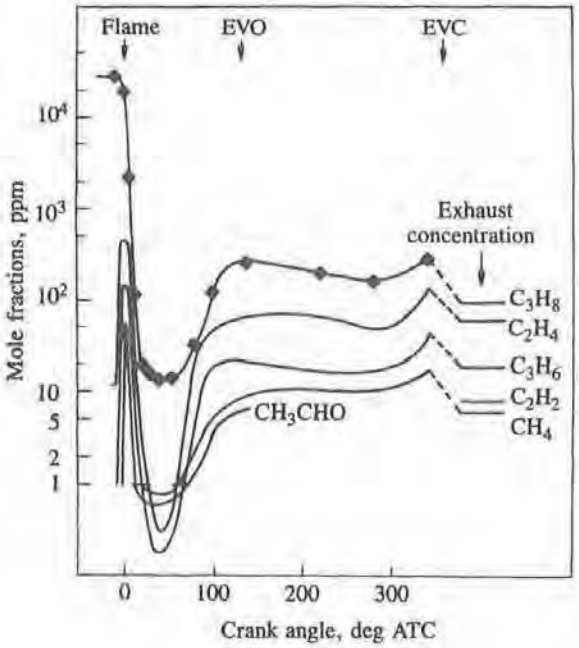


FIGURE 11-25
Concentrations (mole fractions) of selected hydrocarbons adjacent to combustion chamber wall, as a function of crank angle during combustion, expansion, and exhaust processes. Mass sampled with rapid-acting valve held constant at 7.6×10^{-6} g per pulse. Total exhaust HC = 400 ppm C. Engine speed = 1250 rev/min, imep = 380 kPa, equivalence ratio = 0.9, MBT spark timing, no EGR.[44]

Though quench layers on clean smooth combustion chamber walls are not a significant source of unburned hydrocarbons, it has been shown that wall surface finish does affect exhaust HC levels. Comparisons have been made between the standard "rough" as-cast cylinder head surfaces and the same cylinder heads when smoothed. The average exhaust HC concentration decreased by 103 ppm C, or 14 percent; the smoothed surface area was 32 percent of the total combustion chamber surface area.[45] Buildup of deposits on the combustion chamber surfaces also affect HC emission levels, as will be discussed later.

CREVICE HC MECHANISM. The crevices in the combustion chamber walls—small volumes with narrow entrances—into which the flame is unable to penetrate have been shown to be a major source of unburned HC. The largest of these crevice regions is the volumes between the piston, piston rings, and cylinder wall. Other crevice volumes in production engines are the threads around the spark plug, the space around the plug center electrode, crevices around the intake and exhaust valve heads, and the head gasket crevice. Table 8.1 shows the size and relative importance of these crevice regions in one cylinder of a production V-6 engine determined from measurements of cold-engine components. Total crevice volume is a few percent of the clearance volume and the piston and ring pack crevices are the dominant contributor.

The important crevice processes occurring during the engine cycle are the following. As the cylinder pressure rises during compression, unburned mixture is forced into the crevice regions. Since these volumes are thin they have a large surface/volume ratio; the gas flowing into each crevice cools by heat transfer to close to the wall temperature. During combustion, while the pressure continues to rise, unburned mixture continues to flow into the crevice volumes. When the

flame arrives at each crevice, it can either propagate into the crevice and fully or partially burn the fuel and air within the crevice or it can quench at the crevice entrance. Whether the flame quenches depends on crevice entrance geometry, the composition of the unburned mixture, and its thermodynamic state as described in Sec. 11.4.2. After flame arrival and quenching, burned gases will flow into each crevice until the cylinder pressure starts to decrease. Once the crevice gas pressure is higher than the cylinder pressure, gas flows back from each crevice into the cylinder.

The most important of these crevices, the volumes between the piston, piston rings, and cylinder wall, is shown schematically in Fig. 8-27. This crevice consists of a series of volumes, connected by flow restrictions such as the ring side clearance and ring gap whose geometry changes as the ring moves up and down in the ring groove sealing either at the top or bottom ring surface. The gas flow, pressure distribution, and ring motion are therefore coupled, and their behavior during the compression and expansion strokes has already been discussed in Sec. 8.6. During compression and combustion, mass flows *into* the volumes in this total crevice region. Once the cylinder pressure starts to decrease (after about 15° ATC) gas flows out of the top of these crevice regions in Fig. 8-27 into the cylinder at low velocity adjacent to the cylinder wall. The important result is that the fraction of the total cylinder charge (5 to 10 percent) trapped in these regions at the time of peak cylinder pressure escapes the primary combustion process. Most of this gas flows back into the cylinder during the expansion process. Depending on spark plug location in relation to the position of the top ring gap, well above 50 percent of this gas can be unburned fuel-air mixture. Its potential contribution to unburned HC emissions is obvious.

There is substantial evidence to support the above description of crevice HC phenomena and the piston ring crevice region in particular. Visualization studies in a special engine have identified the spark plug crevice outflow, low-velocity gas expansion out of the volume above the first ring after the time of peak pressure, and the jet-like flows through the top ring gap later in the expansion process when the pressure difference across the ring changes sign.[46] Gas sampling from the volume above the top ring, using a rapid-acting sample valve mounted in the piston crown, has shown that the gas composition in this region corresponds to unburned fuel-air mixture until flame arrival at the crevice entrance closest to the sampling valve location. Next, product gases enter the crevice as the cylinder pressure continues to rise. Then, during expansion as gas flows out of this region, the composition of the gas sampled reverts back toward that of the unburned mixture which enters the crevice region earlier.[47]

Direct evidence that the piston and ring crevice regions are a major contributor to exhaust HC emissions comes from experiments where the volume of this crevice region was substantially changed. Wentworth[48] almost completely eliminated this crevice by moving the top piston ring as close to the crown of the piston as possible, and sealing this ring at top and bottom in its groove with O rings. Tests of this sealed ring-orifice design in a production engine showed reductions of between 47 and 74 percent from baseline HC levels over a range of

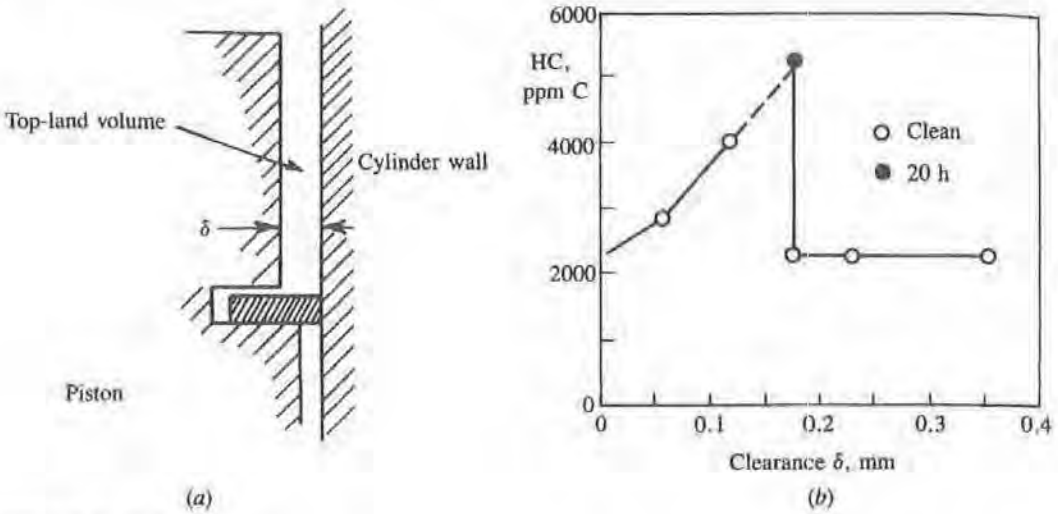


FIGURE 11-26
(*a*) Piston top-land crevice volume. (*b*) Effect of increasing top-land clearance on exhaust hydrocarbon emissions. Unthrottled spark-ignition engine, $r_c = 6$, 885 rev/min, $A/F = 13$, MBT timing.[49]

speeds and loads. Haskell and Legate,[49] in experiments in a single-cylinder CFR engine, steadily increased the piston top-land clearance (see Fig. 11-26*a*) and measured the effect on exhaust HC emissions. Figure 11-26*b* shows the results: HC emissions increase as the top-land clearance increases until the clearance equals about 0.18 mm, when emissions drop to the zero clearance level. This clearance (0.18 mm) is close to the two-plate quench distance estimated from Eq. (11.27). For piston top-land clearances above this value, the flame can enter the crevice and burn up much of the crevice HC.

The relative importance of the different crevices in the combustion chamber walls has been examined by using the cylinder head and piston of a four-cylinder production engine to form two constant-volume reactors or combustion bombs.[50] The cylinder head was sealed with a steel plate across the head gasket plane to make one reactor; the piston and ring pack and cylinder wall, again sealed with a plate at the head gasket plane, formed the second reactor. Each reactor was filled with a propane-air mixture and combustion initiated with a spark discharge across a spark plug; following combustion the burned gases were exhausted, sampled, and analyzed. The crevices were sequentially filled with epoxy or viton rubber, and after filling each crevice, the exhaust HC emission level determined. It was found that the ring pack crevices produced approximately 80 percent of the total scaled HC emissions, the head gasket crevice about 13 percent, and the spark plug threads 5 percent. All other HC sources in these reactors produced less than 2 percent of the total HC. While these numbers cannot be applied directly to an operating engine (the crevice filling and emptying rates in the bomb experiments are substantially different from these rates in an engine), they do underline the importance of the ring pack crevice region.

Blowby is the gas that flows from the combustion chamber, past the piston and into the crankcase. It is forced through any leakage paths afforded by the

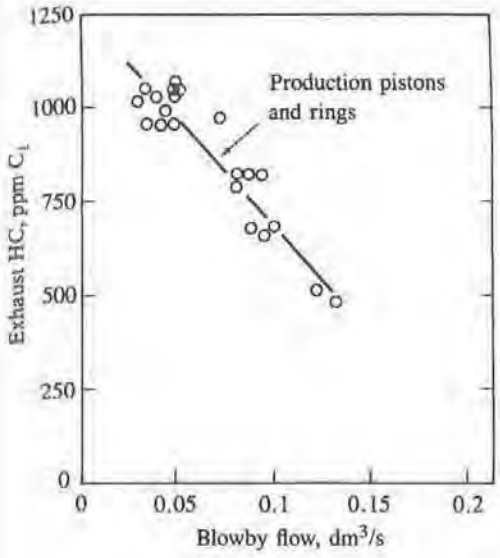


FIGURE 11-27
Effect of increasing crankcase blowby on exhaust hydrocarbon emissions. Production pistons and rings. SI engine at 1200 rev/min, intake manifold pressure 0.6 atm, $A/F = 14.2$.[51]

piston-bore-ring assembly in response to combustion chamber pressure. Blowby of gases from the cylinder to the crankcase removes gas from this crevice region and thereby prevents some of the crevice gases from returning to the cylinder. Crankcase blowby gases used to be vented directly to the atmosphere and constituted a significant source of HC emissions. The crankcase is now vented to the engine intake system, the blowby gases are recycled, and this source of HC emissions is now fully controlled. Blowby at a given speed and load is controlled primarily by the greatest flow resistance in the flow path between the cylinder and the crankcase. This is the smallest of the compression ring ring-gap areas. Figure 8-30 shows how blowby increases linearly with the smallest gap area. Figure 11-27 shows how exhaust HC levels decrease as blowby increases and more crevice HC flows to the crankcase. Crankcase blowby gases represent a direct performance loss. They are a smaller efficiency loss because crankcase gases are now recycled to the engine intake system.

The location of the ring gap in relation to the spark plug also affects HC emission levels. Experiments have shown that HC emissions are highest when the top ring gap is farthest from the spark plug; the gas flowing into the crevice directly above the gap is then unburned mixture for the longest possible time. With the top ring gap closest to the spark plug, HC exhaust levels are lowest because burned gas reaches the gap location at the earliest time in the combustion process. The difference, highest to lowest, was between 9 and 42 percent of the average level for any set of operating conditions, and in most cases was above 20 percent.[51]

The fate of these crevice HC when they flow back into the cylinder during expansion and exhaust is not well understood. Both jet-like flows (e.g., that from the ring gap) and low-velocity creeping flows (e.g., that from the piston top-land crevice) have been observed (see Fig. 8-29). While the former could mix rapidly with the high-temperature bulk burned gases, the latter will enter the cool gases

TABLE 11.6
Amount of gas flowing into and out of crevice regions†

	% mass	ppm C
Total gas in all crevice regions	8.2	
Total gas back to combustion chamber	7.0	
Unburned back to combustion chamber	3.7–7.0‡	5000–9400
Unburned to blowby	0.5–1.2‡	
Total unburned escaping primary combustion	4.2–8.2‡	

† For V-6 engine operating at 2000 rev/min and wide-open throttle.
‡ Depends on spark plug and ring gap location.

in the cylinder wall boundary layer and mix and (probably) burn much more slowly. Hydrocarbon transport and oxidation processes are discussed more fully below.

Table 11.6 presents a summary of estimates of the total mass of gas and mass of unburned mixture in the piston, ring, and cylinder wall crevice region for a typical spark-ignition engine.[46] When compared to exhaust HC levels, it is clear that these crevices are a major source of unburned hydrocarbons.

ABSORPTION AND DESORPTION IN ENGINE OIL. The presence of lubricating oil in the fuel or on the walls of the combustion chamber is known to result in an increase in exhaust hydrocarbon levels. In experiments where exhaust HC concentrations rose irregularly with time, with engine operating conditions nominally constant, it was shown that oil was present on the piston top during these high emission periods. When engine oil was added to the fuel, HC emissions increased, the amount of additional HC in the exhaust increasing with the increasing amount of oil added. The increase in exhaust HC was primarily unreacted fuel (isooctane) and not oil or oil-derived compounds.[51] The increase in HC can be substantial: exhaust HC levels from a clean engine can double or triple when operated on a fuel containing 5 percent lubricating oil over a period of order 10 minutes. (With deposits from leaded-fuel operation present on the combustion chamber walls, however, a much smaller increase in exhaust HC was observed.) It has been proposed that fuel vapor absorption into and desorption from oil layers on the walls of the combustion chamber could explain these phenomena.[49]

The absorption and desorption mechanism would work as follows. The fuel vapor concentration within the cylinder is close to the inlet manifold concentration during intake and compression. Thus, for about one crankshaft revolution, any oil film on the walls will absorb fuel vapor. During the latter part of compression, the fuel vapor pressure is increasing so, by Henry's law, absorption will continue even if the oil was saturated during intake. During combustion the fuel vapor concentration in the bulk gases goes essentially to zero so the absorbed fuel vapor will desorb from the liquid oil film into the gaseous combustion products. Desorption could continue throughout the expansion and exhaust strokes.

Some of the desorbed fuel vapor will mix with the high-temperature combustion products and oxidize. However, desorbed vapor that remains in the cool boundary layer or mixes with the cooler bulk gases late in the cycle may escape full oxidation and contribute to unburned HC emissions.

Experiments, where measured amounts of oil were placed on the piston crown, confirm that oil layers on the combustion chamber surface increase exhaust HC emissions. The exhaust HC levels increased in proportion to the amount of oil added when the engine was fueled with isooctane. Addition of 0.6 cm^3 of oil produced an increase of 1000 ppm C in exhaust HC concentration. Fuel and fuel oxidation species, not oil oxidation products, were responsible for most of this increase. Similar experiments performed with propane fuel showed no increase in exhaust HC emissions when oil was added to the cylinder. The increase in exhaust HC is proportional to the solubility of the fuel in the oil. The exhaust HC levels decreased steadily back to the normal engine HC level before oil addition, over a period of several minutes. At higher coolant temperatures, the increase in HC on oil addition is less, and HC concentrations decreased back to the normal level more quickly. Increasing oil temperature would decrease viscosity, increasing the rate of drainage into the sump. It also changes the solubility and diffusion rate of the fuel in the oil.[52]

At the outer surface of the oil layer, the concentration of fuel vapor dissolved in the oil is given by Henry's law for dilute solutions in equilibrium:

$$\tilde{x}_f = \frac{p_f}{H} \tag{11.32}$$

where $\tilde{x}_f$ is the mole fraction of fuel vapor in the oil, p_f is the partial pressure of fuel vapor in the gas, and H is Henry's constant. If the oil layer is sufficiently thin, and hence diffusion sufficiently rapid, Eq. (11.32) can be used to estimate the mole fraction of the fuel dissolved in the oil. Since $p_f = n_{f,c}\tilde{R}T/V$ (where $n_{f,c}$ is the number of moles of fuel in the cylinder, T is the temperature, and V the cylinder volume) and $x_f = n_{f,o}/(n_{f,o} + n_o) = n_{f,o}/n_o$ for $n_o \gg n_{f,o}$ (where $n_{f,o}$ is the number of moles of fuel dissolved in the oil and n_o is the number of moles of oil),[53] then

$$\frac{n_{f,o}}{n_{f,c}} = \frac{n_o \tilde{R}T}{HV} \tag{11.33}$$

Diffusion is sufficiently rapid for Eq. (11.33) to be valid if the diffusion time constant τ_d is much less than characteristic engine times: i.e.,

$$\tau_d \approx \frac{\delta^2}{D} \ll N^{-1}$$

where δ is the oil layer thickness, D is the diffusion coefficient for fuel vapor in the oil, and N is engine speed. D for a hydrocarbon through a motor oil is of order 10^{-6} cm^2/s at 300 K and of order 10^{-5} cm^2/s at 400 K. Oil film thicknesses on the cylinder wall vary during the operating cycle between about 1 and 10 μm.[54, 55] Thus diffusion times for engine conditions are 10^{-1} to 10^{-3} s; for the thinnest oil layers approximate equilibration would be achieved. A theoretical

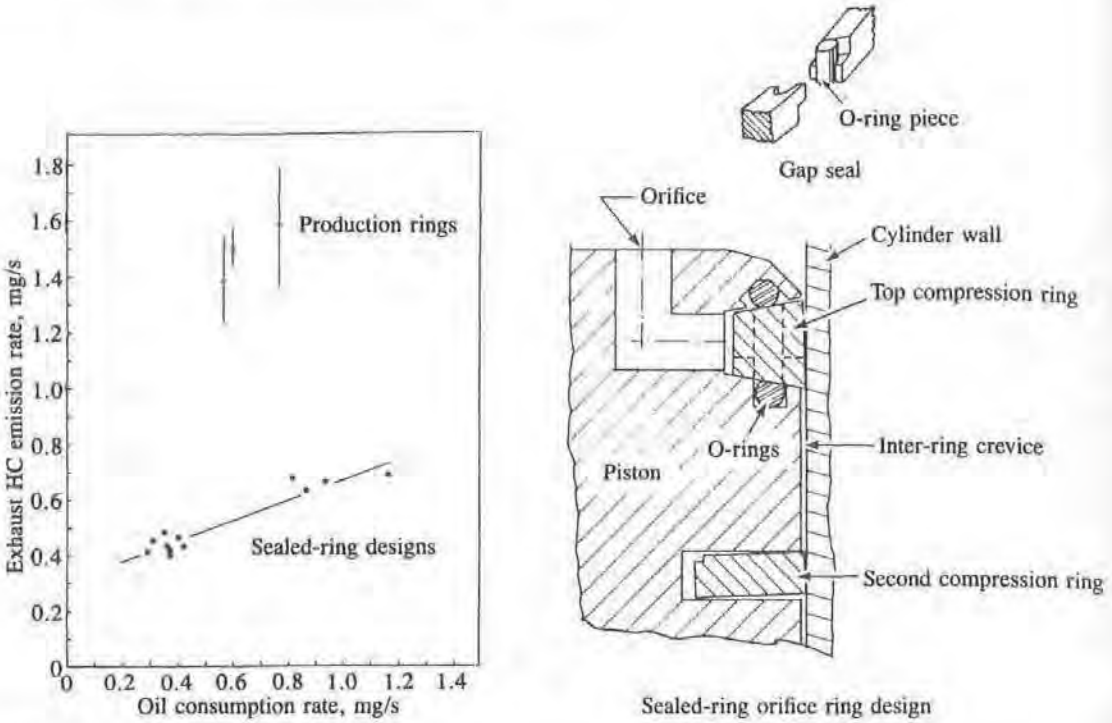


FIGURE 11-28
Correlation between exhaust hydrocarbon emissions and oil consumption rate. Production piston rings and sealed ring–orifice ring designs. SI engine at 1600 rev/min, imep = 422 kPa, equivalence ratio = 0.9, r_c = 8.0, intake pressure = 54 kPa, MBT spark timing.[57]

study of this problem—the one-dimensional cyclic absorption and desorption of a dilute amount of gas in a thin (constant thickness) isothermal liquid layer where diffusion effects are important—has been carried out. It suggests that oil layers on the cylinder wall could be a significant contributor to HC emission levels.[56]

Correlations between engine oil consumption and exhaust HC emissions provide a perspective on the relative importance of oil absorption/desorption and crevice mechanisms. Wentworth measured oil consumption and HC emissions in a spark-ignition engine for a range of piston ring designs.[57] Some of these designs were of the sealed ring–orifice type which effectively eliminates all the crevices between the piston, piston rings, and cylinder, and prevents any significant gas flow into or out of the ring region. HC emissions increase with increasing oil consumption for both production ring designs and the sealed ring–orifice designs, as shown in Fig. 11-28. Extrapolation to zero oil consumption from normal consumption levels shows a reduction in exhaust HC levels, but this decrease is significantly less than the difference in emission levels between the production and the sealed ring–orifice designs which effectively remove the major crevice region. The production piston used had a chamfered top land. The HC emissions for a normal piston top-land design would probably be higher.

POOR COMBUSTION QUALITY. Flame extinction in the bulk gas, before all of the flame front reaches the wall, is a source of HC emissions under certain engine

operating conditions. As the cylinder pressure falls during the expansion stroke, the temperature of the unburned mixture ahead of the flame decreases. This slows the burning rate [the laminar flame speed decreases so the burning rate in Eq. (9.52) decreases]. If the pressure and temperature fall too rapidly, the flame can be extinguished. This type of bulk quench has been observed in spark-ignition engines; it results in very high HC concentrations for that particular cycle. Engine conditions where bulk quenching is most likely to occur are at idle and light load where engine speed is low and the residual gas fraction is high, with high dilution with excessive EGR or overly lean mixtures, and with substantially retarded combustion. Even if steady-state engine calibrations of A/F, EGR, and spark-timing are such that bulk quenching does not occur, under transient engine operation these variables may not be appropriately set to avoid bulk quenching in some engine cycles due to the different dynamic characteristics of the engine subsystems which control these variables.

The existence of zones of stable and unstable engine operation with lean or dilute mixtures has already been discussed (see Sec. 9.4.3). Detailed engine combustion studies have shown that, as mixture composition becomes more dilute (e.g., by increasing EGR) and unburned gas temperature and pressure during combustion become lower, combustion quality (or variability) and engine stability deteriorate. The standard deviation in a parameter such as indicated mean effective pressure (which depends for its magnitude on the proper timing of the start of combustion and on the duration of the combustion process) increases due first to an increase in the number of slower burning cycles, then as conditions worsen to the occurrence of partial burning cycles, and finally to some misfiring cycles. Figure 9-36 showed how unburned hydrocarbon emissions from a spark-ignition engine rise as the EGR rate is increased at constant load and speed, and combustion quality (defined by the ratio of standard deviation in imep to the average imep) deteriorates. Initially the increase in HC is modest and is caused by changes in the other HC emission mechanisms described above. However, when partial burning cycles are detected, HC emissions rise more rapidly due to incomplete combustion of the fuel in the cylinder in these cycles. When misfiring cycles—no combustion—occur the rise in HC becomes more rapid still.

The relative importance of bulk gas quenching in a fraction of the engine's operating cycles due to inadequate combustion quality as a source of HC, compared with the other sources described in this section, has yet to be established. However, one obvious technique for reducing its importance, burning the mixture faster so that combustion is completed before conditions conducive to slow and partial burning exist in the cylinder, does reduce engine exhaust HC emissions. Figure 11-29 shows a comparison of HC emissions from a moderate burn rate engine with HC emissions with a faster burn rate [i.e., with improved combustion quality—lower coefficient of variation in imep, COV_{imep}, Eq. (9.50)], achieved by the use of two spark plugs instead of one.[58] The exhaust measurements show lower HC emissions when significant amounts of EGR are used for NO_x control for the faster, and hence less variable, combustion process. Such evidence suggests that occasional partial burning cycles may occur, even under

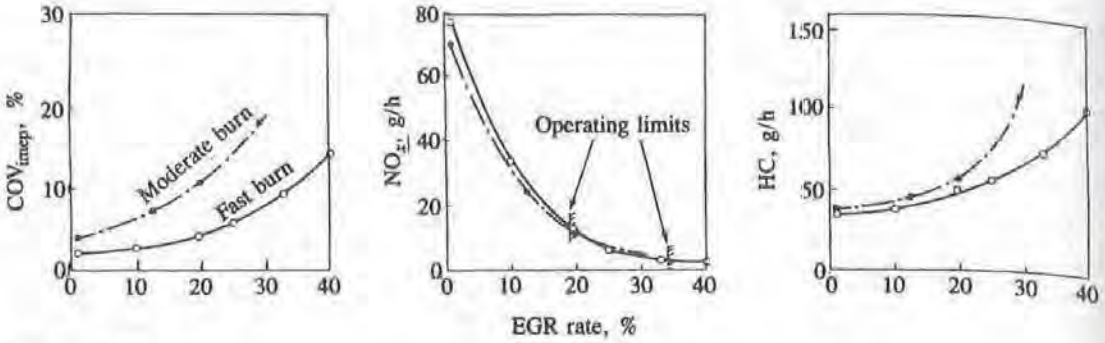


FIGURE 11-29
Effect of increasing burn rate on tolerance to recycled exhaust gas (EGR) and HC and NO_x emissions levels. COV_{imep} defined by Eq. (9.50). SI engine at 1400 rev/min, 324 kPa imep, equivalence ratio = 1.0, MBT timing.[58]

conditions where combustion appears to be "normal," and that this mechanism is important in practice.

EFFECT OF DEPOSITS. Deposit buildup on the combustion chamber walls (which occurs in vehicles over several thousands of miles) is known to increase unburned HC emissions. With leaded gasoline operation, the increase in HC emissions varies between about 7 and 20 percent. The removal of the deposits results typically in a reduction in HC emissions to close to clean engine levels. With unleaded gasoline, while the deposit composition is completely different (carbonaceous rather than lead oxide), the increase in HC emissions with accumulated mileage is comparable. Soft sooty deposits, such as those which accumulate after running the engine on a rich mixture, also cause an increase in HC emissions. Again, when the deposits were removed the emission rate fell about 25 percent to the original level.[59] Studies with simulated deposits (pieces of metal-foam sheet 0.6 mm thick) attached to the cylinder head and piston also showed increases in HC emissions. The increase varied between about 10 and 100 ppm C/cm^2 of simulated deposit area. The effect for a given area of deposit varied with deposit location. Locations close to the exhaust valve, where the flow direction during the exhaust process would be expected to be directly into the exhaust port, showed the highest increase in emissions.[45]

It is believed that absorption and desorption of hydrocarbons by these surface deposits is the mechanism that leads to an increase in emissions. Deposits can also build up in the piston ring crevice regions. A reduction in volume of these crevice regions would decrease HC emissions (and such a decrease has been observed). However, changes in piston–cylinder wall clearance due to deposits can affect the flame-quenching process and could increase emissions.[49]

HYDROCARBON TRANSPORT MECHANISMS. All of the above mechanisms (except misfire) result in high hydrocarbon concentrations adjacent to the combustion chamber walls. While any jet-type flows out of crevices during the expan-

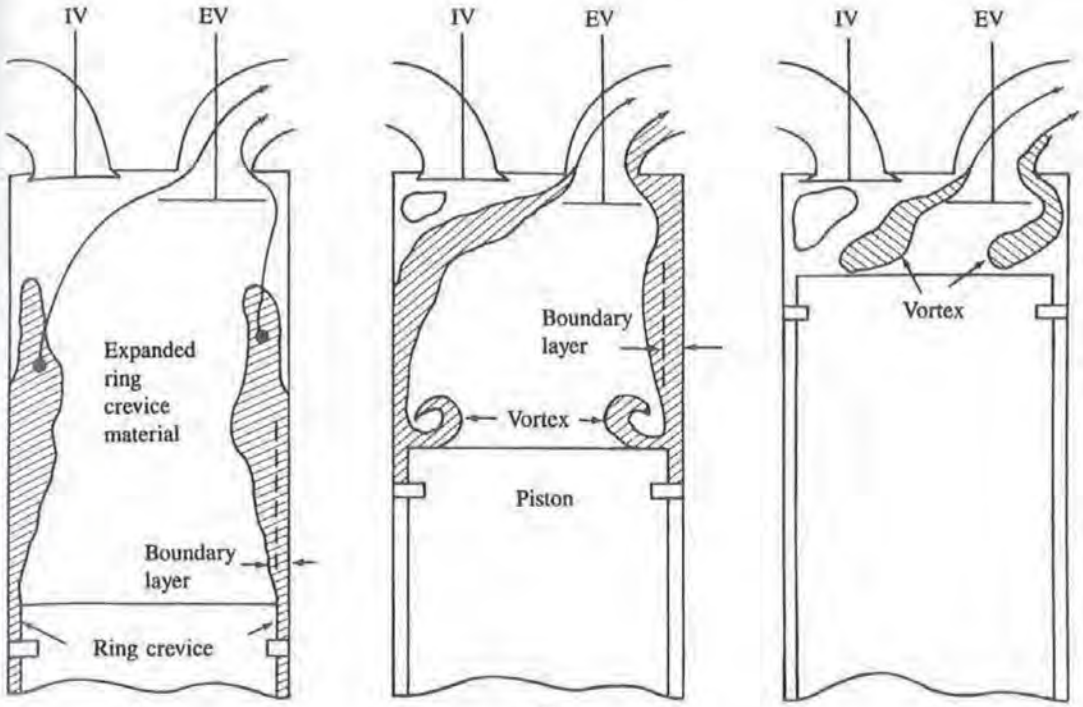


FIGURE 11-30
Schematic of flow processes by which ring crevice HC and HC desorbed from cylinder wall oil film exit the cylinder: (*a*) exhaust blowdown process; (*b*) during exhaust stroke; (*c*) end of exhaust stroke.[60]

sion and exhaust strokes can transport unburned HC into the bulk gases, most of the HC will remain near the wall. Two mechanisms by which gas near the cylinder wall exits the cylinder have been demonstrated. One is entrainment in the vigorous gas flow out of the cylinder which occurs during the exhaust blowdown process. The other is the vortex generated in the piston crown–cylinder wall corner during the exhaust stroke.

Figure 11-30 illustrates these flow processes. In Fig. 11-30*a* the engine cylinder is shown as the exhaust valve opens during the blowdown process. At this time the unburned HC from the ring crevice regions, laid along the wall during expansion (and possibly HC from the oil film on the cylinder wall), is expanding into the cylinder as the cylinder pressure falls. Some of this material will be entrained by the bulk gases in the rapid motion which occurs during exhaust blowdown (see Sec. 6.5). The rapid thinning of the thermal boundary-layer regions on the combustion chamber walls during blowdown, which would result from entrainment of the denser hydrocarbon-containing gas adjacent to the wall, has been observed in schlieren movies taken in a transparent engine.[46] This process, plus entrainment of any HC from the spark plug and head gasket crevices, would contribute to unburned HC in the blowdown gases which contain about half the total HC emissions (see Fig. 11-24). During the exhaust stroke this bulk gas entrainment process will continue, exhausting additional unburned HC, as shown in Fig. 11-30*b*.

The second mechanism starts at the beginning of the exhaust stroke in the piston crown–cylinder wall corner. The piston motion during the exhaust stroke scrapes the boundary-layer gases off the cylinder wall (which contain the remainder of the piston and ring crevice hydrocarbons), rolls them up into a vortex, and pushes them toward the top of the cylinder. This piston crown–cylinder wall corner flow is discussed in Sec. 8.7, and has been observed in transparent engines as well as in water-flow engine analog studies. At the end of the exhaust stroke, the height of this vortex is comparable to the engine clearance height. As shown in Fig. 11-30*c*, a recirculation flow is likely to build up in the upper corner of the cylinder away from the exhaust valve, causing the vortex to detach from the wall and partly sweep out of the cylinder. In the corner nearest the valve, the flow is deflected around the valve, also tending to pull part of the vortex out of the chamber. In this way it is possible for a large part of the vortex, which now contains a substantial fraction of the unburned HC originally located adjacent to the cylinder wall, to leave the cylinder at the end of the exhaust stroke. This vortex flow is thought to be the mechanism that leads to the high HC concentrations measured at the end of the exhaust process, which contributes the other half of the exhausted HC mass (see Fig. 11-24), and to be responsible for the HC concentrations measured in the residual gases being much higher than average exhaust HC levels.[42] This study showed that at close to wide-open-throttle conditions, only about two-thirds of the HC which fail to oxidize inside the cylinder were exhausted, though 95 percent of the gas within the cylinder flows out through the exhaust valve. The residual gas HC concentration was about 11 times the average exhaust level. At part-throttle conditions, where the residual gas fraction is higher, it has been estimated that only about half of the unreacted HC in the cylinder will enter the exhaust.[61]

HYDROCARBON OXIDATION. Unburned hydrocarbons which escape the primary engine combustion process by the mechanisms described above must then survive the expansion and exhaust process without oxidizing if they are to appear in the exhaust. Since the formation mechanisms produce unburned HC at temperatures close to the wall temperature, mixing with bulk burned gas must take place first to raise the HC temperature to the point where reaction can occur. The sequence of processes which links the source mechanisms to hydrocarbons at the exhaust exit is illustrated in Fig. 11-31; it involves mixing and oxidation in both the cylinder and the exhaust system.

There is considerable evidence that substantial oxidation does occur. The oxidation of unburned HC in the quench layers formed on the combustion chamber walls on a time scale of order 1 ms after the flame is extinguished has already been discussed. Because the quench layers are thin, diffusion of HC into the bulk burned gas is rapid. Because the burned gases are still at a high temperature, oxidation then occurs quickly. Measurements of in-cylinder HC concentrations by gas sampling prior to exhaust valve opening show levels about 1.5 to 2 times the average exhaust level.[44, 63] The exhaust unburned HC are a mixture of fuel hydrocarbon compounds and pyrolysis and partial oxidation pro-

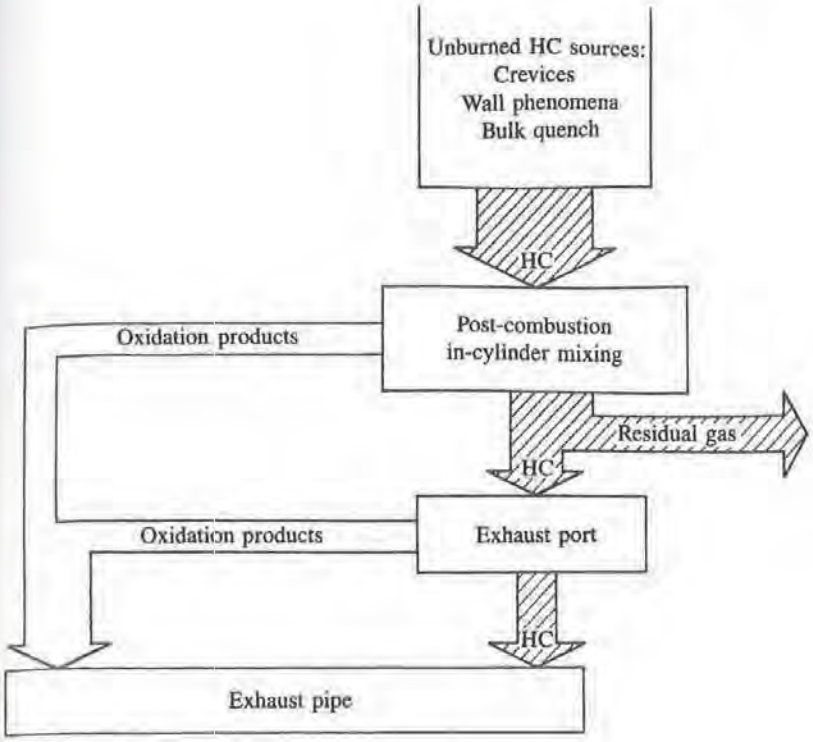


FIGURE 11-31
Schematic of complete SI engine HC formation and oxidation mechanism within the cylinder and exhaust system.[62]

ducts. While the relative proportion of fuel compared to reaction product hydrocarbon compounds varies substantially with engine operating conditions, an average value for passenger car vehicle exhausts is that fuel compounds comprise 40 percent of the total HC. Though partially reacted HC are produced in the flame-quenching process, these are closest to the high-temperature burned gases and are likely to mix and burn rapidly. That such a large fraction of the exhaust HC are reaction products indicates that substantial postformation HC reactions are occurring. There is direct evidence that HC oxidation in the exhaust system occurs.[64] Since in-cylinder gas temperatures are higher, it is likely that mixing of unburned HC with the bulk cylinder gases limits the amount of oxidation rather than the reaction kinetics directly.

Overall empirically based expressions for the rate of oxidation of hydrocarbons of the form of Eq. (11.31) have been developed and used to examine in-cylinder and exhaust burnup. A characteristic time τ_{HC} for this burnup process can be defined:

$$\frac{1}{\tau_{HC}} = \frac{1}{[HC]} \frac{d[HC]}{dt} \tag{11.34}$$

Using an expression similar to Eq. (11.31) for $d[HC]/dt$, Weiss and Keck[63] have shown that any HC mixing with the burned gases in the cylinder prior to exhaust

blowdown will oxidize. The in-cylinder gas temperature prior to blowdown generally exceeds 1250 K; the characteristic reaction time τ_{HC} is then less than 1 ms. During blowdown the temperature falls rapidly to values typically less than 1000 K; τ_{HC} is then greater than about 50 ms. An experimental study of HC exiting from a simulated crevice volume has shown that complete HC oxidation only occurs when the cylinder gas temperature is above 1400 K.[65] Thus a large fraction of the HC leaving crevice regions or oil layers during the exhaust process can be expected to survive with little further oxidation. Gas-sampling data show little decrease in in-cylinder HC concentrations during the exhaust stroke, thus supporting this conclusion.[44, 63] Overall, probably about half of the unburned HC formed by the source mechanisms described above will oxidize within the engine cylinder (the exact amount cannot yet be predicted with any accuracy; it is likely to depend on engine design and operating conditions[61]).

As shown schematically in Fig. 11-31, oxidation of HC in the exhaust system can occur. Often this is enhanced by air addition into the port region to ensure that adequate oxygen for burnup is available. However, since the gas temperature steadily decreases as the exhaust gases flow through the exhaust port and manifold, the potential for HC burnup rapidly diminishes. To oxidize the hydrocarbons in the gas phase, a residence time of order 50 ms or longer at temperatures in excess of 600°C are required. To oxidize carbon monoxide temperatures in excess of 700°C are required. Average exhaust gas temperatures at the cylinder exit (at the exhaust valve plane) are about 800°C; average gas temperatures at the exhaust port exit are about 600°C.† Figure 6-21 shows an example of the measured cylinder pressure, measured gas temperature at the exhaust port exit, and estimated mass flow rate into the port and gas temperature in the cylinder, during the exhaust process at a part-throttle operating condition. Port residence time and gas temperatures vary significantly through the process. Precise values of these variables obviously depend on engine operating conditions. It is apparent that only in the exhaust port and upstream end of the manifold can any significant gas-phase HC oxidation occur.

The importance of exhaust gas temperature to exhaust system emissions burnup is illustrated by the results shown in Fig. 11-32.[66] The exhaust system of a four-cylinder engine was modified by installing a section of heated and insulated pipe to maintain the exhaust gas temperature constant in the absence of any HC or CO burnup. The exhaust temperature entering this test section was varied by adjusting the engine operating conditions. The figure shows CO and HC concentrations as functions of residence time in the exhaust test section (or effectively as a function of distance from the engine). T_e is the entering gas temperature. The exhaust composition was fuel lean with 3 percent O_2 in the burned

† Note that there is a significant variation in the temperature of the exhaust gases throughout the exhaust process. The gas exhausted first is about 100 K hotter than the gas exhausted at the end of the process (see Sec. 6.5).

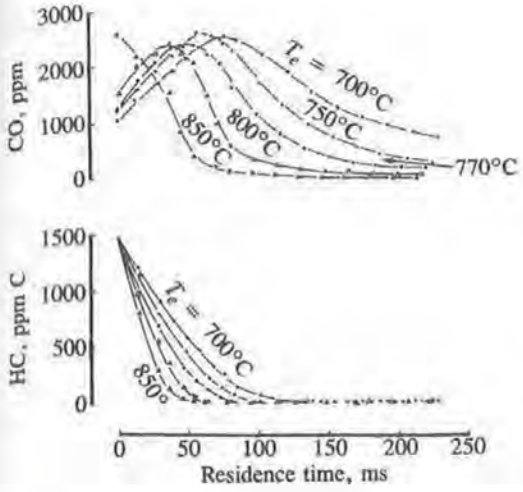


FIGURE 11-32
Effect of exhaust gas temperature on HC and CO burnup in the exhaust. SI engine at 1600 rev/min, engine air flow = 7.7 dm^3/s, lean mixture with 3% O_2 and 13% ($CO + CO_2$) in exhaust.[66]

gas stream. HC oxidation starts immediately (for $T \gtrsim 600°C$), the rate of oxidation increasing rapidly with increasing temperature. Under fuel-lean conditions, incomplete HC oxidation can result in an increase in CO levels. CO oxidation commences later, when the gas temperature rises above the entering value due to heat released by the already occurring HC oxidation. The further heat released by CO oxidation accelerates the CO burnup process. These data underline the importance of the exhaust port heat-transfer and mixing processes. Both mixing between the hotter blowdown gases (with their lower HC concentration) and the cooler end-of-exhaust gases (with their higher HC concentration) and mixing between burned exhaust gas and secondary air are important.

Engine experiments where the exhaust gas reactions were quenched by timed injection of cold carbon dioxide at selected locations within the exhaust port have shown that significant reductions in HC concentration in the port can occur. Parallel modeling studies of the HC burnup process (based on instantaneous mass flow rate, estimated exhaust gas temperature, and an overall hydrocarbon reaction-rate expression), which predicted closely comparable magnitudes and trends, indicated that gas temperature and port residence time are the critical variables. The percent of unburned HC exiting the cylinder which reacted in the exhaust system (with most of the reaction occurring in the port) varied between a few and 40 percent. Engine operating conditions that gave highest exhaust temperatures (stoichiometric operation, higher speeds, retarded spark timing, lower compression ratio) and longest residence times (lighter load) gave relatively higher percent reductions. Air injection at the exhaust valve-stem base, phased to coincide with the exhaust process, showed that for stoichiometric and slightly rich conditions secondary air flow rates up to 30 percent of the exhaust flow substantially increased the degree of burnup. The timing of the secondary air flow relative to the exhaust flow and the location of the air injection point in the port are known to be critical.[64]

Reductions in exhaust port heat losses through the use of larger port cross-sectional areas (to reduce flow velocity and surface area per unit volume), inser-

tion of port liners to provide higher port wall temperatures, and attention to port design details to minimize hot exhaust gas impingement on the walls are known to increase the degree of reaction occurring in the port.

SUMMARY. It will be apparent from the above that the HC emissions formation process in spark-ignition engines is extremely complex and that there are several paths by which a small but important amount of the fuel escapes combustion. It is appropriate here to summarize the overall structure of the spark-ignition engine hydrocarbon emission problem and identify the key factors and engine variables that influence the different parts of that problem. Table 11.7 provides such a summary. The total process is divided into four sequential steps: (1) the formation of unburned hydrocarbon emissions; (2) the oxidation of a fraction of these HC emissions within the cylinder, following mixing with the bulk gases; (3) the flow of a fraction of the unoxidized HC from the cylinder into the exhaust; (4) the oxidation in the exhaust system of a fraction of the HC that exit the cylinder. The detailed processes and the design and operating variables that influence each of these steps in a significant way are listed.

The four separate formation mechanisms identified in step 1 have substantial, though as yet incomplete, evidence behind them. They are listed in the most likely order of importance. Each has been extensively described in this section. It is through each of these mechanisms that fuel or fuel-air mixture escapes the primary combustion process. That fuel must then survive the expansion and exhaust processes and pass through the exhaust system without oxidation if it is to end up in the atmosphere as HC emissions. The rate of mixing of these unburned HC with the hot bulk cylinder gases, the temperature and composition of the gases with which these HC mix, and the subsequent temperature-time and composition-time histories of the mixture will govern the amount of in-cylinder oxidation that occurs. The distribution of these HC around the combustion chamber is nonuniform (and changes with time); they are concentrated close to the walls of the chamber. The fraction of these HC that will exit the chamber during the exhaust process will depend on the details of the in-cylinder flow patterns that take them through the exhaust valve. Overall, the magnitude of the residual fraction will be one major factor; the residual gas is known to be much richer in HC than the average exhaust. In particular, the flow patterns in the cylinder toward the end of the exhaust stroke as the gas scraped off the cylinder wall by the piston moves toward the exhaust valve will be important. Finally, a fraction of the unburned HC which leave the cylinder through the exhaust valve will burn up within the exhaust system. Gas-phase oxidation in the exhaust ports and hotter parts of the exhaust manifold is significant. The amount depends on the gas temperature, composition, and residence time. If catalysts or a thermal reactor are included in the exhaust system, very substantial additional reduction in HC emission levels can occur. These devices and their operating characteristics are described in Sec. 11.6.

TABLE 11.7
Critical factors and engine variables in HC emissions mechanisms

1. *Formation of HC*
   - (*a*) Crevices
     - (1) Crevice volume
     - (2) Crevice location (relative to spark plug)
     - (3) Load
     - (4) Crevice wall temperature
     - (5) Mixture composition†
   - (*b*) Oil layers
     - (1) Oil consumption
     - (2) Wall temperature
     - (3) Speed
   - (*c*) Incomplete combustion
     - (1) Burn rate and variability
     - (2) Mixture composition†
     - (3) Load
     - (4) Spark timing‡
   - (*d*) Combustion chamber walls
     - (1) Deposits
     - (2) Wall roughness
2. *In-cylinder mixing and oxidation*
   - (*a*) Mixing rate with bulk gas
     - (1) Speed
     - (2) Swirl ratio
     - (3) Combustion chamber shape
   - (*b*) Bulk gas temperature during expansion and exhaust
     - (1) Speed
     - (2) Spark timing‡
     - (3) Mixture composition†
     - (4) Compression ratio
     - (5) Heat losses to walls
   - (*c*) Bulk gas oxygen concentration
     - (1) Equivalence ratio
   - (*d*) Wall temperature
     - (1) Important if HC source near wall
     - (2) For crevices: importance depends on geometry
3. *Fraction HC flowing out of cylinder*
   - (*a*) Residual fraction
     - (1) Load
     - (2) Exhaust pressure
     - (3) Valve overlap
     - (4) Compression ratio
     - (5) Speed
   - (*b*) In-cylinder flow during exhaust stroke
     - (1) Valve overlap
     - (2) Exhaust valve size and location
     - (3) Combustion chamber shape
     - (4) Compression ratio
     - (5) Speed
4. *Oxidation in exhaust system*
   - (*a*) Exhaust gas temperature
     - (1) Speed
     - (2) Spark timing‡
     - (3) Mixture composition†
     - (4) Compression ratio
     - (5) Secondary air flow
     - (6) Heat losses in cylinder and exhaust
   - (*b*) Oxygen concentration
     - (1) Equivalence ratio
     - (2) Secondary air flow and addition point
   - (*c*) Residence time
     - (1) Speed
     - (2) Load
     - (3) Volume of critical exhaust system component
   - (*d*) Exhaust reactor§
     - (1) Oxidation catalyst
     - (2) Three-way catalyst
     - (3) Thermal reactor

† Fuel/air equivalence ratio and burned gas fraction (residual plus recycled exhaust gas).
‡ Relative to MBT timing.
§ Of at least as great an importance as engine details if present in total emission control system. See Sec. 11.6.

11.4.4 Hydrocarbon Emission Mechanisms in Diesel Engines

BACKGROUND. Diesel fuel contains hydrocarbon compounds with higher boiling points, and hence higher molecular weights, than gasoline. Also, substantial pyrolysis of fuel compounds occurs within the fuel sprays during the diesel combustion process. Thus, the composition of the unburned and partially oxidized hydrocarbons in the diesel exhaust is much more complex than in the spark-ignition engine and extends over a larger molecular size range. Gaseous hydrocarbon emissions from diesels are measured using a hot particulate filter (at 190°C) and a heated flame ionization detector. Thus the HC constituents vary from methane to the heaviest hydrocarbons which remain in the vapor phase in the heated sampling line (which is also maintained at about 190°C). Any hydrocarbons heavier than this are therefore condensed and, with the solid-phase soot, are filtered from the exhaust gas stream upstream of the detector. The particulate emission measurement procedure measures a portion of total engine hydrocarbon emissions also. Particulates are collected by filtering from a diluted exhaust gas stream at a temperature of 52°C or less. Those hydrocarbons that condense at or below this temperature are absorbed onto the soot. They are the extractable fraction of the particulate: i.e., that fraction which can be removed by a powerful solvent, typically between about 15 and 45 percent of the total particulate mass. This section discusses gaseous hydrocarbon emissions; particulate emissions—soot and extractable material—are discussed in Sec. 11.5.

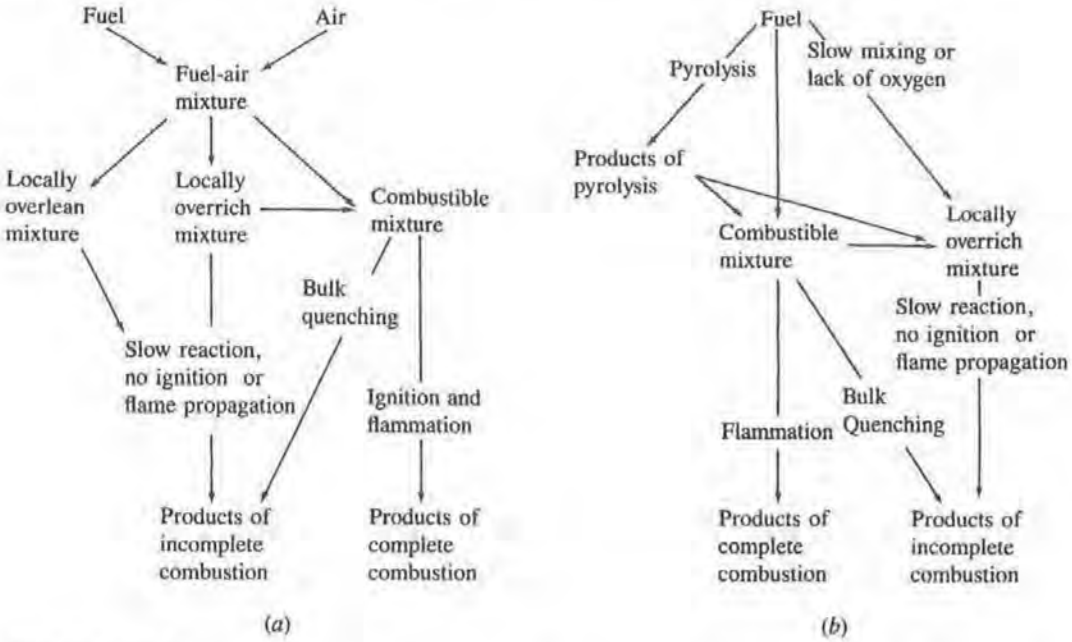


FIGURE 11-33
Schematic representation of diesel hydrocarbon formation mechanisms: (*a*) for fuel injected during delay period; (*b*) for fuel injected while combustion is occurring.[23]

The complex heterogeneous nature of diesel combustion, where fuel evaporation, fuel-air and burned-unburned gas mixing, and combustion can occur simultaneously, has been discussed extensively in Chap. 10. As a result of this complexity, there are many processes that could contribute to diesel engine hydrocarbon emissions. In Chap. 10 the diesel's compression-ignition combustion process was divided into four stages: (1) the ignition delay which is the time between the start of injection and ignition; (2) the premixed or rapid combustion phase, during which the fuel that has mixed to within combustible limits during the delay period burns; (3) the mixing controlled combustion phase, during which the rate of burning depends on the rate of fuel-air mixing to within the combustible limits; (4) the late combustion phase where heat release continues at a low rate governed by the mixing of residual combustibles with excess oxygen and the kinetics of the oxidation process. There are two primary paths by which fuel can escape this normal combustion process unburned: the fuel-air mixture can become too lean to autoignite or to support a propagating flame at the conditions prevailing inside the combustion chamber, or, during the primary combustion process, the fuel-air mixture may be too rich to ignite or support a flame. This fuel can then be consumed only by slower thermal oxidation reactions later in the expansion process after mixing with additional air. Thus, hydrocarbons remain unconsumed due to incomplete mixing or to quenching of the oxidation process.†

Figure 11-33 shows schematically how these processes can produce incomplete combustion products. Fuel injected during the ignition delay (Fig. 11-33*a*) will mix with air to produce a wide range of equivalence ratios. Some of this fuel will have mixed rapidly to equivalence ratios lower than the lean limit of combustion (locally overlean mixture), some will be within the combustible range, and some will have mixed more slowly and be too rich to burn (locally overrich mixture). The overlean mixture will not autoignite or support a propagating flame at conditions prevailing inside the combustion chamber (though some of this mixture may burn later if it mixes with high-temperature burned products early in the expansion stroke). In the "premixed" combustible mixture, ignition occurs where the local conditions are most favorable for autoignition. Unless quenched by thermal boundary layers or rapid mixing with air, subsequent autoignition or flame fronts propagating from the ignition sites consume the combustible mixture. Complete combustion of overrich mixture depends on further mixing with air or lean already-burned gases within the time available before rapid expansion and cooling occurs. Of all these possible mechanisms, the overlean mixture path is believed to be the most important.[23]

For the fuel injected after the ignition delay period is over (Fig. 11-33*b*), rapid oxidation of fuel or the products of fuel pyrolysis, as these mix with air,

† Note that under normal engine operating conditions, the combustion inefficiency is less than 2 percent; see Sec. 4.9.4 and Fig. 3-9.

results in complete combustion. Slow mixing of fuel and pyrolysis products with air, resulting in overrich mixture or quenching of the combustion reactions, can result in incomplete combustion products, pyrolysis products, and unburned fuel being present in the exhaust.[23]

Hydrocarbon emission levels from diesels vary widely with operating conditions, and different HC formation mechanisms are likely to be most important at different operating modes. Engine idling and light-load operation produce significantly higher hydrocarbon emissions than full-load operation. However, when the engine is overfueled, HC emissions increase very substantially. As will be explained more fully below, overmixing (overleaning) is an important source of HC, especially under light-load operation. Undermixing, resulting in overrich mixture during the combustion period, is the mechanism by which some of the fuel remaining in the injector nozzle sac volume escapes combustion, and is also the cause of very high HC emissions during overfueling. Wall temperatures affect HC emissions, suggesting that wall quenching is important, and under especially adverse conditions very high cyclic variability in the combustion process can cause an increase in HC due to partial burning and misfiring cycles.

OVERLEANING. As soon as fuel injection into the cylinder commences, a distribution in the fuel/air equivalence ratio across the fuel sprays develops. The amount of fuel that is mixed leaner than the lean combustion limit ($\phi_L \sim 0.3$) increases rapidly with time.[23] Figure 11-34 illustrates this equivalence ratio distribution in the fuel spray at the time of ignition. In a swirling flow, ignition occurs in the slightly lean-of-stoichiometric region downstream of the spray core

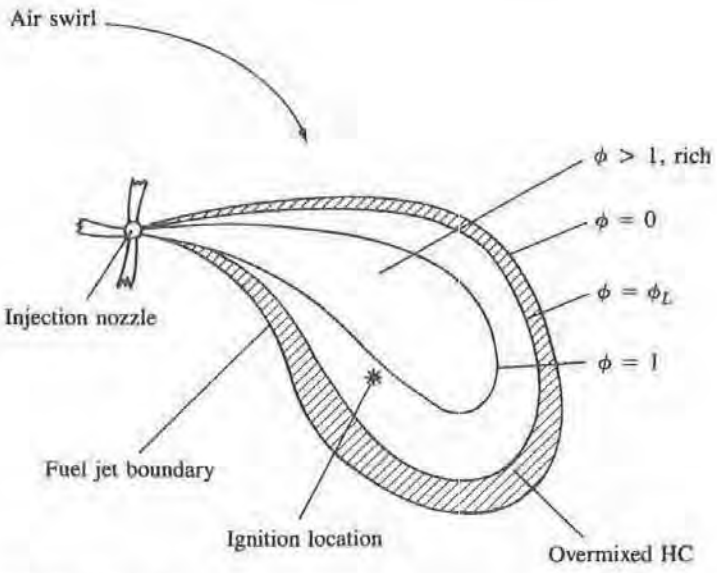


FIGURE 11-34
Schematic of diesel engine fuel spray showing equivalence ratio (ϕ) contours at time of ignition. ϕ_L = equivalence ratio at lean combustion limit (≈ 0.3). Shaded region contains fuel mixed leaner than ϕ_L.[67]

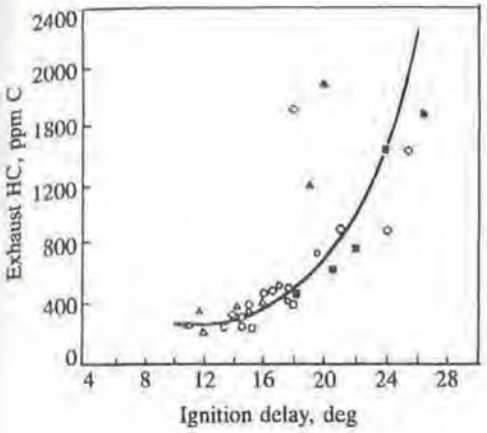


FIGURE 11-35
Correlation of exhaust HC concentration with duration of ignition delay for DI diesel engine. Various fuels, engine loads, injection timings, boost pressures, at 2800 rev/min.[67]

where the fuel which has spent most time within the combustible limits is located. However, the fuel close to the spray boundary has already mixed beyond the lean limit of combustion and will not autoignite or sustain a fast reaction front. This mixture can only oxidize by relatively slow thermal-oxidation reactions which will be incomplete. Within this region, unburned fuel, fuel decomposition products, and partial oxidation products (aldehydes and other oxygenates) will exist; some of these will escape the cylinder without being burned. The magnitude of the unburned HC from these overlean regions will depend on the amount of fuel injected during the ignition delay, the mixing rate with air during this period, and the extent to which prevailing cylinder conditions are conducive to autoignition. A correlation of unburned HC emissions with the length of the ignition delay would be expected. The data in Fig. 11-35 from a direct-injection naturally aspirated engine show that a good correlation between these variables exists. As the delay period increases beyond its minimum value (due to changes in engine operating conditions), HC emissions increase at an increasing rate.[67] Thus, overleaning of fuel injected during the ignition delay period is a significant source of hydrocarbon emissions, especially under conditions where the ignition delay is long.

UNDERMIXING. Two sources of fuel which enter the cylinder during combustion and which result in HC emissions due to slow or under mixing with air have been identified. One is fuel that leaves the injector nozzle at low velocity, often late in the combustion process. The most important source here is the nozzle sac volume, though secondary injections can increase HC emissions if the problem is severe. The second source is the excess fuel that enters the cylinder under overfueling conditions.

At the end of the fuel-injection process, the injector sac volume (the small volume left in the tip of the injector after the needle seats) is left filled with fuel. As the combustion and expansion processes proceed, this fuel is heated and vaporizes, and enters the cylinder at low velocity through the nozzle holes. This fuel vapor (and perhaps large drops of fuel also) will mix relatively slowly with air

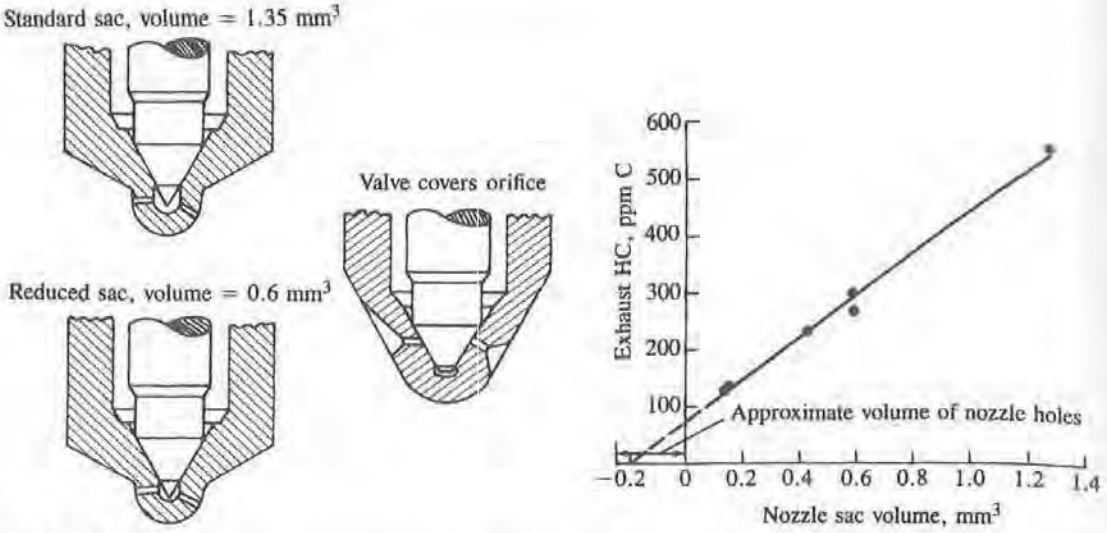


FIGURE 11-36
Effect of nozzle sac volume on exhaust HC concentration, DI diesel engine, at minimum ignition delay. $V_d = 1$ dm³/cylinder, 1700–2800 rev/min.[67]

and may escape the primary combustion process. Figure 11-36 shows HC emissions at the minimum ignition delay for a direct-injection diesel engine as a function of sac volume, along with drawings of some of the injector nozzles used. The correlation between HC emissions (under conditions when the overleaning mechanism is least significant) and sac volume is striking. The extrapolation to zero HC emissions suggests that the fuel in the nozzle holes also contributes. Not all the fuel in the sac volume is exhausted as unburned hydrocarbons. For example, in Fig. 11-36 a volume of 1 mm³ gives 350 ppm C_1 while 1 mm³ of fuel would give 1660 ppm C_1. The sac volume may not be fully filled with fuel. Also, the higher-boiling-point fractions of the fuel may remain in the nozzle. Significant oxidation may also occur. In indirect-injection engines, similar trends have been observed, but the HC emission levels at short ignition delay conditions are substantially lower. The sac volume in current production nozzles helps to equalize the fuel pressures immediately upstream of the nozzle orifices. A small sac volume makes this equalization less complete and exhaust smoke deteriorates. The contribution of sac and hole volumes to exhaust HC can be reduced to below 0.75 g/kW · h for a 1 dm³ per cylinder displacement DI engine.[67]

In DI engines, exhaust smoke limits the full-load equivalence ratio to about 0.7. Under transient conditions as the engine goes through an acceleration process, overfueling can occur. Even though the overall equivalence ratio may remain lean, locally overrich conditions may exist through the expansion stroke and into the exhaust process. Figure 11-37 shows the effect of increasing the amount of fuel injected at constant speed, with the injection timing adjusted to keep the ignition delay at its minimum value (when HC emissions from overleaning are lowest). HC emissions are unaffected by an increasing equivalence ratio until a critical value of about 0.9 is reached when levels increase dramatically. A

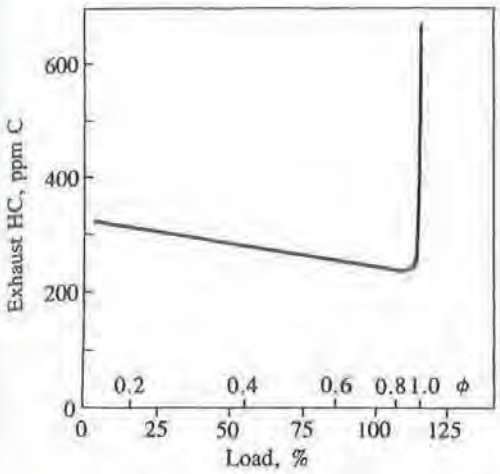


FIGURE 11-37
Effect of overfueling on exhaust HC concentration. DI diesel engine, speed = 1700 rev/min, injection timing at full-load 15° BTC.[67]

similar trend exists for IDI engines.[67] This mechanism is not significant under normal operating conditions, but can contribute HC emissions under acceleration conditions if overfueling occurs. However, it produces less HC than does overleaning at light load and idle.[23]

QUENCHING AND MISFIRE. Hydrocarbon emissions have been shown to be sensitive to oil and coolant temperature: when these temperatures were increased from 40 to 90°C in a DI diesel, HC emissions decreased by 30 percent. Since ignition delay was maintained constant, overmixing phenomena should remain approximately constant. Thus, wall quenching of the flame may also be a significant source of HC, depending on the degree of spray impingement on the combustion chamber walls.

While cycle-by-cycle variation in the combustion process in diesel engines is generally much less than in spark-ignition engines, it can become significant under adverse conditions such as low compression temperatures and pressures and retarded injection timings. Substantial variations, cycle-by-cycle, in HC emissions are thought to result. In the limit, if misfire (no combustion) occurs in a fraction of the operating cycles, then engine HC emissions rise as the percentage of misfires increases. However, complete misfires in a well-designed and adequately controlled engine are unlikely to occur over the normal operating range.[23]

SUMMARY. There are two major causes of HC emissions in diesel engines under normal operating conditions: (1) fuel mixed to leaner than the lean combustion limit during the delay period; (2) undermixing of fuel which leaves the fuel injector nozzle at low velocity, late in the combustion process. At light load and idle, overmixing is especially important, particularly in engines of relatively small cylinder size at high speed. In IDI engines, the contribution from fuel in the nozzle sac volume is less important than with DI engines. However, other sources of low velocity and late fuel injection such as secondary injection can be significant.

11.5 PARTICULATE EMISSIONS

11.5.1 Spark-Ignition Engine Particulates

There are three classes of spark-ignition engine particulate emissions: lead, organic particulates (including soot), and sulfates.

Significant sulfate emissions can occur with oxidation-catalyst equipped engines. Unleaded gasoline contains 150 to 600 ppm by weight sulfur, which is oxidized within the engine cylinder to sulfur dioxide, SO_2. This SO_2 can be oxidized by the exhaust catalyst to SO_3 which combines with water at ambient temperatures to form a sulfuric acid aerosol. Levels of sulfate emissions depend on the fuel sulfur content, the operating conditions of the engine, and the details of the catalyst system used. Typical average automobile sulfate emission rates are 20 mg/km or less.[68]

For automobile engines operated with regular and premium leaded gasolines (which contain about 0.15 g Pb/liter or dm^3) the particulate emission rates are typically 100 to 150 mg/km. This particulate is dominated by lead compounds: 25 to 60 percent of the emitted mass is lead.[69] The particulate emission rates are considerably higher when the engine is cold, following start-up. The exhaust temperature has a significant effect on emission levels. The particle size distribution with leaded fuel is about 80 percent by mass below 2 μm diameter and about 40 percent below 0.2 μm diameter. Most of these particles are presumed to form and grow in the exhaust system due to vapor phase condensation enhanced by coagulation. Some of the particles are emitted directly, without settling. Some of the particles either form or are deposited on the walls where agglomeration may occur. Many of these are removed when the exhaust flow rate is suddenly increased, and these particles together with rust and scale account for the increase in mass and size of particles emitted during acceleration. Only a fraction (between 10 and 50 percent) of the lead consumed in the fuel is exhausted, the remainder being deposited within the engine and exhaust system.

Use of unleaded gasoline reduces particulate emissions to about 20 mg/km in automobiles without catalysts. This particulate is primarily soluble (condensed) organic material. Soot emissions (black smoke) can result from combustion of overly rich mixtures. In properly adjusted spark-ignition engines, soot in the exhaust is not a significant problem.

11.5.2 Characteristics of Diesel Particulates

MEASUREMENT TECHNIQUES. Diesel particulates consist principally of combustion generated carbonaceous material (soot) on which some organic compounds have become absorbed. Most particulate material results from incomplete combustion of fuel hydrocarbons; some is contributed by the lubricating oil. The emission rates are typically 0.2 to 0.6 g/km for light-duty diesels in an automobile. In larger direct-injection engines, particulate emission rates are 0.5 to 1.5 g/brake kW · h. The composition of the particulate material depends on the conditions in the engine exhaust and particulate collection system. At tem-

peratures above 500°C, the individual particles are principally clusters of many small spheres or spherules of carbon (with a small amount of hydrogen) with individual spherule diameters of about 15 to 30 nm. As temperatures decrease below 500°C, the particles become coated with adsorbed and condensed high molecular weight organic compounds which include: unburned hydrocarbons, oxygenated hydrocarbons (ketones, esters, ethers, organic acids), and polynuclear aromatic hydrocarbons. The condensed material also includes inorganic species such as sulfur dioxide, nitrogen dioxide, and sulfuric acid (sulfates).

The objective of most particulate measurement techniques is to determine the amount of particulate being emitted to the atmosphere. Techniques for particulate measurement and characterization range from simple smoke meter opacity readings to analyses using dilution tunnels. Most techniques require lengthy sample-collection periods because the emission rate of individual species is usually low. The physical conditions under which particulate measurements are made are critical because the emitted species are unstable and may be altered through loss to surfaces, change in size distribution (through collisions), and chemical interactions among other species in the exhaust at any time during the measurement process (including sampling, storage, or examination). The most basic information is normally obtained on a mass basis: for example, grams per kilometer for a vehicle, grams per kilowatt-hour for an engine, grams per kilogram of fuel or milligrams per cubic meter of exhaust (at standard conditions). Smoke meters measure the relative quantity of light that passes through the exhaust or the relative reflectance of particulate collected on filter paper. They do not measure mass directly. They are used to determine visible smoke emissions and provide an approximate indication of mass emission levels. Visible smoke from heavy-duty diesels at high load is regulated. In the standard mass emission measurement procedure, dilution tunnels are used to simulate the physical and chemical processes the particulate emissions undergo in the atmosphere. In the dilution tunnel, the raw exhaust gases are diluted with ambient air to a temperature of 52°C or less, and a sample stream from the diluted exhaust is filtered to remove the particulate material.

PARTICULATE COMPOSITION AND STRUCTURE. The structure of diesel particulate material is apparent from the photomicrographs shown in Fig. 11-38 of particulates collected from the exhaust of an IDI diesel engine. The samples are seen to consist of collections of primary particles (spherules) agglomerated into aggregates (hereafter called particles). Individual particles range in appearance from clusters of spherules to chains of spherules. Clusters may contain as many as 4000 spherules. Occasional liquid hydrocarbon and sulfate droplets have been identified. The spherules are combustion generated soot particles which vary in diameter between 10 and 80 nm, although most are in the 15 to 30 nm range. Figure 11-39 shows a typical distribution of spherule size (solid line) determined by sizing and counting images in the photomicrographs. The number-mean diameter ($=\sum N_i d_i/N$) is 28 nm. The volume contribution of these

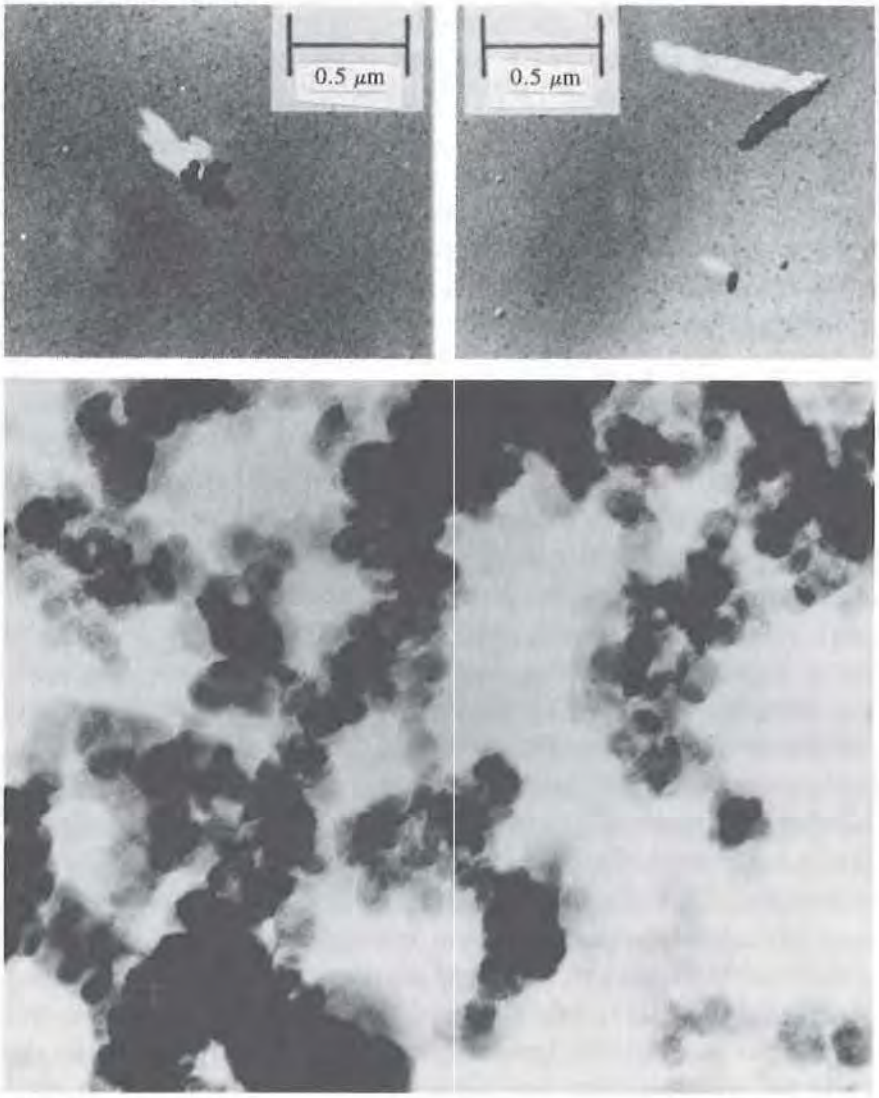


FIGURE 11-38
Photomicrographs of diesel particulates: cluster (upper left), chain (upper right), and collection from filter (bottom).[70]

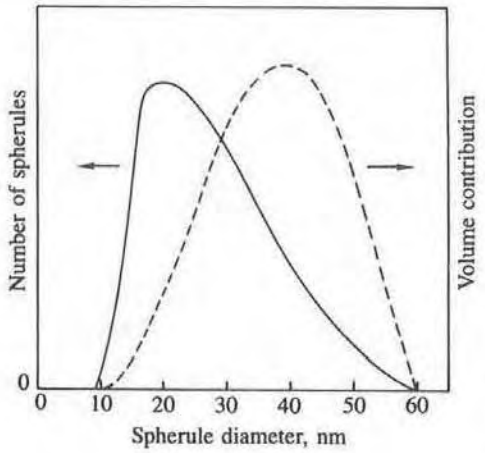


FIGURE 11-39
Typical distributions of spherule diameter and volume.[70]

TABLE 11.8
Chemical composition of particular matter[70]

	Idle	48 km/h
Extractable composition	$C_{23}H_{29}O_{4.7}N_{0.21}$	$C_{24}H_{30}O_{2.6}N_{0.18}$
H/C	1.26	1.63
Dry soot composition	$CH_{0.27}O_{0.22}N_{0.01}$	$CH_{0.21}O_{0.15}N_{0.01}$
H/C	0.27	0.21

spherules is shown as the dashed curve in Fig. 11-39. The volume-mean diameter, $(\sum N_i d_i^3/N)^{1/3}$, is 31 nm.

Determination of the *particle* size distribution with a similar technique involves assigning a single dimension to a complex and irregular aggregate, and introduces uncertainties arising from only having two-dimensional images of particles available. Other approaches based on inertial impactors and electrical aerosol analysers have been used. Some of the data suggest that the particle size distribution is bimodal. The smaller-size range is thought to be liquid hydrocarbon drops and/or individual spherules characterized by number-mean diameters of 10 to 20 nm; the larger-size range is thought to be the particles of agglomerated spherules characterized by number-mean diameters of 100 to 150 nm. However, other particulate samples have not shown a bimodal distribution: volume-mean diameters ranged from 50 to 220 nm with no notable trend with either speed or load.[70]

The exhaust particulate is usually partitioned with an extraction solvent into a soluble fraction and a dry-soot fraction. Two commonly used solvents are dichloromethane and a benzene-ethanol mixture. Typically 15 to 30 mass percent is extractable, though the range of observations is much larger ($\sim$10 to 90 percent). Thermogravimetric analysis (weighing the sample as it is heated) produces comparable results. Typical average chemical compositions of the two particulate fractions are given in Table 11.8. Dry soot has a much lower H/C ratio than the extractable material. Although most of the particulate emissions are formed through incomplete combustion of fuel hydrocarbons, engine oil may also contribute significantly. The number-average molecular weight of the extractable material shown in Table 11.8 ranged from about 360 to 400 for a variety of engine conditions. This fell between the average molecular weight of the fuel (199) and that of the lubricating oil (443 when fresh and 489 when aged).[70] Radioactive tracer studies in a light-duty IDI diesel have shown that the oil was the origin of between 2 to 25 percent by mass of the total particulate and 16 to 80 percent of the extractable organic portion, the greatest percentages being measured at the highest engine speed studied (3000 rev/min). All of the oil contribution appeared in the extractable material. The contributions from the different individual compounds in the fuel have also been studied. All the compounds tested—paraffins,



FIGURE 11-40
Lattice-imaging micrograph of a diesel particulate.[72]

olefins, and aromatics—contributed to the particulate emissions; as a group, aromatics were the greatest contributors. Eighty percent of the carbon-14 used to tag individual fuel compounds was found in the *insoluble* fraction and 20 percent in the *soluble* particulate fraction.[71]

In addition to the elements listed in Table 11.8, trace amounts of sulfur, zinc, phosphorus, calcium, iron, silicon, and chromium have been found in particulates. Sulfur and traces of calcium, iron, silicon, and chromium are found in diesel fuel; zinc, phosphorus, and calcium compounds are frequently used in lubricating oil additives.[70]

A lattice image of a diesel particle is shown in Fig. 11-40; it suggests a concentric lamellate structure arranged around the center of each spherule. This arrangement of concentric lamellas is similar to the structure of carbon black. This is not surprising; the environment in which diesel soot is produced is similar to that in which oil furnace blacks are made. The carbon atoms are bonded together in hexagonal face-centered arrays in planes, commonly referred to as platelets. As illustrated in Fig. 11-41, the mean layer spacing is 0.355 nm (only slightly larger than graphite). Platelets are arranged in layers to form crystallites. Typically, there are 2 to 5 platelets per crystallite, and on the order of 10^3 crys-

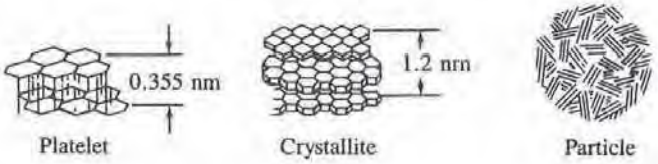


FIGURE 11-41
Substructure of carbon particle.[73]

tallites per spherule. The crystallites are arranged with their planes more or less parallel to the particle surface. This structure of unordered layers is called turbostatic. The spherules, 10 to 50 nm in diameter, are fused together to form particles as shown in Fig. 11-40. A single spherule contains 10^5 to 10^6 carbon atoms.[70, 73]

A surface area of about 200 m^2/g has been measured for diesel soot. A smooth-surfaced 30-nm diameter sphere with a density of 2 g/cm^3 would have a surface/mass ratio of 100 m^2/g, so the measured value is about twice the superficial area. Approximating a particle of agglomerated spherules by a single sphere of 200 nm diameter gives a surface/mass ratio of 15 m^2/g.[70] These data and estimates of superficial area per unit mass indicate that diesel soot has low porosity.

SOLUBLE FRACTION COMPONENTS. The extractable organic fraction of diesel particulate emissions includes compounds that may cause health and environmental hazards. Thus chemical and biological characterization of the soluble organic fraction are important. Both soxhlet and sonification methods are used to extract the organic fraction from particulate samples. Because the particulates are mixtures of polar and nonpolar components, full extraction requires different solvents; any one solvent is a compromise. Methylene chloride is the most commonly used extractant, however. Since a complex mixture of organic compounds is associated with diesel particulates, a preliminary fractionation scheme is used to group similar types of compounds before final separation and identification. The scheme most frequently used results in seven fractions generally labeled as: basics, acidics, paraffins, aromatics, transitionals, oxygenates, and ether insolubles. Table 11.9 indicates the types of components in each fraction and the approximate proportions. The biological activity of the soluble organic fraction and its subfractions is most commonly assessed with the Ames *Salmonella*/microsomal test. With this test, a quantitative dose-response curve showing the mutagenicity of a sample compound is obtained. The Ames test uses a mutant strain of *Salmonella typhimurium* that is incapable of producing histidine. Mutagenicity is defined as the ability of a tested compound to revert—back-mutate—this bacterium to its wild state, where it regains its ability to produce histidine.[35]

11.5.3 Particulate Distribution within the Cylinder

Measurements have been made of the particulate distribution within the combustion chamber of operating diesel engines. The results provide valuable information on the particulate formation and oxidation processes and how these relate to the fuel distribution and heat-release development within the combustion chamber. Techniques used to obtain particulate concentration data include: use of rapid-acting poppet or needle valves which draw a small gas sample from the cylinder at a specific location and time for analysis (e.g., Refs. 21

TABLE 11-9
Components of the soluble organic fraction[35]

Fraction	Components of fraction	Percent of total
Acidic	Aromatic or aliphatic Acidic functional groups Phenolic and carboxylic acids	3–15
Basic	Aromatic or aliphatic Basic functional groups Amines	<1–2
Paraffin	Aliphatics, normal and branched Numerous isomers From unburned fuel and/or lubricant	34–65
Aromatic	From unburned fuel, partial combustion, and recombination of combustion products; from lubricants Single ring compounds Polynuclear aromatics	3–14
Oxygenated	Polar functional groups but not acidic or basic Aldehydes, ketones, or alcohols Aromatic phenols and quinones	7–15
Transitional	Aliphatic and aromatic Carbonyl functional groups Ketones, aldehydes, esters, ethers	1–6
Insoluble	Aliphatic and aromatic Hydroxyl and carbonyl groups High molecular weight organic species Inorganic compounds Glass fibers from filters	6–25

and 74), optical absorption techniques (e.g., Refs. 75 and 76), and cylinder dumping where the cylinder contents are rapidly emptied into an evacuated tank at a preset time in the cycle (e.g., Ref. 77). Both DI and IDI engines have been studied. Of course, concentration data taken at specific locations in the cylinder during the engine cycle are not necessarily representative of the cylinder contents in general; nor do they represent the time history of a given mass of gas. The fuel distribution, mixing, and heat-release patterns in the cylinder are highly nonuniform during the soot-formation process, and the details of gas motion in the vicinity of the sampling location as the piston changes position are usually unknown.

In direct-injection diesel engines, the highest particulate concentrations are found in the core region of each fuel spray where local average equivalence ratios are very rich (see Secs. 10.5.6 and 10.7.2). Soot concentrations rise rapidly soon after combustion starts. Figure 11-42 shows a set of sample-valve soot-concentration data from a large (30.5-cm bore, 38.1-cm stroke), quiescent, direct-

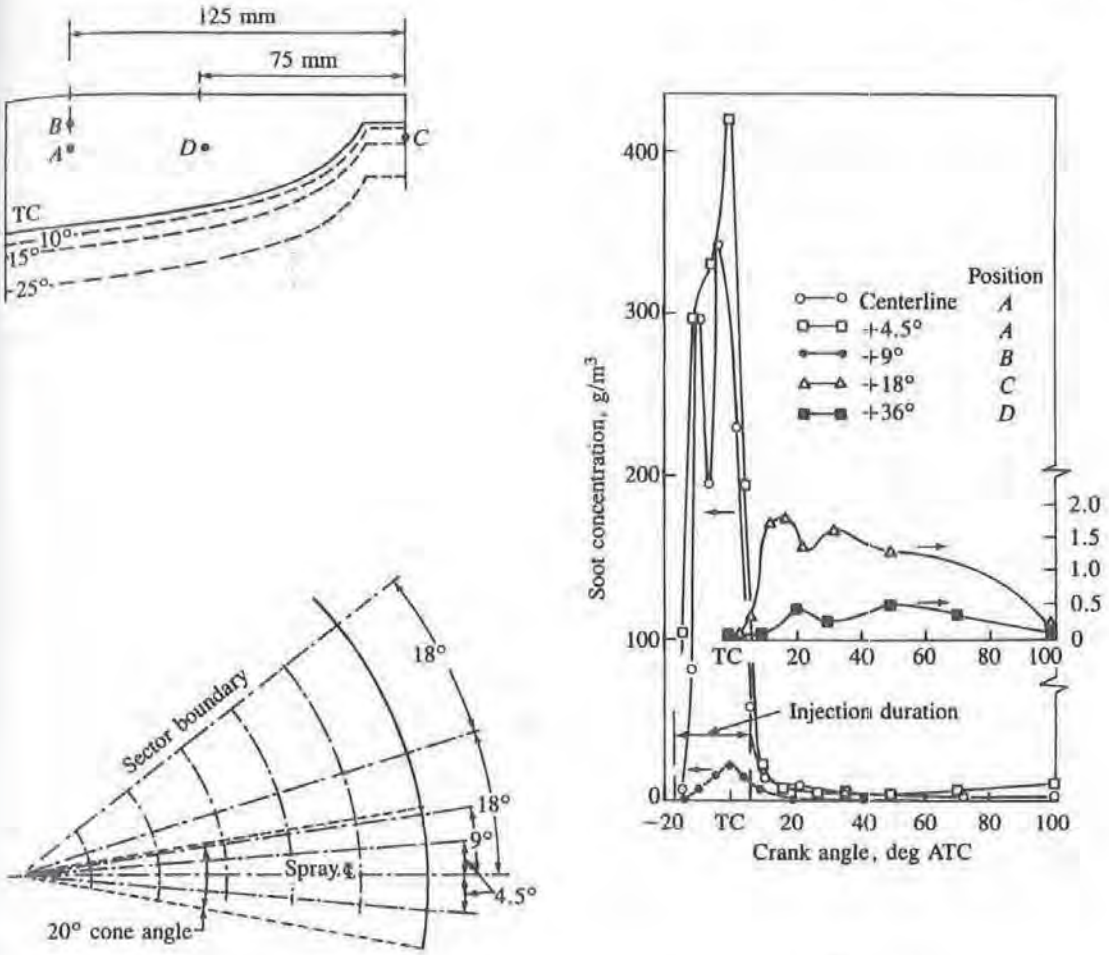


FIGURE 11-42
Particulate concentrations, in g/m³ at standard temperature and pressure, in various regions of the fuel spray as a function of crank angle in quiescent DI diesel engine, measured with rapid sampling valve. Different sample valve locations in combustion chamber and spray indicated on left. Cylinder bore = 30.5 cm, stroke = 38.1 cm, r_c = 12.9, engine speed = 500 rev/min, bmep = 827 kPa.[74]

injection diesel engine which illustrates these points.[74] The particulate concentrations on the fuel spray axis close to the injector orifice are remarkably high (~200 to 400 g/m³ at standard temperature and pressure). This corresponds to a large fraction of the fuel carbon in the extremely rich fuel vapor core being sampled as particulate (as soot and condensed HC species). Such high particulate fractions of the local fuel carbon (~50 percent) have also been found in the very fuel rich cores of high-pressure liquid-fueled turbulent diffusion flames. Pyrolysis of the fuel is therefore an important source of soot. These very high local soot concentrations decrease rapidly once fuel injection ceases and the rich core mixes to leaner equivalence ratios. Soot concentrations in the spray close to the piston bowl outer radius and at the cylinder wall rise later, are an order of magnitude less, and decay more slowly. Away from the fuel spray core, soot concentrations

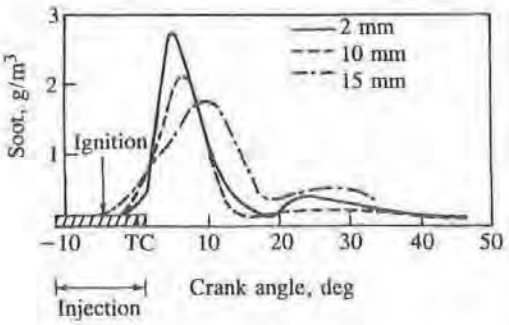


FIGURE 11-43
Particulate concentrations at various distances from wall of precharnber in swirl-chamber IDI diesel engine, measured with rapid sampling valve. Engine speed = 1000 rev/min, injection at 12° BTC, ignition at 5° BTC.[21]

decrease rapidly with increasing distance from the centerline. A useful comparison with these soot concentrations is the fuel concentration in a *stoichiometric* mixture, about 75 g fuel/m^3. Approximate estimates of the mean soot concentration inside the cylinder through the combustion process suggests that almost all (over 90 percent) of the soot formed is oxidized prior to exhaust. Similar results have been obtained in a small direct-injection engine with swirl.[78, 79] Peak soot concentrations in the outer regions of the fuel spray were comparable ($\sim$10 g/m^3). Measurements were not made in the spray core near the injector orifice; however, based on the equivalence ratio results in Fig. 10-46, soot concentrations would be expected to be lower due to the more rapid mixing with air that occurs with swirl.

Similar data are available from sampling in the prechamber of an IDI swirl chamber engine.[21] Figure 11-43 shows soot concentrations 2, 10, and 15 mm from the wall of the prechamber. Equivalence ratio distributions from this study have already been shown in Fig. 11-17. Concentrations peak 5 to 10° ATC at levels $\sim$2 g/m^3; these are substantially lower than DI engine peak soot concentrations (presumably due to the more rapid mixing of fuel and air in the IDI engine). Concentrations in the prechamber at these locations then decrease substantially.

A better indication of average concentrations within the cylinder is given by total cylinder sampling experiments. Measurements of the total number of soot particles and soot volume fraction through the combustion process have been made in an IDI passenger car diesel. The contents of the engine cylinder, at a preselected point in the cycle, were rapidly expelled through a blowdown port, diluted, and collected in a sample bag. Figure 11-44 shows one set of results. Particles first appear shortly after the start of combustion (4 to 5° ATC). The number density rises to a maximum at 20° ATC and then falls rapidly as a result of particle coagulation and, possibly, oxidation. The exhaust particulate number density is less than one-tenth of the peak value. The volume fraction soot data (soot mass concentration is proportional to volume fraction) show a much flatter maximum earlier in the combustion process and a decrease (due to oxidation) from 20 to 40° ATC to about one-third of the peak value. Oxidation apparently ceases at about 40° ATC at these conditions.

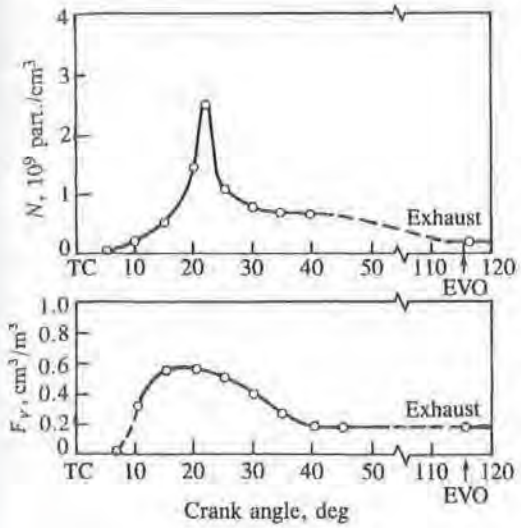


FIGURE 11-44
Cylinder-average particle-number density N and particle-volume fraction F_V, as a function of crank angle in IDI diesel engine determined from cylinder-dumping experiments. 1000 rev/min, $\phi = 0.32$, injection starts at 3.5° BTC. Gas volumes at standard temperature and pressure.[77]

11.5.4 Soot Formation Fundamentals

The soot particles, whose characteristics have been described in the above two sections, form primarily from the carbon in the diesel fuel. Thus, the formation process starts with a fuel molecule containing 12 to 22 carbon atoms and an H/C ratio of about 2, and ends up with particles typically a few hundred nanometers in diameter, composed of spherules 20 to 30 nm in diameter each containing some 10^5 carbon atoms and having an H/C ratio of about 0.1. Most of the information available on the fundamentals of soot formation in combustion comes from studies in simple premixed and diffusion flames, stirred reactors, shock tubes, and constant-volume combustion bombs. A recent review[80] summarizes the extensive literature available from such studies. Also, the production of carbon black requires a high yield of soot from pyrolysis of a hydrocarbon feedstock, and the literature from that field has much to contribute (see Ref. 81). However, the characteristics of diesel combustion which make it unsuitable for more fundamental studies—the high gas temperatures and pressures, complex fuel composition, dominance of turbulent mixing, the unsteady nature of the process, and the three-dimensional geometry—also make it difficult to interpret fundamental ideas regarding soot formation in the diesel context. There is much about the soot formation process in diesel engines, therefore, that is poorly and incompletely understood.

Soot formation takes place in the diesel combustion environment at temperatures between about 1000 and 2800 K, at pressures of 50 to 100 atm, and with sufficient air *overall* to burn fully all the fuel. The time available for the formation of solid soot particles from a fraction of the fuel is in the order of milliseconds. The resulting aerosol—dispersed solid-phase particles in a gas—can be characterized by the total amount of condensed phase (often expressed as the soot volume fraction, F_V, the volume of soot/total volume), the number of soot particles per unit volume (N), and the size of the particles (e.g., average diameter d). F_V, N, and d are mutually dependent [e.g., for spherical particles $F_V =$

$(\pi/6)Nd^3$], and any two of these variables characterize the system. It is most convenient to consider N and F_V as the independent variables since they each relate to the "almost-separate" stages of soot particle generation (the source of N) and soot particle growth (the source of F_V).

These stages can be summarized as follows:[80]

1. Particle formation, where the first condensed phase material arises from the fuel molecules via their oxidation and/or pyrolysis products. These products typically include various unsaturated hydrocarbons, particularly acetylene and its higher analogues ($C_{2n}H_2$), and polycyclic aromatic hydrocarbons (PAH). These two types of molecules are considered the most likely precursors of soot in flames. The condensation reactions of gas-phase species such as these lead to the appearance of the first recognizable soot particles (often called nuclei). These first particles are very small ($d < 2$ nm) and the formation of large numbers of them involve negligible soot loading in the region of their formation.
2. Particle growth, which includes both surface growth, coagulation, and aggregation. Surface growth, by which the bulk of the solid-phase material is generated, involves the attachment of gas-phase species to the surface of particles and their incorporation into the particulate phase. Figure 11-45, where the log of the molecular weight of a species is plotted against its hydrogen mole fraction $\tilde{x}_H$, illustrates some important points about this process. Starting with a fuel molecule of $\tilde{x}_H \gtrsim 0.5$ it is apparent that neither purely polyacetylene chain

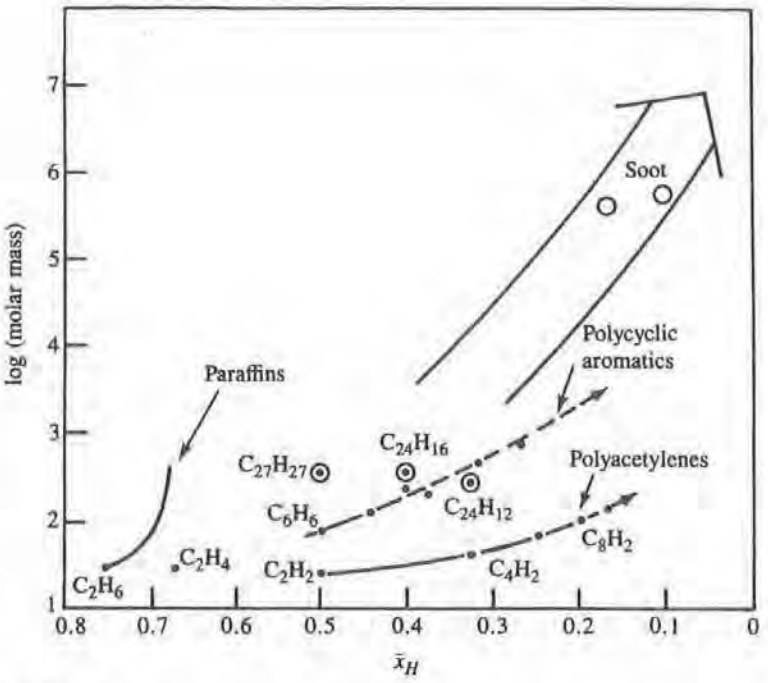


FIGURE 11-45
Paths to soot formation on plot of species molecular weight M versus hydrogen mole fraction $\tilde{x}_H$.[80]

growth nor purely PAH growth would lead to soot particles which have $\tilde{x}_H$ in the range 0.1 to 0.2. What is required is condensation of species with the right hydrogen content, or condensation of species with higher hydrogen content followed by dehydrogenation, or a combination of both these processes. Obviously some polyacetylenes and some PAH can satisfy these requirements, as can saturated platelets (e.g., $C_{27}H_{27}$; see Sec. 11.5.2). Surface growth reactions lead to an increase in the amount of soot (F_v) but the number of particles (N) remains unchanged. The opposite is true for growth by coagulation, where the particles collide and coalesce, which decreases N with F_v constant. Once surface growth stops, continued aggregation of particles into chains and clusters can occur.

These stages of particle generation and growth constitute the soot formation process. At each stage in the process oxidation can occur where soot or soot precursors are burned in the presence of oxidizing species to form gaseous products such as CO and CO_2. The eventual emission of soot from the engine will depend on the balance between these processes of formation and burnout. The emitted soot is then subject to a further mass addition process as the exhaust gases cool and are diluted with air. Adsorption into the soot particle surface and condensation to form new particles of hydrocarbon species in the exhaust gases occurs in the exhaust system and in the dilution tunnel which simulates what happens in the atmosphere. Figure 11-46 illustrates the relationship between these processes.[70] Although they are illustrated as discrete processes, there is some overlap, and they may occur concurrently in a given elemental mixture region within the diesel combustion chamber. Of course, due also to the nonhomogeneous nature of the mixture and the duration of fuel injection and its overlap with combustion, at any given time different processes are in progress in different regions or packets of fluid. The fundamentals of each of these processes will now be reviewed.

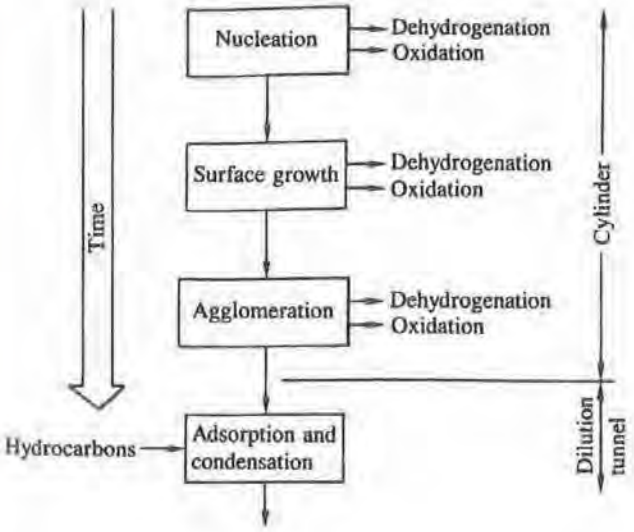


FIGURE 11-46
Processes leading to net production of diesel particulates.[70]

SOOT PARTICLE FORMATION. Empirically, it has been found useful to define the composition of the fuel-oxidizer mixture at the onset of soot formation in flames by the carbon/oxygen ratio. Equilibrium considerations indicate that soot formation should occur when, in

$$C_m H_n + yO_2 \rightarrow 2_y CO + \frac{n}{2} H_2 + (m - 2y)C_S \tag{11.35}$$

m becomes larger than $2y$: i.e., the C/O ratio exceeds unity. The corresponding fuel/air equivalence ratio is given by

$$\phi = 2\left(\frac{C}{O}\right)(1 + \delta) \tag{11.36}$$

where $\delta = n/(4m)$; ϕ is 3 for $(C/O) = 1$, with $n/m = 2$. The experimentally observed critical C/O ratios are less than unity, however, varying with fuel composition and details of the experimental setup from about 0.5 to 0.8. The critical C/O ratio for soot formation increases with increasing temperature but is only weakly dependent on pressure. Beyond the carbon formation limit, the yield of soot increases rapidly with increasing C/O ratio and is strongly enhanced by increasing pressure.[80]

It is obvious that soot formation is a nonequilibrium process. Yet despite decades of study, the precise details of the chemistry leading to the establishment of soot nuclei still elude investigators. Several different theories have been advanced to explain the pyrolysis process—the extensive decomposition and atomic rearrangement of the fuel molecules—that culminates in nucleation. Reviews of these theories can be found in Refs. 73, 80, and 81. Often-cited mechanisms are thermal cracking that results in fragmentation of fuel molecules into smaller ones, condensation reactions and polymerization that result in larger molecules, and dehydrogenation that lowers the H/C ratio of the hydrocarbons destined to become soot. Three different paths to the production of soot appear to exist, depending on the formation temperature. At the lowest temperatures ($\lesssim$1700 K) only aromatics or highly unsaturated aliphatic compounds of high molecular weight are very effective in forming solid carbon through pyrolysis. At intermediate temperatures typical of diffusion flames ($\gtrsim$1800 K), all normally used hydrocarbon fuels produce soot if burned at sufficiently rich stoichiometry, but appear to do so by following a different path. At very high temperatures, above the range of interest for diesel combustion, a third nucleation process seems likely that involves carbon vapor.[70]

A simple mechanistic model for nucleation in the low and intermediate temperature ranges which has considerable experimental support for its basic features has been advanced by Graham et al.[82] It is illustrated in Fig. 11-47. At low temperatures, an aromatic hydrocarbon can produce soot via a relatively fast direct route that involves condensation of the aromatic rings into a graphitelike structure. Above about 1800 K, however, a slower, less-direct route is favored that entails ring breakup into smaller hydrocarbon fragments. These fragments then polymerize to form larger unsaturated molecules that ultimately produce

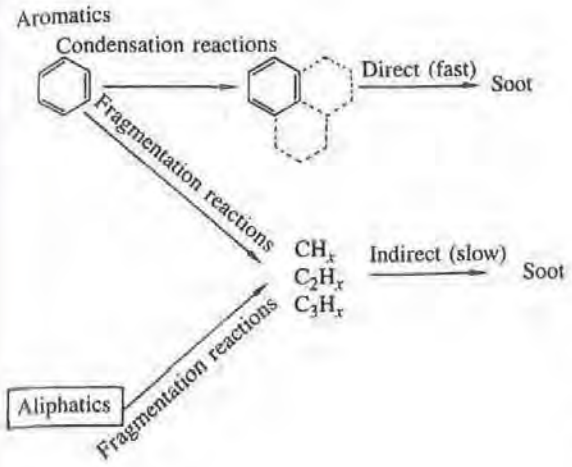


FIGURE 11-47
Mechanistic model for formation of soot from aromatic and aliphatic hydrocarbon compounds.[70]

soot nuclei. Aliphatic molecules can only follow this latter less-direct route. Experimental measurements in flames suggest that polyunsaturated hydrocarbon compounds are involved in nucleation, and acetylenes and polyacetylenes have been detected that decrease in concentration as the mass of carbon formed increases. Such observations fit the indirect path in Fig. 11-47. Results of studies of pyrolysis of benzene between 1300 and 1700 K support a physical condensation mechanism for the low-temperature path. This mechanism begins with the transformation of the initial hydrocarbon into macromolecules by a gas-phase reaction. The partial pressure of these macromolecules grows until supersaturation becomes sufficient to force their condensation into liquid microdroplets. These become nuclei, and subsequently formed gaseous macromolecules then contribute to nuclei growth.[70]

SOOT PARTICLE GROWTH. Nucleation produces a large number of very small particles with an insignificant soot loading. The bulk of the solid-phase material is generated by surface growth, which involves the gas-phase deposition of hydrocarbon intermediates on the surfaces of the spherules that develop from the nuclei. A qualitative description of the changes that occur as a function of time in a premixed flame during nucleation and surface growth is shown in Fig. 11-48. The soot fraction F_V, in units of soot volume per unit volume of gas, is related to the number density N and the volume-mean diameter of the soot particles by

$$F_V = \frac{\pi}{6} N d^3 \tag{11.37}$$

d is the actual diameter of the spherules, or the diameter of a sphere of equivalent volume to an agglomerated particle. The rate of change of particle number density with time t can be written

$$\frac{dN}{dt} = \dot{N}_n - \dot{N}_a \tag{11.38}$$

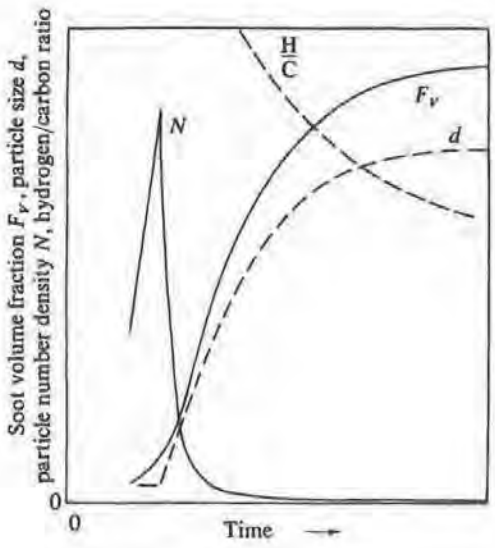


FIGURE 11-48
Variation in soot volume fraction F_V, particle number density N, particle size d, and soot hydrogen/carbon ratio with time in a flame.[70]

where $\dot{N}_n$ is the rate at which fresh nuclei appear and $\dot{N}_a$ is the rate of agglomeration of spherules or particles that collide and stick. At the peak of the N curve, $\dot{N}_n = \dot{N}_a$. To the left of the peak, $\dot{N}_n > \dot{N}_a$, the particle diameter remains essentially constant at the minimum detectable diameter and the (small) rise in soot volume is dominated by nucleation. To the right of the peak in the N curve, $\dot{N}_a > \dot{N}_n$. The number of agglomerating collisions is high because of the high number density; at the same time nucleation ends because there is enough dispersed surface area for gaseous deposition of hydrocarbon intermediates so the probability of generating new nuclei falls to zero. With nucleation halted slightly to the right of the N curve peak, all the subsequent increase in soot volume fraction (the majority) stems from surface growth. To the right of the N curve peak, the number density falls in the case illustrated by three orders of magnitude. This is the result of agglomeration, which is responsible for a portion of the increase in particle diameter. Agglomeration does not contribute to the rise in soot volume fraction, F_V. Surface growth that takes place on nuclei and on spherules is responsible for forming the concentric shells (somewhat distorted and warped) that constitute the outer portions of spherules and which are distinct from the less-organized spherule center (see Figs. 11-40 and 11-41). Surface growth on agglomerated particles may partly fill in the crevices at the junctures of adjoining spherules to provide the nodular structure evident in Fig. 11-40.[70]

Once particles have formed, interparticle collisions can lead to agglomeration, thereby decreasing the number of particles and increasing their size. Three types of agglomeration have been identified in soot formation. During the early stages of particle growth, collision of two spherical particles may result in their *coagulation* into a single spheroid. This is easy to visualize in hydrocarbon pyrolysis where the beginnings of a soot particle may have the viscosity of a tarry liquid.[70] Also, when the individual particles are small, rapid surface growth will quickly restore the original spherical shape.[73] This process occurs up to diameters of about 10 nm. On the other hand, if spherules have solidified before colli-

sion and surface growth rates have diminished, the resulting particles resemble a cluster in which the original spherules retain much of their individual identity. After surface growth essentially ceases, continued coalescence of the soot particles results in the formation of chainlike structures of discrete spherules. This suggests electrostatic forces are significant. Positive charge measured on these particle chains is claimed to be the cause of their chainlike structure.[70, 73] This latter coalescence once surface growth ceases is termed *aggregation.*

It has been shown experimentally that during coagulation the rate of decrease of particle number density was proportional to the product of a coagulation coefficient and the square of the number density:

$$-\frac{dN}{dt} = KN^2 \tag{11.39}$$

This is the Smoluchowski equation for coagulation of a liquid colloid. Based on brownian motion, this equation is applicable when the Knudsen number (ratio of mean free path to particle diameter) exceeds 10. K depends on such factors as particle size and shape, size distribution, and the temperature, pressure, and density of the gas. Equation (11.39) has been used to predict coagulation rates in low-pressure sooting flames.[73, 80] It has also been modified so that it applies where the particle size and mean free path are comparable by using a more complex expression for K (see Ref. 83). These studies show that under conditions approximating those in engine flames, the fraction of the initial number density N_0 remaining at time t is given approximately by

$$\frac{N}{N_0} \approx (KN_0 t)^{-1} \tag{11.40}$$

Thus as t increases, N/N_0 decreases rapidly. Although these coagulation calculations are simplistic (in that many of the assumptions made are not strictly valid since soot particles are not initially distributed homogeneously in the combustion space, they are not monodisperse, and surface growth and oxidation may be taking place during agglomeration), an overall conclusion is that the rate of coagulation of spherules and particles to larger particles is very sensitive to number density. Thus the number of particles decreases rapidly with advancing crank angle in the diesel engine during the early part of the expansion process (see Fig. 11-44) and agglomeration is essentially complete well before the exhaust valve opens.

Throughout the soot formation process in a flame, the H/C ratio of the hydrocarbons formed in the pyrolysis and nucleation process and of the soot particles continually decreases. The H/C ratio decreases from a value of about 2, typical of common fuels, to of order 1 in the youngest soot particles that can be sampled, and then to 0.2 to 0.3 once surface growth has ceased in the fully agglomerated soot.[80] The latter stages of this process are indicated in Fig. 11-48. The addition of mass to the soot particles occurs by reaction with gas-phase molecules. The reacting gas-phase hydrocarbons appear to be principally acetylenes, with larger polymers adding faster than the smaller. Small polyacetylenes

undergo further polymerization in the gas phase, presumably by the same mechanism leading to nucleation. As a result of preferential addition of the larger polymers, the H/C ratio of the particles decreases toward its steady-state value. Thus most of the polyacetylenes added must be of very high molecular weight or dehydrogenation must also take place.[73, 80]

11.5.5 Soot Oxidation

In the overall soot formation process, shown schematically in Fig. 11-46, oxidation of soot at the precursor, nuclei, and particle stages can occur. The engine cylinder soot-concentration data reviewed in Sec. 11.5.3 indicate that a large fraction of the soot formed is oxidized within the cylinder before the exhaust process commences. In the discussion of diesel combustion movies in Sec. 10.3.1, dark brown regions were observed in the color photographs (see color plate, Fig. 10-4); these were interpreted as soot particle clouds, and were seen to be surrounded by a diffusion flame which appeared white from the luminosity of the high-temperature soot particles consumed in this flame. As air mixed with this soot-rich region, the white flame eradicated the dark soot clouds as the particles were burned up.

In general, the rate of heterogeneous reactions such as the oxidation of soot depends on the diffusion of reactants to and products from the surface as well as the kinetics of the reaction. For particles less than about 1 μm diameter, diffusional resistance is minimal. The soot oxidation process in the diesel cylinder is kinetically controlled, therefore, since particle sizes are smaller than this limit. There are many species in or near the flame that could oxidize soot: examples are O_2, O, OH, CO_2, and H_2O. Recent reviews of soot formation[70, 73, 80] have concluded that at high oxygen partial pressures, soot oxidation can be correlated with a semiempirical formula based on pyrographite oxidation studies. For fuel-rich and close-to-stoichiometric combustion products, however, oxidation by OH has been shown to be more important than O_2 attack, at least at atmospheric pressure.

It is argued on the basis of structural similarities that the rates of oxidation of soot and of pyrographites should be the same. This is a significant simplification. It has proved difficult to follow the oxidation of soot aerosols in flames, and if care is taken to avoid diffusional resistance, studies of bulk samples of pyrographite can then be used as a basis for understanding soot oxidation. The semiempirical formula of Nagle and Strickland-Constable has been shown[84] to correlate pyrographite oxidation for oxygen partial pressures $p_{O_2} < 1$ atm and temperatures between 1100 and 2500 K. This formula is based on the concept that there are two types of sites on the carbon surface available for O_2 attack. For the more reactive type A sites, the oxidation rate is controlled by the fraction of sites not covered by surface oxides (and therefore is of mixed order, between 0 and 1 in p_{O_2}). Type B sites are less reactive, and react at a rate which is first order in p_{O_2}. A thermal rearrangement of A sites into B sites is also allowed (with rate constant k_T). A steady-state analysis of this mechanism gives a surface mass oxi-

TABLE 11.10
Rate constants for Nagle and Strickland-Constable soot oxidation mechanism[84]

Rate constant	Units
$k_A = 20 \exp(-15{,}100/T)$	$g/cm^2 \cdot s \cdot atm$
$k_B = 4.46 \times 10^{-3} \exp(-7640/T)$	$g/cm^2 \cdot s \cdot atm$
$k_T = 1.51 \times 10^5 \exp(-48{,}800/T)$	$g/cm^2 \cdot s$
$k_Z = 21.3 \exp(2060/T)$	atm^{-1}

dation rate w (g C/cm$^2 \cdot$ s):

$$\frac{w}{12} = \left(\frac{k_A p_{O_2}}{1 + k_Z p_{O_2}}\right) x + k_B p_{O_2}(1 - x) \tag{11.41}$$

where x is the fraction of the surface occupied by type A sites and is given by

$$x = \left(1 + \frac{k_T}{p_{O_2} k_B}\right)^{-1} \tag{11.42}$$

The empirical rate constants determined by Nagle and Strickland-Constable for this model are listed in Table 11.10. According to this mechanism, the reaction is first order at low oxygen partial pressures, but approaches zero order at higher pressures. At a given oxygen pressure, the rate initially increases exponentially with temperature (equivalent activation energy is k_A/k_Z or 34,100 cal/mol). Beyond a certain temperature the rate decreases as the thermal rearrangement favors formation of less reactive B sites. When, at sufficiently high temperature, the surface is completely covered with B sites, the rate is first order in oxygen partial pressure and increases again with temperature.[80]

Park and Appleton[84] have compared this formula with oxidation rate data obtained from pyrographite samples, carbon black particles, and with the available flame soot oxidation data. Figure 11-49 shows both the soot oxidation rate predicted by Eqs. (11.41) and (11.42) as a function of temperature and oxygen partial pressure, and the above-mentioned data. The formula correlates the data shown to within a factor of 2. Under diesel engine conditions, the O_2 partial pressure can be high ($\sim$several atmospheres), as can the temperatures of close-to-stoichiometric mixtures ($\lesssim$2800 K).

Equations (11.41) and (11.42) have been used to estimate the amount of soot that can be oxidized in a typical IDI diesel engine. It was assumed that soot was present in stoichiometric combustion products at selected times in the cycle and that mixing with air leaned out the burned gas mixture at different rates until the overall fuel/air equivalence ratio was reached. The surface recession rate during this process was computed. Figure 11-50 shows sample results at an engine speed of 1600 rev/min and an overall cylinder equivalence ratio of 0.58. Fast, intermediate, and slow mixing occurred in 30, 70, and 140°, respectively. The surface recession rate rises to a maximum as p_{O_2} increases and then decreases as the

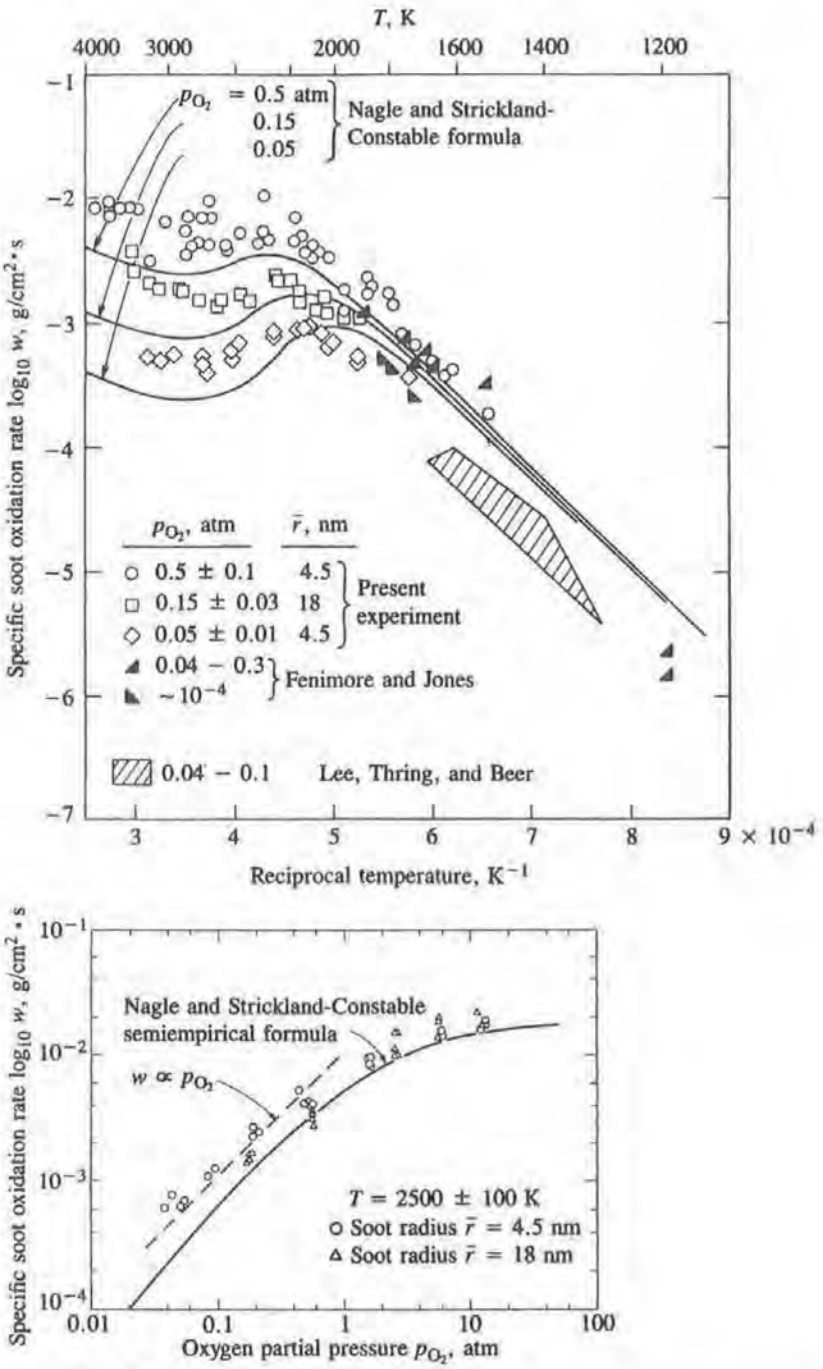


FIGURE 11-49
Specific soot oxidation rate measurements and predictions as a function of temperature and oxygen partial pressure.[84]

falling gas temperature more than offsets the increasing oxygen concentration. While the shape of the recession rate versus time curves depends on the mixing rate, the total amount of carbon burned (the area under each curve in Fig. 11-50*b*) is about the same (0.1 μg/mm^2). However, the point in the cycle at which the soot-containing burned gas mixture passes through stoichiometric is much

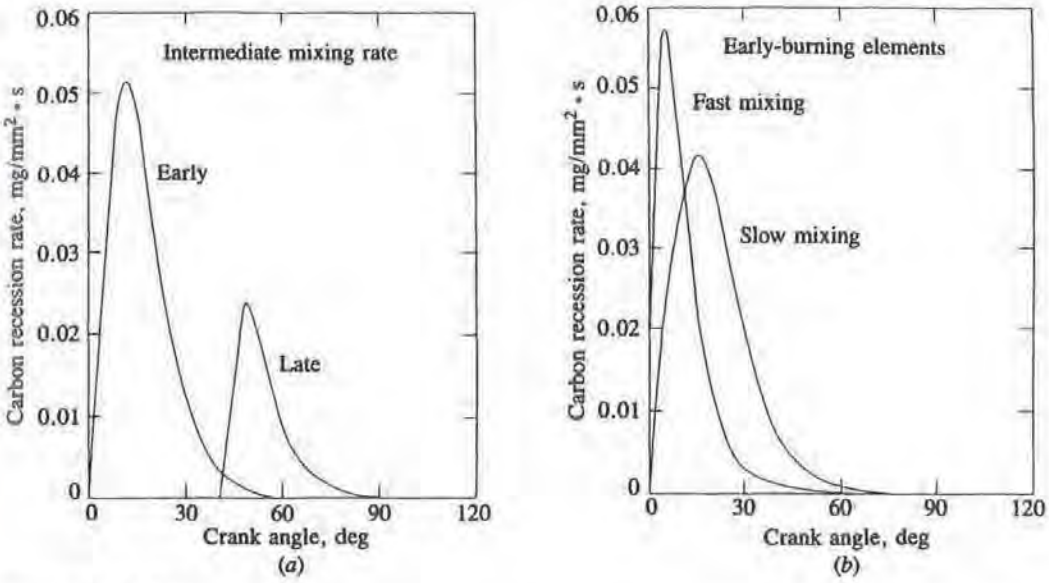


FIGURE 11-50
Soot particle burnup rate in diesel combustion environment: (*a*) in early- and late-burned fuel-air elements with intermediate mixing rate; (*b*) for fast and slow mixing for early-burning elements.[83]

more important. For the late mixing element shown (mixing lean of stoichiometric at 40° ATC), the total carbon mass oxidized is only 40 percent of that for the early mixing calculation. This is due primarily to the decreasing gas temperatures as the expansion stroke proceeds, and not the longer time available for burnup.[83]

For a spherical particle, the mass burning rate w (g/cm^2 · s) can be converted to a surface recession rate using

$$\frac{dr}{dt} = \frac{-w}{\rho}$$

where ρ is the density (≈ 2 g/cm^3). The integrated values of $w(t)$ when divided by ρ then give the maximum radius of a soot particle that can be burned up. Integrated values of 0.1 μg/mm^2 (estimated for TC start of burnup) correspond to a radius of about 50 nm or diameter of 100 nm. Individual spherule diameters are about 30 nm, so soot which mixes with air early in the expansion stroke is likely to be fully burned. Thus the soot present in the exhaust would be expected to come from regions which mix with air too late for the oxidation rate to be sufficient for particle burnup.

Agglomeration will have an indirect influence on the amount of soot oxidized through its effect on surface area. In the limiting case of a spherical cluster, n monodisperse spherules ($10 \lesssim n \lesssim 100$) can be imagined as compacted into a single solid sphere of equal volume. Alternatively, the same n spherules can be imagined compacted into a cylinder of diameter equal to that of the original spherules. Since oxidative attack is essentially an exterior surface phenomenon, the surface/volume ratio is the appropriate measure of the effect of particle shape on soot mass burnup rate. It can be shown that the surface/volume ratios for the

single sphere, cylinder, and individual spherule are in the ratio $n^{-1/3}$, $\frac{2}{3}$, and 1, respectively. Thus agglomeration will decrease the relative oxidation rate. In the limit spherical clusters are less desirable than a chain; the larger the cluster the bigger the relative reduction in surface area. However, the densely packed spherule limit does not appear to be approached in practice. A specific surface area, of about 200 m^2/g for diesel soot, has been measured.[85] A smooth-surfaced 30-nm diameter spherule with a 2-g/cm^3 density has a surface/mass ratio of 100 m^2/g; the measured value is about twice this value, indicating low porosity and an agglomerate structure which is loosely rather than densely packed.[83]

Equation (11.41) shows a maximum recession rate in combustion products corresponding to a fuel/air equivalence ratio of about 0.9. Recent evidence shows that in an atmospheric pressure environment with rich and close-to-stoichiometric combustion products where O_2 mole fractions are low, oxidation by OH radical attack is much more significant than oxidation by O or O_2. The OH radical may be important in oxidizing soot in the flame zone under close-to-stoichiometric conditions.

11.5.6 Adsorption and Condensation

The final process in the particulate formation sequence illustrated in Fig. 11-46 is adsorption and condensation of hydrocarbons. This occurs primarily after the cylinder gases have been exhausted from the engine, as these exhaust gases are diluted with air. In the standard particulate mass emission measurement process this occurs in a dilution tunnel which simulates approximately the actual atmospheric dilution process. A diluted exhaust gas sample is filtered to remove the particulate. After equilibrating the collection filter at controlled conditions to remove water vapor, the particulate mass is obtained by weighing. In the prescribed EPA procedure, the filter temperature must not exceed 52°C. For a given exhaust gas temperature, the filter (and sample) temperature depends on the dilution ratio, as shown in Fig. 11-51.

The effect of the dilution ratio (and the dependent sample temperature) on collected particulate mass is shown in Fig. 11-52 for a standard dilution tunnel,

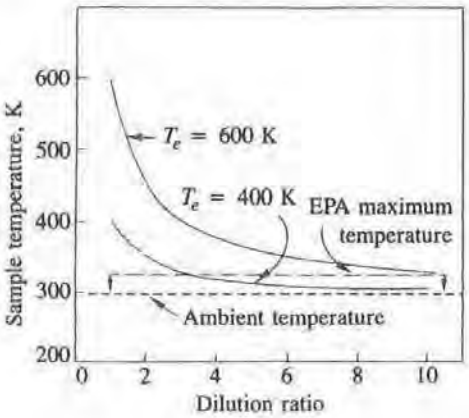


FIGURE 11-51
Effect of exhaust gas dilution ratio on the temperature of the collected particulate sample as a function of engine exhaust temperature T_e.[70]

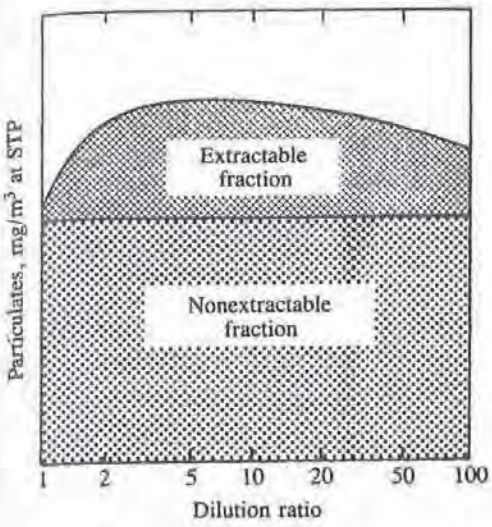


FIGURE 11-52
Typical effect of dilution ratio on particulate mass emission and its partitioning between extractable and nonextractable fractions.[70]

where the total sample is partitioned into extractable and nonextractable fractions. The nonextractable fraction is the carbonaceous soot generated during combustion and is not affected by the dilution process. With no dilution (dilution ratio of unity) the difference between the total and nonextractable mass is small; the bulk of the extractable fraction is acquired after the exhaust gas is mixed with dilution air. Extensive studies of this dilution process have shown that both adsorption and condensation occur. Adsorption involves the adherence of molecules of unburned hydrocarbons to the surfaces of the soot particles by chemical or physical (van der Waals) forces. This depends on the fraction of the available particle surface area occupied by hydrocarbons and on the partial pressure of the gaseous hydrocarbons that drives the adsorption process. As the dilution ratio increases from unity, the effect of decreasing temperature on the number of active sites dominates and, as shown in Fig. 11-52, the extractable fraction increases. At high dilution ratios, the sample temperature becomes insensitive to the dilution ratio (see Fig. 11-51) but the decreasing hydrocarbon partial pressure causes the extractable mass to fall again. Condensation will occur whenever the vapor pressure of the gaseous hydrocarbon exceeds its saturated vapor pressure. Increasing dilution decreases hydrocarbon concentrations and hence vapor pressure. However, the associated reduction in temperature does reduce the saturation pressure. High exhaust concentrations of hydrocarbons are the conditions where condensation is likely to be most significant, and the hydrocarbons most likely to condense are those of low volatility. Sources of low-volatility hydrocarbons are the high-boiling-point end of the fuel, unburned hydrocarbons that have been pyrolyzed but not consumed in the combustion process, and the lubricating oil.[70]

Experiments with a passenger car IDI diesel, where the oil was tagged with a radioactive tracer, have shown that the oil can contribute from 2 to 25 percent of the total particulate mass, with the greatest contribution occurring at high speed. On average, over half of the extractable mass was traceable to the oil. All the material traceable to the oil was found in the extractable fraction, indicating that the oil did not participate in the combustion process. However, the oil is not

always a significant contributer: in another engine, fuel was the dominant source of extractable material.[70, 71]

11.6 EXHAUST GAS TREATMENT

11.6.1 Available Options

Our discussion so far has focused on *engine* emissions. Further reductions in emissions can be obtained by removing pollutants from the exhaust gases in the engine exhaust system. Devices developed to achieve this result include catalytic converters (oxidizing catalysts for HC and CO, reducing catalysts for NO_x, and three-way catalysts for all three pollutants), thermal reactors (for HC and CO), and traps or filters for particulates.

The temperature of exhaust gas in a spark-ignition engine can vary from 300 to 400°C during idle to about 900°C at high-power operation. The most common range is 400 to 600°C. Spark-ignition engines usually operate at fuel/air equivalence ratios between about 0.9 and 1.2 (see Sec. 7.1). The exhaust gas may therefore contain modest amounts of oxygen (when lean) or more substantial amounts of CO (when rich). In contrast, diesel engines, where load is controlled by the amount of fuel injected, always operate lean. The exhaust gas therefore contains substantial oxygen and is at a lower temperature (200 to 500°C). Removal of gaseous pollutants from the exhaust gases after they leave the engine cylinder can be either thermal or catalytic. In order to oxidize the hydrocarbons in the gas phase without a catalyst, a residence time of order or greater than 50 ms and temperatures in excess of 600°C are required. To oxidize CO, temperatures in excess of 700°C are required. Temperatures high enough for some homogeneous thermal oxidation can be obtained by spark retard (with some loss in efficiency) and insulation of the exhaust ports and manifold. The residence time can be increased by increasing the exhaust manifold volume to form a *thermal reactor* (see Sec. 11.6.3). However, this approach has limited application.

Catalytic oxidation of CO and hydrocarbons in the exhaust can be achieved at temperatures as low as 250°C. Thus effective removal of these pollutants occurs over a much wider range of exhaust temperatures than can be achieved with thermal oxidation. The only satisfactory method known for the removal of NO from exhaust gas involves catalytic processes. Removal of NO by catalytic oxidation to NO_2 requires temperatures <400°C (from equilibrium considerations) and subsequent removal of the NO_2 produced. Catalytic reaction of NO with added ammonia NH_3 is not practical because of the transient variations in NO produced in the engine. Reduction of NO by CO, hydrocarbons, or H_2 in the exhaust to produce N_2 is the preferred catalytic process. It is only feasible in spark-ignition engine exhausts. Use of catalysts in spark-ignition engines for CO, HC, and NO removal has become widespread. Catalysts are discussed in Sec. 11.6.2.

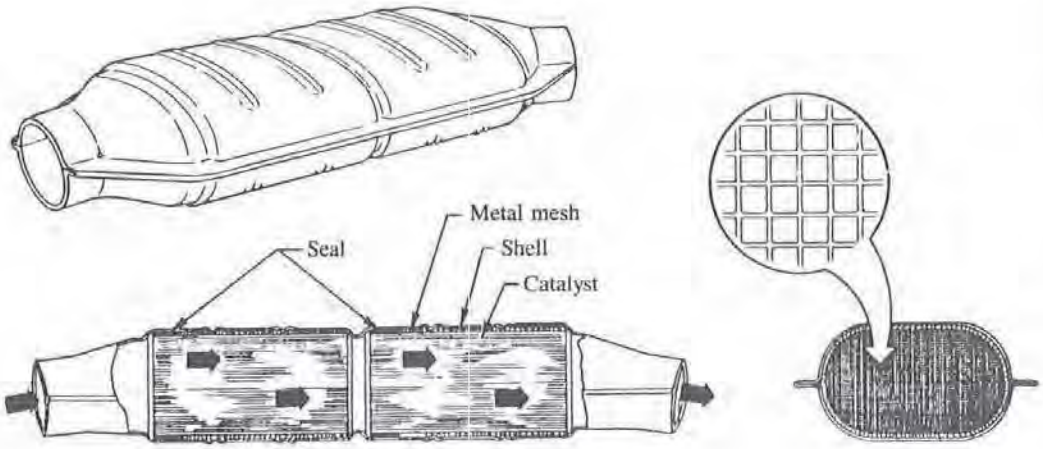
Particulates in the exhaust gas stream can be removed by a trap. Due to the small particle size involved, some type of filter is the most effective trapping

method. The accumulation of mass within the trap and the increase in exhaust manifold pressure during trap operation are major development problems. Diesel particulates, once trapped, can be burned up either by initiating oxidation within the trap with an external heat source or by using a trap which contains catalytically active material. The operation of particulate traps is reviewed briefly in Sec. 11.6.4.

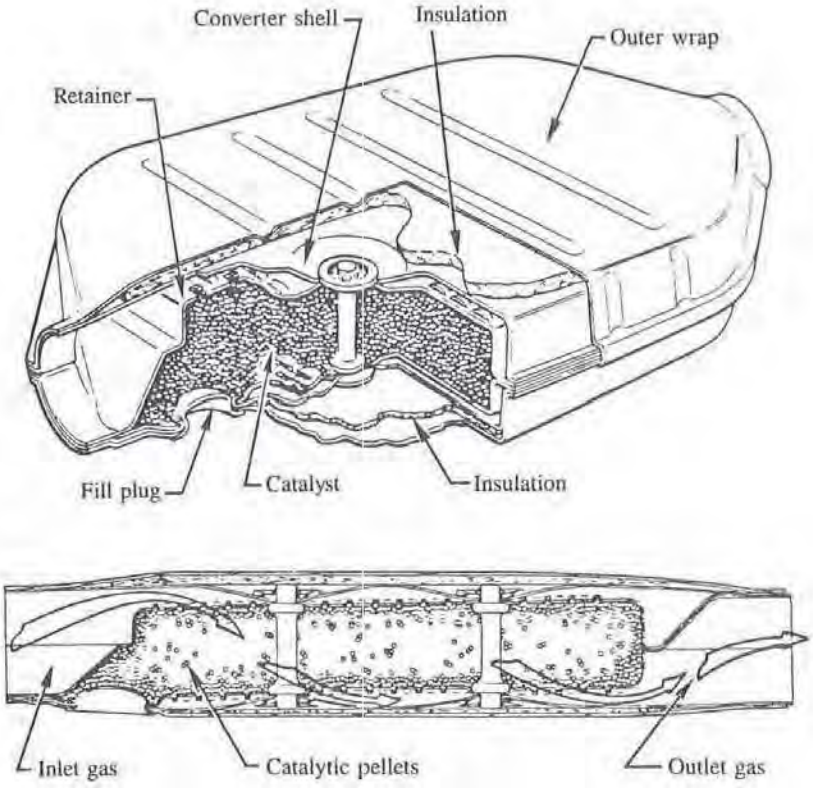
11.6.2 Catalytic Converters

The catalytic converters used in spark-ignition engines consist of an active catalytic material in a specially designed metal casing which directs the exhaust gas flow through the catalyst bed. The active material employed for CO and HC oxidation or NO reduction (normally noble metals, though base metals oxides can be used) must be distributed over a large surface area so that the mass-transfer characteristics between the gas phase and the active catalyst surface are sufficient to allow close to 100 percent conversion with high catalytic activity. The two configurations commonly used are shown in Fig. 11-53. One system employs a ceramic honeycomb structure or monolith held in a metal can in the exhaust stream. The active (noble metal) catalyst material is impregnated into a highly porous alumina washcoat about 20 μm thick that is applied to the passageway walls. The typical monolith has square-cross-section passageways with inside dimensions of $\sim$1 mm separated by thin (0.15 to 0.3 mm) porous walls. The number of passageways per square centimeter varies between about 30 and 60. The washcoat, 5 to 15 percent of the weight of the monolith, has a surface area of 100 to 200 m^2/g. The other converter design uses a bed of spherical ceramic pellets to provide a large surface area in contact with the flow. With pellet catalysts, the noble metal catalyst is impregnated into the highly porous surface of the spherical alumina pellets (typically 3 mm diameter) to a depth of about 250 μm. The pellet material is chosen to have good crush and abrasion resistance after exposure to temperatures of order 1000°C. The gas flow is directed down through the bed as shown to provide a large flow area and low pressure drop. The gas flow is turbulent which results in high mass-transfer rates; in the monolith catalyst passageways, it is laminar.

OXIDATION CATALYSTS. The function of an oxidation catalyst is to oxidize CO and hydrocarbons to CO_2 and water in an exhaust gas stream which typically contains $\sim$12 percent CO_2 and H_2O, 100 to 2000 ppm NO, $\sim$20 ppm SO_2, 1 to 5 percent O_2, 0.2 to 5 percent CO, and 1000 to 6000 ppm C_1 HC, often with small amounts of lead and phosphorus. About half the hydrocarbons emitted by the SI engine are unburned fuel compounds. The saturated hydrocarbons (which comprise some 20 to 30 percent) are the most difficult to oxidize. The ease of oxidation increases with increasing molecular weight. Sufficient oxygen must be present to oxidize the CO and HC. This may be supplied by the engine itself



(*a*)



(*b*)

FIGURE 11-53
Catalytic converters for spark-ignition engine emission control: (*a*) monolith design; (*b*) pelletized design.[62]

running lean of stoichiometric or with a pump that introduces air into the exhaust ports just downstream of the valve. Venturi air addition into the exhaust port using the pressure pulsations generated by the exhaust process can also be used to add the required air.

Because of their high intrinsic activity, noble metals are most suitable as the catalytic material. They show higher specific activity for HC oxidation, are more thermally resistant to loss of low-temperature activity, and are much less deactivated by the sulfur in the fuel than base metal oxides. A mixture of platinum (Pt) and palladium (Pd) is most commonly used. For the oxidation of CO, olefins, and methane, the specific activity of Pd is higher than that of Pt. For the oxidation of aromatic compounds, Pt and Pd have similar activity. For oxidation of paraffin hydrocarbons (with molecular size greater than C_3), Pt is more active than Pd. Pure noble metals sinter rapidly in the 500 to 900°C temperature range experienced by exhaust catalysts. Since catalytic behavior is manifested exclusively by surface atoms, the noble metals are dispersed as finely as possible on an inert support such as γ-A_2O_3 which prevents particle-to-particle metal contact and suppresses sintering. The particle size of the noble metal particles in a fresh catalyst is less than 50 nm. This can increase to $\sim$100 nm when the catalyst is exposed to the high temperatures of the exhaust in vehicle operation. Typical noble metal concentrations in a commercial honeycomb catalyst are between 1 and 2 g/dm^3 of honeycomb volume, with Pt/Pd = 2 on a weight basis. As a rough rule of thumb, the ceramic honeycomb volume required is about half the engine displaced volume. This gives a space velocity through the converter (volume flow rate of exhaust divided by converter volume) over the normal engine operating range of 5 to 30 per second.[68]

The *conversion efficiency* of a catalyst is the ratio of the rate of mass removal in the catalyst of the particular constituent of interest to the mass flow rate of that constituent into the catalyst: e.g., for HC,

$$\eta_{cat} = \frac{\dot{m}_{HC,in} - \dot{m}_{HC,out}}{\dot{m}_{HC,in}} = 1 - \frac{\dot{m}_{HC,out}}{\dot{m}_{HC,in}} \tag{11.43}$$

The variation of conversion efficiency of a typical oxidizing catalytic converter with temperature is shown in Fig. 11-54. At high enough temperatures, the steady-state conversion efficiencies of a new oxidation catalyst are typically 98 to 99 percent for CO and 95 percent or above for HC. However, the catalyst is ineffective until its temperature has risen above 250 to 300°C. The term *light-off temperature* is often used to describe the temperature at which the catalyst becomes more than 50 percent effective.

The above numbers apply to fresh noble metal oxidation catalysts; as catalysts spend time in service their effectiveness deteriorates. Catalysis involves the adsorption of the reactants onto surface sites of high activity, followed by chemical reaction, then desorption of the products. Catalyst degradation involves both the deactivation of these sites by catalyst poisons and a reduction in the effective area of these sites through sintering. Poisoning affects both the warm-up and

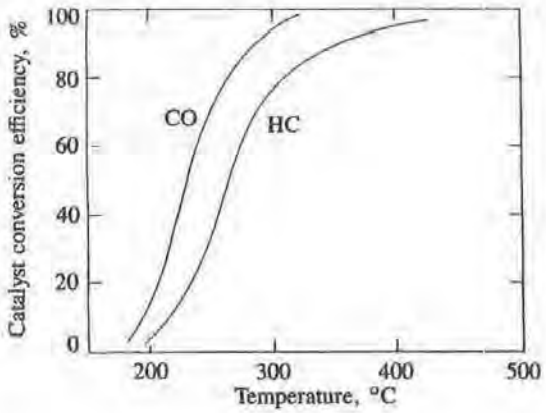


FIGURE 11-54
Conversion efficiency for CO and HC as a function of temperature for typical oxidizing catalytic converter.[62]

steady-state performance of the catalyst. When poisoning occurs, catalytic activity is impeded through prolonged contact with interfering elements that either physically block the active sites or interact chemically with the active material. The lead in fuel antiknock agents and the phosphorus in oil additives are the most important poisons. Though lead antiknock agents are not added to the gasoline used with catalyst-equipped vehicles, this "unleaded" fuel can be contaminated with small amounts ($\sim$10 mg Pb/dm^3) from the fuel distribution system. Between 10 and 30 percent of the lead in the fuel ends up on the catalyst. Its effect on catalyst conversion efficiency depends on the amount of lead on the catalyst, as shown in Fig. 11-55. Lead depresses the catalytic oxidation of HC to a greater extent than oxidation of CO. The oxidation activity of saturated hydrocarbons is particularly depressed. The extent of the poisoning that results from traces of critical elements in the fuel and oil depends on which elements are present and the amounts absorbed, as well as the composition of the catalyst and its operating conditions (especially its temperature).[68] Sintering is promoted by exposure of the catalyst to high operating temperatures. It involves the migration and agglomeration of sites, thus decreasing their active surface area. Sintering slows warm-up but has minimal effect on the steady-state conversion efficiency.

The oxidation kinetics of CO over Pt and Pd noble metal catalysts can be described by

$$\frac{d[\mathrm{CO}]}{dt} = \frac{K_1 p_{\mathrm{CO}} p_{\mathrm{O_2}}}{(1 + K_2 p_{\mathrm{CO}} + K_3 p_{\mathrm{HC}})^2 (1 + K_4 p_{\mathrm{NO}}^n)} \tag{11.44}$$

where K_1 to K_4 and n are constants at any given temperature, and p_{CO}, $p_{\mathrm{O_2}}$, p_{HC}, and p_{NO} are the partial pressures of carbon monoxide, oxygen, hydrocarbons, and nitric oxide, respectively. A similar relationship can be written for the olefinic and aromatic HC oxidation rate (these being the most reactive hydrocarbons). These relationships incorporate the fact that the rates of CO and HC oxidation are inhibited by high CO and reactive HC concentrations, and that NO concentrations in the range 0 to 1000 ppm strongly inhibit oxidation also. The oxidation rate of paraffin hydrocarbons varies with the first power of the HC partial pres-

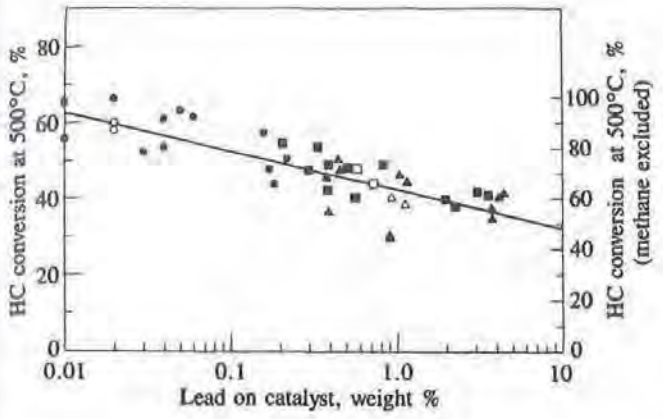


FIGURE 11-55
HC conversion efficiency as a function of lead concentration on catalyst. Total HC conversion on left; nonmethane HC conversion on right. 0.001–0.013 g Pb/dm^3 in fuel.[68]

sure, is inhibited by CO, olefins, and NO, and increases as the O_2 partial pressure is decreased to near-stoichiometric values.[68]

It will be apparent from the above that two extremely important considerations for successful use of catalysts for automotive applications are the test procedure that is used to measure emissions and the methods used to determine if the catalyst has the required durability. The U.S. Federal Test Procedure requires that the vehicle under test be at a temperature of 16 to 30°C for 12 hours prior to the test and that emissions are measured from the time the ignition key is turned on until the test has ended. In spark-ignition engines the mixture fed into the engine during start-up is enriched substantially (carburetors have a choke to accomplish this; additional fuel is injected with port or manifold fuel injection). The rationale is that if sufficient fuel is added to the inlet air, enough will evaporate to start the engine. However, until the rest of the fuel is consumed, the engine then runs rich and emits high concentrations of CO and HC. The catalyst is cold at this time, and until it warms up, these emissions will pass through without reaction. It is important that the catalyst be brought to its light-off temperature as quickly as possible (preferably in less than 60 s) and that mixture enrichment during start-up be held to a minimum. Thus catalysts should have low thermal inertia for rapid warm-up and low light-off temperatures for CO and HC, so they become effective quickly. The closer they are placed to the engine the faster they will reach light-off. However, they will then experience higher temperatures when fully warmed up and so be more susceptible to thermal degradation. While it is not too difficult to prepare catalysts that are highly effective when fresh, it is much more difficult to maintain effectiveness over extended mileage (50,000 miles) in which the catalyst is exposed to high temperatures and catalyst poisons. These can degrade both cold-start and warmed-up performance. Also, catalyst durability is affected by engine durability. Any engine malfunction that will expose the catalyst to excessive amounts of unburned fuel (such as ignition failure, misfire with too lean a mixture, or excessively rich operation) will severely overheat the catalyst.

Oxidation-catalyst-equipped vehicles may emit sulfuric acid aerosol. Unleaded gasoline contains 150 to 600 ppm by weight of S, which leaves the

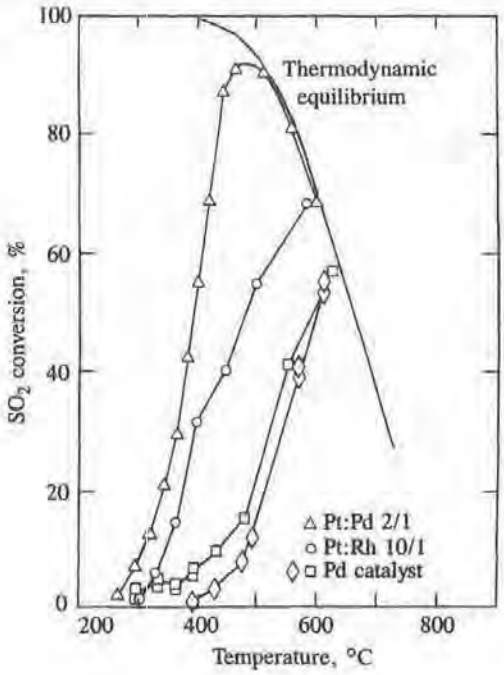


FIGURE 11-56
SO_2 conversion to SO_3 as a function of temperature with 5% O_2 concentration and no reducing gases present. Space velocity (volume flow per unit volume) ~ 10 s^{-1}. Results for Pt–Pd, Pt–Rh, and Pd catalysts.[68]

combustion chamber as SO_2. This SO_2 can be oxidized by the catalyst to SO_3 which combines with water at ambient conditions to form an H_2SO_4 aerosol. The SO_3 can be chemisorbed on the alumina catalyst surface; when large pellet beds are used, considerable storage of SO_3 at temperatures $<500°C$ can occur. At higher catalyst temperatures, this stored SO_3 is emitted as an SO_3–SO_2 mixture. SO_3 production can be controlled by lowering or raising the catalyst temperature. Figure 11-56 shows that at low temperatures SO_3 production is kinetically limited; at high temperatures SO_3 production is thermodynamically limited. Palladium and rhodium produce less SO_3 than Pt and have comparable HC and CO catalytic activity. By decreasing oxygen concentrations leaving the catalyst to ~1 percent, SO_3 production can be substantially reduced.[68]

NO CATALYSIS. NO is removed by reduction using the CO, hydrocarbons, and H_2 in the exhaust. The reactions are shown in Table 11.11. No catalyst is available for the decomposition of NO to O_2 and N_2 (thermodynamically favored at exhaust temperatures) which is sufficiently active for use in engine exhausts. NO reduction can be carried out under rich conditions where there is an excess of reducing species over oxidizing species. The catalyst used under these conditions is referred to as an *NO reduction catalyst*. Such a system requires a follow-up oxidation catalyst, together with addition of air from an air pump before the oxidation catalyst, to remove the remaining CO and hydrocarbons. Such a two-bed system can remove all three pollutants (NO, CO, and HC) from the exhaust. However, the rich operation necessary for NO reduction results in a fuel consumption penalty and constrains the performance of the NO catalyst since a fraction of the NO removed is converted to ammonia NH_3 rather than N_2. NH_3

TABLE 11.11
Possible NO reactions under reducing conditions[68]

1. $NO + CO \rightarrow \frac{1}{2}N_2 + CO_2$
2. $2NO + 5CO + 3H_2O \rightarrow 2NH_3 + 5CO_2$
3. $2NO + CO \rightarrow N_2O + CO_2$
4. $NO + H_2 \rightarrow \frac{1}{2}N_2 + H_2O$
5. $2NO + 5H_2 \rightarrow 2NH_3 + 2H_2O$
6. $2NO + H_2 \rightarrow N_2O + H_2O$

Reactions 3 and 6 occur at 200°C, which is below that usually found in auto exhausts.

formation under rich operation in the first bed must be small in this two-bed system because the second (oxidation) catalyst readily oxidizes NH_3 back to NO. Reduction of NO by CO or H_2 can be accomplished by base metal catalysts (e.g., CuO, NiO) in the temperature range 350 to 600°C. However, these catalyst materials are deactivated by sulfur and have shown limited thermal stability when used in vehicle exhausts. Alumina-supported noble metal catalysts reduce NO with CO–H_2 mixtures. Their NO-reduction activity is in the order Ru > Rh > Pd > Pt. Ruthenium (Ru) and rhodium (Rh) produce considerably less NH_3 than Pd or Pt under slightly rich conditions. While these properties make ruthenium a desirable NO catalyst, it forms volatile oxides under oxidizing conditions which results in loss of ruthenium from the alumina support.[68]

THREE-WAY CATALYSTS. If an engine is operated at all times with an air/fuel ratio at or close to stoichiometric, then both NO reduction and CO and HC oxidation can be done in a single catalyst bed. The catalyst effectively brings the exhaust gas composition to a near-equilibrium state at these exhaust conditions; i.e., a composition of CO_2, H_2O, and N_2. Enough reducing gases will be present to reduce NO and enough O_2 to oxidize the CO and hydrocarbons. Such a catalyst is called a *three-way catalyst* since it removes all three pollutants simultaneously. Figure 11-57 shows the conversion efficiency for NO, CO, and HC as a function of the air/fuel ratio. There is a narrow range of air/fuel ratios near stoichiometric in which high conversion efficiencies for all three pollutants are achieved. The width of this window is narrow, about 0.1 air/fuel ratios (7×10^{-3} in equivalence ratio units) for catalyst with high mileage use, and depends on catalyst formulation and engine operating conditions.

This window is sufficiently narrow to be beyond the control capabilities of an ordinary carburetor, though it can sometimes be achieved with sophisticated carburetors and fuel-injection systems. Thus closed-loop control of equivalence ratio has been introduced. An oxygen sensor in the exhaust is used to indicate whether the engine is operating on the rich or lean side of stoichiometric, and provide a signal for adjusting the fuel system to achieve the desired air-fuel mixture (see Sec. 7.4). Holding the equivalence ratio precisely on the chosen near-

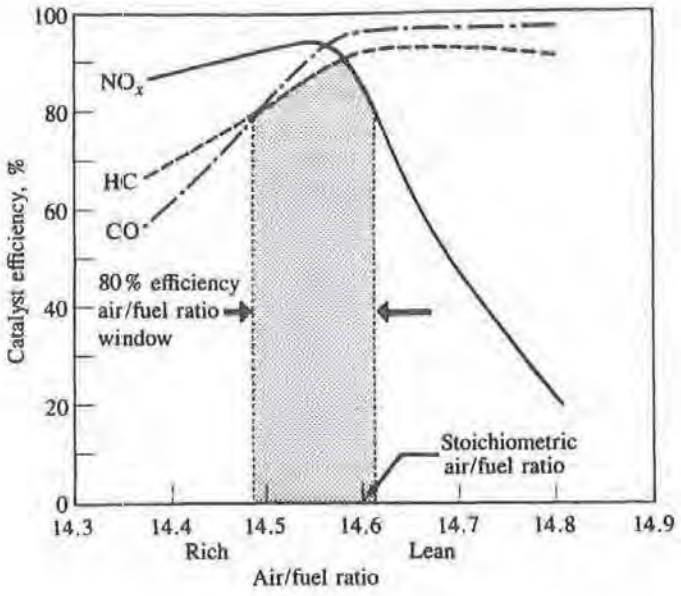


FIGURE 11-57
Conversion efficiency for NO, CO, and HC for a three-way catalyst as a function of exhaust gas air/fuel ratio.[68]

stoichiometric value is not a practical expectation of such a feedback system, and the equivalence ratio oscillates around the set point in an approximately periodic manner as the fuel flow is varied. Experimental data show that there is a considerable widening of the air/fuel ratio window where all three pollutants are effectively removed, with cyclic variation of the fuel flow. The maximum conversion in the middle of the window is reduced, however, from its value when there are no fluctuations. The effect of fluctuations depends on the frequency; frequencies of about 0.5 to 1 hertz are most effective and the usable window (at lower conversion efficiencies) can be broadened to about 1 air/fuel ratio. Some of the benefits of fluctuations in equivalence or air/fuel ratios are available even without any deliberate attempt to produce such variations with closed-loop feedback. Open-loop systems exhibit variations in the air/fuel ratio during normal vehicle operation.

Because of these cyclic variations in exhaust gas composition about a set point close to stoichiometric, it is desirable that the catalyst be able to reduce NO when a slight excess of oxygen is present (on the lean side) and remove CO and HC when there is a slight deficiency of oxygen (on the rich side). Rhodium is the principal ingredient used in commercial catalysts to remove NO. It is very active for NO reduction, is much less inhibited by CO and sulfur compounds, and produces less NH_3 than Pt. To remove NO under slightly lean-of-stoichiometric conditions, the catalyst must react the CO, H_2, or HC with NO rather than with O_2, as the exhaust gas passes through the catalyst bed. Rhodium shows some NO reduction activity slightly lean of stoichiometric. On the rich side, the three-way catalyst window is determined by hydrocarbon and CO removal. Platinum is most commonly used for HC and CO oxidation; it has good activity under stoichiometric and slightly lean conditions. When sufficient rhodium is present, the participation of Pt in NO removal is minimal. In the rich

regime, the three-way catalyst consumes all the oxygen that is present in the exhaust, and as a consequence removes an equivalent amount of CO, H_2, and hydrocarbons; it is thought that the H_2 is removed first. In addition, the water-gas shift reaction

$$CO + H_2O = H_2 + CO_2$$

and the steam-reforming reaction

$$\text{Hydrocarbon} + H_2O \rightarrow CO, CO_2, H_2$$

can consume CO and HC. The exhaust contains an H_2/CO ratio of about $\frac{1}{3}$ (see Sec. 4.9.1), where the equilibrium ratio at 500°C is about 4. Considerable CO removal can be expected if the water-gas shift equilibrium is approached. Platinum is active in promoting this equilibrium. For large molecular weight paraffin hydrocarbons, and for olefins and aromatic hydrocarbons, the equilibrium for the steam-reforming reactions lies to the right. This reaction can therefore lead to considerable hydrocarbon removal. Rhodium is particularly active in the steam-reforming reaction; platinum is also active.[68]

The conversions of NO, CO, and hydrocarbons in a three-way catalyst operated with cyclical variations in equivalence ratio are larger than estimates based on summation of steady-state values during the cycle. At least part of the improved performance is thought to be due to the ability of the catalyst to undergo reduction-oxidation reactions. Such a catalyst component is usually referred to as an oxygen-storage component. In its oxidized state it can provide oxygen for CO and hydrocarbon oxidation in a rich exhaust gas environment, and in the process be reduced. When the exhaust cycles to lean conditions, this reduced component can react with O_2 or NO (which removes NO directly or indirectly by reducing the O_2 concentration). The oxidized component can then oxidize CO and HC in the next rich cycle, etc. Components such as ReO_2 or CeO_2 which exhibit this "redox" behavior can be included in three-way catalyst formulations. Commercial three-way catalysts contain platinum and rhodium (the ratio Pt/Rh varying substantially in the range 2 to 17) with some A_2O_3, NiO, and CeO_2. Alumina is the preferred support material.[68]

11.6.3 Thermal Reactors

In Secs. 11.3 and 11.4.2 it was explained that oxidation of CO and HC occurred during the expansion and exhaust processes in the cylinder of a conventional spark-ignition engine and, under certain circumstances, in the exhaust system. Oxidation after passage through the exhaust port can be enhanced with a *thermal reactor*—an enlarged exhaust manifold that bolts directly onto the cylinder head. Its function is to promote rapid mixing of the hot exhaust gases with any secondary air injected into the exhaust port (required with fuel-rich engine operation to produce a net oxidizing atmosphere), to remove nonuniformities in temperature and composition in the exhaust gases, and to retain the gases at a high enough

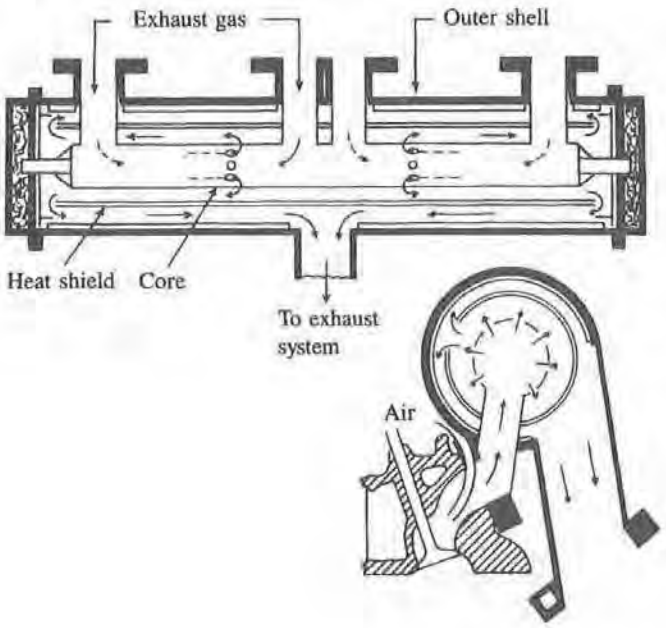


FIGURE 11-58
Schematic of exhaust thermal reactor for HC and CO oxidation.

temperature for sufficient time to oxidize much of the HC and CO which exits the cylinder. An example of a thermal reactor design is shown in Fig. 11-58.

The temperature levels typically required for bulk gas oxidation of HC and CO in a reactor are about 600 and 700°C, respectively. Note that they are considerably higher than those required for equivalent conversion in a catalytic converter and that higher temperatures are required for CO oxidation than for HC oxidation. The exhaust gas temperature in the manifold of a conventional engine is not sufficient to achieve any substantial reduction in engine exhaust port emissions. To achieve greater reductions, the reactor must be designed to reduce heat losses and increase residence time. In addition, to achieve rapid warm-up after engine start, a low thermal inertia reactor is desirable. Typically, a thin steel liner acts as the core of the reactor inside a cast-iron outer casing; with suitably arranged flow paths, this construction holds heat losses to a minimum by thermally isolating the core.

The effectiveness of the reactor depends on its operating temperature, the availability of excess oxygen mixed throughout the reacting gases, and the reactor volume. The operating temperature depends on the reactor inlet gas temperature, heat losses, and the amount of HC, CO, and H_2 burned up in the reactor. This latter factor is important: 1.5 percent CO removal results in a 220 K temperature rise. As a consequence, reactors with fuel-rich cylinder exhaust gas and secondary air give greater fractional reductions in HC and CO emissions than reactors with fuel-lean cylinder exhaust (which do not require any secondary air). As has already been explained, a higher core gas temperature is required to burn up the same fraction of CO which enters the reactor as of HC which enters. For lean engine exhaust gas, where the reactor core gas temperatures are a hundred degrees K lower than under fuel-rich operation, substan-

tial reductions in CO emissions are difficult to achieve. For very lean operation, HC burnup becomes marginal.

A practical limitation to reactor effectiveness with fuel-rich engine operation is mixing of secondary air and engine exhaust gases in the exhaust port and the reactor core. The secondary air flow with a conventional air pump is effectively shut off by the exhaust blowdown process, and virtually no oxidation occurs in the exhaust port because the air and exhaust gases are segregated. Mixing in the reactor itself is promoted by suitably arranging the reactor inlet and exit ports and by using baffles. In systems with conventional secondary air pumps, maximum reductions in CO and HC occur with 10 to 20 percent excess air in the mixture. However, even with very high reactor core gas temperatures, 100 percent HC and CO oxidation is not achieved due to incomplete mixing. Improved control of secondary air flow has been shown to increase significantly CO emissions burnup.

11.6.4 Particulate Traps

An exhaust treatment technology that substantially reduces diesel engine particulate emissions is the trap oxidizer. A temperature-tolerant filter or trap removes the particulate material from the exhaust gas; the filter is then "cleaned off" by oxidizing the accumulated particulates. This technology is difficult to implement because: (1) the filter, even when clean, increases the pressure in the exhaust system; (2) this pressure increase steadily rises as the filter collects particulate matter; (3) under normal diesel engine operating conditions the collected particulate matter will not ignite and oxidize; (4) once ignition of the particulate occurs, the burnup process must be carefully controlled to prevent excessively high temperatures and trap damage or destruction. Trap oxidizers have been put into production for light-duty automobile diesel engines. Their use with heavy-duty diesel engines poses more difficult problems due to higher particulate loading and lower exhaust temperatures.

Types of particulate filters include: ceramic monoliths, alumina-coated wire mesh, ceramic foam, ceramic fiber mat, woven silica-fiber rope wound on a porous tube. Each of these has different inherent pressure loss and filtering efficiency. Regeneration of the trap by burning up the filtered particulate material can be accomplished by raising its temperature to the ignition point while providing oxygen-containing exhaust gas to support combustion and carry away the heat released. Diesel particulate matter ignites at about 500 to 600°C. This is above the normal temperature of diesel exhaust so either the exhaust gas flowing through the trap during regeneration must be heated (positive regeneration) or ignition must be made to occur at a lower temperature with catalytic materials on the trap or added to the fuel (catalytic regeneration). Catalytic coatings on the trap reduce the ignition temperature by up to 200°C.

Figure 11-59 shows a ceramic-coated trap oxidizer mounted on the exhaust system of a turbocharged IDI diesel engine. The trap is a ceramic honeycomb with half the cells closed at the inlet end and the other half of the cells closed at

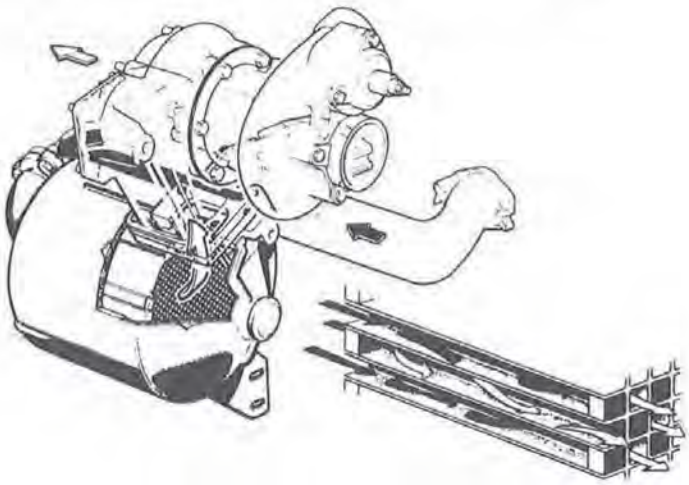


FIGURE 11-59
Catalytic ceramic-monolith particulate trap oxidizer mounted on exhaust of turbocharged automobile diesel engine.[86]

the exit end. Thus the particulate laden exhaust is forced to flow through the porous ceramic cell walls. The outside of the honeycomb is insulated and the trap is mounted close to the engine to maintain as high a trap temperature as possible. The pressure drop across the unloaded trap increases from 0.02 atm at 1000 rev/min to 0.15 atm at the maximum engine speed of 4500 rev/min. As the trap loads up, the pressure drop increases, requiring more fuel to be injected to compensate for the loss in power. This leads to higher exhaust temperature which eventually results in catalytic ignition of the particulate. The particulate oxidation rate depends on the trap temperature. With suitable trap location and design, the regeneration process is largely self-regulating. The particulate emissions from the engine are reduced by 70 percent or more.[86]

PROBLEMS

11.1. Figure 11-2 shows concentrations of NO, CO, and HC in a spark-ignition engine exhaust as a function of fuel/air equivalence ratio. Assume the concentration scale is parts per million. Explain the trends shown as the mixture is first made richer and then leaner than stoichiometric.

11.2. Figure 11-2 is for a spark-ignition engine. Construct a similar qualitative graph of NO, CO, and HC concentrations versus equivalence ratio for a direct-injection four-stroke cycle diesel engine.

11.3. A spark-ignition engine driving a car uses, on average, 120 grams of gasoline per mile traveled. The average emissions from the engine (upstream of the catalyst) are 1.5, 2, and 20 grams per mile of NO_x (as NO_2), HC, and CO, respectively. The engine operates with a stoichiometric gasoline-air mixture. Find the average concentrations in parts per million of NO_x, HC (as ppm C_1), and CO in the engine exhaust.

11.4. Calculate the average combustion inefficiency corresponding to the spark-ignition engine emissions levels given in Prob. 11.3. Include any hydrogen you estimate would be present in the exhaust stream.

11.5. A three-way catalytic converter is used with the spark-ignition engine in Prob. 11.3. For 10 percent of the driving time, the catalyst is cold and ineffective, and does not reduce the engine's emissions. For 90 percent of the time, the catalyst is hot and has conversion efficiencies as given in Fig. 11-57. Estimate the average *vehicle* emissions of NO_x, HC, and CO in grams per mile.

11.6. Figure 15-11 shows the variation in NO and HC emissions as concentrations (ppm) in the exhaust of a spark-ignition engine as a function of speed and load. Convert these data to graphs of indicated specific NO and HC emissions (g/kW · h) versus speed and imep. Assume η_v (based on atmospheric air density) = imep (kPa) $\times 10^{-3}$.

11.7. Use the data in Fig. 11-44 to estimate:

(*a*) The exhaust particulate emissions as a fraction of the maximum particulate loading during the cycle.

(*b*) The maximum measured soot loading and the exhaust soot loading as fractions of the fuel carbon.

(*c*) The equivalent sphere size of each soot particle at the number density peak (22° ATC) and in the exhaust.

Assume a particulate density of 2 g/cm^3. Note that the gas volumes in Fig. 11-44 are determined at standard temperature and pressure.

11.8. Explain the following emissions trends. Highest marks will be given for succinct summaries of the *important* technical issues.

(*a*) Nitric oxide (NO) emissions from diesels and spark-ignition engines as the equivalence ratio is varied show significantly different behavior (see Figs. 11-9 and 11-16). Redraw these graphs on the same plot and explain the different trends for these two types of engines as ϕ decreases on the lean side of stoichiometric.

(*b*) Recirculation of a fraction of the exhaust gases to the intake is used to control engine nitric oxide emissions at part load. Exhaust gas recycle is usually more effective with spark-ignition engines than with diesels, as shown in Fig. P11-8. Explain why these trends are different.

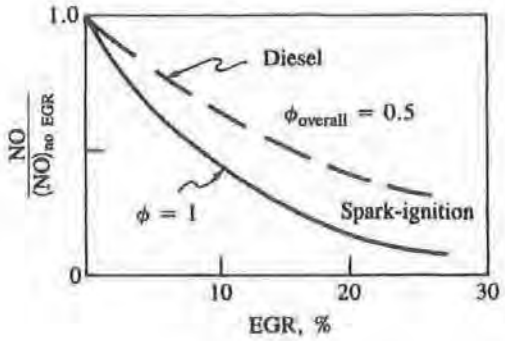


FIGURE P11-8

(*c*) Brake specific particulate emissions from diesels are a major problem. Particulate emissions from conventional spark-ignition engines are negligible. Briefly explain why the particulate emission levels from these two types of engines are so different in magnitude.

(*d*) Diesels have low carbon monoxide (CO) emissions. Spark-ignition engine CO emissions when *averaged* over a typical urban automobile trip (cold engine start, warm-up, cruise, idle, acceleration, etc.) are substantial and require a catalyst for effective control. Explain this difference in average CO emissions (upstream of any catalyst) from these two types of engines.

11.9. The following questions refer to an engine with these geometric and operating characteristics (see Fig. 11-26*a*): $\phi = 1.0$; compression ratio = 8 : 1; bore = 100 mm; stroke = 100 mm; piston diameter above top ring = 99.4 mm; distance from piston crown top to top ring = 9.52 mm; volumetric efficiency = 0.8; temperature in cylinder at the start of compression = 333 K; pressure in cylinder at start of compression = 1 atm; mixture temperature before entering cylinder = 30°C; brake specific fuel consumption = 300 g/kW · h.

A substantial fraction of spark-ignition engine hydrocarbon emissions comes from the crevice between the piston crown and cylinder wall. Gas is forced into this crevice as the cylinder pressure increases and flows out of this crevice as the cylinder pressure decreases. The gas in the crevice can be assumed to be at the wall temperature, 400 K. The gas pushed into the crevice ahead of the flame is unburned mixture; the gas pushed in behind the flame is burned mixture. About two-thirds of the crevice gas is unburned. The maximum cylinder pressure is 3 MPa.

(*a*) Calculate the mass fraction of the cylinder gas which is in the crevice between the piston and cylinder wall and above the first piston ring, at the time of peak pressure.

(*b*) Assuming that half of the unburned fuel in this region is oxidized within the cylinder and a further one-third is oxidized in the exhaust port, calculate the engine HC emissions from this source in parts per million (ppm C_1) by volume.

(*c*) Calculate the ratio of brake specific hydrocarbon emissions to brake specific fuel consumption.

(*d*) Calculate the brake specific hydrocarbon emissions in grams of HC per kilowatt-hour.

11.10. Nitric oxide, NO, forms via reactions (11.1) to (11.3). Reaction (11.1) is "slow" and reactions (11.2) and (11.3) are "fast," so the initial rate of formation of NO is given by Eq. (11.8):

$$\frac{d[\mathrm{NO}]}{dt} = 2k_1^+[\mathrm{N_2}]_e[\mathrm{O}]_e$$

where [ ] denote concentrations in gram-moles per cubic centimeter, k_1^+ is the rate constant for reaction (11.1), and the factor of 2 enters because the N atom formed in (11.1) immediately reacts via (11.2) or (11.3) to give an additional NO molecule:

$$k_1^+ = 7.6 \times 10^{13} \exp\left(\frac{-38{,}000}{T}\right) \quad \mathrm{cm^3/gmol \cdot s}$$

where T is in kelvin.

Using the equilibrium composition data provided for mole fraction atomic oxygen (O), molecular nitrogen (N_2), and nitric oxide (NO):

(*a*) Plot the formation rate of NO as a function of the equivalence ratio at 3000 K and 5.5 MPa, and as a function of temperature for a stoichiometric mixture at 5.5 MPa.

(*b*) Estimate approximately the time taken to reach equilibrium NO levels at $\phi = 1$, 2750 K and 3000 K, 5.5 MPa.

(*c*) If the stoichiometric mixture inducted into the engine reaches 3000 K and 5.5 MPa after combustion, in the absence of any exhaust gas recirculation, calculate the percentage of the exhaust that must be recycled to the intake (at the initial intake temperature) to reduce the NO formation rate by a factor of 4 (assume the final pressure 5.5 MPa stays the same; of course, the final temperature decreases as the exhaust gas is recycled).

$p = 5.5$ MPa

		Mole fraction	
ϕ	T(K)	O	N_2
0.9	3000	2.1×10^{-3}	0.73
1.0	3000	1.5×10^{-3}	0.73
1.1	3000	1×10^{-3}	0.73

$\phi = 1.0$, $p = 5.5$ MPa

	Mole fraction		
T(K)	O	N_2	NO
2500	6×10^{-5}	0.73	—
2750	5×10^{-4}	0.73	4×10^{-3}
3000	1.5×10^{-3}	0.73	8×10^{-3}

REFERENCES

1. Bowman, C. T.: "Kinetics of Pollutant Formation and Destruction in Combustion," *Prog. Energy Combust. Sci.*, vol. 1, pp. 33–45, 1975.
2. Lavoie, G. A., Heywood, J. B., and Keck, J. C.: "Experimental and Theoretical Investigation of Nitric Oxide Formation in Internal Combustion Engines," *Combust. Sci. Technol.*, vol. 1, pp. 313–326, 1970.
3. Heywood, J. B., Fay, J. A., and Linden, L. H.: "Jet Aircraft Air Pollutant Production and Dispersion," *AIAA J.*, vol. 9, no. 5, pp. 841–850, 1971.
4. Newhall, H. K., and Shahed, S. M.: "Kinetics of Nitric Oxide Formation in High-Pressure Flames," in *Proceedings of Thirteenth International Symposium on Combustion*, pp. 381–390, The Combustion Institute, 1971.
5. Hilliard, J. C., and Wheeler, R. W.: "Nitrogen Dioxide in Engine Exhaust," SAE paper 790691, *SAE Trans.*, vol. 88, 1979.
6. Merryman, E. L., and Levy, A.: "Nitrogen Oxide Formation in Flames: The Roles of NO_2 and Fuel Nitrogen," in *Proceedings of Fifteenth International Symposium on Combustion*, p. 1073, The Combustion Institute, 1975.
7. Komiyama, K., and Heywood, J. B.: "Predicting NO_x Emissions and Effects of Exhaust Gas Recirculation in Spark-Ignition Engines," SAE paper 730475, *SAE Trans.*, vol. 82, 1973.
8. Alperstein, M., and Bradow, R. L.: "Exhaust Emissions Related to Engine Combustion Reactions," SAE paper 660781, *SAE Trans.*, vol. 75, 1966.
9. Starkman, E. S., Stewart, H. E., and Zvonow, V. A.: "Investigation into Formation and Modification of Exhaust Emission Precursors," SAE paper 690020, 1969.
10. Lavoie, G. A.: "Spectroscopic Measurement of Nitric Oxide in Spark-Ignition Engines," *Combust. Flame*, vol. 15, pp. 97–108, 1970.
11. Blumberg, P., and Kummer, J. K.: "Prediction of NO Formation in Spark-Ignition Engines—An Analysis of Methods of Control," *Combust. Sci. Technol.*, vol. 4, pp. 73–96, 1971.
12. Sakai, Y., Miyazaki, H., and Mukai, K.: "The Effect of Combustion Chamber Shape on Nitrogen Oxides," SAE paper 730154, 1973.
13. Quader, A. A.: "Why Intake Charge Dilution Decreases Nitric Oxide Emission from Spark Ignition Engines," SAE paper 710009, *SAE Trans.*, vol. 80, 1971.

14. Benson, J. D., and Stebar, R. F.: "Effects of Charge Dilution on Nitric Oxide Emission from a Single-Cylinder Engine," SAE paper 710008, *SAE Trans.*, vol. 80, 1971.
15. Toda, T., Nohira, H., and Kobashi, K.: "Evaluation of Burned Gas Ratio (BGR) as a Predominant Factor to NO_x," SAE paper 760765, *SAE Trans.*, vol. 85, 1976.
16. Lavoie, G. A., and Blumberg, P. N.: "A Fundamental Model for Predicting Fuel Consumption, NO_x and HC Emissions of the Conventional Spark-Ignited Engine," *Combust. Sci. Technol.*, vol. 21, pp. 225–258, 1980.
17. Lavoie, G. A., and Blumberg, P. N.: "Measurements of NO Emissions from a Stratified Charge Engine: Comparison of Theory and Experiment," *Combust. Sci. Technol.*, vol. 8, p. 25, 1973.
18. Aoyagi, Y., Kamimoto, T., Matsui, Y., and Matsuoka, S.: "A Gas Sampling Study on the Formation Processes of Soot and NO in a DI Diesel Engine," SAE paper 800254, SAE Trans., vol. 89, 1980.
19. Vioculescu, I. A., and Borman, G. L.: "An Experimental Study of Diesel Engine Cylinder-Averaged NO_x Histories," SAE paper 780228, *SAE Trans.*, vol. 87, 1978.
20. Mansouri, S. H., Heywood, J. B., and Radhakrishnan, K.: "Divided-Chamber Diesel Engine, Part I: Cycle-Simulation Which Predicts Performance and Emissions," SAE paper 820273, *SAE Trans.*, vol. 91, 1982.
21. Duggal, V. K., Priede, T., and Khan, I. M.: "A Study of Pollutant Formation within the Combustion Space of a Diesel Engine," SAE paper 780227, *SAE Trans.*, vol. 87, 1978.
22. Liu, X., and Kittelson, D. B.: "Total Cylinder Sampling from a Diesel Engine (Part II)," SAE paper 820360, 1982.
23. Yu, R. C., and Shahed, S. M.: "Effects of Injection Timing and Exhaust Gas Recirculation on Emissions from a D.I. Diesel Engine," SAE paper 811234, *SAE Trans.*, vol. 90, 1981.
24. Plee, S. L., Myers, J. P., and Ahmed, T.: "Flame Temperature Correlation for the Effects of Exhaust Gas Recirculation on Diesel Particulate and NO_x Emissions," SAE paper 811195, *SAE Trans.*, vol. 90, 1981.
25. Plee, S. L., Ahmad, T., and Myers, J. P.: "Diesel NO_x Emissions—A Simple Correlation Technique for Intake Air Effects," in *Proceedings of Nineteenth International Symposium on Combustion*, pp. 1495–1502, The Combustion Institute, Pittsburgh, 1983.
26. Ahmad, T., and Plee, S. L.: "Application of Flame Temperature Correlations to Emissions from a Direct-Injection Diesel Engine," SAE paper 831734, *SAE Trans.*, vol. 92, 1983.
27. Harrington, J. A., and Shishu, R. C.: "A Single-Cylinder Engine Study of the Effects of Fuel Type, Fuel Stoichiometry, and Hydrogen-to-Carbon Ratio and CO, NO, and HC Exhaust Emissions," SAE paper 730476, 1973.
28. Newhall, H. K.: "Kinetics of Engine-Generated Nitrogen Oxides and Carbon Monoxide," in *Proceedings of Twelfth International Symposium on Combustion*, pp. 603–613, Mono of Maryland, 1968.
29. Keck, J. C., and Gillespie, D.: "Rate-Controlled Partial-Equilibrium Method for Treating Reacting Gas Mixtures," *Combust. Flame*, vol. 17, pp. 237–241, 1971.
30. Delichatsios, M. M.: "The Kinetics of CO Emissions from an Internal Combustion Engine," S.M. Thesis, Department of Mechanical Engineering, MIT, June 1972.
31. Johnson, G. L., Caretto, L. S., and Starkman, E. S.: "The Kinetics of CO Oxidation in Reciprocating Engines," paper presented at the Western States Section, The Combustion Institute, Spring Meeting, April 1970.
32. Jackson, M. W.: "Analysis for Exhaust Gas Hydrocarbons—Nondispersive Infrared Versus Flame-Ionization," *J. Air Pollution Control Ass.*, vol. 16, p. 697–702, 1966.
33. Jackson, M. W.: "Effect of Catalytic Emission Control on Exhaust Hydrocarbon Composition and Reactivity," SAE paper 780624, *SAE Trans.*, vol. 87, 1978.
34. Patterson, D. J., and Henein, N. A.: *Emissions from Combustion Engines and Their Control*, Ann Arbor Science Publishers, Ann Arbor, Michigan, 1972.
35. "Diesel Technology, Impacts of Diesel-Powered Light-Duty Vehicles," report of the Technology Panel of the Diesel Impacts Study Committee, National Research Council, National Academy Press, Washington, D.C., 1982.
36. Lavoie, G. A.: "Correlations of Combustion Data for S.I. Engine Calculations—Laminar Flame

Speed, Quench Distance and Global Reaction Rates," SAE paper 780229, *SAE Trans.*, vol. 87, 1978.

37. Adamczyk, A. A., Kaiser, E. W., Cavolowsky, J. A., and Lavoie, G. A.: "An Experimental Study of Hydrocarbon Emissions from Closed Vessel Explosions," in *Proceedings of Eighteenth International Symposium on Combustion*, pp. 1695–1702, The Combustion Institute, 1981.
38. Westbrook, C. K., Adamczyk, A. A., and Lavoie, G. A.: "A Number Study of Laminar Wall Quenching," *Combust. Flame*, vol. 40, pp. 81–91, 1981.
39. Kaiser, E. W., Adamczyk, A. A., and Lavoie, G. A.: "The Effect of Oil Layers on the Hydrocarbon Emissions Generated During Closed Vessel Combustion," in *Proceedings of Eighteenth International Symposium on Combustion*, pp. 1881–1890, The Combustion Institute, 1981.
40. Tabaczynski, R. J., Heywood, J. B., and Keck, J. C.: "Time-Resolved Measurements of Hydrocarbon Mass Flow Rate in the Exhaust of a Spark-Ignition Engine," SAE paper 720112, *SAE Trans.*, vol. 81, 1972.
41. Ekchian, A., Heywood, J. B., and Rife, J. M.: "Time Resolved Measurements of the Exhaust from a Jet Ignition Prechamber Stratified Charge Engine," SAE paper 770043, *SAE Trans.*, vol. 86, 1977.
42. Daniel, W. A., and Wentworth, J. T.: "Exhaust Gas Hydrocarbons—Genesis and Exodus," SAE paper 486B, March 1962; also SAE Technical Progress Series, vol. 6, p. 192, 1964.
43. Daniel, W. A.: "Flame Quenching at the Walls of an Internal Combustion Engine," in *Proceedings of Sixth International Symposium on Combustion*, p. 886, Reinhold, New York, 1957.
44. LoRusso, J. A., Lavoie, G. A., and Kaiser, E. W.: "An Electrohydraulic Gas Sampling Valve with Application to Hydrocarbon Emissions Studies," SAE paper 800045, *SAE Trans.*, vol. 89, 1980.
45. Wentworth, J. T.: "More on Origins of Exhaust Hydrocarbons—Effects of Zero Oil Consumption, Deposit Location, and Surface Roughness," SAE paper 720939, *SAE Trans.*, vol. 81, 1972.
46. Namazian, M., and Heywood, J. B.: "Flow in the Piston-Cylinder-Ring Crevices of a Spark-Ignition Engine: Effect on Hydrocarbon Emissions, Efficiency and Power," SAE paper 820088, *SAE Trans.*, vol. 91, 1982.
47. Furuhama, S., and Tateishi, Y.: "Gases in Piston Top-Land Space of Gasoline Engine," *Trans. SAEJ*, no. 4, 1972.
48. Wentworth, J. T.: "The Piston Crevice Volume Effect on Exhaust Hydrocarbon Emission," *Combust. Sci. Technol.*, vol. 4, pp. 97–100, 1971.
49. Haskell, W. W., and Legate, C. E.: "Exhaust Hydrocarbon Emissions from Gasoline Engines—Surface Phenomena," SAE paper 720255, 1972.
50. Adamczyk, A. A., Kaiser, E. W., and Lavoie, G. A.: "A Combustion Bomb Study of the Hydrocarbon Emissions from Engine Crevices," *Combust. Sci. Technol.*, vol. 33, pp. 261–277, 1983.
51. Wentworth, J. T.: "Piston and Ring Variables Affect Exhaust Hydrocarbon Emissions," SAE paper 680109, *SAE Trans.*, vol. 77, 1968.
52. Kaiser, E. W., LoRusso, J. A., Lavoie, G. A., and Adamczyk, A. A.: "The Effect of Oil Layers on the Hydrocarbon Emissions from Spark-Ignited Engines," *Combust. Sci. Technol.*, vol. 28, pp. 69–73, 1982.
53. Kaiser, E. W., Adamczyk, A. A., and Lavoie, G. A.: "The Effect of Oil Layers on the Hydrocarbon Emissions Generated during Closed Vessel Combustion," in *Proceedings of Eighteenth International Symposium on Combustion*, pp. 1881–1890, The Combustion Institute, 1981.
54. McGeehan, J. A.: "A Literature Review of the Effects of Piston and Ring Friction and Lubricating Oil Viscosity on Fuel Economy," SAE paper 780673, *SAE Trans.*, vol. 87, 1978.
55. Shin, K., Tateishi, Y., and Furuhama, S.: "Measurement of Oil-Film-Thickness between Piston Ring and Cylinder," SAE paper 830068, *SAE Trans.*, vol. 92, 1983.
56. Carrier, G. F., Fendell, F. E., and Feldman, P. S.: "Cyclic Absorption/Desorption of Gas in a Liquid Wall Film," *Combust. Sci. Technol.*, vol. 25, pp. 9–19, 1981.
57. Wentworth, J. T.: "Effects of Top Compression Ring Profile on Oil Consumption and Blowby with the Sealed Ring–Orifice Design," SAE paper 820089, 1982.
58. Kuroda, H., Nakajima, Y., Sugihara, K., Takagi, Y., and Muranaka, S.: "The Fast Burn with Heavy EGR, New Approach for Low NO_x and Improved Fuel Economy," SAE paper 780006, *SAE Trans.*, vol. 87, 1978.

59. Jackson, M. W., Wiese, W. M., and Wentworth, J. T.: "The Influence of Air-Fuel Ratio, Spark Timing, and Combustion Chamber Deposits on Exhaust Hydrocarbon Emissions," SAE paper 486A, in *Vehicle Emissions*, vol. TP-6, SAE, 1962.
60. Lavoie, G. A., Lorusso, J. A., and Adamczyk, A. A.: "Hydrocarbon Emissions Modeling for Spark Ignition Engines," in J. N. Mattavi and C. A. Amann (eds.), *Combustion Modeling in Reciprocating Engines*, pp. 409–445, Plenum Press, 1978.
61. Daniel, W. A.: "Why Engine Variables Affect Exhaust Hydrocarbon Emission," SAE paper 700108, *SAE Trans.*, vol. 79, 1970.
62. Amann, C. A.: "Control of the Homogeneous-Charge Passenger-Car Engine—Defining the Problem," SAE paper 801440, 1980.
63. Weiss, P., and Keck, J. C.: "Fast Sampling Valve Measurements of Hydrocarbons in the Cylinder of a CFR Engine," SAE paper 810149, *SAE Trans.*, vol. 90, 1981.
64. Caton, J. A., Heywood, J. B., and Mendillo, J. V.: "Hydrocarbon Oxidation in a Spark Ignition Engine Exhaust Port," *Combust. Sci. Technol.*, vol. 37, nos. 3 and 4, pp. 153–169, 1984.
65. Green, R. M., Smith, J. R., and Medina, S. C.: "Optical Measurement of Hydrocarbons Emitted from a Simulated Crevice Volume in an Engine," SAE paper 840378, *SAE Trans.*, vol. 93, 1984.
66. Nakagawa, Y., Etoh, Y., and Maruyama, R.: "A Fundamental Analysis of HC and CO Oxidation Reaction in the Exhaust System," *JSAE Rev.*, no. 1, pp. 98–106, 1978.
67. Greeves, G., Khan, I. M., Wang, C. H. T., and Fenne, I.: "Origins of Hydrocarbon Emissions from Diesel Engines," SAE paper 770259, *SAE Trans.*, vol. 86, 1977.
68. Kummer, J. T.: "Catalysts for Automobile Emission Control," *Prog. Energy Combust. Sci.*, vol. 6, pp. 177–199, 1981.
69. Cadle, S. H., Nebel, G. J., and Williams, R. L.: "Measurements of Unregulated Emissions from General Motors' Light-Duty Vehicles," SAE paper 790694, *SAE Trans.*, vol. 88, 1979.
70. Amann, C. A., and Siegla, D. C.: "Diesel Particulates—What They Are and Why," *Aerosol Sci. Technol.*, vol. 1, pp. 73–101, 1982.
71. Mayer, W. J., Lechman, D. C., and Hilden, D. L.: "The Contribution of Engine Oil to Diesel Exhaust Particulate Emissions," SAE paper 800256, *SAE Trans.*, vol. 89, 1980.
72. Lahaye, J., and Prado, G.: "Morphology and Internal Structure of Soot and Carbon Blacks," in D. C. Siegla and G. W. Smith (eds.), *Particulate Carbon Formation during Combustion*, pp. 33–55, Plenum Press, 1981.
73. Smith, O. I.: "Fundamentals of Soot Formation in Flames with Application to Diesel Engine Particulate Emissions," *Prog. Energy Combust. Sci.*, vol. 7, pp. 275–291, 1981.
74. Whitehouse, N. D., Clough, E., and Uhunmwangho, S. O.: "The Development of Some Gaseous Products during Diesel Engine Combustion," SAE paper 800028, 1980.
75. Greeves, G., and Meehan, J. O.: "Measurement of Instantaneous Soot Concentration in a Diesel Combustion Chamber," paper C88/75, in *Combustion in Engines*, pp. 73–82, Institution of Mechanical Engineers, 1975.
76. Chang, Y. J., Kobayashi, H., Matsuzawa, K., and Kamimoto, T.: "A Photographic Study of Soot Formation and Combustion in a Diesel Flame with a Rapid Compression Machine," Proceedings of International Symposium on *Diagnostics and Modeling of Combustion in Reciprocating Engines*, COMODIA 85, pp. 149–157, Tokyo, Japan, September 4–6, 1985.
77. Du, C. J., and Kittelson, D. B.: "Total Cylinder Sampling from a Diesel Engine: Part III—Particle Measurements," SAE paper 830243, *SAE Trans.*, vol. 92, 1983.
78. Aoyagi, Y., Kamimoto, T., Matsui, Y., and Matsuoka, S.: "A Gas Sampling Study on the Formation Processes of Soot and NO in a DI Diesel Engine," SAE paper 800254, *SAE Trans.*, vol. 89, 1980.
79. Matsui, Y., Kamimoto, T., and Matsuoka, S.: "Formation and Oxidation Processes of Soot Particles in a D.I. Diesel Engine—An Experimental Study Via the Two-Color Method," SAE paper 820464, *SAE Trans.*, vol. 91, 1982.
80. Haynes, B. S., and Wagner, H. G.: "Soot Formation," *Prog. Energy Combust. Sci.*, vol. 7, pp. 229–273, 1981.
81. Lahaye, J., and Prado, G.: "Mechanisms of Carbon Black Formation," in P. L. Walker and P. A.

Thrower (eds.), *Chemistry and Physics of Carbon*, vol. 14, pp. 168–294, Marcel Dekker, New York, 1978.

82. Graham, S. C., Homer, J. B., and Rosenfeld, J. L. J.: "The Formation and Coagulation of Soot Aerosols Generated by the Pyrolysis of Aromatic Hydrocarbons," *Proc. R. Soc. Lond.*, vol. A344, pp. 259–285, 1975.
83. Amann, C. A., Stivender, D. L., Plee, S. L., and MacDonald, J. S.: "Some Rudiments of Diesel Particulate Emissions," SAE paper 800251, *SAE Trans.*, vol. 89, 1980.
84. Park, C., and Appleton, J. P.: "Shock-Tube Measurements of Soot Oxidation Rates," *Combust. Flame*, vol. 20, pp. 369–379, 1973.
85. Otto, K., Sieg, M. H., Zinbo, M., and Bartosiewicz, L.: "The Oxidation of Soot Deposits from Diesel Engines," SAE paper 800336, *SAE Trans.*, vol. 89, 1980.
86. Abthoff, J., Schuster, H., Langer, H., and Loose, G.: "The Regenerable Trap Oxidizer—An Emission Control Technique for Diesel Engines," SAE paper 850015, 1985.

CHAPTER 12

ENGINE HEAT TRANSFER

12.1 IMPORTANCE OF HEAT TRANSFER

The peak burned gas temperature in the cylinder of an internal combustion engine is of order 2500 K. Maximum metal temperatures for the inside of the combustion chamber space are limited to much lower values by a number of considerations, and cooling for the cylinder head, cylinder, and piston must therefore be provided. These conditions lead to heat fluxes to the chamber walls that can reach as high as 10 MW/m^2 during the combustion period. However, during other parts of the operating cycle, the heat flux is essentially zero. The flux varies substantially with location: regions of the chamber that are contacted by rapidly moving high-temperature burned gases generally experience the highest fluxes. In regions of high heat flux, thermal stresses must be kept below levels that would cause fatigue cracking (so temperatures must be less than about 400°C for cast iron and 300°C for aluminum alloys). The gas-side surface of the cylinder wall must be kept below about 180°C to prevent deterioration of the lubricating oil film. Spark plug and valves must be kept cool to avoid knock and preignition problems which result from overheated spark plug electrodes or exhaust valves. Solving these engine heat-transfer problems is obviously a major design task.

Heat transfer affects engine performance, efficiency, and emissions. For a given mass of fuel within the cylinder, higher heat transfer to the combustion chamber walls will lower the average combustion gas temperature and pressure,

and reduce the work per cycle transferred to the piston. Thus specific power and efficiency are affected by the magnitude of engine heat transfer. Heat transfer between the unburned charge and the chamber walls in spark-ignition engines affects the onset of knock which, by limiting the compression ratio, also influences power and efficiency. Most critical is heat transfer from the hot exhaust valve and piston to mixture in the end-gas region. Changes in gas temperature due to the heat-transfer impact on emission formation processes, both within the engine's cylinder and in the exhaust system where afterburning of CO and HC occurs. The exhaust temperature also governs the power that can be obtained from exhaust energy recovery devices such as a turbocharger turbine. Friction is both affected by engine heat transfer and contributes to the coolant load. The cylinder liner temperature governs the piston and ring lubricating oil film temperature, and hence its viscosity. Piston and liner distortion due to temperature nonuniformities have a significant impact on the piston component of engine friction. Some of the mechanical energy dissipated due to friction must be rejected to the atmosphere by the cooling system. The fan and water pump power requirements are determined by the magnitude of the heat rejected. The importance of engine heat transfer is clear.

To examine heat transfer more fully, it is helpful to divide the engine into its subsystems. The intake system consists of intake manifold and inlet ports and valves. Heat transfer to the inflowing charge reduces volumetric efficiency (see Sec. 6.2.1). However, in spark-ignition engines, the intake mixture is heated, with carbureted and single-point injected engines, to aid in vaporizing the fuel (see Sec. 7.6.3). Within the engine cylinder, the temperature of the charge relative to the wall temperature and the flow field vary enormously throughout the cycle. Both of these variables have a major influence on heat transfer. During the intake process, the incoming charge is usually cooler than the walls and the flow velocities are high. During compression the charge temperature rises above the wall temperature, and gas velocities decrease (see Sec. 8.2.2). Heat transfer is now from the cylinder gases to the chamber walls. During combustion gas temperatures increase substantially and the gas expansion which occurs on combustion produces increased gas motion. This is the period when heat-transfer rates to the walls are highest. Also, as the cylinder pressure rises, a small fraction of the cylinder charge is forced into crevice regions, resulting in additional heat transfer (see Sec. 8.6). During expansion, gas temperatures decrease so heat-transfer rates decrease. When the exhaust valve opens, however, the blowdown process (Sec. 6.5) produces high velocities within the cylinder, and past the exhaust valve and in the exhaust port. Substantial heat transfer from the exhausting gases to the valve, port, and (to a lesser extent) manifold occurs during the exhaust process. An example of how the heat-transfer rate to the total combustion chamber walls varies throughout the four-stroke operating cycle of a spark-ignition engine is shown in Fig. 14-9. The heat-transfer rate was estimated from the cylinder pressure, unburned and burned gas temperatures, combustion chamber surface area, and wall temperature, assuming gas velocities scaled with mean piston speed. An ability to predict the magnitude of the heat transfer between the working fluid,

the walls of the intake system, combustion chamber, and exhaust system, and to the coolant is of obvious importance to the engine designer.

12.2 MODES OF HEAT TRANSFER

The following modes of heat transfer are important.

12.2.1 Conduction

Heat is transferred by molecular motion, through solids and through fluids at rest, due to a temperature gradient. The heat transfer by conduction, per unit area per unit time, $\dot{\mathbf{q}}$, in a steady situation is given by Fourier's law:

$$\dot{\mathbf{q}} = -k\nabla T \tag{12.1}$$

where k is the thermal conductivity. For a steady one-dimensional temperature variation

$$\dot{q}_x = \frac{\dot{Q}}{A} = -k\frac{dT}{dx}$$

Heat is transferred by conduction through the cylinder head, cylinder walls, and piston; through the piston rings to the cylinder wall; through the engine block and manifolds.

12.2.2 Convection

Heat is transferred through fluids in motion and between a fluid and solid surface in relative motion. When the motion is produced by forces other than gravity, the term *forced convection* is used. In engines the fluid motions are turbulent (see Chap. 8).

Heat is transferred by forced convection between the in-cylinder gases and the cylinder head, valves, cylinder walls, and piston during induction, compression, expansion, and exhaust processes. Heat is transferred by forced convection from the cylinder walls and head to the coolant (which may be liquid or gas), and from the piston to the lubricant or other piston coolant. Substantial convective heat transfer occurs to the exhaust valve, exhaust port, and exhaust manifold during the exhaust process. Heat transfer by convection in the inlet system is used to raise the temperature of the incoming charge. Heat is also transferred from the engine to the environment by convection.

In steady-flow forced-convection heat-transfer problems, the heat flux $\dot{q}$ transferred to a solid surface at temperature T_w from a flowing fluid stream at temperature T is determined from the relation

$$\dot{q} = h_c(T - T_w) \tag{12.2}$$

where h_c is called the heat-transfer coefficient. For many flow geometries (such as flow through pipes or over a plate), h_c is given by relations of the form

$$\left(\frac{h_c L}{k}\right) = \text{constant} \times \left(\frac{\rho v L}{\mu}\right)^m \left(\frac{c_p \mu}{k}\right)^n \tag{12.3}$$

where L and v are a characteristic length and velocity. The terms in brackets from left to right are the Nusselt, Reynolds, and Prandtl dimensionless numbers, respectively. For gases, the Prandtl number ($c_p \mu/k$) varies little and is about 0.7 (see Sec. 4.8).

When boiling occurs at the surface (i.e., vapor is formed in the liquid), as may be the case in high heat flux areas on the coolant side in water-cooled engines, then different relationships for h_c must be used.

12.2.3 Radiation

Heat exchange by radiation occurs through the emission and absorption of electromagnetic waves. The wavelengths at which energy is transformed into thermal energy are the visible range (0.4 to 0.7 μm) and the infrared (0.7 to 40 μm). Heat transfer by radiation occurs from the high-temperature combustion gases and the flame region to the combustion chamber walls (although the magnitude of this radiation heat transfer relative to convective heat transfer is only significant in diesel engines). Heat transfer by radiation to the environment occurs from all the hot external surfaces of the engine.

The theory of radiant heat transfer starts from the concept of a "black body," i.e., a body that has a surface that emits or absorbs equally well radiation of all wavelengths and that reflects none of the radiation falling on it. The heat flux from one plane black body at temperature T_1 to another at temperature T_2 parallel to it across a space containing no absorbing material is given by

$$\dot{q} = \sigma(T_1^4 - T_2^4) \tag{12.4}$$

where σ is the Stefan-Boltzmann constant 5.67×10^{-8} W/m$^2 \cdot$ K^4. Real surfaces are not "black" but reflect radiation to an extent which depends on wavelength. Gases are far from this black-body idealization. They absorb and emit radiation almost exclusively within certain wavelength bands characteristic of each species. These departures from black-body behavior are usually dealt with by applying a multiplying factor (an emissivity, ε) to Eq. (12.4). Similarly, a "shape factor" is applied to account for the fact that the angle of incidence of the radiation usually varies over any actual surface. These factors can be calculated for simple cases.

12.2.4 Overall Heat-Transfer Process

Figure 12-1 shows, schematically, the overall heat-transfer process from the gases within the cylinder through the combustion chamber wall to the coolant flow. The heat flux into the wall has in general both a convective and a radiation component. The heat flux is conducted through the wall and then convected from

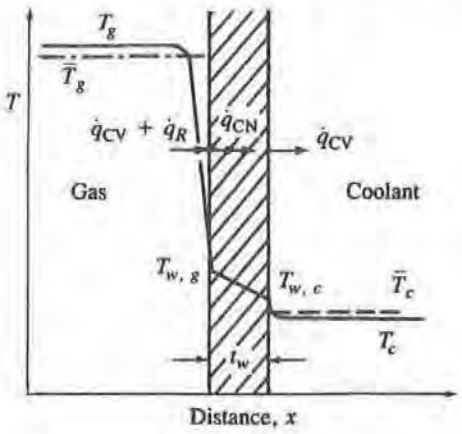


FIGURE 12-1
Schematic of temperature distribution and heat flow across the combustion chamber wall.

the wall to the coolant. A schematic temperature profile, and mean gas and coolant temperatures, $\bar{T}_g$ and $\bar{T}_c$, are shown.

In internal combustion engines, throughout each engine operating cycle, the heat transfer takes place under conditions of varying gas pressure and temperature, and with local velocities which vary more or less rapidly depending on intake port and combustion chamber configuration (see Chap. 8). In addition, the surface area of the combustion chamber varies through the cycle. The heat flux into the containing walls changes continuously from a small negative value during the intake process to a positive value of order several megawatts per square meter early in the expansion process. The flux variation lags behind the change in gas temperature. This lag between heat flux and driving temperature difference is clearly perceptible[1] but the precision of measurements to date suffice only for a rough estimate of its magnitude. Generally, investigators have concluded that the assumption that the heat-transfer process is *quasi steady* is sufficiently accurate for most calculation purposes. However, gas temperature and gas velocities vary significantly across the combustion chamber. The heat flux distribution over the combustion chamber walls is, therefore, nonuniform.

For a steady one-dimensional heat flow through a wall as indicated in Fig. 12-1, the following equations relate the heat flux $\dot{q} = \dot{Q}/A$ and the temperatures indicated:

Gas side:
$$\dot{q} = \dot{q}_{CV} + \dot{q}_R = h_{c,g}(\bar{T}_g - T_{w,g}) + \sigma\varepsilon(\bar{T}_g^4 - T_{w,g}^4) \tag{12.5}$$

where ε is the emissivity. The radiation term is generally negligible for SI engines.

Wall:
$$\dot{q} = \dot{q}_{CN} = \frac{k(T_{w,g} - T_{w,c})}{t_w} \tag{12.6}$$

Coolant side:
$$\dot{q} = \dot{q}_{CV} = h_{c,c}(T_{w,c} - \bar{T}_c) \tag{12.7}$$

If $h_{c,g}$ and $h_{c,c}$ are known, the temperatures $\bar{T}_g$, $T_{w,g}$, $T_{w,c}$, and $\bar{T}_c$ can be related to each other.

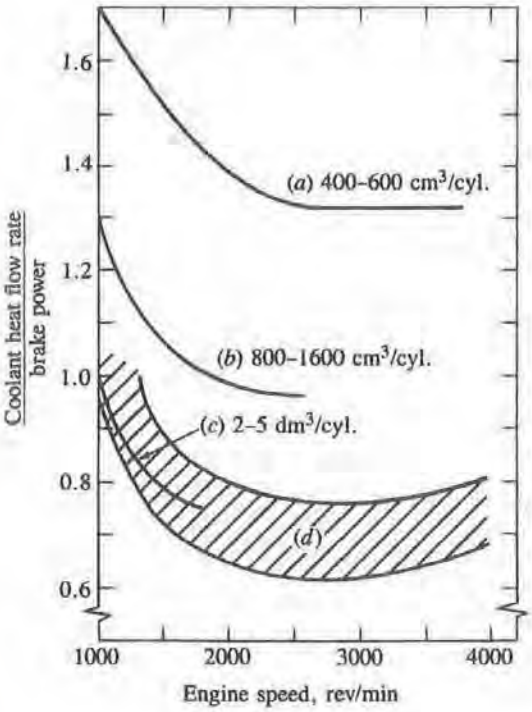


FIGURE 12-2
Ratio of coolant heat flow rate to brake power as a function of engine speed. Different size and types of engines: (*a*) small automotive diesels; (*b*) larger automotive diesels; (*c*) various diesels; (*d*) spark-ignition engines. (*Developed from Howarth.*[2])

12.3 HEAT TRANSFER AND ENGINE ENERGY BALANCE

Figure 12-2 shows the magnitude of the heat-rejection rate to the coolant relative to the brake power for a range of engine types and sizes at maximum power. This ratio decreases with increasing engine speed and with increasing engine size. The smaller diesel engine designs use higher gas velocities to achieve the desired fuel-air mixing rates and have less favorable surface/volume ratios (see Sec. 10.2).

An overall first law energy balance for an engine provides useful information on the disposition of the initial fuel energy. For a control volume which surrounds the engine (see Fig. 3-8), the steady-flow energy-conservation equation is

$$\dot{m}_f h_f + \dot{m}_a h_a = P_b + \dot{Q}_{\text{cool}} + \dot{Q}_{\text{misc}} + (\dot{m}_f + \dot{m}_a)h_e \tag{12.8}$$

where P_b is the brake power, $\dot{Q}_{\text{cool}}$ is the heat-transfer rate to the cooling medium, $\dot{Q}_{\text{misc}}$ is the heat rejected to the oil (if separately cooled) plus convection and radiation from the engine's external surface. It proves convenient to divide the exhaust enthalpy h_e into a sensible part $h_{e,s} = h_e(T) - h_e(298\ \text{K})$, plus the exhaust reference state enthalpy (see Sec. 4.5). Then Eq. (12.8) can be written:

$$P_b + \dot{Q}_{\text{cool}} + \dot{Q}_{\text{misc}} + \dot{H}_{e,\text{ic}} + \dot{m}h_{e,s} = \dot{m}_f Q_{\text{LHV}} \tag{12.9}$$

where $\dot{H}_{e,\text{ic}}$ represents the exhaust enthalpy loss due to incomplete combustion. Typical values of each of these terms relative to the fuel flow × heating value are given in Table 12.1.

The energy balance within an engine is more complicated and is illustrated

TABLE 12.1
Energy balance for automotive engines at maximum power

	P_b	$\dot{Q}_{cool}$	$\dot{Q}_{misc}$	$\dot{H}_{e,ic}$	$\dot{m}h_{e,s}$
	(percentage of fuel heating value)				
SI engine	25–28	17–26	3–10	2–5	34–45
Diesel	34–38	16–35	2–6	1–2	22–35

Sources: From Khovakh,[3] Sitkei,[4] and Burke *et al.*[5]

in the energy flow diagram in Fig. 12-3. The indicated power is the sum of the brake power and the friction power. A substantial part of the friction power (about half) is dissipated between the piston and piston rings and cylinder wall and is transferred as thermal energy to the cooling medium. The remainder of the friction power is dissipated in the bearings, valve mechanism, or drives auxiliary devices, and is transferred as thermal energy to the oil or surrounding environment (in $\dot{Q}_{misc}$). The enthalpy initially in the exhaust gases can be subdivided into the following components: a sensible enthalpy (60 percent), an exhaust kinetic energy (7 percent), an incomplete combustion term (20 percent), and a heat transfer to the exhaust system (12 percent) (part of which is radiated

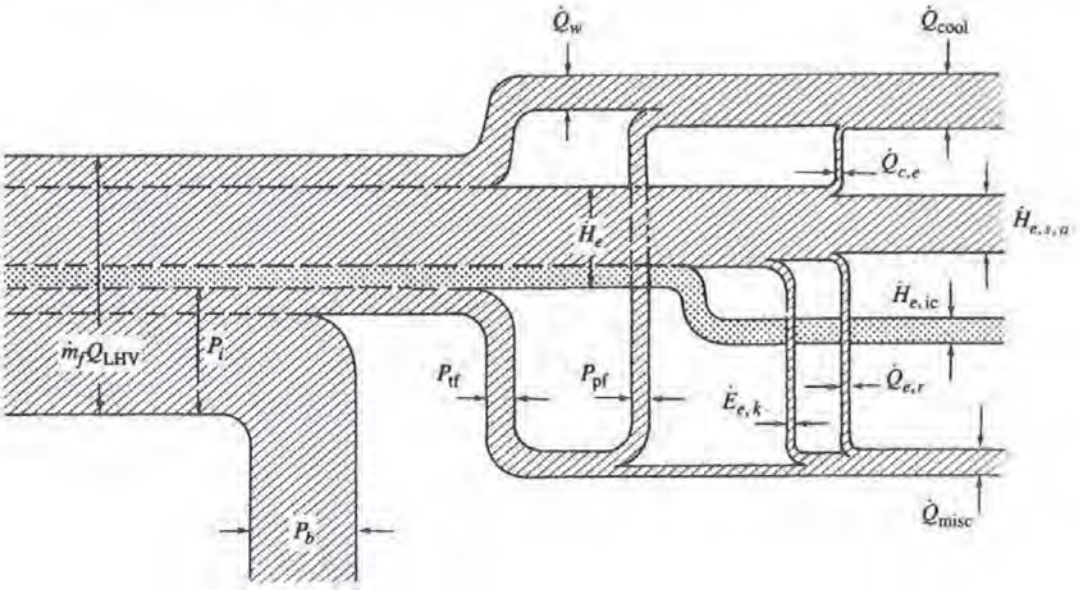


FIGURE 12-3
Energy flow diagram for IC engine. ($\dot{m}_f Q_{LHV}$) = fuel flow rate × lower heating value, $\dot{Q}_w$ = heat-transfer rate to combustion chamber wall, $\dot{H}_e$ = exhaust gas enthalpy flux, P_b = brake power, P_{tf} = total friction power, P_i = indicated power, P_{pf} = piston friction power, $\dot{Q}_{cool}$ = heat-rejection rate to coolant, $\dot{Q}_{c,e}$ = heat-transfer rate to coolant in exhaust ports, $\dot{H}_{e,s,a}$ = exhaust sensible enthalpy flux entering atmosphere, $\dot{H}_{e,ic}$ = exhaust chemical enthalpy flux due to incomplete combustion, $\dot{Q}_{e,r}$ = heat flux radiated from exhaust system, $\dot{E}_{e,k}$ = exhaust kinetic energy flux, $\dot{Q}_{misc}$ = sum of remaining energy fluxes and transfers.

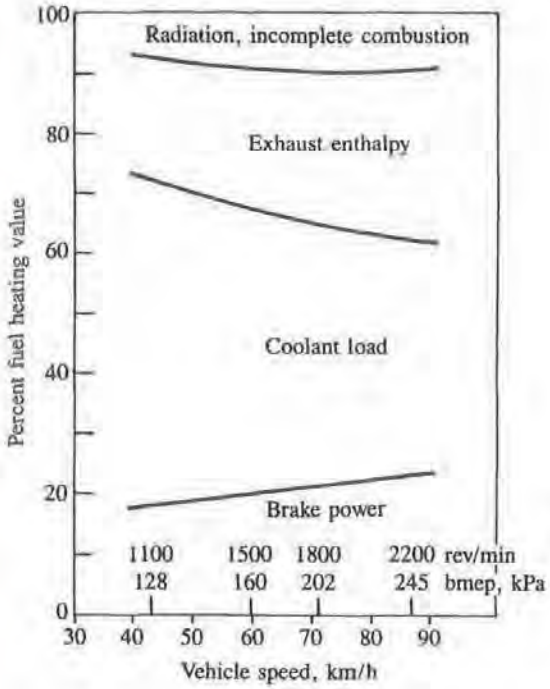


FIGURE 12-4
Brake power, coolant load, sensible exhaust enthalpy, and miscellaneous energy transfers as percent of fuel flow × heating value for spark-ignition engine at road-load operating conditions.[6]

to the environment and the remainder ends up in the cooling medium).† Thus the heat carried away by the coolant medium consists of heat transferred to the combustion chamber walls from the gases in the cylinder, heat transferred to the exhaust valve and port in the exhaust process, and a substantial fraction of the friction work.

At part-load, a greater fraction of the fuel heating value is absorbed into the coolant. Figure 12-4 shows data for a six-cylinder SI engine operated at road-load over a range of vehicle speeds. At low speeds and loads, the coolant heat-transfer rate is 2 to 3 times the brake power.

Although the heat losses are such a substantial part of the fuel energy input, elimination of heat losses would only allow a fraction of the heat transferred to the combustion chamber walls to be converted to useful work. The remainder would leave the engine as sensible exhaust enthalpy. Consider this example for an automotive high-speed naturally aspirated CI engine with a compression ratio of 15. The indicated efficiency is 45 percent, and 25 percent of the fuel energy is carried away by the cooling water. Of this 25 percent, about 2 percent is due to friction. Of the remaining 23 percent, about 8 percent is heat loss during combustion, 6 percent heat loss during expansion, and 9 percent heat loss during exhaust. Of the 8 percent lost during combustion about half (or 4 percent of the fuel energy) could be converted into useful work on the piston (see Fig. 5-9). Of the 6 percent heat loss during expansion, about one-third (or 2 percent) could

† The percentages are approximate.

have been utilized. Thus, of the 25 percent lost to the cooling system, only about 6 percent could have been converted to useful work on the piston, which would increase the indicated efficiency of the engine from 45 to 51 percent.

For a spark-ignition engine, the conversion to useful work will be lower, because the compression ratio is lower. However, as shown in Fig. 12-4, the heat losses at part-load (an important operating regime for automobile use) are a substantially larger fraction of the fuel heating value. Studies with computer simulations of the SI engine operating cycle indicate that at typical part-load conditions a proportional reduction in combustion-chamber-wall heat losses of 10 percent results in a proportional increase (improvement) in brake fuel conversion efficiency of about 3 percent.[7]

12.4 CONVECTIVE HEAT TRANSFER

12.4.1 Dimensional Analysis

While the overall time-averaged heat transfer to the coolant medium is adequate for some design purposes, the instantaneous heat flux during the engine cycle is a necessary input for realistic cycle calculations (see Sec. 14.4) and provides the fundamental input for obtaining the heat flux distribution to various parts of an operating engine. Equations (12.5), (12.6), and (12.7) provide the framework for calculating the heat flux $\dot{q}$, based on the assumption that at each point in the cycle the heat-transfer process is quasi steady. For example, neglecting radiation, if $\bar{T}_g$, $\bar{T}_{w,g}$, and $h_{c,g}$ can be calculated at each point in the cycle, $q(\theta)$ is obtained. Alternatively, if $\bar{T}_c$, $h_{c,c}$, $\bar{T}_g$, and $h_{c,g}$ are known, $\dot{q}$, $T_{w,g}$, and $T_{w,c}$ can be computed.

Dimensional analysis can be used to develop the functional form of relationships which govern the gas-side heat-transfer coefficient.[8] The engine convective heat-transfer process can be characterized geometrically by a length dimension—say the bore B—and a number of length ratios y_1, y_2, y_3, etc. (of which one will be the axial cylinder length z divided by the bore z/B), which define the cylinder and combustion chamber geometry. The flow pattern, similarly, may be characterized by one chosen velocity v and a set of velocity ratios u_1, u_2, u_3, etc. The gas properties of importance are the thermal conductivity k, the dynamic viscosity μ, the specific heat c_p, and the density ρ. If there is combustion, then the chemical energy release rate per unit volume $\dot{q}_{ch}$ may be important. The engine speed N and relative position in the cycle denoted by crank angle θ introduce the cyclical nature of the process. Thus

$$f(h_c, B, z, y_1, y_2, \ldots, y_m, v, u_1, u_2, \ldots, u_n, k, \mu, c_p, \rho, \dot{q}_{ch}, N, \theta) = 0$$

Applying dimensional analysis, with mass, length, time, and temperature as the independent dimensions, reduces the variables to four-fewer nondimensional groups:

$$F\left(\frac{h_c B}{k}, \frac{\rho v B}{\mu}, \frac{c_p \mu}{k}, \frac{c_p T}{v^2}, \frac{NB}{v}, \frac{\dot{q}_{ch}}{\rho c_p N T}, \frac{z}{B}, y_1, \ldots, y_m, u_1, \ldots, u_n, \theta\right) = 0$$

The first three groups are the familiar Nusselt, Reynolds, and Prandtl numbers, respectively. The next has the nature of a Mach number since $c_p T$ is proportional to the square of the sound speed. For Mach numbers much less than 1, the Mach number dependence is known to be small and can be omitted. It is usual to take for v the mean piston speed $\bar{S}_p = 2LN$. Then, by introducing the bore/stroke ratio B/L, the term NB/v is eliminated. z/B is a function of the compression ratio r_c, the ratio of connecting rod to crank radius $R = l/a$, and θ. Thus

$$F\left(\frac{h_c B}{k}, \frac{\rho \bar{S}_p B}{\mu}, \frac{c_p \mu}{k}, \frac{B}{L}, \frac{\dot{q}_{ch}}{\rho c_p N T}, r_c, R, y_1, \ldots, y_m, \theta, u_1, \ldots, u_n\right) = 0 \quad (12.10)$$

The dimensionless groups may be varied (but not reduced in number) by combination. While Eq. (12.10) reveals nothing about the functional form of the relationship between the groups, it does provide a basis for evaluating the correlations which have been proposed.

Many formulas for calculating instantaneous engine heat-transfer coefficients have been proposed (see Ref. 9 for a review). Only those with a functional form which fits Eq. (12.10) will be summarized here. The basis of these correlations is the assumption that the Nusselt, Reynolds, and Prandtl number relationship follows that found for turbulent flow in pipes or over flat plates:

$$\mathrm{Nu} = a\,\mathrm{Re}^m\,\mathrm{Pr}^n \quad (12.11)$$

Distinctions should be made between correlations intended to predict the *time-averaged* heat flux to the combustion chamber walls, the *instantaneous spatially averaged* heat flux to the chamber walls (which is required for engine performance analysis), and the *instantaneous local* heat fluxes (which are not uniform over the combustion chamber and may be required for thermal stress calculations). In using these heat-transfer correlations, the critical choices to be made are (1) the velocity to be used in the Reynolds number; (2) the gas temperature at which the gas properties in Eq. (12.11) are evaluated; and (3) the gas temperature used in the convective heat-transfer equation (12.2).

The most widely used correlations and the basis of their derivation will now be summarized. Because the experimental data for evaluating these correlations in CI engines includes both convective and radiative heat fluxes, comparison of these correlations with data is deferred to Sec. 12.6.

12.4.2 Correlations for Time-Averaged Heat Flux

Taylor and Toong[10] have correlated overall heat-transfer data from 19 different engines. It was assumed that coolant and wall temperatures varied little between designs and that the effects of geometrical differences were small. Thus, at a given fuel/air ratio, the convective part of the heat flux should correlate with Reynolds number. To allow for variations in fuel/air ratio, Taylor and Toong defined an

average effective gas temperature $T_{g,a}$ such that

$$\int Ah_c(T - T_{g,a})d\theta = 0$$

over the engine cycle. $T_{g,a}$ is the temperature at which the wall would stabilize if no heat was removed from outside. $T_{g,a}$ was obtained by extrapolating average heat-transfer data plotted versus gas-side combustion chamber surface temperature back to the zero heat-transfer axis. The Nusselt number, defined as

$$\text{Nu} = \frac{\bar{Q}B}{(\pi B^2/4)(T_{g,a} - T_c)k_g} = \frac{4\bar{Q}}{\pi B k_g(T_{g,a} - T_c)} \tag{12.12}$$

plotted against Reynolds number, defined as

$$\text{Re} = \frac{\dot{m}B}{\mu_g(\pi B^2/4)} = \frac{4\dot{m}}{\pi\mu_g B} \tag{12.13}$$

where $\dot{m}$ is the charge mass flow rate, is shown in Fig. 12-5. Taylor and Toong proposed a power law of 0.75. Annand[8] suggests three separate lines for the three different types of engines covered, with slope 0.7. The diesel line is about 25 percent higher than the spark-ignition engine line (which corresponds in part to the radiative heat flux component present in diesels). The air-cooled engine line is lower than the liquid-cooled line, presumably because surface temperatures are higher. The average gas temperature values developed by Taylor and Toong are shown in the insert in Fig. 12-5.

12.4.3 Correlations for Instantaneous Spatial Average Coefficients

Annand[8] developed the following convective heat-transfer correlation to match previously published experimental data on instantaneous heat fluxes to selected cylinder head locations:

$$\left(\frac{h_c B}{k}\right) = a\left(\frac{\rho \bar{S}_p B}{\mu}\right)^b \tag{12.14}$$

The value of a varied with intensity of charge motion and engine design. With normal combustion, $0.35 \leq a \leq 0.8$ with $b = 0.7$, and a increases with increasing intensity of charge motion. Gas properties are evaluated at the cylinder-average charge temperature $\bar{T}_g$:

$$\bar{T}_g = \frac{pVM}{m\tilde{R}} \tag{12.15}$$

The same temperature is used in Eq. (12.2) to obtain the convective heat flux.

Note that in developing this correlation, the effects of differences in geometry and flow pattern between engines [the ratios $y_1, \ldots, y_m$ and $u_1, \ldots, u_n$ in Eq. (12.10)] have been incorporated in the proportionality constant a, and the

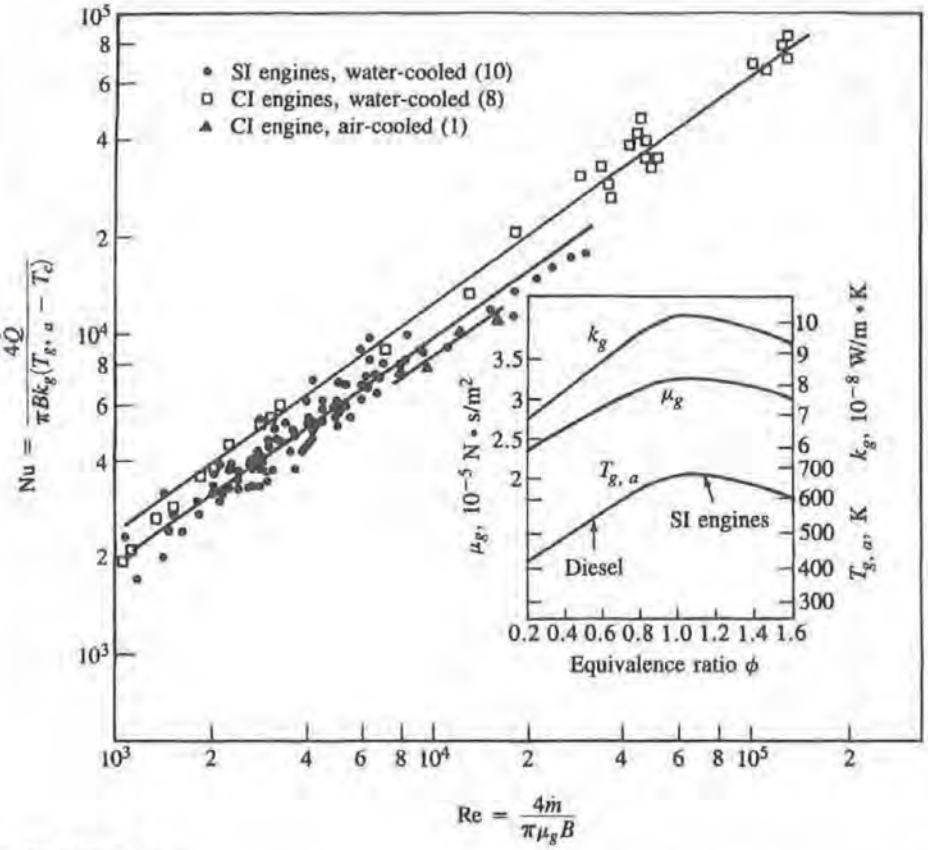


FIGURE 12-5
Overall engine heat-transfer correlation: gas-side Nusselt number versus Reynolds number for different types of IC engines. See text for definition of symbols. Insert gives effective gas temperature (wall temperature for adiabatic operation), gas viscosity μ_g and thermal conductivity k_g. Lines have slope 0.7.[8, 10]

effect of chemical energy release is omitted. While only data from cylinder head thermocouple locations were used as a basis for this correlation, it has often been used to estimate instantaneous spatial average heat fluxes for the entire combustion chamber.

Woschni[11] assumed a correlation of the form

$$\mathrm{Nu} = 0.035\ \mathrm{Re}^m \tag{12.16}$$

With the cylinder bore B taken as the characteristic length, with w as a local average gas velocity in the cylinder, and assuming $k \propto T^{0.75}$, $\mu \propto T^{0.62}$, and $p = \rho RT$, the above correlation can be written

$$h_c = CB^{m-1} p^m w^m T^{0.75-1.62m} \tag{12.17}$$

During intake, compression, and exhaust, Woschni argued that the average gas velocity should be proportional to the mean piston speed. During combustion and expansion, he attempted to account directly for the gas velocities induced by the change in density that results from combustion ($\sim$10 m/s), which are comparable to mean piston speeds. Thus a term proportional to the pressure

rise due to combustion ($p - p_m$) was added (p_m is the motored cylinder pressure). The coefficients relating the local average gas velocity w to the mean piston speed and ($p - p_m$) were determined by fitting the correlation, integrated over the engine cycle, to time-averaged measurements of heat transfer to the coolant for a wide range of engine operating conditions for a direct-injection four-valve diesel without swirl. T in Eq. (12.17) is the mean cylinder gas temperature defined by Eq. (12.15); the same temperature is used to obtain the heat flux from the heat-transfer coefficient h_c. Thus this correlation represents *spatially averaged* combustion chamber heat fluxes.

The average cylinder gas velocity w (meters per second) determined for a four-stroke, water-cooled, four-valve direct-injection CI engine without swirl was expressed as follows:

$$w = \left[C_1 \bar{S}_p + C_2 \frac{V_d T_r}{p_r V_r} (p - p_m) \right] \tag{12.18}$$

where V_d is the displaced volume, p is the instantaneous cylinder pressure, p_r, V_r, T_r are the working-fluid pressure, volume, and temperature at some reference state (say inlet valve closing or start of combustion), and p_m is the motored cylinder pressure at the same crank angle as p.

For the gas exchange period: $C_1 = 6.18, \quad C_2 = 0$
For the compression period: $C_1 = 2.28, \quad C_2 = 0$
For the combustion and expansion period: $C_1 = 2.28, \quad C_2 = 3.24 \times 10^{-3}$

Subsequent studies in higher-speed engines with swirl indicated higher heat transfer than these velocities predicted. For engines with swirl, cylinder averaged gas velocities were given by Eq. (12.18) with:

For the gas exchange period: $C_1 = 6.18 + 0.417 \frac{v_s}{\bar{S}_p}$

For the rest of cycle: $C_1 = 2.28 + 0.308 \frac{v_s}{\bar{S}_p}$

where $v_s = B\omega_p/2$ and ω_p is the rotation speed of the paddle wheel used to measure the swirl velocity (see Sec. 8.3.1).[12] Spark-ignition engine tests showed that the above velocities gave acceptable predictions for this type of engine also.[13]

Woschni's correlation, with the exponent in Eq. (12.17) equal to 0.8, can be summarized as:

$$h_c(\mathrm{W/m^2 \cdot K}) = 3.26 B(\mathrm{m})^{-0.2} p(\mathrm{kPa})^{0.8} T(\mathrm{K})^{-0.55} w(\mathrm{m/s})^{0.8} \tag{12.19}$$

with w defined above.

Hohenberg[14] examined Woschni's formula and made changes to give better predictions of time-averaged heat fluxes measured with probes in a direct-injection diesel engine with swirl. The modifications include use of a length based on instantaneous cylinder volume instead of bore, changes in the effective gas velocity, and in the exponent of the temperature term.

12.4.4 Correlations for Instantaneous Local Coefficients

LeFeuvre *et al.*[15] and Dent and Sulaiman[16] have proposed the use of the flat-plate forced convection heat-transfer correlation formula

$$\left(\frac{h_c l}{k}\right) = 0.036\left(\frac{\rho v l}{\mu}\right)^{0.8}\left(\frac{\mu c_p}{k}\right)^{0.333} \tag{12.20}$$

where l is the length of the plate and v the flow velocity over the plate. This formula has been applied to DI diesel engines with swirl, with l and v evaluated at a radius r as

$$l = 2\pi r \qquad v = r\omega$$

ω being the solid-body angular velocity of the charge. The heat flux at any radius r (with Pr = 0.73) is then given by

$$\dot{q}(r) = 0.023\,\frac{k}{r}\left(\frac{\omega r^2}{\nu}\right)^{0.8}[\bar{T}_g(r) - T_w(r)] \tag{12.21}$$

This equation can be used if the swirl variation with crank angle is known (see Sec. 8.3) and an appropriate local gas temperature can be determined. It would not be consistent to use the cylinder average gas temperature given by Eq. (12.15) because during combustion substantial temperature nonuniformities exist between burned gases and air or mixture which has yet to burn or mix with already burned gas.

An alternative approach is zonal modeling, where the combustion chamber is divided into a relatively small number of zones each with its own temperature, heat-transfer coefficient, and heat-transfer surface area history. This approach has been applied to spark-ignition engines (e.g., Ref. 17), where the division of the in-cylinder gases during combustion into a higher-temperature burned gas region behind the flame and lower-temperature unburned gas region ahead of the flame is clear (see Fig. 9-4). The heat transfer to the combustion chamber surfaces in contact with the unburned and burned gas zones [analagous to Eq. (12.2)] is given by

$$\dot{Q}_u = A_{u,w}\,h_{c,u}(T_u - T_w) \qquad \dot{Q}_b = A_{b,w}\,h_{c,b}(T_b - T_w) \tag{12.21a,b}$$

respectively. Since h_c depends on local gas properties and velocities, $h_{c,u}$ and $h_{c,b}$ are not necessarily the same. Examples of how the burned gas wetted areas on the piston, cylinder head, and liner vary during the combustion process are given in Fig. 14-8. Since the burned gas temperature T_b is much larger than the unburned gas temperature, the heat flux from the burned gas zone dominates.

One useful development of this two-zone approach is the division of the burned gas zone into an adiabatic core and a thermal boundary layer. The advantages are: (1) this corresponds more closely to the actual temperature distribution (see Sec. 12.6.5); (2) a model for the boundary-layer flow provides a more fundamental basis for evaluating the heat-transfer coefficient. The local heat

flux is then given by[18]

$$\dot{q} = \frac{k_e(T_{ac} - T_w)}{\delta} \tag{12.22}$$

where k_e is the effective thermal conductivity in the boundary layer, T_{ac} is the adiabatic core temperature, and δ the boundary-layer thickness. In the laminar regime δ would grow as $t^{1/2}$; in the turbulent regime δ would grow as $t^{0.8}$. Both growth regimes are observed.

Zonal models have also been used to describe DI diesel engine heat transfer.[19] A bowl-in-piston chamber was divided into three flow regions and two gas-temperature zones during combustion. An effective velocity

$$w = (U_x^2 + U_y^2 + 2k)^{1/2}$$

was used to obtain the heat-transfer coefficient, where U_x and U_y are the two velocity components parallel to the surface outside the boundary layer and k is the turbulent kinetic energy. Zonal models would be expected to be more accurate than global models. However, only limited validation has been carried out.

12.4.5 Intake and Exhaust System Heat Transfer

Convective heat transfer in the intake and exhaust systems is driven by much higher flow velocities than in-cylinder heat transfer. Intake system heat transfer is usually described by steady, turbulent pipe flow correlations.[9] With liquid fuel present in the intake, the heat-transfer phenomena become especially complicated (see Sec. 7.6). Exhaust flow heat-transfer rates are the largest in the entire cycle due to the very high gas velocities developed during the exhaust blowdown process and the high gas temperature (see Sec. 6.5). Exhaust system heat transfer is important since it affects emissions burnup in the exhaust system, catalyst, or particulate trap, it influences turbocharger performance, and it contributes significantly to the engine cooling requirements.

The highest heat-transfer rates occur during blowdown, to the exhaust valve and port. Detailed exhaust port convective heat-transfer correlations have been developed and tested. These are based on Nusselt-Reynolds number correlations. For the valve open period, relations of the form

$$\mathrm{Nu} = K\ \mathrm{Re}_j^n \tag{12.23}$$

have been proposed and evaluated.[20] For $L_v/D_v \lesssim 0.2$, the flow exits the valve as a jet, and $\mathrm{Re}_j = v_j D_v/\nu$, where D_v is the valve diameter, v_j the velocity of the exhaust gases through the valve opening, and ν the kinematic velocity. For $L_v/D_v \gtrsim 0.2$, the port is the limiting area and a pipe flow model with $\mathrm{Re} = v_p D_p/\nu$ is more appropriate. v_p is the velocity in the port and D_p is the port diameter. For the valve closed period, the correlation

$$\mathrm{Nu} = 0.022\ \overline{\mathrm{Re}}_D^{0.8} \tag{12.24}$$

was developed. Here $\overline{\mathrm{Re}}_D = \bar{v}_p D_p/\nu$, where $\bar{v}_p$ is the time-averaged exhaust port gas velocity and D_p is the port diameter. For straight sections of exhaust pipe downstream of the port, an empirical correlation based on measurements of average heat-transfer rates to the pipe has been derived:[21]

$$\mathrm{Nu} = 0.0483\ \mathrm{Re}^{0.783} \tag{12.25}$$

The Reynolds number is based on pipe diameter and velocity. Heat-transfer correlations for steady developing turbulent flow in pipes predict values about half that given by Eq. (12.25).

12.5 RADIATIVE HEAT TRANSFER

There are two sources of radiative heat transfer within the cylinder: the high-temperature burned gases and the soot particles in the diesel engine flame. In a spark-ignition engine, the flame propagates across the combustion chamber from the point of ignition through previously mixed fuel and air. Although the flame front is slightly luminous (see color plate, Fig. 9-1), all the chemical intermediaries in the reaction process are gaseous. Combustion is essentially complete early in the expansion stroke. In the compression-ignition engine (and in fuel-injected stratified-charge engines), most of the fuel burns in a turbulent diffusion flame as fuel and air mix together. There can be many ignition locations, and the flame conforms to the shape of the fuel spray until dispersed by air motion (see color plate, Figs. 10-4 and 10-5). The flame is highly luminous, and soot particles (which are mostly carbon) are formed at an intermediate step in the combustion process.

The radiation from soot particles in the diesel engine flame is about five times the radiation from the gaseous combustion products. Radiative heat transfer in conventional spark-ignition engines is small in comparison with convective heat transfer. However, radiative heat transfer in diesel engines is not negligible; it contributes 20 to 35 percent of the total heat transfer and a higher fraction of the maximum heat-transfer rate.

12.5.1 Radiation from Gases

Gases absorb and emit radiation in narrow wavelength bands rather than in a continuous spectrum as do solid surfaces. The simpler gas molecules such as H_2, O_2, and N_2 are essentially transparent to radiation. Of the gases important in combustion, CO, CO_2, and H_2O emit sufficient energy to warrant consideration. In gases, emission and absorption will occur throughout the gas volume. These processes will be governed by the number of molecules along the radiation path. For each species, this will be proportional to the product of the species partial pressure p_i and the path length l. In addition the radiative capacity depends on gas temperature T_g. Thus the emissivity of the gas ε_g can be expressed as

$$\varepsilon_g = f(T_g, p_1 l, \ldots, p_n l) \tag{12.26}$$

The mean path length for a volume V with surface area A is given with sufficient accuracy by

$$l = 0.9 \times \frac{4V}{A} \tag{12.27}$$

$4V/A$ is the mean path length for a hemispherical enclosure.

Standard methods have been developed for estimating ε_g for mixtures of CO_2 and H_2O by Hottel and others (see Ref. 22). Charts based on experimental data give ε_{CO_2} and ε_{H_2O} as functions of $p_i l$ and T_g. Correction factors are applied for total pressures above one atmosphere and for the overlapping of spectral bands of CO_2 and H_2O. Estimates for engine combustion gases at peak conditions give $\varepsilon_g \approx 0.1$ and peak heat fluxes due to gas radiation of order 0.2 MW/m^2. This amounts to ~ 5 percent of the peak convective heat transfer. Since gas radiation is proportional to T_g^4, this radiative flux falls off more rapidly from peak values than convective heat flux and, when integrated over the cycle, can be neglected.

12.5.2 Flame Radiation

Flame radiation is a much more complex process because the detailed geometry and chemical composition of the radiating region are not well known. Since the radiation from the optically transparent or nonluminous flames of spark-ignition engines is small, we will deal only with luminous nontransparent flames where the radiation comes from incandescent soot particles and has a continuous spectrum. Because the particle size distribution, number density and temperature, and flame geometry in a diesel engine are not well defined, flame emissivities cannot be calculated from first principles. Direct measurements of flame emissivities are required. A number of measurements of the magnitude and spectral distribution of radiation from a diesel engine combustion chamber have been made (see Ref. 9 for a summary). The most extensive of these by Flynn *et al.*[23] in a direct-injection engine used a monochromator to measure intensity of radiation at seven wavelengths. The viewing path cut through the piston crown into the central region of the bowl-in-piston combustion chamber. Fuel was injected through a five-hole nozzle and some air swirl was provided. At any given crank angle, the distribution of energy over the seven wavelengths was used to reconstruct the complete energy spectrum and to calculate the apparent radiation temperature and optical thickness.

The energy distribution was skewed from that of a grey-body model (for which emissivity is independent of wavelength), and the monochromatic emissivity was well fitted by the equation

$$\varepsilon_\lambda = 1 - \exp\left(\frac{-kl}{\lambda^{0.95}}\right) \tag{12.28}$$

used to describe the emissivity variation from clouds of small particles. Figure 12-6 shows sample results for the monochromatic emissive power and monochro-

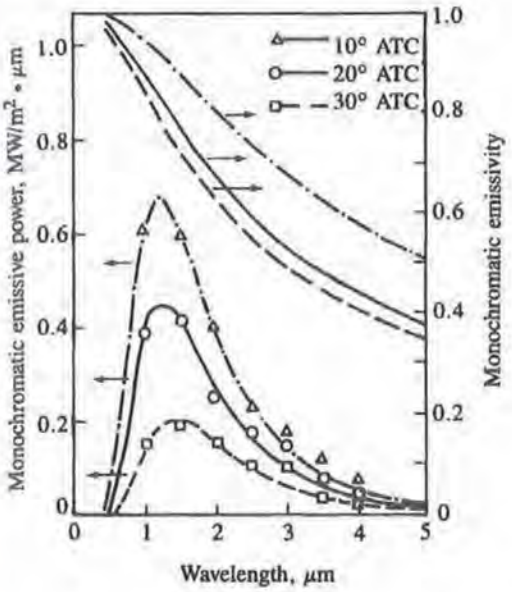


FIGURE 12-6
Variation in monochromatic emissive power and emissivity, with wavelength, at three different crank angles. DI diesel engine with 114 mm bore, 1995 rev/min, overall equivalence ratio 0.46. Radiation from piston bowl measured through cutout in piston crown.[23]

matic emissivity. Equation (12.28), combined with Planck's equation for blackbody monochromatic emissive power

$$e_{b,\lambda} = \frac{2\pi K_1}{\lambda^5 (e^{K_2/\lambda T_R} - 1)} \tag{12.29}$$

where $K_1 = 0.59548 \times 10^{-16}$ W · m² and $K_2 = 1.43879$ cm · K, defined an apparent radiation temperature T_R and optical thickness kl for the radiating medium. An apparent grey-body emissivity ε_a was also calculated from the standard equation

$$\varepsilon_a = \frac{\int \varepsilon_\lambda e_{b,\lambda} d\lambda}{\int e_{b,\lambda} d\lambda}$$

Figure 12-7 shows sample results for four equivalence ratios at an engine speed of 2000 rev/min. The radiation flux has approximately the same shape and time span as the net heat-release rate curve (which was determined from the cylinder pressure curve). During the period of maximum radiation, the apparent emissivity is 0.8 to 0.9; it then decreases as the expansion process proceeds.[23] In previous experiments on the same engine, instantaneous total heat fluxes had been measured at various locations on the cylinder head.[24] A comparison of radiant and total heat fluxes (both peak and average) showed that the radiation heat flux can be a substantial fraction of the peak heat flux. The average radiant flux is about 20 percent of the average total flux: the percentage varies significantly with load. These conclusions are supported by other experimental data summarized in the next section.

The radiation or apparent flame temperatures measured in diesels by several investigators show consistent results (see Fig. 12-8). Also included in the figure during the combustion and expansion process are typical values of: (1) the

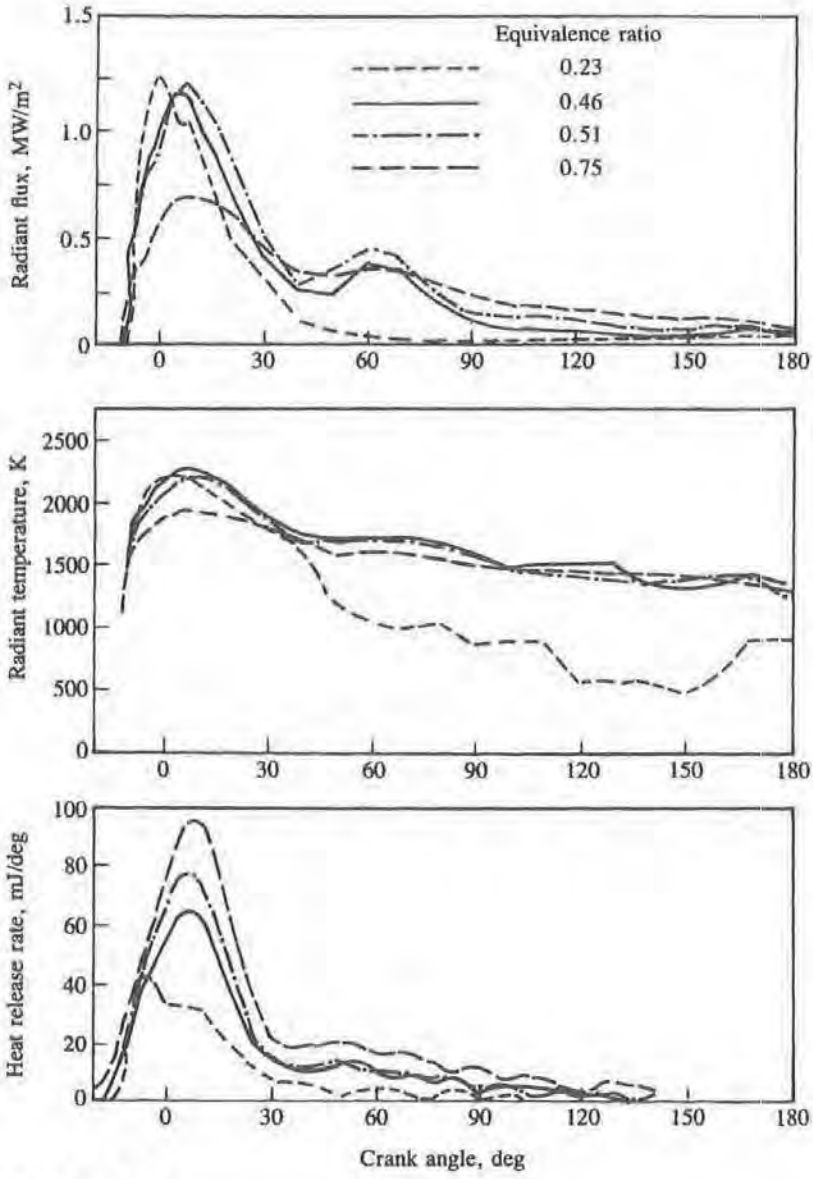


FIGURE 12-7
Radiant heat flux, apparent radiant temperature and net heat-release rate as function of crank angle for DI diesel engine at four different loads. Engine and measurement details as in Fig. 12-6; 2000 rev/min.[23]

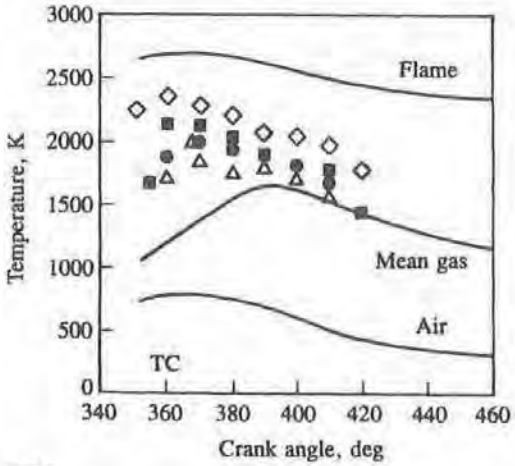


FIGURE 12-8
Apparent radiation temperatures measured in diesel engines, compared to calculated maximum adiabatic flame, cylinder-mean and air temperatures, during the combustion period. Adiabatic flame temperature is temperature attained by burning air at air temperature with fuel for equivalence ratio of 1.1. (*Data from Dent and Sulaiman,*[16] *Flynn* et al.,[23] *Lyn,*[25] *Kamimoto* et al.;[26] *calculated curves from Assanis and Heywood.*[27])

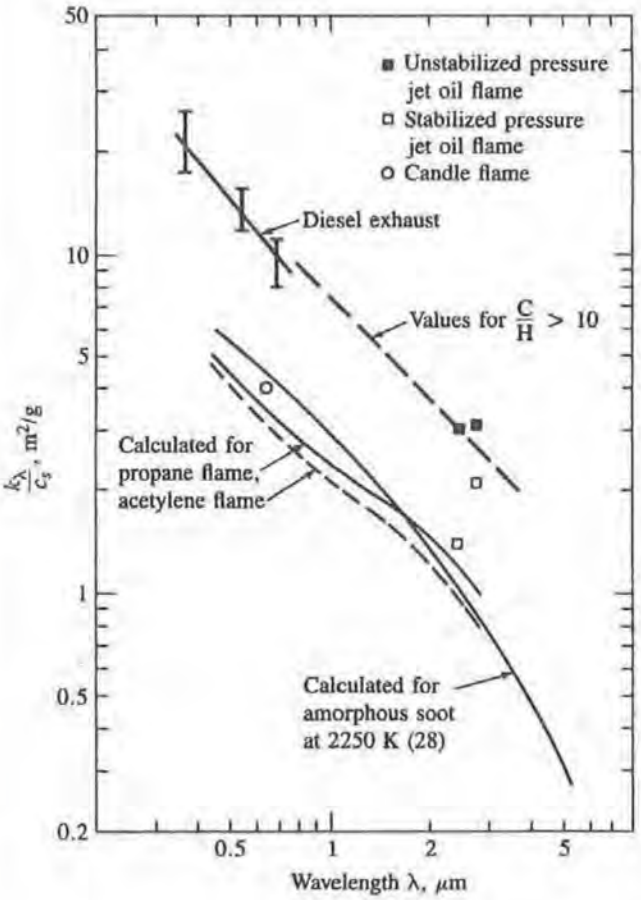


FIGURE 12-9
Measured and calculated values of k_λ/c_s as a function of wavelength λ. k_λ is monochromatic absorption coefficient, c_s is the soot concentration. (*From Field* et al.[28] *and Greeves and Meehan.*[29])

temperature of any air not yet mixed with fuel or burned gases; (2) the average temperature of the cylinder contents; and (3) the maximum possible flame temperature [corresponding to combustion of a slightly rich mixture ($\phi = 1.1$) with air at the temperature shown]. The measured radiation temperatures fall between the maximum flame temperatures and the bulk temperature. Such a model has been proposed, fits the available data, and has been used.[27] Zonal models have been proposed (e.g., the burned gas region is stoichiometric[16, 19]) to define an appropriate flame temperature.

The emissivity of an incandescent soot-burning flame can be calculated from a knowledge of the monochromatic absorption coefficient, which is given by

$$k_\lambda = 36\pi \frac{c_s}{\rho_s} \frac{n^2\kappa}{\lambda[(n^2 + n^2\kappa^2)^2 + 4(n^2 - n^2\kappa^2 + 1)]} = 36\pi \frac{c_s}{\rho_s} f(\lambda, T) \quad (12.30)$$

where n is the refractive index, κ is the absorption term in the complex refractive index, c_s is the soot concentration in kilograms per cubic meter, and ρ_s is the density of the soot particles (≈ 2 g/m^3).[28] The absorption coefficient depends on wavelength and temperature, is independent of particle size, and depends only on the soot mass loading. Figure 12-9 shows several estimates of k_λ/c_s as a function of λ. The strong dependence on λ shows that clouds of soot particles are markedly not grey. There is a considerable spread in the different estimates shown.

This could be the result of different soot compositions (the C/H ratio affects the optical properties) and temperatures. To find a mean value for the absorption coefficient of a wide spectrum of radiation, the expression

$$k_a = \frac{\int k_\lambda e_{b,\lambda}\, d\lambda}{\int e_{b,\lambda}\, d\lambda}$$

must be evaluated. For example, for radiation from a black body at temperature 1800 K, the mean absorption coefficient is $\approx 1300 c_s$ per meter, where c_s is in kilograms per cubic meter. At higher black-body temperatures, the value of k_a would be higher.

Annand[30] has applied this approach to a diesel engine. The apparent flame emissivity was related to the apparent mean absorptivity by

$$\varepsilon_a = 1 - \exp(-k_a l) \tag{12.31}$$

For Flynn's data, the peak emissivity is 0.8 which gives $k_a l = 1.6$. Since $l \approx 0.07$ m, this gives $k_a \approx 22\ \text{m}^{-1}$ and $c_s \approx 16\ \text{g/m}^3$ ($\approx 1\ \text{g/m}^3$ at NTP), which is a soot loading comparable with values measured in diesel engines during combustion (see Figs. 11-42 to 11-44).

12.5.3 Prediction Formulas

Well-accepted prediction formulas for radiant heat flux in an engine are not available. Annand has proposed a radiation term of the form

$$\dot{q}_R = \beta\sigma(\bar{T}_g^4 - T_w^4) \tag{12.32}$$

where σ is the Stefan-Boltzmann constant, $\bar{T}_g$ is the mean gas temperature, and T_w is the wall temperature. This term was coupled with a convective heat flux term to give a correlation for predicting total heat flux. In a first evaluation, when coupled with Eq. (12.14), $\beta = 0.6$ was proposed.[8] In a later study with a modified convective heat-transfer correlation,[31] $\beta \approx 1.6$ was proposed. (Note that since the temperature used is the average gas temperature and not the apparent flame temperature, β is not an emissivity.) The limited evaluation of this approach shows that $\beta = 0.6$ gave approximately correct magnitude for $\dot{q}_R$ for one engine and was too low for another.[32] $\beta = 1.6$ gave radiant heat fluxes higher than experimental data.[33]

Flynn *et al.*[23] developed an empirical expression for instantaneous radiant heat flux to fit their data, of the form

$$\dot{q}_R = 2\bar{\dot{q}}_R\, b(a+1)\left(\frac{\theta - \theta_s}{360}\right)^a \exp\left[\frac{(\theta - \theta_s)^{a+1}}{360}\right] \tag{12.33}$$

where θ_s is the crank angle at the start of the radiation pulse. Correlations for $\bar{\dot{q}}_R$, a, b, and θ_s in terms of engine speed, manifold pressure, crank angle at the start of fuel injection, and the equivalence ratio were obtained and presented. This corre-

lation gave a reasonable match to Flynn's data, an example of which was shown in Fig. 12-7.

It has been proposed that the apparent absorptivity should be proportional to pressure.[4, 313] The assumption is then made that the proportionality constant would be a unique function of the equivalence ratio and crank angle. Although k_a is dependent on p for gas radiation, it is not clear that the same proportionality should apply to soot radiation.

12.6 MEASUREMENTS OF INSTANTANEOUS HEAT-TRANSFER RATES

12.6.1 Measurement Methods

Values of instantaneous heat flux into the combustion chamber walls have been obtained from measurements of the instantaneous surface temperature. The temperature variation at the wall is a result of the time-varying boundary condition at the gas/wall interface. It is damped out within a small distance (~ 1 mm) from the wall surface, so measurements must be made at the surface. Various types of thermocouple or thermistor have been used.[9] One-dimensional unsteady heat conduction into the wall is then assumed:

$$\frac{\partial T}{\partial t} = \frac{1}{\rho c}\frac{\partial}{\partial x}\left(k\frac{\partial T}{\partial x}\right) \tag{12.34}$$

A sinusoidal variation with time of heat flux into a semi-infinite solid can be shown to produce a sinusoidal variation of surface temperature of the same frequency displaced in phase by 90°. The surface temperature T_w is expressed as a Fourier series:

$$T_w = T_m + \sum_{n=1}^{N} [A_n \cos(n\omega t) + B_n \sin(n\omega t)] \tag{12.35}$$

where T_m is the time-averaged value of T_w, A_n and B_n are Fourier coefficients, n is a harmonic number, and ω is the angular frequency (radians per second). The boundary conditions are $T = T_w(t)$ at $x = 0$ and $T = T_l$ (constant) at $x = l$. The solution of Eq. (12.35) is[1]

$$T(x, t) = T_m - (T_m - T_l)\frac{x}{l} + \sum_{n=1}^{N} \exp(-\phi_n x) F_n(x, t) \tag{12.36}$$

where

$$F_n = A_n \cos(n\omega t - \phi_n x) + B_n \sin(n\omega t - \phi_n x)$$

and $\phi_n = (n\omega/2\alpha)^{1/2}$, where α is the thermal diffusivity of the wall material $k/(\rho c)$.

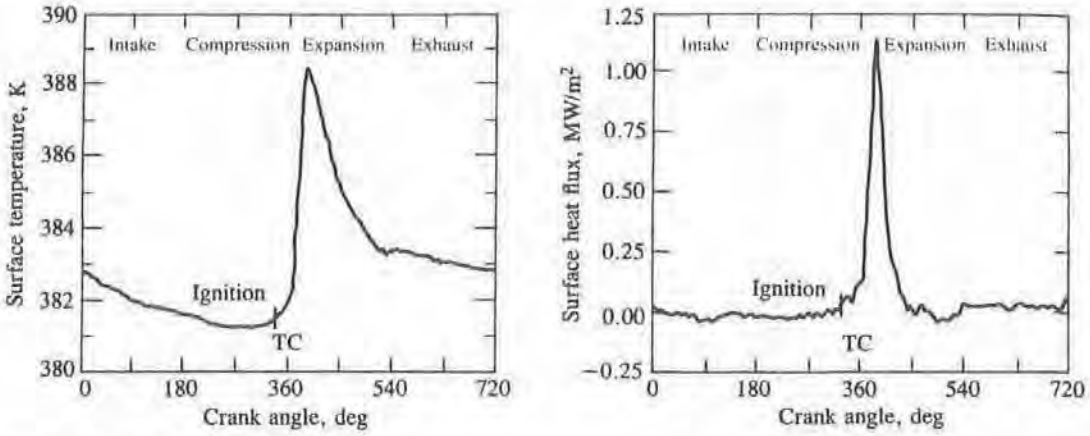


FIGURE 12-10
Surface temperature measured with thermocouple in cylinder head, and surface heat flux calculated from surface temperature, as a function of crank angle. Spark-ignition engine operated at part-load.[34]

The heat flux components at each frequency that caused that variation can be calculated via Fourier's law [Eq. (12.1)], and summed to give the total fluctuation of heat flux with time:

$$\dot{q}_w = \frac{k}{l}(T_m - T_l) + k\sum_{n=1}^{N} \phi_n[(A_n + B_n)\cos(n\omega t) - (A_n - B_n)\sin(n\omega t)] \quad (12.37)$$

Alternative approaches for solving Eq. (12.34) are through use of an electrical analogy to heat flow and by numerical methods. The latter become necessary if wall material properties depend significantly on temperature, as do combustion chamber deposits and some insulating ceramic materials. Several measurements of this type in spark-ignition and diesel engines have been made. A summary of these measurements can be found in Ref. 9.

Radiant heat fluxes are determined by a variety of techniques: e.g., photodetector and infrared monochromator; thermocouple shielded by a sapphire window; pyroelectric thermal detector.

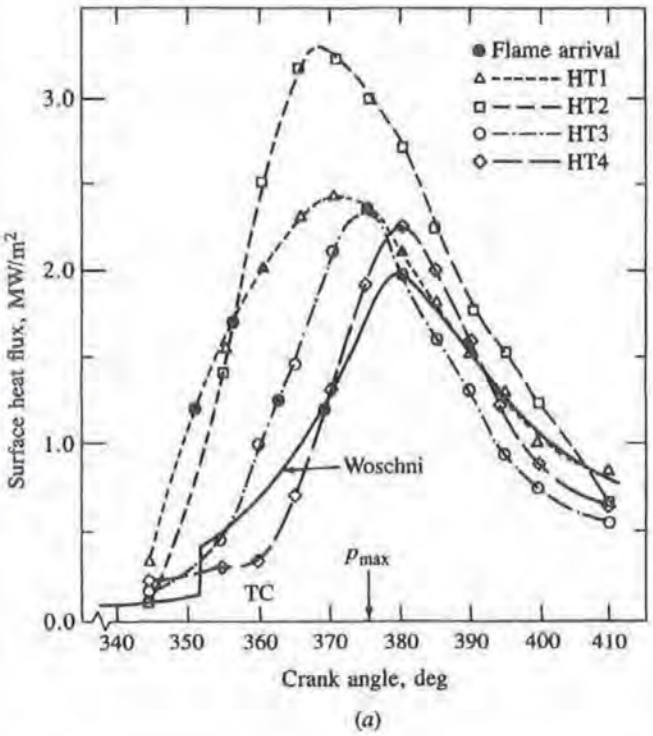
12.6.2 Spark-Ignition Engine Measurements

Figure 12-10 shows the surface temperature variation with crank angle, and the heat flux variation calculated from it, on the cylinder head of a spark-ignition engine at a part-load low-speed operating condition. The swing in surface temperature at this point (about halfway from the on-the-cylinder-axis spark plug to the cylinder wall) is 7 K. The heat flux rises rapidly when the flame arrives at the measurement location, has its maximum at about the time of peak cylinder pressure when gas temperatures peak (see Section 9.2.1), and then decays to relatively low levels by 60° ATC as expansion cools the burned gases. Peak heat fluxes on the cylinder head of 1.5 to 3 MW/m^2 were measured over the normal engine speed and load range.[34, 35]

The heat flux profile varies significantly with location and from one cycle to the next. Figure 12-11 illustrates both these effects. When the rapid rise in heat

flux occurs depends on the flame arrival time at the measurement location. Thus the heat fluxes determined from surface temperature data averaged over many cycles show their rapid rise later, the further the distance from the spark plug location (Fig. 12-11*a*). The individual cycle data in Fig. 12-11*b* show how variations in the flame arrival time from one cycle to the next essentially shift the rising portion of the heat flux profile in time. Note that due to this cyclic variation, the average profile shows a less rapid rise in heat flux than do individual cycles.

Such measurements show that increasing engine speed and increasing engine load increase the surface heat flux. Retarding timing delays the rise in heat



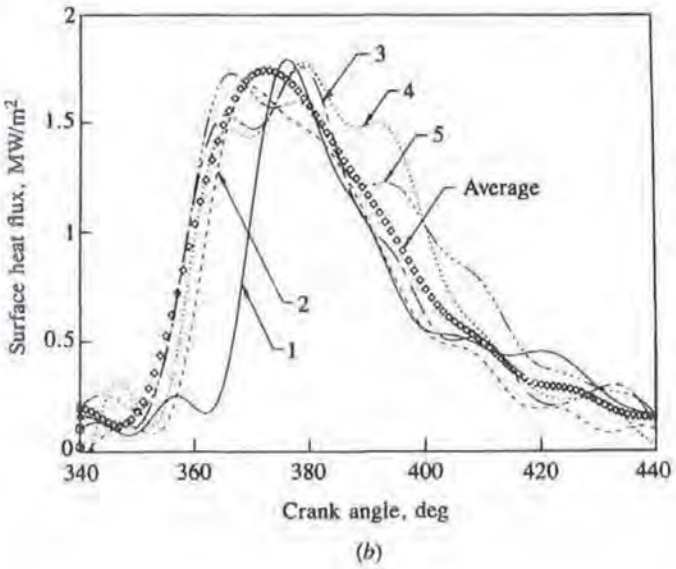


FIGURE 12-11
(*a*) Variation of surface heat flux with crank angle at four temperature measurement locations in the cylinder head of a spark-ignition engine. Each curve is an average over many cycles. Distances from on-axis spark plug are: HT1, 18.7 mm; HT2, 27.5 mm; HT3, 37.3 mm; HT4, 46.3 mm. Bore = 104.7 mm, 2000 rev/min, part-load $\eta_v = 40$ percent, $A/F = 18$, MBT timing. Solid curve shows heat flux predicted by Woschni's correlation.[34] (*b*) Heat flux histories for five consecutive individual cycles and 198-cycle average at location HT1. 1500 rev/min, $A/F = 18$, $\eta_v = 40$ percent, MBT timing.[35]

flux and reduces the peak value. Maximum heat fluxes occur with close-to-stoichiometric mixtures.[34, 35] All these trends would be expected from the variations in burned gas temperature that result from these changes in engine operation.

12.6.3 Diesel Engine Measurements

Measurements of instantaneous heat fluxes in diesel engines show similar features. The heat flux distribution is usually highly nonuniform. There may also be significant variations between the heat flux profiles from individual cycles. Figure 12-12 shows surface heat fluxes at two locations in a medium-swirl DI diesel, one over the piston bowl (higher heat flux) and the other over the piston squish area, in relation to the heat-release profile. The heat flux increases rapidly once combustion starts, reaches a maximum at close to the time of maximum cylinder pressure, and decreases to a low value by 40 to 60° ATC. Peak heat fluxes to the primary combustion chamber surfaces (the piston bowl and head directly above the bowl) are of order 10 MW/m^2.

In smaller diesel engines with swirl, the mean heat flux to the piston within the piston bowl is usually higher than the mean heat fluxes to the cylinder head and the annular squish portion of the piston crown (by about a factor of two).[16, 31] This would be expected since the piston bowl is the zone where most of the combustion takes place and gas velocities are highest. There are, in addition, substantial variations in heat flux at different locations within the piston bowl, on the head, and on the annular region of the piston crown.

In contrast to the above results obtained on smaller high-speed (~10-cm bore) diesels with swirl with deep bowl-in-piston combustion chambers of diameter about half the piston diameter, results from tests on a medium-speed 30-cm bore quiescent shallow-bowl piston direct-injection supercharged diesel showed a much more uniform heat flux distribution over the combustion chamber walls.[37]

Heat fluxes to the cylinder liner are much lower still (an order of magnitude less than the peak flux to the combustion chamber surface) and are also nonuniform. Figure 12-13 compares heat fluxes to the cylinder head with three locations along the liner. Even at the top of the liner, the peak heat flux is only 15 to 20

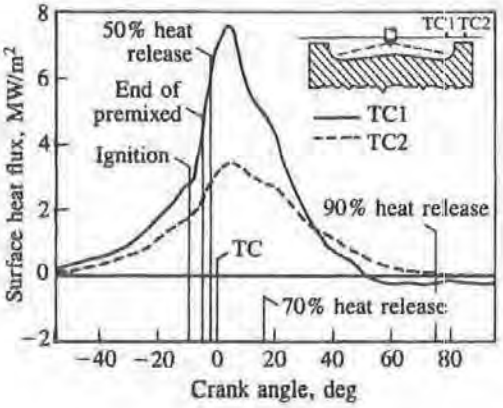


FIGURE 12-12
Measured surface heat flux at two locations in the cylinder head of a medium-swirl DI diesel engine. TC1 above the piston bowl, TC2 above the piston squish area as shown. Percentages of heat release are indicated. Bore = stroke = 114 mm, $r_c = 16$, 2000 rev/min, overall equivalence ratio = 0.5, intake pressure = 1.5 atm.[36]

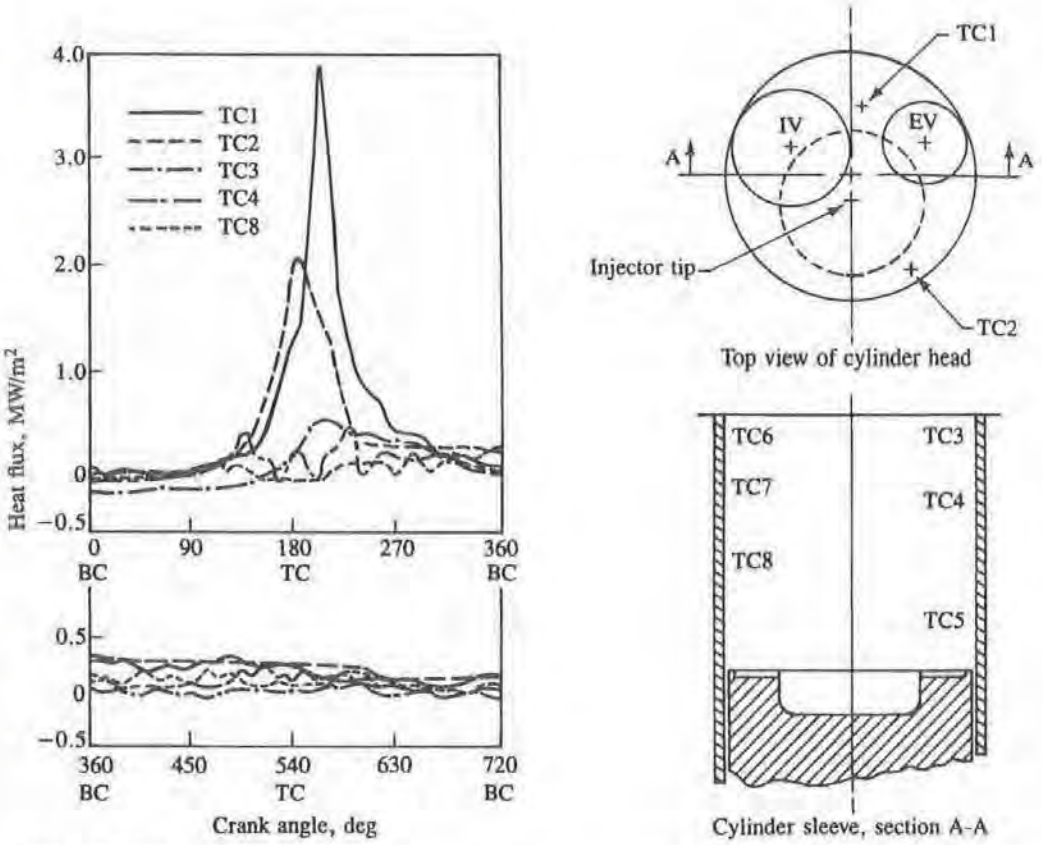


FIGURE 12-13
Measured surface heat fluxes at different locations in cylinder head and liner of naturally aspirated four-stroke cycle DI diesel engine. Bore = stroke = 114 mm, 2000 rev/min, overall equivalence ratio = 0.45.[15]

percent of the flux to the primary combustion chamber surfaces. Again this would be expected, since the combustion gases do not contact the lower parts of the cylinder wall until later in the expansion stroke when their temperature is much below the peak value.

Figure 12-14 shows examples of radiant heat flux measured above the piston bowl of a medium-swirl DI diesel engine as a function of engine speed and load.[16] The limited radiant heat flux data available exhibit the following trends. The rapid increase in radiant heat flux following combustion is delayed relative to the start of pressure rise due to combustion (by about 5°); this delay increases with increasing speed. The peak radiant flux remains approximately constant with increasing equivalence ratios up to $\phi \approx 0.5$. Further increases in the equivalence ratio produce a drop in level of radiant flux. The time-averaged radiant heat flux increased approximately linearly with increasing manifold pressure; however, peak radiative flux levels remained essentially unchanged. Peak and time-averaged values of the radiant heat flux decreased as injection timing was retarded.

In diesel engines, the relative importance of radiant heat transfer (as a percentage of the total heat flux) depends on the location on the combustion

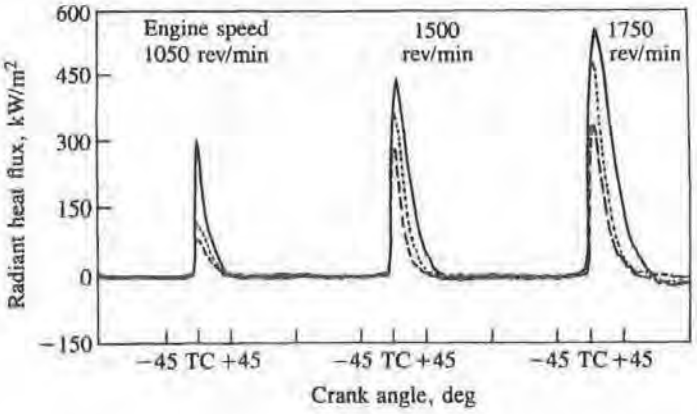


FIGURE 12-14
Measured radiant heat flux to cylinder head above the piston bowl in a high-swirl DI diesel engine when load and speed are varied. Solid curve: 80 percent load. Dotted curve: 40 percent load. Dashed curve: no load.[16]

chamber surface, crank angle, engine load, engine size, and engine design. The time-averaged radiant heat transfer increases as a proportion of the total heat transfer, with increasing load, as indicated in Fig. 12-15.[9] At high load, the total radiant heat flux is between 25 and 40 percent of the total time-averaged heat flux.

12.6.4 Evaluation of Heat-Transfer Correlations

The convective (or combined convective plus radiative) heat flux correlations have been compared with instantaneous engine heat-transfer measurements. One difficulty in this evaluation is the determination of spatially averaged combustion-chamber heat fluxes from the experimental data for comparison with correlations intended to predict the mean chamber heat flux as a function of crank angle. The area-averaged instantaneous heat flux prediction using Woschni's equation (12.19) for the spark-ignition engine conditions shown in Fig. 12-11*a* is comparable in magnitude to, though lower than, the measured heat fluxes to the cylinder head.

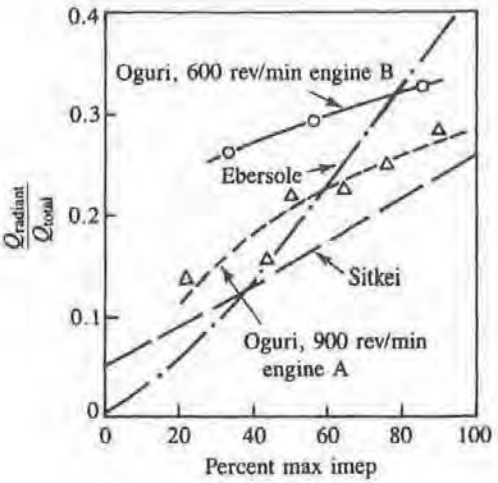


FIGURE 12-15
Radiant heat flux as fraction of total heat flux over the load range of several different diesel engines.[9]

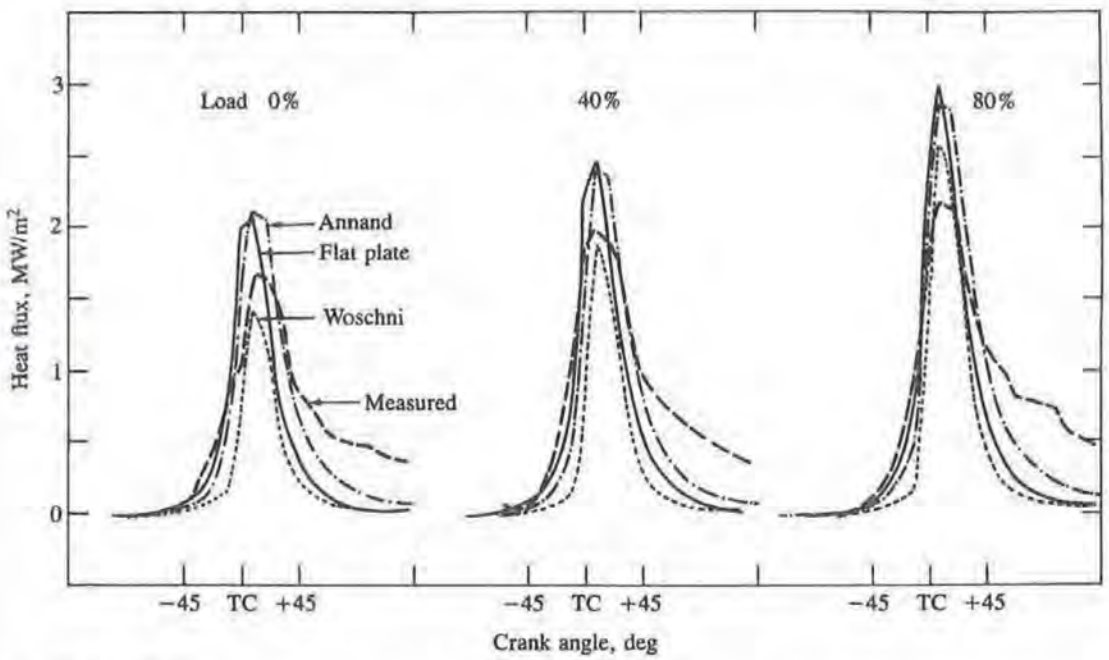


FIGURE 12-16
Comparison of measured mean heat fluxes on the cylinder head at 1050 rev/min in a fired high-swirl DI diesel engine with various prediction equations. Annand, Eq. (12.14), Woschni, Eq. (12.19), flat plate, Eq. (12.20) using measured gas motion.[16]

More extensive comparisons have been made of predictions with data for diesel engines. Annand's correlations, Eqs. (12.14) and (12.32) with $a = 0.06$, $b = 0.85$, and β (for the combustion phase only) $= 0.57$, gave reasonable agreement with instantaneous cylinder head heat fluxes, and overall time-averaged heat fluxes for a medium-speed quiescent DI engine design.[37] In a small high-speed diesel with swirl, values of $a = 0.13$, $b = 0.7$, and $\beta = 1.6$ gave an approximate fit to estimates of the instantaneous area-mean heat flux[31] and time-averaged heat flux to the piston.[38] Comparisons of the Annand and Woschni correlations generally show that the Annand correlation predicts higher heat fluxes at the same crank angle.[11, 24] The most careful comparison of all three correlations summarized in Secs. 12.4.3 and 12.4.4 with experimental data has been made by Dent and Sulaiman in a small high-speed diesel engine with swirl.[16] The mean experimental heat flux was estimated from a number of thermocouple measurements located at different points around the combustion chamber surface. Figure 12-16 shows the comparison. The Woschni correlation falls below the others at light load because the combustion-induced velocity term is smaller. Expansion stroke heat fluxes are underpredicted by all three correlations. Given the uncertainty in converting the measurements to an average heat flux value, the agreement is reasonably good.

Dent examined additional modifications to the flat plate formula [Eq. (12.20)], which was based on a cylinder-mean gas temperature. During combustion a two-zone model is more appropriate. Assuming an equivalence ratio

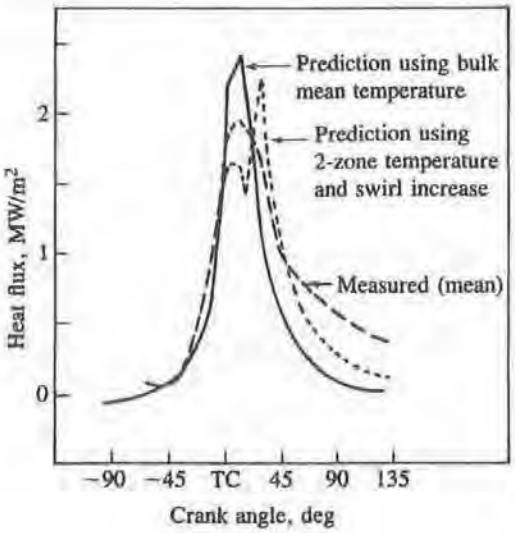


FIGURE 12-17
Measured heat fluxes on cylinder head in fired high-swirl DI diesel engine at 1050 rev/min and 40 percent load compared with predictions based on bulk mean gas temperature and using temperatures based on two-zone (air and burned gas) model.[16]

for the burned gas (Dent assumed stoichiometric), a combustion zone temperature can be determined from the relation

$$\bar{T}_b = \frac{m\bar{T}_g - m_a T_a}{m_b}$$

where m_a is the mass of air, T_a is the air temperature, and m_b is the burned gas mass, $m_b = m - m_a$. In addition, the observed swirl enhancement which occurs due to the combustion was included by multiplying the swirl velocity used in the heat-transfer correlation by the square root of the ratio (density of air in the motored case)/(density of burned gas in fired case). The combination of both effects (see Fig. 12-17) improves the shape of the predictions by broadening and lowering the peak.

Each of the convective-heat-transfer correlations described has limited experimental support. However, under engine design and operating conditions different from those under which they were derived, the predictions should be viewed with caution. Woschni's correlation is the correlation used most extensively for predicting spatially averaged instantaneous convective heat fluxes. However, the empirical constants which relate the mean piston speed and combustion-induced motion to the velocity used in the Reynolds number, determined by Woschni, will not necessarily apply to all the different types of engine. If local velocities are known, the flat-plate-based correlations provide the best available approach. Annand's correlation has the advantage of being the simplest correlation to use. Since the radiation component in diesel engine heat transfer is normally 20 to 40 percent of the total an approximate estimate of its value may suffice.

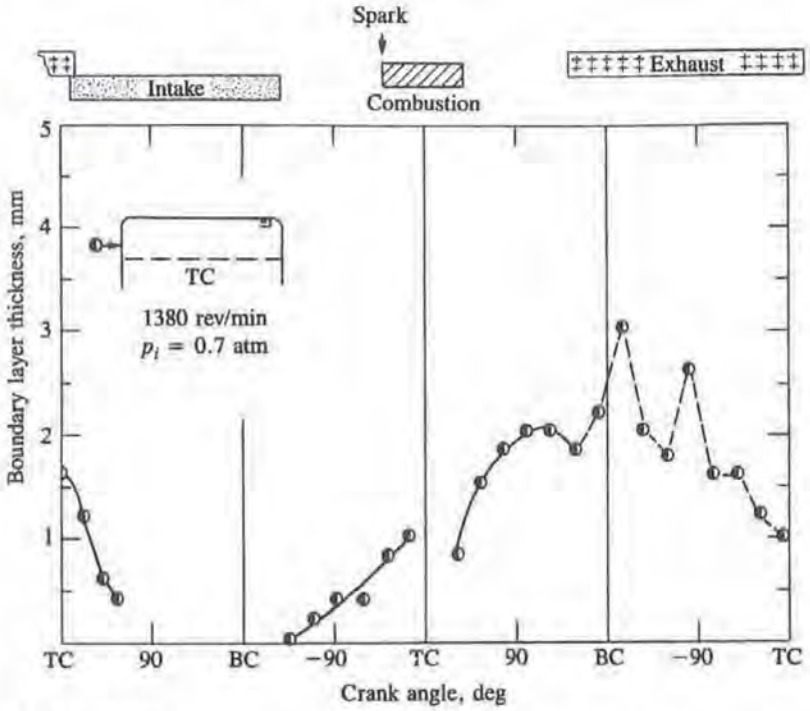


FIGURE 12-18
Thermal boundary-layer thickness, at the top of the cylinder wall in the clearance volume, determined from schlieren photographic measurements in a special visualization square-piston spark-ignition engine.[39]

12.6.5 Boundary-Layer Behavior

Measurements of thermal boundary-layer thickness in an operating spark-ignition engine have been made using schlieren photography in a special flow-visualization engine. Figure 12-18 shows one set of measurements on the cylinder wall in the clearance volume opposite the spark plug. The boundary-layer thickness decreases during intake and increases steadily during compression and expansion to about 2 mm. It stops growing and becomes unstable during the exhaust process, separating from the cylinder wall and becoming entrained into the bulk gas leaving the cylinder. The thickness of the thermal boundary layer varies substantially at different locations throughout the chamber. While the trends with crank angle were similar, the layers on the cylinder head and piston crown were substantially (up to 2 to 3 times) thicker during compression and expansion in the simple disc-shaped chamber studied.[39] This different behavior probably results because there is no bulk flow adjacent to the head and piston crown.

Estimates of thermal boundary-layer thickness in spark-ignition engines, based on convective-heat-transfer correlations and thermal energy conservation for the growing layer give thicknesses comparable to these measurements. Note that a substantial fraction of the cylinder mass is contained within the thermal

boundary layer. For example, for an average thickness of 3 mm at 90° ATC during expansion, the volume of the boundary layer is 20 percent of the combustion chamber volume for typical engine dimensions. Since the average density in the boundary layer is about twice that in the bulk gases, some 30 to 40 percent of the cylinder mass would be contained within this boundary layer.

12.7 THERMAL LOADING AND COMPONENT TEMPERATURES

The heat flux to the combustion chamber walls varies with engine design and operating conditions. Also, the heat flux to the various parts of the combustion chamber is not the same. As a result of this nonuniform heat flux and the different thermal impedances between locations on the combustion chamber surface and the cooling fluid, the temperature distribution within engine components is nonuniform. This section reviews the variation in temperature and heat flux in the components that comprise the combustion chamber.

12.7.1 Component Temperature Distributions

Figures 12-19 to 12-22 show illustrative examples of measured temperature distributions in various engine components. Normally, the heat flux is highest in the center of the cylinder head, in the exhaust valve seat region, and to the center of the piston. It is lowest to the cylinder walls. Cast-iron pistons run about 40 to 80°C hotter than aluminum pistons. With flat-topped pistons (typical of spark-ignition engines) the center of the crown is hottest and the outer edge cooler by 20 to 50°C. Diesel engine piston crown surface temperatures are about 50°C higher than SI engine equivalent temperatures. As shown in Fig. 12-19, the maximum piston temperatures with DI diesel engine pistons are at the lip of the

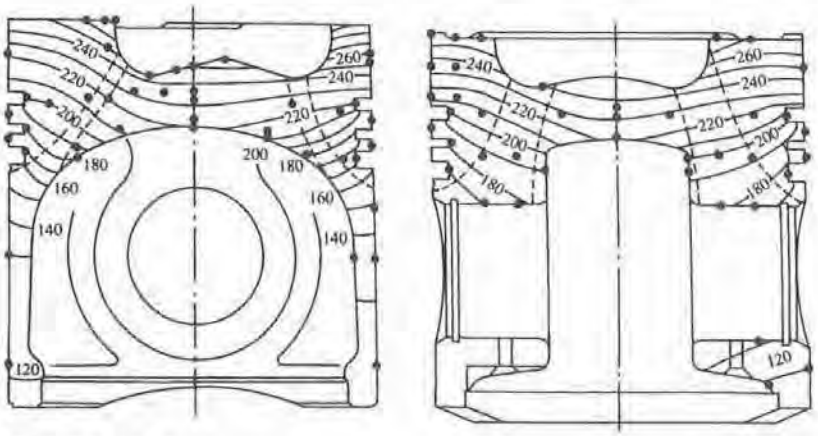


FIGURE 12-19
Isothermal contours (solid lines) and heat flow paths (dashed lines) determined from measured temperature distribution in piston of high-speed DI diesel engine. Bore 125 mm, stroke 110 mm, $r_c = 17$, 3000 rev/min, and full load.[40]

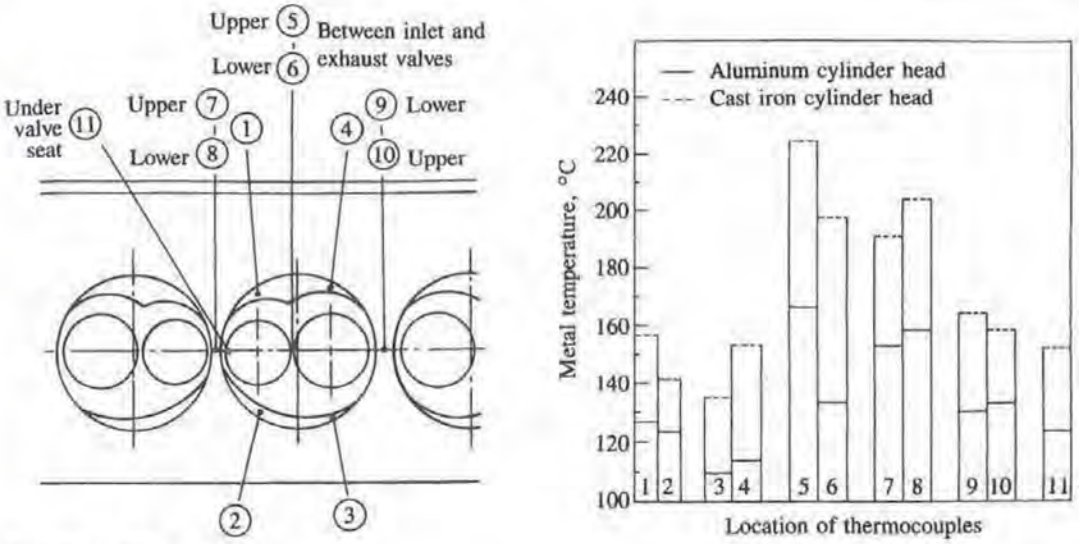


FIGURE 12-20
Variation of cylinder head temperature with measurement location in spark-ignition engine operating at 2000 rev/min, wide-open throttle with coolant water at 95°C and 2 atm.[41]

bowl. In IDI diesel engines, maximum piston temperatures occur where the prechamber jet impinges on the piston crown.

Figure 12-20 shows the temperatures at various locations on a four-cylinder SI engine cylinder head. The maximum temperatures occur where the heat flux is high and access for cooling is difficult. Such locations are the bridge between the valves and the region between the exhaust valves of adjacent cylinders. Figure 12-21 shows how the average heat flux and temperature vary along the length of a DI diesel engine liner. Because the lower regions of the liner are only exposed to combustion products for part of the cycle after significant gas expansion has occurred, the heat flux and temperature decrease significantly with distance from

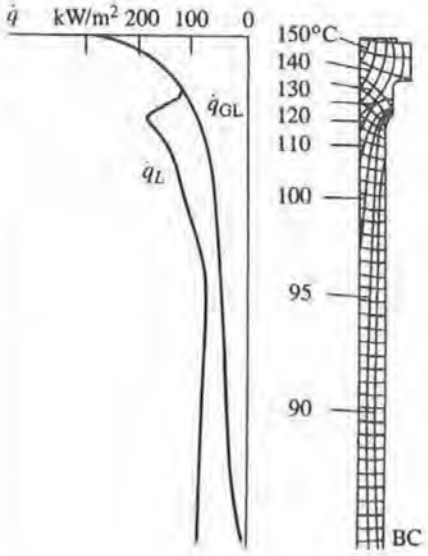


FIGURE 12-21
Temperature and heat flux distribution in the cylinder liner of a high-speed DI diesel engine at 1500 rev/min and bmep = 11 bar. $\dot{q}_L$ is heat flux into the liner; $\dot{q}_{GL}$ is heat flux from the gas to the liner. Difference is friction-generated heat flux.[42]

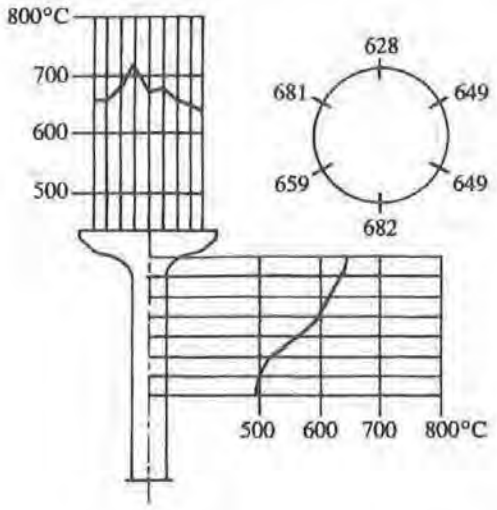


FIGURE 12-22
Temperature distribution in one of the four exhaust valves of a two-stroke-cycle uniflow DDA 4-53 DI diesel engine. Bore = 98 mm, stroke = 114 mm.[43]

the cylinder head. Note that the heat generated by friction between the piston and the liner, the difference between $\dot{q}_{GL}$ (the gas to liner heat flux) and $\dot{q}_L$ (the total heat flux into the liner), is a significant fraction of the liner thermal loading.

The exhaust valve is cooled through the stem and the guide, and the valve seat. In small-size valves the greater part of the heat transfer occurs through the stem; with large-size valves, the valve seat carries the higher thermal load.

Temperature distributions in engine components can be calculated from a knowledge of the heat fluxes across the component surface using finite element analysis techniques. For steady-state engine operation, the depth within a component to which the unsteady temperature fluctuations (caused by the variations in heat flux during the cycle) penetrate is small, so a quasi-steady solution is satisfactory. Results from such calculations for a spark-ignition engine piston illustrate the method.[44] A mean heat-transfer coefficient from the combustion chamber gases to the piston crown and a mean chamber gas temperature were defined (using the input from a cycle simulation of the type described in Sec.

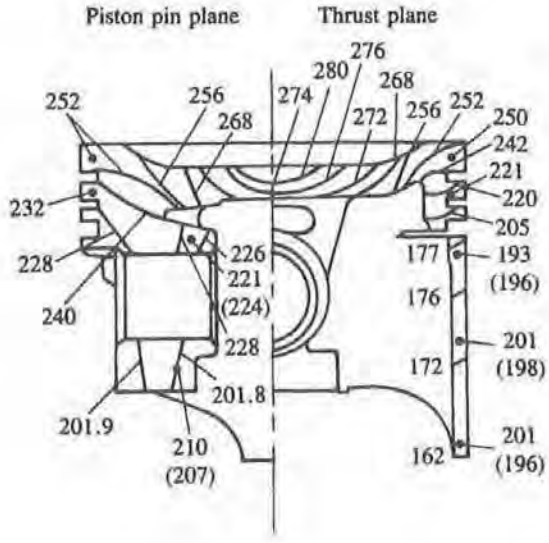


FIGURE 12-23
Measured (dots) and calculated temperature (°C) distributions in piston pin and thrust planes of the piston of a four-cylinder 2.5-dm^3 spark-ignition engine at 4600 rev/min and wide-open throttle.[44]

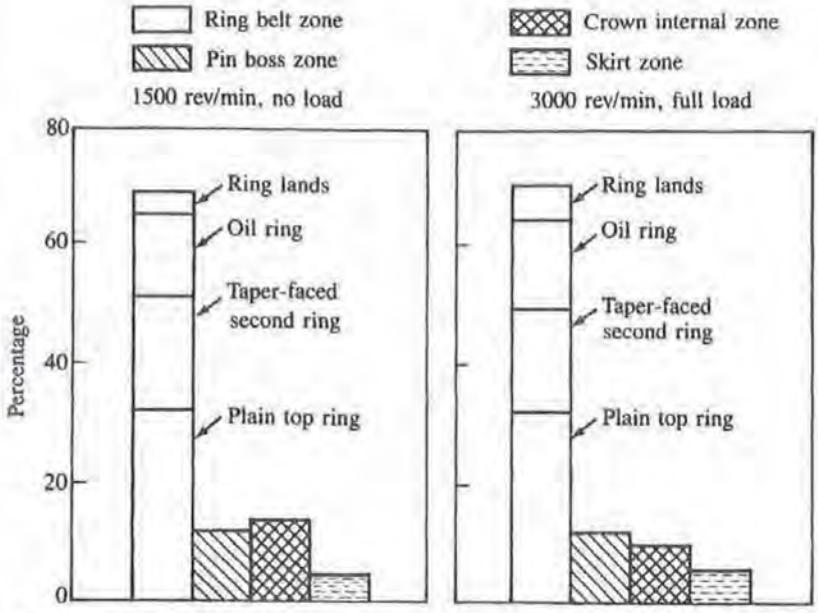


FIGURE 12-24
Heat outflow from various zones of piston as percentage of heat flow in from combustion chamber. High-speed DI diesel engine, 125 mm bore, 110 stroke, $r_c = 17$.[40]

14.4). These define the time-averaged heat flux into the piston. Heat-transfer coefficients for the different surfaces of the piston (underside of dome, ring-land areas, ring regions, skirt outer and inner surfaces, wrist pin bearings, etc.) were estimated. The actual piston shape was approximated with a three-dimensional grid for one quadrant of the piston. A standard finite element analysis of the heat flow through the piston yields the temperature distribution within the piston. The thermal stresses can therefore be calculated and added to the mechanical stress field to determine the total stress distribution. This can be used to define the potential fatigue regions in the actual piston design. Figure 12-23 shows the temperature distribution calculated with this approach, compared with measurements (indicated by dots). The agreement is acceptable, except in the piston skirt where the heat-transfer rate between the skirt and cylinder liner has been overestimated.

Detailed measurements of the temperature distribution in the piston allow the relative amounts of heat which flow out of the different piston surfaces to be estimated. Figure 12-24 shows examples of such estimates for a DI diesel engine at no-load and full-load. About 70 percent of the heat flows out through the ring zone, and much smaller amounts through the pin boss zone, underside of the crown and skirt. In larger diesel engines and highly loaded diesel engines, one or more cooling channels are incorporated into the piston crown. This reduces the heat flow out through the ring area significantly.[45]

12.7.2 Effect of Engine Variables

The following variables affect the magnitude of the heat flux to the different surfaces of the engine combustion chamber and the temperature distribution in the

components that comprise the chamber: engine speed; engine load; overall equivalence ratio; compression ratio; spark or injection timing; swirl and squish motion; mixture inlet temperature; coolant temperature and composition; wall material; wall deposits. Of these variables, speed and load have the greatest effect. Equation (12.19), derived from the Nusselt-Reynolds number relation

$$h_c = \text{constant} \times B^{-0.2} p^{0.8} T^{-0.55} w^{0.8}$$

and the relation for heat-transfer rate per unit area [Eq. (12.2)]

$$\dot{q} = h_c(T - T_w)$$

are useful for predicting trends as engine operating and design variables change.

The effect of the above variables on engine and component heat flux will now be summarized. The comments which follow apply primarily to spark-ignition engines. In compression-ignition engines, the distribution of heat flux and temperature varies greatly with the size of cylinder and form of the combustion chamber.

SPEED, LOAD, AND EQUIVALENCE RATIO. Predictions of spark-ignition engine heat transfer as a function of speed and load are shown in Fig. 12-25. The cycle heat transfer is expressed as a percent of the fuel's chemical energy (mass of fuel $\times$ Q_{LHV}). The heat transfer to the total combustion chamber surface (excluding the exhaust port) was calculated using a thermodynamic-based cycle simulation (see Sec. 14.4). The relative importance of heat losses *per cycle* decreases as speed and load increase: the *average* heat transfer *per unit time*, however, increases as speed and load increase.

Since speed and load affect p, T, and w in Eq. (12.19), simpler correlations have been developed to predict component heat fluxes from experimental data. Time-averaged heat fluxes at several combustion chamber locations, determined from measurements of the temperature gradient in the chamber walls, have been fitted with the empirical expression

$$\dot{q} = \text{constant} \times \left(\frac{\dot{m}_f}{A_p}\right)^n \tag{12.38}$$

with n between 0.5 and 0.75 (the value of n depending on engine type and location within the combustion chamber). Results for a modern four-cylinder SI

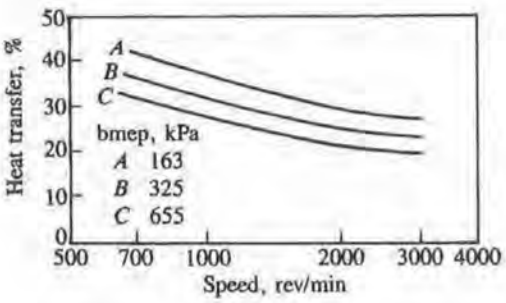


FIGURE 12-25
Predicted average heat-transfer rate (as percent of fuel flow rate $\times$ Q_{LHV}) to combustion chamber walls of an eight-cylinder 5.7-dm^3 spark-ignition engine as a function of speed and load. Stoichiometric operation; MBT timing.[46]

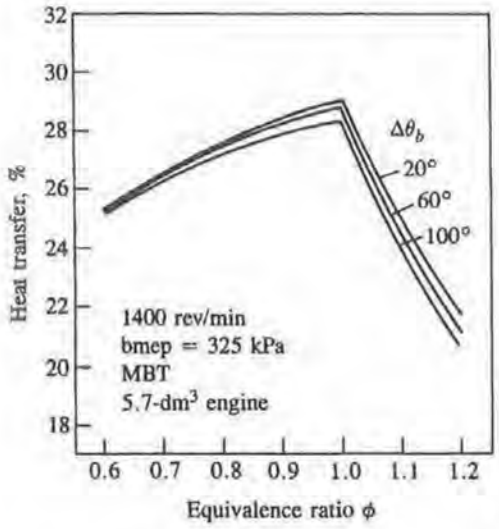


FIGURE 12-26
Predicted average heat-transfer rate (as percent of fuel flow rate × Q_{LHV}) to combustion chamber walls of an eight-cylinder 5.7-dm³ spark-ignition engine as a function of equivalence ratio and burn rate ($\Delta\theta_b$ = combustion duration).[46]

engine and several diesel engine designs, with appropriate values of n, can be found in Refs. 47 to 49. While this correlation is not dimensionless and does not satisfy Eq. (12.19), it provides a convenient method for reducing the experimental data. The heat flux to the cylinder head and liner for a spark-ignition engine were well correlated by Eq. (12.38) with $n = 0.6$. The flux distribution over the cylinder head at a fuel flow rate per unit piston area of 0.195 kg/s · m² for several different DI diesel engines were comparable in magnitude. The effect of speed at wide-open throttle on component temperatures for a spark-ignition engine can be found in Ref. 47. Exhaust valve, piston crown and top ring groove, and nozzle throat temperatures for a Comet prechamber diesel as a function of fuel flow rate can be found in Ref. 49.

The peak heat flux in an SI engine occurs at the mixture equivalence ratio for maximum power $\phi \approx 1.1$, and decreases as ϕ is leaned out or enriched from this value.[50] The major effect is through the gas temperature in Eqs. (12.2) and (12.19). However, as a fraction of the fuel's chemical energy, the heat transfer per cycle is a maximum at $\phi = 1.0$ and decreases for richer and leaner mixtures, as shown by the thermodynamic-based cycle-simulation predictions in Fig. 12-26. In CI engines, the air/fuel ratio variation is incorporated directly in the load variation effects.

COMPRESSION RATIO. Increasing the compression ratio in an SI engine decreases the total heat flux to the coolant until $r_c \approx 10$; thereafter heat flux increases slightly as r_c increases.[50] The magnitude of the change is modest; e.g., a 10 percent decrease in the maximum heat flux (at the valve bridge) occurs for an increase in r_c from 7.1 to 9.4.[47] Several gas properties change with increasing compression ratio (at fixed throttle setting): cylinder gas pressures and peak burned gas temperatures increase; gas motion increases; combustion is faster; the surface/volume ratio close to TC increases; the gas temperature late in the expansion stroke and during the exhaust stroke is reduced. Measured mean exhaust temperatures confirm the last point, which probably dominates the trend at lower

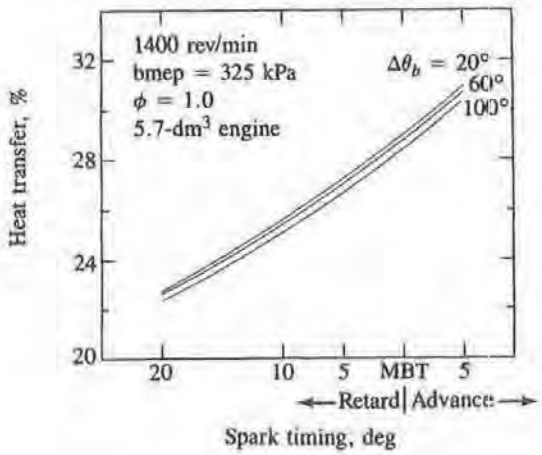


FIGURE 12-27
Predicted average heat-transfer rate (as percentage of fuel flow rate × Q_{LHV}) to combustion chamber walls of an eight-cylinder 5.7-dm^3 spark-ignition engine as a function of spark timing and burn rate ($\Delta\theta_b$ = combustion duration).[46]

compression ratios. As the compression ratio increases further, the other factors (which all increase heat transfer) become important.

The effect of changes in compression ratio on component temperatures depends on location. Generally, head and exhaust valve temperatures decrease with increasing compression ratio, due to lower expansion and exhaust stroke temperatures. The piston and spark plug electrode temperatures increase, at constant throttle setting, due to the higher peak combustion temperatures at higher compression ratios. If knock occurs (see Sec. 9.6), increases in heat flux and component temperatures result; see below.

SPARK TIMING. Retarding the spark timing in an SI engine decreases the heat flux as shown in Fig. 12-27. A similar trend in CI engines with retarding injection timing would be expected. The burned gas temperatures are decreased as timing is retarded because combustion occurs later when the cylinder volume is larger. Temperature trends vary with component. Piston and spark plug electrode temperatures change most with timing variations; exhaust valve temperature increases as timing is retarded due to higher exhausting gas temperatures.[47]

SWIRL AND SQUISH. Increased gas velocities, due to swirl or squish motion, will result in higher heat fluxes. Equation (12.19) indicates that the effect on local heat flux, relative to quiescent engine designs, should be proportional to (local gas velocity)$^{0.8}$. There is no direct evidence to support this correlation but there is evidence that use of a shrouded value to increase gas velocities within the cylinder increases the total heat transfer.[50]

INLET TEMPERATURE. The heat flux increases linearly with increasing inlet temperature; the gas temperatures throughout the cycle are increased. An increase of 100 K gives a 13 percent increase in heat flux.[51]

COOLANT TEMPERATURE AND COMPOSITION. Increasing liquid coolant temperature increases the temperature of components directly cooled by the liquid coolant. Figure 12-28 shows the result of a 50-K rise in coolant tem-

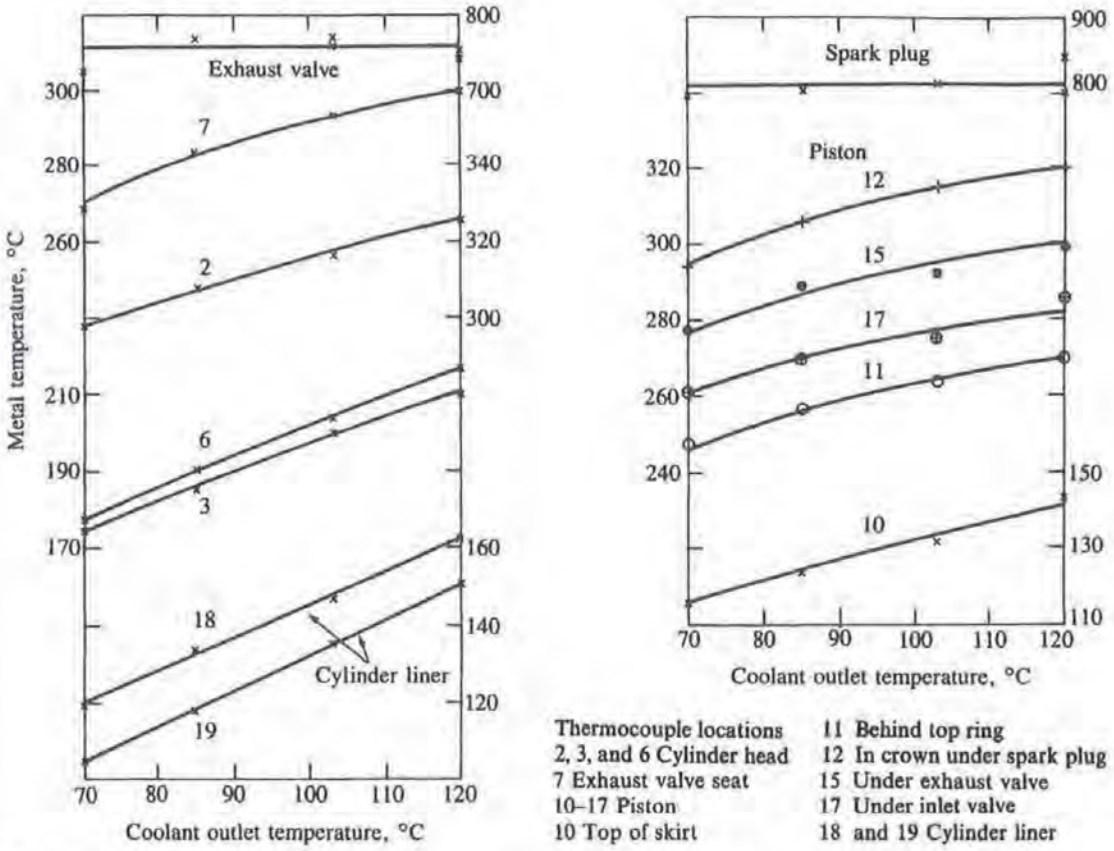


FIGURE 12-28
Effect of coolant temperature on cylinder head, liner, exhaust valve, valve seat, piston, and spark plug metal temperatures. Spark-ignition engine at 5520 rev/min and wide-open throttle. $r_c = 8.5$.[47]

perature in a spark-ignition engine. The exhaust valve and spark plug temperatures are unchanged. The smaller response of the metal temperatures to coolant temperature change occurs at higher heat flux locations (such as the valve bridge), and indicates that heat transfer to the coolant has entered the nucleate-boiling regime in that region. The response is greater where heat fluxes are lower (e.g., the cylinder liner), indicating that there heat transfer to the coolant is largely by forced convection. When nucleate boiling occurs (i.e., when steam bubbles are formed in the liquid at the metal surface, although the bulk temperature of the coolant is below the saturation temperature), the metal temperature is almost independent of coolant temperature and velocity. Addition of antifreeze (ethylene glycol) to coolant water changes the thermodynamic properties of the coolant.

WALL MATERIAL. While the common metallic component materials of cast iron and aluminum have substantially different thermal properties, they both operate with combustion chamber surface temperatures (200 to 400°C) that are low relative to burned gas temperatures. There is substantial interest in using materials that could operate at much higher temperatures so that the heat losses from the working fluid would be reduced. Ceramic materials, such as silicon nitride and

TABLE 12.2
Thermal properties of wall materials

Material	Thermal conductivity k, W/m·K	Density ρ, kg/m^3	Specific heat c, J/kg·K	Thermal diffusivity α, m^2/s	$k\rho c$	Skin depth δ, mm	Peak temperature swing, K
Cast iron	54	7.2×10^3	480	1.57×10^{-5}	1.8×10^8	2.8	18
Aluminum	155	2.75×10^3	915	6.2×10^{-5}	3.9×10^8	5.4	12
Reaction-bonded silicon nitride	5–10	2.5×10^3	710	2.8×10^{-6}	1.3×10^7	1.2	70
Sprayed zirconia	1.2	5.2×10^3	732	3.2×10^{-7}	4.6×10^6	0.39	95

zirconia, have lower thermal conductivity than cast iron, would operate at higher temperatures, and thereby insulate the engine. The thermal properties of some of these materials are listed in Table 12.2. With these thermally insulating materials it is possible to reduce the heat transfer through the wall by a substantial amount.

This approach is most feasible for diesel engines where there is the possibility of eliminating the conventional engine coolant system and improving engine efficiency. Since the coolant-side heat transfer is essentially steady during each cycle, a high enough thermal resistance in the wall material can bring the net heat transfer close to zero. However, there is still substantial heat transfer between the working fluid in the cylinder and the combustion chamber walls. Figure 12-29 illustrates these heat-transfer processes by comparing the mean gas temperature to the piston surface temperature for metal and ceramic combustion chamber wall materials. The results come from a thermodynamic simulation of a turbocompounded diesel engine system operating cycle. From Eq. (12.2) the heat transfer is *from* the gas when $T_g > T_w$ and *to* the gas when $T_g < T_w$. With the ceramic material at about 800 K surface temperature, the *net* heat transfer is much reduced compared with the metal case. However, there is substantial heat transfer to the gas from the ceramic walls during intake (which reduces volumetric efficiency) and compression (which increases compression stroke work), and still substantial heat transfer from the gas during combustion and expansion.

The heat transfer from the hot walls to the incoming charge makes thermally insulating materials unattractive for spark-ignition engines. Such heat transfer would increase the unburned mixture temperature leading to earlier onset of knock (see Sec. 9.6).

The variation in ceramic surface temperature in Fig. 12-29 indicates the inherently unsteady nature of the heat-transfer interaction with the wall. During combustion and expansion, the thermal energy transferred from the gas to the wall is stored in a thin layer of wall material adjacent to the surface. While some

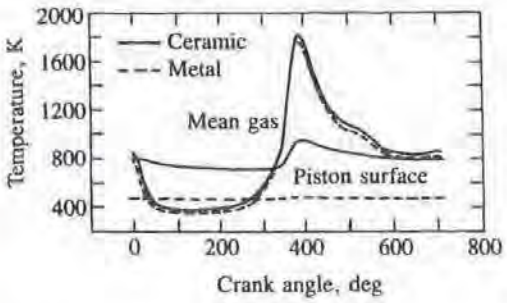


FIGURE 12-29
Mean gas temperature and piston surface temperature profiles predicted by turbocompounded DI diesel engine simulation for water-cooled metal combustion chamber walls and for partly insulated engine with ceramic walls.[27]

of this thermal energy diffuses through the wall, during intake and compression much of it is transferred back to the now low-temperature cylinder contents. The depth of penetration of the thermal wave into the material, the skin depth δ, is proportional to $\sqrt{\alpha/\omega}$, where $\alpha = k/(\rho c)$ is the thermal diffusivity and ω the frequency of the wave (proportional to engine speed). Values of α and δ are given in Table 12.2 for an engine speed of 1900 rev/min: $\sqrt{\alpha}/\delta = 1.4$, a constant. The magnitude of the temperature fluctuation (important because it is a source of fluctuating thermal stress) is proportional to $(\delta\rho c)^{-1}$: this varies as $(k\rho c)^{-1/2}$. Estimated peak temperature swings for the materials in Table 12.2 are tabulated.

KNOCK. Knock in an SI engine is the spontaneous ignition of the unburned "end-gas" ahead of the flame as the flame propagates across the combustion chamber. It results in an increase in gas pressure and temperature above the normal combustion levels (see Sec. 9.6). Knock results in increased local heat fluxes to regions of the piston, the cylinder head, and liner in contact with the end-gas. Increases to between twice and three times the normal heat flux in the end-gas region have been measured.[13, 52] It is thought that the primary knock damage to the piston crown in this region is due to the combination of extremely high local pressures and higher material temperatures.

PROBLEMS

12.1. If radiation in the combustion chamber is negligible, Eqs. (12.5), (12.6), and (12.7) can be combined into the following overall equation approximating the time-averaged heat transfer from the engine:

$$\dot{q} = h_{c,a}(\bar{T}_g - \bar{T}_c)$$

Derive the expression for $h_{c,a}$.

12.2. Given that the average heat flux through a particular zone in a cast iron liner 1 cm thick is 0.2 MW/m^2, the coolant temperature is 85°C, and the coolant side heat-transfer coefficient is 7500 W/m$^2 \cdot$K, find the average surface temperature on the combustion chamber and coolant sides of the liner at that zone.

12.3. Figure 12-1 gives a schematic of the temperature profile from the gas inside the combustion chamber out to the coolant. Draw an equivalent figure showing schematically the temperature profiles at the following points in the engine cycle: (*a*) intake; (*b*) just prior to combustion; (*c*) just after combustion; (*d*) during the exhaust stroke. Your sketch should be carefully proportioned.

12.4. Using dimensional analysis, compare the relative heat losses of two geometrically similar SI engines (same bore/stroke ratio, same connecting rod/stroke ratio) operating at the same imep and power. Engine A has twice the displacement per cylinder of engine B. Assume that the wall temperature and the gas temperature for both engines are the same.

12.5. (*a*) Using Woschni's correlation, evaluate the percentage increase in heat transfer expected from an engine with a mean piston speed of 10 m/s when the swirl ratio is raised from 0 to 5. Do your comparison for the intake process only. The engine bore is 0.15 m and the engine speed is 2000 rev/min.

(*b*) Explain how both the generation of swirl and the change in heat transfer that results affect the volumetric efficiency of an engine.

12.6. (*a*) Explain how you would estimate the thermal boundary-layer thickness on the combustion chamber wall of an internal combustion engine.

(*b*) Using representative data, make a rough estimate of the thickness of the thermal boundary layer in the combustion chamber of an SI engine just after the completion of combustion and the fraction of the cylinder mass contained within the boundary layer. $B \approx 100$ mm. Transport properties given in Sec. 4.8.

12.7. (*a*) Using the analysis found in Sec. 12.6.1, calculate the depth below the surface where the amplitude of the temperature oscillations has attenuated to 1 percent of the amplitude at the surface. The wall material is aluminum and the four-stroke cycle engine is operating at 2500 rev/min. For this estimate, consider only the temperature oscillations which have a frequency equal to the engine firing frequency ($\omega = 2\pi N/n_R$).

(*b*) Repeat the calculation for the engine operating at 5000 rev/min.

(*c*) What is the dependence of the penetration depth on the amplitude of surface temperature fluctuations?

12.8. The instantaneous heat-transfer rate $\dot{Q}$ from the cylinder gases to the combustion chamber walls in a spark-ignition engine may be estimated approximately from the equation

$$\dot{Q} = h_c A(\bar{T}_g - \bar{T}_w)$$

where h_c is the heat-transfer coefficient, A is the surface area, $\bar{T}_g$ is the average temperature of the gas in the cylinder, and $\bar{T}_w$ is the average wall temperature. The heat-transfer coefficient can be obtained from the Nusselt, Reynolds, and Prandtl number relationship:

$$\mathrm{Nu} = C(\mathrm{Re})^m(\mathrm{Pr})^n$$

where $C = 0.4$, $m = 0.75$, $n = 0.4$. The characteristic velocity and length scale used in this relation are the mean piston speed and the cylinder bore.

Assuming appropriate values for the engine geometry and operating conditions at wide-open throttle with the wall temperature at 400 K, at an engine speed of 2500 rev/min, and using the cylinder pressure versus crank angle curve of Fig. 14-9, calculate the following:

(*a*) The *average* temperature of the gas in the cylinder at $\theta = -180°, -90°, 0°, 20°, 40°, 90°, 150°$.

(*b*) The instantaneous heat-transfer coefficient h_c and heat-transfer rate $\dot{Q}$ from the gas to the combustion chamber walls of one cylinder at these crank angles. Plot these results versus θ.

(c) Estimate the fraction of the fuel energy that is transferred to the cylinder walls during compression and expansion.

Assume for the gas that the viscosity $\mu = 7 \times 10^{-5}$ kg/m · s, the thermal conductivity $k = 1.5 \times 10^{-1}$ J/m · s · K, the molecular weight = 28, and the Prandtl number is 0.8. Assume that the combustion chamber is disc-shaped with $B = 102$ mm, $L = 88$ mm, and $r_c = 9$. (The calculations required for this problem are straightforward; do not attempt anything elaborate.)

REFERENCES

1. Overbye, V. D., Bennethum, J. E., Uyehara, O. A., and Myers, P. S.: "Unsteady Heat Transfer in Engines," SAE paper 201C, *SAE Trans.*, vol. 69, pp. 461–494, 1961.
2. Howarth, M. H.: *The Design of High Speed Diesel Engines*, chap. 5, Constable, London, 1966.
3. Khovakh, M. (ed.): *Motor Vehicle Engines*, chap. 12, Mir Publishers, Moscow, 1971.
4. Sitkei, G.: *Heat Transfer and Thermal Loading in Internal Combustion Engines*, Akademiai Kiado, Budapest, 1974.
5. Burke, C. E., Nagler, L. H., Campbell, E. C., Zierer, W. E., Welch, H. L., Lundstrom, L. C., Kosier, T. D., and McConnell, W. A.: "Where Does All the Power Go," *SAE Trans.*, vol. 65, pp. 713–738, 1957.
6. Ament, F., Patterson, D. J., and Mueller, A.: "Heat Balance Provides Insight into Modern Engine Fuel Utilization," SAE paper 770221, 1977.
7. Novak, J. M., and Blumberg, P. N.: "Parametric Simulation of Significant Design and Operating Alternatives Affecting the Fuel Economy and Emissions of Spark-Ignited Engines," SAE paper 780943, *SAE Trans.*, vol. 87, 1978.
8. Annand, W. J. D.: "Heat Transfer in the Cylinders of Reciprocating Internal Combustion Engines," *Proc. Instn Mech. Engrs*, vol. 177, no. 36, pp. 973–990, 1963.
9. Borman, G., and Nishiwaki, K.: "A Review of Internal Combustion Engine Heat Transfer," *Prog. Energy Combust. Sci.*, vol. 13, pp. 1–46, 1987.
10. Taylor, C. F., and Toong, T. Y.: "Heat Transfer in Internal Combustion Engines," ASME paper 57-HT-17, 1957.
11. Woschni, G.: "Universally Applicable Equation for the Instantaneous Heat Transfer Coefficient in the Internal Combustion Engine," SAE paper 670931, *SAE Trans.*, vol. 76, 1967.
12. Sihling, K., and Woschni, G.: "Experimental Investigation of the Instantaneous Heat Transfer in the Cylinder of a High Speed Diesel Engine," SAE paper 790833, 1979.
13. Woschni, G., and Fieger, J.: "Experimental Investigation of the Heat Transfer at Normal and Knocking Combustion in Spark Ignition Engines," *MTZ*, vol. 43, pp. 63–67, 1982.
14. Hohenberg, G. F.: "Advanced Approaches for Heat Transfer Calculations," SAE paper 790825, *SAE Trans.*, vol. 88, 1979.
15. LeFeuvre, T., Myers, P. S., and Uyehara, O. A.: "Experimental Instantaneous Heat Fluxes in a Diesel Engine and Their Correlation," SAE paper 690464, *SAE Trans.*, vol. 78, 1969.
16. Dent, J. C., and Sulaiman, S. J.: "Convective and Radiative Heat Transfer in a High Swirl Direct Injection Diesel Engine," SAE paper 770407, *SAE Trans.*, vol. 86, 1977.
17. Krieger, R. B., and Borman, G. L.: "The Computation of Apparent Heat Release for Internal Combustion Engines," ASME paper 66-WA/DGP-4, in *Proceedings of Diesel Gas Power*, ASME, 1966.
18. Borgnakke, C., Arpaci, V. S., and Tabaczynski, R. J.: "A Model for the Instantaneous Heat Transfer and Turbulence in a Spark Ignition Engine," SAE paper 800287, 1980.
19. Morel, T., and Keribar, R.: "A Model for Predicting Spatially and Time Resolved Convective Heat Transfer in Bowl-in-Piston Combustion Chambers," SAE paper 850204, 1985.
20. Caton, J. A., and Heywood, J. B.: "An Experimental and Analytical Study of Heat Transfer in an Engine Exhaust Port," *Int. J. Heat Mass Transfer*, vol. 24, no. 4, pp. 581–595, 1981.
21. Malchow, G. L., Sorenson, S. C., and Buckius, R. O.: "Heat Transfer in the Straight Section of an Exhaust Port of a Spark Ignition Engine," SAE paper 790309, 1979.

22. Hottel, H. C., and Sarofim, A. F.: *Radiative Transfer*, McGraw-Hill, 1967.
23. Flynn, P., Mizuszwa, M., Uyehara, O. A., and Myers, P. S.: "Experimental Determination of Instantaneous Potential Radiant Heat Transfer within an Operating Diesel Engine," SAE paper 720022, *SAE Trans.*, vol. 81, 1972.
24. LeFeuvre, T., Myers, P. S., and Uyehara, O. A.: "Experimental Instantaneous Heat Fluxes in a Diesel Engine and Their Correlation," SAE paper 690464, *SAE Trans.*, vol. 78, 1969.
25. Lyn, W. T.: "Diesel Combustion Study by Infra Red Emission Spectroscopy," *J. Instn Petroleum*, vol. 43, 1957.
26. Kamimoto, T., Matsuoka, S., Matsui, Y., and Aoyagi, Y.: "The Measurement of Flame Temperature and Thermodynamic Analysis of the Combustion Process in a Direct Injection Diesel Engine," paper C96/75, in *Proceedings of Conference on Combustion in Engines*, Cranfield, Institution of Mechanical Engineers, 1975.
27. Assanis, D. N., and Heywood, J. B.: "Development and Use of Computer Simulation of the Turbocompounded Diesel System for Engine Performance and Components Heat Transfer Studies," SAE paper 860329, 1986.
28. Field, M. A., Gill, D. W., Morgan, B. B., and Hawksley, P. G. W.: "*Combustion of Pulverised Coal*, British Coal Utility Research Association, Leatherhead, U.K., 1967.
29. Greeves, G., and Meehan, J. O.: "Measurements of Instantaneous Soot Concentration in a Diesel Combustion Chamber," paper C88/75, in *Proceedings of Conference on Combustion in Engines*, Cranfield, Institution of Mechanical Engineers, 1975.
30. Annand, W. J. D.: "Heat Transfer from Flames in Internal Combustion Engines," in N. Afgan and J. M. Beer (eds.), *Heat Transfer from Flames*, chap. 24, John Wiley, 1974.
31. Annand, W. J. D., and Ma, T. H.: "Instantaneous Heat Transfer Rates to the Cylinder Head Surface of a Small Compression-Ignition Engine," *Proc. Instn Mech. Engrs*, vol. 185, no. 72/71, pp. 976–987, 1970–1971.
32. Oguri, T., and Inaba, S.: "Radiant Heat Transfer in Diesel Engines," SAE paper 720023, *SAE Trans.*, vol. 81, 1972.
33. Kunitomo, T., Matsuoka, K., and Oguri, T.: "Prediction of Radiative Heat Flux in a Diesel Engine," SAE paper 750786, *SAE Trans.*, vol. 84, 1975.
34. Alkidas, A. C.: "Heat Transfer Characteristics of a Spark-Ignition Engine," *Trans. ASME, J. Heat Transfer*, vol. 102, pp. 189–193, 1980.
35. Alkidas, A. C., and Myers, J. P.: "Transient Heat-Flux Measurements in the Combustion Chamber of a Spark-Ignition Engine," *Trans. ASME, J. Heat Transfer*, vol. 104, pp. 62–67, 1982.
36. Van Gerpen, J. H., Huang, C.-W., and Borman, G. L.: "The Effects of Swirl and Injection Parameters on Diesel Combustion and Heat Transfer," SAE paper 850265, 1965.
37. Whitehouse, N. D.: "Heat Transfer in a Quiescent Chamber Diesel Engine," *Proc. Instn Mech. Engrs*, vol. 185, no. 72/71, pp. 963–975, 1970–1971.
38. Ramchandani, M., and Whitehouse, N. D.: "Heat Transfer in a Piston of a Four Stroke Diesel Engine," SAE paper 760007, 1976.
39. Lyford-Pike, E. J., and Heywood, J. B.: "Thermal Boundary Layer Thickness in the Cylinder of a Spark-Ignition Engine," *Int. J. Heat Mass Transfer*, vol. 27, no. 10, pp. 1873–1878, 1984.
40. Furuhama, S., and Suzuki, H.: "Temperature Distribution of Piston Rings and Piston in High Speed Diesel Engine," *Bull. JSME*, vol. 22, no. 174, pp. 1788–1795, 1979.
41. Finlay, I. C., Harris, D., Boam, D. J., and Parks, B. I.: "Factors Influencing Combustion Chamber Wall Temperatures in a Liquid-Cooled, Automotive, Spark-Ignition Engine," *Proc. Instn Mech. Engrs*, vol. 199, no. D3, pp. 207–214, 1985.
42. Woschni, G.: "Prediction of Thermal Loading of Supercharged Diesel Engines," SAE paper 790821, 1979.
43. Worthen, R. P., and Raven, D. G.: "Measurements of Valve Temperatures and Strain in a Firing Engine," SAE paper 860356, 1986.
44. Li, C-H.: "Piston Thermal Deformation and Friction Considerations," SAE paper 820086, 1982.
45. Woschni, G., and Fieger, J.: "Determination of Local Heat Transfer Coefficients at the Piston of a High Speed Diesel Engine by Evaluation of Measured Temperature Distribution," SAE paper 790834, *SAE Trans.*, vol. 88, 1979.

46. Watts, P. A., and Heywood, J. B.: "Simulation Studies of the Effects of Turbocharging and Reduced Heat Transfer on Spark-Ignition Engine Operation," SAE paper 800289, 1980.
47. French, C. C. J., and Atkins, K. A.: "Thermal Loading of a Petrol Engine," *Proc. Instn Mech. Engrs*, vol. 187, 49/73, pp. 561–573, 1973.
48. Brock, E. K., and Glasspoole, A. J.: "The Thermal Loading of Cylinder Heads and Pistons on Medium-Speed Oil Engines," in *Proceedings of Symposium on Thermal Loading of Diesel Engines*, vol. 179, part 3C, pp. 3–18, Institution of Mechanical Engineers, 1964–1965.
49. French, C. C. J., and Hartles, E. R.: "Engine Temperatures and Heat Flows under High Load Conditions," in *Proceedings of Symposium on Thermal Loading of Diesel Engines*, vol. 179, part 3C, pp. 126–135, Institution of Mechanical Engineers, 1964–1965.
50. Kerley, R. V., and Thurston, K. W.: "The Indicated Performance of Otto-Cycle Engines," *SAE Trans.*, vol. 70, pp. 5–30, 1962.
51. Taylor, C. F.: *The Internal Combustion Engine in Theory and Practice*, vol. 1, chap. 8, MIT Press, 1966.
52. Lee, W., and Schaefer, H. J.: "Analysis of Local Pressures, Surface Temperatures and Engine Damages Under Knock Conditions," SAE paper 830508, *SAE Trans.*, vol. 92, 1983.

CHAPTER 13

ENGINE FRICTION AND LUBRICATION

13.1 BACKGROUND

Not all the work transferred to the piston from the gases contained inside the cylinder—the indicated work—is available at the drive shaft for actual use. That portion of the work transferred which is not available is usually termed *friction* work. It is *dissipated* in a variety of ways within the engine and engine auxiliaries. The friction work or power is a sufficiently large fraction of the indicated work or power—varying between about 10 percent at full load and 100 percent at idle or no-load—for the topic to be of great practical importance in engine design. Friction losses affect the maximum brake torque and minimum brake specific fuel consumption directly; often the difference between a good engine design and an average engine is the difference in their frictional losses. A large part of the friction losses appear as heat in the coolant and oil which must be removed in the radiator and oil cooler system. Thus, friction losses influence the size of the coolant systems. A knowledge of friction power is required to relate the combustion characteristics of an engine—which influence the indicated power—and the useful output—the brake power.

The friction work, defined as the difference between the work delivered to the piston while the working fluid is contained within the cylinder (i.e., during the

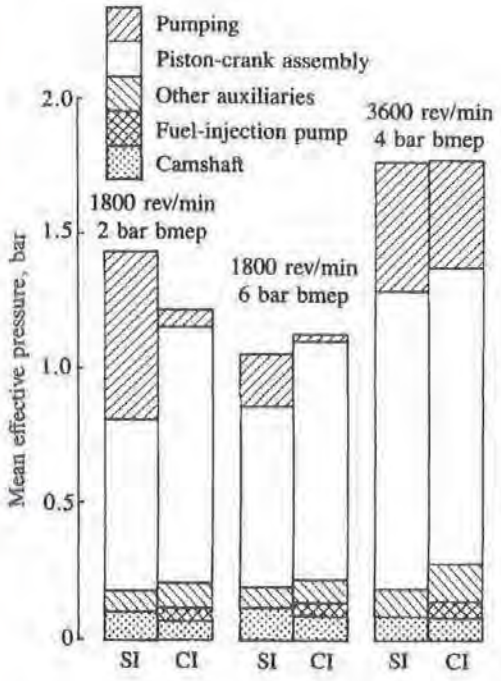


FIGURE 13-1
Comparison of major categories of friction losses: friction mean effective pressure at different loads and speeds for 1.6-liter four-cylinder overhead-cam automotive spark-ignition (SI) and compression-ignition (CI) engines.[1]

compression and expansion strokes) and the usable work delivered to the drive shaft, is expended as follows:

1. To draw the fresh mixture through the intake system and into the cylinder, and to expel the burned gases from the cylinder and out of the exhaust system. This is usually called the pumping work.
2. To overcome the resistance to relative motion of all the moving parts of the engine. This includes the friction between the piston rings, piston skirt, and cylinder wall; friction in the wrist pin, big end, crankshaft, and camshaft bearings; friction in the valve mechanism; friction in the gears, or pulleys and belts, which drive the camshaft and engine accessories.
3. To drive the engine accessories. These can include: the fan, the water pump, the oil pump, the fuel pump, the generator, a secondary air pump for emission control, a power-steering pump, and an air conditioner.

All this work is eventually dissipated as heat; the term friction work or power is therefore appropriate. Figure 13-1 indicates the relative importance of these components in typical four-cylinder automotive SI and diesel engines at different loads and speeds. The magnitudes of the friction from the major items in 1, 2, and 3 above are shown for an SI and a CI engine. The absolute value of the total friction work varies with load, and increases as speed increases. The pumping work for SI engines is larger than for equivalent CI engines and becomes comparable to rubbing friction at light loads as the engine is increasingly throttled. The piston and crank assembly contributes the largest friction component.

13.2 DEFINITIONS

The following terminology will be used in discussing engine friction.

Pumping work W_p. The net work per cycle done by the piston on the in-cylinder gases during the inlet and exhaust strokes. W_p is only defined for four-stroke cycle engines. It is the area $(B + C)$ in Fig. 2-4.†

Rubbing friction work W_{rf}. The work per cycle dissipated in overcoming the friction due to relative motion of adjacent components within the engine. This includes all the items listed in 2 above.

Accessory work W_a. The work per cycle required to drive the engine accessories; e.g., pumps, fan, generator, etc. Normally, only those accessories essential to engine operation are included.

Total friction work W_{tf}. The total friction work is the sum of these three components, i.e.,

$$W_{tf} = W_p + W_{rf} + W_a \tag{13.1}$$

It is convenient to discuss the difference between indicated and brake output in terms of *mean effective pressure*, mep, the work per cycle per unit displaced volume:

$$\text{mep} = \frac{W_c}{V_d}$$

and power. Power and mep are related by

$$P = \text{mep} \times V_d \times \frac{N}{n_R}$$

where n_R (the number of revolutions per cycle) = 1 or 2 for the two-stroke or four-stroke cycle, respectively. Hence, from W_p, W_{rf}, W_a, and W_{tf} we can define pumping mean effective pressure and power (pmep and P_p), rubbing friction mean effective pressure and power (rfmep and P_{rf}), accessory mean effective pressure and power (amep and P_a), and total friction mean effective pressure and power (tfmep and P_{tf}), respectively.

Brake mean effective pressure and power (bmep and P_b), indicated mean effective pressure and power (imep and P_i), and mechanical efficiency have already been defined in Secs. 2.3, 2.4, 2.5, and 2.7. Note that for four-stroke cycle engines, two definitions of indicated output are in common use. These have been designated as:

† This definition gives $W_p > 0$ for naturally aspirated engines. For supercharged and turbocharged engines at high load, where p_i is usually greater than p_e, this definition gives $W_p < 0$. For such engines the sign convention for pumping work is often changed in order to maintain W_p as a positive quantity.

Gross indicated mean effective pressure, imep_g. The work delivered to the piston over the compression and expansion strokes, per cycle per unit displaced volume.

Net indicated mean effective pressure, imep_n. The work delivered to the piston over the entire four strokes of the cycle, per unit displaced volume.

From the above definitions it follows that

$$\text{imep}_g = \text{imep}_n + \text{pmep} \tag{13.2a}$$

$$\text{tfmep} = \text{pmep} + \text{rfmep} + \text{amep} \tag{13.2b}$$

$$\text{bmep} = \text{imep}_g - \text{tfmep} \tag{13.2c}$$

$$\text{bmep} = \text{imep}_n - \text{rfmep} - \text{amep} \tag{13.2d}$$

[Note that all the quantities in Eqs. (13.2*a* to *d*) are positive, except for pmep when $p_i > p_e$.]

That two different definitions of indicated output are in common use follows from two different approaches to determining friction work or power. In the standard engine test code procedures[2] friction power is measured in a hot motoring test: the engine is motored with water and oil temperatures held at the firing engine values, with the throttle setting unchanged from its firing engine position (in an SI engine). This measures (approximately) the sum of pumping, rubbing friction, and auxiliary power. The sum of brake power, and friction power determined in this way, is the gross indicated power. Alternatively, when an accurate record of cylinder pressure throughout the whole cycle is available, pumping power can be determined directly: the sum of rubbing friction and accessory power is then the difference between the net indicated power—determined from $\int p\, dV$ over the whole cycle—and the brake power.

For the reasons explained in Sec. 2.4, the gross indicated output is preferred and used in this text. The distinction is most important for SI engines at part load where the pumping power and rubbing friction power are comparable in magnitude. For unthrottled engines at low speeds, the distinction becomes less important (Fig. 13-1 shows the relative importance of pumping work under both these conditions).

13.3 FRICTION FUNDAMENTALS

The friction losses outlined in Sec. 13.1 can be classified into two groups, depending on the type of dissipation which occurs. One type is friction between two metal surfaces in relative motion, with a lubricant in between. The other type is turbulent dissipation.

13.3.1 Lubricated Friction

A primary problem in understanding friction between lubricated surfaces in engines is the wide variation in the magnitude of the forces involved. Thus

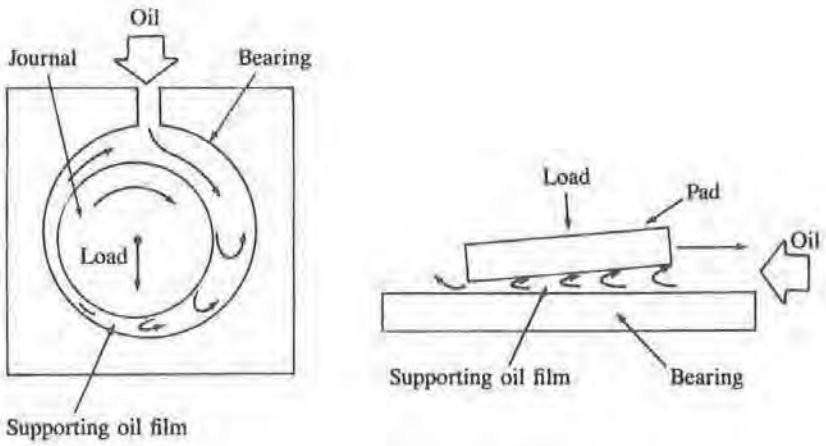


FIGURE 13-2
Schematic of a lubricated journal and a slider bearing.

various regimes of lubrication can occur. Figure 13-2 shows the operating conditions of two common geometries for lubricated parts: a journal and a slider bearing. The different regimes of lubricated friction can be illustrated by means of the Stribeck diagram shown in Fig. 13-3, where the coefficient of friction f (tangential force/normal force) for a journal bearing is plotted against a dimensionless duty parameter $\mu N/\sigma$, where μ is the dynamic viscosity of the lubricant, N is the rotational speed of the shaft, and σ is the loading force per unit area. For sliding surfaces the dimensionless duty parameter becomes $\mu U/(\sigma b)$, where U is the relative velocity of the two surfaces and b is the width of the sliding pad in the direction of motion.

The coefficient of friction can be expressed as

$$f = \alpha f_s + (1 - \alpha) f_L \tag{13.3}$$

where f_s is the metal-to-metal coefficient of dry friction, f_L is the hydrodynamic coefficient of friction, and α is the metal-to-metal contact constant, varying between 0 and 1. As $\alpha \to 1, f \to f_s$ and the friction is called *boundary*, i.e., close to solid friction. The lubricating film is reduced to one or a few molecular layers and cannot prevent metal-to-metal contact between surface asperities. As $\alpha \to 0, f \to f_L$ and the friction is called *hydrodynamic* or *viscous* or *thick film*. The lubricant film is sufficiently thick to separate completely the surfaces in relative motion. In between these regimes, there is a *mixed* or *partial* lubrication regime where the transition from boundary to hydrodynamic lubrication occurs. While Fig. 13-3 applies to journal bearings, this discussion holds for any pair of engine parts in relative motion with lubricant in between.

Under boundary lubrication conditions, the friction between two surfaces in relative motion is determined by surface properties as well as by lubricant properties. The important surface properties are roughness, hardness, elasticity, plasticity, shearing strength, thermal conductivity, and wettability with respect to the lubricant. The important lubricant properties are mainly surface ones or

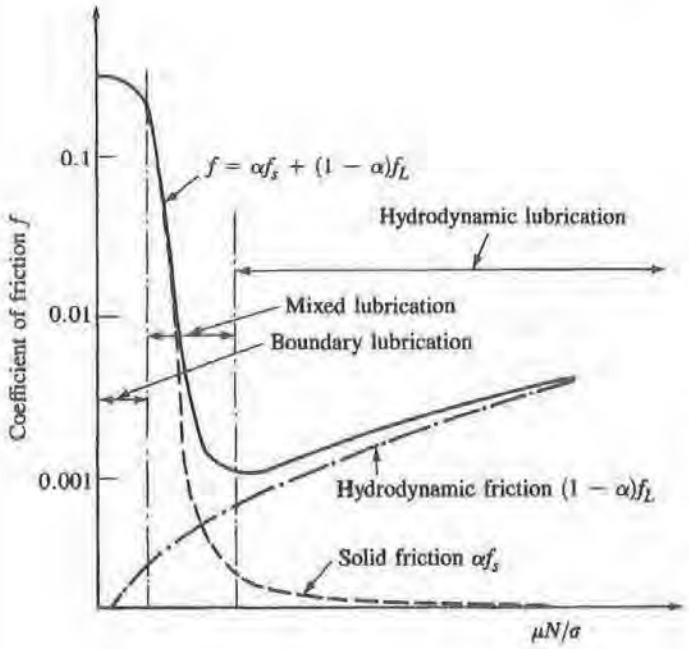


FIGURE 13-3
Stribeck diagram for journal bearing: coefficient of friction f versus dimensionless duty parameter $\mu N/\sigma$, where μ is the lubricant dynamic viscosity, N is rotational speed of shaft, σ is the loading force per unit area.

chemical ones, which govern the ability of lubricant (or additive) molecules to attach themselves to the solid surfaces. Figure 13-4 shows two surfaces under boundary lubrication conditions. Due to the surface asperities, the real contact area is much less than the apparent contact area. The real contact area A_r is equal to the normal load F_n divided by the yield stress of the material σ_m:

$$A_r = \frac{F_n}{\sigma_m}$$

The force required to cause tangential motion is the product of the real contact area and the shear strength of the material τ_m:

$$F_t = A_r \tau_m$$

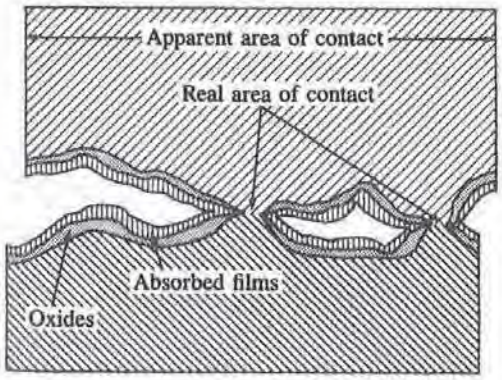


FIGURE 13-4
Schematic of two surfaces in relative motion under boundary lubrication conditions.[3]

Thus the coefficient of friction f is

$$f = \frac{F_t}{F_n} = \frac{\tau_m}{\sigma_m} \tag{13.4}$$

For dissimilar materials, the properties of the weaker material dominate the friction behavior. Since, as shown in Fig. 13-4, the surfaces are covered by oxide films and adsorbed lubricant films, the shear strength of the material in Eq. (13.4) is effectively the shear strength of the surface film.[3] Under boundary lubrication conditions, the coefficient of friction is essentially independent of speed. Boundary lubrication occurs between engine parts during starting and stopping (bearings, pistons, and rings), and during normal running at the piston ring/cylinder interface at top and bottom center crank positions, between heavily loaded parts, and between slow moving parts such as valve stems and rocker arms, and crankshaft timing gears and chains.[4]

Hydrodynamic lubrication conditions occur when the shape and relative motion of the sliding surfaces form a liquid film in which there is sufficient pressure to keep the surfaces separated. Resistance to motion results from the shear forces within the liquid film, and not from the interaction between surface irregularities, as was the case under boundary lubrication. The shear stress τ in a liquid film between two surfaces in relative motion is given by

$$\tau = \mu\left(\frac{dv}{dy}\right)$$

where μ is the fluid viscosity and (dv/dy) the velocity gradient across the film. Hence, the friction coefficient (shear stress/normal load stress) in this regime will be proportional to viscosity × speed ÷ loading: i.e., a straight line on the Stribeck diagram. Full hydrodynamic lubrication or viscous friction is independent of the material or roughness of the parts, and the only property of the lubricant involved is its viscosity. Hydrodynamic lubrication is present between two converging surfaces, moving at relatively high speed in relation to each other and withstanding a limited load, each time an oil film can be formed. This type of lubrication is encountered in engine bearings, between piston skirt and cylinder liner, and between piston rings and liners for high sliding velocities.

Hydrodynamic lubrication breaks down when the thickness of the fluid film becomes about the same as the height of the surface asperities. To the viscous friction is then added metal-to-metal solid friction at the peaks of the asperities. Both hydrodynamic and boundary conditions coexist. The surface texture controls this transition from hydrodynamic to mixed lubrication: rougher surfaces make the transition at lower loads.[3] Abrupt load or speed variations or mechanical vibration may cause this transition to occur. This phenomenon occurs in connecting rod and crankshaft bearings where periodic metal-to-metal contact results from sudden breaks in the oil film. The contact area between rings and cylinders is a zone where, due to sudden variations in speed, load, and temperature, lubrication is of the mixed type. Intermittent metal-to-metal contacts occur as the result of breaks in the oil film.

13.3.2 Turbulent Dissipation

Part of the total friction work is spent in pumping fluids through flow restrictions. The cylinder gases, cooling water, and oil are pumped through the engine; the fan pumps air over the engine block. This work is eventually dissipated in turbulent mixing processes. The pressure difference required to pump these fluids around their flow paths is proportional to ρv^2, where v is a representative fluid velocity. The proportionality constant essentially depends only on flow-path geometry. Hence the friction forces associated with fluid pumping will be proportional to N^2 (or $\bar{S}_p^2$ if the piston motion forces the flow).

13.3.3 Total Friction

The work per cycle for each component i of the total friction is given by integrating the friction force $F_{f,i}$ times its displacement dx around the cycle:

$$W_{f,i} = \int F_{f,i}(\theta)\, dx$$

The friction force components are either independent of speed (boundary friction), proportional to speed (hydrodynamic friction) or to speed squared (turbulent dissipation), or some combination of these. It follows that the total friction work per cycle (and thus the friction mean effective pressure) for a given engine geometry engine will vary with speed according to

$$W_{tf} \text{ (or tfmep)} = C_1 + C_2 N + C_3 N^2 \tag{13.5}$$

Some of the components of hydrodynamic lubrication friction and turbulent dissipation will be dependent on mean piston speed rather than crankshaft rotational speed N. Examples are piston skirt and ring friction, and the pressure losses associated with gas flow through the inlet and exhaust valves. For conventional engine geometries, crankshaft rotational speed is usually used to scale the total friction data rather than mean piston speed,[5, 6] though more detailed models must include both these variables.

13.4 MEASUREMENT METHODS

A true measurement of friction in a firing engine can only be obtained by subtracting the brake power from the indicated power determined from accurate measurements of cylinder pressure throughout the cycle. However, this method is not easy to use on multicylinder engines, both because of cylinder-to-cylinder differences in indicated power and due to the difficulties in obtaining sufficiently accurate pressure data. As a result, friction is often measured in a motored engine. Friction in a firing and a motored engine are different for the reasons outlined below. First, the common measurement methods will be described.

1. *Measurement of fmep from imep.* The gross indicated mean effective pressure is obtained from $\int p\, dV$ over the compression and expansion strokes for a four-

stroke engine, and over the whole cycle for a two-stroke engine. This requires accurate and in-phase pressure and volume data. Accurate pressure versus crank angle data must be obtained from each cylinder with a pressure transducer and crank angle indicator. Volume versus crank angle values can be calculated. Great care must be exercised if accurate imep data are to be obtained.[7] Both $imep_g$ and pmep are obtained from the p-V data. By subtracting the brake mean effective pressure, the combined rubbing friction plus auxiliary requirements, rfmep + amep, are obtained.

2. *Direct motoring tests.* Direct motoring of the engine, under conditions as close as possible to firing, is another method used for estimating friction losses. Engine temperatures should be maintained as close to normal operating temperatures as possible. This can be done either by heating the water and oil flows or by conducting a "grab" motoring test where the engine is switched rapidly from firing to motored operation. The power required to motor the engine includes the pumping power. In tests on SI engines at part-load, the throttle setting is left unchanged. "Motoring" tests on a progressively disassembled engine can be used to identify the contribution that each major component of the engine makes to the total friction losses.
3. *Willans line.* An approximate equivalent of the direct motoring test for diesel engines is the Willans line method. A plot of fuel consumption versus brake output obtained from engine tests at a fixed speed is extrapolated back to zero fuel consumption. An example is shown in Fig. 13-5. Generally, the plot has a slight curve, making accurate extrapolation difficult. Agreement with a motored test result is shown.
4. *Morse test.* In the Morse test, individual cylinders in a multicylinder engine are cut out from firing, and the reduction in brake torque is determined while maintaining the same engine speed. The remaining cylinders drive the cylinder cut out. Care must be taken to determine that the action of cutting out one cylinder does not significantly disturb the fuel or mixture flow to the others.

Only the first of these four methods has the potential for measuring the true friction of an operating engine. The last three methods measure the power requirements to motor the engine. The motoring losses are different from the firing losses for the following reasons:

1. Only the compression pressure and not the firing pressure acts on the piston, piston rings, and bearings. The lower gas loadings during motoring lower the rubbing friction.
2. Piston and cylinder bore temperatures are lower in motored operation. This results in greater viscosity of the lubricant and therefore increased viscous friction. In addition, piston-cylinder clearances are greater during motoring operation which tends to make friction lower. However, in firing operation, the lubrication of the top ring near the top of the stroke is inadequate to maintain normal hydrodynamic lubrication with the higher gas pressures

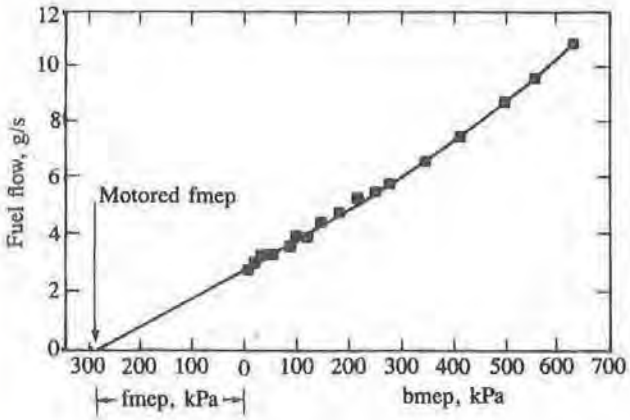


FIGURE 13-5
Willans line method for determining friction mean effective pressure.[5]

behind the ring. The resulting boundary friction in this region makes friction in the firing engine higher. Overall, the net effect of lower piston and cylinder temperatures during motoring is unclear.

3. In motored operation, the exhaust blowdown phase is missing and the gases discharged later in the exhaust stroke have a higher density than under firing conditions. These effects can result in different pumping work.
4. When motoring, net work is done during the compression and expansion strokes because of heat loss from the gas to the walls, and because of gas loss through blowby. This work is not part of the true total friction work in a firing engine and should not be deducted from the indicated work of the firing engine to obtain the brake work; heat losses and blowby are additional energy transfers to the indicated work, friction work, and brake work.

Figure 13-6 shows pumping mep, rubbing friction plus auxiliary mep, and total friction mep for an SI engine over the entire range of throttle positions for firing and motoring tests. Firing test data come from imep and bmep measurements. The engine was a special four-cylinder, in-line, overhead-valve, 3.26-dm^3 displacement tractor SI engine of rugged design and 12 : 1 compression ratio. The pmep values are closely comparable; the rubbing friction mep values diverge

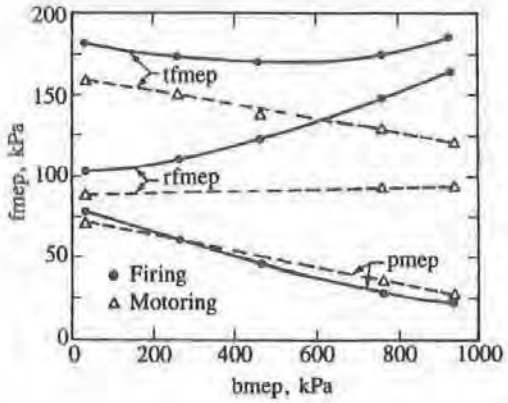


FIGURE 13-6
Total friction mean effective pressure (tfmep), rubbing friction mep (rfmep), and pumping mep (pmep) as a function of load for four-cylinder 3.26-dm^3 spark-ignition engine with bore = 95.3 mm, stroke = 114 mm, and r_c = 12, operated at 1600 rev/min. Motoring and firing conditions.[8]

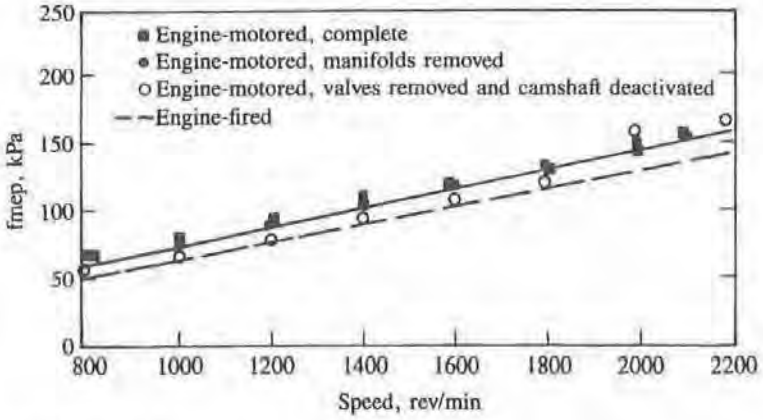


FIGURE 13-7
Rubbing friction and auxiliary mep for six-cylinder diesel engine under motored and fired conditions. Effect of removing manifolds, valves, and camshaft drive under motored conditions also shown.[9]

significantly as load increases.[8] However, the firing friction is not necessarily higher than the motoring test values. Figure 13-7 shows rubbing plus auxiliary mep for a six-cylinder diesel. The firing data are slightly lower than the motored data for this case.[9]

13.5 ENGINE FRICTION DATA

13.5.1 SI Engines

Figure 13-8 shows total motored friction mep for several four-stroke cycle four-cylinder SI engines between 845 and 2000 cm^3 displacement, at wide-open throttle, as a function of engine speed.[6] The data are well correlated by an equation of the form of (13.5):

$$\text{tfmep(bar)} = 0.97 + 0.15\left(\frac{N}{1000}\right) + 0.05\left(\frac{N}{1000}\right)^2 \tag{13.6}$$

where N is in revolutions per minute. Mean piston speed did not provide as good a correlation as rotational speed for this friction data. The importance of avoiding high engine speeds in the interests of good mechanical efficiency are evident. Under normal automobile engine operating conditions, a reduction in total friction mean effective pressure by about 10 kPa results in about a 2 percent improvement in fuel consumption.[10]

Figure 13-9 shows how mechanical efficiency and the relative importance of pumping work vary over the load range idle to wide-open throttle under mid-speed operating conditions.

The effect of compression ratio on rubbing friction and pumping losses, as a function of load at 1600 rev/min, is shown in Fig. 13-10.[8] At the same bmep, both friction and pumping mep are higher at a higher compression ratio. Friction is higher because peak cylinder pressures are higher. Pumping is higher at fixed bmep because the engine is throttled more because the efficiency is higher.

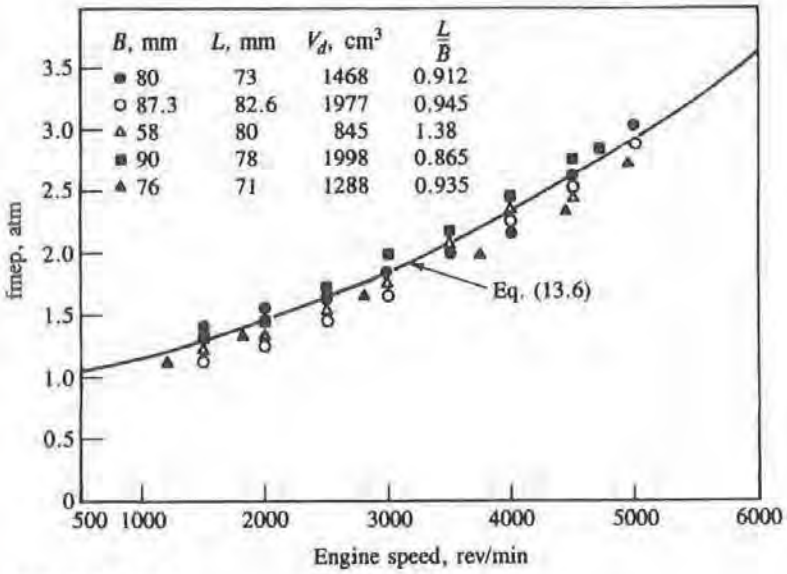


FIGURE 13-8
Friction mean effective pressure under motored conditions at wide-open throttle for several four-cylinder spark-ignition engines.[6]

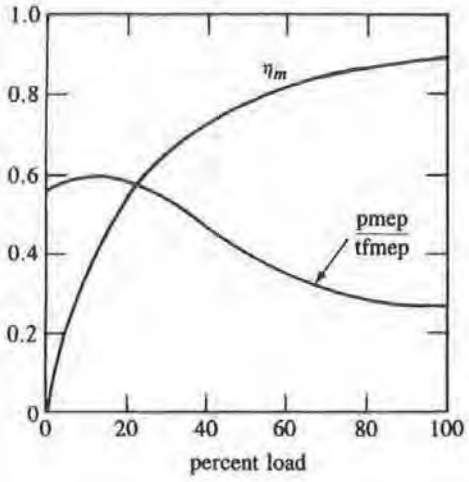


FIGURE 13-9
Mechanical efficiency η_m and ratio of pumping mep to total friction mep as a function of load for a typical spark-ignition engine at fixed speed.[3]

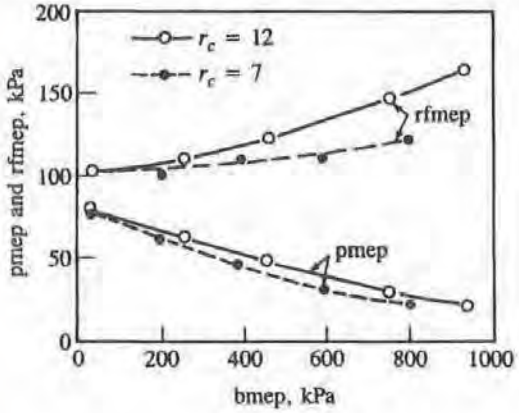


FIGURE 13-10
Pumping mep (pmep) and rubbing friction mep (rfmep) as a function of load for $r_c = 12$ and 7, four-cylinder SI engine with $B = 95.3$ mm and $L = 114$ mm. 1600 rev/min.[8]

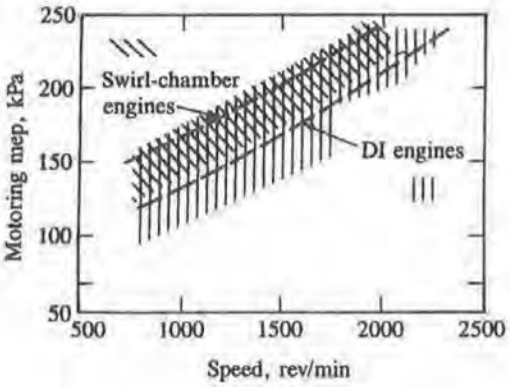


FIGURE 13-11
Motored total friction mean effective pressure as a function of speed for several DI diesels (bores in range 100 to 137 mm) and IDI swirl-chamber diesels (bores in range 100 to 121 mm). Correlations for $r_c = 15$ and $L = 142$ mm (DI engine) and $r_c = 16$ and $L = 142$ mm (IDI engine).[5]

13.5.2 Diesel Engines

Figure 13-11 shows total friction as determined from motoring tests for both direct-injection and swirl-chamber indirect-injection four- and six-cylinder CI engines in the 10 to 14 cm bore range. The higher compression ratio IDI engines lie in the upper half of the scatter band. Correlations for a typical engine of each type are shown, of the form:

$$\text{Motoring mep (kPa)} = C_1 + 48\left(\frac{N}{1000}\right) + 0.4\bar{S}_p^2 \tag{13.7}$$

where N is in revolutions per minute and $\bar{S}_p$ in meters per second. For the direct-injection engine $C_1 = 75$ kPa; for the large swirl chamber IDI engine $C_1 = 110$ kPa. Mean piston speed was found to give a better correlation for the last term in Eq. (13.5) which is mainly pumping mep. Figure 13-12 shows similar results for small swirl-chamber IDI engines. The same correlation, Eq. (13.7) with $C_1 = 144$ kPa, is a good fit to the data.

Friction mep increases as engine size decreases. Also, the *motoring* friction loss for the swirl-chamber engines is higher than for direct-injection engines, primarily because of heat transfer to the prechamber throat and not due to extra pumping losses which are small. Comparative motoring tests show the increase in motored fmep to be about 27 kPa and essentially independent of speed. This is typical of a heat-loss effect, whereas a pumping loss would increase as the square

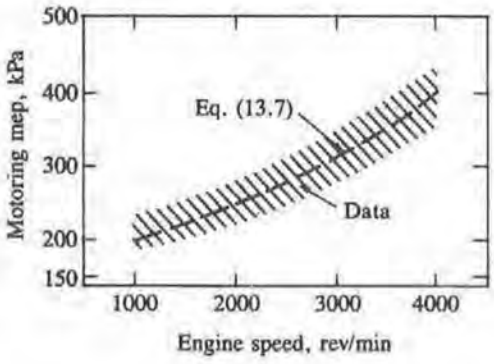


FIGURE 13-12
Motored total friction mean effective pressure as a function of speed for smaller IDI swirl-chamber diesel engines (bores in range 73 to 93 mm). Correlation for $r_c = 21$ and $L = 95.3$ mm.[5]

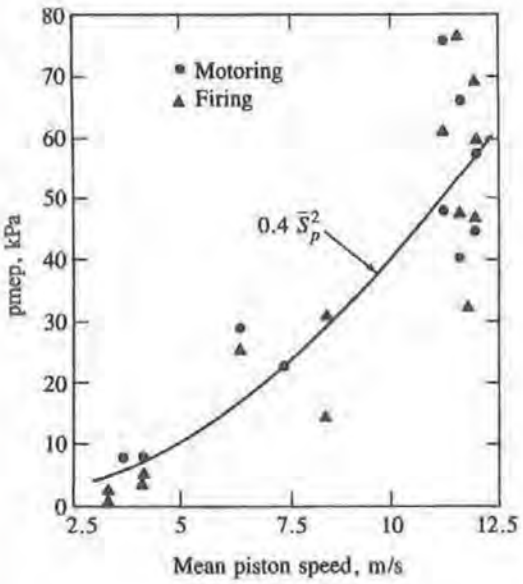


FIGURE 13-13
Pumping mean effective pressure as a function of mean piston speed for several naturally aspirated diesel engines.[5]

of the speed.[5] This extra heat loss is not part of the difference between indicated and brake output in a firing engine, as noted previously.

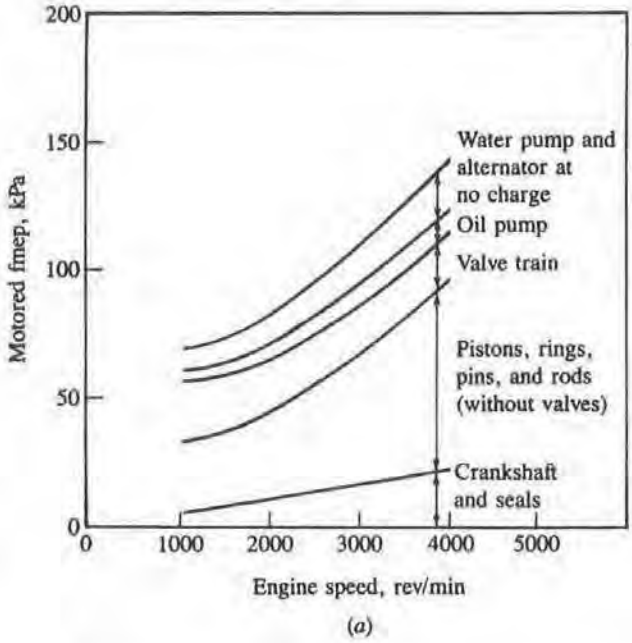
Pumping mean effective pressure data for a series of naturally aspirated diesels under both firing and motored conditions is shown in Fig. 13-13. The solid line is the term $0.4\bar{S}_p^2$, with $\bar{S}_p$ in meters per second; this is the last term in the overall motored engine friction correlation [Eq. (13.7)].

13.6 ENGINE FRICTION COMPONENTS

In this section, a more detailed analysis of the major components of engine friction is presented and, where possible, equations for predicting or scaling the different components are developed.

13.6.1 Motored Engine Breakdown Tests

Motored engine tests, where the engine is disassembled or broken down in stages, can be used to determine the friction associated with each major engine assembly. While this test procedure does not duplicate the combustion forces of actual engine operation, such tests are useful for assessing the relative importance of individual friction components. Figure 13-14 shows results of breakdown tests on a spark-ignition engine and DI diesel engines. These tests show the large contribution from the piston assembly (piston, rings, rod, including compression loading effects), with the valve train, crankshaft bearings, and water and oil pumps all making significant contributions to the total. An approximate breakdown of rubbing and accessory friction is: piston assembly 50 percent; valve train 25 percent; crankshaft bearings 10 percent; accessories 15 percent. Their relative importance varies over the speed range, however. In the sections that follow, total engine friction will be discussed under the following headings:



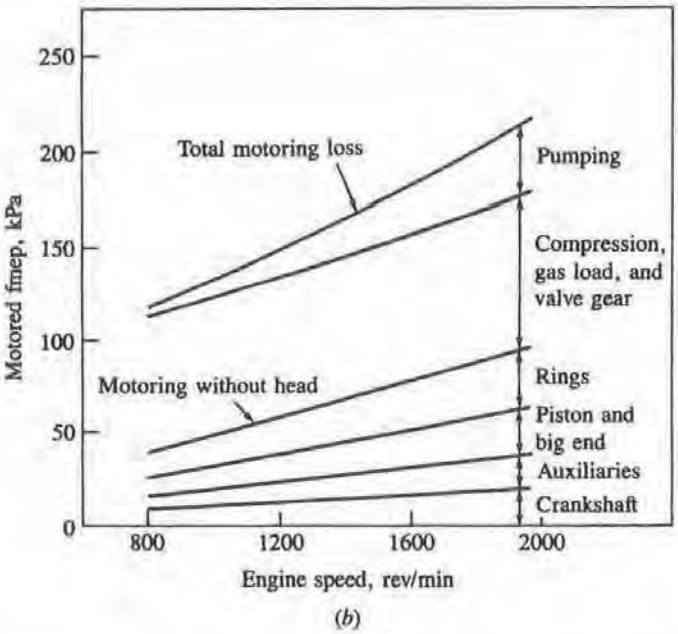


FIGURE 13-14
Motored friction mean effective pressure versus engine speed for engine breakdown tests. (*a*) Four-cylinder spark-ignition engine.[10] (*b*) Average results for several four- and six-cylinder DI diesel engines.[5]

pumping friction, piston assembly friction, valve train friction, crankshaft bearing friction, and (in Sec. 13.7) accessory power requirements.

13.6.2 Pumping Friction

Engine pumping mep data for SI and CI engines, as a function of speed and load, were given in Sec. 13.5. A more detailed breakdown of pumping work is developed here. Figure 13-15 shows the pumping loop for a firing four-stroke cycle spark-ignition engine. The pumping work per cycle (see Fig. 2-4) is the $\int p\,dV$

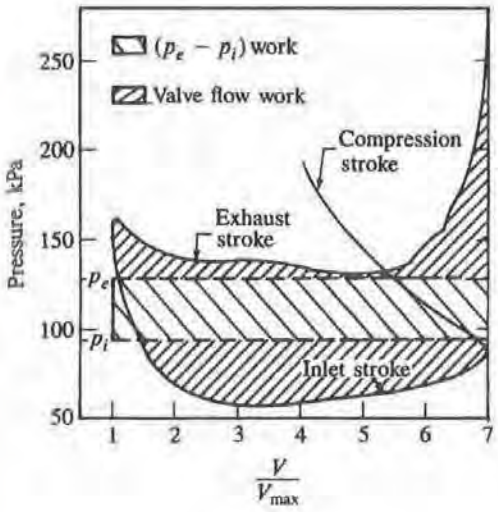


FIGURE 13-15
Pumping loop diagram for spark-ignition engine under firing conditions, showing throttling work $V_d(p_e - p_i)$ and valve flow work.[11]

over the inlet and exhaust strokes. In Fig. 13-15, the firing pumping loop is compared with the inlet and exhaust manifold pressures, p_i and p_e. The work $V_d(p_i - p_e)$ measures the effect of restrictions outside the cylinder, in the inlet and exhaust systems: air filter, carburetor, throttle valve, intake manifold (on the inlet side); exhaust manifold and tail pipe, catalytic converter, and muffler (on the exhaust side). The other area, shown as *valve flow work*, corresponds mainly to pressure losses in the inlet and exhaust valves, and to a lessor extent in the inlet and exhaust ports. As load is reduced in an SI engine, the throttle restriction is increased, the $V_d(p_e - p_i)$ term—called *throttling work*—will increase, and the valve flow work will decrease. The increase in throttling work is much more rapid than the decrease in valve flow work. Both throttling work and valve flow work increase as speed increases at constant load.

The manifold pressures in naturally aspirated engines can be related to imep through a set of equations developed by Bishop:[11, 12]

$$\text{imep}_c = 12.9p_a\left(\frac{p_{i,a}}{p_a} - 0.1\right) \tag{13.8}$$

where $p_{i,a}$ is the absolute inlet manifold pressure and p_a is the atmospheric pressure. (All pressures are in kilopascals.)

For SI engines,

$$p_{i,g} = p_a - \frac{\text{imep}_c}{12.9} - 10 \tag{13.9}$$

$$p_{e,g} = p'_{e,g}\left[\left(\frac{\text{imep}_c}{3904}\right)\left(\frac{N}{1000}\right)\right]^2 \tag{13.10}$$

For diesel engines (naturally aspirated),

$$p_{i,g} = 0 \quad \text{and} \quad \text{imep}_c[\text{in Eq. (13.8)}] = 972 \text{ kPa} \tag{13.11}$$

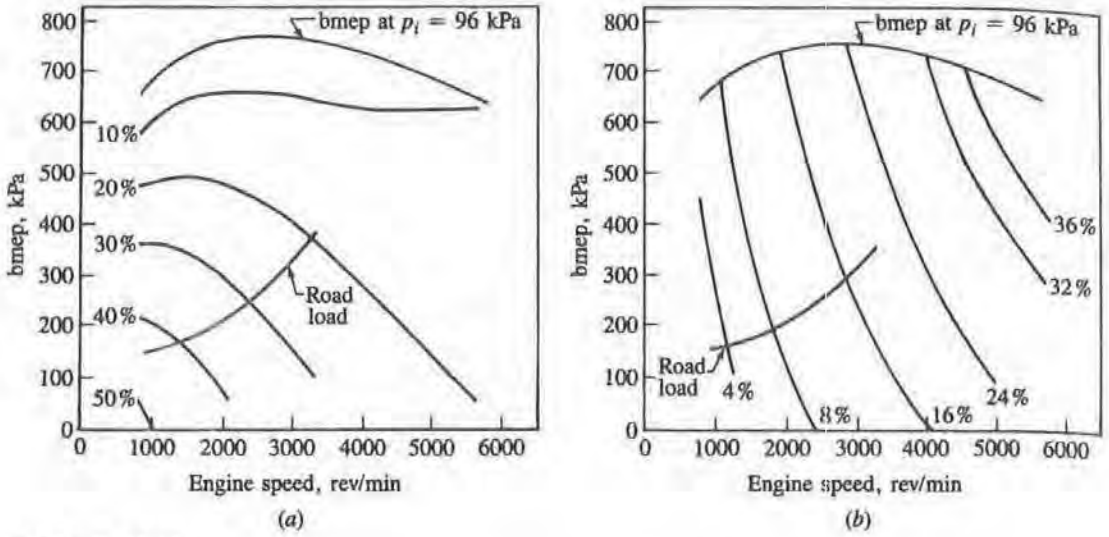


FIGURE 13-16
Relative importance of (*a*) throttling friction mep and (*b*) valve pumping friction mep, for spark-ignition engine, as percent of total friction mep on engine load versus speed map.[12]

Here $p_{i,g}$ and $p_{e,g}$ are the intake and exhaust manifold *gauge* pressures (both are positive numbers), p_a is the atmospheric pressure, and $p'_{e,g}$ is the exhaust gauge pressure (all in kilopascals) at 4000 rev/min and full load.

The *throttling mep* for firing engine operation is then given by

$$\text{mep(throttling)} = p_{i,g} + p_{e,g} \tag{13.12}$$

The *valve-pumping mep* was correlated by

$$\text{mep (valve pump)} = 8.96\left(\frac{\text{imep}_c}{1124}\right)^{0.5}\left(\frac{N}{1000}\right)^{1.7}\left(\frac{2.98}{F}\right)^{1.28} \tag{13.13}$$

where

$$F = \frac{n_{\text{iv}}\, n_c\, D_{\text{iv}}^2}{V_d} \qquad \text{m}^{-1}$$

and n_{iv} is the number of inlet valves per cylinder, n_c the number of cylinders, D_{iv} the inlet valve head diameter, and V_d the displaced volume. For diesel engines, in Eq. (13.13), $\text{imep}_c = 1124$ kPa.

Figure 13-16 shows the relative importance of the throttling and valve pumping losses as a percentage of the total friction mep over the speed and load range of a typical SI engine. The curves are obtained with the equations given above for a six-cylinder, 9 : 1 compression ratio, 3.3-liter (202 in^3) displacement engine. The trends of increasing importance of valve pumping with increasing speed and increasing importance of throttling losses with decreasing load are evident.

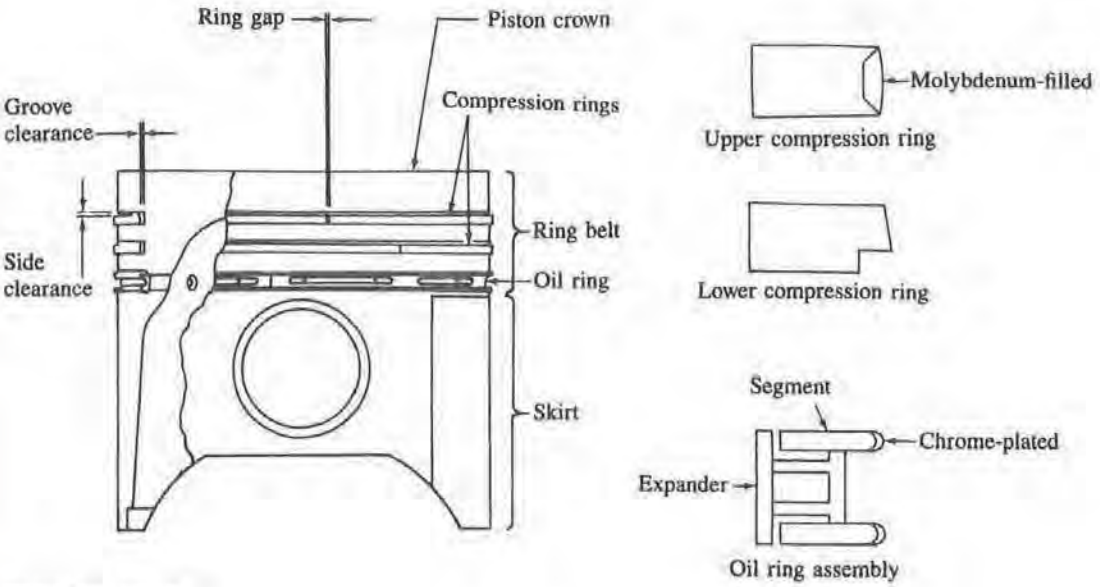


FIGURE 13-17
Construction and nomenclature of typical piston and ring assembly.[10]

13.6.3 Piston Assembly Friction

The construction and nomenclature of a typical piston and ring assembly is shown in Fig. 13-17. The piston skirt is a load-bearing surface which keeps the piston properly aligned within the cylinder bore. The piston lands and skirt carry the side load which is present when the connecting rod is at an angle to the cylinder axis. The rings control the lubrication between these surfaces and the liner. Two types of rings—compression and oil rings—perform the following tasks: (1) seal the clearance between the piston and cylinder to retain gas pressure and minimize blowby; (2) meter adequate lubricant to the cylinder surface to sustain high thrust and gas force loads at high surface speed and at the same time control oil consumption to acceptable limits; and (3) control piston temperatures by assisting in heat transfer to the cylinder walls and coolant. Automobile engines normally use three rings, though two-ring designs exist. Larger diesel engines may use four rings.

Many designs of compression ring are employed,[13] the differences between them being in the cross-sectional shapes (and hence relative flexibility) and in their use of wear-resistant surface treatments. Top compression rings are usually made of cast iron. The axial profiles are chosen to facilitate hydrodynamic lubrication. Common shapes are a rectangular cross section with inner and outer edges chamfered to prevent sticking in the groove, or with a barrel-shaped working surface which can accommodate the rotation of the piston which occurs with short piston skirts. Wear-resistant coatings (either a hard chromium-plated overlay or a molybdenum-filled inlay) are usually applied to the outer ring surface. The second compression ring serves principally to reduce the pressure drop across the top ring. Since the operating environment is less arduous, the

second ring can be made more flexible to give better oil control. The objective is to compensate for the torsional deflection of the ring under load so that top-edge contact with the cylinder liner is avoided. Top-edge contact tends to pump oil toward the combustion chamber, detracting from the performance of the oil control ring. Bottom-edge contact provides an oil scraping action on the downstroke. The oil control ring meters and distributes the oil directed onto the cylinder liner by the crankshaft system, returning excess oil to the crankcase sump. It must exert sufficient pressure against the cylinder, possess suitably shaped wiping edges (usually two thin steel rings), and provide adequate oil drainage. Slotted or composite rings are normally used.[14]

The tension in all the piston rings holds them out against the cylinder wall and hence contributes to friction. The gas pressure behind the compression rings increases this radial force. The gas pressures behind the second ring are substantially lower than behind the first ring. The gas pressures behind the rings are a function of speed and load. An approximate rule for estimating ring friction is that each compression ring contributes about 7 kPa (1 lb/in^2) mep.[5] Oil rings, due to their substantially higher ring tension, operate under boundary lubrication; they contribute about twice the friction of each compression ring.[15]

The piston assembly is the dominant source of engine rubbing friction. The components that contribute to friction are: compression rings, oil control rings, piston skirt, and piston pin. The forces acting on the piston assembly include: static ring tension (which depends on ring design and materials); the gas pressure forces (which depend on engine load); the inertia forces (which are related to component mass and engine speed). The major design factors which influence piston assembly friction are the following: ring width, ring face profile, ring tension, ring gap (which governs inter-ring gas pressure), liner temperature, ring-land width and clearances, skirt geometry, skirt-bore clearance.[3]

Piston assembly friction is dominated by the ring friction. The forces acting on a typical compression ring, lubricated by a thin oil film, are shown in Fig. 13-18. The analysis of this hydrodynamic contact is complex because the forces acting on the ring vary with time and slight changes in ring face geometry can have large effects on the computed results. Cylinder pressure p_c normally acts on the top and back of the ring. The inter-ring gas pressure p_{ir} (which depends on cylinder pressure and the geometry of the lands, ring grooves, and ring, especially the ring gap), acts on the oil film and bottom part of the ring. The character of the gas flow into and out of the inter-ring regions and its effect on ring motion were discussed in Sec. 8.6. Late in the expansion stroke, pressure reversals can occur which may cause the ring to move to the upper surface of the groove or to flutter in between. Ring tension acts to force the ring against the liner. The pressure in the lubricating oil film is generated as shown by the surface A-B in Fig. 13-18 as the ring moves downward. It is believed that the film cavitates between B and C so the pressure decreases to a low value and then increases to p_c. When the direction of motion is reversed, C-B becomes the pressure-generating surface.

Models for the ring and oil film behavior have been developed. For the practical case where the oil film thickness h is much less than the ring width, the

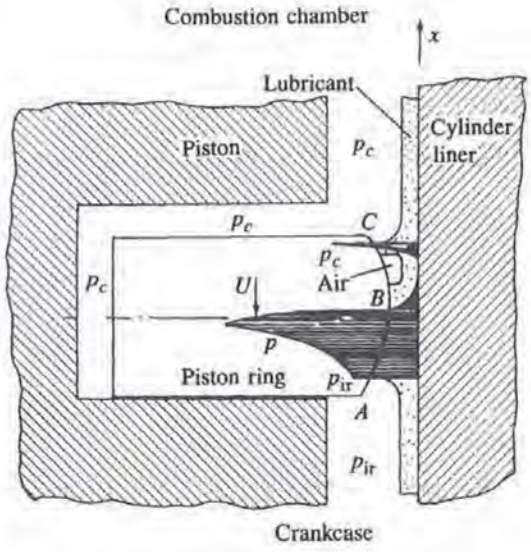


FIGURE 13-18
Schematic of pressure distribution in the lubricating oil film and around a compression ring during expansion stroke. Pressure profile in the oil film indicated by horizontal shading.[3]

Navier-Stokes equation for the liquid film motion reduces to a Reynolds equation of the form:

$$\frac{\partial}{\partial x}\left(h^3 \frac{\partial p}{\partial x}\right) = 6U\mu \frac{\partial h}{\partial x} + 12\mu \frac{\partial h}{\partial t} \tag{13.14}$$

where h is the local film thickness, μ the liquid viscosity, and U the relative velocity between the two surfaces. This equation, along with the appropriate force balances on the ring, can then be solved for the coupled film and ring behavior (e.g., see Ref. 15).

Measured oil film thicknesses in an operating direct-injection diesel engine are shown in Fig. 13-19. A capacitance technique with electrodes embedded in the top compression ring was used to make the measurements.[16] At top-center during combustion, the thickness is a minimum (≈ 1 μm); it then increases as gas loading on the rings decreases and piston velocity increases during the expansion stroke to a value an order of magnitude higher. Higher engine load results in higher gas loading on the rings. It also results in higher lubricant temperatures and lower viscosity, which reduce the film thickness during intake, compression, and exhaust. This large change in film thickness over one cycle is the reason the ring friction regime changes from boundary lubrication to thick-film hydrodynamic lubrication. When the oil film thickness drops below about 1 μm, asperity contact will begin.†

An analysis of the side thrust between the piston and cylinder wall helps explain piston design trends. A force balance on the crank/connecting rod mechanism of Fig. 2-1 leads to the following. An axial force balance relates the piston

† The critical film thickness depends on both the cylinder liner and ring surface finish.

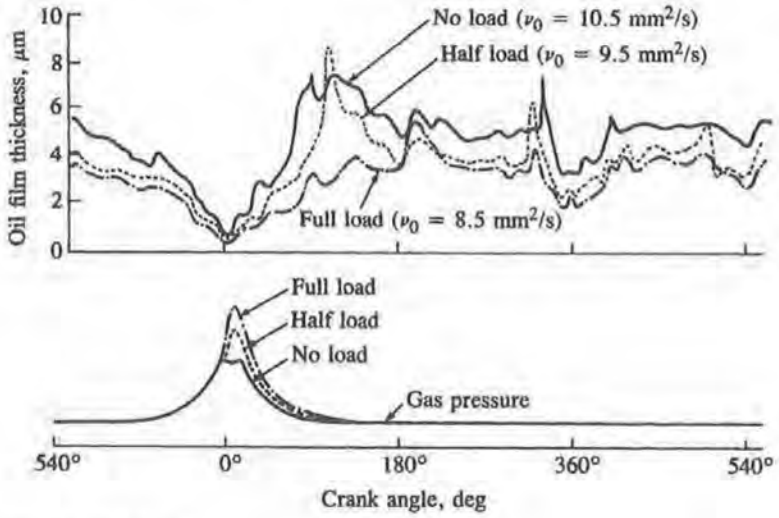


FIGURE 13-19
Measured oil film thickness between top ring and cylinder liner of a DI diesel engine, operated at 1300 rev/min. Bore = 139.7 mm, stroke = 152.4 mm. ν_0 is estimated oil viscosity. Reprinted by permission of the Society of Tribologists and Lubrication Engineers (STLE), formerly the American Society of Lubrication Engineers (ASLE).[16]

mass m and acceleration to the net axial force:

$$m\frac{dS_p}{dt} = -F_r\cos\phi + \frac{\pi B^2}{4}p \mp F_f \tag{13.15}$$

where ϕ is the angle between the cylinder axis and connecting rod, and p is the cylinder *gauge* pressure. A transverse force balance gives

$$F_t = F_r\sin\phi = \left(-m\frac{dS_p}{dt} + \frac{\pi B^2}{4}p \mp F_f\right)\tan\phi \tag{13.16}$$

Here F_r is the force in the connecting rod (positive when in compression) and F_f is the friction force on the piston assembly (− when piston is moving toward the crank; + when piston moves away from the crank). dS_p/dt is the piston acceleration obtained by differentiating the equation for piston velocity [Eq. (2.11)]:

$$\frac{dS_p}{dt} = \frac{d^2s}{dt^2} = \pi^2 N\bar{S}_p\left[\cos\theta + \frac{R^2\cos 2\theta + \sin^4\theta}{(R^2 - \sin^2\theta)^{3/2}}\right] \tag{13.17}$$

The side thrust F_t given by Eq. (13.16) is transmitted to the liner via the rings and piston skirt. It changes direction as the piston passes through top- and bottom-center positions. Since the friction force changes sign at these locations and the gas pressure during expansion is greater than during compression, the side thrust during expansion is greater.

The piston skirt carries part of this side thrust so it contributes to piston assembly friction. The large contact area between the skirt and liner, relative to

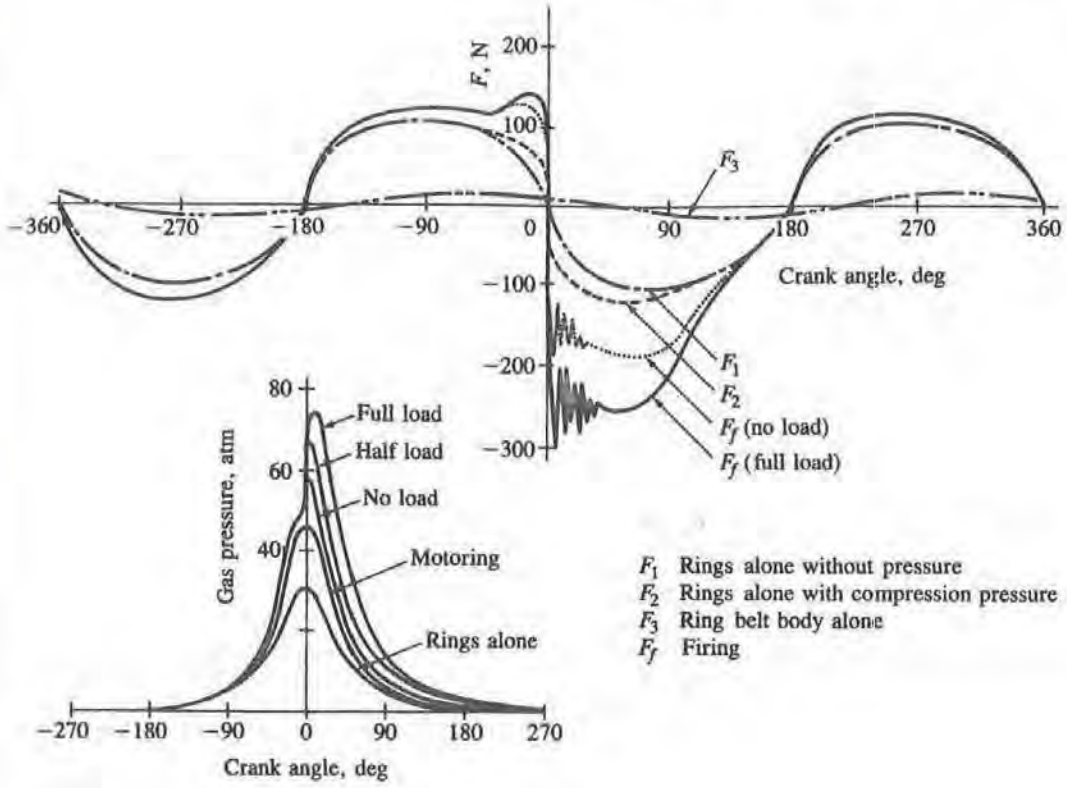


FIGURE 13-20
Measured frictional force on cylinder liner of 137 mm bore and 135 mm stroke single-cylinder DI diesel engine. 1200 rev/min, coolant temperature 80°C, cylinder liner inside temperature 97°C.[18]

the ring contact area, results in lighter loading (force/area) and promotes hydrodynamic lubrication. Piston skirt areas have been reduced substantially in recent years to reduce piston mass (which reduces side thrust) and contact area. An additional reduction in side thrust, leading to reduced skirt friction, has been achieved with the use of an offset wrist-pin. By offsetting the pin axis by 1 to 2 mm without changing its vertical location, the crank angle at which the piston traverses the bore and "slaps" the other side of the cylinder is advanced so it occurs before combustion has increased the cylinder gas pressure significantly.[17]

Direct measurements of the friction force associated with the piston assembly have been made. The most common technique involves the use of a special engine where the axial force on the cylinder liner is measured directly with a load transducer (e.g., Ref 18). Figure 13-20 shows the friction forces measured in such an engine (a DI diesel engine) through the engine's operating cycle. Friction forces are highest just before and after top-center at the end of the compression stroke. The high values at the start of the expansion stroke under firing conditions are caused by the piston slap impulse and the high side-thrust force as well as the combustion gas pressure loading on the rings.

Bishop[12] has developed correlations for piston and ring friction in the following categories: boundary condition friction (primarily between the rings and

the cylinder wall due to ring tension, and gas pressure behind the compression rings) and viscous ring and piston friction. He argued that boundary condition friction was primarily due to breakdown of the oil film between the rings and cylinder wall over part of the piston travel. Assuming that the transition to boundary lubrication occurred at a critical speed, he showed that fmep due to boundary friction was proportional to stroke/bore^2, i.e.:

$$(\text{fmep})_{\text{boundary}} \propto \text{loading} \times \frac{L}{B^2} \tag{13.18}$$

The ring loading has two components. The component due to ring tension is essentially constant. The component due to gas pressure behind the rings will depend on load. Bishop assumed it to be proportional to inlet manifold pressure. The viscous piston friction—friction between the piston and rings and cylinder wall under hydrodynamic lubrication conditions—was correlated by

$$(\text{fmep})_{\text{hydrodyn}} \propto \frac{\bar{S}_p A_{p,\text{eff}}}{LB^2} \tag{13.19}$$

where $A_{p,\text{eff}}$ is the effective area of the piston skirt in contact with the cylinder liner.

The relative importance of the boundary lubrication piston and ring friction, and viscous piston and ring friction over the load and speed range, is as follows. The viscous friction component increases in importance with increasing speed. The boundary lubrication friction component increases with increasing load as the cylinder gas pressures increase.

13.6.4 Crankshaft Bearing Friction

Crankshaft friction contributions come from journal bearings (connecting rod, main and accessory or balance shaft bearings) and their associated seals. A schematic of a journal bearing operating under hydrodynamic lubrication is shown in Fig. 13-21. Large loads can be carried by journal bearings with low energy losses under normal operating conditions, due to the complete separation of the two surfaces in relative motion by the lubricant film. Loads on crankshaft journal bearings vary in magnitude and direction because they result primarily from the inertial loads of the piston/connecting rod mechanism and the cylinder gas loads [see Eq. (13.15)]. Typical loads and the resulting journal eccentricity diagram for a connecting rod bearing are shown in Fig. 13-22. From the journal eccentricity diagram the minimum oil film thickness is determined. This quantity, the minimum separation distance between the journal and bearing surfaces, is a critical bearing design parameter. If the film thickness is too low, asperities will break through the oil film and substantially increase the friction and wear. Journal bearings are usually designed to provide minimum film thicknesses of about 2 μm.

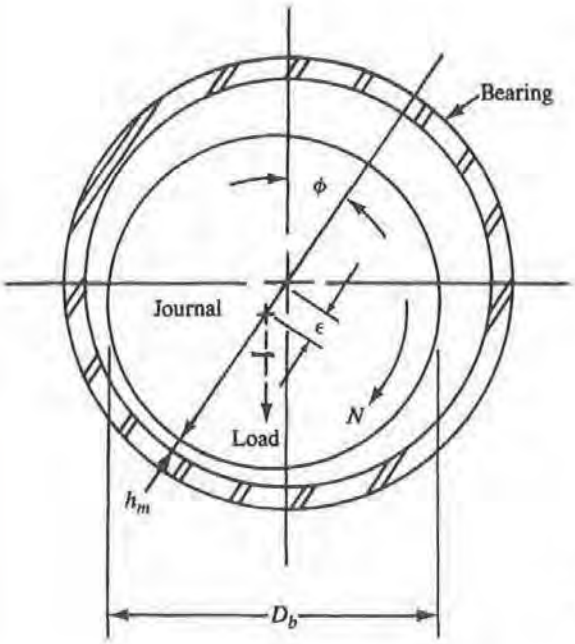
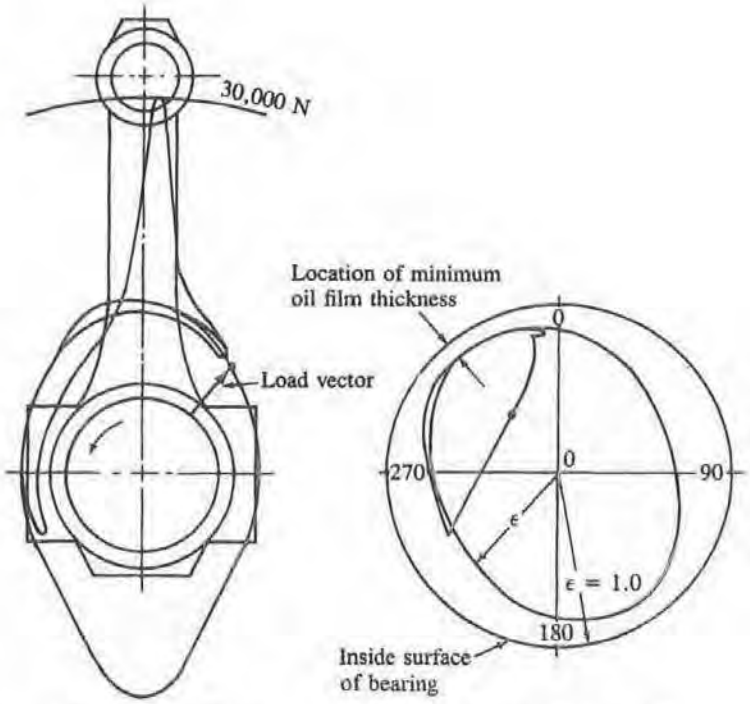


FIGURE 13-21
Schematic of hydrodynamically lubricated journal bearing.[3]



Polar load diagram for connecting rod bearing

Eccentricity of journal in connecting rod bearing

FIGURE 13-22
Typical engine journal bearing load and eccentricity diagrams.[3]

The friction force F_f in the bearing is given approximately by the product of the bearing area, the oil viscosity, and the mean velocity gradient in the oil:

$$F_f \approx (\pi D_b L_b)\mu\left(\frac{\pi D_b N}{\bar{h}}\right) = \frac{\pi^2 \mu D_b^2 L_b N}{\bar{h}} \tag{13.20}$$

where D_b and L_b are the bearing diameter and length, $\bar{h}$ is the mean radial clearance, and N is the shaft rotational speed. A more sophisticated analysis of the friction in a hydrodynamically lubricated bearing yields the relation[19]

$$F_f = \frac{\pi^2 \mu D_b^2 L_b N}{(1-\varepsilon^2)^{1/2}\bar{h}} + \frac{\bar{h}\varepsilon W}{D_b} \sin \phi \tag{13.21}$$

where ε is the eccentricity ratio $(\bar{h} - h_m)/\bar{h}$ and h_m is the minimum clearance. The first term closely matches the approximation given in Eq. (13.20). The factor $1/(1-\varepsilon^2)^{1/2}$ and the second term correct for the offset of the journal center relative to the bearing center: W is the bearing load and ϕ the attitude angle. To first order, with hydrodynamic lubrication the friction power does not depend significantly on the bearing load. If σ is the loading per unit projected area of the bearing $[W/(L_b D_b)]$, then the coefficient of friction f is given by

$$f = \frac{F_f}{W} \approx \frac{\pi^2 \mu D_b^2 L_b N}{\sigma L_b D_b \bar{h}} = \frac{\pi^2 D_b}{\bar{h}} \frac{\mu N}{\sigma} \tag{13.22}$$

For a given bearing, or series of geometrically similar bearings, the friction coefficient is proportional to $\mu N/\sigma$. However, at low values of $\mu N/\sigma$ the hydrodynamic pressure in an actual bearing will be insufficient to support the shaft load and the oil film becomes incomplete. The friction coefficient increases rapidly as mixed lubrication then occurs.

Bishop[12] summed the friction power loss in all crankshaft and con rod journal bearings and divided by the displaced volume per unit time to obtain the following correlation for bearing friction mep (in kilopascals):

$$\text{fmep (bearings)} = 41.4\left(\frac{B}{L}\right)\left(\frac{N}{1000}\right) K \tag{13.23}$$

where

$$K = \frac{D_{mb}^2 L_{mb} + D_{rb}^2 L_{rb}/m + D_{as}^2 L_{as}}{B^3} \tag{13.24}$$

In Eq. (13.24), D_{mb} is the main bearing diameter, L_{mb} the total main bearing length ÷ number of cylinders, D_{rb} the rod bearing diameter, L_{rb} the rod bearing length, m the number of pistons per rod bearing, D_{as} the accessory shaft bearing diameter, L_{as} the total length of all accessory shaft bearings ÷ number of cylinders, and all dimensions are in millimeters. The similarity between engines is such that $K \approx 0.14$ for spark-ignition engines and $K \approx 0.29$ for diesel engines.

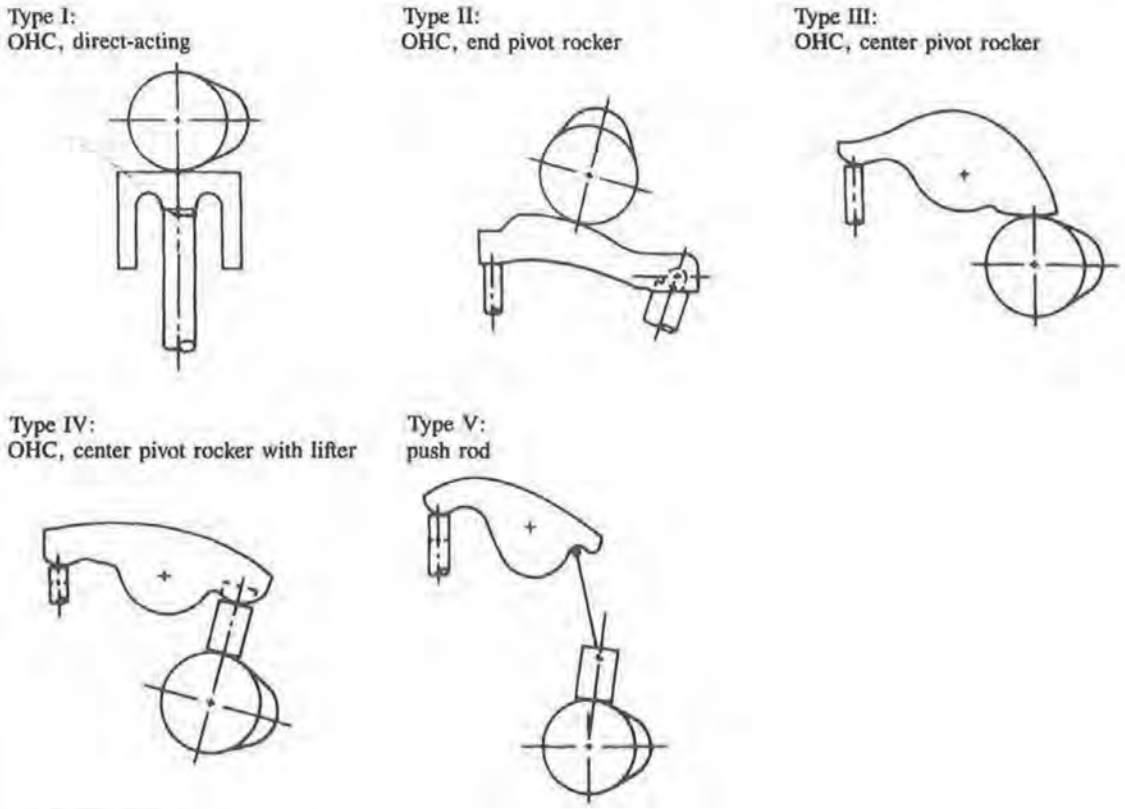


FIGURE 13-23
Different valve train configurations.[21]

The front and rear main bearing seals[20] also contribute to crankshaft assembly friction. At 1500 rev/min they are responsible for about 20 percent of the friction attributable to the crankshaft.[10]

13.6.5 Valve Train Friction

The valve train carries high loads over the entire speed range of the engine. Loads acting on the valve train at lower speeds are due primarily to the spring forces, while at higher speeds the inertia forces of the component masses dominate. Valve train designs can be classified by type of configuration, as indicated in Fig. 13-23. Large valves and high rated speeds generally increase spring and inertia loads and friction. Friction differences between these systems are difficult to quantify. For example, measurements of valve train friction mean effective pressure for several of these valve train types showed significant variations (± 30 percent): see Fig. 13-24*a*.[10,21] However, when the data were adjusted to a common spring load, Fig. 13-24*b*, the low-speed friction mep values converged and the high-speed fmep differences were reduced.[10]

The total valve train friction can be broken down by critical contact regions: camshaft journal bearings, rocker arm/fulcrum and cam/tappet interface.

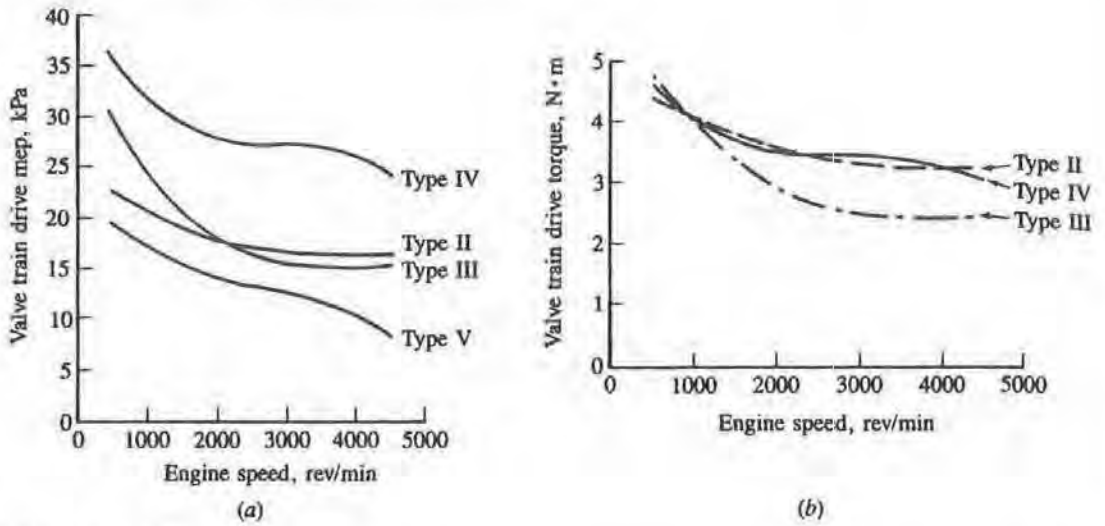


FIGURE 13-24
(*a*) Total valve train friction mean effective pressure as a function of speed for four engines with different valve configurations (see Fig. 13-23). (*b*) Valve train friction torque for three of these engines after adjusting to common valve spring load.[10]

The shape of the valve train mep versus speed curve indicates that the predominant regime of lubrication in the valve train at lower engine speeds is boundary lubrication. The cam/lifter interface usually contributes the largest friction loss due to the very high loads and small contact areas.[22]

Effective methods of reducing valve train friction are: (1) spring load and valve mass reduction; (2) use of tappet roller cam followers; (3) use of rocker arm fulcrum needle bearings. One such low-friction valve train design is shown in Fig. 13-25.[22] The roller cam-followers provide the largest benefit especially at lower speeds: reductions of order 50 percent in valve train friction can be achieved.

Bishop[12] developed a correlation for valve train friction from design data on valve spring loads and valve weights, and experimental data from dynamometer tests of push rod engines. He shows that

$$\text{fmep (valve train)} = \frac{C[1 - 0.133(N/1000)]n_{iv} D_{iv}^{1.75}}{B^2 L} \tag{13.25}$$

where n_{iv} is the number of inlet valves per cylinder, D_{iv} is the inlet valve head diameter, and B and L are bore and stroke. This relation does not include camshaft bearing friction, which is included in Eq. (13.23). The functional form of Eq. (13.25) is an acceptable fit to more modern engine data. Bishop's value for C (1.2×10^4 with fmep in kilopascals, N in revolutions per minute, and dimensions in millimeters) gives valve train fmep values (which exclude camshaft bearing losses) about two-thirds the total valve train friction of current production engines. This is consistent with the data in Fig. 13-24.

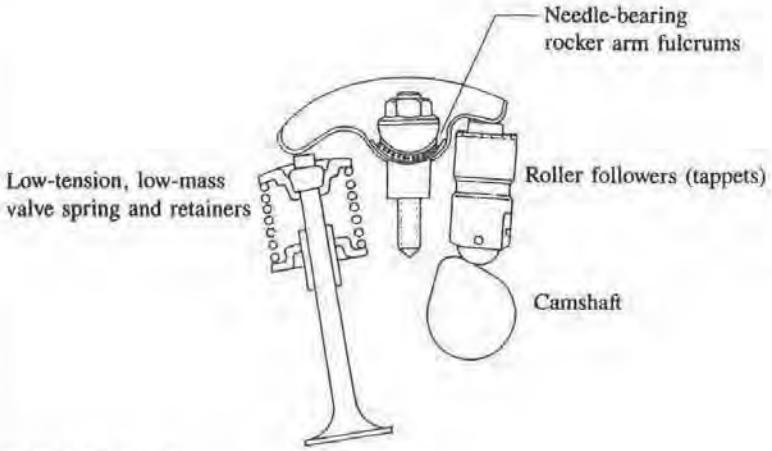


FIGURE 13-25
Low friction valve train.[22]

13.7 ACCESSORY POWER REQUIREMENTS

The coolant water pump and oil pump are built-in accessories, essential to engine operation, and are normally considered part of the basic engine.[2] A fully equipped engine usually includes additional accessories—a fan and generator; in automobile use it often includes a power-steering pump, an air conditioner, and an air pump for emission control. The power delivered by the fully equipped engine (the net power) is lower than the power delivered by the basic engine due to the power requirements of these additional accessories.

The friction mean effective pressures associated with driving the water pump and alternator, and oil pump are shown in Fig. 13-14*a*. Together they comprise about 20 percent of the total (motored) engine friction. The water pump is typically less than about 7 kPa at 1500 rev/min;[10] the oil pump 4 to 10 kPa at this speed;[10] the alternator requires 7 to 10 kPa.[23] These numbers vary significantly with component design details. The generator power depends on the electrical load to be met and the generator blower design. A requirement of about two-thirds of the peak is indicated for average generator power.[23]

The power requirements for a fan, generator, and power-steering pump typical of a 5.7-liter engine are shown in Fig. 13-26. The fan requirements are the largest and with a direct drive increase with the cube of the speed. Alternative couplings such as a viscous drive reduce the fan speed at high engine speed and thereby reduce its power significantly. The power-steering pump is only required to provide high pressures intermittently. Here only the fluid pumping losses are charged against the engine.

Air-conditioning is standard on a majority of U.S. cars; additional power is required for the air-conditioning compressor. Also, since the compressed refrigerant is condensed in a second radiator, a larger-than-standard fan is required to pull additional air through the combined radiator systems. An air pump which pumps air into the engine exhaust ports may be part of an SI engine emission

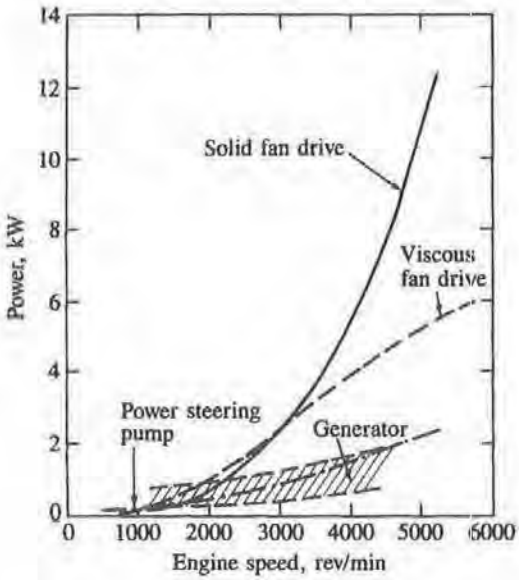


FIGURE 13-26
Power requirements for engine fan, generator, and power-steering pump typical of 5.7-liter eight-cylinder engine.[23, 24]

control system (see Sec. 11.6). Its power requirements (~1 kW at normal engine speeds) must then be added to the accessory friction requirements.

13.8 LUBRICATION

The lubricant and the lubricating system perform the following functions:[25]

1. Reduce the frictional resistance of the engine to a minimum to ensure maximum mechanical efficiency.
2. Protect the engine against wear.
3. Contribute to cooling the piston and regions of the engine where friction work is dissipated.
4. Remove all injurious impurities from lubricated regions.
5. Hold gas and oil leakage (especially in the ring region) at an acceptable minimum level.

13.8.1 Lubrication System

The principle moving parts of an engine are positively lubricated by introducing a supply of oil from a pressurized system. An example of a lubrication system (for an air-cooled diesel engine) is shown in Fig. 13-27. The oil pump draws oil from the engine sump and delivers it through a control valve to the oil cooler. The oil then passes through the filter to the main oil gallery. From the main oil gallery it is branched to the main, the big end, and the camshaft bearings. Oil is also ducted to the injection pump. Through a passage in the camshaft bearing the oil flows to the tappet bridges. As the oil passages of tappets and tappet bridges line up during tappet motion, rocker arms and valve stems are pulse-lubricated

1 Sump
2 Suction pipe
3 Lube oil pump
4 Oil pressure control valve
5 Pressure pipe
6 Bypass pipe or alternative
7 Cooling coil or, alternatively:
8 Block-type oil cooler
9 Oil filter
10 Safety valve
11 Main oil gallery
12 Main bearing
13 Big end bearing
14 Camshaft bearing
15 Tappet (with timing groove to pulse-lubricate rocker arm)
16 Push rod (hollow, used as rocker arm oil feed pipe)
17 Rocker arm bearing
18 Metering plug (to control valve lubrication)
19 Push rod duct (used as cylinder-head-to-crankcase oil return pipe)
20 Splash hole to lubricate timing gears
21 Piston cooling nozzle
22 Oil pressure gauge adaptor
23 Oil pressure gauge

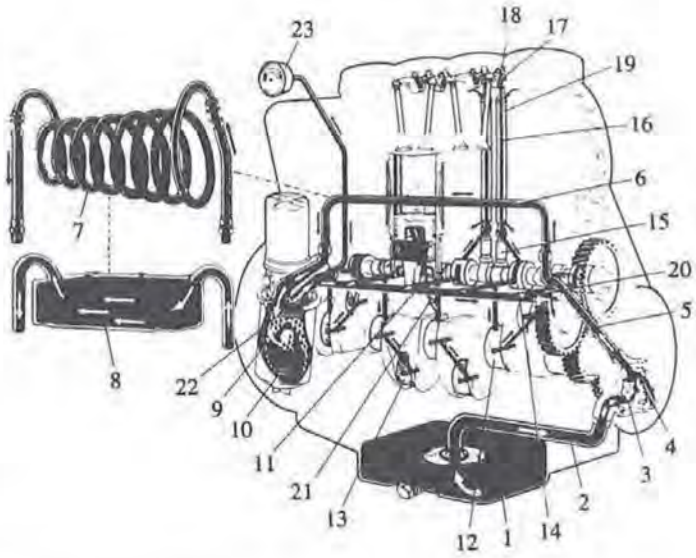


FIGURE 13-27
Lubrication system layout for air-cooled DI diesel engine. (*Courtesy Klöckner-Humboldt-Deutz AG.*)

through the tappets and pushrods. For cooling pistons and lubricating cylinders, oil is thrown against the underside of the piston through nozzles connected to the main bearings. Spring-loaded ball valves incorporated in the nozzles interrupt the jet cooling at low engine speeds to insure that the oil pressure remains above a safe level. The gears of the main timing train are splash-lubricated. The oil is returned from the injection pump and rocker chamber cover to the sump.

13.8.2 Lubricant Requirements

Table 13.1 lists the qualities required of engine oils to perform the main lubrication system functions. These qualities can be summarized under the following headings.[25]

OXIDATION STABILITY. The temperature of the oil and engine parts it contacts, the presence of oxygen, the nature of the metal surfaces and debris, and the products of the fuel combustion, all influence the oxidation of the hydrocarbon components in lubricating oil. High temperatures are the primary factor, and the top piston ring groove and the crankcase are the critical regions. The temperature of the top ring groove can easily reach 250°C. The lubricating oil when subject to these conditions must not, through oxidation, contribute to deposit formation, even after long periods of running. These deposits would eventually

TABLE 13.1
Functions and qualities required of engine oils

Main functions required	Where and when	Qualities required
Reduce frictional resistance	During cold-starting	Low enough viscosity to provide good pumping and avoid undue cranking resistance
	Between con-rod/ crankshaft bearings, and journals	Minimum viscosity without risk of metal-to-metal contact under the varying conditions of temperature, speed, and load
	Between pistons, rings, and cylinders	Sufficiently high viscosity at high temperatures; good lubrication property outside the hydrodynamic condition, especially at top-center
		Antiseizure properties, especially during the run-in period
Protect against corrosion and wear	During shut-down or when running at low temperature	Must protect metallic surfaces against corrosive action of fuel decomposition products (water, SO_2, HBr, HCl, etc.)
		Must resist degradation (resist oxidation, have good thermal stability)
	In normal running	Must counteract action of fuel and lubricant decomposition products at high temperatures, especially on non-ferrous metals
		By intervention in the friction mechanism must reduce the consequences of unavoidable metal-to-metal contact
		Must resist deposit formations which would affect lubrication (detergency or dispersive action)
		Must contribute to the elimination of dust and other contaminants (dispersive action)
Assist sealing	In the ring zone, especially at TC	Must have sufficient viscosity at high temperatures and low volatility
		Must limit ring and liner wear
		Must not contribute to formation of deposits in ring grooves and must prevent such formation
Contribute to cooling	Chiefly of pistons, rings, and con-rod bearings	Must have good thermal stability and oxidation resistance
		Must have low volatility
		Viscosity must not be too high
Facilitate the elimination of undesirable products	During oil drains to eliminate atmospheric dust, soot from diesel engines, Pb salts, wear debris, organic products from burned fuel and lubricants, and other contaminants which promote deposits or accelerate wear	Must be able to maintain in fine suspension all solid material (dispersivity) whatever the temperature and physical and chemical conditions (water)
		Must be able to solubilize certain organic compounds, particularly heavy oxidation products

Source: From Schilling.[25]

lead to ring sticking which results in excessive blowby. At high temperatures, deposits are related to the oxidized fraction of the oil.

The oil temperature in the crankcase is 120 to 130°C, or higher. Oil maintained at this temperature should neither form any acid products capable of attacking the bearing alloys nor form insoluble products which form deposits. Good-quality mineral oils cannot withstand these temperatures, so antioxidant and anticorrosive additives are used to control these problems. While antioxidants help to reduce deposit formation, detergent/dispersant additives are required to maintain any insoluble materials formed through oxidation in suspension.

DETERGENCY/DISPERSION. Except for deposits formed in the combustion chamber, deposits in the oil are controlled by its detergency. The amount of deposits formed depends on the fuel used, the quality of combustion, the temperature of the lubricating oil and coolant, and on the effectiveness of gas sealing at the piston rings. The detergency property is given to straight mineral oils by additives; the function of the detergent additive is to reduce the amount of deposits formed and make their removal easier.

At low temperatures, deposits are mainly byproducts of fuel combustion, and the detergency function is to keep them in suspension or solution in the oil. At high temperatures, deposits come from the oxidized fractions of the oil. The detergency function here is both to keep these products in suspension and to inhibit the reactions that lead to the formation of varnishes and lacquers. In addition, in diesel engines, the detergency helps in neutralizing the acidic reaction products from the sulfur compounds in the fuel.

WEAR REDUCTION. Wear is due to the individual and combined effects of corrosion, adhesion (i.e., metal-to-metal contact), and abrasion.

Corrosive attack by acidic products of combustion is one of the chief causes of cylinder and ring wear. The effect is worst at low cylinder wall temperatures. In diesel engines, the sulfur in the fuel increases the corrosive wear. Corrosive wear is effectively prevented by the use of detergent oils which neutralize the corrosive acids as they form, and by designing the cooling system to give appropriate metal temperatures.

Adhesive wear affects certain parts of the engine. In the upper cylinder, metal-to-metal contact between piston, rings, and cylinder walls takes place each time the engine is started (most significant during cold-starts) because there is insufficient oil in the top portion of the engine. Oils with antiwear additives and low viscosity at low temperatures provide a partial remedy. Adhesive wear also occurs on components such as cams, tappets, drive gears, rocker arm ends, and valve stems.

Abrasion results from the presence of atmospheric dust, and metallic debris from corrosive and adhesive wear, in the lubricating oil. Efficient air filtration is therefore most important (see Ref. 26 for a discussion of air filters). Elimination of

abrasive particle impurities from the oil system by filtration and periodic oil change is essential.

VISCOSITY. For low resistance to cranking and ease of starting, and rapid distribution of the oil while the engine is cold, a low oil viscosity at low ambient temperatures is required. When the engine (and oil) is fully warmed up, viscosity in the proper range is important for adequate sealing of the piston, acceptable oil consumption, and low friction losses. The viscosity of the oil at both low and normal engine temperatures (a spread of some 200 K) is, therefore, important. The viscosity of lubricating oils decreases with increasing temperature. The *pour point*, *viscosity*, and *viscosity index* are used to characterize the behavior of a lubricating oil for these aspects of engine operation.

The *pour point* is determined by cooling a sample of oil in a test jar until, when the jar is rotated from the vertical to the horizontal, no perceptible movement of the oil will occur within 5 s; 5°F above this temperature is the pour point.

The viscosity of lubricating oils is determined by measuring the time required for a specified volume of oil to flow through a capillary tube or orifice, contained in a constant temperature water bath. The *kinematic viscosity*, ν ($\nu = \mu/\rho$), is determined by this method. Use of a Saybolt tube with an orifice of specified diameter is the standard U.S. measurement practice. The viscosity is then given by the time t (in seconds) required to flow 60 cm^3 of oil, and is expressed as Saybolt universal seconds, SUS. Approximate conversion to centistokes (1 centistoke = 10^{-6} m^2/s) can be obtained via

$$\nu = at - \frac{b}{t}$$

where for $115 > t > 34$ s, $a = 0.224$ and $b = 185$; for $215 > t > 115$ s, $a = 0.223$ and $b = 155$; and for $t > 215$ s, $a = 0.2158$ and $b = 0$.[27]

The viscosity of lubricating oils decreases with increasing temperature. Since engine oils must operate over a range of temperatures, a measure of the rate of decrease is important. The *viscosity index*, an empirical number indicating the effect of temperature changes on viscosity, is used for this purpose;[28] a low viscosity index indicates a relatively large change of viscosity with temperature. To increase the viscosity index, lubricating oils incorporate additives called "viscosity-index improvers." These are high molecular weight compounds (molecular weight $\approx 10^3$ to 10^4) whose primary function is to reduce the viscosity variation with temperature.

The lubricating oil classification used most extensively is the SAE classification.[29] It depends solely on the viscosity of the oil. The seven different classification numbers 5W, 10W, 20W, 20, 30, 40, and 50 correspond to viscosity ranges; increasing numbers correspond to increasing viscosity, as shown in Fig. 13-28. SAE numbers followed by W (abbreviation for winter) refer to oils for use in cold climates, and viscosity is determined at −18°C (0°F). SAE numbers without W are applied to engine oils commonly used under warmer conditions;

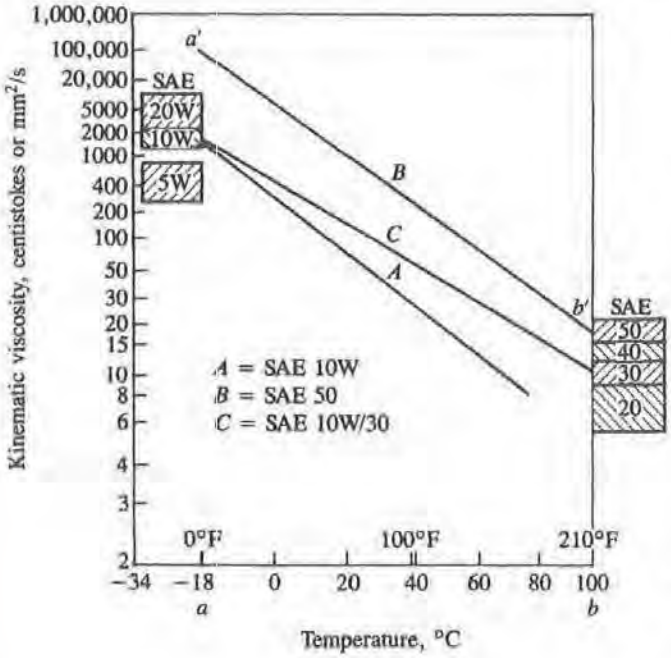


FIGURE 13-28
Viscosity versus temperature curves illustrating SAE lubricating oil classification.[25]

they are based on viscosity at 99°C (210°F). Multigrade oils (for example, 10W-40) satisfy service requirements at low as well as high temperatures in terms of the SAE classification. The first number indicates the viscosity at −18°C; the second number at 99°C. Examples are shown in Fig. 13-28. Multigrade oils have a higher viscosity index than single-grade oils, which make them more attractive for engine use.

PROBLEMS

13.1. (*a*) Show how friction mean effective pressure for a four-stroke cycle engine can be obtained from the brake power P_b, engine speed N, displaced volume V_d, and $\int p\,dV$ over the compression and expansion strokes ($= W_{c,ig}$).

(*b*) How is pumping mean effective pressure related to $\int p\,dV$ over the compression and expansion strokes and $\int p\,dV$ over the full four-stroke cycle?

(*c*) Find the brake power, total friction power, total friction imep, and pumping imep for a four-stroke cycle SI engine operating at 1800 rev/min with a measured brake torque of 32 N · m, a gross imep of 933 kPa, and a net imep of 922 kPa. $V_d = 0.496$ dm^3.

13.2. Three categories of friction are described in Sec. 13.3: boundary friction, hydrodynamic (or fully lubricated) friction, and turbulent dissipation. By means of Eq. (13.6), estimate the relative proportion of total friction work per cycle in each category for a four-cylinder automobile spark-ignition engine operating at 3000 rev/min.

13.3. For four-stroke cycle naturally aspirated multicylinder spark-ignition and diesel automobile engines at full load and one-third full load, at mid speed (2000 rev/min), give approximate estimates of the percentages of total friction mep in these three categories: pumping mep, rubbing friction mep, and accessory friction mep. State explicitly how you develop these estimates and what you include as accessories.

13.4. All of the friction measurement procedures except the difference between brake and gross indicated power or mep measured directly assume that motored engine friction and firing engine friction are closely comparable. This is not an accurate assumption for the pumping component. Summarize the differences between the gas exchange processes under motoring and firing conditions for a spark-ignition engine at a fixed part-load throttle setting that will result in the pumping work being significantly different under these two conditions.

13.5. On separate accurately proportioned sketches of the piston, cylinder, connecting rod, and crank mechanism (similar to Fig. 2-1), during the intake stroke (at 120° ATC), compression stroke (at 60° BTC), expansion stroke (at 60° ATC), and exhaust stroke (at 120° BTC), draw an arrow for each of the forces acting on the piston (pressure forces, force from connecting rod, friction force, inertia force). Mark clearly the *positive* direction of each force. Express each force in terms of cylinder pressure p_c, crankcase pressure p_{cc}, friction force F_f, piston area A_p, effective piston (and part of connecting rod) mass m_p, piston acceleration a, connecting rod force F_{cr}.

13.6. (*a*) For the DI diesel engine for the friction force data in Fig. 13-20, estimate the maximum pressure force on the piston (under full-load conditions) and the approximate magnitude of the inertia force [mass of piston plus part of the connecting rod (7 kg) × $\bar{S}_p$ × $(N/4)$]. Compare these forces with the piston friction force at time of peak pressure.

(*b*) Figure 13-6 shows the variation in friction force acting on the piston of a DI diesel engine under no-load and full-load firing conditions. Carefully sketch the shape (indicating direction and rough magnitude) of the cylinder pressure force on the piston, the piston velocity, and the piston acceleration, as functions of crank angle on the same graph as these friction forces. Use these graphs to explain the variation of piston friction force throughout the four strokes of the cycle.

13.7. (*a*) Show by dimensional analysis of the variables that govern the friction in a journal bearing (friction force F_f, oil viscosity μ, bearing diameter D_b, length L_b, mean clearance $\bar{h}$, shaft rotational speed N) that

$$\frac{F_f}{\mu D_b^2 N} = f\left(\frac{L_b}{D_b}, \frac{\bar{h}}{D_b}\right)$$

What additional physical assumptions are then required to obtain an equation of the form of (13.20)?

(*b*) Under what conditions can Eq. (13.23), an empirically developed relation for engine bearing fmep, be obtained from Eq. (13.20)?

13.8. Explain whether each of the following components of engine friction would be expected to depend on (1) crankshaft rotational speed N, (2) mean piston speed $\bar{S}_p$, (3) or both of these variables. Crankshaft journal bearings, connecting rod bearings, valve train, piston rings, piston skirt, water pump, fan, valve flow loss (resistance to flow through the inlet and exhaust valves).

REFERENCES

1. Ball, W. F., Jackson, N. S., Pilley, A. D., and Porter, B. C.: "The Friction of a 1.6 Litre Automotive Engine-Gasoline and Diesel," SAE paper 860418, 1986.
2. SAE Test Code J816b.

3. Rosenberg, R. C.: "General Friction Considerations for Engine Design," SAE paper 821576, 1982.
4. Schilling, A.: *Automobile Engine Lubrication*, Scientific Publication, 1972.
5. Millington, B. W., and Hartles, E. R.: "Frictional Losses in Diesel Engines," paper 680590, *SAE Trans.*, vol. 77, 1968.
6. Barnes-Moss, H. W.: "A Designer's Viewpoint," in *Passenger Car Engines, Conference Proceedings*, pp. 133–147, Institution of Mechanical Engineers, London, 1975.
7. Lancaster, D. R., Krieger, R. B., and Lienesch, J. H.: "Measurement and Analysis of Engine Pressure Data," paper 750026, *SAE Trans.*, vol. 84, 1975.
8. Gish, R. E., McCullough, J. D., Retzloff, J. B., and Mueller, H. T.: "Determination of True Engine Friction," *SAE Trans.*, vol. 66, pp. 649–661, 1958.
9. Brown, W. L.: "The Caterpillar IMEP Meter and Engine Friction," paper 730150, *SAE Trans.*, vol. 82, 1973.
10. Kovach, J. T., Tsakiris, E. A., and Wong, L. T.: "Engine Friction Reduction for Improved Fuel Economy," SAE paper 820085, 1982.
11. Cleveland, A. E., and Bishop, I. N.: "Several Possible Paths to Improved Part-Load Economy of Spark-Ignition Engines," SAE paper 150A, 1960.
12. Bishop, I. N.: "Effect of Design Variables on Friction and Economy," *SAE Trans.*, vol. 73, pp. 334–358, 1965.
13. *Piston Rings*, Mobil Technical Bulletin.
14. Nunney, M. J.: *The Automotive Engine*, Newnes-Butterworths, London, 1974.
15. Furuhama, S., Takiguchi, M., and Tomizawa, K.: "Effect of Piston and Piston Ring Designs on the Piston Friction Forces in Diesel Engines," SAE paper 810977, *SAE Trans.*, vol. 90, 1981.
16. Furuhama, S., Ashi, C., and Hiruma, M.: "Measurement of Piston Ring Oil Film Thickness in an Operating Engine," ASLE preprint 82-LC-6C-1, 1982.
17. McGeehan, J. A.: "A Literature Review of the Effects of Piston and Ring Friction and Lubricating Oil Viscosity on Fuel Economy," SAE paper 780673, *SAE Trans.*, vol. 87, 1978.
18. Furuhama, S., and Takiguchi, M.: "Measurement of Piston Frictional Force in Actual Operating Diesel Engine," SAE paper 790855, *SAE Trans.*, vol. 88, 1979.
19. Cameron, A.: *The Principles of Lubrication*, Wiley, New York, 1966.
20. McGeehan, J. A.: "A Survey of the Mechanical Design Factors Affecting Engine Oil Consumption," SAE paper 790864, *SAE Trans.*, vol. 88, 1979.
21. Armstrong, W. B., and Buuck, B. A.: "Valve Gear Energy Consumption: Effect of Design and Operational Parameters," SAE paper 810787, 1981.
22. Staron, J. T., and Willermet, P. A.: "An Analysis of Valve Train Friction in Terms of Lubrication Principles," SAE paper 830165, *SAE Trans.*, vol. 92, 1983.
23. Burke, C. E., Nagler, L. H., Campbell, E. C., Lundstrom, L. C., Zierer, W. E., Welch, H. L., Kosier, T. D., and McConnell, W. A.: "Where Does All the Power Go," *SAE Trans.*, vol. 65, pp. 713–737, 1957.
24. Dean, J. W., and Casebeer, H. M.: "Chrysler 340 Cu In. V-8 Engine Produces 275 HP at 5000 RPM," SAE paper 680019, 1968.
25. Schilling, A.: *Motor Oils and Engine Lubrication*, Scientific Publications, 1968.
26. Annand, W. J., and Roe, G. E.: *Gas Flow in the Internal Combustion Engine*, Haessner Publishing, 1974.
27. ASTM Standards, Part 17, Petroleum Products.
28. ASTM D2270-64.
29. SAE J300a.

CHAPTER 14

MODELING REAL ENGINE FLOW AND COMBUSTION PROCESSES

14.1 PURPOSE AND CLASSIFICATION OF MODELS

In engineering, modeling a process has come to mean developing and using the appropriate combination of assumptions and equations that permit critical features of the process to be analyzed. The modeling of engine processes continues to develop as our basic understanding of the physics and chemistry of the phenomena of interest steadily expands and as the capability of computers to solve complex equations continues to increase. Modeling activities can make major contributions to engine engineering at different levels of generality or detail, corresponding to different stages of model development, by:

1. Developing a more complete understanding of the process under study from the discipline of formulating the model;
2. Identifying key controlling variables to provide guidelines for more rational and therefore less costly experimental development efforts;
3. Predicting engine behavior over a wide range of design and operating variables to screen concepts prior to major hardware programs, to determine

trends and tradeoffs, and, if the model is sufficiently accurate, to optimize design and control;

4. Providing a rational basis for design innovation.

Each of these contributions is valuable. Whether a model is ready to pass from one stage to the next depends on the accuracy with which it represents the actual process, the extent to which it has been tested and validated, and the time and effort required to use the model for extensive sets of calculations and to interpret the results.

This chapter reviews the types of models and their primary components that are being developed and used to describe engine operating and emissions characteristics. These models describe the thermodynamic, fluid-flow, heat-transfer, combustion, and pollutant-formation phenomena that govern these performance aspects of engines. Many of the building blocks for these models have been described in the previous chapters. The purpose here is to show how fluid dynamics, heat-transfer, thermodynamics, and kinetics fundamentals can be combined at various levels of sophistication and complexity to predict, with varying degrees of completeness, internal combustion engine combustion and emissions processes, and hence engine operating characteristics.

For the processes that govern engine performance and emissions, two basic types of models have been developed. These can be categorized as *thermodynamic* or *fluid dynamic* in nature, depending on whether the equations which give the model its predominant structure are based on energy conservation or on a full analysis of the fluid motion. Other labels given to thermodynamic energy-conservation-based models are: zero-dimensional (since in the absence of any flow modeling, geometric features of the fluid motion cannot be predicted), phenomenological (since additional detail beyond the energy conservation equations is added for each phenomenon in turn), and quasi-dimensional (where specific geometric features, e.g., the spark-ignition engine flame or the diesel fuel spray shapes, are added to the basic thermodynamic approach). Fluid-dynamic-based models are often called multidimensional models due to their inherent ability to provide detailed geometric information on the flow field based on solution of the governing flow equations.

Some general observations about models of engine processes provide a context for the details that follow. The processes themselves are extremely complex. While much is known about these processes, they are not adequately understood at a fundamental level. At present, it is not possible to construct models that predict engine operation from the basic governing equations alone. Thus the objectives of any model development effort should be clearly defined, and the structure and detailed content of the model should be appropriate to these objectives. It is impractical to construct models that attempt to describe *all* important aspects of engine operation: more limited objectives are appropriate.

Due to this complexity of engine processes and our inadequate understanding at a fundamental level, most engine models are incomplete. Empirical relations and *ad hoc* approximations are often needed to bridge gaps in our

understanding of critical phenomena. Hence, since models will continue to develop greater completeness and generality, the emphasis in this chapter is on the basic relationships used in engine process models rather than the current status of these models.

Finally, an important issue in any overall engine model is balance in complexity and detail amongst the process submodels. A model is no more accurate than its weakest link. Thus critical phenomena should be described at comparable levels of sophistication.

14.2 GOVERNING EQUATIONS FOR OPEN THERMODYNAMIC SYSTEM

It is often required to model a region of the engine as an open thermodynamic system. Examples are the cylinder volume and the intake and exhaust manifolds (or portions of these volumes). Such a model is appropriate when the gas inside the open system boundary can be assumed uniform in composition and state at each point in time, and when that state and composition vary with time due to heat transfer, work transfer and mass flow across the boundary, and boundary displacement. Such an open system is illustrated in Fig. 14-1. The important equations are mass and energy conservation. These equations for an open system, with time or crank angle as the independent variable, are the building blocks for thermodynamic-based models.

14.2.1 Conservation of Mass

The rate of change of the total mass m of an open system is equal to the sum of the mass flows into and out of the system:

$$\dot{m} = \sum_j \dot{m}_j \tag{14.1}$$

Mass flows into the system are taken as positive; mass flows out are taken as negative. For conservation of the fuel chemical elements, it is convenient to use the fuel fraction f, which is defined as m_f/m, where m_f denotes the mass of fuel (or

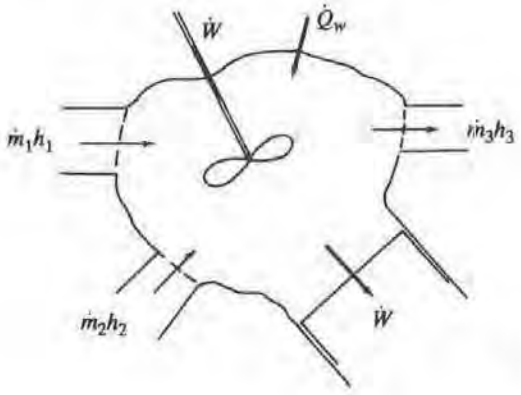


FIGURE 14-1
Open thermodynamic system.

fuel elements in the combustion products) in the open system:

$$\dot{m}_f = \frac{d}{dt}(mf) = \sum_j \dot{m}_{f,j} = \sum_j \dot{m}_j f_j \tag{14.2}$$

Differentiation of Eq. (14.2) leads to an equation for the rate of change of fuel fraction:

$$\dot{f} = \sum_j \left(\frac{\dot{m}_j}{m}\right)(f_j - f) \tag{14.3}$$

The fuel/air equivalence ratio ϕ is related to f via $\phi = f/[(F/A)_s(1 - f)]$. Hence the rate of change of equivalence ratio of the material in the open system is

$$\dot{\phi} = \frac{1}{(F/A)_s}\frac{\dot{f}}{(1-f)^2} \tag{14.4}$$

14.2.2 Conservation of Energy

The first law of thermodynamics for the open system in Fig. 14-1 can be written:

$$\dot{E} = \dot{Q}_w - \dot{W} + \sum_j \dot{m}_j h_j \tag{14.5}$$

$\dot{Q}_w$ is the total heat-transfer rate into the system, across the system boundary, and equals the sum of the heat-transfer rates across each part of the boundary, $\sum_i \dot{Q}_{w,i}$. $\dot{W}$ is the work-transfer rate out of the system across the boundary; where the piston is displaced, the work-transfer rate equals $p\dot{V}$. Because all energies and enthalpies are expressed relative to the same datum (see Sec. 4.5.3), it is not necessary to include the heat released by combustion in Eq. (14-5); this is already accounted for in the energy and enthalpy terms.

The goal is to define the rate of change of state of the open system in terms of $\dot{T}$ and $\dot{p}$. Two approaches are commonly used, depending on whether the thermodynamic property routines provide values for internal energy u or enthalpy h. Thus $\dot{E}$ in Eq. (14.5) can be expressed as

$$\dot{E} = \frac{d}{dt}(mu) \qquad \text{or} \qquad \dot{E} = \frac{d}{dt}(mh) - \frac{d}{dt}(pV) \tag{14.6a, b}$$

It is assumed that the system can be characterized by T, p, and ϕ; thus

$$u = u(T, p, \phi) \qquad h = h(T, p, \phi) \qquad \rho = \rho(T, p, \phi) \tag{14.7}$$

and the rate of change of u, h, and ρ can be written in the form

$$\dot{\alpha} = \left(\frac{\partial \alpha}{\partial T}\right)\dot{T} + \left(\frac{\partial \alpha}{\partial p}\right)\dot{p} + \left(\frac{\partial \alpha}{\partial \phi}\right)\dot{\phi} \tag{14.8}$$

where α is u, h, or ρ. Using the ideal gas law in its two forms, $p = \rho RT$ and $pV = mRT$, and Eq. (14.8) for $\dot{p}$, an equation for $\dot{p}$ can be derived:

$$\dot{p} = \frac{\rho}{\partial\rho/\partial p}\left(-\frac{\dot{V}}{V} - \frac{1}{\rho}\frac{\partial\rho}{\partial T}\dot{T} - \frac{1}{\rho}\frac{\partial\rho}{\partial\phi}\dot{\phi} + \frac{\dot{m}}{m}\right) \tag{14.9}$$

Returning now to the energy conservation equation, expressing $\dot{E}$ in terms of $\dot{u}$ or $\dot{h}$, and $\dot{u}$ or $\dot{h}$ in terms of partial derivatives with respect to T, p, and ϕ, and substituting for $\dot{p}$ with Eq. (14.9), one can obtain equations for $\dot{T}$:

$$\dot{T} = \left[B - \frac{p}{D}\frac{\partial u}{\partial p}\left(\frac{\dot{m}}{m} - \frac{\dot{V}}{V} + \frac{\partial R}{\partial\phi}\frac{\dot{\phi}}{R}\right) - \frac{\partial u}{\partial\phi}\dot{\phi}\right] \Big/ \left(\frac{\partial u}{\partial T} + \frac{C}{D}\frac{p}{T}\frac{\partial u}{\partial p}\right) \tag{14.10}$$

where

$$B = -RT\frac{\dot{V}}{V} + \frac{1}{m}\left(\dot{Q}_w + \sum_j \dot{m}_j h_j - \dot{m}u\right)$$

$$C = 1 + \frac{T}{R}\frac{\partial R}{\partial T}$$

$$D = 1 - \frac{p}{R}\frac{\partial R}{\partial p}$$

(see Ref. 1, for example). From Ref. 2,

$$\dot{T} = \frac{B'}{A'}\left[\frac{\dot{m}}{m}\left(1 - \frac{h}{B'}\right) - \frac{\dot{V}}{V} - \frac{C'}{B'}\dot{\phi} + \frac{1}{B'm}\left(\sum_j \dot{m}_j h_j - \dot{Q}_w\right)\right] \tag{14.11}$$

where

$$A' = \frac{\partial h}{\partial T} + \frac{\partial\rho/\partial T}{\partial\rho/\partial p}\left(\frac{1}{\rho} - \frac{\partial h}{\partial p}\right)$$

$$B' = \frac{1 - \rho(\partial h/\partial p)}{\partial\rho/\partial p}$$

$$C' = \frac{\partial h}{\partial\phi} + \frac{\partial\rho/\partial\phi}{\partial\rho/\partial p}\left(\frac{1}{\rho} - \frac{\partial h}{\partial p}\right)$$

Equations (14.1), (14.3), (14.4), (14.9), and (14.10) or (14.11) can now be solved to obtain the state of the open system as a function of time. $\dot{V}$ is obtained from Eq. (2.6), and the thermodynamic properties and their derivatives from the models described in Chap. 4.

Often, for specific applications, the above equations can be simplified substantially. For the intake and exhaust systems (or sections of these systems such as the manifold or plenum, etc.), $\dot{V}$ is zero and effects of dissociation (the terms $\partial u/\partial p$, $\partial h/\partial p$, and $\partial R/\partial p$) can usually be neglected. For the cylinder during compression, dissociation can usually be neglected, also. Application of these equations during combustion must be related to the combustion model used. For the single-zone model often used in diesel engine simulations (see Sec. 10.4) the whole

of the combustion chamber is treated as one system. For the two-zone model used for spark-ignition engine simulations, the unburned mixture zone and the burned mixture zone are each treated as separate open systems, with volumes V_u and V_b, respectively, where $V_u + V_b = V$. If a thermal boundary-layer region is included (see Sec. 12.6.5) an additional open system must be defined.

14.3 INTAKE AND EXHAUST FLOW MODELS

14.3.1 Background

The behavior of the intake and exhaust systems are important because these systems govern the air flow into the engine's cylinders. Inducting the maximum air flow at full load at any given speed and retaining that mass within the engine's cylinders is a primary design goal. The higher the air flow, the larger the amount of fuel that can be burned and the greater the power produced. The important parameters are volumetric efficiency (for four-stroke cycle engines) or scavenging and trapping efficiencies (for two-stroke cycle engines), along with equal air flows to each engine cylinder (see Secs. 6.2, 6.6, and 7.6.2).

The objectives of any manifold model have an important bearing on its complexity and structure. If the goal is to provide the input or boundary conditions to a detailed model of in-cylinder processes, then sophisticated intake and exhaust system models are not necessarily required. If the manifold flows are the primary focus, then models that adequately describe the unsteady gas-flow phenomena which occur are normally required. Then simple models for the in-cylinder phenomena usually suffice to connect the intake and exhaust processes. The valves and ports, which together provide the major restriction to the intake and exhaust flow, largely decouple the manifolds from the cylinders.

Three types of models for calculating details of intake and exhaust flows have been developed and used:

1. Quasi-steady models for flows through the restrictions which the valve and port (and other components) provide
2. Filling and emptying models, which account for the finite volume of critical manifold components
3. Gas dynamic models which describe the spatial variations in flow and pressure throughout the manifolds

Each of these types of models can be useful for analyzing engine behavior. The appropriate choice depends on objectives, and the time and effort available. Each will now be reviewed.

14.3.2 Quasi-Steady Flow Models

Here the manifolds are considered as a series of interconnected components, which each constitute a significant flow restriction: e.g., air cleaner, throttle, port,

and valve for the intake system. The flow restriction each of these components represents is defined by their geometry and discharge coefficient, usually determined empirically under steady-state conditions. The gas flow rate through each component is computed using steady one-dimensional flow equations [see App. C, Eqs. (C.8) and (C.9)]: the actual flow is assumed to be quasi steady. These components are connected by the gas flow passing through them and the pressure ratios across them; mass accumulation between components is neglected.

Quasi-steady models are often used to calculate the flow into and out of the cylinder through the inlet and exhaust valves (see Secs. 6.3 and 6.5 and Fig. 6-20). If the pressure variation with time upstream of the valve is known or is small, as usually occurs with large plenums and short manifold pipe lengths, such methods are accurate enough to be useful. This approach has been used extensively with engine cycle simulations which predict engine performance characteristics from a thermodynamics-based analysis, to calculate the mass flow rates into and out of the cylinder (see Sec. 14.4). Such methods are not able to predict the variation of volumetric efficiency with engine speed, however, because many of the phenomena which govern this variation are omitted from this modelling approach (see Sec. 6.2 and Fig. 6-9).

14.3.3 Filling and Emptying Methods

In "filling and emptying" models, the manifolds (or sections of manifolds) are represented by finite volumes where the mass of gas can increase or decrease with time. Such models can range from treating the whole intake or exhaust system as a single volume to dividing these systems into many sections, with flow restrictions such as the air cleaner, throttle valve, or inlet valve at the beginning, in between volumes, or at the end. Each volume is then treated as a control volume (an open system of fixed volume) which contains gas at a uniform state. The mass and energy conservation equations developed in Sec. 14.2 [Eqs. (14.1), (14.3), (14.9), and (14.10) or (14.11)], coupled with information on the mass flow rates into and out of each volume [e.g., determined by the equations for flow through a restriction, Eqs. (C.8) and (C.9)] are used to define the gas state in each control volume. For intake and exhaust flows these equations can be simplified since the volumes are fixed ($\dot{V} = 0$), gas composition can be assumed frozen ($\partial u/\partial p$, $\partial h/\partial p$, and $\partial R/\partial p$ are then zero), unless backflow occurs or recycled exhaust is used for emission control changes in fuel fraction are not significant, and for intake systems it may be acceptable to omit heat transfer to the walls ($\dot{Q}_w$). Such methods characterize the contents of the manifold (or a region thereof) with a single gas temperature, pressure, and composition. These vary periodically with time as each cylinder in turn draws on the intake system and discharges to the exhaust system. Also, under transient conditions when engine load and/or speed change with time, manifold conditions will vary until the new engine steady-state conditions are established. Watson and Janota[3] discuss the application of filling and emptying models to manifolds in more detail. Such models can characterize these time-varying phenomena, spatially averaged over each mani-

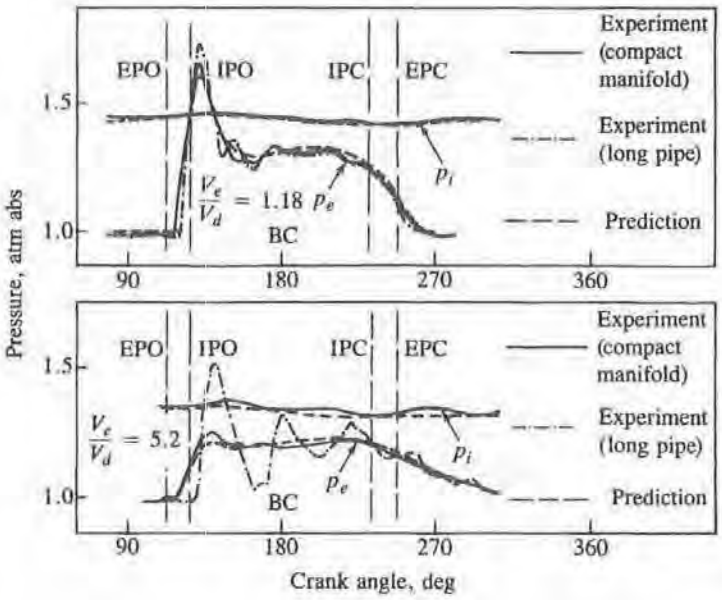


FIGURE 14-2
Comparison of intake and exhaust manifold pressures, p_i and p_e, predicted by filling and emptying model, with experimental data. Single-cylinder two-stroke loop-scavenged direct-injection diesel engine. Different ratios of exhaust system volume V_e to displaced volume V_d, and exhaust manifold shapes.[4]

EPO Exhaust port opens
IPO Inlet port opens
IPC Inlet port closes
EPC Exhaust port closes

fold region corresponding to each volume analyzed: however, they cannot describe the spatial variation of pressure (and other gas properties) due to unsteady gas dynamics in the manifolds.

A simple application of a filling and emptying model to the intake manifold of a spark-ignition engine was described in Sec. 7.6.2. The manifold was analyzed as a single control volume with the throttle plate controlling mass flow into the manifold and the engine cylinders controlling mass flow out. An equation for the rate of change of manifold pressure [Eq. (7.22)] was derived and used to explain how the air flow past the throttle varied as the throttle open angle was increased, as would occur at the start of a vehicle acceleration at part-throttle conditions (see Fig. 7-24).

A second example will illustrate the conditions under which filling and emptying models give sufficiently accurate predictions to be useful.[4] It concerns a single-cylinder two-stroke cycle loop-scavenged direct-injection diesel engine. The engine was modeled as three open systems (the intake system, the cylinder, the exhaust system) connected by flow restrictions. Various exhaust manifold volumes and shapes were examined, using nozzles at the manifold exit to simulate the exhaust-driven turbine. The in-cylinder models were calibrated to match the measured engine performance. Figure 14-2 shows the predicted and measured pressure variation at the exhaust system exit for two exhaust system volumes (V_e). With the compact manifold the measured and predicted pressures were in good agreement. With the larger exhaust system shown in the figure ($V_e/V_d = 5.2$) and the compact manifold, good agreement is again obtained. Only with the larger volume and long pipe exhaust system is there evidence in the measured pressure variation of substantial unsteady gas dynamic effects. For small manifolds, and manifolds that are compact in shape, filling and emptying models can be a useful predictive tool.

14.3.4 Gas Dynamic Models

Many induction and exhaust system design variables determine overall performance. These variables include the length and cross-sectional area of both primary and secondary runners, the volume and location of the plenums or junctions which join the various runners, the entrance or exit angles of the runners at a junction, the number of engine cylinders and their dimensions, intake and exhaust port and valve design, and valve lift and timing (see Secs. 6.2, 6.3, 6.7, and 7.6). Most of this geometric detail is beyond the level which can be incorporated into the models discussed above. Coupled with the pulsating nature of the flow into and out of each cylinder, these details create significant gas dynamic effects on intake and exhaust flows which require a more complete modeling approach.

Gas dynamic models have been in use for a number of years to study engine gas exchange processes. These models use the mass, momentum, and energy conservation equations for the unsteady compressible flow in the intake and exhaust. Normally, the one-dimensional unsteady flow equations are used.† These models often use a thermodynamic analysis of the in-cylinder processes to link the intake and exhaust flows. In the past, the method of characteristics was used to solve the gas dynamic equations. Finite difference techniques are used in more recent intake and exhaust flow models. The basic equations and assumptions of these models will now be reviewed.[5, 6]

UNSTEADY FLOW EQUATIONS. Consider the flow through the control volume within a straight duct shown in Fig. 14-3. It is assumed that the area change over the length dx of the control volume is small so the flow is essentially one-

† Two- and three-dimensional effects can be important and can be modeled with multidimensional flow models described in Sec. 14.5.

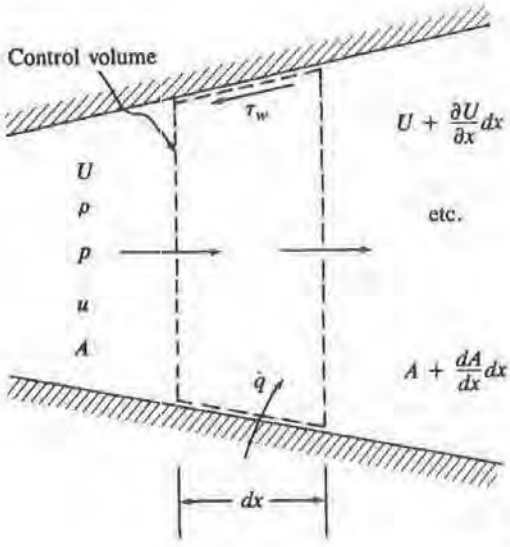


FIGURE 14-3
Control volume for unsteady one-dimensional flow analysis.

dimensional. Mass conservation requires that the rate of change of mass within the control volume equals the net flow into the control volume: i.e.,

$$\frac{\partial}{\partial t}(\rho A\, dx) = \rho AU - \left[\rho AU + \frac{\partial}{\partial x}(\rho AU)\, dx\right] \tag{14.12}$$

Retaining only first-order quantities, this equation simplifies to

$$\frac{\partial \rho}{\partial t} + \frac{\partial}{\partial x}(\rho U) + \frac{\rho U}{A}\frac{dA}{dx} = 0 \tag{14.13}$$

The momentum conservation equation states that the net pressure forces plus the wall shear force acting on the control volume surface equal the rate of change of momentum within the control volume plus the net flow of momentum out of the control volume. The net forces and momentum changes are given by:

Pressure forces:

$$pA - \left(p + \frac{\partial p}{\partial x}\, dx\right)\left(A + \frac{dA}{dx}\, dx\right) + p\frac{dA}{dx}\, dx = -A\frac{\partial p}{\partial x}\, dx$$

Shear forces:

$$-\tau_w \pi D\, dx = -\xi \frac{\rho U^2}{2}\pi D\, dx$$

where D is the equivalent diameter $(4A/\pi)^{1/2}$ and ξ is the friction coefficient given by $\tau_w/(\frac{1}{2}\rho U^2)$.

The rate of change of momentum within the control volume is

$$\frac{\partial}{\partial t}(U\rho A\, dx)$$

and the net efflux of momentum across the control volume surface is

$$\left(\rho + \frac{\partial \rho}{\partial x}\, dx\right)\left(U + \frac{\partial U}{\partial x}\, dx\right)^2\left(A + \frac{dA}{dx}\, dx\right) - \rho U^2 A = \frac{\partial}{\partial x}(\rho U^2 A)\, dx$$

Combining these terms into the momentum equation yields

$$-A\frac{\partial p}{\partial x}\, dx - \xi\frac{\rho U^2}{2}\pi D\, dx = \frac{\partial}{\partial t}(\rho UA\, dx) + \frac{\partial}{\partial x}(\rho U^2 A)\, dx \tag{14.14}$$

This can be rearranged and combined with the mass conservation equation (14.13) to give

$$\frac{\partial U}{\partial t} + U\frac{\partial U}{\partial x} + \frac{1}{\rho}\frac{\partial p}{\partial x} + 2\xi\frac{U^2}{D} = 0 \tag{14.15}$$

ENERGY CONSERVATION. The first law of thermodynamics for a control volume states that the energy within the control volume changes due to heat and shear work transfers across the control volume surface and due to a net efflux of

stagnation enthalpy resulting from flow across the control volume surface. The stagnation enthalpy h_0 is

$$h_0 = h + \frac{U^2}{2} = u + \frac{p}{\rho} + \frac{U^2}{2}$$

where u is the specific internal energy of the fluid (often approximated by $c_v T$). The shear work transfer across the control volume surface is zero.

The heat-transfer rate $\dot{Q}_w$ is given by

$$\delta\dot{Q}_w = \dot{q}\rho A \; dx$$

where $\dot{q}$ is the heat transfer per unit mass of fluid per unit time into the control volume.

The rate of change of energy within the control volume is

$$\frac{\partial E}{\partial t} = \frac{\partial}{\partial t}\left[(\rho A\, dx)\left(u + \frac{U^2}{2}\right)\right]$$

The net efflux of stagnation enthalpy is

$$\frac{\partial}{\partial x}\left[(\rho U A)\left(u + \frac{p}{\rho} + \frac{U^2}{2}\right)\right] dx$$

Hence, the equation for energy conservation becomes

$$\frac{\partial}{\partial t}\left[(\rho A\, dx)\left(u + \frac{p}{\rho} + \frac{U^2}{2}\right)\right] + \frac{\partial}{\partial x}\left[(\rho U A)\left(u + \frac{p}{\rho} + \frac{U^2}{2}\right)\right] dx - \dot{q}\rho A\, dx = 0 \tag{14.16}$$

Additional simplifications are possible. Expanding Eq. (14.16) and using the mass and momentum conservation equations yields

$$\frac{\partial u}{\partial t} + U\frac{\partial u}{\partial x} = \dot{q} + 2\xi\frac{U^3}{D} - \frac{p}{\rho A}\frac{\partial (UA)}{\partial x} \tag{14.17}$$

If u can be represented by $c_v T$ and $R/c_v = \gamma - 1$ is constant, Eq. (14.17) can be rearranged and simplified to give

$$\frac{\partial p}{\partial t} + U\frac{\partial p}{\partial x} - a^2\left(\frac{\partial \rho}{\partial t} + U\frac{\partial \rho}{\partial x}\right) - (\gamma - 1)\rho\left(\dot{q} + 2\xi\frac{U^3}{D}\right) = 0 \tag{14.18}$$

where the sound speed a for an ideal gas is given by

$$a^2 = \left(\frac{\partial p}{\partial \rho}\right)_s = \gamma\frac{p}{\rho} \tag{14.19}$$

If friction and heat-transfer effects are small enough to be neglected, Eqs. (14.15) and (14.18) can be considerably simplified. In the absence of these effects the flow is *isentropic*; it has uniform entropy which is constant with time and is often called *homentropic* flow.[6] If the duct area can be neglected then the continuity equation, (14.13), can be simplified also.

These one-dimensional unsteady flow equations have been used for a number of years to study the flow in the intake and exhaust systems of spark-ignition and diesel engines, both naturally aspirated and turbocharged. Two types of methods have been used to solve these equations: (1) the method of characteristics and (2) finite difference procedures. The characteristic methods have a numerical accuracy that is first order in space and time, and require a large number of computational points if resolution of short-wavelength variations is important. Finite difference techniques can be made higher order and prove to be more efficient;[7, 8] this approach is now preferred. Methods for treating the boundary conditions will also be described.

METHOD OF CHARACTERISTICS. The method of characteristics is a well-established mathematical technique for solving hyperbolic partial differential equations. With this technique, the partial differential equations are transformed into ordinary differential equations that apply along so-called characteristic lines. Pressure waves are the physical phenomenon of practical interest in the unsteady intake flow, and these propagate relative to the flowing gas at the local sound speed. In this particular application, the one-dimensional unsteady flow equations, (14.13) and (14.15), are rearranged so that they contain only the local fluid velocity U and local sound speed a.

Since the absolute velocity of small amplitude sound waves is $U + a$ in the direction of flow and $U - a$ opposite to the flow direction, the lines of slope $U \pm a$ are the *position* characteristics of the propagating pressure waves which define the position x of the pressure wave at time t. *Compatability conditions* accompanying the position characteristics relate U to a. The compatability relationships are expressed in terms of variables (called Riemann invariants) which are constant along the position characteristics for constant-area homentropic flow, though they vary if these restrictions do not apply. Thus, the solution of the mass and momentum conservation equations for this one-dimensional unsteady flow is reduced to the solution of a set of ordinary differential equations.

The equations are usually solved numerically using a rectangular grid in the x and t directions. The intake or exhaust system is divided into individual pipe sections which are connected at junctions. A mesh is assigned to each section of pipe between junctions. From the initial values of the variables at each mesh point at time $t = 0$, the values of the Riemann variables at each mesh point at subsequent time steps are then determined. Gas pressure, density, and temperature can then be calculated from the energy conservation equation and the ideal gas law. Additional details of the method are given by Benson *et al.*[5, 6]

FINITE DIFFERENCE METHODS. Finite difference methods for solving the one-dimensional unsteady flow equations in intake and exhaust manifolds are proving more efficient and flexible than the method of characteristics. The conservation equations, (14.13), (14.14), and (14.16), can be rearranged and written in

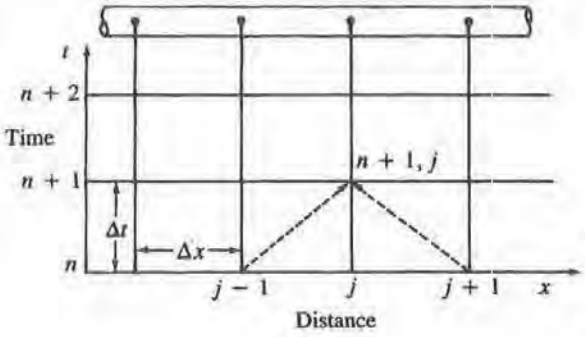


FIGURE 14-4
Mesh in time-distance plane for application of one-step Lax-Wendroff method to intake or exhaust pipe.

matrix form as

$$\frac{\partial}{\partial t}\begin{pmatrix}\rho\\ \rho U\\ \rho u\end{pmatrix}+\frac{\partial}{\partial x}\begin{pmatrix}\rho U\\ \rho U^2+p\\ pU+\rho Uu\end{pmatrix}=\begin{pmatrix}-\rho U\dfrac{dA}{dx}\\ -\rho\dfrac{U^2}{A}\dfrac{dA}{dx}-\rho\dfrac{2\xi U|U|}{D}\\ -\dfrac{4h_c(T-T_w)}{D\rho}-\dfrac{1}{A}\dfrac{dA}{dx}\left(\dfrac{1}{2}\rho U^3+\dfrac{\gamma}{\gamma-1}Up\right)\end{pmatrix} \tag{14.20}$$

The fluid viscous shear is small relative to friction at the wall in the momentum equation, and heat conduction and viscous dissipation prove negligible relative to convective heat transfer at the wall in the energy conservation equation. These equations have the vector form:

$$\frac{\partial F}{\partial t}+\frac{\partial G}{\partial x}=H \tag{14.21}$$

where G and H are functions of F only. Several finite difference methods have been used to solve Eq. (14.21) (see Refs. 7, 8, and 9). The one-step Lax-Wendroff method will be illustrated.[8] Equation (14.21) can be developed into a Taylor series with respect to time, and the time and space derivatives approximated by central differences around the mesh point, shown in Fig. 14-4, as

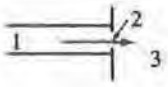
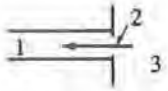
$$F_j^{n+1}=F_j^n-\frac{1}{2}\frac{\Delta t}{\Delta x}(G_{j+1}^n-G_{j-1}^n)+\Delta tH_j^n$$
$$+\frac{1}{4}\left(\frac{\Delta t}{\Delta x}\right)^2[(G'^n_{j+1}+G'^n_j)(G^n_{j+1}-G^n_j)-(G'^n_j+G'^n_{j-1})(G^n_j-G^n_{j-1})] \tag{14.22}$$

where $G'=\partial G/\partial F$. This equation is first-order accurate, unless H is small. For stability in the integration process, the time step and mesh size must satisfy the requirement that

$$C=(|U|+a)\frac{\Delta t}{\Delta x}<1 \tag{14.23}$$

where C is the Courant number.

TABLE 14.1
Boundary conditions for unsteady one-dimensional finite element analysis[9]

Pipe ends			
Out-flow	Mass	$\rho_1 U_1 A_1 = \rho_2 U_2 A_2$	
	Energy	$c_p T_1 + \frac{U_1^2}{2} = c_p T_2 + \frac{U_2^2}{2}$	
	Isobaric	$p_2 = p_3$	
In-flow	Mass	$\rho_1 U_1 A_1 = \rho_2 U_2 A_2$	
	Energy	$c_p T_3 = c_p T_2 + \frac{U_2^2}{2} = c_p T_1 + \frac{U_1^2}{2}$	
	Isentropic	$p_2/\rho_2^\gamma = p_3/\rho_3^\gamma$	
Pipe junctions			
	Mass	$V\frac{\partial \rho}{\partial t} = \sum_i \rho_i U_i A_i$	
	Energy	$\rho V \frac{\partial u}{\partial t} = \sum_i (\rho_i U_i A_i)\left(c_p T_i + \frac{U_i^2}{2}\right)$	
	Pressure	$p_1 - \Delta p_1 = p_2 + \Delta p_2 = p_3 + \Delta p_3 = \cdots$ $\Delta p_i/p_i = C_i(U_i/a_i)^2$	

These finite difference solution methods usually require the introduction of some form of dissipation or damping to prevent instabilities and large nonphysical oscillations from occurring with nonlinear problems with large gradients (e.g., a shock wave in the exhaust system). Amplification of the physical viscosity and the addition of artificial viscosity, damping, and smoothing terms to Eq. (14.22) are frequently used techniques.[8, 9]

The boundary conditions at pipe ends and junctions are obtained from the appropriate conservation equations and pressure relations, as illustrated in Table 14.1. Out-flows and in-flows obviously conserve mass and energy. For the flow out through a restriction, there is no pressure recovery downstream: for flow in through a restriction, the flow upstream of the restriction is isentropic. For pipe junctions, the conservation equations are applied to the control volume contained within the dashed line in the sketch in the table. The pressure boundary conditions are most easily estimated by modifying the simple constant-pressure assumption with pressure losses at each pipe exit or entry, calculated from experimentally determined loss coefficients (see Fig. 6-5).[9]

Calculations of intake and exhaust flows using these techniques predict the variations in intake and exhaust manifold pressure with crank angle (as shown, for example, in Fig. 6-7), in single and multicylinder engines, with acceptable accuracy.[7, 9] Measured volumetric efficiency variations with engine speed, manifold design, and valve dimensions and timing are adequately predicted also. Figure 14-5*a* shows the instantaneous exhaust and intake mass flow rates for cylinder number 1 of a four-cylinder spark-ignition engine at wide-open throttle at 1500 rev/min. Note how gas dynamic effects distort the exhaust flow. Note also the "reverse" flows into the cylinder past the exhaust valve and out of the

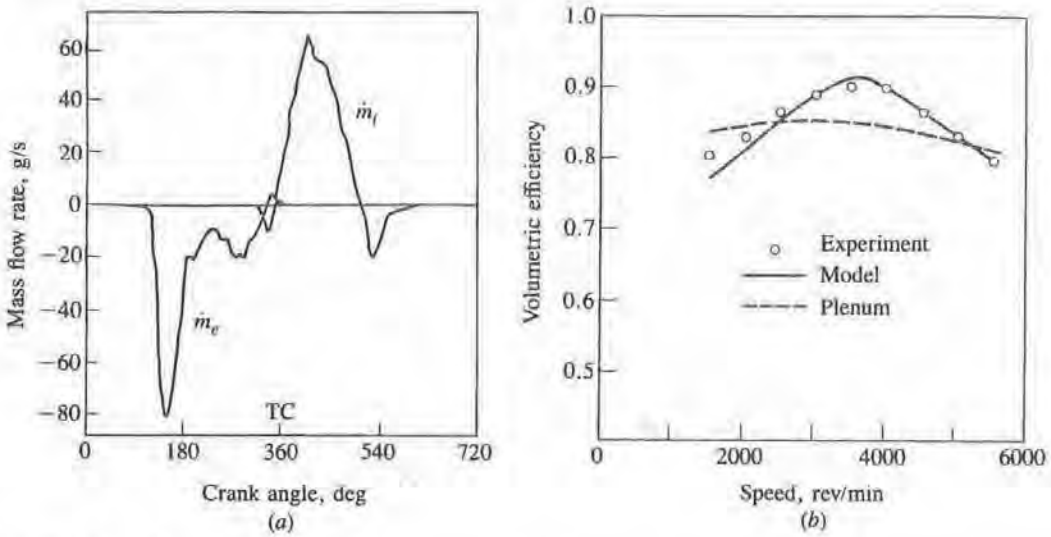


FIGURE 14-5
(*a*) Predicted mass flow rate through the exhaust valve $\dot{m}_e$ and through the intake valve $\dot{m}_i$ in cylinder 1, four-cylinder four-stroke-cycle spark-ignition engine at wide-open throttle and 1500 rev/min. Flows into cylinder are positive; flows out are negative. (*b*) Predicted and measured volumetric efficiency at wide-open throttle for four-cylinder spark-ignition engine. Solid line: one-dimensional unsteady flow model. Dashed line: quasi-steady flow calculation based on infinite plenums for manifolds.[7]

cylinder past the intake valve at the end of the exhaust process, and the larger reverse flow at the end of the intake process at this low engine speed. Figure 14-5*b* shows the volumetric efficiency for this engine based on these predicted mass flow rates, as a function of speed. Experimental values and values predicted with quasi-steady flow equations and infinite plenums for manifolds are also shown. These results clearly demonstrate the important role that intake and exhaust system gas dynamics play in determining both the engine speed at which peak breathing efficiency occurs and the air charging characteristics over the full engine speed range.[7]

14.4 THERMODYNAMIC-BASED IN-CYLINDER MODELS

14.4.1 Background and Overall Model Structure

If the mass transfer into and out of the cylinder during intake and exhaust, the heat transfer between the in-cylinder gases and the cylinder head, piston, and cylinder liner, and the rate of charge burning (or energy release from the fuel) are all known, the energy and mass conservation equations permit the cylinder pressure and the work transfer to the piston to be calculated. Engine models of this type have been developed and used extensively to predict engine operating characteristics (indicated power, mean effective pressure, specific fuel consumption, etc.) and to define the gas state for emission calculations. These models effectively follow the changing thermodynamic and chemical state of the working fluid through the engine's intake, compression, combustion, expansion, and exhaust processes; they are often called engine *cycle simulations.*

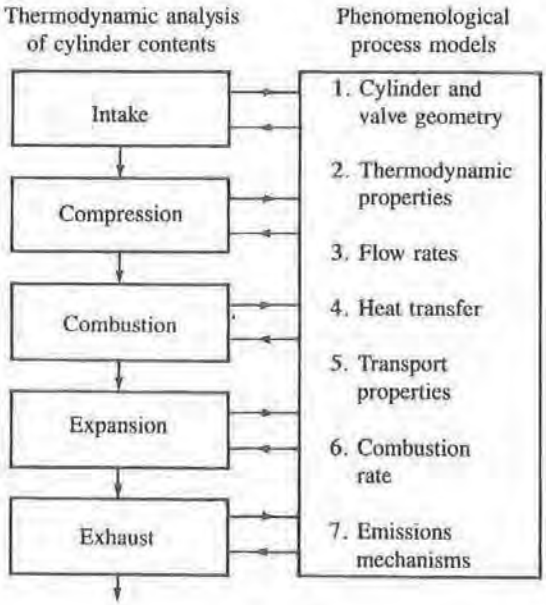


FIGURE 14-6
Logic structure of thermodynamic-based simulations of internal combustion engine operating cycle.

The starting point for these cycle simulations is the first law of thermodynamics for an open system, developed in Sec. 14.2. This is applied to the cylinder volume for the intake, compression, combustion, expansion, and exhaust processes that in sequence make up the engine's operating cycle. The structure of this type of engine simulation is indicated in Fig. 14-6. Then, during each process, submodels are used to describe geometric features of the cylinder and valves or ports, the thermodynamic properties of the unburned and burned gases, the mass and energy transfers across the system boundary, and the combustion process.

During intake and compression, the cylinder volume is modeled as a single open system. Application of the conservation equations in the form of Eqs. (14.1), (14.3), and (14.10) or (14.11) for the intake and then the compression process gives[2]

Intake:

$$\dot{m} = \dot{m}_i - \dot{m}_e \tag{14.24}$$

$$\dot{f} = \frac{\dot{m}_i}{m}(f_i - f) - \frac{\dot{m}_e}{m}(f_e - f) \tag{14.25}$$

$$\dot{T} = \frac{B}{A}\left[\frac{\dot{m}}{m}\left(1 - \frac{h}{B}\right) - \frac{\dot{V}}{V} - \frac{C}{B}\dot{\phi} + \frac{1}{Bm}(\dot{m}_i h_i - \dot{m}_e h_e - \dot{Q}_w)\right] \tag{14.26}$$

where m is the mass of gas in the cylinder, $\dot{m}_i$ and $\dot{m}_e$ are the mass flow rates through the inlet valve and the exhaust valve, and f is the fuel fraction m_f/m. The subscripts i and e denote properties of the flow through the intake and exhaust valves, respectively. The thermodynamic properties for these flows are the values upstream of the valves and therefore depend on whether the flow is into or out of the cylinder.

Compression:

$$\dot{m} = 0 \qquad \dot{f} = 0 \tag{14.27a, b}$$

$$\dot{T} = \frac{B}{A}\left(-\frac{\dot{V}}{V} - \frac{Q_w}{Bm}\right) \tag{14.28}$$

The pressure is then determined from Eq. (14.9).

During intake and compression, the working fluid composition is frozen. The composition and thermodynamic properties can be determined using the models described in Secs. 4.2 and 4.7. Mass flows across open valves are usually calculated using one-dimensional compressible flow equations for flow through a restriction (see App. C and Secs. 6.3.2 and 14.3.2) or filling and emptying models (Sec. 14.3.3). The more accurate unsteady gas dynamic intake (and exhaust) flow models described in Sec. 14.3.4 are sometimes used to calculate the mass flow into the engine cylinder in complete engine cycle simulations when the variation in engine flow rate with speed is especially important:[10] the disadvantage is much increased computing time. Heat transfer during intake and compression is calculated using one of the Nusselt-Reynolds number relations for turbulent convective heat transfer described in Sec. 12.4.5. The transport properties, viscosity, and thermal conductivity used in these correlations can be obtained from relations such as Eqs. (4.52) to (4.55).

During combustion which starts with the spark discharge in spark-ignition engines and with spontaneous ignition of the developing fuel-air jets in compression-ignition engines, the actual processes to be modeled become much more complex. Many approaches to predicting the burning or chemical energy release rate have been used successfully to meet different simulation objectives. The simplest approach has been to use a one-zone model where a single thermodynamic system represents the entire combustion chamber contents and the energy release rate is defined by empirically based functions specified as part of the simulation input. At the other extreme, quasi-geometric models of turbulent premixed flames are used with a two-zone analysis of the combustion chamber contents—an unburned and a burned gas region—in more sophisticated simulations of spark-ignition engines. In compression-ignition engines, multiple-zone models of the developing fuel-air jets have been used to provide more detailed predictions of the combustion process and nonuniform cylinder composition and state. These combustion models will be reviewed in the following sections (14.4.2 and 14.4.3) and the appropriate conservation equations for the *combustion process* will be developed there. In diesels, radiation heat transfer becomes important during the combustion process (see Sec. 12.5).

The *expansion process* is either treated as a continuation of the combustion process or, once combustion is over, can use the form of the mass, fuel, and energy conservation equations which hold during compression [Eqs. (14.27) and (14.28)]. The exhaust process conservation equations for a one-zone open-system model of the cylinder contents are[2]

Exhaust:

$$\dot{m} = -\dot{m}_e \qquad \dot{f} = -\frac{\dot{m}_e}{m}(f_e - f) \tag{14.29a, b}$$

$$\dot{T} = \frac{B}{A}\left[-\frac{\dot{m}_e}{m}\left(1 - \frac{h}{B}\right) - \frac{\dot{V}}{V} - \frac{C}{B}\dot{\phi} + \frac{1}{Bm}(-\dot{m}_e h_e - \dot{Q}_w)\right] \tag{14.30}$$

where h_e, the enthalpy of the flow through the exhaust valve, is the cylinder average enthalpy for flow *out* of the cylinder and the exhaust system gas enthalpy if reverse flow occurs.

The engine operating cycle should end with the working fluid at the same state that it started out. For the first calculations of the sequence of processes in Fig. 14-6, property values defining the initial state of the fluid in the cylinder were assumed. If the values of these properties at the end of the first cycle differ from the assumed values, the cycle calculation is repeated with the appropriate new initial values until the discrepancy is sufficiently small. Convergence with these cycle simulations occurs within a few iterations.

The working fluid state is now defined throughout the operating cycle. The work transfer to the piston per cycle

$$W_c = \oint p\, dV \tag{14.31}$$

can now be obtained. From W_c, the masses of fuel and air inducted, m_f and m_a, and engine speed N, all the engine *indicated* performance parameters can be calculated: power, torque, mean effective pressure, specific fuel consumption, fuel-conversion efficiency; as well as volumetric efficiency, residual gas fraction, total heat transfer, etc. With a friction model, the indicated quantities can be converted to brake quantities.

The more sophisticated of these thermodynamic-based engine cycle simulations define the working fluid state throughout the cycle in sufficient detail for useful predictions of engine emissions to be made. The discussion in Chap. 11 of emission-formation mechanisms indicates that our understanding of how some of these pollutants form (e.g., NO_x, CO) is reasonably complete, and can be modeled accurately. The formation processes of the other pollutants (unburned hydrocarbons and particulates) are not adequately understood, though modeling activities are continuing to contribute to that understanding. The key features of models for predicting engine emissions were discussed in Chap. 11.

Cycle simulations and combustion models which have been developed for spark-ignition engines, where the fuel, air, residual gas mixture is essentially uniformly mixed, are discussed in Sec. 14.4.2. Compression-ignition engine simulations and combustion models are then discussed in Sec. 14.4.3. The special features required for prechamber engine models are reviewed in Sec. 14.4.4. Finally, thermodynamic-based models for more complex engine systems—multicylinder, turbocharged, and turbocompounded engines—are discussed in Sec. 14.4.5.

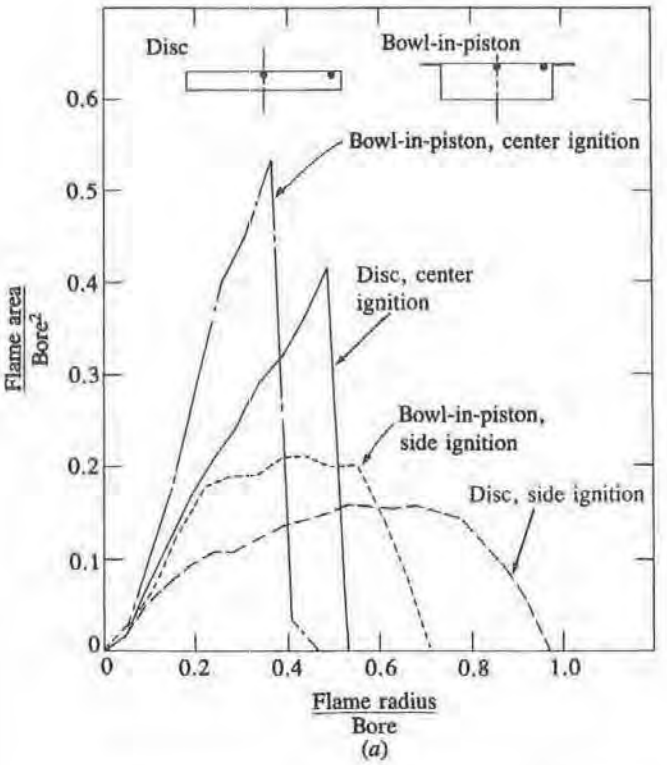
14.4.2 Spark-Ignition Engine Models

These models have usually followed the conceptual structure indicated in Fig. 14-6. Our focus here is on the combustion submodels that have been developed and used successfully. Features of the spark-ignition engine combustion process that permit major simplifying assumptions for thermodynamic modeling are: (1) the fuel, air, residual gas charge is essentially uniformly premixed; (2) the volume occupied by the reaction zone where the fuel-air oxidation process actually occurs is normally small compared with the clearance volume—the flame is a thin reaction sheet even though it becomes highly wrinkled and convoluted by the turbulent flow as it develops (see Sec. 9.3); thus (3) for thermodynamic analysis, the contents of the combustion chamber during combustion can be analyzed as two zones—an unburned and a burned zone.

Useful combustion chamber design information can be generated with simple geometric models of the flame. In the absence of strong swirl, the surface which defines the leading edge of the flame can be approximated by a portion of the surface of a sphere. Thus the mean burned gas front can also be approximated by a sphere. Then, for a given combustion chamber shape and assumed flame center location (e.g., the spark plug), the spherical burning area A_b [see Eq. (9.40)], the burned gas volume V_b [see Eq. (9.39)], and the combustion chamber surface "wetted" by the burned gases can be calculated for a given flame radius r_b and piston position (defined by crank angle) from purely geometric considerations.† The practical importance of such "model" calculations is that (1) the mass burning rate for a given burning speed S_b (which depends on local turbulence and mixture composition) is proportional to the spherical burning area A_b as given by Eq. (9.44); (2) the heat transfer occurs largely between the burned gases and the walls and is proportional to the chamber surface area wetted by the burned gases $A_{b,w}$ [see Eq. (12.21)]. Using the fact that the density ratio across the flame ρ_u/ρ_b is approximately constant and equal to 4, the unburned and burned gas volumes V_u and V_b can be related to the unburned and burned mass fractions $(1 - x_b)$ and x_b, respectively.

Examples of the results of such flame geometry calculations are shown in Figs. 14-7 and 14-8.[11] Figure 14-7*a* shows spherical flame areas A_b as a function of flame radius r_b for two different chambers and two plug locations and the TC piston position. The much larger flame area and shorter flame travel length of the central plug location are obvious. Such area data can be plotted as a function of burned gas volume V_b, as shown in Fig. 14-7*b*, so that comparisons of $A_b(r_b)$ for different chambers at the same mass fraction burned can be made. The advantage of a more compact chamber with higher central clearance height is apparent. Figure 14-8 shows that burned-gas-wetted wall area on the cylinder head, cylin-

† Note that the center of this sphere may be convected away from the spark plug location, especially if some swirl is present. However, only strong swirling and squish flows produce major distortions to the flame surface shape.



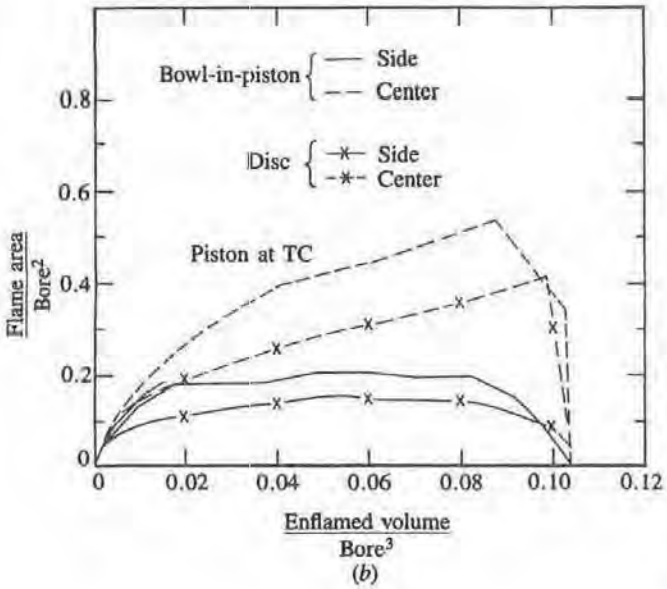


FIGURE 14-7
Calculated spark-ignition engine spherical flame surface area: (*a*) as a function of flame radius for different combustion chamber shapes and spark plug locations and (*b*) as a function of enflamed volume. Piston in top center position.[11]

der wall, and piston as a function of flame radius and crank angle for an open chamber with central ignition. The cylinder head and piston are the dominant areas early in the expansion stroke when the burned gas temperatures and heat fluxes are highest.

Mass fraction burned versus crank angle profiles determined from a first law analysis of cylinder pressure data, as shown in Figs. 9-2, 9-5, and 9-8, have an essentially universal dimensionless shape, as indicated in Fig. 9-13. Much useful

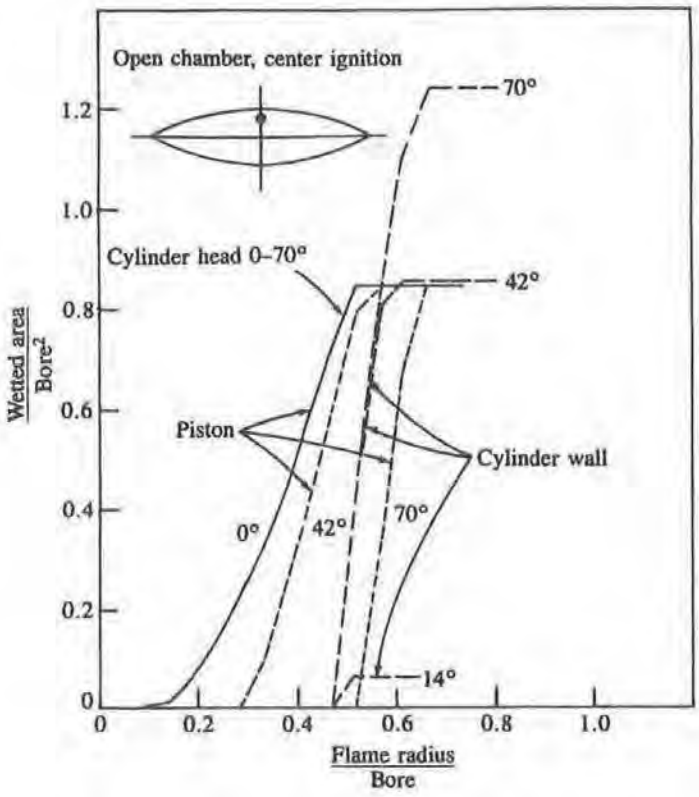


FIGURE 14-8
Calculated burned-gas-wetted wall area as a function of radius based on spherical flame model of an open-chamber SI engine with center plug location, for piston locations of 0°, 42°, and 70°.[11]

analysis has been done with engine simulations where this universal combustion profile has been used as a calculation input. The S-shaped mass fraction burned profile is often represented by the Wiebe function:

$$x_b = 1 - \exp\left[-a\left(\frac{\theta - \theta_0}{\Delta\theta}\right)^{m+1}\right] \tag{14.32}$$

where θ is the crank angle, θ_0 is the start of combustion, $\Delta\theta$ is the total combustion duration ($x_b = 0$ to $x_b \approx 1$), and a and m are adjustable parameters which fix the shape of the curve. Actual mass fraction burned curves have been fitted with $a = 5$ and $m = 2$.[12]

The conservation equations for an open system [Eqs. (14.1) and (14.10) or (14.11)] are now applied to the unburned gas zone ahead of the flame and to the burned zone behind the flame, in turn (see Fig. 9-4). For premixed engines, f and ϕ are zero. During combustion, $\dot{m}$ and $\dot{m}_j$ in Eq. (14.10) or Eq. (14.11) are the mass flow rate across the flame sheet. This is $-\dot{m}_b$ for the unburned zone system and $+\dot{m}_b$ for the burned zone system; $\dot{m}_b$ is given by $m\dot{x}_b$, with $\dot{x}_b$ obtained by differentiating Eq. (14.32).

To calculate the effect of heat transfer on the burned gas state more accurately, the burned gas zone in Fig. 9-4 can be modeled in two parts: an adiabatic core and a boundary-layer region. The intent here is to account for the fact that heat loss to the walls primarily cools the burned gas adjacent to the wall, and only indirectly affects the core gas through the change in pressure that results

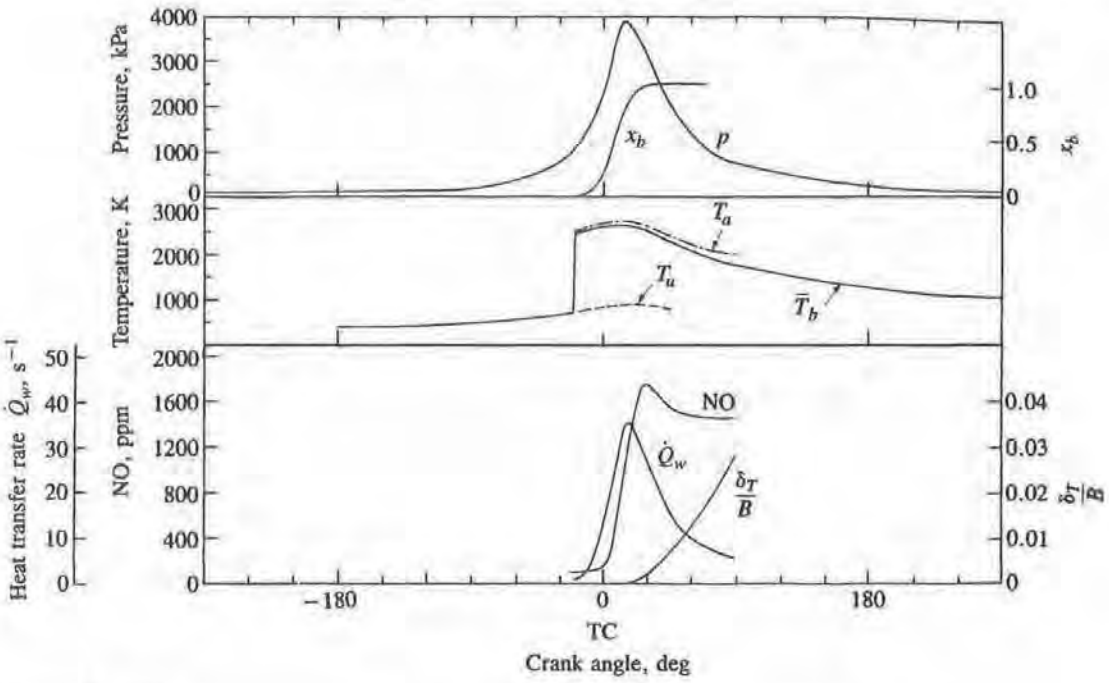


FIGURE 14-9
Cylinder pressure p, mass fraction burned x_b, unburned and burned gas temperatures (T_u = unburned, T_a = adiabatic burned core, $\bar{T}_b$ = mean burned gas temperatures), heat-transfer rate $\dot{Q}_w$ (normalized by fuel flow rate × heating value), thermal boundary-layer thickness δ_T, and mean nitric oxide concentration in the burned gases, through a four-stroke engine operating cycle, predicted by thermodynamic-based cycle simulation. 5.7-dm^3 displacement eight-cylinder engine operating at wide-open throttle, 2500 rev/min, with equivalence ratio = 1.1. Gross indicated mean effective pressure is 918 kPa and specific fuel consumption is 254 g/kW · h.[13]

from heat loss. The open-system conservation equations, (14-1) and (14.10) or (14.11), are now applied to the core and boundary-layer region separately. The boundary-layer region covers that portion of the combustion chamber wall wetted by the burned gases, as shown in Fig. 9-4, and is of thickness δ_T, which increases with time. The temperature of the boundary-layer zone (assumed uniform) is usually taken to be the mean of the wall temperature and burned gas core temperature. Equation (14.10) or Eq. (14.11) is used to relate the enthalpy flux due to the mass flow across the inner edge of the boundary layer (which has an enthalpy equal to the core gas enthalpy), the heat transfer to the wall, the changing energy within the boundary-layer system due to its increasing mass and changing state, and the work transfer due to its changing volume.

An example of predictions of cylinder pressure, unburned and burned gas temperatures, heat-transfer rate, and boundary-layer thickness, based on an assumed 50° total burn duration for a 5.7-dm^3 eight-cylinder engine at wide-open throttle and 2500 rev/min is shown in Fig. 14-9.[13] Appropriately based predictions of overall engine performance parameters made with this type of thermodynamic model agree well with engine data. Figure 14-10 shows predictions of indicated specific fuel consumption and exhaust gas temperature as a function of

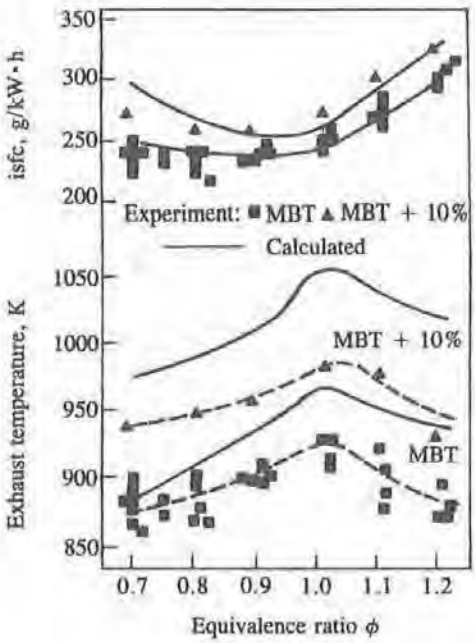


FIGURE 14-10
Predicted and measured indicated specific fuel consumption and exhaust temperature as a function of the fuel/air equivalence ratio for a spark-ignition engine operated at 1250 rev/min and imep of 379 kPa. MBT: maximum brake torque timing. MBT + 10%: combustion timing retarded to give 10 percent fuel consumption penalty.[14]

the fuel/air equivalence ratio at fixed load and speed. The isfc predictions and data agree well (except for very lean mixtures with retarded timing where cycle-by-cycle combustion variations are sufficiently large so predictions based on the average cycle lose accuracy); the predicted curves for exhaust temperature show the same trends as the experimental data. However, they are higher due to underestimation of the heat losses during the exhaust process.[14]

The output from such thermodynamic-based cycle simulations has replaced the fuel-air cycle as a predictor of effects of major variables on engine performance and efficiency. An instructive example of the value of such predictions is shown in Fig. 14-11, where fuel consumption at constant equivalence ratio, load, and speed has been computed as a function of total burn duration and heat loss to the chamber walls: increasing burn duration and heat loss both worsen fuel consumption.[15] Such data can be used to assess the efficiency improvements that should result from reduced heat transfer (e.g., reduced chamber surface area) and increased burn rate. Obviously the dependence of burn rate on engine design and operating parameters has not been modeled; the burn rate profile was a calculation input. Such models are most useful either (1) when the burn rate profile is *not critical* to the problem under study or (2) when predictions for a *range* of assumed burn rate profiles provide the required information.

So far we have discussed engine cycle simulations where details of the combustion process have been specified as input. The same thermodynamic-based simulation structure can be used in conjunction with a combustion model which *predicts* the rate of fuel burning. Various combustion models have been proposed and used for this purpose. Some of these are empirically based; some are based on the highly wrinkled, thin reaction-sheet flame model described in Sec. 9.3. All

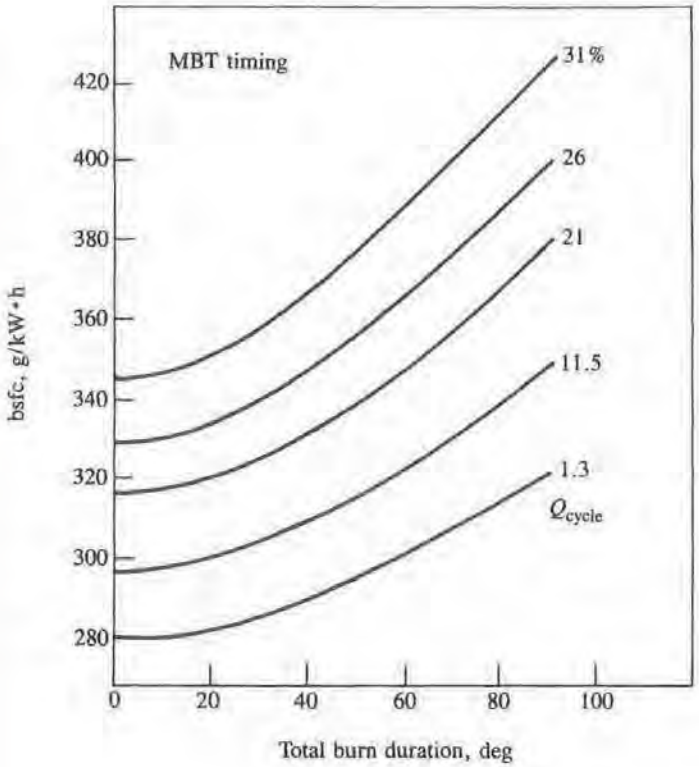


FIGURE 14-11
Predicted brake specific fuel consumption as a function of heat transfer per cycle to the combustion chamber walls (as a percent of the fuel's heating value) and total burn duration [$\Delta\theta$ in Eq. (14.32)]. 1250 rev/min, 262 kPa bmep, fuel/air equivalence ratio = 0.91, maximum brake torque spark timing.[15]

these models assume that the overall flame shape approximates a portion of a sphere centered at or near the spark plug. Empirical flame models have difficulty appropriately describing the three phases of the combustion process—flame development, rapid burning, and termination—with sufficient generality to be widely useful. One such model, based on the experimental data shown in Fig. 9-30, has been used successfully to evaluate different combustion chambers.[16, 17] The burning speed S_b [defined by Eq. (9.44)] is related empirically to the laminar flame speed S_L (see Sec. 9.3.3), the local rms velocity fluctuation u'_F [see Eq. (8.22)] under motored engine conditions, the firing and motored cylinder pressure at the same crank angle, and spark advance. While a good fit to the data in Fig. 9-30 for engine flames during their turbulent rapid-burning phase was obtained, during the flame development period a correction factor was required to fit the data.

Spark-ignition engine combustion models with a more fundamental framework have been developed and used. Based on coupled analysis of flame front location and cylinder pressure data, Keck and coworkers[18–20] have derived the following burning law:

$$\frac{dm_b}{dt} = \rho_u A_f S_L + \frac{\mu}{\tau_b} \tag{14.33}$$

$$\frac{d\mu}{dt} = \rho_u A_f u_T (1 - e^{-t/\tau_b}) - \frac{\mu}{\tau_b} \tag{14.34}$$

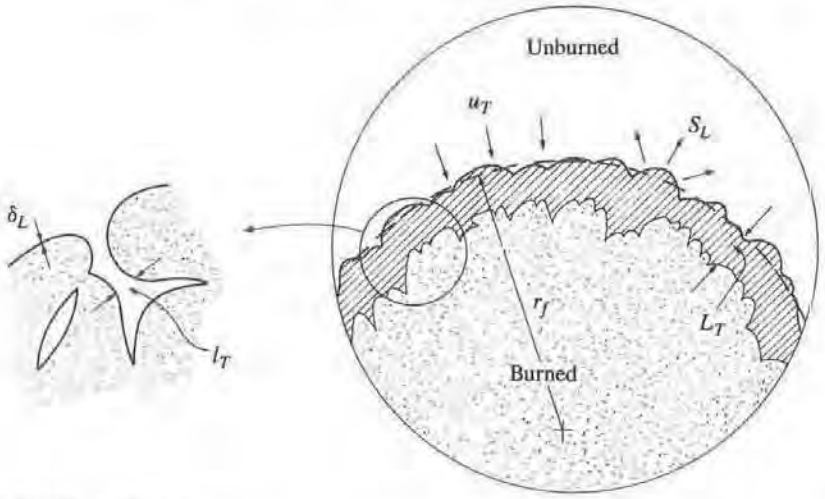


FIGURE 14-12
Schematic of turbulent premixed spark-ignition engine flame, illustrating the physical basis for burning law of Eqs. (14.33) to (14.35). The approximately spherical front of the "thick" turbulent flame (dashed line) diffuses outward at the laminar flame speed S_L. Fresh mixture also crosses this front at a characteristic velocity u_T due to turbulent convection. Schematic on left shows detailed flame structure: δ_L is a reaction-sheet thickness, l_T is characteristic scale of wrinkles in the sheet.

where

$$\mu = m_e - m_b = \rho_u(V_f - V_b) = \rho_u l_T(A_L - A_f) \tag{14.35}$$

is a parametric mass (interpreted as the mass entrained within the flame region that has yet to burn), u_T a characteristic speed, and $\tau_b = l_T/S_L$ is a characteristic burning time. l_T, A_L, V_f, A_f, V_b are defined in Sec. 9.3.4.

Figure 14-12 illustrates the physical basis for this model. The first term in Eq. (14.33) represents the laminar (diffusive) propagation forward of the approximately spherical front of the "thick" turbulent flame; the second term represents the burning of mixture already entrained within this flame front. In Eq. (14.34), which describes the rate of change of *unburned* mixture mass μ within the flame zone, the first term represents the turbulent convection of unburned mixture across the spherical front of the flame and the second term represents the mass rate of burning of entrained but not yet burned mixture which is contained within the "wrinkles" and "islands," which the distorting and stretching of the thin reaction sheet by the turbulent flow produces. This has been called an "entrainment" or "eddy-burning" model for the above reasons. The exponential term in brackets in Eq. (14.34) allows for the fact that the flame sheet initially is spherical and laminarlike: it requires a time of about τ_b to develop into a turbulent flame.

The behavior of Eqs. (14.33) and (14.34) in four important limits is:

1. For a quiescent mixture, $u_T \to 0$ or $l_T \to \infty$,

$$S_b \to S_L \tag{14.36a}$$

2. Initially, as $t \to 0$,

$$S_b \to S_L \tag{14.36b}$$

3. Quasi-steady state, $d\mu/dt \approx 0$,

$$S_b \approx u_T + S_L \tag{14.36c}$$

4. Final burning stage after the flame front reaches the wall, $t \geq t_w$ (when $A_f \to 0$),

$$\frac{\dot{m}_b}{\dot{m}_b(t_w)} = e^{-(t-t_w)/\tau_b} \tag{14.36d}$$

To apply Eqs. (14.33) and (14.34), the quantities u_T and τ_b (or $l_T = \tau_b S_L$) must be evaluated. Two approaches have been taken: (1) use of empirical correlations for these variables, derived from engine flame data (such as that described in Sec. 9.3.4); (2) use of more fundamental models to predict these quantities.

Keck has derived the following correlations for u_T and l_T, based on the application of Eqs. (14.33) and (14.34) to several sets of engine combustion data:

$$u_T = 0.08\bar{u}_i\left(\frac{\rho_u}{\rho_i}\right)^{1/2} \tag{14.37}$$

$$l_T = 0.8L_{iv}\left(\frac{\rho_i}{\rho_u}\right)^{3/4} \tag{14.38}$$

u_T was found to be proportional to $\sqrt{\rho_u}$ (at time of spark) and to correlate well with mean inlet gas speed $\bar{u}_i = \eta_v(A_p/A_{iv})\bar{S}_p$, where η_v is volumetric efficiency, A_p is piston area, A_{iv} is the maximum open area of the inlet valve, $\bar{S}_p$ is mean piston speed. l_T appears to scale with valve lift, L_{iv}; it decreases with increasing density at a rate proportional to $\rho_u^{-3/4}$. While u_T and l_T are not constant during the combustion process, their variation is modest.[18]

A quantitative comparison of predicted and measured flame radius as a function of time is shown in Fig. 14-13 for hydrogen and propane fuel-air mixtures which exhibit widely different behavior:[18] the figure indicates both the behavior and validity of the model. Predicted burned gas expansion speeds u_b [see Eq. (9.43)] are shown in Fig. 14-13*a* as a function of burned gas radius; the parameters u_T and l_T were chosen to fit the propane data. Figure 14-13*b* shows that the measured flame front radii, r_f, are in good agreement with the predicted flame and burned gas radii, r_f and r_b, for these two fuels. The initial expansion speed of hydrogen is about 10 times that of propane. Since $r_f \approx r_b$ for early times, $S_b \approx S_L$ and this ratio is expected. As r_b become large, $(r_f - r_b) \to u_T\tau_b$, which is several times smaller for hydrogen mixtures than for propane mixtures.

An adaption of this approach developed by Tabaczynski and coworkers[21, 22] is based on the following model of turbulent flame propagation. The vorticity in the turbulent flow field is concentrated in vortex sheets which are

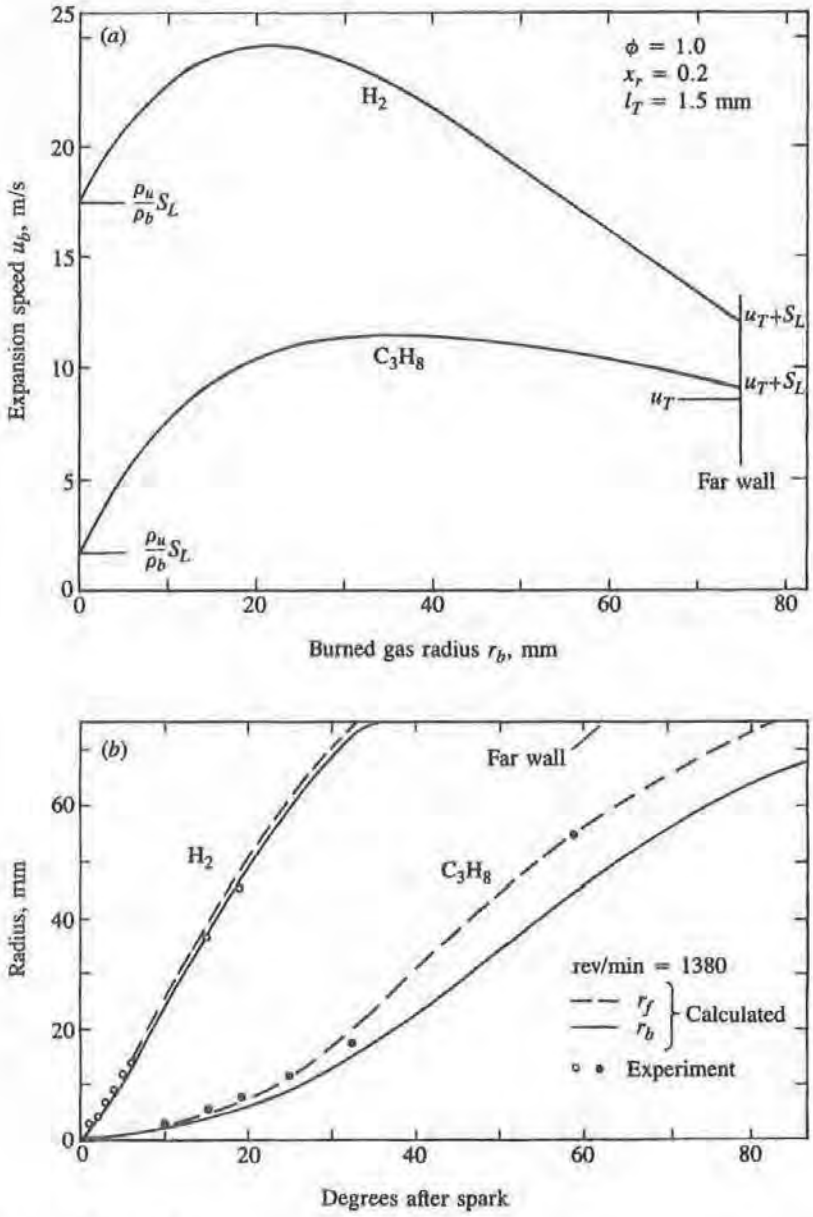


FIGURE 14-13
(*a*) Calculated burned gas expansion speed u_b for stoichiometric hydrogen-air and propane-air mixtures as a function of burned gas radius r_b. (*b*) Comparison of experimentally measured (points) and calculated (dashed curve) flame radii r_f for these mixtures as a function of crank angle. Also shown (solid curve) is the burned gas radius r_b.[18]

of a size comparable to the Kolmogorov scale l_K [see Eq. (8-11)]. These vortex sheets are assumed to have a characteristic spacing which is of the order of the Taylor microscale l_M, which is a function of the integral length scale l_I and the turbulent Reynolds number as indicated by Eq. (8.15). From these turbulence assumptions it is argued that ignition sites propagate along the vortex sheets with a velocity $u' + S_L$, where u' is the local turbulence intensity. The propagation of the reaction front between the vortex sheets is assumed to be a laminar process.

Thus, in Eqs. (14.33) and (14.34), u_T and τ_b are given by

$$u_T \approx u' \qquad \text{and} \qquad \tau_b = \frac{l_T}{S_L} \approx \frac{l_M}{S_L} \tag{14.39}$$

where l_M, the microscale, is determined from the integral scale and the turbulent Reynolds number via Eq. (8.15), assuming that the turbulence is homogeneous and isentropic. The task therefore becomes one of evaluating u' and l_I.

One approach used is to relate the turbulence intensity at the start of the combustion process to the mean intake flow velocity through the valve: e.g.,[23]

$$u'_0 = \frac{C\bar{S}_p B^2}{L_{\text{iv}} D_{\text{iv}}} \tag{14.40}$$

where $\bar{S}_p$ is the mean piston speed, B the bore, and L_{iv} and D_{iv} the lift and diameter of the inlet valve. It is assumed that the integral length scale at the start of combustion, $l_{I,0}$, is proportional to a characteristic flow dimension, usually the clearance height h. Then, during combustion, the unburned portion of the charge is assumed to undergo isentropic compression sufficiently rapidly that the angular momentum of the "eddies" is conserved and the length scale follows the eddy size, i.e., a simple rapid distortion process occurs:

$$u' = u'_0\left(\frac{\rho}{\rho_0}\right)^{1/3} \qquad l_I = l_{I,0}\left(\frac{\rho_0}{\rho}\right)^{1/3} \tag{14.41}$$

This model predicts an increase in turbulence intensity and decrease in length scale with compression, which is only partly confirmed by experiment.

A more sophisticated approach is to describe the dynamic behavior of the turbulence with one or more rate equations for the key turbulence parameters: k the turbulent kinetic energy and ε the dissipation rate of k. Turbulence is generated, diffused, and dissipated by the flow field, so the rate of change of turbulent kinetic energy k can be written:

$$\frac{dk}{dt} = P_k + D_k - \rho\varepsilon \tag{14.42}$$

where the term P_k represents the volumetric production of turbulence and the diffusion term D_k can be modeled as a gradient diffusion with an effective turbulent viscosity which dominates the laminar diffusion process. In this application, Eq. (14.42) is integrated over the combustion chamber (or a region of the chamber) to provide spatially averaged turbulence predictions. Then the diffusion terms become boundary fluxes: e.g., the transport of kinetic energy across the combustion chamber boundary due to flow through the inlet or exhaust valve. The dissipation rate ε is related to the integral length scale via

$$\varepsilon = \frac{C_D k^{3/2}}{l_I} \qquad C_D = 0.09 \tag{14.43}$$

l_I can be taken as proportional to the clearance height ($l_I \approx 0.22\ h$), or an additional rate equation for a second turbulence parameter, the dissipation rate ε, can

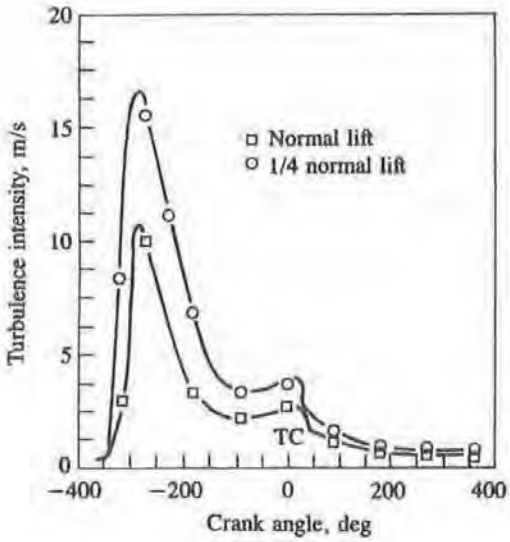


FIGURE 14-14
Predicted turbulence intensity u' as a function of crank angle and valve lift in engine operating at 1500 rev/min, 414 kPa imep, with a compression ratio of 10.[27]

be used. In the more complete of these $k - \varepsilon$ turbulence models,[24] the ε equation is similar to the k equation with production, diffusion, and dissipation terms. These $k - \varepsilon$ turbulence models are discussed more fully in Sec. 14.5.2.

The application of this turbulence model to the spark-ignition engine combustion chamber becomes complicated and the reader is referred to references for the details.[25–28] Considerable success with predicting trends in mass burning rate has been achieved with this type of model. Design variables examined include: swirl, squish, valve lift, bore/stroke ratio. The advantage of such models is that they are straightforward computationally so that extensive parametric sets of calculations are feasible. The major disadvantage is the *ad hoc* nature of the turbulence and flame models which involve plausible but arbitrary assumptions. Sample predictions are shown in Figs. 14-14 and 14-15.[27,28] Figure 14-14 shows the variation in turbulence intensity u' in an engine with a disc-shaped combustion chamber, throughout the operating cycle. A normal valve-lift profile and

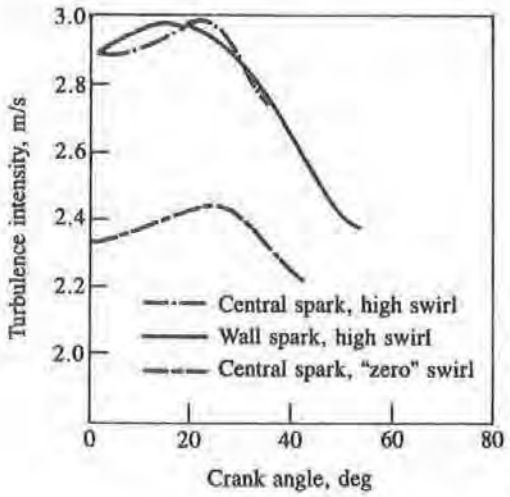


FIGURE 14-15
Predicted turbulence intensity during combustion for high and "zero" swirl levels for central and cylinder wall spark plug locations. Same engine and operating conditions as in Fig. 14-14.[28]

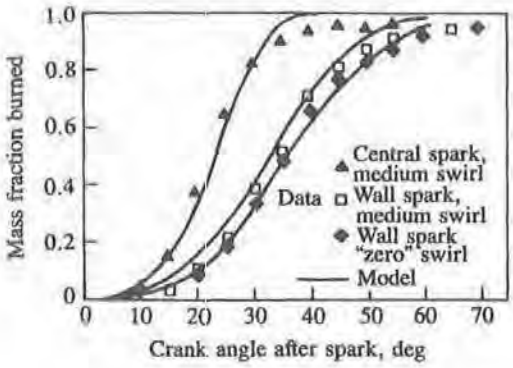


FIGURE 14-16
Comparisons of predicted and measured mass fraction burned versus crank angle profiles for same swirl levels and plug locations as Fig. 14-15.[28]

reduced maximum valve-lift profile (one-quarter normal) are shown. The high levels of turbulence generated during the first half of the intake process decay substantially before the latter stages of the compression stroke produce some amplification. Reduced valve lift produces higher levels of turbulence intensity at combustion, as is well known.[29] Figure 14-15 shows the predicted turbulence behavior during combustion for a disc-shaped chamber for different swirl levels and plug locations. Swirl is shown to increase the turbulence intensity. Comparison of predicted and measured mass fraction burned profiles versus crank angle for different swirl levels and plug locations are shown in Fig. 14-16. The large flame area effects (shown here in the two limiting plug locations: side wall and center) and significant though lesser effect of swirl are correctly modeled. Such models are useful for relating changes in spark-ignition engine design and operating variables to changes in engine performance, via predictions of changes in flame development and propagation.

The above type of combustion model has been used to obtain explicit relations for the flame development and rapid burning angles as functions of engine design and operating variables.[30] The equation for the mass burning rate, (14.33), was effectively integrated over the relevant portion of the total combustion process; the turbulent characteristic velocity was assumed proportional to $\bar{S}_p$, the mean piston speed. The flame development angle was found to vary as

$$\Delta\theta_d = C(\bar{S}_p \nu)^{1/3}\left(\frac{h}{S_L}\right)^{2/3} \tag{14.44}$$

where ν is the kinematic viscosity ($\nu = \mu/\rho$) and h is the clearance height at ignition. C is a constant which depends on engine geometry and is determined by matching Eq. (14.44) with engine data. The rapid burn angle (here taken as the crank angle between $x_b = 0.01$ and 1.0) is given by

$$\Delta\theta_b = C'\left(\frac{B}{h^*}\right)\left(\frac{\rho_i}{\rho_u^*}\right)^{10/9}(\bar{S}_p \nu^*)^{1/3}\left(\frac{h_i}{S_L^*}\right)^{2/3} \tag{14.45}$$

where C' is a constant which depends on engine geometry, B is the bore, the subscript i denotes the value at ignition, and the superscript $*$ denotes the value

at cylinder conditions where $x_b = 0.5$. These expressions show reasonable agreement with observed trends in $\Delta\theta_d$ and $\Delta\theta_b$.

14.4.3 Direct-Injection Engine Models

In direct-injection compression-ignition and stratified-charge engines, the liquid fuel is injected into the cylinder as one or several jets just prior to ignition. In large direct-injection compression-ignition engines, the air flow is essentially quiescent. However, in medium and smaller size DI engines, the air flow is usually swirling about the cylinder axis at up to 10 times the crankshaft rotational speed; this air-flow pattern increases the rate of entrainment of air into the fuel jet to increase the fuel-air mixing rate. Thus modeling of the ignition and combustion processes for direct-injection types of engines is much more complex than for premixed-charge spark-ignition engines. The unsteady liquid-fuel jet phenomena—atomization, liquid jet and droplet motion, fuel vaporization, air entrainment, fuel-air mixing, and the ignition chemistry—all play a role in the heat-release process (see Chap. 10). It is not yet possible to model all these phenomena from a fundamental basis, even with the most sophisticated fluid-dynamic-based codes now available (see Sec. 14.5), since many of these processes are not yet adequately understood. However, models at various levels of detail and empiricism have been developed and have proven useful in direct-injection diesel and stratified-charge engine analysis. This section reviews the important features of single-zone heat-release models and phenomenological jet-based combustion models. Their relative simplicity and modest computer time requirements make them especially useful for diesel cycle simulation and more complex engine system studies.

Single-zone models assume that the cylinder contents can be adequately described by property values representing the average state, and use one or more algebraic formulas to define the heat-release rate. The functional forms of these formulas are chosen to match experimentally observed heat-release profiles (see Sec. 10.4.2). Coefficients in these formulas, which may vary with engine design details and operating conditions, are determined empirically by fitting with data. The phenomenological description of diesel combustion developed by Lyn (see Sec. 10.3) comprises three primary phases: the ignition delay period, the premixed fuel-burning phase, and the mixing-controlled fuel-burning phase. Ignition delay correlations are reviewed in Sec. 10.6.6. Here models for the second and third phases, when the major heat release occurs, are summarized (see Ref. 31 for a more extensive review). The attraction of the one-zone heat-release approach is its simplicity: however, since it cannot fully describe the complex phenomena which comprise the compression-ignition engine combustion process, substantial empirical input must be used. Several one-zone heat-release models have been proposed and used (e.g., Refs. 32 to 34). These use simple equations to describe the rate of release of the fuel's energy, sometimes modeled on the presumed controlling physical or chemical process and always calibrated by comparison with data.

One extensively used model of this type developed by Watson *et al.*[35] is especially appropriate for use in total diesel system simulations where the combustion process details are not the primary focus. It is based on Lyn's description of compression-ignition combustion—a rapid premixed burning phase followed by a slower mixing controlled burning phase. The fraction of the injected fuel that burns in each of these phases is empirically linked to the duration of the ignition delay. One algebraic function is used to describe the premixed heat-release phase and a second function to describe the mixing-controlled heat-release phase. These two functions are weighted with a phase proportionality factor, β, which is largely a function of the ignition delay. Thus:

$$\frac{m_{f,b}(t')}{m_{f,0}} = \beta f_1 + (1 - \beta) f_2 \tag{14.46}$$

where $m_{f,b}$ is the mass of fuel burned, $m_{f,0}$ is the total fuel mass injected per cycle per cylinder, and t' is time from ignition non-dimensionalized by total time allowed for combustion $[=(t - t_{ign})/\Delta t_{comb}]$.† The premixed-burning function is

$$f_1 = 1 - (1 - t'^{K_1})^{K_2} \tag{14.47}$$

and the mixing-controlled function is

$$f_2 = 1 - \exp(-K_3 t'^{K_4}) \tag{14.48}$$

where K_1, K_2, K_3, and K_4 are empirical coefficients. The proportionality factor β is given by

$$\beta = 1 - \frac{a\phi^b}{\tau_{id}^c} \tag{14.49}$$

where ϕ is the overall fuel/air equivalence ratio and a, b, and c are empirical constants.

Correlation with data from a typical turbocharged truck engine gave the following values for K_1 to K_4:

$$\begin{aligned} K_1 &= 2 + 1.25 \times 10^{-8}(\tau_{id} N)^{2.4} \\ K_2 &= 5000 \\ K_3 &= \frac{14.2}{\phi^{0.644}} \\ K_4 &= 0.79 K_3^{0.25} \end{aligned} \tag{14.50}$$

where τ_{id}, the ignition delay, is in milliseconds and N, engine speed, is in revolutions per minute. It also gave these ranges for a, b, c:[35]

$$0.8 < a < 0.95; \qquad 0.25 < b < 0.45; \qquad 0.25 < c < 0.5$$

† The combustion duration at Δt_{comb} is an arbitrary period within which combustion must be completed. A value of 125° was used above.

Such single-zone heat-release models are useful because of their simplicity. They obviously cannot relate engine design and operating variables explicitly to the details of the combustion process. Experience indicates that those models with only one function are not usually able to fit experimentally determined heat-release profiles with sufficient accuracy. All single-zone heat-release models should be checked against experimentally derived heat-release profiles, and recalibrated if necessary, before being used for predictions.

Many thermodynamic-based direct-injection engine simulations incorporate an explicit model for each fuel spray which attempts to describe how the spray develops with time. The spray starts out as a liquid fuel jet which then vaporizes, entrains air and (later) burned gases. Mixture preparation can be limited by the availability of either fuel vapor or air, the former limited by droplet evaporation and the latter by air entrainment. While there is evidence in the literature to support both of these phenomena as rate-limiting, more recent studies[36] show that most (70 to 95 percent) of the injected fuel is in the vapor phase at the start of combustion, whereas only 10 to 35 percent of the vaporized fuel is mixed to within the combustion limits (equivalence ratio between 0.3 and 3). This suggests that the combustion process in typical heavy-duty direct-injection compression-ignition engines is mixing controlled rather than vaporization controlled.

While spray geometry is an essential aspect of the fuel-air mixing process, it may not be necessary to model the precise details of the actual configuration. For the purpose of heat-release and emission analysis, it suffices in many phenomenological models to calculate the evolution of the fuel mass, composition, volume, and temperature of critical regions of the spray based on a generic spray geometry. Alternate approaches attempt to provide a detailed structure for the fuel spray to improve the modeling of air entrainment, effects of swirl/spray interaction, and heat transfer. The more commonly used approaches are illustrated in Fig. 14-17.

The schematic in Fig. 14-17*a* illustrates the simplest approach: it is assumed that the growth and motion of the spray or jet within the chamber can be analyzed as a quasi-steady one-dimensional turbulent gaseous jet.[38–40] The intent here is to describe the position of the jet within the combustion chamber and the overall jet size as a function of time. Entrainment of air into the jet is assumed to take place at each point along the jet surface at a rate proportional to the velocity difference between the jet and surrounding air at that point. Two empirical entrainment coefficients[41] are used for the proportionality constants for the relative motion in the jet axial and transverse directions. Conservation equations for fuel mass and total mass, and momentum (in two or three orthogonal directions) are used to determine the jet trajectory and size. The jet slows down due to air entrainment. Deflection of the jet results from the entrainment of air with a momentum component normal to the jet axis, and from drag forces due to the normal component of air flow past the jet. This approach does not define the velocity and concentration profiles across the jet: it only calculates the mean values at any jet axial position. Experimentally determined radial profiles for

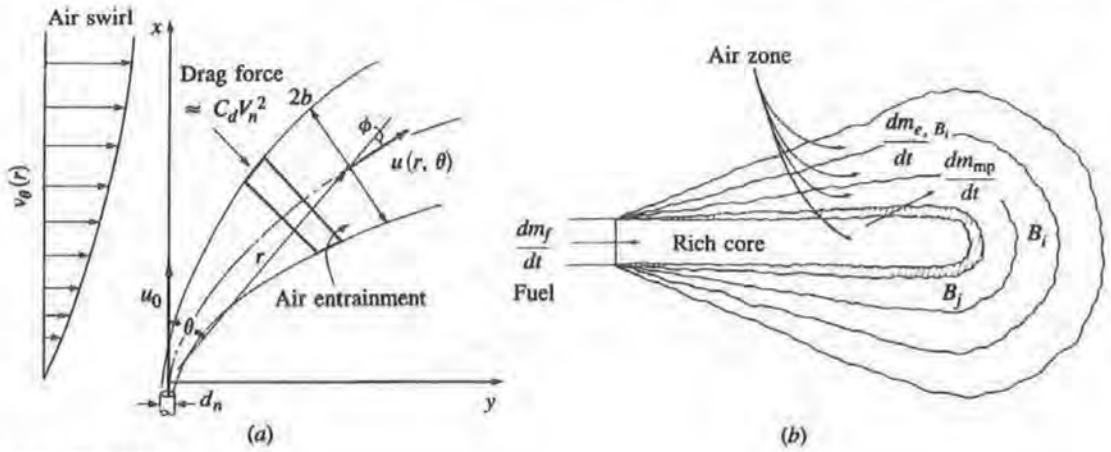


FIGURE 14-17
(*a*) Schematic of one-dimensional quasi-steady fuel spray model used to define spray centerline trajectory and width as radially outward-moving spray interacts with swirling air flow. (*b*) Schematic of multizone model for fuel spray which, based on empirically calculated spray motion and assumed concentration distributions in the spray, successfully evolves discrete combustion zones (each containing a fixed fraction of the fuel) as fuel is injected, vaporized, and mixed with air. (dm_f/dt) = rate of fuel injection into rich core; (dm_{mp}/dt) = rate of preparation of mixture for burning; $(dm_{e,B_i}/dt)$ = rate of entrainment of air into zone B_i.[37]

axisymmetric turbulent jets[42] are often assumed to apply. Although the fuel spray is initially pure liquid, the liquid fuel drops soon become a small fraction of the jet volume due to vaporization and air entrainment. Downstream of the initial liquid breakup region, the velocity of the small drops relative to the vaporized fuel and air is small, so the spray acts as a gas jet. Adding a combustion model to this quasi-steady gaseous jet model for fuel-air mixing is an additional major step.

A comparison between this type of gas jet model and an experimental engine spray is shown in Fig. 14-18. A single fuel jet was injected into a disc-shaped chamber in the location shown, and schlieren photography used to observe the spray trajectory. Good agreement was obtained for the spray centerline: note the significant effect of swirl. Reasonable agreement was also obtained between predicted and measured spray boundaries.

Figure 14-17*b* shows a multizone model for each fuel spray which has been used extensively for engine performance and emissions studies in quiescent DI diesels.[37,43] The spray is modeled as a gas jet, with penetration, trajectory and spreading rate determined from empirical equations based on axisymmetric turbulent jet data. These equations describe the approximate spray geometry. The fuel-air distribution within the spray is determined by using a normal distribution across the spray cross section and a hyperbolic profile along the axis of the spray. Progressively evolving, discrete combustion zones, each containing a fixed fraction of the total fuel mass, are then superimposed on the geometrically defined fuel-air distribution. Outer zones are diluted with air and inner zones are added as fuel vaporizes and mixes, as injection and combustion proceeds. The model implicitly assumes that combustion does not affect the mixing rates. With careful

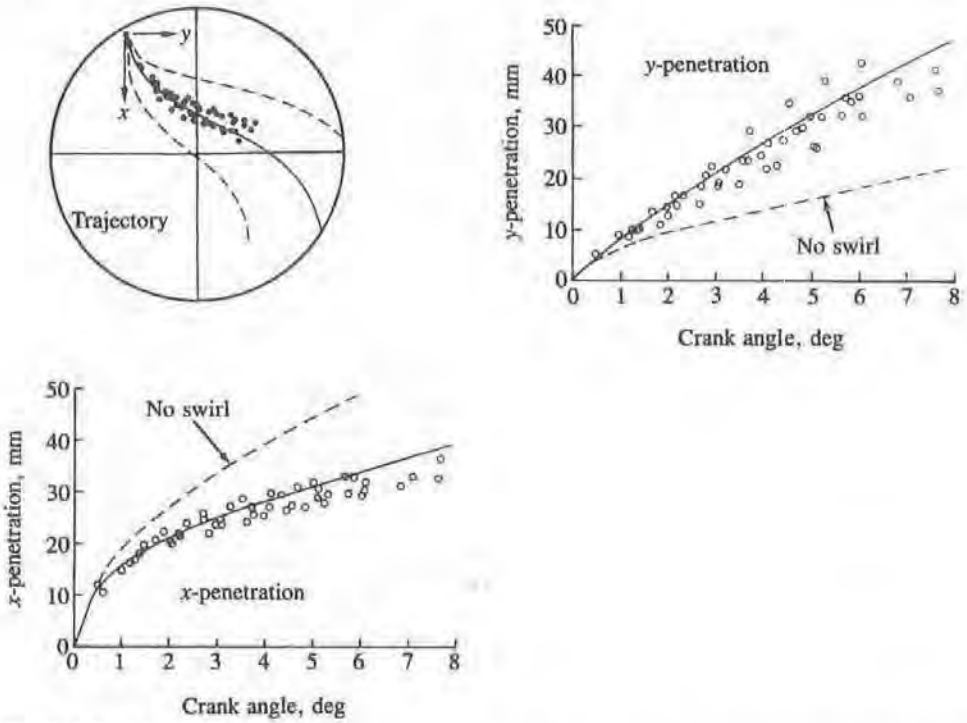


FIGURE 14-18
Spray trajectory and width calculated using one-dimensional quasi-steady spray model of type illustrated in Fig. 14-17*a*, compared with experimental data taken in special visualization direct-injection stratified-charge engine.[39]

adjustment of calibrating constants, this model describes engine performance variations with reasonable accuracy as major design and operating variables change.

More detailed geometric models of the fuel-air mixing and combustion processes in engine sprays have been developed (e.g., Ref. 44). The intent is to follow the spray development in a swirling air flow and the spray interaction with the combustion chamber wall. Figure 14-19 illustrates the approach. The liquid fuel which enters the chamber through the injector nozzle is divided into many small equal mass "elements." The spray motion is defined by an experimentally based correlation. Air entrainment is calculated from momentum conservation and the spray velocity decrease predicted by this correlation. The processes which occur within each element are also illustrated in Fig. 14-19. The fuel drops evaporate and fuel vapor mixes with entrained air. When ignition occurs combustible mixture prepared before ignition burns rapidly: it is assumed to burn at the stoichiometric composition. The continuation of the burning process then depends on the composition of the element: it may be limited by either the rate of production of fuel vapor by evaporation or the availability of air by the rate of entrainment (paths *A* and *B* in Fig. 14-19).

The growth of the spray is determined from the air entrainment into each element and the combustion-produced expansion of each element, as indicated in Fig. 14-20. When impingement on the wall occurs, the spray is assumed to spread

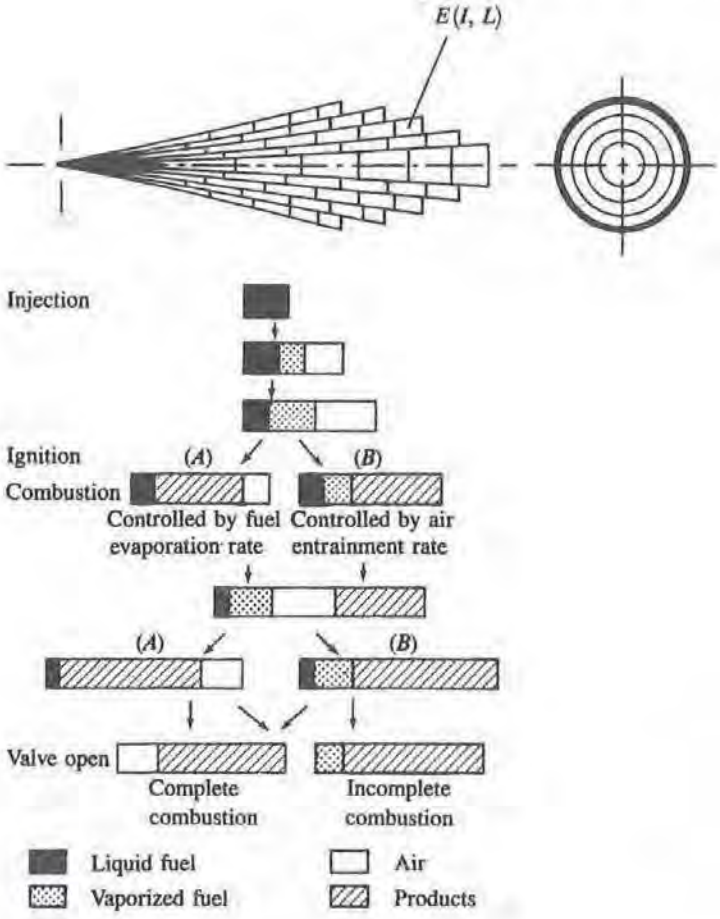


FIGURE 14-19
Schematic of spray model with many small packages, each with the same fuel mass, and of the processes that occur within each package, developed and used by Hiroyasu *et al.*[44]

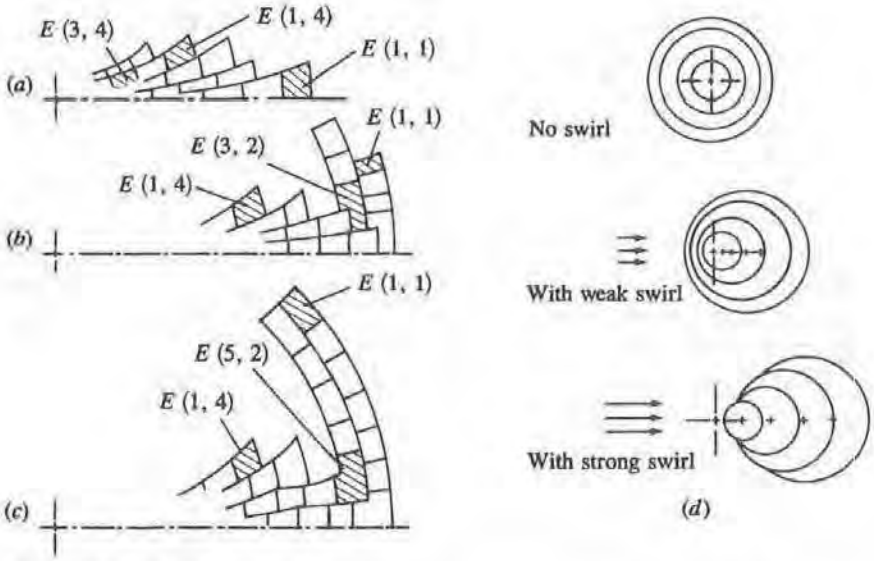


FIGURE 14-20
Method used with model of Fig. 14-19 to compute spray and flame configuration: (*a*) prior to impingement of spray on wall—shaded elements indicate combustion; (*b*) and (*c*) show spray behavior following impingement on the cylindrical bowl wall of the DI diesel combustion chamber; (*d*) shows effect of swirl on spray and flame configuration.[44]

along the wall with a constant thickness as shown in Fig. 14-20. When the periphery of the spray reaches that of a neighboring spray the sideways growth of the spray is then prevented and the thickness of the elements along the wall increases. Swirl effects are calculated from tangential momentum considerations. Each annular cone ring element is shifted sideways by the swirl as indicated in Fig. 14-20.

The heat-release rate in the combustion chamber is obtained by summing up the heat release in each element. Nitric oxide and soot formation calculations are based on the time histories of temperature, vaporized fuel, air and combustion products in each element. The overall structure of this particular complete diesel engine performance and emissions model is indicated in Fig. 14-21: it is typical of the type of compression-ignition engine simulation used to study engine performance and emissions. Figure 14-22 shows an example of the output from the above model. The injection rate diagram, the assumed Sauter mean drop size of the spray, and the air swirl determine the spray development which leads to the heat-release rate predictions. This determines the cylinder pressure profile. Predicted engine performance results show reasonable but not precise agreement with experimental data. That is not surprising given the complexity of the phenomena being modeled. A review of these types of jet models is given by Hiroyasu.[46]

14.4.4 Prechamber Engine Models

Small high-speed compression-ignition engines use an auxiliary combustion chamber, or prechamber, to achieve adequate fuel-air mixing rates. The prechamber is connected to the main combustion chamber above the piston via a nozzle, passageway, or one or more orifices (see Secs. 1.8, 8.5, and 10.2.2). Auxiliary chambers are sometimes used in spark-ignition engines, also. The plasma and flame-jet ignition systems described in Sec. 9.5.3 enclose the spark plug in a cavity or small prechamber which connects to the main chamber via one or more orifices. The function of the prechamber is to increase the initial growth rate of the flame. Combustion in the main chamber is initiated by one or more flame jets emanating from the prechamber created by the ignition process and subsequent energy release within the prechamber. If the mixture within the prechamber is richer than in the main chamber (due to fuel injection or a separate prechamber intake valve—see Sec. 1.9) these are called stratified-charge engines.

The additional phenomena which these prechambers introduce beyond those already present in conventional chamber engines are: (1) gas flows through the nozzle or orifice between the main chamber and prechamber due to piston motion; (2) gas flows between these chambers due to the combustion-generated pressure rise; (3) heat is transferred to the nozzle or passageway walls due to these flows. The first of these phenomena results in nonuniform composition and temperature distributions between the main and prechamber due to gas displacement primarily during compression, and determines the nature of the flow field within the prechamber toward the end of compression just prior to combustion.

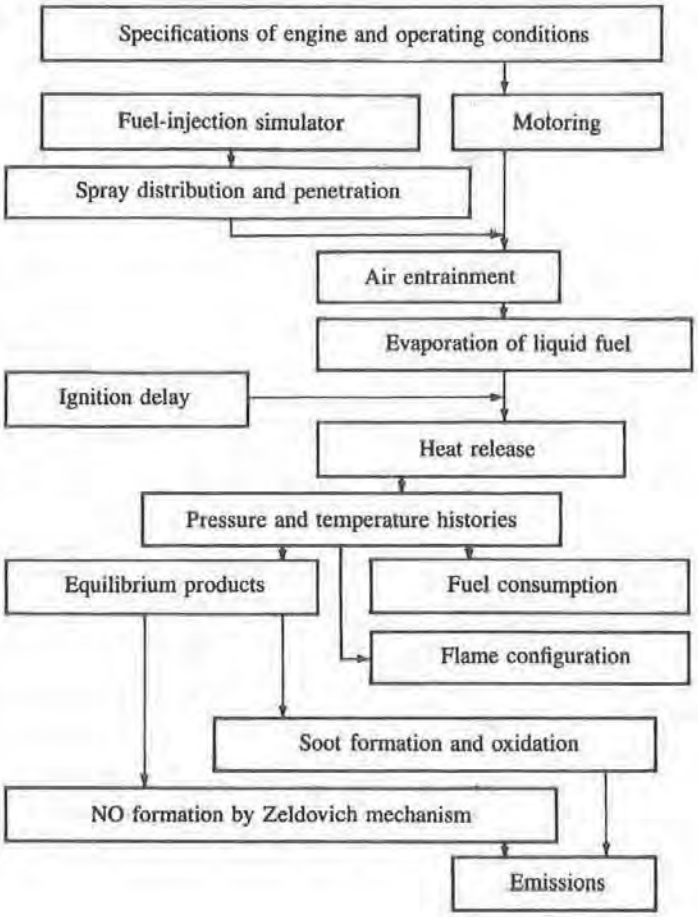


FIGURE 14-21
Structure of thermodynamic-based DI diesel simulation for predicting engine performance and emissions. Simulation incorporates spray model of type illustrated in Figs. 14-19 and 14-20.[45]

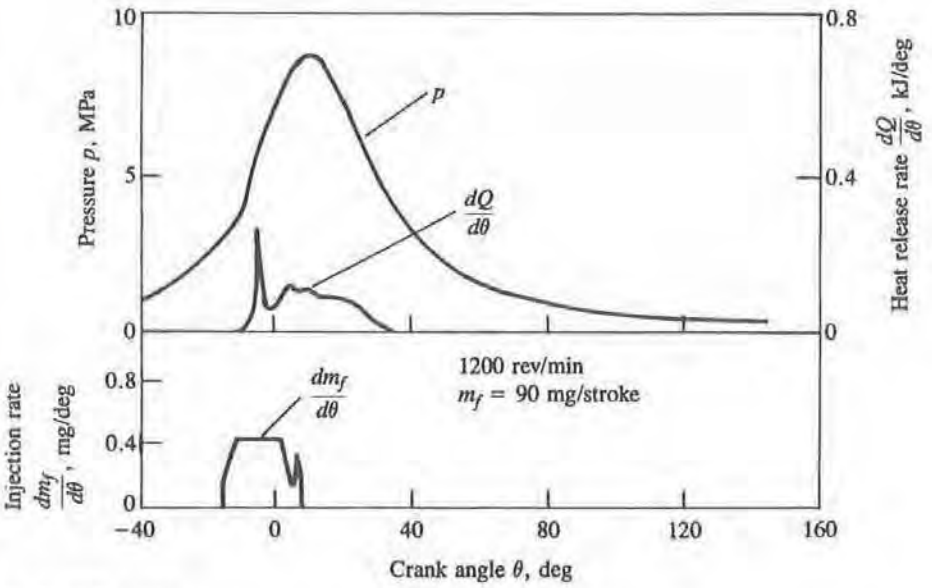


FIGURE 14-22
Fuel-injection rate, heat-release rate profile, and cylinder pressure predicted with thermodynamic-based DI diesel simulation with spray and combustion model of type shown in Fig. 14-21.[45]

The second phenomena controls the rate of energy release in the main chamber. The heat losses in the passageway and to the additional chamber surface area of the prechamber designs relative to conventional open chambers result in decreased engine performance and efficiency. Thus the prechamber concept adds additional complexity to the engine processes that must be modeled to predict engine behavior.

The following variables are important to prechamber engine performance and emissions characteristics, in addition to the design and operating variables which govern single-chamber engine behavior: prechamber geometry—size, shape, flow area and shape of connecting passageway(s); prechamber location in relation to main chamber geometry; geometry and timing of any auxiliary prechamber valve; fuel metering strategy in prechamber compression-ignition or stratified-charge engine. Thermodynamic-based models have been developed and used to examine the overall impact of these variables (see Ref. 47). Computational fluid dynamic models (see Sec. 14.5 and Fig. 8-26) have also been used to examine specific prechamber engine flow and combustion processes.

Useful predictions of fuel, air, and residual gas distributions and the corresponding temperature within the prechamber and main chamber can be obtained with simple gas displacement models. Only during combustion is the pressure difference across the nozzle or orifice sufficiently large in magnitude for its modeling to be essential; the assumption of uniform pressure during compression, the critical process for determining conditions just prior to combustion, introduces little error into calculations of the flows between the chambers. Section 8.5 develops the appropriate equations for these piston-motion driven gas displacements. Use of the conservation equations for an open system, for total mass, fuel mass, residual gas, and energy given in Sec. 14.2, for the main chamber and the prechamber, then give the mean composition and temperature variation in each chamber as a function of time due to this flow. Figure 8-25 illustrates the mean composition variation in the prechamber that results during the compression stroke of a three-valve stratified-charge engine.

During combustion, the pressure difference across the connecting passageway or orifice is the driving force for the flow between chambers. Since combustion starts in the prechamber, the initial flow is into the main chamber; later, as the heat release in the main chamber becomes dominant, the flow may reverse direction and be into the prechamber. In thermodynamic-based models, the equations for one-dimensional quasi-steady ideal gas flow through a restriction given in App. C are used to relate these flows to the pressure difference between the two chambers. Open-system conservation equations are again used to calculate mean properties in each chamber.

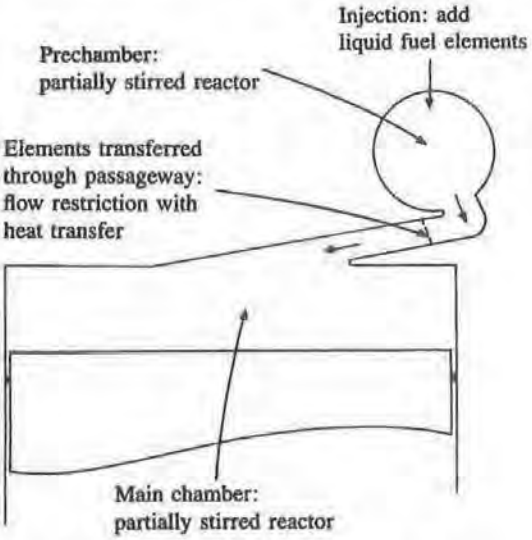
Combustion models used are either empirically based [e.g., using specified heat-release or mass burning rates such as Eq. (14.32)[48]] or are developed from direct-injection compression-ignition engine models with spray evaporation, fuel-air mixing, and ignition delay processes explicitly included.[49] Because of the complexity of these processes in the prechamber engine geometry, substantial simplifying assumptions and empiricism must be used.

Heat transfer to the passageway and chamber walls is affected by the flows between the chambers: high velocities within the passageway result in high heat-transfer rates to the passageway walls, and the vigorous flows set by the passageway exit flow entering the prechamber or the main chamber increase heat-transfer rates to the walls of these chambers. The standard engine heat-transfer correlations which relate the heat-transfer coefficient to mean flow field variables via Nusselt-Reynolds number relationships (see Sec. 12.4) are normally used to describe these heat-transfer processes. The length scales are chosen to match the prechamber or main chamber or passageway dimensions. The characteristic velocities in these relationships are equated with velocities which are representative of the flow in each of these regions at the relevant time in the engine operating cycle.[50, 51]

The utility of the more sophisticated of these prechamber engine performance and emissions models is illustrated by the sample results shown in Fig. 14-23. This simulation of the indirect-injection compression-ignition engine's flow and combustion processes describes, through the use of stochastic mixing models, the development of the fuel/air ratio distribution and fuel-energy release distribution, and hence the development of the gas pressure and gas temperature distribution, within the prechamber and main chambers of the engine. With the (nonuniform) gas composition and state defined, the models for NO formation described in Sec. 11.2.1 was used to predict NO_x emissions. The approaches used to describe the evolution of the prechamber, main chamber, and passageway contents are summarized in Fig. 14-23*a*.

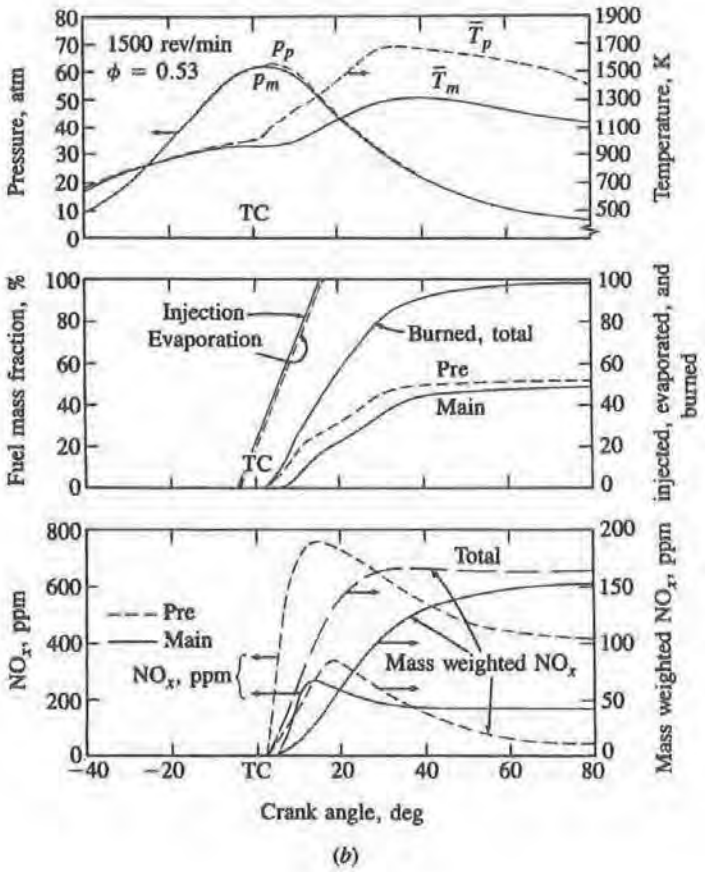
The cylinder contents were divided up into a large number of elements. Pairs of elements are selected at random to undergo "turbulent mixing" interactions at a frequency related to the turbulence in each region. Rate processes—evaporation, ignition, NO formation, etc.—proceed within each element between these mixing interactions. Figure 14-23*b* shows sample results. At about TC, after some of the injected fuel has evaporated and the ignition delay is over, combustion starts in the prechamber and the prechamber pressure p_p rises above the main chamber pressure p_m. This forces air, fuel, and burned gases to flow from the prechamber into the main chamber; fuel and rich products can now mix with air and burn in the main chamber. NO starts to form in each mass element, once it burns, at a rate dependent on each element's composition and state. Most of the NO forms within the prechamber and then flows into the main chamber as the expansion process proceeds. The attractive feature of this type of emission calculation is that the kinetically controlled NO formation calculations are based directly on local gas composition and temperature in a manner that approximately simulates the mean and turbulent nonuniformities in these variables. Predictions of engine operation and emissions showed good agreement with data.[52]

Fluid-dynamic-based models have been used to study fluid flow, combustion, and pressure wave phenomena in prechamber engines. Section 14.5 reviews this type of engine model. Additional details of these applications can be found in Refs. 53 and 54.



Partially stirred reactors contain many equal mass elements. These elements may be air (plus residual), liquid fuel, unburned mixture (fuel vapor, air, burned gas), and burned mixture

(*a*)



(*b*)

FIGURE 14-23
(*a*) Schematic of IDI diesel engine illustrating how stochastic mixing models are applied to prechamber, main chamber, and passageway to simulate turbulent mixing processes and pressure-driven flows. (*b*) Example of simulation predictions through the engine's operating cycle. Shown are prechamber and main chamber pressures, prechamber and main chamber average gas temperatures; fuel mass injected, evaporated, and burned in prechamber and main chamber, average NO concentration in each chamber (and total) in ppm by volume and mass weighted ppm (mass in chamber × NO concentration in chamber/total mass in cylinder).[52]

14.4.5 Multicylinder and Complex Engine System Models

The models discussed in the previous parts of Sec. 14.4 focus on the processes occurring within *each* cylinder of an internal combustion engine. Most engines are multicylinder engines and the individual cylinders interact via the intake and exhaust manifolds. Also, many engine systems are more complex: internal combustion engines can be supercharged, turbocharged, or turbocompounded, and the manifolds then connect to the atmosphere via compressors or turbines (see Fig. 6-37 and Sec. 6.8). Thermodynamic-based simulations of the relevant engine processes, constructed from the types of model components already described, prove extremely useful for examining the behavior of these more complex engine systems. By describing the mass and energy flows between individual components and cylinders of such systems throughout the engine's operating cycle, the total system preformance can be predicted. Such models have been used to examine steady-state engine operation at constant load and speed (where time-varying conditions in the manifolds due to individual cylinder filling and emptying events affect multicylinder engine behavior), and how the total system responds to changes in load and speed during engine transients.

The block diagram of a turbocharged and turbocompounded diesel engine system in Fig. 14-24 illustrates the interactions between the system components. By describing the mass and energy flows between components and the heat and work transfers within each component, total system behavior can be studied. In such engine simulations, the reciprocator cylinders, the intake manifold, and the various sections of the exhaust system are treated as connected open systems. The flows into and out of these volumes are usually analyzed using the quasi-steady emptying and filling approach described in Sec. 14.3.3, using the open-system conservation equations of Sec. 14.2. The reciprocator cycle is treated as a sequence of processes within each cylinder: intake, compression, combustion (including expansion), and exhaust. These are modeled using the approaches described previously in Secs. 14.4.1 to 14.4.4. Heat transfer has, of course, an important effect on the in-cylinder processes. It also is important in the exhaust system since the performance of the turbocharger turbine and of any compounded turbine depends on the gas state at the turbine inlet. The performance of the turbomachinery components is normally defined by maps that interrelate efficiency, pressure ratio, mass flow rate, and shaft speed for each component (see Secs. 6.8.2 to 6.8.4). Special provisions are usually required in the logic of the turbomachinery map interpolation routines to avoid problems with the compressor surge and turbine choking operating limits of these devices.

When the reciprocator is coupled with turbomachinery its manifolds no longer connect directly with the atmosphere: matching procedures are required to ensure that the pressure levels and mass flow rates of the compressor and turbines match with those of the engine. The following matching process is typical of those used for turbocharged engines (one compressor and one turbine only). At a given time, the values of the variables describing the state of the

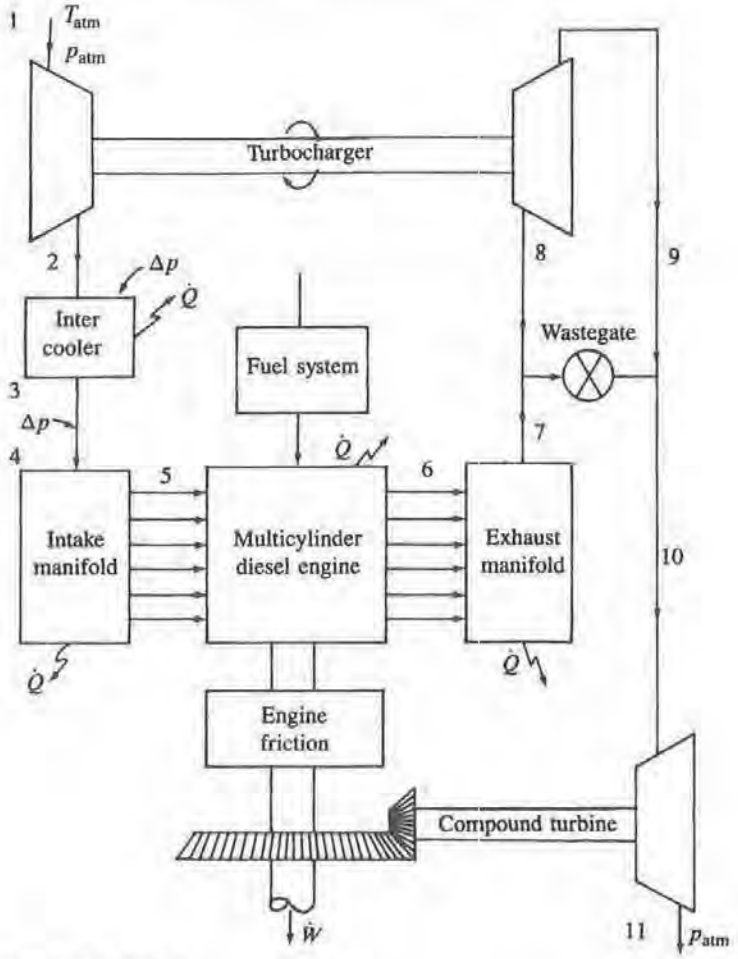


FIGURE 14-24
Block diagram of turbocharged turbocompounded diesel engine system.

various system components are known (from integration of the system governing equations over the previous time step). These include the intake and exhaust manifold pressures and the turbocharger rotor speed. The compressor inlet pressure is atmospheric pressure less the intake air-filter pressure drop. The turbine exit pressure is atmospheric plus the muffler pressure drop. By relating the compressor discharge pressure to the intake manifold pressure and the turbine inlet pressure to the exhaust manifold pressure (through suitable pressure drops) the pressure ratio across each machine is determined. Hence, the compressor and turbine maps can be entered using the calculated pressure ratios, and the rotor speed (same for both turbomachines) as inputs. The output from the map interpolation routines determines the mass flow rate and efficiency of each component for the next time step. From these the power required to drive the compressor ($-\dot{W}_C$) and to drive the turbine ($\dot{W}_T$) are determined from Eqs. (6.42) and (6.48), respectively. Any excess power (or power deficiency) will result in a change of

rotor speed according to the turbocharger dynamics equation

$$\dot{W}_C + \dot{W}_T = I_{TC}\,\omega\,\frac{d\omega}{dt} + B\omega^2 \tag{14.51}$$

where I_{TC} is the rotational inertia of the turbocharger, ω is angular velocity, and B is the rotational damping. The values of the other state variables for the next time step are determined from the solution of the mass and energy conservation equations for each open system, with the compressor and turbine mass flows taken from the output of the turbomachinery map interpolation routines.

This approach can be used to establish the steady-state engine operating characteristics from an assumed initial set of state variables. (Of course, due to the pulsating nature of the flows into and out of the cylinders, these state variables will vary in a periodic fashion throughout the engine cycle at a fixed engine load and speed.) This approach can also be used to follow transient engine behavior as load or speed is varied from such a steady-state condition.[35] The additional inputs required are the fuel pump delivery characteristics as a function of fuel pump rack position and speed, with the latter evaluated from an appropriate model for dynamic behavior of the governor.[55] From the brake torque of the engine (determined by subtracting friction torque from the indicated torque), the torque required by the load T_L, the inertia of the engine and load I_E and I_L, the dynamic response of the engine and load to changing fuel rate or engine speed can be obtained from

$$T_B - T_L = (I_E + I_L)\,\frac{d\omega}{dt} \tag{14.52}$$

An example of the output from this type of engine model is shown in Fig. 14-25. The response of a turbocharged DI diesel engine to an increase in load from 0 to 95 percent of full load is shown. The predictions come from a model of the type shown in Fig. 14-24, and engine details correspond to the experimental configuration.[55] The simulation follows the data through the engine transient with reasonable accuracy. Note that with the assumed constant governor setting, during this transient the equivalence ratio of the trapped mixture rises to close to stoichiometric because the increase in air flow lags the increase in fuel flow. This would result in excessive smoke emissions. Such models prove extremely useful for exploring the effect of changes in engine system design on transient response.[56]

For two-staged turbocharged or turbocompounded systems the engine-turbocharger matching process is more complicated. The division of the pressure ratio between the exhaust manifold and atmosphere between the two turbines in Fig. 14-24 is not known a priori. Nor, with two compressors, is the intake pressure ratio distribution known. Iterative procedures based on an assumed mass flow rate are used to determine the pressure level between the two turbines such that mass flow and pressure continuity through the exhaust system is satisfied (e.g., Ref. 2).

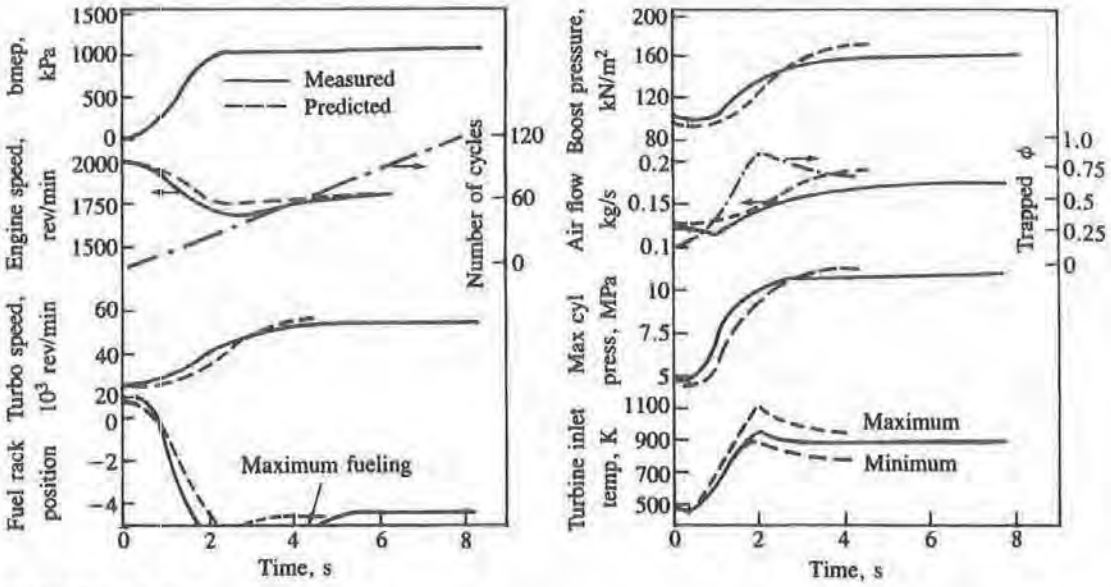


FIGURE 14-25
Predicted (---) and measured (—) response of a turbocharged direct-injection diesel engine to an increase in load.[55]

14.4.6 Second Law Analysis of Engine Processes

The first-law-based methods for evaluating power plant performances do not explicitly identify those processes within the engine system that cause unrecoverable degradation of the thermodynamic state of the working fluid. However, second-law-based analysis methods do provide the capability to identify and quantify this unrecoverable state degradation. Thus, cause and effect relationships which relate these losses to individual engine processes can be determined. The first law analysis approaches summarized in this section (14.4) are based on the fact that energy is conserved in every device and process. Thus, they take account of the conversion of energy from one form to another: e.g., chemical, thermal, mechanical. Although energy is conserved, second law analysis indicates that various forms of energy have differing levels of ability to do useful mechanical work. This ability to perform useful mechanical work is defined as *availability*.

The availability of a system at a given state is defined as the amount of useful work that could be obtained from the combination of the system and its surrounding atmosphere, as the system goes through reversible processes to equilibrate with the atmosphere. It is a property of the system and the environment with which the system interacts, and its value depends on both the state of the system and the properties of the atmosphere. Availability is not a conserved property; availability is destroyed by irreversibilities in any process the system undergoes. When availability destruction occurs, the potential for the system to do useful mechanical work is permanently decreased. Thus to make a proper evaluation of the processes occurring within an engine system both energy and availability must be considered concurrently.

The basis for an availability analysis of realistic models of internal com-

TABLE 14.2
Available energy equations for various processes

Mechanism	Equation
Work transfer	$dA_W = dW$
Heat transfer	$dA_Q = dQ(1 - T_0/T)$
Gas transfer	$dA_g = dm_g[(h - h_0) - T_0(s - s_0)]$
Liquid fuel transfer†	$dA_f = dm_f(1.0338Q_{LHV})$
Control volume storage	$dA_{CV} = d\{m_{CV}[(u - u_0) - T_0(s - s_0) + p_0(v - v_0)]\}$

† The availability of the fuel is 1.0338 times its lower heating value; see Sec. 5.7.

bustion engine processes has already been developed in Sec. 5.7. The change in availability of any system undergoing any process where work, heat, and mass transfers across the system boundary occur (see Fig. 5.13) can be written:

$$\Delta A = A_{in} - A_{out} - A_{destroyed} \tag{14.53}$$

where A_{in} and A_{out} represent the availability transfers into and out of the system across the boundary. Since availability is not a conserved quantity, this equation can only be used to solve for the availability destruction term, $A_{destroyed}$. Table 14.2 summarizes the equations for the availability change of the system and the availability transfers associated with work, heat and mass transfer across the system boundary, developed in Sec. 5.7.

This availability balance is applied to the internal combustion engine operating cycle as follows. A first-law-based cycle analysis of the type described above in this section (14.4) is used to define the variation in working fluid thermodynamic state, and the work, heat, and mass transfers that occur in each of the processes that make up the total engine cycle. Integration of the availability balance over the duration of each process then defines the magnitude of the availability destruction that occurs during that process.

To illustrate this procedure, consider the operating cycle of a 10-liter six-cylinder turbocharged and aftercooled direct-injection four-stroke cycle compression-ignition engine, operating at its rated power and speed of 224 kW and 2100 rev/min. The variations in temperature, energy, and entropy are determined with a first-law-based analysis. Figure 14-26 shows the T-s diagram for the working fluid as it goes through the sequence of processes from air inlet from the atmosphere (state 1) to exhaust gas exit to the atmosphere (state 10).[57] The incoming air is compressed (with some irreversibility) in the turbocompressor to state 2 and cooled with an aftercooler to state 3. The air at state 3 is drawn into the cylinder and mixed (irreversibly) with residual gases until, at the end of the intake, the cylinder gases are represented by state 4. That mixture is subsequently compressed (with modest heat loss) to state 5. Fuel addition commences close to state 5; subsequent burning increases the combustion chamber pressure and temperature along the line 5-6. At 6 the heat release, heat transfer, and volume change rate are such that the maximum cylinder pressure is reached (a few degrees after TC). From 6 to 7 combustion continues to completion, the burned

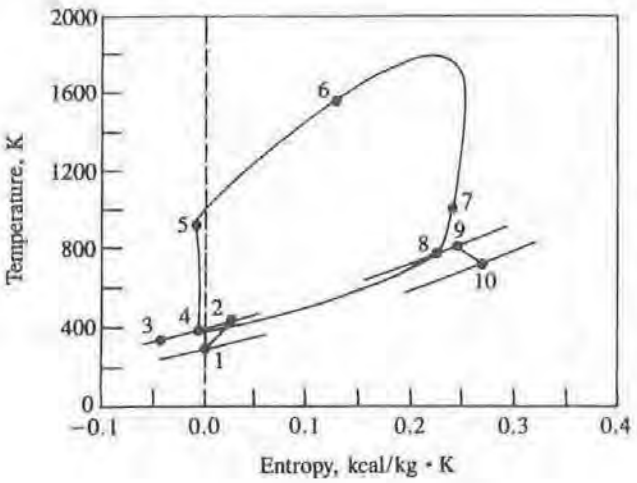


FIGURE 14-26
T-s diagram for the working fluid as it goes through the sequence of processes from air inlet to exhaust in turbocharged aftercooled DI compression-ignition engine. The 10-liter six-cylinder engine is operated at its rated power (224 kW) and speed (2100 rev/min). The text relates processes to numbered end states.[57]

gases continue to expand, doing work on the piston and losing heat to the walls. At state 7 the exhaust valve opens initiating a rapid pressure equilibration with the exhaust manifold to a pressure corresponding to point 8. Gases are expelled from the cylinder to the exhaust manifold. After the intake valve opens, cylinder residual gases are mixed with incoming air at state 3 to yield gases at state 4 to complete the in-cylinder cycle. The exhaust gases that have been expelled from the cylinder experience additional thermodynamic losses and can be represented by state 9. These gases then pass through the turbocharger turbine to state 10 to provide the work to drive the compressor.

A first law and second law analysis of a naturally aspirated diesel engine are compared in Table 14.3. Also shown is a second law analysis of a turbocharged version of the naturally aspirated diesel. These results illustrate the value of defining the losses in availability that occur in each process.

Consider the first and second law analysis results for the naturally aspirated engine. While 25.1 percent of the fuel energy leaves the combustion chamber in the form of heat transfer, the availability transfer corresponds to 21.4 percent of the fuel's availability. It is this latter number that indicates the maximum amount of the heat transfer that can be converted to work. The table shows that 34.6 percent of the fuel energy is carried out of the engine in the exhaust gases. However, the second law analysis shows that the exhaust contains only 20.4 percent of the available energy of the fuel. The ratio of these quantities shows that only about 60 percent of the exhaust energy can be converted to work using ideal thermodynamic devices.† The exhaust gas leaves the system in a high-temperature, ambient pressure state and therefore has high entropy (relative to the p_0, T_0 reference state). This, via the gas-transfer equation in Table 14.2, reduces the available energy of the exhaust gas stream.

† Of course, real thermodynamic devices will produce less work than ideal devices.

TABLE 14.3
Comparison of first and second law analysis for six-cylinder 14-liter naturally aspirated and turbocharged diesel engine at 2100 rev/min[58]

	Naturally aspirated		Turbocharged
	First law, % fuel energy	Second law, % fuel availability	
Indicated work†	40.3	39.1	43.9
Combustion loss	—	15.9	19.2
Cylinder heat transfer	25.1	21.4	17.6
Internal valve throttling	—	0.7	0.7
Exhaust valve throttling	—	2.5	2.3
Loss in compressor	—	—	1.4
Loss in turbine	—	—	0.8
Exhaust to ambient	34.6	20.4	14.1
Total	100.0	100.0	100.0
Brake power, kW	185	185	220

† Note that the indicated work for the second law balance is a lower percentage than for the first law. This occurs because the availability of the fuel is 1.0317 times the fuel's heating value.

The quantity referred to as combustion loss in Table 14.3 is determined from an availability balance for the combustion chamber over the duration of the combustion period. The "availability destroyed" term in Eq. (14.53) then represents the deviation of the actual combustion process from a completely reversible process. The second law analysis shows that the availability loss associated with the combustion irreversibilities is 15.9 percent of the fuel's availability. This loss depends on the overall equivalence ratio at which the engine is operating, as indicated in Fig. 5-17. Combustion of leaner air/fuel ratios would give a higher fractional availability loss due to mixing of the fuel combustion products with increased amounts of excess air and the lower bulk temperature.

Overall, the most important point emerging from this comparison is that the work-producing potential of the heat loss to the combustion chamber walls and the exhaust mass flow out of the engine is not as large as the magnitude of the energy transferred: some of these energy transfers, even with ideal thermodynamic work-producing devices, must ultimately be rejected to the environment as heat.

A comparison of the second and third columns in Table 14.3, both obtained with a combined first and second law analysis, illustrates how turbocharging improves the performance of a naturally aspirated engine. The brake fuel conversion efficiency of the turbocharged engine is considerably improved—from 33.9 to 39.2 percent. The table indicates that through turbocharging, the availability transfers associated with the heat loss and exhaust gas flow are reduced from 41.8

to 31.7 percent (a difference of 10.1 percentage points), while the combustion and added turbomachinery availability losses increase from 15.9 to 21.4 percent (a difference of 5.5 percentage points). By turbocharging, advantage has been taken of the following changes. While the leaner air/fuel ratio operation of the turbocharged engine increases the combustion availability losses due to the use of a greater portion of the chemical energy of the fuel to mix with and heat excess air, the lower burned gas temperature this produces results in reduced heat losses and lower cylinder exhaust temperature. In addition, the turbocharger transfers available energy from the cylinder exhaust to the inlet air. The reduced heat loss and lower final exhaust availability level give a substantial performance improvement.[58]

To interpret the second law analysis results, one must remember that the desired output is brake work and increases in this quantity (for a given fuel flow) represent improved performance. All other availability terms represent losses or undesirable transfers from the system; decreasing these terms constitutes an improvement. These undesirable available energy transfer and destruction terms fall into five categories: (1) heat transfer, (2) combustion, (3) fluid flow, (4) exhaust to ambient, (5) mechanical friction. The available energy flows identified as heat transfer represent the summation of all availability transfers that occur due to heat transfers. The most significant of these are the in-cylinder and aftercooler heat rejection. The combustion loss represents the amount of available energy destroyed due to irreversibilities occurring in releasing the chemical potential of the fuel as thermal energy and mixing the combustion products with any excess air. The fluid flow losses include the available energy destroyed within the working fluid in the compressor, aftercooler, intake valve, exhaust valve, exhaust manifold, and turbine due to fluid shear and throttling. The availability destroyed due to fluid shear and mechanical rubbing, exterior to the working fluid, are contained in the mechanical friction category. The effect of variations in engine load and speed on these five categories of losses or transfers will now be described.

Figure 14-27 shows the availability transfers or losses in each of these categories for a turbocharged six-cylinder 10-liter displacement direct-injection diesel engine, expressed as a percentage of the fuel availability, as a function of engine load. The percentage of fuel availability associated with the heat transfers varies

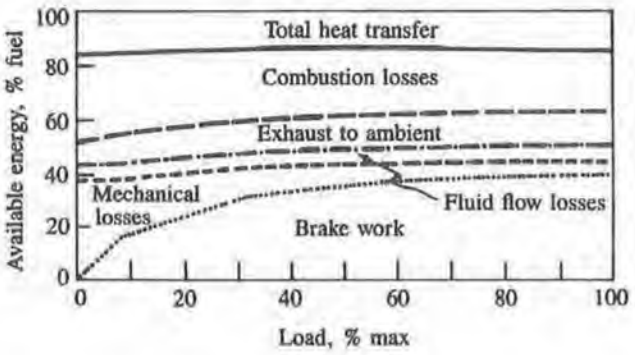


FIGURE 14-27
Distribution of available energy into major categories for the engine of Fig. 14-26 as a function of engine load.[57]

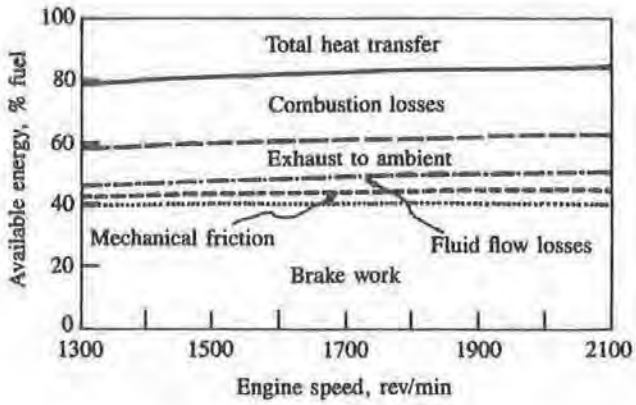


FIGURE 14-28
Distribution of available energy into major categories for the engine of Fig. 14-26 as a function of engine speed.[57]

little over the load range. The combustion loss increases from 21.8 to 32.5 percent as load is decreased due to an increasingly lean operation of the engine. Fluid friction losses, as a percentage, increase slightly as load increases due to larger mass flow rates. Since friction is approximately constant in absolute magnitude, its relative importance increases drastically as the brake output goes to zero. Exhaust flow available energy decreases from 12.2 to 8 percent as load is decreased from 100 to 0 percent.[57]

The effect of varying engine speed (at full load) is shown in Fig. 14-28. The availability associated with heat transfers changes over the speed range shown from 15.6 to 21 percent: more time during each cycle is available for heat transfer at lower speeds. Fluid flow and friction losses decrease with decreasing speed. Other availability losses remain essentially constant as a percentage of the fuel's availability.[57]

14.5 FLUID-MECHANIC-BASED MULTIDIMENSIONAL MODELS

14.5.1 Basic Approach and Governing Equations

The prediction of the details of the flow field within engines, and the heat-transfer and combustion processes that depend on those flow fields, by numerical solution of the governing conservation equations has become a realizable goal. Such methods have been under development for more than a decade, during which time they have steadily improved their ability to analyze the flow field in realistic engine geometries. While the overall dynamic characteristics of intake and exhaust flows can usefully be studied with one-dimensional unsteady fluid dynamic computer calculations (see Sec. 14.3.4), flows within the cylinder and in intake and exhaust ports are usually inherently unsteady and three dimensional. Recent increases in computing power, coupled with encouraging results with two-dimensional calculations, indicate that useful three-dimensional calculations are now feasible. However, they still do not have the capability to predict accurately